ORIGIN AND EVOLUTION OF THE MESOARCHEAN AOUÉOUAT GREENSTONE BELT AND ASSOCIATED GOLD MINERALISATION

PhD Thesis

2016

Kyle Heron



Trinity College Dublin
Coláiste na Tríonóide, Baile Átha Cliath
The University of Dublin

DECLARATION

I declare that this thesis has not been submitted as an exercise for a degree at this or any other university and it is entirely my own work.

I agree to deposit this thesis in the University's open access institutional repository or allow the library to do so on my behalf, subject to Irish Copyright Legislation and Trinity College Library conditions of use and acknowledgement.

Kyle Heron

Abstract:

Origin and evolution of the Mesoarchean Aouéouat greenstone belt and associated gold mineralisation

Kyle Heron

This Aouéouat greenstone belt is situated in the Tasiast-Tijirit Terrane of the Reguibat Shield, part of the West African Craton. Petrographic, geochronological, geochemical and isotopic studies of the Aouéouat greenstone belt and surrounding rocks were undertaken in order to elucidate its geological evolution. The Aouéouat greenstone belt is comprised of three major stratigraphic units; the Temeimichat assemblage ultramafic to mafic volcanic rocks, the Aouéouat assemblage mafic to felsic volcanic rocks, and the Tasiast assemblage sedimentary rocks. The greenstone belt is bound on all sides by Tonalite-Trondhjemite-Granodiorite (TTG) intrusive rocks. The volcanic rocks of the Temeimichat assemblage are interpreted as mantle plume-derived juvenile rocks which formed at ~3.01 Ga, likely being extruded into a rift basin which developed on 3.32-3.17 Ga pre-existing continental crust. The Aouéouat assemblage formed between 3.00 Ga and 2.99 Ga, and contains a crustal component attained on its eruption through the pre-existing basement. Partial convective overturn of these volcanic rocks resulted in emplacement of the TTG suite between 2.97 Ga and 2.91 Ga, with the resulting tectonic displacement consequently leading to deposition of the Tasiast assemblage sedimentary rocks. The Tasiast assemblage clastic sedimentary rocks were sourced from all lithologies present in the region by ~2.95 Ga including the TTG rocks. A hydrothermal event at ~2.84 Ga utilised faults and shear zones in the Aouéouat greenstone belt as fluid pathways and traps, liberating gold from the juvenile Temeimichat assemblage, resulting in formation of the Tasiast gold deposit in the overlying Aouéouat and Tasiast assemblages.

The evolution of the Aouéouat greenstone belt and associated rocks has a significant bearing on our understanding of Archean geological processes such as crustal and mantle evolution, development of plate tectonics, and formation of orogenic gold deposits. The temporal evolution of these processes has been aided by development of a new analytical approach to minimise the effects of Pb-loss in zircons, thus reducing uncertainties on calculated U-Pb and Pb-Pb ages. Two episodes of crustal growth are recorded in the Aouéouat greenstone belt, one at ~3.27 Ga, and one at ~3.01 Ga, adding new data to current crustal evolution models. The Temeimichat assemblage is a significant example of Mesoarchean juvenile volcanism, being sourced from a depleted mantle reservoir. Isotopic and geochemical data from the Temeimichat assemblage rocks indicate that its source was more depleted than current depleted mantle evolution curves, so these data could help to constrain mantle evolution models of the Early Earth. The formation of the Aouéouat greenstone belt at ~3.0 Ga places it at at a significant time in relation to plate tectonic models, and the debate of whether subduction was active at this time. Results suggest that vertical tectonics were the driving force behind the formation of the Aouéouat greenstone belt and surrounding rocks between 3.0 Ga and 2.9 Ga, thus precluding the necessity for active subduction in this part of the West African Craton at this time. Finally, the gold mineralisation at ~2.84 Ga is one of the oldest gold occurrences yet known, and is significant in relation to our understanding of the evolution of orogenic gold deposits during the Mesoarchean.

ACKNOWLEDGEMENTS

I would like to thank:

Quentin for having faith in me both prior to my PhD, and throughout it. Your patience and accommodation for my needs and requests were greatly appreciated throughout. Sorry I was not as good a training partner as you may have hoped for.

Keith for setting up the project, arranging everything for my fieldwork at Tasiast, and always being available when needed. I hope you are pleased with the end result.

Michael for his endless help with the geochemistry; from sample preparation through to the write up of the results. I couldn't have completed it without you. Also for the numerous late night discussions over a whisky or a beer, my final few months were not the same without them.

Dave for help with the apatite analysis, and also for the numerous late night discussions over a whisky. You never failed to keep me amused with your constant delusional ramblings about some rugby team or another.

Cora for help with all lab work, and the patience you showed throughout my time in the lab. It was great to have a fellow Irn-Bru lover as well.

Frank for help with sample preparation, but mostly for the constant cheer and amusement you spread to not only me, but everyone in the department.

Balz for helping with the direction of my thesis, making resources available to me, and being there to answer any queries when required.

Kinross Gold for funding the project, and everyone who I met with at Tasiast, or was involved with my thesis at some point of its journey to completion.

Mags, Neil, Maura and Noel for always being there to answer queries, aid with sample preparation, or provide me with elusive sample bags.

John for the time we spent together on the Mayo fieldtrips, which will always remain one of the greatest memories of my time in the department, Ian for your assistance with petrography, and George for the conversations we had, and the frequent use of your Leinster season ticket.

Abi, Ben and Kieran for welcoming me to the department when I first arrived as one of Quentin's mystery students.

Gavin for your constant nonsense, Clare for the URL, the Rave Cave and Cork, Saskia for the LRL and volunteering, Meabh for our shared love of fried cheese, Nathan for time spent in the pub, Daniel and Antoinette for time in the URL, and Chris for your amusing chat.

DU Orienteers for our many trips together, with the two Jukola trips being the highlight.

My parents, Jim and Lorna, for their support in allowing me to get to where I am. Without you I could not have achieved what I have.

Ceana for her company during late nights up, and her visits to Ireland, including of course your 21st birthday.

My greatest appreciation goes to my wife Rosalind. You encouraged me to undertake this PhD initially, and supported me with patience throughout it. More so however I appreciate the years we have spent, and the experiences we have had together over the years. I am delighted to finally be able to join you, and savour many future adventures together.

TABLE OF CONTENTS

Abstract

Acknowledgements

Chapter 1: Introduction 1

1.1 Mauritania 1
1.2 Kinross Gold 1
1.3 Motivation for this study 2
1.4 Objectives 3

Chapter 2: Literature Review 5

2.1 Granite-greenstone terrane geology 5
2.1.1 Archean geology 5
2.1.2 Granite-greenstone terrane geology 7
2.1.2.1 Ultramafic to mafic volcanic rocks 8
2.1.2.2 Intermediate to felsic volcanic rocks 9
2.1.2.3 Syn-volcanic intrusive rocks 10
2.1.2.4 Sedimentary successions 10
2.1.2.5 TTG rocks 11
2.1.2.6 Relationship to basement 12
2.1.2.7 Metamorphism and metasomatism 12
2.1.2.8 Structural geology 13
2.1.3 Granite-greenstone terrane formation 14
2.1.3.1 Ultramafic to mafic volcanic rocks 14
2.1.3.2 Intermediate to felsic volcanic complex 15
2.1.3.3 Sedimentary succession 16
2.1.3.4 TTG rocks 17
2.1.4 Summary of granite-greenstone terrane geology 18
2.2 Crustal and mantle evolution 19
2.2.1 Crustal evolution 19
2.2.1.2 Detrital zircon 20

2.2.1.3 Alternative isotope systems 22
2.2.1.4 Formation of the continental crust 25
2.2.1.5 Supercontinent formation 26
2.2.2 Mantle evolution 28
2.3 Plate tectonic evolution 32
2.3.1 Horizontal tectonics 33
2.3.2 Vertical tectonics 34
2.3.3 The onset of modern day plate tectonics 36
2.3.3.1 Hadean 37
2.3.3.2 Eoarchean 38
2.3.3.3 Paleoarchean 39
2.3.3.4 Mesoarchean 39
2.3.3.5 Neoarchean 40
2.3.3.6 Proterozoic 41
2.3.4 Alternative models 41
2.3.5 Horizontal versus vertical tectonics 45
2.3.5.1 Arc signature of TTG rocks 45
2.3.5.2 Greenstone volcanic rocks as ophiolites 47
2.3.5.3 Further arguments for Archean subduction 50
2.3.5.4 Further arguments against Archean subduction 53
2.3.6 Summary of plate tectonic evolution 56
2.4 Gold in greenstone belts 57
2.4.1 Orogenic gold 57
2.4.2 Timing of gold deposition 58
2.4.3 Crustal evolution, mantle evolution, and orogenic gold 59
2.4.4 Plate tectonics and orogenic gold 61
2.4.5 Source of orogenic gold 62
2.4.6 Mesoarchean gold 63
2.4.7 Summary of orogenic gold 64
2.5 West African Craton, Reguibat Shield and Aouéouat Greenstone Belt 65
2.5.1 West African Craton 65
2.5.2 Reguibat Shield 66
2.5.2.1 Tasiast-Tijirit Terrane 67
2.5.2.2 Amsaga Complex 70

2.5.2.3 Tâçarât-Inemmaûdene Shear Zone 71
2.5.2.4 Tiris Complex 71
2.5.2.5 Ghallaman Complex 72
2.5.2.6 Late dyke swarms 73
2.5.2.7 Tectonic relationships of the Reguibat Shield 73
2.5.3 Aouéouat Greenstone Belt and surrounding rocks 77
2.5.3.1 Temeimichat Assemblage 79
2.5.3.2 Aouéouat Assemblage 79
2.5.3.3 Tasiast Assemblage 80
2.5.3.4 Imkebdene-Kneffissat Greenstone Belt 80
2.5.3.5 TTG rocks 80
2.5.3.6 Basement 81
2.5.4 Gold in Aouéouat Greenstone Belt 82

Chapter 3: Methodology 85

3.1 Petrography 85
3.2 Fieldwork 85
3.3 Sample processing and mineral separation 88
3.4 Analysis and data reduction 88
3.4.1 U-Pb dating 88
3.4.2 Chemical abrasion (CA) LA-ICP-MS 92
3.4.3 Major element analysis 93
3.4.4 Trace element analysis 94
3.4.5 Sm-Nd isotope analysis 95
3.4.6 Pb-Pb isotope analysis 95

Chapter 4: Results 97

4.1 Petrography 97
4.1.1 Temeimichat assemblage 97
4.1.2 Aouéouat assemblage 101
4.1.3 Tasiast assemblage 107
4.1.4 TTG rocks 112

4.1.5 Banded iron formation 119
4.1.6 Pegmatite 121
4.1.7 Quartz-carbonate veins 124
4.2 Geochronology 128
4.2.1 Temeimichat assemblage 128
4.2.2 Aouéouat assemblage 130
4.2.3 Tasiast assemblage 135
4.2.4 TTG rocks 145
4.2.5 Banded iron formation 152
4.2.6 Pegmatite 153
4.2.7 Quartz-carbonate veins 153
4.3 Geochemistry 162
4.3.1 Element mobility 162
4.3.2 Temeimichat assemblage 164
4.3.3 Aouéouat assemblage 167
4.3.4 Aouéouat greenstone belt volcanic and plutonic rocks 169
4.3.4.1 Nd isotopes 176
4.3.5 Tasiast assemblage 177
4.3.6 TTG rocks 180
4.3.7 Banded iron formation 185
4.2.7 Pegmatite 186
4.4 Pb-Pb isotopes 187

Chapter 5: Discussion 189

5.1 The Aouéouat greenstone belt and associated rocks 189
5.1.1 Temeimichat assemblage 189
5.1.2 Aouéouat assemblage 191
5.1.3 Tasiast assemblage 195
5.1.4 TTG rocks 197
5.1.5 Banded iron formation 199
5.1.6 Pegmatite 200
5.1.7 Quartz-carbonate veins 200
5.2 Gold in the Aouéouat greenstone belt 202

5.3 Reguibat Shield and proposed model 206
5.3.1 Tasiast-Tijirit Terrane 206
5.3.2 Reguibat Shield 211
5.3.3 West African Craton 214
5.3.4 Tectonic model 215
5.4 Crustal, mantle and tectonic evolution 221
5.4.1 Crustal evolution 221
5.4.1.1 Detrital zircon 221
5.4.1.2 Alternative isotope systems 224
5.4.1.3 Crustal evolution summary 225
5.4.2 Mantle evolution 226
5.4.3 Plate tectonic evolution 227
5.4.3.1. Plate tectonic evolution summary 231
5.5 Comparison of the Aouéouat greenstone belt with greenstone belts worldwide 233
5.5.1 East Pilbara Craton 234
5.5.2 Barberton greenstone belt 235
5.5.3 Greenstone belts ~3.0 Ga in age 236
5.5.4 Kalgoorlie Terrane and Abitibi greenstone belt 237
5.5.5 Summary of greenstone belt comparisons 238
5.6 Methodology discussion 240
5.6.1 Chemical Abrasion (CA) LA-ICP-MS 240
5.6.2 Pb-Pb isotope analysis using Q-LA-ICP-MS 243
5.7 Future studies 244
5.7.1 Isotope studies 244
5.7.2 TTG rocks and orthogneissic basement 245
5.7.3 Additional geochronology 247
5.7.4 Banded iron formation 247

Chapter 6: Conclusion 249

References 252

Appendices: 274
1. Models incorporating vertical tectonics 274

2. Table of samples 277
3. Rock crushing and mineral separation instructions 278
4. EDS spectra of gold 288
5. U-Pb zircon data table 289
6. U-Pb apatite data table 312
7. Major element, trace element and Sm-Nd isotope data table 315
8. Pb-Pb data table 320
9. Heron et al. (2015) 321
10. Crowley et al. (2014) 330

Chapter 1: Introduction

This study is focussed on the Aouéouat greenstone belt and associated Tasiast gold deposit, both of which form part of the Tasiast-Tijirit Terrane, Mauritania. The Tasiast-Tijirit Terrane in turn forms part of the Reguibat Shield of the West African Craton. Neither the Tasiast gold deposit, nor the Aouéouat greenstone belt, have been studied in detail in the past. This thesis therefore represents the first comprehensive, modern geological study of the region. Original detailed petrography, geochronology and geochemistry are presented and used to elucidate the timing and formation of the Aouéouat greenstone belt, surrounding rocks, and also the Tasiast gold deposit itself. These new findings are discussed in relation to global Archean geology, in particular to that of crustal and mantle evolution, the advent of plate tectonics, and the development of a generic model for Archean orogenic gold deposits worldwide.

1.1. Mauritania:

The Islamic Republic of Mauritania (Mauritania) is situated in West Africa, bordered by Morocco to the north, Algeria to the northeast, Mali to the east and Senegal to the south. To the west there is 700 km of Atlantic coast. The capital city is Nouakchott, and the second city is Nouâdhibou, both of which lie on the coast (Figure 1.1). The country includes the western edge of the Sahara Desert, with 90% of the land surface covered by sand dunes and gravel (Taylor et al., 2012), while subtropical conditions in the Tertiary formed a continuous laterite layer that is generally ~40 m deep. This land surface, as well as the flat topography makes it a difficult environment for mineral exploration, however exposure of the West African Craton has resulted in a high potential for mineral resources being present, resulting in exploration in the country increasing in recent years.

1.2. Kinross Gold:

Kinross Gold are a Canadian gold mining company who own the exploration permit for a region of the Tasiast-Tijirit Terrane, in the Reguibat Shield of the West African Craton through the subsidiary company Kinross Tasiast. The exploration permit includes the Aouéouat greenstone belt, the Imkebdene-Kneffissat greenstone belt, and surrounding TTG plutonic rocks. Commercial gold production began in 2008, with the opening of the Tasiast Mine exploiting the West Branch and Piment deposits, and has been expanding since this time with exploration ongoing in the surrounding area. As of 2013 the Tasiast Deposit was listed as the 29th largest gold producing mine in the world with a resource of 15.5 million oz (NRH, 2013). The project area is located in

northwest Mauritania, in the southwest corner of the Reguibat Shield, ~300 km north of Nouakchott and ~250 km southeast of Nouâdhibou (Figure 1.1). Gold is hosted in a number of quartz-carbonate veins and disseminated in the country rocks surrounding the veins, which are found in a ~N-S trending corridor associated with several faults and shear zones within the Aouéouat greenstone belt.

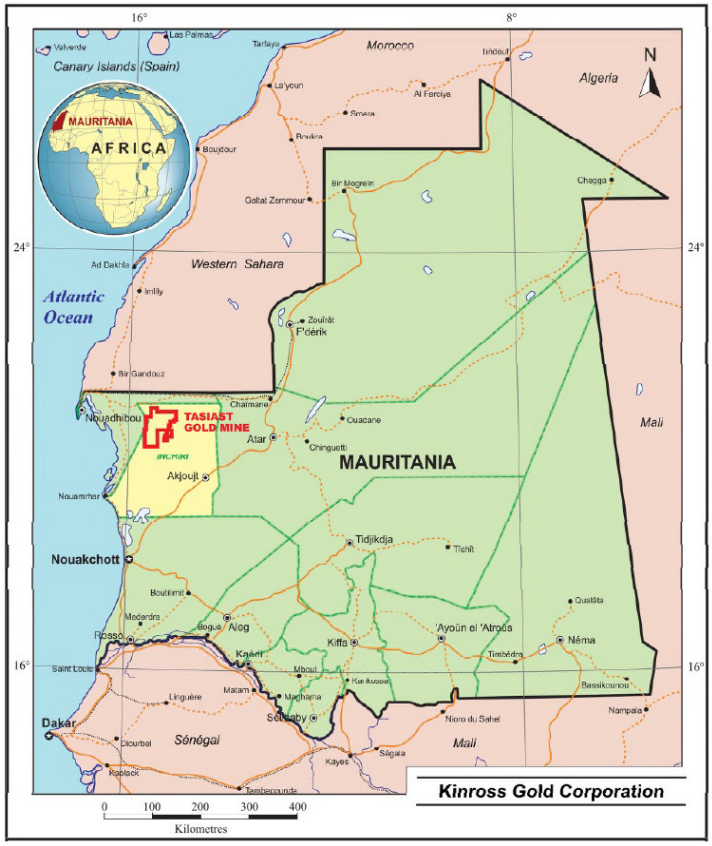


Figure 1.1: Map of Mauritania, highlighting the location and extent of the Kinross Tasiast exploration permit in red (Sims, 2014).

1.3. Motivation for this study:

There are a number of motives involved in driving this research, which combined will be of great benefit to Kinross Gold, the scientific community, and the global community.

With respect to the interests of Kinross Gold; little is known about the timing and origin of the Aouéouat greenstone belt and the surrounding rocks. It is evident that significant gold deposits are hosted within the region, as indicated by the Tasiast deposit, and typically orogenic gold deposits do not occur as single occurrences, but rather as clusters of deposits (Taylor et al., 2012). This study will aid in the understanding of the entire Aouéouat greenstone belt and surrounding region, allowing targeted exploration to locate further associated gold deposits.

With respect to the scientific community this thesis adds to a global database of Archean geology. New data are presented which constitute one of the most detailed studies carried out on rocks of the Reguibat Shield, adding considerable new knowledge to the geological evolution of both the Reguibat Shield, and West African Craton. Studies on Archean greenstone belts not only improve our understanding of specific terranes, but also contribute to an improved awareness of the geological processes active at the time of their formation. In this regard, this thesis also provides valuable data contributing to the study of crustal and mantle evolution, and the temporal development of plate tectonic processes. Greenstone belts are also renowned worldwide for the significant gold deposits they may host (e.g. the Barberton greenstone belt, Kaapvaal Craton (De Ronde et al., 1991) and the Kalgoorlie greenstone belt of the Yilgarn Craton (Barley et al., 2008)). By determining the age of gold mineralisation relative to tectonothermal events, new data can improve our understanding of the genetic links between the geological evolution of granite-greenstone terranes, and mineralising events which lead to formation of associated gold deposits.

With respect to modern society, minerals underpin every aspect of our daily life (Lusty and Gunn, 2014). Particularly due to population growth, there is a higher demand than ever for minerals which are needed to meet the requirements of new technology, and support economic growth (Lusty and Gunn, 2014). As well as a historical significance, gold has a wide variety of functions in modern society, from financial and economic security, to electronic and medical applications to name a few. By improving the prospects of gold exploration at the Tasiast Deposit, this thesis will aid in not only the development of exploration in the Reguibat Shield, but also with mineral deposit formation models for other Archean orogenic gold deposits, and therefore exploration models worldwide.

1.4. Objectives:

The two main objectives of this study are: 1) to elucidate the timing of, and mechanisms by which the Aouéouat greenstone belt was formed, and 2) to date the gold mineralisation event that formed the Tasiast Deposit.

Previous studies on the Reguibat Shield have provided only a single date, of ~2965 Ma (Key et al., 2008) for the timing of greenstone belt formation. If representative, this ~2965 Ma date would constrain formation of this region of the West African Craton in the middle of the Mesoarchean, a very interesting time in the geological calendar. Three major aspects of the early Earth's evolution are strongly debated; crustal and mantle evolution, and the timing of development of plate

tectonics. Previous studies on other granite-greenstone terranes have been used as a basis to propose numerous different models pertaining to the Earth's geological evolution during the Mesoarchean (e.g. Bleeker, 2003, Moyen et al., 2006, Van Kranendonk et al., 2007b). It is therefore envisaged that this thesis will enhance current knowledge in these themes and help to reach a consensus on crustal and mantle processes operating in the early Earth.

Dating gold mineralisation at Tasiast is a primary aim of this thesis. Providing an absolute age for gold deposits in general is challenging, mainly due to the fact that datable minerals with high closure temperatures are rare in hydrothermal systems (Kerrich and Cassidy, 1994).Groves et al. (2003) stated that the lack of precise dating of mineralisation events has limited the development of viable genetic models, and as such dating should be a priority, particularly for giant and world class deposits. The location of the Tasiast Deposit is of particular interest, as some parts of Africa, including the West African Craton, require more robust dating of gold deposits in order to improve our understanding of the distribution of mineral deposits through time (Groves, 2003). In addition to the dating of gold deposits, the source and evolution of orogenic gold is also the subject of much debate. Due to late-tectonic granitic rocks being correlated with the genesis of world class gold deposits, understanding the timing of emplacement of these rocks associated with granite-greenstone terranes is important for both economic and geological reasons (Sanislav et al., 2014). This thesis will add valuable information to the global database of gold deposits and help to improve our understanding of how mineral deposits have evolved through time. It will also aid in the understanding of gold deposits in relation to granite-greenstone terranes, a topic which is still widely debated.

Chapter 2: Literature Review

2.1. Granite-greenstone terrane geology:

2.1.1. Archean geology:

Archean rocks, where present on Earth, have been preserved to the current day as part of large, tectonically stable Precambrian cratons. Cratons are segments of continental crust that have become, and remained stable for a large part of Earth's history, with subsequent tectonic activity being confined to their margins (Pearson, 1999). Although the term craton can be used to define any section of long-term stable crust, it is most commonly applied to those of an Archean, and occasionally early Proterozoic, age (Bleeker, 2003), hence the term 'Archean craton'. The reason for this long-term stability is primarily attributed to the fact that Archean cratons have developed a relatively thick and cool lithospheric keel or root known as the sub-continental lithospheric mantle (SCLM) (e.g. Jordan, 1988, Lenardic et al., 2003) (Figure 2.1.1) preventing them from being recycled into the convecting asthenosphere. The processes involved in the formation of a lithospheric keel are still debated, with possible models including repeated collisional thickening (Jordan, 1988), or buoyant subduction (Helmstaedt, 1989), though age data suggest the keel forms synchronously with or immediately after the crust (Davis et al., 2003). The buoyancy of the SCLM keel relative to the surrounding mantle, along with its thickness, makes it difficult to destroy by either subduction or delamination, thus resulting in its longevity.

Archean cratons are present on every continent, with their being no apparent process controlling their distribution (Figure 2.1.2). Many studies have attempted to correlate Archean cratons to each other (e.g. Zegers et al., 1998, de Kock et al., 2009), however there is a great difficulty in doing so. This can be highlighted by using the example of the Lewisian Gneiss in Scotland (Moorbath et al., 1969, Rollinson and Windley, 1980, Crowley et al., 2015). Less than 100 Ma, before the formation of the North Atlantic Ocean (e.g. Driscoll et al., 1995, Pe-Piper et al., 2007), these were part of the Nain Craton of South Greenland (Park, 1995), yet the two successions are now > 2000 Km apart. In addition to this continental drift, it is known that not all Archean crust has been preserved. In the same way that modern crust has been destroyed,

Archean crust must also have been destroyed, although the processes involved may have been different. This means that what is currently preserved is only a percentage of what once existed, and a large proportion of the rock record has been lost. When the complexity of Archean cratons

are combined with the great time intervals that have passed since their creation, i.e. > 2500 Myrs, and the missing information, it can be seen how challenging it may be to link current Archean cratons to one another. This is not to say that such connections cannot be made, and there are some cases where work has been focussed on strong links between certain successions, e.g. between Kaapvaal and Pilbara (de Kock et al., 2009), however a number of methods and techniques must be used in combination to support such links.

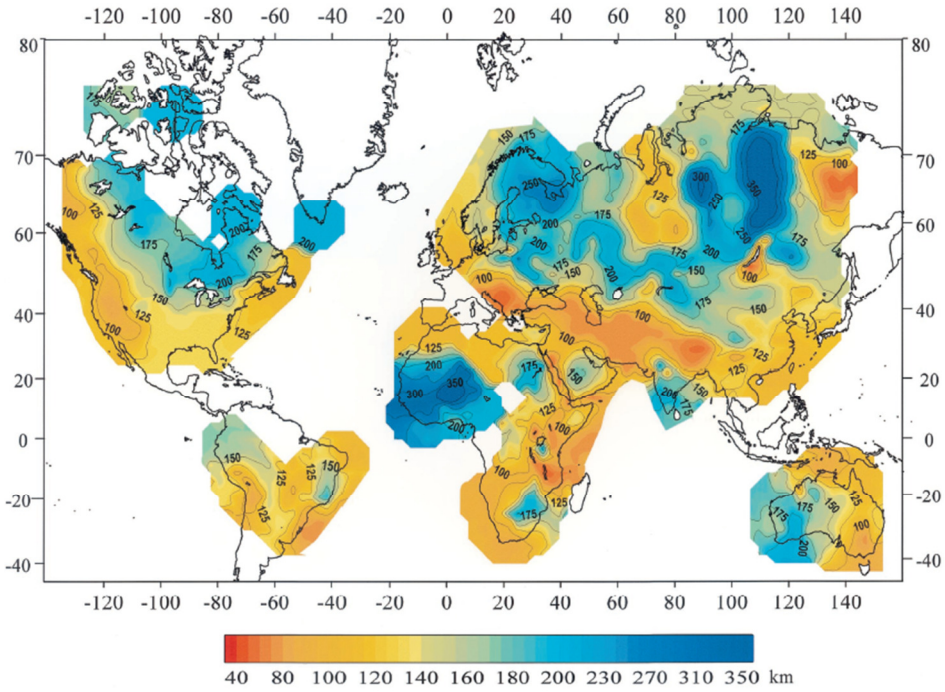


Figure 2.1.1: Map of lithospheric thermal thickness based on seismic tomography and mantle xenoliths. Note the particularly thick lithosphere beneath West Africa (Artemieva and Mooney, 2001).

There are two major lithological categories that constitute the majority of rocks in Archean cratons: 1) high grade gneisses and granulites mostly of a felsic composition, and 2) granite-greenstone terranes (e.g. Condie, 1981, Martin et al., 2005, Anhaeusser, 2014). These two sequences typify Archean cratons (Sanislav et al., 2014), and although high grade gneiss and granulite terranes are formed today in collisional orogenies (e.g. the Himalaya; (Yin and Harrison, 2000)), there does not appear to be a modern day analogue of granite-greenstone terranes (e.g. Bagas et al., 2008, Bédard et al., 2013). The fact that there are > 260 preserved Archean granite-greenstone successions worldwide (Kusky, 2004), yet there are no such sequences preserved in Phanerozoic rocks highlights this further. This has led to granite-greenstone terranes being the focus of an increasing number of scientific studies as they provide a window into Archean Earth processes that may have been different to those that are known today.

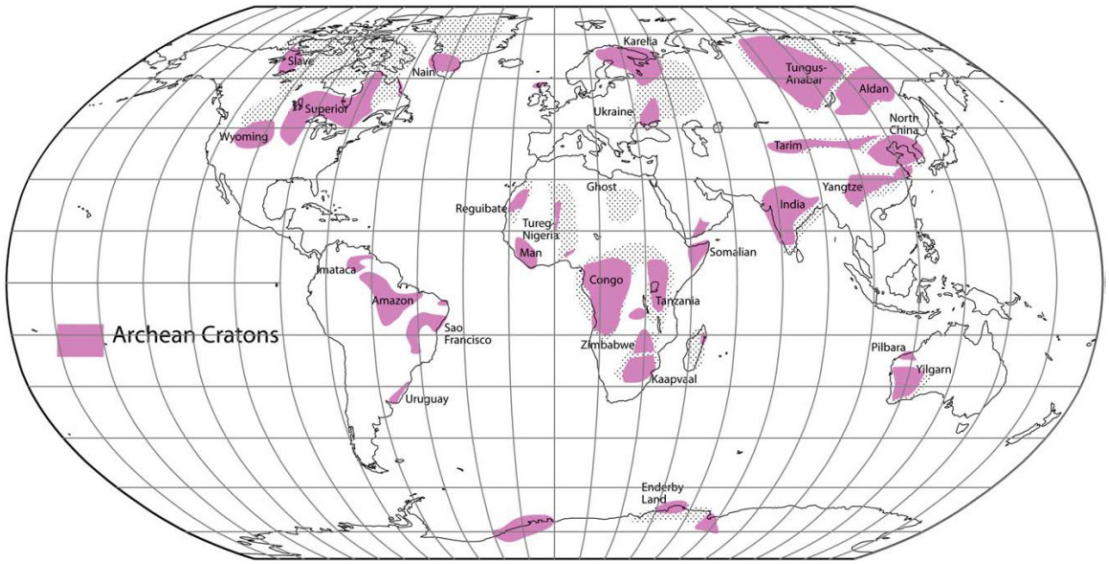


Figure 2.1.2: Global distribution of Archean cratons (Condie et al., 2009).

As well as being used to develop early Earth tectonic models, rocks preserved in Archean cratons are also used to study many other aspects of Earth's evolution. These include crustal formation (e.g. Condie et al., 2009, Hawkesworth et al., 2010), the development of early life on Earth (e.g. Schopf et al., 2007, Sugitani et al., 2007), atmospheric evolution (e.g.Holland, 1984, Mukhopadhyay et al., 2014) and oceanic evolution (e.g. Holland, 2005, Bekker et al., 2010). Archean cratons host many economic deposits, including platinum group elements (PGEs), uranium and gold, which has resulted in a large number of studies, many of which have advanced our fundamental understanding of Archean geology in general (e.g. Gapais et al., 2014, Doyle et al., 2015).

2.1.2. Granite-greenstone terrane geology:

There is evidence for greenstone successions being present in rocks through to the end of the Precambrian era, however these are not accompanied by the granitic plutons associated with the greenstones prevalent in the Archean (Furnes et al., 2015). It is difficult to strictly and simply define a greenstone belt, as highlighted by de Wit (1991) in the statement that "*they are far more complicated than even the staunchest uniformitarians would have previously predicted*". Generally, granite-greenstone terranes are composed of elongate belts of predominantly ultramafic to felsic volcanic and intrusive rocks, and associated sedimentary rocks of various facies, that have been deformed and metamorphosed to some degree, usually upper greenschist to lower amphibolite. The almost ubiquitous presence of granitic plutons in the vicinity of, or intruding greenstone belts is what gives rise to the term granite-greenstone terrane. There are many major difficulties involved when studying greenstone belts that need to be overcome in

order to form stratigraphic models; sections are often isoclinally folded, formations may be thinned, thickened or entirely removed due to deformation, marker horizons are uncommon resulting in difficulty when correlating across structural or igneous discontinuities, and outcrops are often of poor quality (i.e. deeply weathered). There are however a number of rock sequences worldwide that typify granite-greenstone terranes, as outlined below.

2.1.2.1. Ultramafic to mafic volcanic rocks:

The predominant rock type in greenstone belts, typically 70-90% of the volcanic sequence, are the ultramafic to mafic volcanic rocks, of which the mafic volcanic rocks are the most common (Bédard et al., 2013). These are in fact the rocks that give the name 'greenstone' to the lithologic succession due to the presence of green minerals, particularly post-metamorphism, e.g. chlorite, epidote and hornblende. They generally form the lower stratigraphy of greenstone belts, being composed of flow dominated ultramafic komatiites, basaltic komatiites and tholeiitic basaltic lavas, often pillowed.

Komatiites are Mg-rich ultramafic volcanic rocks composed of olivine, clinopyroxene, plagioclase and chromite, and are not formed on modern day Earth, making them an interesting product of a different environment. They can reach up to 25% volume of the ultramafic to mafic complex (Hunter and Stowe, 1997), however are often only a minor component of greenstone belts overall. When preserved without a high degree of alteration or metamorphism komatiites exhibit a classic spinifex texture (Figure 2.1.3), and also form cumulate zones which can be composed of almost pure olivine. In most cases komatiites are altered to serpentinite (from olivine), talc and tremolite (from clinopyroxene), and often occur as talc-tremolite schists. Individual flows are extremely thin, typically ~2 cm, presumably due to their very low viscosity as lavas, while cumulate and spinifex layers were able to build where these flows accumulated as small lava lakes or ponds.

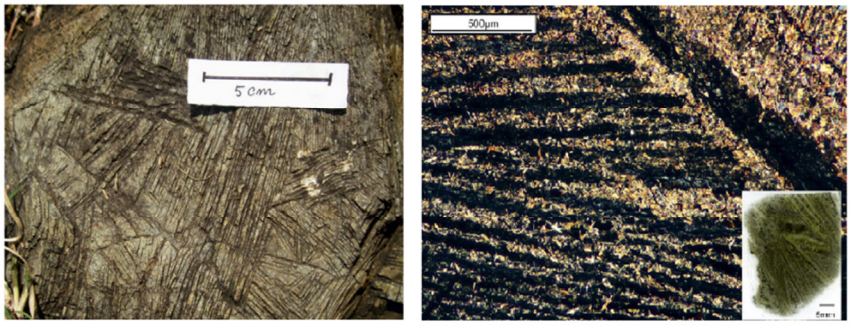


Figure 2.1.3: Field photo and photomicrograph of spinifex texture in komatiite (Chaudhuri et al., 2015).

Basaltic volcanic rocks are the predominant component of ultramafic to mafic complexes in granite-greenstone terranes. Basaltic rocks are also common in modern day environments, forming in mid ocean ridge environments such as the Atlantic Ocean (e.g. Langmuir et al., 1977, Andres et al., 2004) and in large igneous provinces such as the sub aerial North Atlantic Igneous Province (e.g. Kent and Fitton, 2000, Saunders et al., 2013) or the sub aqueous 33-43 km thick Ontong-Java Plateau (e.g. Neal, 1997, Kerr, 2003). Composed primarily of pyroxene and plagioclase, there does not appear to be good mineralogical reason to distinguish greenstone belt basalts from modern day basalts. Basaltic komatiites lie compositionally between basalts and komatiites, their composition being largely dependent on the temperature of the source region, with a higher temperature and corresponding higher degree of partial melting resulting in a lava with a more komatiitic composition being erupted, and likewise a lower degree of melting results in lavas with a more basaltic composition being erupted.

Ultramafic to mafic volcanic rocks are the most difficult lithologies to date using U-Pb isotopes; this is due to their composition resulting in a lack of datable minerals being present (e.g. a lack of primary zircon or monazite). Occasionally minerals datable using the U-Pb technique are present, but there is a strong likelihood that they are inherited from the surrounding crust, and therefore do not temporally constrain the volcanic rock itself. Due to the lack of suitable minerals for U-Pb dating, alternative techniques are often used on these lithologies, for example: Re-Os (e.g. Puchtel et al., 2004, Connolly et al., 2011), Pb-Pb isotope dating (Dupré and Arndt, 1990, Khanna et al., 2011) or Sm-Nd dating (e.g. Dupré et al., 1984, Mole et al., 2013), however these methods are more laborious to obtain than U-Pb data, all involving plotting isochrons often through a small number of data points, and make the assumption that all samples are contemporaneous.

2.1.2.2. Intermediate to felsic volcanic rocks:

Intermediate to felsic volcanic rocks are found in many greenstone belt sequences, often overlying the ultramafic to mafic volcanic rocks. Their common presence towards the top of greenstone belt volcanic sequences highlights that these often form during the later stages of volcanic activity in the region (Condie, 1981). The composition of these felsic to intermediate rocks range from dacitic to rhyolitic and can be in the form of either lava or pyroclastic flows (Anhaeusser, 2014). Intermediate to felsic volcanic rocks contribute a small volume of rock to the overall stratigraphy of a greenstone belt relative to greenstones of the ultramafic to mafic volcanic complex and overlying sedimentary rocks, however they can locally be several kilometres thick (e.g. in the East Pilbara Craton; (Van Kranendonk et al., 2007b)). Although not the dominant rock type, intermediate to felsic volcanic rocks are of great importance for a number of reasons.

They appear to signal the end of volcanic activity in many greenstone belts, being overlain by sedimentary sequences, and a number of studies have linked them to the TTG plutons that form in granite-greenstone terranes (DiMarco and Lowe, 1989, Hickman, 2004). From a geochronological perspective the felsic volcanic rocks are very useful, as unlike the ultramafic to mafic volcanic rocks, datable minerals such as zircon are often present. Dating crystallisation ages from the intermediate to felsic volcanic rocks provides the highest precision age constraints of volcanism in most greenstone belts worldwide.

2.1.2.3. Syn-volcanic intrusive rocks:

Often found interbedded with the volcanic successions of greenstone belts are a number of volumetrically minor intrusive dykes or sills. These are not always part of the later TTG plutonism related to the greenstone belt as may initially be expected. In fact many are interpreted to be part of the plumbing system of the greenstone volcanic rocks, and can be fractionated derivatives of the magma feeding these rocks. The systems sourcing the ultramafic to mafic volcanic rocks include for example anorthosites (Naqvi and Hussain, 1979), quartz-diorites, or gabbros (Zhou, 2013), while those associated with the felsic volcanic rocks often include quartz-feldspar porphyries (Van Kranendonk et al., 2009).

2.1.2.4. Sedimentary successions:

The sedimentary rocks in greenstone belts tend to form the top of the succession, overlying the volcanic rocks and signalling the end of volcanism (Anhaeusser, 2014). A classic example of this is the Barberton greenstone belt where the Fig Tree and Moodies sedimentary groups overlie the Onverwacht volcanic rocks (Eriksson, 1980, Foster and Piper, 1993). Greenstone belt sedimentary rocks typically constitute < 10 % of the rocks in a greenstone sequence (Bédard et al., 2013) and the largest source rock for the sediments are mafic and ultramafic volcanic rocks, indicating that a large portion of the Earth's surface during the Archean was composed of mafic and ultramafic volcanic rocks (Kamber, 2015). The lithologies present in sedimentary successions include: shallow water clastic sediments, turbiditic sequences (usually greywackes), chemical sediments (predominantly banded iron formations), and occasionally stromatolitic carbonates or deep water shales.

2.1.2.5. TTG Rocks:

Two disclaimers should be made before discussing trondhjemite-tonalite-granodiorite plutons. The first of these is that the term 'granite-greenstone terrane' does not accurately reflect the composition of the intrusive plutons present along with the greenstones in these terranes, as the majority of these rocks are not technically granites. The plutons present are mostly trondhjemite-tonalite-granodiorite rocks, termed 'TTG' rocks, and the use of the term 'granite' refers to these being granitoid in nature. Secondly, the term 'pluton' in this instance is used to encompass all intrusive rock bodies, and not only the typical plutonic shape (a non-tabular intrusive mass of rock several km wide) which is often inferred when using the term pluton. TTG rocks are estimated to constitute around 90% of continental crust formed during the Archean and mineralogically are generally composed of quartz-plagioclase-biotite with a minor component of K-feldspar, and occasional hornblende (Martin et al., 2005). TTG rocks form large intrusive bodies that appear to puncture through the greenstones which then occupy the interstitial space between the plutons. This can be seen clearly in the Pilbara Craton of Western Australia where the light coloured and ovoid (due to the present day erosive surface) TTG bodies are in contrast to the darker linear greenstones between them (Figure 2.1.4). A combination of deformation and the large volumes of granitic rocks relative to greenstone belt lithologies mean that in most granite-greenstone terranes the TTG rocks are volumetrically dominant, and occupy the majority of the exposed terrane (e.g. Van Kranendonk et al., 2007b, Boily et al., 2009). There appears to be a temporal progression within a particular granite-greenstone terrane from TTG rocks (which always remain the dominant lithology) representing the oldest granitoids, to more evolved rocks, such as sanukitoid-like rocks, and finally granites and even syenites representing the youngest granitoids. This is seen in granite-greenstone terranes in all continents, with two examples being the Abitibi greenstone belt (Feng and Kerrich, 1992) and the Pilbara Craton (Figure 2.1.5) (Kamber, 2015).



Figure 2.1.4: Satellite image of the Pilbara Craton showing the contrast between TTG rocks (light) and greenstone belts (dark) (Map data: TerraMetrics, Google).

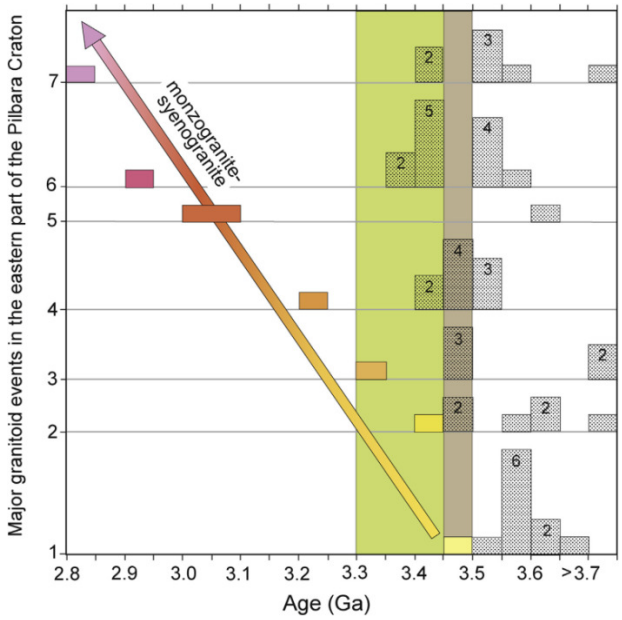


Figure 2.1.5: Granitoid evolution in the East Pilbara craton in which granitoids become increasingly evolved through time. Note: stippled boxes are Nd-model ages, the grey bar is the main TTG forming event and the green bar is the timing of SCLM formation (Kamber, 2015).

2.1.2.6. Relationship to basement:

One of the major uncertainties in Archean granite-greenstone terranes is that of the nature of the basement upon which the volcanic rocks were erupted (Condie, 1981). In most cases it is impossible to tell the true nature of the relationship between the base of the volcanic sequence, and the basement upon which it was erupted, with either continental or oceanic crust being possible settings (Hunter and Stowe, 1997). This is due to the basement contact often being faulted, sheared, poorly exposed, or the greenstones being adjacent to younger intrusive rocks with the original contact no longer existing. There is evidence in a number of greenstone belts that the volcanic rocks were erupted onto gneissic basement with the original contact being that of an unconformity (e.g. Slave Craton (Thurston, 2002) and Pilbara Craton (Van Kranendonk et al., 2007b)), however many gneissic basement rocks also contain xenoliths of greenstones, and so in these cases there must have been earlier episodes of greenstone volcanism that are no longer fully discernible (Condie, 1981).

2.1.2.7. Metamorphism and metasomatism:

Almost all greenstone belts have undergone metamorphism to some extent, with many different factors interplaying to produce the resultant rocks. Two of the main factors influencing the metamorphic grade of greenstone belt rocks are the intrusion of granitoid plutons, and regional

deformation events. The pre-existing fabric of the rocks within greenstone belts themselves (i.e. flow volcanics or sedimentary deposits as opposed to massive igneous intrusions) make them susceptible to deformation, and often greenstone belts appear to be zones of weakness accommodating much of the faulting and shearing associated with regional deformation events, unlike the neighbouring more massive intrusive bodies (Anhaeusser, 2014). The grade of metamorphism can vary both within a greenstone belt and also from belt to belt, however greenschist facies metamorphism is the predominant grade, and this is partly the reason the term greenstone belt was given to these successions. Under greenschist conditions ultramafic to mafic lithologies are converted to tremolite-actinolite-chlorite-hornblende assemblages, with talc and carbonate formed in ultramafic rocks and epidote and albite in mafic rocks. In siliceous rocks minerals are converted to quartz-albite-sericite. The proximity of intrusive plutons to specific greenstone sequences has an effect on metamorphic grade, with greenstones adjacent to intrusive rock bodies commonly being metamorphosed to amphibolite grade rocks, and granulites also being formed in some instances as contact aureoles. This can result in a larger proportion of hornblende, as well as andalusite and garnet being formed as metamorphic minerals (Hunter and Stowe, 1997). The presence of regional high grade deformation events also affects the metamorphic grades within greenstone belts, as does the size of the belt itself, with larger greenstone belts apparently being less susceptible to metamorphism (Anhaeusser, 2014).

Most greenstone belts have undergone later metasomatism to varying degrees by the migration of hydrothermal and magmatic fluids through the rocks. The most common types of alteration in these rocks are silicification, albitisation and sulphidisation. Although such processes pose problems when it comes to identifying and attempting to deduce the original rock composition, it is worth noting that this metasomatic mineral replacement has resulted in greenstone belts being a valuable source of natural resources. Metasomatic processes often result in greenstone belts being endowed with gold, copper and other valuable metals, as well as hosting an increased grade of iron ore deposits related to banded iron formations (Anhaeusser, 2014).

2.1.2.8. Structural geology:

A detailed structural analysis of greenstone belts is beyond the intended scope of this thesis. Structural geology will only be touched on where it is necessary for the understanding of the main aims of this study. The structural geology of greenstone belts is often very complicated with multiple deformation events resulting in a complex folding, faulting and shearing history. Some of this structural/deformational activity is syn-volcanic or syn-sedimentary in nature and therefore has a direct influence in the formation of the greenstone belt itself (e.g. syn volcanic granitoid

emplacement in the Abitibi greenstone belt; (Benn, 2004)), while other deformation events postdate the greenstone belt formation completely (e.g. late shearing in the Pilbara Craton; (Beintema, 2003)). A particular structural specificity seen in greenstone belts, as well as Archean cratons as a whole, is the presence of steeply dipping fabrics and steeply plunging lineations (Gapais et al., 2009). Large strains are seen in these regions despite a lack of major metamorphic gaps (Jaguin et al., 2012).

2.1.3. Granite-greenstone terrane formation:

There is little debate on the generalised stratigraphy of granite-greenstone terranes as outlined above, as this is mainly based on field observations and geological mapping. The setting and processes under which the stratigraphy formed however is often strongly debated, as many of the features are not seen in modern day environments. Each of the main rock-types featured in greenstone belts is subject to ongoing discussion and debate on mode of formation and process operating during their genesis. Some of these main issues and debates are discussed below.

2.1.3.1. Ultramafic to mafic volcanic rocks:

Komatiites are common in Archean and Paleoproterozoic greenstone belts, yet are almost completely absent in rocks < 2.0 Ga due to their inability to be formed in modern day environments (Furnes et al., 2014). This leads to the simple conclusion that at least some processes or factors involved in their creation are not active today. There is general agreement that for the formation of komatiites, and in many other early Precambrian processes for that matter, that the mantle temperature had to be hotter than present (e.g. Kamber et al., 2002, Herzberg et al., 2010). Komatiites have been modelled to contain a very high degree melt (30-50%) and to have been erupted at 1500-1600°C (300°C hotter than modern day hot melt) (Sleep and Windley, 1982). This is known through the modelling of Mg content in the rocks, as a higher mantle temperature results in deeper melt initiation and partial melting progressing to a larger degree (McKenzie and Bickle, 1988, van Thienen et al., 2004). Furthermore, the finite amount of iron available in the melt will be diluted relative to Mg, resulting in the characteristically low Fe/Mg ratios of komatiites. The reason for a hotter mantle in the early Earth is generally considered to be due to greater heat output resulting from a higher concentration of radioactive parent isotopes. One theory on the formation of komatiites is that this greater heat output resulted in mantle plume activity being more commonplace. This mantle plume activity could then have been able to produce enough heat to melt dry peridotites (Arndt et al., 2008). An alternative suggestion is that komatiites could have been formed during the partial melting of a

hydrated mantle slab in a subduction zone similar to modern day boninites (Parman and Grove, 2004), but the latter model necessitates some kind of subduction process to exist, which is not universally agreed for the Archean.

Basaltic volcanic rocks are common in modern day environments, and therefore there does not appear to be a need to develop a specific model for the conditions needed to form these rocks in Archean times, however there is still much debate on specific environments and processes resulting in them being extruded onto the Earth's surface. Archean basalts are often tholeiitic and high-Mg, which likely reflects the hotter mantle conditions relative to the Phanerozoic (Herzberg et al., 2010), and agrees with the analogous theory behind komatiite formation. The composition of tholeiitic basalts is similar to that of Phanerozoic intra-oceanic plateaus, like that of the Ontong-Java Plateau (Manikyamba and Kerrich, 2012), and so has led to the comparison between Archean greenstone belts and modern day oceanic plateaus or LIPs (e.g. Tomlinson and Condie, 2001, Kamber, 2010). It is also argued that these basaltic volcanic rocks could have been formed through sea floor spreading, similar to mid-ocean ridge basalts today, and greenstone belts may represent obducted portions of primitive ocean crust and therefore ancient ophiolites (Furnes et al., 2014). The ophiolite model forms a large part of the debate on the formation of granite-greenstone terranes and is discussed further in chapter 2.3.5.2.

Basaltic komatiites lie compositionally between basalts and komatiites, with their formation dependant on the composition and temperature of the source, and so are not a unique lithology requiring a different formation setting. Their presence however does highlight that there is not simply a bi-modal production of end member mafic volcanics, but rather an entire range along a mixing line likely predominantly depending on source characteristics and conditions of partial melting.

2.1.3.2. Intermediate to felsic volcanic rocks:

The intermediate to felsic volcanic rocks, as mentioned above are generally agreed to be dacitic to rhyolitic lavas or pyroclastic flows (Anhaeusser, 2014). Many different models have been proposed to explain the formation of the intermediate to felsic volcanic rocks in greenstone belts. One possibility is that felsic components evolved through fractional crystallisation of ultramafic to mafic volcanic rocks similar to modern day environments (Condie, 1981) and that these eruptions were therefore only possible late in greenstone belt formation. Another proposed model favours the source of these volcanic rocks as being the partial melt of mafic to ultramafic volcanic rocks which have been buried to depths great enough for partial melting to occur due to the thickness

to which the ultramafic to mafic rock sequences can reach (Smithies et al., 2003). Such a process has been invoked to occur in Iceland today (Willbold et al., 2009). The relatively late extrusion of the intermediate to felsic volcanic rocks also concurs with the above model, as the ultramafic to mafic volcanic sequence must be thick enough for melting at its base to begin. It is known that TTG rocks form late relative to greenstone belt formation, so these too may be formed by partial melting of pre-existing mafic to ultramafic lithologies. It may be that some, or all of the felsic volcanic rocks are the extrusive equivalent of the TTG rocks themselves (Van Kranendonk et al., 2004). Similarities have been made between the intermediate to felsic volcanic rocks and the intermediate crust formed in modern day arc settings, and this has been used to propose an Archean volcanic arc setting as a further possibility for formation environment (e.g. McLennan and Taylor, 1991, Barrie et al., 1993). As can be seen, there are still many theories used to explain formation of intermediate to felsic volcanic rocks, all of which seem to be possible. A factor that makes the debate more difficult is that these rocks are particularly difficult to preserve, as seen by the fact they are commonly silicified to such an extent that they are often difficult to distinguish from bedded chert horizons (Hofmann et al., 2013).

2.1.3.3. Sedimentary succession:

Sedimentary rocks can be used to reconstruct both the environment of deposition, e.g. deltaic or deep water, and the tectonic history of their formation region using many different methods, e.g. sequence stratigraphy, sedimentary structures, isotope composition and petrography. They are therefore the focus of many studies which attempt to reconstruct the deposition environment, or elucidate the tectonic processes which may have operated at their time of formation. A number of models exist which suitably explain the sedimentary sequence stratigraphy of greenstone belts. Not all greenstone belts formed in the same environment, and so these sequences differ from example to example. In one model, seen in the Wabigoon subprovince of the Superior craton in Canada, coarse grained clastic sediments form a fluvial-deltaic system over TTG basement. This sequence then transgresses due to basin subsidence, eventually giving way to carbonates and banded iron formations due to sediment starvation (Kamber et al., 2004). In some cases, there is evidence for full continental rupture, e.g. in the Slave Craton of Canada (Bleeker and Hall, 2007) in which a similar sequence to the Wabigoon subprovince is deposited on continental TTG rocks, and the cessation of continental rupture is signalled by the eruption of ultramafic to mafic volcanic rocks. It is not uncommon that the sedimentary sequences are largely starved of clastic and terrigeneous input (except for minor ash fall deposits). In such cases the predominant facies is banded iron formation, in particular Algoma-type, which usually forms far from any continental landmass through hydrothermal deposition or sea-water precipitation. One environment for

deposition in an ocean environment is proposed to be similar to that of a modern day oceanic plateau, e.g. the Ontong-Java Plateau, in which there is a thick sequence of mafic volcanic rocks overlain by a relatively thin sedimentary sequence (Kamber, 2010).

No matter what the sedimentary sequence, it is possible to propose a model for deposition, with the majority of greenstone belt sedimentary rocks having a modern day analogue. So although the sediments deposited may be different, e.g. TTG derived clastics, or Algoma-type banded iron formation, both requiring different source chemistries other than modern day equivalents, the general processes involved in sedimentary deposition appear to be largely similar to those of today.

2.1.3.4. TTG rocks:

TTG rocks are granitic rocks composed of largely the same component minerals as granites, formed by the partial or complete melting of pre-existing crust or mantle. The compositional difference between TTG rocks and granites is that TTG rocks are largely sodic, with a minor potassium constituent, i.e. they don't contain much alkali feldspar (Moyen, 2011). The reason for this is they are derived largely from the melting of a hydrous basaltic source which is largely devoid of potassic minerals to begin with (Drummond and Defant, 1990). It is therefore not difficult to envisage that the source of TTG rocks associated with greenstone belts, is in fact the greenstones themselves, which are largely basaltic in nature. A difficulty arises in that basaltic source rocks must almost certainly be hydrated to produce TTG rocks (Arndt, 2013). Source rocks must also be at a great enough depth, or be subjected to a sufficiently high heat flow in order for partial melting to take place. Subduction is seen as the simple answer to this conundrum, with the process taking hydrated sea floor basalts to depths great enough for them to melt, however this model does not necessarily fully fit in with the stratigraphy of granite-greenstone terranes, and other theories have been proposed, e.g. volcanic resurfacing; the burial of a thickened oceanic plateau due to the continued addition of extrusive volcanics at its surface (Kamber et al., 2005). TTG rocks, in particular due to their similarities with modern day adakites, are one of the main sources of contention when it comes to the debate on how granite-greenstone terranes were formed, and are discussed in detail in chapter 2.3.5.1.

In addition to TTG granitoids, many granite-greenstone terranes also possess potassic granites and even syenites (Moyen et al., 2007). These are formed from the melting of a pre-enriched crustal source, and could therefore form from re-melting of enriched TTG rocks or could involve

the melting of sedimentary sequences that overlie or are interbedded with the ultramafic to mafic volcanic rocks.

2.1.4. Summary of granite-greenstone terrane geology:

It is important to note that the 'typical' rock sequences described above do not necessarily all need to be present, and there is no set order of these rocks in order for the term granite-greenstone terrane to be applied. This is a simplified model and in reality many of these sequences are often repeated in individual greenstone belts. Certain features can however be defined across almost all greenstone belts (Condie, 1981); 1) there is a decrease in volume of both ultramafic and mafic volcanic rocks with stratigraphic height, 2) there is an increase in the amount of felsic lavas and pyroclastic flows with stratigraphic height, 3) immature clastic sediments often dominate the upper parts of greenstone successions, 4) mature clastic sediments, carbonates and alkali-rich volcanic rocks are not common in Archean greenstone successions.

2.2. Crustal and mantle evolution:

2.2.1. Crustal evolution:

The Earth's continental crust contains rock sequences spanning almost the entire history of the Earth, including some > 4.0 Ga (Bowring et al., 1989). The continental crust is therefore the primary archive of Earth's geological history, and can be used to decipher the evolution of the early Earth (Roberts et al., 2014). The continental crust varies in thickness from 20-70 km, averaging ~35-40 km (Mooney et al., 1998) (Figure 2.2.1). The entire lithospheric thickness including the sub-continental lithospheric mantle (SCLM) is generally < 60-80 km beneath Phanerozoic regions as evidenced through the lack of garnet in mantle xenoliths (Lee et al., 2011). Beneath Archean cratons however, SCLM thickness is much greater, typically 200-220 km, and in some cratons the SCLM is > 300 km (e.g. West Africa) (Artemieva and Mooney, 2001) (Figure 2.1.1). 'Crustal evolution', or 'crustal growth' is the process by which the volume of continental crust we see today has formed through time (termed 'crustal formation' or 'crustal generation'), relative to the volume of continental crust that has subsequently been destroyed (e.g. Voice et al., 2011, Cawood and Hawkesworth, 2013, Hawkesworth et al., 2013). Note that crustal formation is used solely to describe the formation of new crust, juvenile in nature and which has been sourced directly from the mantle, whereas 'crustal recycling' consists of any process that reworks crustal material (McLennan, 1988). For crustal evolution to be possible there must have been a net gain of continental crust through time, however the rates at which this crust has been formed and preserved are debated, with many different models having been proposed (Figure 2.2.2). Included

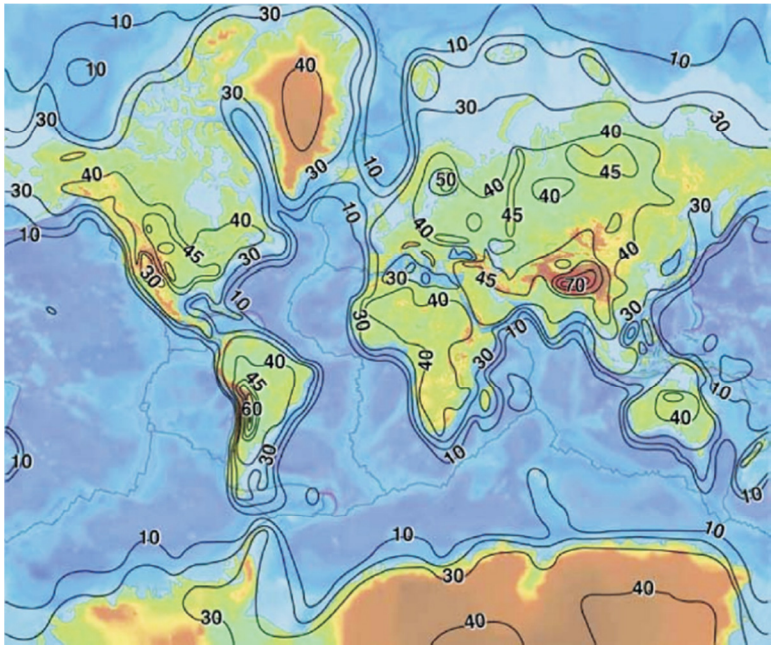


Figure 2.2.1: Map highlighting the thickness of the Earth's crust (Voice et al., 2011, Cawood and Hawkesworth, 2013).

in these models are: 1) a uniformitarian model, in which the present day volume of continental crust was formed early in the Earth's history and has since then been destroyed and replaced at a constant rate resulting in equilibrium (Armstrong and Harmon, 1981), 2) a model in which there was little crustal formation during the Hadean or Archean with most crust being formed during the Proterozoic (Allègre and Rousseau, 1984), 3) a model in which the majority of crust was formed during the Meso-Neoarchean, with relatively little crust present before, or added after this time period (Taylor, 1985), and 4) the model of Dhuime et al. (2012), which predicts two steady rates of crustal growth through time with a point of inflection at 3.0 Ga. The importance of crustal evolution models to this thesis is that they are all particularly relevant when studying rocks from the Archean, in particular the Mesoarchean, as any new data could have implications for one or more models. At the present day there appears to be no net addition to the continental crust, with possibly even a slight reduction in continental crustal volume occurring (Stern, 2011, Hawkesworth et al., 2013). In an attempt to decipher the complexities of crustal evolution a number of different methods have been used, and are discussed below.

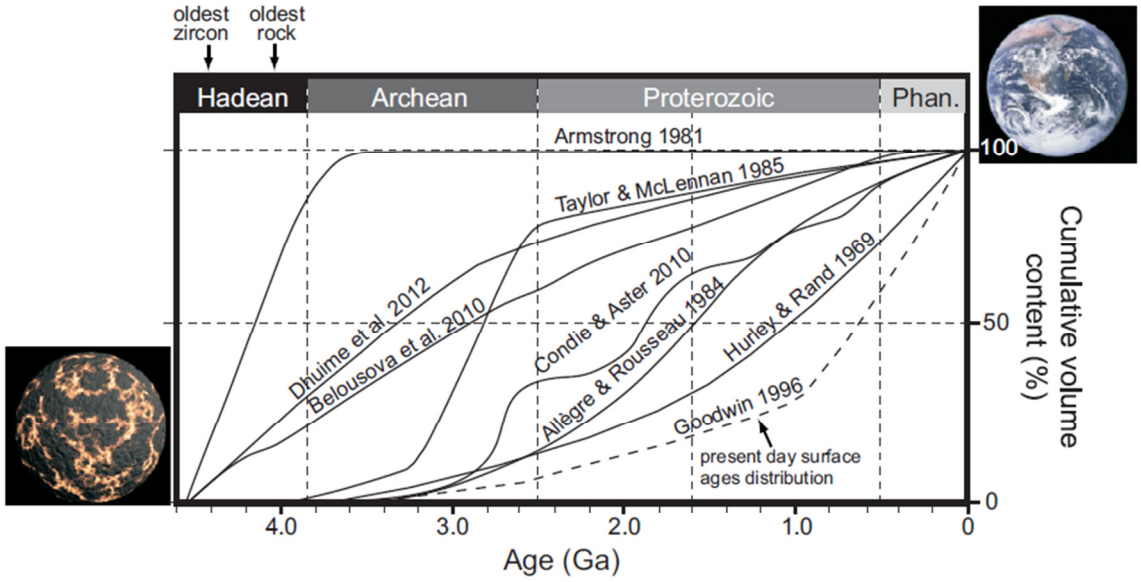


Figure 2.2.2: Plot of numerous crustal evolution models, also highlighting present day surface rock age distributions (Cawood and Hawkesworth, 2013).

2.2.1.2. Detrital zircon:

The most common method used for modelling crustal evolution is the detrital zircon record. The physical and chemical resilience of zircons, and the fact they are derived largely from felsic volcanic rocks makes zircon an important archive of the crustal record (Cawood and Hawkesworth, 2013). If the entire zircon record is used however, there will be a strong bias

towards felsic igneous rocks, and a large proportion of Earth's rocks will remain unaccounted for. In a bid to reduce this bias, detrital zircons are used for modelling crustal evolution, as they sample a range of rocks in their catchment areas and therefore provide a more representative record of the ages of rocks present, both from felsic igneous rock and other lithology types. It must be noted however that the detrital zircon record is still biased; younger source rocks are more accessible to erosion and re-deposition, resulting in older source rocks being underrepresented in the detrital zircon record (Allègre and Rousseau, 1984), and methods other than zircon U-Pb are used to model crustal evolution (e.g. Pb, Sr, Nd radiogenic isotope systems (Armstrong and Harmon, 1981, Allègre and Rousseau, 1984)).

When examining the age spectra from the U-Pb detrital zircon record, it is immediately apparent that there are a number of distinct U-Pb zircon crystallisation age peaks throughout Earth's history (e.g. Condie, 2005, Voice et al., 2011) (Figure 2.2.3). These are interpreted by many to represent large scale crustal formation events (e.g. Condie, 2004, Campbell and Allen, 2008, Voice et al., 2011). It is difficult to envisage a tectonic model that could explain punctuated crustal growth as opposed to it being a continuous process (Cawood and Hawkesworth, 2013), though possibilities could be episodic subduction (O'Neill et al., 2007), or increased magmatic arc activity due to continental breakup (Stern and Scholl, 2010). The current favoured mechanism proposed that could form this intermittent crustal growth pattern however is episodic mantle plume activity (Condie, 2004), as this negates the need for a complicated tectonic model. The zircon age peaks also match times of supercontinent formation, which has led to the suggestion that this pattern could be more of an artefact of preservational bias as opposed crustal formation (Condie and Aster, 2010, Hawkesworth et al., 2010, Hawkesworth et al., 2013). Cawood et al. (2013) highlighted that during times of supercontinent formation (e.g. the Himalaya in modern day Eurasia) there was a preservational bias in zircon as they are formed a large distance from destructive plate margins and are therefore less likely to be recycled into the mantle. This is the opposite of those formed in arc settings (e.g. the Andes) where destruction is much more likely through subduction. The probability of zircons being preserved in sedimentary sequences is clearly affected by this isolation from plate margins, but also due to the fact that more sedimentary rocks are produced during continental collision (Clift, 2010). The detrital zircon record therefore almost certainly overestimates the volume of crust formed during supercontinent cycles, and it is in fact likely that a greater volume of new crust is formed in arc settings where there is a mantle source for the rocks as opposed to crustal recycling being the dominant process (Hawkesworth and Kemp, 2006). For the reasons discussed above, care must be taken when interpreting the detrital zircon record, and it must be noted that analysis of U-Pb detrital zircon ages alone is unlikely to provide an accurate representation of crustal evolution.

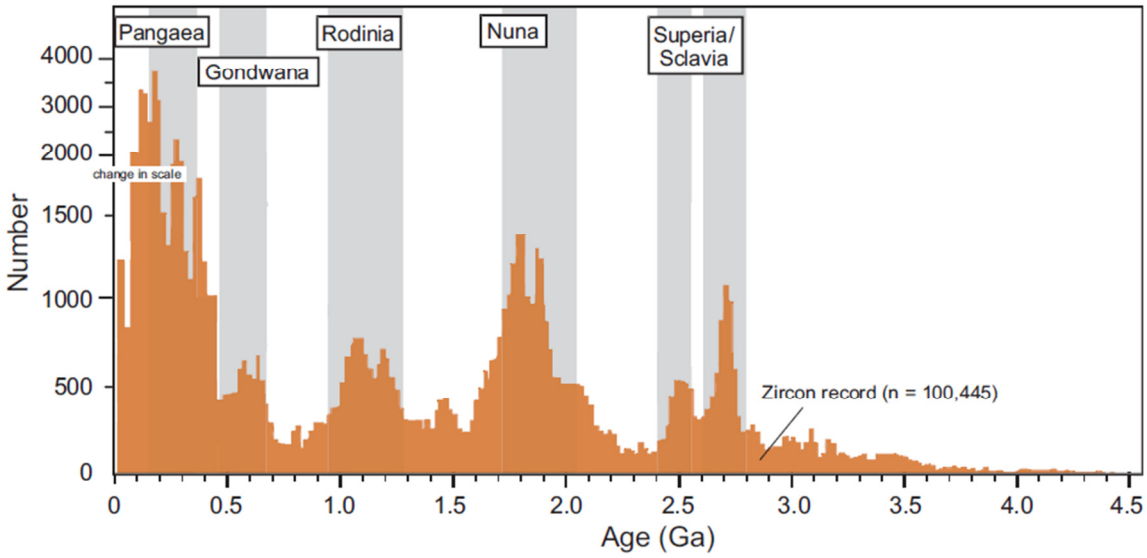


Figure 2.2.3: Histogram of over 100,000 detrital zircon analyses highlighting peaks in their U-Pb crystallisation ages through time, and their similarities to the ages of supercontinents (modified from Cawood and Hawkesworth, 2013).

2.2.1.3. Alternative isotope systems:

In order to better model the Earth's crustal evolution a number of different isotope systems can be used, including Sm-Nd isotopes, Lu-Hf isotopes and O isotopes, which are discussed here.

From a petrogenetic perspective, the Sm-Nd isotope system is most commonly used for whole rock samples to determine evolution of the rock with respect to bulk Earth or mantle composition through time. ^{147}Sm decays to ^{143}Nd with a half-life of $1.06x10^{11}$ years. This is used to calculate the initial $^{143}Nd/^{144}Nd$ ratio of a rock, which in turn can be used to determine the timing of partial melting when initial separation from a mantle reservoir occurred (termed the Nd model age or $T_{DM;}$ (DePaolo, 1981)). Many ultramafic to mafic rocks are derived directly from mantle plume activity and therefore represent true first stage crustal formation events; however these lithology types are generally missing from crustal formation models which use only the detrital zircon record. By using Nd model ages on these rocks, the time at which their magmatic source was separated from the mantle can be calculated. In fact one of the first crustal evolution models was based on the Nd model ages of shales, which were used to represent the continental crustal average composition (Allègre and Rousseau, 1984). The key assumption in calculating model ages is that the ratio of the parent-daughter isotope changes in the processes involved when new crust is generated, but cannot be fractionated by any later event within the continental crust (Hawkesworth et al., 2010). This is a reasonable assumption, as both Sm and Nd are REE, and

generally immobile. A further assumption is that the mantle is formed from a 'chondritic uniform reservoir' (abbreviated to CHUR, (DePaolo and Wasserburg, 1976)) which has undergone chondritic evolution, allowing calculation of when a particular rock or reservoir was separated from the mantle. Due to the Nd isotope signature being unaffected by crustal processes, this allows a model age to be calculated irrelevant of later tectonic or re-melting events. This is most commonly calculated using the 'depleted mantle' giving a depleted mantle model age (T_{DM}). A second calculation which can be carried out using the Sm-Nd isotope system is that of εNd. εNd is the measure of the deviation in the Nd isotope ratio of a sample from the expected Nd isotope ratio of a sample of that age from CHUR (DePaolo and Wasserburg, 1976) (present day $^{143}Nd/^{144}Nd$ value of 0.512638 (Jacobsen and Wasserburg, 1979)). High positive εNd values can lie directly on the depleted mantle evolution curve, highlighting that the rock is juvenile in nature and was extracted from a depleted mantle source close to the time of crystallisation, while lower εNd values suggest that the rock comes from a reworked source, or a mixture of juvenile and reworked sources. One problem with calculating depleted mantle model ages is the uncertainty in depleted mantle evolution lines (e.g. Babechuk and Kamber, 2011, Kamber, 2015), which is discussed in chapter 2.2.2.

For crustal evolution models, Lu-Hf ratios are generally calculated for zircons at the single grain, or sub-grain scale (i.e. by LA-MC-ICP-MS or SIMS), with an obvious disadvantage when compared to the Sm-Nd whole rock method being that the Lu-Hf method used in this way only represents rocks which crystallise zircon. The Lu/Hf ratio in zircons is particularly low due to Hf being concentrated in zircons, and so $^{176}Hf/^{177}Hf$ isotope ratios in zircons are similar to those of the magma from which they crystallised (Patchett et al., 1982). As with Sm and Nd, both Lu and Hf are generally immobile elements and the assumption is made that these are not fractionated by crustal processes. The mantle reservoir that is used in these calculations is that of the depleted mantle (e.g. Griffin et al., 2000, Wyche et al., 2012) and the resulting ages calculated are Hf depleted mantle model ages (T_{DM}), i.e. the time at which the source magma from which the zircon crystallised was separated from the depleted mantle (Roberts and Spencer, 2014). This can also be termed the crustal residence age, and is a useful indicator of when new crust was formed. Zircon can survive multiple crustal recycling events with the possibility that at high-grade events the U-Pb system may be reset thus resulting in earlier-formed zircons giving a younger (reset) U-Pb age, however the Lu-Hf isotope system used to calculate Hf model ages is unaffected by crustal reworking events (Cawood et al., 2013). This allows an age of initial crustal formation to be calculated for a rock using Hf isotopes, which can complement U-Pb zircon ages to provide a more detailed history of a rock (Flowerdew et al., 2006).

Oxygen isotopes in zircons are commonly used in relation to crustal evolution studies. Oxygen isotopes cannot be used to temporally constrain mantle extraction or crystallisation, however they can be used to distinguish whether or not a zircon has already been subjected to a rock cycle (Hawkesworth et al., 2010). The $^{18}O/^{16}O$ ratio ($\delta^{18}O$) is altered by low temperature hydrothermal alteration, which is achieved in a sedimentary cycle (Valley, 2003) yet it is thought to be unaffected by metamorphism or diagenetic processes, and so the $\delta^{18}O$ of a magma will reflect that of its source (Roberts and Spencer, 2014). It is therefore possible to perceive whether the source magma contained a contribution from sedimentary rocks, or solely a first cycle contribution. If a sedimentary contribution is present, it is clear that this rock, or mineral, does not represent an age of crustal formation (i.e. crustal recycling was an important process in rock formation).

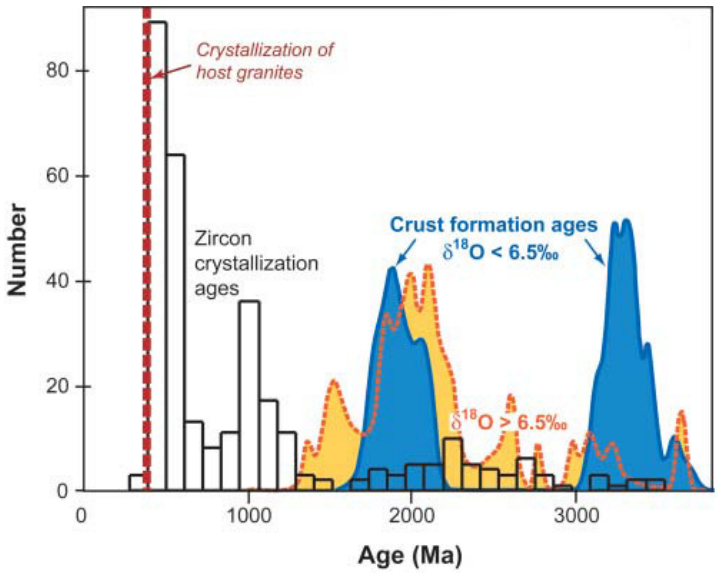


Figure 2.2.4: Plot highlighting the difference between zircon U-Pb ages, and Hf model ages from 'first cycle' zircon with mantle like $\delta^{18}O$ (blue) and recycled zircon(orange) (Hawkesworth et al., 2010).

There are clear benefits in using multiple isotope systems to model crustal evolution as seen from the individual methods described above. Neodymium model ages are particularly useful for ultramafic to mafic rocks in which zircons are not present, and as mentioned a number of primitive rocks are ultramafic to mafic in composition. Zircons however allow a number of different analyses to be carried out on the same crystal. U-Pb ages are the most common and most accurate ages calculated for zircons, and can be easily obtained *en masse* from the literature. These however could potentially represent resetting ages. Crustal recycling and the partial melting of pre-existing crust can result in the resetting of the U-Pb chronometer in zircon which retains a corresponding older T_{DM} recording the initial crustal extraction age. Hafnium model ages provide the time at which the source magma was separated from the mantle for a

rock, however if the zircons analysed come from a mixture of recycled rocks and first phase rocks then a mixed Hf model age will be calculated. By also analysing O isotopes, first cycle zircons (i.e. those not subjected to low-temperature alteration during rock weathering and erosion) can be selected for Hf isotope analysis resulting in the greatest degree of certainty that the results are providing a crustal formation age unaffected by other factors. An example of this is seen in a compilation of zircons with mantle like $\delta^{18}O$ which form two distinctive Hf model age peaks at 3.4-3.1 Ga, and 2.1-1.7 Ga. These peaks differ from those seen using other methods (e.g. detrital zircon), and suggest that large periods of crustal formation occurred in the Mesoarchean (Figure 2.2.4) (Hawkesworth et al., 2010).

2.2.1.4. Formation of the continental crust:

The earliest physical record of the presence of an evolved lithospheric crust on Earth comes from the Jack Hills conglomerate detrital zircons, which formed ~4.4 Ga, from the Yilgarn Craton, Australia (Compston and Pidgeon, 1986, Harrison et al., 2005, Bell et al., 2014). It is thought that these are probably remnants of the first small felsic continents on the early Earth (Hawkesworth et al., 2010). The oldest known rocks are from the 4.02 Ga Acasta Gneiss of the Slave Craton in northwest Canada (Bowring et al., 1989), and the oldest terrane composed of different stratigraphies is that of the 3.9-3.8 Ga Isua Greenstone Belt in the North Atlantic Craton, Greenland (Furnes et al., 2007). These all provide evidence an evolved crust was present probably from ~4.4 Ga, but certainly from 4.02 Ga. This poses the question of whether or not these extremely small crustal remnants are representative of the fact that there was very little crust formed at this time, or if it is a case that the early crust on Earth was subsequently mostly destroyed, or reworked. It has been suggested through modelling using a combination of isotope systems that a similar volume of crust as is present today was formed during the Hadean; however it was entirely recycled back into the mantle by the onset of the Archean (Harrison et al., 2005). One theory used to explain such a scenario is that the late heavy meteorite bombardment destroyed almost all Hadean crust, and the fact that we do not see much evidence for an extensive Hadean crust today does not mean that crust was not formed at this time (Van Kranendonk, 2011, Kamber, 2015). Others however argue that there was very little crust present this early in Earth's history (e.g. Poupinet and Shapiro, 2009, Condie and Aster, 2010).

The oldest known major sections of continental crust still present today were formed between 3.7 Ga and 3.4 Ga, currently forming parts of the Kaapvaal and Pilbara cratons, thought to have originally comprised part of the Vaalbara supercontinent (Zegers et al., 1998). A number of other Mesoarchean terranes are found across the globe, however these are less expansive in size than

the so-called Vaalbara terranes, and it is not until the Neoarchean where there is an apparent significant increase in crustal formation. The debate concerning crustal evolution in the Neoarchean is similar to that discussed above, in that there is a chance that preservational bias is responsible for a lack of rocks older than Neoarchean in age, and the deeper isotopic signature of rocks can be considered rather than current exposures and zircon crystallisation ages. By using a combination of isotopic systems Dhuime et al. (2012) modelled that ~65% of today's volume of crust was formed by 3.0 Ga, even although this time span represents < 5% of the current exposed continental crust (Figure 2.2.5). A similar suggestion is made by van Kranendonk (2011) where it is proposed there is rapid crustal growth from the end of the late heavy meteorite bombardment (3.85 Ga) through to 3.00 Ga followed by dominantly crustal recycling and a relatively modest rate of net crustal growth. The relevance of these models to the debate regarding the onset of modern day plate tectonics is discussed in chapter 2.3.3. The evidence from the isotope data in the studies discussed above however suggests a uniformitarian model is unlikely, and that there is in fact a real preservational bias of continental crust in supercontinents.

2.2.1.5. Supercontinent formation:

As introduced above, a correlation is thought to exist between supercontinent formation and the dominant detrital zircon age spectra (Figure 2.2.3). It has long been known that the geological record is incomplete (Hutton, 1788), and so if the formation of supercontinents are in fact creating a bias in the record then possible reasons for this can be examined; both the mechanisms by which supercontinents formed, and the reasons zircons temporally corresponding with supercontinent formation appear to dominate the zircon record.

A number of supercontinents have been well documented and constrained through time. The more recent of these, i.e. Rodinia, Gondwana and Pangaea are relatively well constrained in both time and formation (e.g. Li et al., 2008, Powell et al., 1993, Veevers, 2004), and the further back in time, the more uncertain the time and formation of supercontinents become. The oldest of these supercontinents have been proposed as the Mesoarchean Vaalbara supercontinent (Zegers et al., 1998), and the Neoarchean Superia and Sclavia supercontinents (Bleeker, 2003). Although there is little physical evidence explicitly for a supercontinent around this time, there is an increase in crustal formation (through detrital zircon populations) and associated orogenic events proposed, leading to the speculation of possible supercontinent formation.

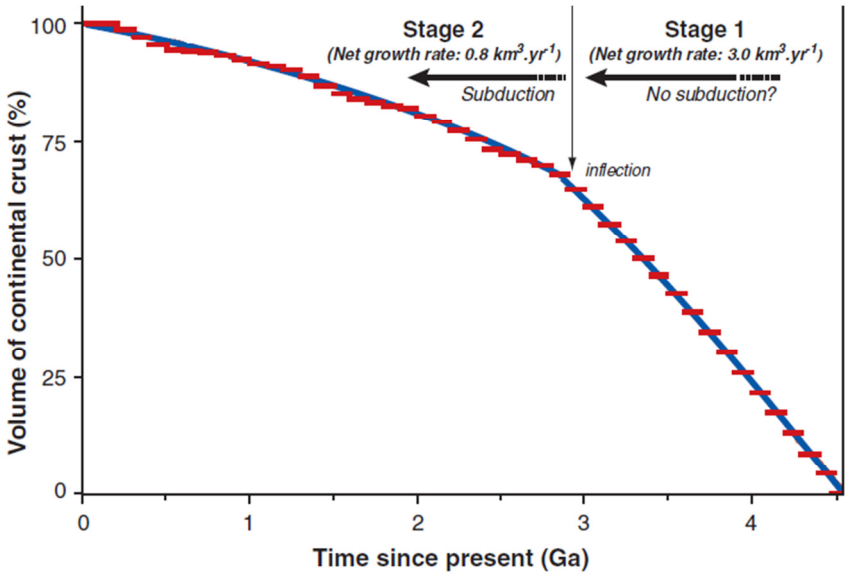


Figure 2.2.5: Continental growth curve calculated using a combination of U-Pb and Hf isotopes. Note the rapid initial growth followed by a more modest rate of crustal growth, possibly due to the onset of modern day plate tectonics at 3.0 Ga (modified from Dhuime et al., 2012).

Two of the major episodes of Precambrian continental growth, Superia and Sclavia (3.0-2.5 Ga) and Nuna (2.15-1.65 Ga) are commonly explained by major mantle overturning in a hotter early Earth (Condie, 2000). The results of mantle overturn were massive decompressional melting and emplacement of TTG rocks, resulting in the formation of a depleted lower crust and a buoyant upper crust. These mantle overturn events are thought to have changed the rheology of the mantle from possessing distinct layers with the potential to build up radiogenic heat, to a whole mantle convection system. This also enabled hot lower mantle to migrate into the upper mantle, possibly replenishing incompatible elements and resulting in increased mantle melting and crustal extraction (Davies, 1995). One possible driving force for mantle overturn is that subducted slabs accumulated at the 660km discontinuity between the upper and lower mantle, and then catastrophically sunk into the lower mantle causing mantle overturn (Stein and Hofmann, 1994). This obviously would require that subduction was active at this time, and although we know that modern supercontinents were formed through collision and subduction processes, Archean supercontinents may not have needed such a tectonic system. Possible methods of supercontinent formation without the implication of subduction is that the continents collated at a geoid low (Condie, 2000), or that continents drifted together mobilised by a 'mantle wind' (Bédard et al., 2013). The Neoarchean episode has been described as a period of 'global crisis' (Rey et al., 2003) due to the intense and protracted magmatic activity led to a near complete reworking of the felsic continental crust (Zibra et al., 2014). This is seen in the Yilgarn Craton of Australia where basement underlying the greenstones was re-melted and assimilated by younger granitic plutons with the only evidence remaining of an older basement crust being several suites

of inherited zircons (Cassidy et al., 2002). The re-melting of older crust during the Neoarchean provides a strong possibility as to why the zircon record is biased towards the Neoarchean relative to preceding eras, and that in fact these events were not true continental growth, but the reworking of older continental crust. We know that later supercontinent formation was due to accretionary plate tectonics, and hence there was a preservational bias, however there was not a major reworking of the crust and so the post Neoarchean zircon record has not been overprinted by younger ages. Therefore the late Archean marks a transition between relatively poor preservation to a strong bias in preservation, and so when studying rocks older than ~2.9 Ga, zircons may provide the best record, as their preservation is less likely to have been affected by a preservational bias effect (Hawkesworth et al., 2010).

2.2.2. Mantle evolution:

Intrinsically linked to crustal evolution is the concept of mantle depletion. In order to form the continental crust, its constituent material had to be extracted from the mantle through partial melting. Partial melting preferentially extracts incompatible elements from the mantle, i.e. the LILE, which preferentially partition into silicate melts. This results in the creation of two complementary geochemical reservoirs (Figure 2.2.6); the enriched crust, and the depleted upper mantle reservoir (e.g. DePaolo, 1981, Bennett, 2003, Hawkesworth and Kemp, 2006). The minerals formed by the silicate melts predominantly have a low density resulting in the continental crust being relatively buoyant and less susceptible to recycling in comparison to oceanic crust (e.g. Cawood and Hawkesworth, 2013, Mole et al., 2013), which is later formed from the re-homogenised residual depleted mantle reservoir after crustal extraction (Hofmann, 1988). On modern day earth, oceanic crust in the form of mid-ocean ridge basalt (MORB) is sampled from the depleted mantle reservoir (Hawkesworth et al., 2010). It is important to note that the depleted mantle reservoir does not encompass the entire mantle, but only the portion of the mantle that has been a part of the differentiation process of crustal extraction. This leaves the possibility that some depleted sections are more depleted than others, or that a large proportion of the mantle (particularly the lower mantle) might still be primitive in nature. An example that highlights this complexity is that we know there are still enriched mantle reservoirs which are seen to source some oceanic island basalts today, e.g. the Azores (Widom et al., 1997). This poses the question of how the depleted mantle reservoir evolved, i.e. mantle evolution.

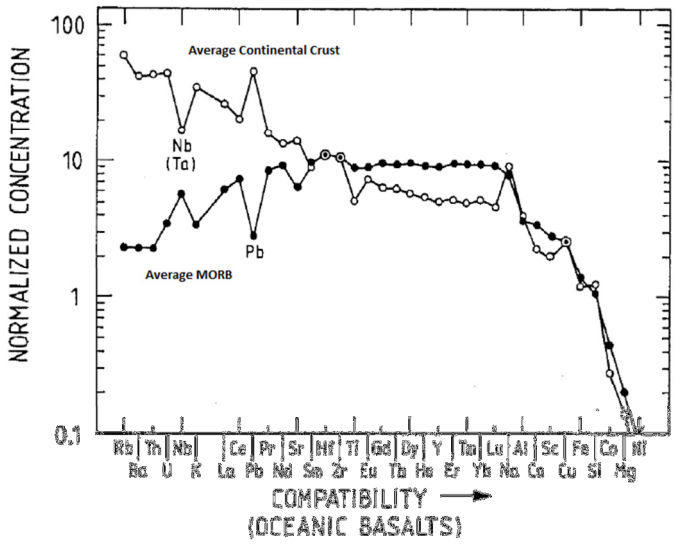


Figure 2.2.6: Normalised element concentrations of average continental crust and MORB. Note the average continental crust is roughly a mirror image of MORB for the incompatible elements (Hofmann, 1988).

The timing of creation of this depleted mantle is modelled to have occurred early in Earth's history (e.g. Kamber et al., 2003, Frei et al., 2004, Shirey et al., 2008). One explanation for this is that crustal formation was already underway soon after Earth's formation, and the extraction of this crust caused the formation of the depleted mantle. Mantle depletion is in fact the main evidence used for significant crustal formation having occurred in the Hadean without a direct geological record of this (e.g. Armstrong and Harmon, 1981, Harrison et al., 2005), and even if this Hadean crust was later destroyed, it would leave a legacy of corresponding depletion in the upper mantle (Cawood et al., 2013). Alternatively, it is possible that early mantle depletion could have been caused by partitioning of the mantle into an early enriched reservoir and a depleted mantle reservoir without the need to form crust, thus allowing models inducing a later crustal extraction (Tolstikhin et al., 2006). This two stage extraction model would mean that the evolution of the depleted mantle has no direct link to crustal extraction (Hawkesworth et al., 2010). It is however generally accepted that the depletion did occur synchronously with, or within a short period following, formation of overlying crust (Pearson, 1999). Formation of the SCLM which has allowed preservation of Archean cratons through to the modern day is also attributed to mantle depletion; however it is still debated as to how and when exactly this happened relative to crustal extraction (e.g. Davis et al., 2003, Rollinson, 2010).

One problem with the presence of a depleted mantle source in the Archean is that there are almost no Archean greenstone belts with HFSE ratios similar to MORB, i.e. those which display a depleted geochemical signature (Condie, 2005). There are a number of theories as to why this is. The depleted source in the upper mantle may have been absent or small during the Archean, and the depleted mantle as evidenced through isotopic models perhaps resided in the deep mantle

only contributing to the extrusion of mantle plume derived rocks (Condie, 2005). This theory is aided by the fact that depleted signatures are sourced from the mantle plume beneath Iceland today (Fitton et al., 1997). Most geological models however agree that the Archean deeper mantle was less depleted or enriched compared to the upper mantle (e.g. Roy, 2002, Polat et al., 2011, Kamber, 2015). If so, this deeper mantle could have re-fertilised the depleted mantle by upwelling through plumes or convection (e.g. Polat et al., 2011, Kamber, 2015), or plumes with an enriched signature themselves could have been the major source of rocks in the Archean (e.g. Macdougall, 1988, Roy, 2002). Evidence for mantle re-enrichment can be seen in different ways, e.g. mantle xenoliths record the process of the depleted mantle being re-fertilised by metasomatism or melt enrichment (Rollinson, 2007), and rocks with an enriched mantle plume source are found in the Pilbara Craton (Van Kranendonk et al., 2007a). Interestingly, in the Pilbara Craton there are also rocks with a depleted mantle source that progressively becomes more depleted through time, suggesting small isolated mantle reservoirs were present (Van Kranendonk et al., 2007a). Further models which could lead to the formation of rocks with an apparent enriched signature include widespread crustal recycling, which would re-enrich the depleted upper mantle, or newly erupted greenstones becoming contaminated during their ascent through a thin continental lithosphere (Tomlinson et al., 2003). If it is the case that the enriched signature is attained through crustal contamination, the prevalence of an enriched signature in Archean greenstone belts worldwide would suggest that the continental lithosphere was extensive, which also links back to the formation of the depleted mantle in the first place.

In order to elucidate which source was utilized, i.e. a depleted mantle source or an enriched source (crustal or mantle), and the time at which the melt was extracted from this source, geochemical fingerprinting and isotopic systems can be used (Hofmann, 1988). The preferred methods used are Nd, Pb and Hf isotopes, REE patterns and trace element ratios (e.g. Nb/Th) (e.g. Condie and Benn, 2006, Babechuk and Kamber, 2011, Khanna et al., 2014). In order to calculate the timing of extraction, model ages are calculated as described in chapter 2.2.1.3. A problem with this method however is that the model age calculation is dependent on the depleted mantle evolution line calculated for a particular isotopic system. The depleted mantle evolution lines used for age calculations assume a constant evolution of the depleted mantle through time (e.g. Nd isotope evolution line (DePaolo and Wasserburg, 1976), Hf isotope evolution line (Griffin et al., 2002) and Pb isotope evolution curves (Kramers and Tolstikhin, 1997)). However, if mantle processes were more complex and there was an open connection between the lower mantle and the depleted upper mantle, the volume and/or composition of the depleted mantle reservoir could vary due to mixing of different reservoirs over time. For example, if there was replenishment from an enriched mantle source, e.g. the re-fertilisation of the depleted upper

mantle, or there were smaller uncoupled depleted reservoirs with different degrees of depletion (due to different volumes of crustal extraction) then these evolution lines will not be representative of the true state of the depleted mantle. This could result in both the calculation of incorrect depleted mantle model ages, and the assumption rocks are sourced from recycled crust when in fact they could be new crustal additions exhibiting isotopic fingerprints from an enriched mantle source (e.g. Babechuk and Kamber, 2011, Kamber, 2015). As is the case when modelling crustal evolution as well as many other geological systems, by using a combination of techniques together, a greater degree of certainty can be achieved. An example of this is the fact that the Pb isotope mantle depletion evolution curve is not applicable to rocks from the Flin Flon Belt, Canada (Figure2.2.7). This could have been interpreted as the rocks having not been sourced from the depleted mantle; however they exhibit strong Light REE depletion which is not possible through crustal contamination or having formed from an enriched source (Babechuk and Kamber, 2011). In order to rectify this problem with depleted mantle evolution lines, Kamber (2015) suggests that geochemical data from unaltered igneous rocks with a demonstrable depleted mantle origin and insignificant crustal contamination should be collated and made available to the geochemical community. This will hopefully result in a more accurate understanding of mantle evolution which will both aid in calculating accurate model ages and might also help to constrain when continental crust was generated.

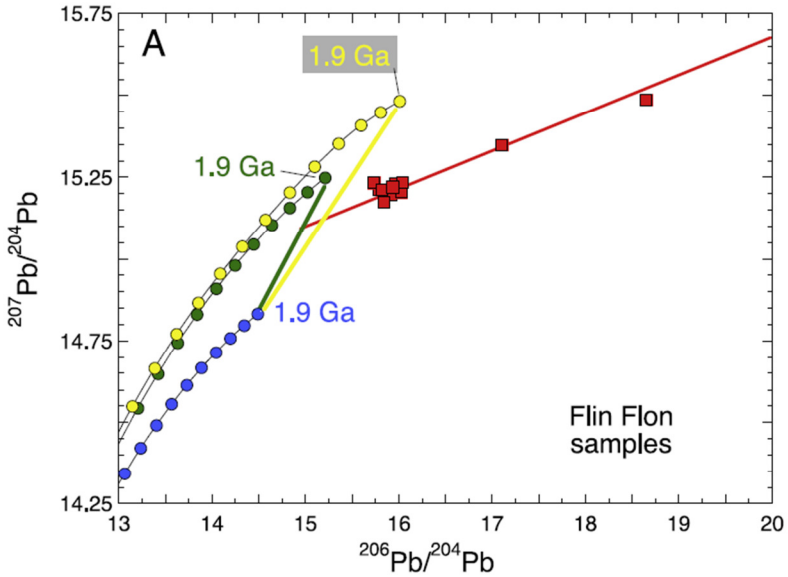


Figure 2.2.7: Pb isotope systematics from 1.9 Ga Flin Flon depleted rocks do not intercept the depleted mantle evolution line (blue circles) of Kramers and Tolstikhin (1997) at 1.9 Ga. Also shown are the primitive mantle evolution line (green circles) of Kamber and Collerson (1999), the average sediment composition (yellow circles) of Kramers and Tolstikhin (1997), and hypothetical mixing lines between these evolution lines. All evolution lines are shown in 100 Ma steps (Babechuk and Kamber, 2011, Kamber, 2015).

2.3. Plate tectonic evolution:

The range of lithologies found in granite-greenstone terranes were discussed in chapter 2.1, along with a number of possible settings in which they could have formed. The formation processes of granite-greenstone terrane lithologies are intrinsically linked to global tectonics that were active at the time. The tectonic processes active during the Archean and Hadean form one of the greatest debates in early Earth geology. The origin of Archean granite-greenstone terranes has been strongly debated in the literature for decades (e.g. Condie, 1981, de Wit and Ashwal, 1997, Cawood et al., 2006, Bédard et al., 2013, Kamber, 2015), and the debate on this subject does not appear to be reaching a consensus. Increased geochemical, geochronological and geophysical data have resulted in a great advancement in what is known of granite-greenstone terranes; however this increased data set has not resulted in the construction of a single conclusive model, with new data each year appearing to help confirm multiple different theories. The fact that most greenstone belts are severely tectonised, recognising possible different tectonic environments and reconstructing them is an extremely difficult task (Hunter and Stowe, 1997), and de Wit (1991) stated that "*a single tectonic environment applicable to greenstone belts does not exist; different tectonic environments can be found within and amongst greenstone belts.*" The greatest debate involving the evolution and formation of granite-greenstone terranes therefore is that of the tectonic processes that were responsible for their formation. If this question relating to the tectonic styles that were active on the early Earth can be resolved there will be a much improved understanding of Archean geodynamics (Condie and Benn, 2006). There are a number of ways this debate can be described; subduction vs sagduction, horizontal tectonics vs vertical tectonics, uniformitarian vs non-uniformitarian. All of these pose the exact same question; did the same tectonic model that we see today, i.e. the Wilson cycle (Wilson, 1966), with sea-floor spreading, subduction and collision, operate throughout Earth's history, or was a different tectonic model responsible for crustal formation and destruction for at least part of the early Earth? The reason this debate has focussed on granite-greenstone terranes is due to the fact that these are so widespread throughout the Precambrian rock record, with > 260 known worldwide (Kusky, 2004), whereas they are absent from the Phanerozoic rock record, with no evidence of any modern day granite greenstone terrane formation currently taking place. This leads to the question of whether or not the plate tectonic system active today was underway during the Precambrian, and if it was, what has changed, and when, to prevent the formation and/or preservation of granite-greenstone terranes.

2.3.1. Horizontal tectonics:

Plate tectonics are a vital process in controlling several aspects of the Earth as we see it today. It is the major mechanism in releasing heat from the Earth's interior and controls the interface between surface and deep Earth processes (Turner et al., 2014). Modern day plate tectonics are universally agreed to be those of the Wilson cycle (Wilson, 1966) (Figure 2.3.1), and are generally classified as horizontal tectonics. That is, the formation of crust at mid ocean ridges, mantle hot-spots, and island arc settings, the convergence of crust at continental collision zones, i.e. the site of major orogenies, and the destruction of crust at subduction zones. The process is largely driven by subduction as the dominant driver, which recycles lithosphere back into the mantle (Furnes et al., 2014). There are other smaller, yet not insignificant processes also known to be involved in modern day plate tectonics, e.g. delamination can destroy crust without subduction, as is occurring beneath the modern day Himalaya (Chung et al., 2003). The proportions of crust modelled to be formed and destroyed in these respective settings are diagrammatically portrayed by Cawood et al. (2013) (Figure 2.3.2).

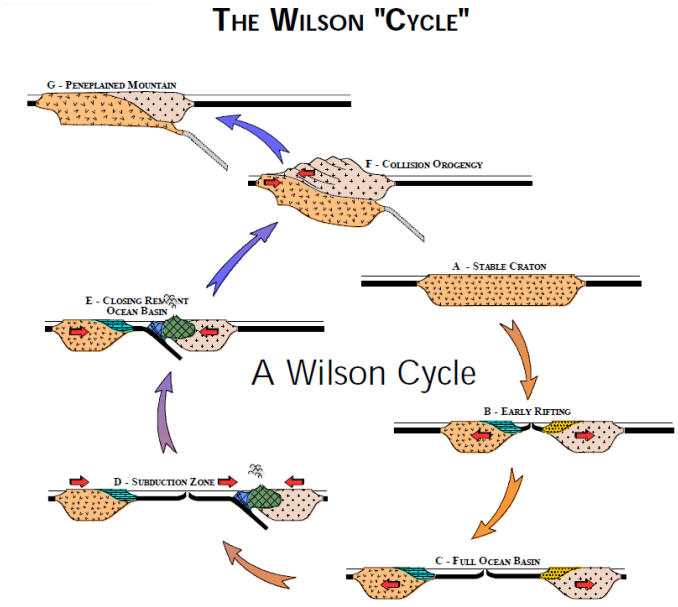


Figure 2.3.1: The Wilson Cycle (Wilson, 1966, James Madison University).

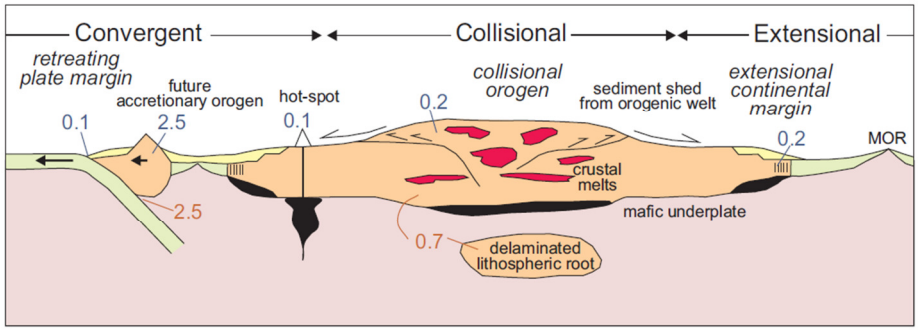


Figure 2.3.2: Schematic cross section of plate boundaries highlighting estimated volumes (in km^3yr^{-1}) of crust formed (blue) and destroyed (red) (Cawood et al., 2013).

2.3.2. Vertical tectonics:

Granite-greenstone terranes of the East Pilbara Craton form large ovoid exposures of TTG and granite domes, separated by thin linear greenstone belts, composed of volcanic and sedimentary rocks and (Figures 2.1.4, 2.3.3). The presence of banded iron formation in the greenstone belts highlights this relationship even more so through aeromagnetic imagery (Figure 2.3.4). A number of terms are associated with this stratigraphy; 'dome and keel' architecture is a name given to the stratigraphy as we see it today, and the processes involved in its creation include models of 'partial convective overturn' (Van Kranendonk, 2011), and 'sagduction' (Macgregor, 1951, Goodwin, 1977), however to generalise as well as to differentiate it from modern day horizontal tectonics, it can be classified as 'vertical tectonics'. The East Pilbara Craton is the best documented example of vertical tectonics, as there are a number of important features preserved that have allowed the dome and keel model to be developed (Van Kranendonk et al., 2004). The greenstone belts that wrap around the granitic domes display a well preserved stratigraphy, which is also laterally continuous (Collins et al., 1998). This lateral continuity highlights that greenstone belt volcanic and sedimentary rocks must have at one stage been more extensive, covering the entirety of the region before emplacement of granitoid plutons. Along with outcrop geology, there are many kinematic indicators that point towards vertical as opposed to horizontal displacement and strain in granite-greenstone terranes. In East Pilbara both strain patterns and fold geometry suggest that the greenstones sank vertically with respect to TTG plutons (Collins et al., 1998). It should be noted however, that even given the extensive evidence supporting vertical tectonics in the East Pilbara Craton some studies still argue for a horizontal tectonic model here (e.g. Zegers et al., 1996, Kloppenburg et al., 2001). Further strong evidence for vertical tectonics in granite-greenstone terranes is provided by vertical shearing in supracrustal rocks in the Dharwar Craton of India where lineations converge towards triple points, and the supracrustal rocks show downward displacement with respect to the TTG basement (Bouhallier et al., 1995) (Figure 2.3.5).

Contrastingly, for example, the Yilgarn Craton of Australia exhibits craton scale parallel high strain zones, elongate granitic bodies and dismembered greenstone belts (Zibra et al., 2014), more in resemblance to Phanerozoic orogenic belts and modern subduction-accretion models than the vertical tectonics of the East Pilbara Craton. This could be due to a shift in tectonic processes during the Meso-Neoarchean, or alternatively perhaps there has been less tectonic reworking in the East Pilbara Craton resulting in the original dome and keel architecture being well preserved.

Although it contains the most compelling field data, it is not only the Pilbara Craton in which there is evidence for vertical tectonics. Other examples include the Dharwar Craton in India, as

mentioned above, (Bouhallier et al., 1995), and the Superior Craton in Canada (Kamber, 2015). These examples highlight that there is a valid geological basis for proposing a different tectonic system operated extensively during the early Earth compared to modern day horizontal tectonics. This leads to the question of whether there is a suitable model that could both accommodate these observations while also incorporating other known features of granite-greenstone terranes that are not present in modern day environments, e.g. komatiites.

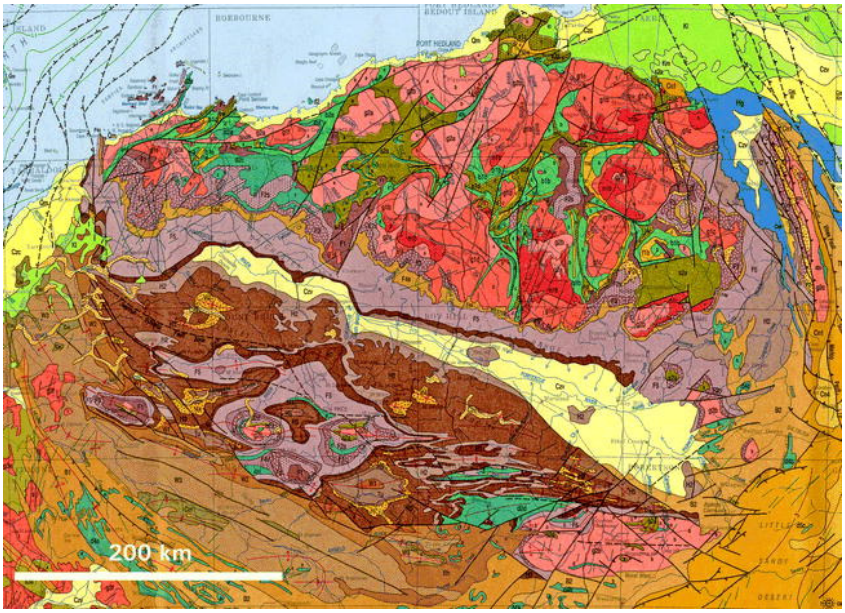


Figure 2.3.3: Geological map of Pilbara Craton (Geological Survey of Australia).

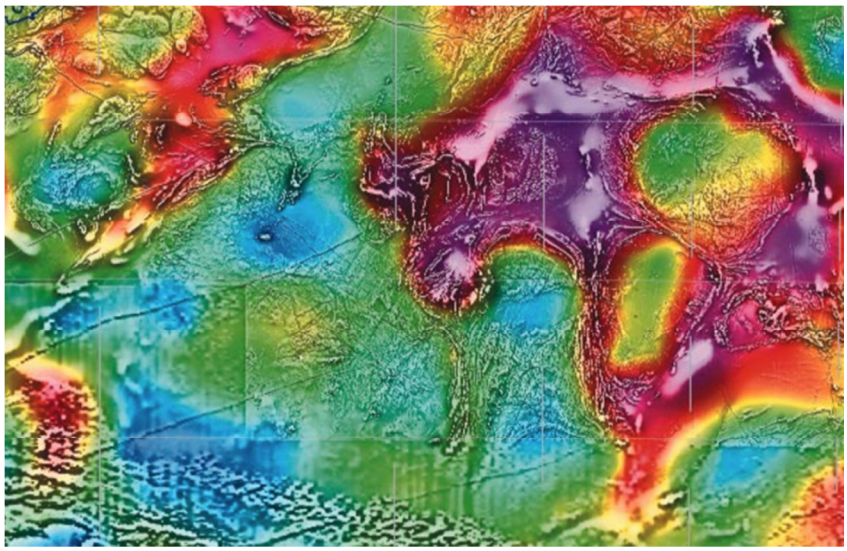


Figure 2.3.4: Aeromagnetic image of Pilbara Craton (source unknown).

The model for partial convective overturn is generally agreed as the best model to explain vertical tectonics. Partial convective overturn involves an initial stage of the greenstone volcanic rocks being deposited in a similar style to a modern day oceanic plateaux or LIP as discussed in chapter

2.1.3.1. When thick enough, the lower crust, whether this is an underlying sialic basement or the base of the LIP, will start to partially melt and fractionate due to high pressure and temperature, forming TTG plutons. This process would be promoted by the presence of a mantle plume through the addition of anomalous heat to the crust. Melting at the base of the LIP would also be aided if the volcanic rocks were erupted onto a sialic basement, as this would result in the burial of heat-producing older granitoid rocks which are rich in U-Th-K relative to the overlying greenstones. Melting at the base of an LIP would create a gravitational instability in the crust, as relatively cool and dense mafic to ultramafic volcanic rocks would overlie warmer less dense TTG rocks resulting in the volcanics sinking into the TTG plutons, or partial convective overturn. The reason it is only partial, and not full, is that if and when the rising plutons were to reach the surface, there would no longer be a thermal buffer and so the convective cell will cool and overturn will cease. Depending on the extent of later erosion, different crustal sections will later be exposed, such as those in the East Pilbara Craton, or those in the Dharwar Craton, and a relative lack of subsequent tectonic activity can allow these to be relatively well preserved. This process of partial convective overturn has been modelled by Mareschal & West (1980), and subsequently modified and expanded to explain many different granite-greenstone terrane formations (e.g. Bouhallier et al., 1995, Collins et al., 1998, Van Kranendonk et al., 2007b, Bédard et al., 2013, Kamber, 2015) (Figure 2.3.5).

Many tectonic models are based on vertical tectonics; some to explain specific granite-greenstone terranes, and others to provide a general model for granite-greenstone terrane formation. Each model has slight differences in approach, or gives an alternative interpretation on one or more geological aspects, however rather than explaining in depth the differences between the models, a number of them are presented in Appendix 1, with the important observation being that all illustrated models use vertical tectonics to explain the formation of one or more granite-greenstone terranes.

2.3.3 The onset of modern day plate tectonics:

The question of whether or not modern day plate tectonics has operated throughout Earth's history may appear in the first instance to be a simple yes/no question, however no matter what the answer to this question is, the Wilson cycle had to initiate at some point. This poses the more complicated question of 'when did modern day plate tectonics start?' Arguments have been presented for a number of possible periods in Earth history for the initiation of modern day plate tectonics, from the Hadean right through to the Proterozoic. Many of these theories are strongly linked to crustal evolution, a theme which was discussed in chapter 2.2.1.

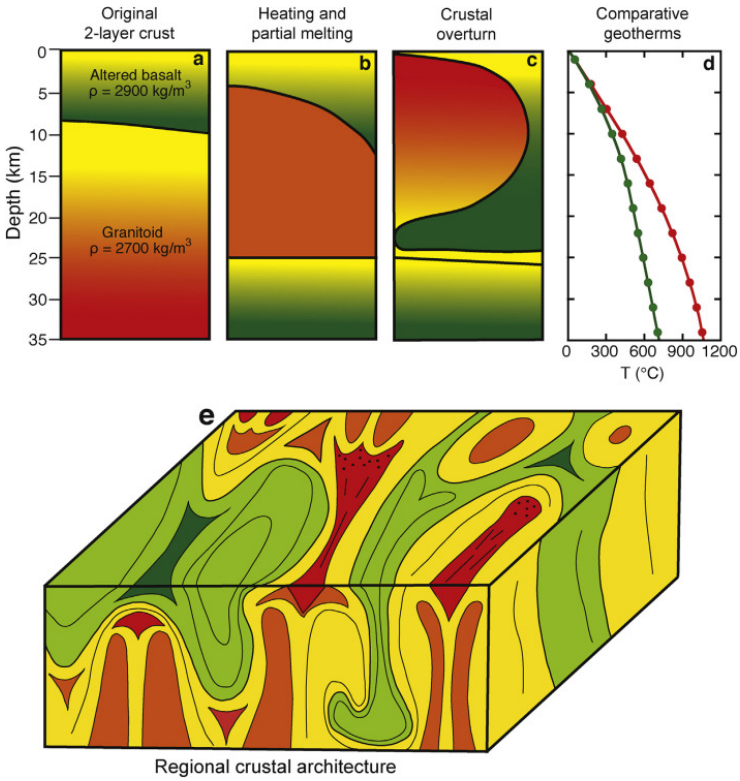


Figure 2.3.5: Diagram indicating the process of partial convective overturn and the resulting crustal architecture as seen in the Dharwar Craton. Green represents relatively cool greenstone volcanic rocks; red represents relatively hot TTG plutons (Bouhallier et al., 1995, Kamber, 2015).

2.3.3.1. Hadean:

In chapter 2.2.1.4 dealing with crustal formation it was discussed that the Jack Hills zircons, dated ~4.4 Ga, are the oldest physical record of when crustal rocks almost certainly existed. These zircons are presumed to have been formed in a felsic rock through the partial melting of an ultramafic to mafic crust, and so this is often used to infer that there must have been an ultramafic to mafic crust before ~4.4 Ga, and that by ~4.4 Ga there were probably the first small felsic continents present on the Earth's surface (Hawkesworth et al., 2010). If the only way of creating first cycle felsic rocks is through the melting and enrichment of mafic rocks in island arc settings, then this would imply that modern day plate tectonics have been active since > 4.4 Ga. It could be argued that allowing time for an initial mafic crust to form, then this represents modern day plate tectonics having existed throughout the Earth's history. There are however other models proposed for the formation of felsic crust without the need for subduction, which are described below, and so the presence of these zircons alone cannot be used to infer that plate tectonic processes were active in the Hadean. It is also worth noting that there are other theories behind the formation of the Jack Hills zircons that do not include continental crust at all, for example the zircons may have formed in the melt sheet created by a bolide impact (Marchi et al., 2014), or small volumes of felsic rocks may have been formed within a dominantly mafic crust due

to the partial hydrous melting of this crust (Rollinson, 2009). It would therefore be erroneous to unequivocally state that modern day plate tectonics existed in the Hadean solely through the presence of the Jack Hills zircons.

Although no direct dating of rocks older than 4.02 Ga (Acasta Gneisses) (Bowring et al., 1989) has been achieved, it has been suggested that the Nuvvuagittuq supracrustal belt in Canada contains 4.4-4.3 Ga old rocks through Sm-Nd isochron ages (O'Neil et al., 2012). This would make it the same age as the lunar crust, and likely related to the lunar impact. Further studies on the Nuvvuagittuq supracrustal belt rocks have suggested that they contain a subduction related signature, and therefore imply that subduction did in fact occur throughout the Earth's history, or at least very shortly after its formation (Turner et al., 2014). The weaknesses in this example however involve the dating of the rocks themselves, with the Nd isotope system in these rocks possibly containing an older component resulting in the 4.4-4.3 Ga isochron ages being inaccurate (Cates et al., 2013), while intruding TTG rocks have been dated between 3.8 Ga and 3.6 Ga (O'Neil et al., 2012). No matter when the Nuvvuagittuq supracrustal rocks were formed, the evidence that they possess subduction like REE signatures is used to infer active subduction (Turner et al., 2014).

2.3.3.2. Eoarchean:

The transition between the Hadean and the Eoarchean in the rock record is marked by Earth's oldest preserved rock outcrop; the Acasta Gneiss in northwest Canada, dated to 4.02 Ga (Bowring et al., 1989). These rocks may have been formed in a setting similar to Iceland today (i.e. an oceanic plateau with anomalously thick mafic crust) (Reimink et al., 2014), however ~4.0 Ga is also suggested as a possible time for the onset of subduction (Nebel et al., 2014) even although it is acknowledged that there is no physical evidence in favour of subduction until 3.9 Ga. This is the time of the formation of the Isua greenstone belt in Greenland, dated between 3.9 Ga and 3.8 Ga (Furnes et al., 2007).

The Isua greenstone belt is one of the strongest pieces of evidence used to imply that subduction was active by the Eoarchean. The rocks here have been interpreted by some to be supra-subduction zone ophiolite sequences, including the sheeted dyke complex missing from many other Archean greenstone belts (Furnes et al., 2007, Friend and Nutman, 2010, Furnes et al., 2014), thus requiring active subduction in order to obduct the sea floor onto continental crust. Some later studies have however argued that there is not enough evidence that these rocks represent an ophiolitic sequence, and in fact that the dykes may not even be Eoarchean in age

(Nutman et al., 2007a). As well as an ophiolitic sequence, some rocks in the Isua greenstone belt have been interpreted as a preserved accretionary prism (Komiya et al., 1999), again suggesting subduction as the active tectonic mechanism in their formation. Geochemical studies also show three of the oldest greenstone complexes (Nuvvuagittuq, Isua and Southern Iron Ore Group (the latter from the Singhbhum Craton of NE India)) to possess subduction influenced geochemical signatures (Furnes et al., 2014). In order to explain the lack of fully preserved ophiolite sequences in the Archean, the topic of a hotter Archean mantle is discussed. A higher rate of convection in a hotter mantle would have resulted in a faster spreading of the plates at mid ocean ridges. If this rate outweighed the ability for new melt to be produced at spreading centres then the sheeted dyke complex would not have been formed in the same way as today, hence its lack of preservation (Hargraves, 1986, Robinson et al., 2008). Needless to say, the argument against greenstone belts representing ophiolitic sequences is that the lack of complete ophiolite sequences (and accretionary prisms) in Archean greenstone belts is taken as evidence to suggest that subduction was not in existence in the Eoarchean (e.g. Bédard et al., 2013, Kamber, 2015).

2.3.3.3. Paleoarchean:

The Paleoarchean is the time at which the first preservation of large scale geological terranes occurs, including both the Pilbara Craton in Australia, and the Kaapvaal Craton in South Africa. The preservation of these terranes is likely due to the first SCLM keels being formed at this time (Smithies et al., 2005), and there do not appear to be any models that predict a Paleoarchean start to modern day plate tectonics. This is likely due to the fact that there is no direct evidence seen in Paleoarchean rocks that is not also seen in Eoarchean rocks e.g. Isua, and so either subduction was active since at least the Eoarchean, or was not underway until after the Paleoarchean.

2.3.3.4. Mesoarchean:

A number of studies suggest that modern day plate tectonics began around 3.0 Ga. The most convincing evidence for this is presented by Shirey and Richardson (2011), who note that this is when the first eclogite inclusions are found in diamonds. Eclogites are metamorphic rocks formed in high pressure environments, generally from a mafic protolith. The environment which can most easily transport mafic rocks to great enough depths is subduction, and so eclogites are commonly used as an indicator of this process. The fact that no eclogites older than 3.0 Ga have been found can be used as evidence against earlier subduction, although it is possible that these were formed in subduction zones > 3.0 Ga, but were unable to be transported to the Archean shallow crust. It

is also possible however for eclogites to form in other environments, for example mafic rocks can be buried to great depths in large igneous provinces, with pressures great enough to allow the formation of an eclogitic restite (Rollinson, 1997), and so a later onset to modern day plate tectonics cannot be ruled out using this model. Some isotopic studies on zircons related to crustal growth have highlighted that there appears to be a decrease in the rate of crustal growth at 3.0 Ga (e.g. Cawood et al., 2006, Dhuime et al., 2012). It is suggested that rather than a decrease in the rate of crustal formation at this time, it could in fact represent the onset of a means by which crust can be destroyed at an increased rate. The method of this destruction is proposed to be the onset of subduction and modern day tectonics.

By the Mesoarchean, a number of granite-greenstone terranes that are both expansive, and well preserved, were fully formed. These include the Pilbara Craton in Australia, and the Kaapvaal Craton in South Africa. The Pilbara Craton is famous for its preservation of classic dome and keel stratigraphy, commonly used as evidence for vertical tectonics as the driving factor to its formation. Technically though, the famous dome and keel stratigraphy is part of the East Pilbara Craton. It has been postulated that the contact between the East Pilbara Craton and the West Pilbara Superterrane, geologically different from one another, is a preserved suture zone, indicating subduction at 3.09-3.07 Ga (Van Kranendonk et al., 2007b). There is also evidence for earlier arc accretion forming a large part of the East Pilbara Terrane (Appendix 1c) (Van Kranendonk et al., 2010). At a similar time period, between 3.23 Ga and 3.08 Ga, structures in the Kaapvaal Craton have been interpreted as those of subduction related sutures and preserved accretionary prisms (e.g. de Ronde and de Wit, 1994, Moyen et al., 2006). These constitute the progression from largely geochemical evidence and small scale geological evidence, to large scale geological evidence for the presence of active subduction. It should be noted here that this evidence for modern day plate tectonics being the driving force is not universally accepted, with some authors arguing that structures interpreted as suture zones could have formed through other tectonic models, and are not unequivocal evidence for subduction (Bédard et al., 2013).

2.3.3.5. Neoarchean:

By the Neoarchean, the rock record had expanded massively due mainly to crustal formation events; however whether these are first order crustal formation events or crustal recycling events is not so clear. Either way there was less crustal recycling of Neoarchean rocks, and a number of stable Archean cratons were formed as preserved today. Cratons formed, or stabilised at this time include the Superior Craton of Canada and the Yilgarn Craton of Australia as two prime examples. This more extensive Neoarchean rock record allows plentiful studies to be carried out on

Neoarchean rocks, including determining whether they were formed through horizontal or vertical tectonic processes. The metamorphic record shows the first evidence for eclogite metamorphism (whole rock, as opposed to the eclogite micro-inclusions found in diamonds discussed earlier in relation to the Mesoarchean), associated with subduction, at around 2.7 Ga, adding another line of evidence towards subduction being active at this time (Brown, 2006, Crowley et al., 2015). An age of ~2.7 Ga is in agreement with formation of the first widely accepted supercontinent formation occurring soon after; that of the Superia and Sclavia supercontinents (Bleeker, 2003). There are however still studies which do not support horizontal tectonics as the active tectonic mechanisms during the Neoarchean. A prime example of this is the debate surrounding the Abitibi greenstone belt in the Superior Craton. For many years the favoured model for this terrane was that of the accretion of a number of allochthonous arc and oceanic plateaux terranes amalgamated through repeated subduction and collision tectonics (e.g. Polat and Kerrich, 2001, Desrochers et al., 1993, Kimura et al., 1993). More recent studies however have suggested that these are not tectonic terrane boundaries, but are all part of the one autochthonous volcanic sequence, that of an oceanic plateaux (e.g. Ayer et al., 2002, Benn, 2006, Kamber, 2015), though even in this model it has been suggested that plate tectonics could still have been active at the time (Benn et al., 2009).

Should any of the above timings be correct for the start of modern day plate tectonics, there is still a major question posed. Why do we not see granite-greenstone terranes after the Neoarchean-Proterozoic boundary, even although they are widespread before this time? This is the argument used by Bedard (2006) to propose that subduction began at around 2.6 Ga, after which granite-greenstone terranes cease to appear in the rock record.

2.3.3.6. Proterozoic:

The final era in which modern day plate tectonics have been proposed to have been initiated is the Neoproterozoic. This is on the basis that the presence of true ophiolite sequences, as well as blueschist facies metamorphic rocks and ultra-high pressure metamorphic terranes are required as evidence for subduction, are not fully preserved until the Neoproterozoic (e.g. Stern, 2005, Hamilton, 2011). It is certain that by this time the Wilson plate tectonic model was fully established.

2.3.4. Alternative models:

As discussed above there are many arguments for different periods in Earth history at which vertical tectonics may have ceased and horizontal tectonics may have been initiated as the main

driving tectonic force. Rather than this being a single catastrophic event that led to the switch in systems, a number of studies have suggested a more gradual change over time, with both systems operating together over a transitionary time period. François et al. (2014) found that there is no incompatibility between subduction and sagduction, with both able to exist simultaneously. Moyen and van Hunen (2012) proposed that Archean subduction was episodic in nature, with successive 'stop and start' events before Earth's convective system matured sufficiently to allow the operation of stable subduction. If there were horizontal tectonics in the earlier Archean, as an alternative to full subduction it is possible that downgoing crust detached through slab break off, drips, or delamination which would lead to a 'stop and start' system as opposed modern day continuous plate tectonics (van Hunen and van den Berg, 2008). Greya et al. (2015) produced a model for episodic subduction which could have been active during the Mesoarchean, the subduction being initiated by the presence of a mantle plume beneath oceanic crust, similar to the Caribbean Large Igneous Province today. It is proposed that these episodes of subduction, or lithospheric drips, related to mantle plumes could provide the link between a largely static lithospheric lid pre-plate tectonic Earth, and modern day plate tectonics. One theory by which stop start subduction developed into continuous plate tectonics is the final breakdown of a mechanical barrier in the uppermost lower mantle. The breakdown of this barrier then allowed recycling of slabs into the lower mantle at the Archean-Proterozoic boundary, as well as re-fertilisation of the depleted upper mantle (Davies, 2008, Kamber, 2015).

One of the more favourable alternative models for Archean tectonics, used to explain the differences between Archean and modern day rocks, is that of shallow subduction. There are not many dissimilarities in principle between modern day tectonics and shallow subduction tectonics, with the only difference being that instead of relatively steeply dipping slabs as seen today, the downgoing slabs descend at shallow angles beneath the overriding palate (e.g. van Hunen and Moyen, 2012, Hynes, 2013). The theory behind this model is that the result of a hotter upper mantle would have been a higher degree of partial melting at oceanic spreading centres. This would have created a thicker oceanic crust as well as a thicker depleted region of the upper mantle (Sleep and Windley, 1982). Modern day plate tectonics are driven by slab pull, with the gravitational pull from dense slabs providing approximately 90% of the driving force (Forsyth and Uyeda, 1975), requiring the negative buoyancy provided by the thin cool dense oceanic lithosphere. A thicker oceanic lithosphere would have been buoyant, so much so that it could have become difficult to subduct (Davies, 1992), which would have led to the development of shallow subduction (Vlaar et al., 1994). This model appears to be a compromise that allows proponents of Archean subduction to argue that subduction has occurred throughout Earth's

history, while also accepting that some small differences did occur, primarily due to the fact that the Archean mantle was hotter than today.

The outcome of shallow subduction could have been the tectonic imbrication of oceanic crustal terranes as a method of forming granite-greenstone terranes (Nutman et al., 2007b) (Figure 2.3.6). It could also be used to explain the common occurrence of TTGs representing modern day adakites, as shallow subduction would have resulted in the absence of, or at most a much thinner mantle wedge, and so the resulting rocks would be derived from the partial melting of oceanic crust as opposed to the partial melting of a mantle wedge like today (Smithies, 2000). It has also been argued however, that in shallow subduction, mantle heat flow is depressed and so there is insufficient heat to initiate melting of the downgoing slab (Van Kranendonk et al., 2007b). In addition to this it has been argued that shallow subduction is not viable, for if the oceanic lithosphere was as buoyant as models suggest, the crust would be almost unsubductable resulting in no driving force for subduction to initiate (van Hunen et al., 2004, van Hunen and Moyen, 2012).

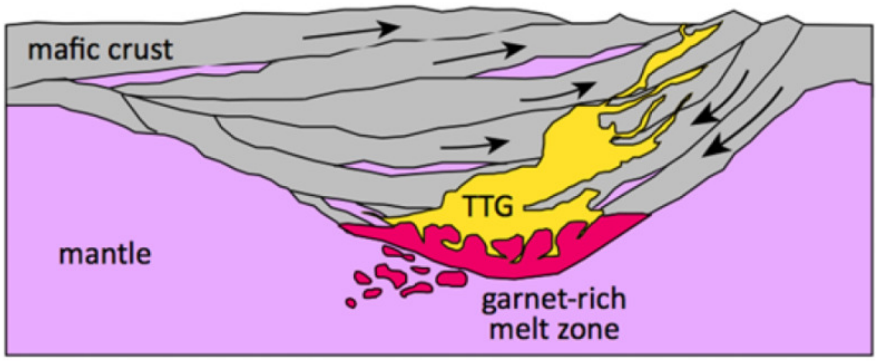


Figure 2.3.6: Tectonic imbrication at convergent plate boundaries due to shallow subduction (Roberts et al., 2014).

Some alternative models have been suggested as a means to explain certain features found in granite-greenstone terranes. One of these is 'pop-down tectonics'. This model attempts to explain how the vertical features seen in greenstone belts could have formed in horizontal tectonically driven system (Gapais et al., 2014) (Figure 2.3.7). A weaker SCLM would allow the displacement needed by horizontal shortening to be accounted for in a downwards motion, as opposed to upwards motions seen in mountain building orogenies today.

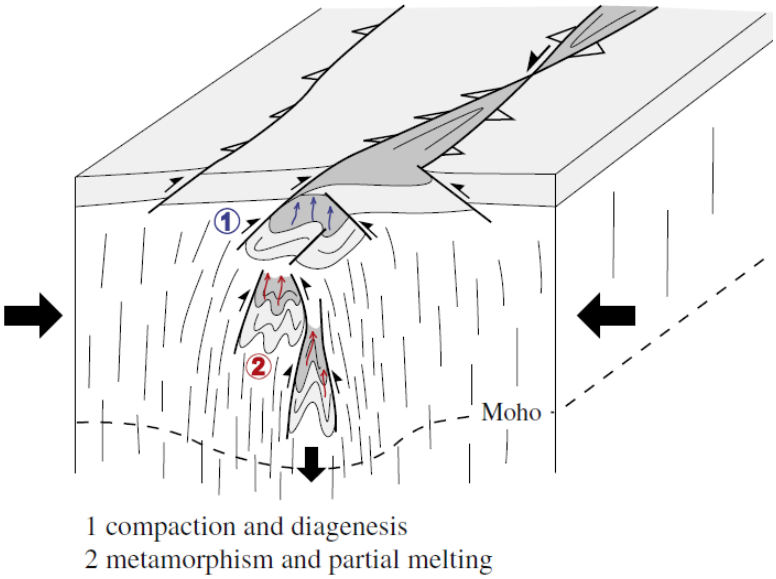


Figure 2.3.7: Model of pop-down tectonics (Gapais et al., 2014).

A further model proposes that greenstone belts formed through the accretion of cratonic keels that drifted into one another, and there was no need for subduction to account for the horizontal amalgamation of continents (Bédard et al., 2013) (Appendix 1d). The driving force behind this is suggested to have been a 'mantle wind', i.e. the force of convecting currents in the mantle (Davies, 1993). The mantle wind is proposed to be a factor on modern day Earth in India, as the Indian continent is still moving north ~50 Myrs after accretion (Becker and Faccenna, 2011), and so it could have been a stronger factor in a hotter Archean with more intense mantle plume activity.

Finally, it is important to raise again that should there not have been subduction throughout the Archean, there must have been a transition to modern day tectonics at some point in the Earth's history. This brings forward the model of episodic subduction through repeated slab-break off, or drips of subducted crust as opposed to continuous subduction. Some possible theories for this are that weak subducting slabs may not have been strong enough to hold their own weight (van Hunen and Moyen, 2012), or that mantle plume activity in the Archean resulted in an increased number of unsubductable oceanic LIPs temporarily halting plate subduction (Condie, 2001). An important point to note with regards this latter model is that repeated slab break off would not allow back arc basins to form. Back arc basins are one of the main settings in which greenstone belts are proposed to have formed should modern day tectonics have been active in the Archean, and so greenstone belts could probably not have been formed in this way until prolonged continuous subduction was established. Possible examples of episodic subduction have been proposed in the Superior Craton (Benn and Moyen, 2008) and the Kaapvaal Craton (van Hunen

and Moyen, 2012) where arc-like rocks appear to form in an episodic nature of 5-10 Myrs, separated by episodes of plume volcanism. However, due to the necessity to have an environment that allows both subduction and mantle plumes to interact a complicated tectonic model would be required, and the general debate of whether vertical or horizontal tectonics were present is more relevant to answer this query.

2.3.5. Horizontal versus vertical tectonics:

The debate between whether horizontal or vertical tectonics were prevalent in the Archean and when/if a changeover occurred has been researched in great detail. Many methods have been used to argue both for and against, ranging from field geology, structural geology, geochronology, geochemistry, and more. Below both the arguments for and against Archean subduction, with a focus on granite-greenstone terranes, are discussed. A particular emphasis is placed on two main aspects that are at the forefront of this debate: that of TTG rocks containing a geochemical signature similar to modern day subduction related rocks, and the debate on whether greenstone volcanics represent modern day ophiolites. These are not the only two arguments, and other points are discussed, however not in as much detail.

2.3.5.1. Arc signature of TTG rocks:

The geochemical signature, in particular that of the trace elements, of TTG rocks has been commonly associated with that of modern island arc, or continental arc rocks present along convergent plate boundaries, and is termed the ‘arc’ signature. This arc signature is caused by the decoupling between large-ion lithophile elements (LILE) and high-field-strength elements (HFSE) (van Hunen and Moyen, 2012). LILE are large cations with small positive charges (e.g. Cs, K, Rb, Sr) and are fluid mobile at > 500°, while HFSE are small cations with large positive charges (e.g. Zr, Hf, Nb, Ta) and are typically not fluid mobile at high temperatures and are also immobile during low temperature alteration (van Hunen and Moyen, 2012). Arc rocks (e.g. arc basalts and andesites) are enriched in LILE but not in HFSE (Pearce, 2008), and due to the “Lanthanide contraction” and increase of compatibility with increasing atomic number for typical garnet bearing mantle mineralogy, feature a strongly fractionated Rare Earth Element (REE) profile. These geochemical attributes suggest there is an enrichment of the mantle source by a LILE-rich, HFSE-poor component, generally accepted to be achieved through fluid fluxed melting of the upper mantle. This occurs in the mantle wedge above a subducting slab, where the fluids released from the dehydration of the subducting slab hydrate and partially melt the mantle wedge, thus creating arc rocks (Tatsumi, 2005).

It is not possible to directly source felsic rocks from the mantle, and so another component is needed to allow the formation of felsic TTG rocks (van Hunen and Moyen, 2012). Studies have led to the general consensus that TTG rocks are formed by the partial melting of mafic rocks previously separated from the mantle and cannot be formed solely by the partial melting of mantle peridotite like modern day arc rocks (Kamber et al., 2002, Moyen, 2011). Melting of the downgoing slab itself is very rare, however there are modern instances in which this appears to be the case. This can happen for example where the subducted lithosphere is very young and therefore relatively hot (Defant and Drummond, 1990), or through slab windows in which the rising mantle can sufficiently heat the surrounding slab to produce a slab melt (Yogodzinski et al., 2001). Adakites are the resulting rocks, with a strongly fractionated REE pattern for the reasons explained above, thought to be produced by the melting of hydrated subducted slabs (e.g. Stern and Kilian, 1996, Rollinson and Tarney, 2005, Arndt, 2013).

Examples of modern adakite melts include those seen in the Andes (e.g. Stern and Kilian, 1996, Bourdon et al., 2002) and Tibet (e.g. Chung et al., 2003, Gao et al., 2007). These modern adakites have very similar REE patterns to Archean TTG rocks, and so it was proposed that TTG rocks represent the direct melting of subducted oceanic lithosphere (Martin et al., 2005). Although rare today, in a hotter Archean Earth, faster mantle convection could have led to a higher rate of mafic crust production which would have resulted in the subduction of hotter lithosphere leading to slab melting being more probable (Martin, 1986). This latter theory has been extremely popular, and is the most convincing argument used in many studies of Archean TTG rocks to claim that they were formed in a subduction setting, and that therefore modern day plate tectonics were in existence throughout the Archean. A main factor in this theory is related to the depletion of heavy REE (HREE) in the TTG rocks. For this to occur, the rocks must form in an environment where a residual is left behind that retains the HREE, with the most likely mineral being garnet (Moyen and Stevens, 2006). Due to garnet being formed under melting at high pressures (> 10-12 kbar), the TTG rocks must have been formed in such an environment (Champion and Smithies, 2003). Subduction seems a likely candidate for this, in particular as some TTG rocks are proposed to have formed at pressures > 18 kbar (Moyen, 2011).

There are however other settings in which rocks could obtain an arc signature, and so there is still a debate as to whether TTGs do in fact represent the melting of a subducted slab. Due to continental crust having a similar signature to arc rocks, the arc signature could be formed by the mixing of continental crust with juvenile melt or the mantle. This could happen by continental crust delaminating into the upper mantle (van Hunen and Moyen, 2012, Johnson et al., 2014),

juvenile melt being contaminated by continental crust as it ascends through it (Arndt and Jenner, 1986), or the mantle itself being primitive (Condie, 2005). It is also possible for hydrated mafic rocks to melt in other settings, e.g. in an oceanic plateau (Willbold et al., 2009), a mid-oceanic ridge (Rollinson, 2009), or through 'lithospheric drips' (Gerya et al., 2015) rather than full-scale subduction transporting oceanic crust into the mantle.

Although a large proportion of Archean igneous rocks plot in the arc related field of many geochemical plots, e.g. Th/Nb ratios (van Hunen and Moyen, 2012), Kamber et al. (2002) concluded that there is a difference between adakites and TTGs, particularly with higher La/Yb, and lower Nb/Ta trace element ratios in TTG rocks, and therefore TTG rocks could not have been formed from the melting of a subducted slab. It is also argued by Kamber et al. (2002) that Archean oceanic lithosphere was not any hotter than that of the modern day at the time of subduction. This is in agreement with other studies, e.g. Kramers (1988) and Nutman et al. (1999), and results in a theoretically simple alternate model in which TTG rocks can be produced through the melting of a hydrous basaltic source without the process of subduction with 'volcanic resurfacing' proposed as a possible mechanism for production of TTG magmas (Kamber et al., 2005). Volcanic resurfacing involves the hydrous melting of the base of a thick volcanic pile, and is compliant with trace element modelling (Nagel et al., 2012), though arguments remain over the feasibility of transporting enough hydrous fluids to depth to produce the volumes of TTG formed (Arndt, 2013). The model of melting at the base of an over thickened volcanic pile, along with the melting of a subducted slab remain the two leading proposed mechanisms by which TTG rocks could have formed with a geochemical arc signature.

2.3.5.2. Greenstone volcanic rocks as ophiolites:

The second major debate in relation to granite-greenstone terranes and tectonics is that of greenstone volcanic rocks and their similarities to modern day ophiolites. There are two sides to this argument; those who believe that greenstone belts represent Archean ophiolites and those who see them as something different, not present on modern day Earth.

Modern day ophiolites are sections of obducted oceanic crust and upper mantle, with their stratigraphy comprising: an ultramafic lower section composed of tectonised harzburgite, i.e. a section of the upper mantle, layered and massive gabbro, a sheeted dyke complex, and pillow basalts, capped by sedimentary facies (Figure 2.3.8). Greenstone belts as discussed earlier have a lower ultramafic stratigraphy, and an upper mafic stratigraphy, capped by sedimentary facies, similar in general stratigraphy to ophiolites. Proponents of greenstone belts as ophiolitic

sequences use this as one of the main pieces of evidence to argue for subduction throughout the Archean (e.g. Kusky and Kidd, 1992, Dilek and Polat, 2008, Furnes et al., 2015). There are however, even accounting for the later deformation and alteration that has affected most greenstone belts, differences between ophiolites and greenstone belts. The greenstone belt ultramafic volcanic rocks are those of komatiitic flow volcanics, and not tectonised upper mantle. There does not appear to be any evidence for the preservation of upper mantle harzburgite in greenstone belts. Although gabbro is preserved in some greenstone belt sequences, this appears to be as relatively small feeder dykes or sills (Zhou, 2013) and not as layered gabbro. Furthermore, there does not appear to be any evidence for sheeted dyke complexes in Archean greenstone belts, although this has been debated (Furnes et al., 2007). It therefore seems likely that greenstone belts are sufficiently different to ophiolites to be considered as non-ophiolitic in origin. Counter-arguments against these apparent differences have been forthcoming in that any missing ophiolitic stratigraphy not present in greenstone belts may perhaps be explained by a hotter Archean mantle. Hotter mantle conditions were unlikely to have been conducive to the production and preservation of these lower ophiolitic sections, with only the upper stratigraphy of the ophiolite being preserved (Hargraves, 1986, Robinson et al., 2008). Should oceanic crust have been thicker than modern oceanic crust due to increased partial melting in a hotter mantle, then deeper portions of the sequence may have been recycled into the mantle at subduction zones and not accreted onto the continents (Condie and Benn, 2006). This leaves only the pillow basalts and sediments to be accounted for, which is done so in the mafic volcanic rocks and banded iron formations seen in Archean greenstone belts worldwide.

Technically, to be classified as an ophiolite, all lithological aspects as described above need to be present, and so there are strictly no ophiolites in Archean greenstone belts, with the oldest true ophiolite being the 1.95 Ga Jormua ophiolite of Finland (Peltonen et al., 1996). This classification however would also result in a number of Phanerozoic ophiolites being ruled out as only 47% of these have evidence of a preserved sheeted dyke complex (Furnes et al., 2014), and so it was suggested that a sheeted dyke complex is not a necessary component for a greenstone belt sequence to be classified as an ophiolite (Robinson et al., 2008). Archean greenstone belts however are missing much more than just the sheeted dyke complex, leaving it difficult to classify them as ophiolites. This does not mean that greenstone belts do not represent Archean ophiolites, and to defend this Dilek & Furnes (2011) redefined ophiolites as *"suites of temporally and spatially associated ultramafic to felsic rocks related to separate melting episodes and processes of magmatic differentiation in particular oceanic tectonic environments"*. This conveniently allowed all greenstone belts to be included in the new classification for ophiolites, however, aware that this would not simply lead to the acceptance that greenstone belts

represent subduction tectonics, two classes of 'subduction related' and 'non-subduction related' ophiolites were formed. With ophiolites traditionally representing an obducted section of oceanic lithosphere above a subduction zone, it seems strange to try and include non-subduction related greenstone belt stratigraphies under the classification, particularly if the argument is that greenstone belts are subduction related. It would appear to have been more logical to decipher a new classification for such a stratigraphy formed under different conditions.

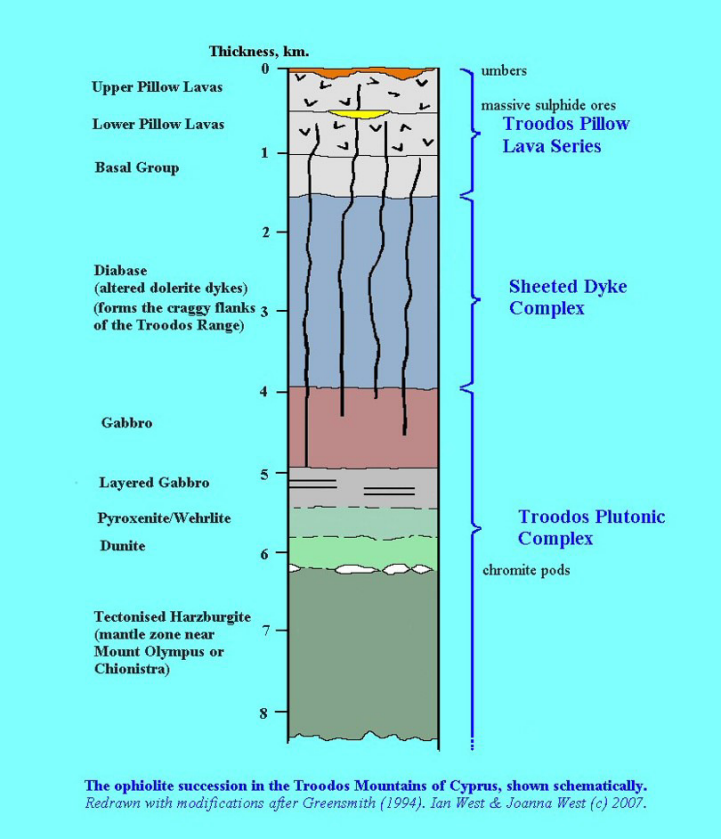


Figure 2.3.8: Typical ophiolite succession, as seen in the Troodos Mountains, Cyprus (West and West, 2007).

Under these new classes of ophiolite, a number of geochemical studies were carried out by Furnes et al. (2014), who concluded that 85% of the Precambrian greenstone sequences are subduction-related including almost all of the Archean greenstone belts analysed. In addition to this it was suggested that < 50% of these are MORB-type, again backing up modern day plate tectonics being active throughout the Archean.

It was discussed in chapter 2.3.3.2 that a great deal of research has been carried out on the Isua greenstone belt in Greenland. Being the oldest greenstone belt on Earth, if it is accepted that modern day plate tectonics were present during its formation, then it can be argued that these have been prevalent throughout the Archean. A number of studies have argued this (e.g. Polat et al., 2011, Furnes et al., 2014, Roberts et al., 2014), though there have also been studies on the

Isua greenstone belt that have shown evidence against a subduction related source (e.g. Kamber et al., 2005, Nutman et al., 2007a) and so it is not widely accepted that subduction was the driving mechanism in its formation.

The argument against Archean greenstone belts representing modern day ophiolites is very strong (e.g. Bédard, 2006, Hamilton, 2011, Kamber, 2015). The chemical alteration caused by seafloor hydrothermal alteration seen in many greenstone belts used to argue for subduction could have been created in non-subduction related environments, e.g. on oceanic plateaus (Hamilton, 2011), and the geochemical signatures of greenstone belt volcanics are very susceptible to crustal contamination which has shown many greenstone belts to have been emplaced onto pre-existing continental crust, i.e. ensialic in origin, as opposed to that of oceanic crust (Kamber, 2015). In some cases where accretion models have been proposed describing greenstone belts as ophiolites, conformable contacts have been present, e.g. in the Zimbabwe Craton (Bolhar et al., 2003) and in the Superior Craton (Tomlinson et al., 2003). Recent studies suggest that the absence of blueschists may be explained by the changing composition of oceanic crust throughout Earth history, with greenschist facies rocks being formed instead of blueschist facies rocks in an Archean subduction setting (Palin and White, 2016). Even if accepting greenstone belts as ophiolites however, in addition to blueschist facies rocks, accretionary prisms are also absent, further putting into question this theory (Bédard, 2006).

It is difficult to accept that, if produced, a full ophiolitic sequence would not be preserved during the Archean. If Archean greenstone belts do represent ophiolites, then the only possible 'ophiolitic' section preserved would be pillow basalts (excluding the sedimentary cover). Although pillow basalts provide evidence that mafic volcanic rocks were erupted sub-aqueously, this is far from proving the existence of active subduction during the Archean. Although geochemical evidence has been proposed to link greenstone belts and ophiolites (e.g. Polat et al., 2011, Furnes et al., 2014), with possible models to explain the missing ophiolitic stratigraphy from greenstone belts (e.g. Furnes et al., 2007, Robinson et al., 2008), it appears that more evidence is required to strengthen this latter interpretation.

2.3.5.3. Further arguments for Archean subduction:

Although the arc signature of TTG rocks and greenstone belts as supra subduction ophiolites are the two main lines of evidence used to support Archean subduction, there are also others. These are briefly discussed below.

The first presence of eclogite inclusions in diamonds at 3.0 Ga is a strong indicator of active subduction at this time (Shirey and Richardson, 2011), and although not specifically citing subduction as the mechanism, the presence of 2.9 Ga sulphur inclusions in diamonds that have undergone mass independent fractionation in an oxygen poor atmosphere indicates that sulphur at this time was transported from the Earth's surface into the mantle (Farquhar et al., 2002). Both the presence of eclogite and the recycling of atmospheric sulphur into the mantle do not need subduction to be possible; eclogite could form through delamination of a restite related to TTG formation, or in an over thickened LIP, and similarly atmospheric sulphur could be transported to the mantle through the delamination of formerly exposed lithospheric crust through volcanic resurfacing, or drip tectonics. Subduction however is the most likely mechanism to achieve both of these outcomes.

A number of geological mapping and geophysical studies have highlighted the likely preservation of ancient suture zones in the crust of Archean Cratons, representing fossilised subduction zones, e.g. the Superior Craton (Benn, 2006) (Figure 2.3.9) or the Kaapvaal Craton (Moyen et al., 2006). An argument used against this is that the crust could have been too weak to thicken significantly, and so these structures could represent lateral flow superimposed on vertical displacements (Chardon et al., 2009) in a hotter, more ductile Archean lithosphere.

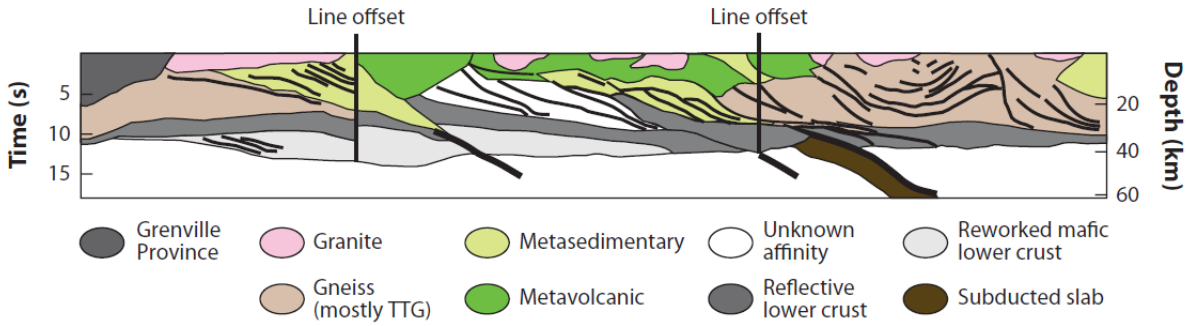


Figure 2.3.9: Geophysical profile of the Abitibi Greenstone Belt with suture zones and a possible fossilised subduction zone (Ludden and Hynes, 2000, Benn, 2006, van Hunen and Moyen, 2012).

The presence of an enriched geochemical signature with respect to Light REE (LREE) is used to argue for primitive melts having been contaminated by crustal material, either in the magma chamber or in their ascent to the surface. This is particularly useful with regards to greenstone volcanics as it can be used to decipher whether they were erupted in a mid ocean ridge (or Archean equivalent), or oceanic plateaux, in which they will keep their original geochemical signature, or if they erupted onto continental crust and are therefore ensialic. In the latter case they will pick up a 'crustal contamination' signature, evidence that they were not formed as

oceanic lithosphere. Furnes et al. (2014) used a method developed by Polat et al. (2006) involving geochemical plots of Nb/Nb* vs TiO_2, Al_2O_3 and MgO to show that ~90% of all greenstone sequences were unaffected by crustal contamination, with any 'arc' signature being obtained through melts from recycled lithosphere and the mantle wedge above subduction zones. It is important to note however that this is only using one element against whole rock geochemistry, and to validate this more geochemical signals should be looked into for a range of greenstone belts, in particular REE patterns, as 90% appears to be a large percentage of greenstone belts to be uncontaminated by continental crust relative to the number of greenstone belts discussed in the literature to be ensialic in origin, for example in the Zimbabwe Craton (Bolhar et al., 2003) and in the Superior Craton (Tomlinson et al., 2003). It is also worth noting that the term 'greenstone sequences' as used by Furnes et al. (2014) includes all Phanerozoic ophiolites which are known to have formed at mid ocean ridges and therefore skew the statistics.

A stronger point made in relation to that of geochemical signatures is that should there have been a major event that caused a change in tectonics, e.g. mantle overturn, we would expect to see an abrupt change in our geochemical records at this time (Davies, 2007). There are however no such changes seen in the geochemical record through the Archean to mark such an event (Furnes et al., 2014).

As well as the aforementioned adakites being modern day arc rocks similar to Archean TTG rocks, another not so common modern arc rock is also argued to be represented in Archean greenstone belts. These are the magnesian volcanic flows termed boninites, which have been compared to the Archean magnesian flows of komatiites. Boninites are thought to form through the second stage melting of the residue left behind after basalt formation in arc settings, resulting in a U-shaped REE pattern (Taylor et al., 1994). These were once thought to be restricted to Phanerozoic arcs (Manikyamba and Kerrich, 2012), however they have been documented in the Superior Craton (Kerrich et al., 1998), the Dharwar Craton (Manikyamba et al., 2005) and the North Atlantic Craton (Polat et al., 2008), which together represent the entire Archean eon. Again, the argument against these Archean examples representing modern day boninites is that there are subtle differences in their geochemistry (Puchtel et al., 2009). Kamber (2015) goes further to say that there needs to be a new outlook when comparing the geochemical signature of modern day rocks to those of ancient rocks in order to infer the same tectonic setting, and whether or not these tectonic settings were actually possible in the early Earth needs to be studied in greater depth.

To explain the presence of alkaline basalts in the Neoarchean Dharwar Craton, Manikyamba & Kerrich (2012) suggest that Mesoarchean crust was subducted into the mantle where it was

incubated for ~500 Myrs before being entrained in mantle plumes; hence a mechanism for subducting this crust was required in the Mesoarchean. Similarly the presence of Archean sanukitoids are thought to have required interaction between crustal rocks and the mantle (Martin et al., 2009, Fowler and Rollinson, 2012), therefore requiring a mechanism to carry these crustal rocks into the mantle, with subduction again being the simplest solution to achieve this.

In conclusion to the arguments for modern day plate tectonics being active throughout the Archean, Polat et al. (2011) found that the Eoarchean to Mesoarchean greenstone belts in southwest Greenland share the lithological and geochemical characteristics of Cenozoic oceanic island arcs and Phanerozoic ophiolites. It is also suggested that higher mantle temperatures and geothermal gradients did not result in a different system than that which operates today. Summing up the work of others it is stated that *"fundamentally, continental crust cannot grow, supercontinents cannot form, and arcs cannot generate melts over millions of years without subduction, collision, subduction of water, and slab dehydration or melting"*. This leads onto the next section, where evidence against subduction being operative throughout the Archean is discussed.

2.3.5.4. Further arguments against Archean subduction:

While proponents of modern day plate tectonics having operated during the early Earth focus on the similarities between Archean rocks and modern rocks, those against them focus on the differences. The difficulty when highlighting the differences is that there then needs to be a valid model proposed that could explain how these differences have come about in an alternative tectonic environment. If an explanation is not forthcoming then there is little weight behind the argument.

TTG rocks are proposed to be Archean equivalents of supra subduction arc rocks formed through the melting of a downgoing slab, i.e. adakites. There are a number of arguments against this theory. In order for the downgoing slab to melt it needs to be hotter than modern day equivalents otherwise modern day arc magmas will be formed (Bédard, 2006). One way of subducting hotter lithosphere is to accelerate plate motion, which would have been possible with a higher rate of mantle convection (Strik et al., 2003). However, faster plates would be more difficult to melt and would have dehydrated very quickly (Harry and Green, 1999). It may also be that the Archean upper mantle was not hotter in the first place if a greater volume of, and thicker oceanic crust was produced to release the additional heat flux (Kamber, 2010). In addition to this, the sheer volume of TTG rocks in granite-greenstone terranes is difficult to explain through subduction (Bédard et

al., 2013). This has been modelled in the Abitibi greenstone belt in the Superior Province, Canada. In order to create the volume of TTG rocks in the time available the plates would have had to converge at an astonishing 15-20 cm/year, which even if possible would be too fast to melt the downgoing plate. In addition to this, to create the volume of TTGs present, up to 10% of the subducted crust would need to be melted, which is too large to be produced from subduction alone (Bédard, 2006). In order to explain the formation of TTG rocks without subduction, the model of partial convective overturn and sagduction was discussed earlier. It has also been modelled in Pilbara that TTG formation occurred in pulses roughly every 20 Myrs (Zegers and van Keken, 2001) which could be related to crustal delamination and the upwelling of mantle in its place. A modern day example of this is proposed to be Tibet where adakites have formed through delamination under the Himalaya, forming the Tibetan Plateau (Chung et al., 2003). This process of TTG formation in place of delaminated crust would also help to form the SCLM and cratonisation (Bédard, 2006).

The TTG and adakite debate also focusses on the geochemical arc signature, as mentioned earlier. This signature can be explained by crustal contamination when the melt passes through continental crust, which negates the need for subduction to be active in order to achieve an arc like signature (Arndt and Jenner, 1986, Polat et al., 2006). Even if accepting that adakites are in fact modern day equivalents of TTG rocks, there are a lack of Archean volcanic rocks that preserve an arc related signature (Bédard et al., 2013). In addition to geochemical evidence, both inherited zircons found in TTG rocks, and isotopic signatures of TTG rocks (e.g. Nd, Hf) imply that there has been continental crustal recycling and not only fractionation in their formation history (Bédard, 2006). Looking at the simple geological model of modern day arc terranes, these involve a background of arc volcanics punctuated by occasional plume related volcanics. This is the opposite of Archean greenstone terranes in which thick basalt dominated sequences are occasionally interbedded by thin felsic volcanic events (Bédard et al., 2013).

Looking from a more simplistic geological viewpoint, there are many differences between granite-greenstone terranes and Phanerozoic geology. The most obvious of these is that there are no modern analogues for dome and keel stratigraphies (Bédard et al., 2013). The characteristics of Phanerozoic active margins are not preserved in greenstone belts (Bleeker, 2002, Van Kranendonk et al., 2004) and neither are those of Atlantic style passive margin sequences (Bédard et al., 2013). There is a lack of large scale linear trends (> 100km) in Archean rocks as are seen in modern day subduction settings and orogenic belts (Zegers and van Keken, 2001), however most Archean terranes have been severely tectonised which may partly account for this. The change from a bi-modal distribution of rocks in the Archean (i.e. TTG and greenstones) to an andesitic composition

of rocks today would also suggest a differing tectonic setting (Van Kranendonk et al., 2010). Today we see a bi-modal distribution of rocks in intraplate continental flood basalt provinces (Mahoney and Coffin, 1997) and not subduction settings, which suggests that a mantle plume origin is also a more likely setting for these rocks to have been formed in the Archean (Cawood et al., 2013). In the Paleoarchean Pilbara and Kaapvaal cratons there is evidence for continuous plume volcanism in one place for > 100 Ma, which has been used to suggest that there was no significant continental drift at this time (de Wit and Hart, 1993). Finally, the scarcity of Archean andesites, and the presence of plume like facies such as komatiites and tholeiites does not match with an arc setting, and is easier explained by a mantle plume setting. In order to generate both arc and plume magmas together requires a complicated tectonic model, for example including slab windows (Figure 2.3.10) (e.g. Benn et al., 2009, Ma et al., 2014), although recent studies have worked on integrating plume derived and subduction derived rocks in the one setting (Gerya et al., 2015).

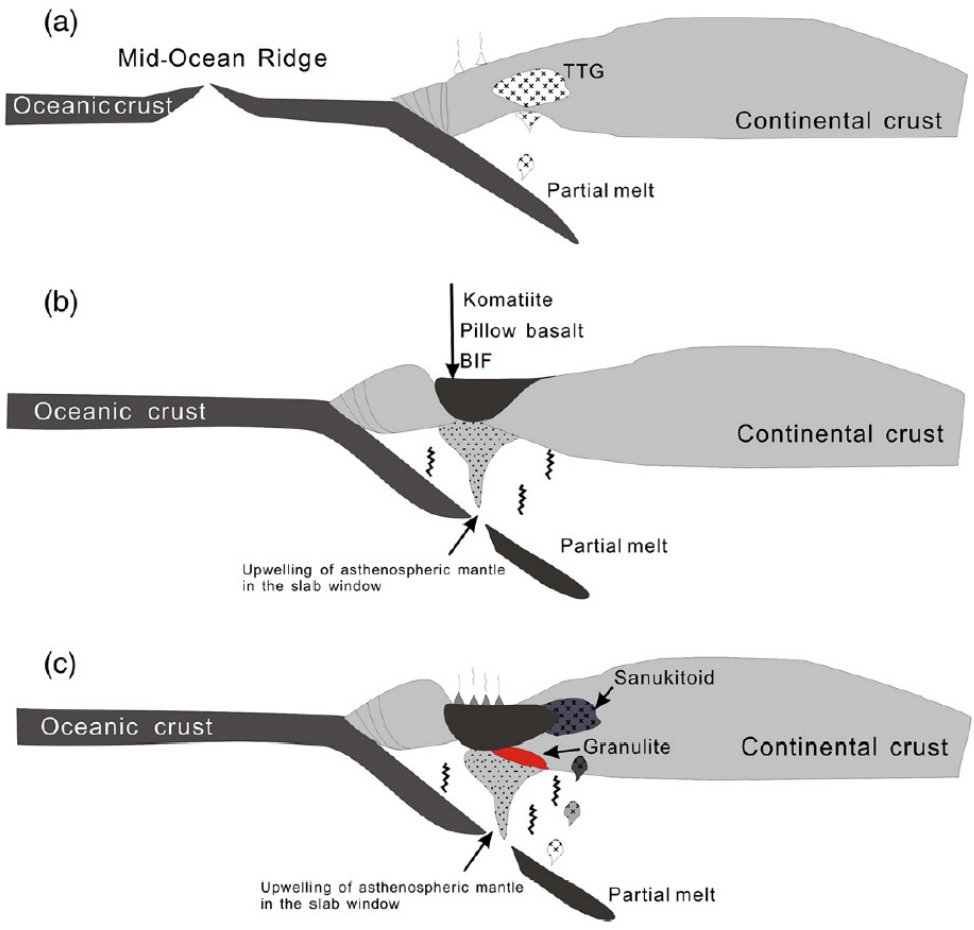


Figure 2.3.10: Model for the formation of plume derived Archean greenstones in an arc setting achieved through the opening of a slab window (Ma et al., 2014).

2.3.6. Summary of plate tectonic evolution:

It is notable that studies on granite-greenstone terranes worldwide has resulted in a variety of tectonic models being formed to explain their formation. It is clear however, that the older the terrane is (e.g. in the Pilbara or Kaapvaal Cratons), the more evidence there is for vertical tectonics relative to horizontal tectonics, and conversely, the younger the terrane (e.g. Superior or Yilgarn Cratons), the more evidence there is for horizontal tectonic processes. The evidence seems to point towards the Meso-Neoarchean as the most likely time at which modern day plate tectonics developed, however there is no set of arguments strong enough to give a definitive answer to this question. Continued studies on granite-greenstone terranes will enhance the geological database of evidence, and at some point it is likely that a preferred model for Archean tectonics will prevail.

2.4. Gold in greenstone belts:

Archean terranes generally host an ore deposit of some kind, i.e. a volume of rock in which an element has been concentrated through natural processes to the point where it can be economically mined (Jenkin et al., 2014). In addition to iron ore and uranium deposits, the economic deposit most commonly associated with Archean rocks, and in particular greenstone belts, is gold. Up to 25% of global gold resources are mined from Archean exposures, which account for only ~6% of the Earth's surface exposure (Goodwin, 1996). This has obvious economic benefits, however Archean gold deposits are also valuable in that they are related to key aspects of early Earth evolution as discussed in chapters 2.2 and 2.3; i.e. crustal formation, mantle evolution and plate tectonic models. Given that the continental crust is essential for capture and storage of ore deposits, it has a first order control on their formation and location (Begg et al., 2010). As is the case when modelling crustal evolution, there is a question here as to whether or not there is a preservational bias at certain time periods in Earth's history related to the formation and storage of ore deposits. Additionally, given that many Archean gold deposits are proximal to juvenile igneous rocks (e.g. Bierlein et al., 2006, Doublier et al., 2014); this poses the question as to whether there is a link between mantle evolution and formation of gold deposits. Finally, Phanerozoic gold deposits are almost all related to subduction related processes (Goldfarb et al., 2001), and many Archean orogenic gold deposits have been related to plate convergence zones, which raises the question as to whether plate tectonics and subduction were also a controlling factor in the formation of Archean gold deposits.

2.4.1. Orogenic gold:

Over 75% of cumulative gold production is sourced from orogenic gold deposits (Phillips, 2013) which have been formed since at least 3.0 Ga (Goldfarb et al., 2001). The term 'orogenic' was introduced by Groves et al. (1998) to replace the term 'mesothermal', previously used to describe the conditions and depths at which these deposits were formed. It was suggested however that the same processes could form gold deposits at different crustal depths, and therefore different temperature conditions. To address this, the term 'orogenic', relating to the fact that these deposits most likely form during the late stages of an orogeny was coined, and if necessary the depth of formation can be added as a descriptive term (Tomkins, 2013). Orogenic deposits are hydrothermal in origin, and are most commonly transported by abundant quartz-carbonate veins, with the gold deposits being vein hosted and disseminated in the surrounding rocks (Goldfarb et al., 2001). The hydrothermal fluids involved in such deposits are chemically distinct compared to other deposit types (e.g. compared to porphyry deposits), and tend to be void of valuable

minerals other than gold (Garofalo and Ridley, 2014). Pressure-temperature conditions for orogenic gold deposits generally range from 1-5 kbar and ~180-700°C and (i.e. conditions found extensively throughout the mid-crust), which differs from other continental margin gold systems that are restricted to the upper crust (< 5km) (Groves, 1993). Maximum temperatures attained in the crust appear to be relevant with respect to localisation of gold mineralisation, with optimal thermal conditions being greenschist facies (Hunter and Stowe, 1997). The defining characteristics of orogenic gold deposits are: deformed and metamorphosed host rocks (particularly greenschist facies), a spatial association with large scale compressional to transpressional structures, and sulphide and carbonate alteration assemblages (e.g. Powell et al., 1991, Robert, 1996, Groves, 2003). The sulphide minerals (e.g. pyrite, pyrrhotite) generally form up to ~3-5% of the deposits, and carbonate minerals (e.g. calcite, dolomite) up to ~5-15%. Commonly albite, chlorite, tourmaline and sericite alteration assemblages are present. Gold grades in orogenic deposits are relatively high (5-30 g/t), however modern mining techniques are exploiting lower grade deposits and expanding around pre-existing mines further from mineralisation centres (Groves et al., 1998). There is no particular lithology within greenstone belts that favours gold mineralisation, with structures being the dominant control, seen at a variety of scales (Hunter and Stowe, 1997). The deposits themselves are located in and around smaller second or third order structures, which have likely acted as traps for the migrating hydrothermal fluids, but there are almost always large scale structures nearby. These larger scale structures (e.g. major shear zones) are likely pathways by which the fluids have transported from deeper in the Earth's crust to their deposition location (e.g. Groves et al., 1998, Gapais et al., 2014).

2.4.2. Timing of gold deposition:

One of the main problems in understanding orogenic gold deposits relates to the timing of mineralisation (e.g. Groves, 2003, Sarma et al., 2011), and as such, one of the main advances in knowledge of orogenic gold deposits has come through an increasing abundance of high precision geochronological studies (Goldfarb et al., 2001). Interestingly all greenstone belt hosted gold deposits significantly postdate greenstone belt formation (Bierlein et al., 2006), and therefore tectonic models, potential fluid source models, and deposition history models related to gold are all improved by precise geochronology of the mineralisation. The timing of gold mineralization can be indirectly constrained by dating minerals which form prior to, or after mineralization, though dating the absolute age of gold deposits remains difficult. This is mainly due to the fact that datable minerals with high closure temperatures are rare in hydrothermal systems (Kerrich and Cassidy, 1994). Xenotime, monazite and titanite are some of the minerals used for U-Pb dating when attempting to carry out these constraints (e.g. Brown et al., 2002, Sarma et al., 2011), or Ar-

Ar dating can be applied to mica alteration (e.g. Marutani, 2005, Doyle et al., 2015). The direct dating of mineralisation is often carried out using associated sulphide minerals and includes Pb-Pb isotope dating (e.g. Jaguin et al., 2012, Khanna et al., 2014) and Re-Os dating (Arne et al., 2001, Doyle et al., 2015). A record of the age of orogenic gold deposits was compiled by Goldfarb et al. (2001) in order to define their global distribution (Figure 2.4.1), however uncertainties remain and many Archean orogenic gold deposits are still undated. Groves et al. (2003) stated that the lack of precise dating of mineralisation events limits the development of viable genetic models and that there need to be better constraints placed on the sources of ore fluids in orogenic gold systems. As such dating should be a priority, particularly for giant and world class deposits.

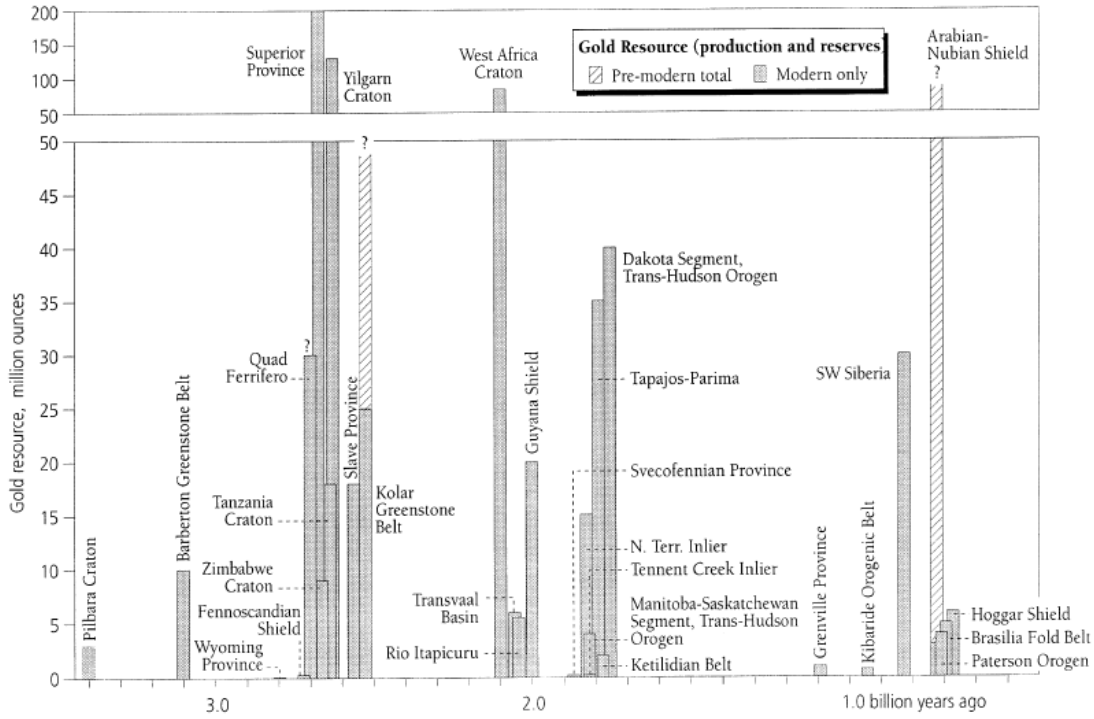


Figure 2.4.1: Gold production vs. best approximation for the age of gold vein formation for Precambrian orogenic gold deposits (Goldfarb et al., 2001).

2.4.3. Crustal evolution, mantle evolution, and orogenic gold:

The exposed Archean crust, in particular that of the Neoarchean, has long been recognised as favourable for hosting the largest orogenic gold deposits, for example in the Yilgarn Craton (Doublier et al., 2014) and the Superior Craton (Tremblay, 2001). Along with this late Archean episode of orogenic gold formation between 2.8 Ga and 2.5 Ga, are smaller but still significant episodes during the Mesoarchean (various ages) and the Paleoproterozoic (2.1-1.8 Ga, particularly prevalent in West Africa) (Goldfarb et al., 2001). Two important observations have been made regarding these Precambrian orogenic gold deposits: their ages correlate with times of global

supercontinent formation (e.g. Goldfarb et al., 2001, Groves et al., 2005), and they are usually proximal to juvenile continental crust (Bierlein et al., 2006).

Goldfarb et al. (2001) highlighted that most exposed orogenic gold deposits throughout Earth history formed at about 3.1, 2.8-2.5, 2.1-1.8, and 0.6-0.05 Ga, which as seen earlier correlate well with times of global supercontinent assembly, often attributed to crustal formation episodes. There is evidently a link between global supercontinent assembly and gold deposition as seen in the age peaks, however again it is likely that this is due to a preservational bias as appears the case with crustal formation ages, and that the ore systems present in these supercontinents have been protected from any extensive erosional processes. When looking at the entire record of orogenic gold deposits versus crustal formation, we see that for example during the 'boring billion' (1.7-0.9 Ga) almost 20% of the preserved crustal record was formed, however < 1% of orogenic gold production is from this time period (Cawood and Hawkesworth, 2013). Similarly the ~7% of exposed Archean greenstone belts which are pre 3.0 Ga in age account for only 2% of Archean orogenic gold, with the vast majority of Archean orogenic gold deposits being Neoarchean in age even although there was extensive continental growth before this time (Goldfarb et al., 2001). This highlights not only that there was relatively little gold deposited in the Proterozoic, but also that there is not a primary relationship between crust formation and orogenic gold deposition, or at least this is not the only controlling factor. However, this may not be entirely accurate, as was discussed that many ages attributed to crustal formation are likely to be ages of crustal recycling and not technically crustal formation ages. Therefore the crucial links between crustal evolution and orogenic gold could in fact be due to crustal recycling and the emplacement of granitoids, and/or there could be a genetic link between formation of orogenic gold deposits and juvenile magmatism.

Archean and Paleoproterozoic orogenic gold systems, particularly giant deposits, typically occur in close proximity to juvenile crust, for example in the Southern Cross deposit in the Yilgarn Craton (Doublier et al., 2014). It has been suggested that juvenile material is the source of the gold, fertilising the crust with metals (e.g. Bierlein et al., 2006, Mole et al., 2013). It is also known that juvenile material is less likely to be emplaced after cratonisation and the formation of the SCLM keel (Bagas et al., 2008), and it is seen that orogenic gold deposits do not form after cratonisation (Mole et al., 2013). For example during the major Neoarchean episode of orogenic gold deposition, a thick SCLM would likely already have been in place below the Mesoarchean crust which had undergone a protracted crustal history. This would prevent the emplacement of juvenile crust and therefore also prevent gold deposition (e.g. the Barberton greenstone belt of the Kaapvaal Craton); hence lithospheric thickness could be seen as a primary control on the

formation of giant gold deposits (Bierlein et al., 2006). It is important to note however that although a likely source for gold, juvenile crust emplacement and the formation of gold deposits are not necessarily contemporaneous. For example, the Southern Cross deposit in the Yilgarn Craton formed 150-350 Myrs after emplacement of juvenile crust (Mole et al., 2013), and likewise in the Barberton Greenstone Belt there was at least a 150 Myr time gap (De Ronde et al., 1991). A link has previously been made in relation to this temporal discrepancy, in that the longer the delay between emplacement of juvenile crust and deposit formation, the smaller the deposit (Bierlein et al., 2006), with for example both of the above mentioned deposits being relatively small compared to the Neoarchean giant deposits that have a time gap < 100 Myrs. A juvenile crustal source may also help explain why the Archean crust is relatively well endowed with metallogenic elements relative to the Phanerozoic, as there would have been a more efficient transfer of metallogenic elements from the mantle to the continental lithosphere (de Wit and Thiart, 2005).

2.4.4. Plate tectonics and orogenic gold:

Two features that are seen to be vital in the process of orogenic gold formation, are the presence of large scale shear zones, and the presence of granitoid plutons (Zibra et al., 2014). As mentioned, the large scale shear zones are seen as a likely pathway to transport metamorphic or magmatic fluids from deeper crustal levels closer to the surface, and granitoid plutons are likely the source of heat and transporting fluids (Czarnota et al., 2010). The final trapping of gold then occurs in relatively small second and third order structures higher in the crust (Zibra et al., 2014). Tectonic models have long been used to explain the processes under which orogenic gold deposits formed. Wyman & Kerrich (1988) and Barley et al. (1989) both provided early models that orogenic gold deposition was related to convergent plate tectonics in the Superior and Yilgarn Cratons respectively, and this model is still commonly used today to explain orogenic gold deposits (Figure 2.4.2). In a convergent plate margin setting, the likely source of the gold is melting associated with subduction; slab dehydration releasing fluids that could dissolve and transport gold from the mantle wedge and/or buried sediments and volcanic rocks (e.g. Groves et al., 1998, Goldfarb et al., 2001). If this latter model is correct, it could be evidence for subduction being active as far back as the Mesoarchean (de Ronde and de Wit, 1994), a theory aided by the fact that almost all Archean greenstone belts that host giant gold deposits have linear geometries (Bierlein et al., 2006) and major tectonic structures (Blewett et al., 2010), often interpreted as ancient suture zones. However, if granite-greenstone terranes were formed by vertical tectonics, i.e. mantle plume activity, the melting of ultramafic to mafic volcanic rocks and the emplacement of granitoid plutons, then this need not be the case. The emplacement of late plutons is a feature

of the vertical tectonic model in the formation of granite-greenstone terranes (e.g. Collins et al., 1998, Van Kranendonk, 2011). These late plutons could be a source of gold bearing fluids, and/or could have induced or reactivated faults along which gold bearing fluids could be transported through and deposited (Hunter and Stowe, 1997). Such a scenario would also help to explain why Archean orogenic gold deposits are always significantly younger than the greenstone belts in which they are hosted. Alternatively, with orogenic gold episodes being related to supercontinent formation, granitoid emplacement could be largely unrelated to the gold deposition, and only served to create a stable crust and related SCLM in which the gold could be preserved (Groves et al., 2005). The synchronicity of granitic magmatism and gold deposition however does suggest there is a stronger link between the two (Bierlein et al., 2006). As both convergent plate margins, and vertical tectonics are viable models in which orogenic gold deposits could have formed, it is difficult to use orogenic gold deposits as a proxy for determining a preferred tectonic model for granite-greenstone terrane formation.

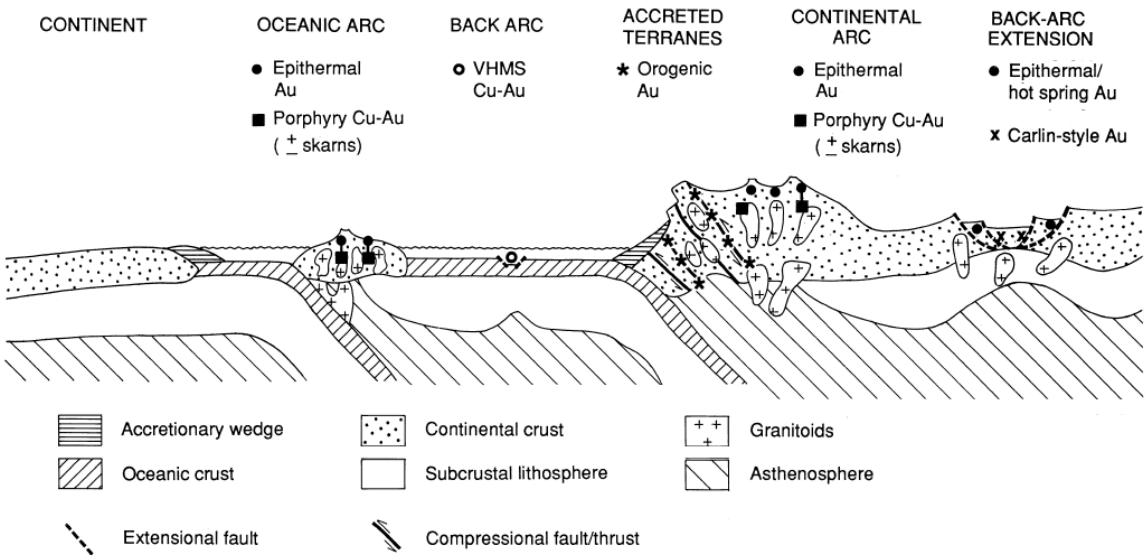


Figure 2.4.2: Tectonic settings of gold deposits (Groves et al., 1998).

2.4.5. Source of orogenic gold:

As with most other aspects of orogenic gold deposits, the source of hydrothermal fluids in orogenic gold deposits is still debated, largely between metamorphic and magmatic sources (Yardley and Cleverley, 2013, e.g. Jenkin et al., 2014). It is noteworthy that available geochemical and isotopic data cannot unequivocally distinguish between these possible end member sources (Groves, 2003). The main debate here involves the role of late stage granitic intrusions, which have been widely correlated with the genesis of world class orogenic gold deposits, though rarely definitively linked (Goldfarb et al., 2001). This temporal link is not surprising, as the metamorphic

conditions under which orogenic gold deposits form are also conducive to forming large volumes of granitic melts (Groves, 2003). One model suggests that through their close spatial and temporal association with the gold deposits, the plutons were actually the source of the hydrothermal fluids (Sillitoe, 1991). Metamorphic transporting fluids were long the favoured method, whether that be through stripping gold from buried sedimentary or volcanic rocks, or deeper still from subducted slabs and the overlying mantle wedge (e.g. Fyfe and Kerrich, 1985, Powell et al., 1991), and therefore synonymous with orogenic gold deposits. It is even possible that mineralising fluids are derived from a deep magmatic source (Ridley, 2000). This led to a distinction being made between orogenic deposits (mesothermal at the time), and a new class of 'intrusion related' deposits (Sillitoe, 1991), and a suggestion that many gold deposits previously classified as orogenic, should in fact be reclassified as intrusion related. It may be that there are different sources for different deposits. Two of the favoured methods used to link granitic intrusions and gold deposits are Pb-Pb isotopes (e.g. Cassidy et al., 1998, Qiu and McNaughton, 1999), and S isotopes (Xue et al., 2013) of ore related minerals.

2.4.6. Mesoarchean gold:

The largest and most famous Archean gold deposits are the Neoarchean deposits from the Superior Craton (e.g. Robert et al., 1991, Tremblay, 2001) and the Yilgarn Craton (e.g. Groves et al., 1998, Qiu and McNaughton, 1999). There are very few known examples of Mesoarchean orogenic gold deposits, which is especially surprising considering it has been estimated that < 80% of all known gold was originally deposited in crust of Mesoarchean age (Frimmel, 2008). This apparent contradiction has been explained by the repeated remobilisation and recycling of gold as evidenced through Os isotopes (Frimmel and Hennigh, 2015). The oldest known orogenic gold deposits are from the Pilbara Craton in Australia which formed at around 3.4 Ga (Neumayr et al., 1998). A larger number of relatively small deposits have been dated from the Barberton greenstone belt to between 3.04 Ga and 2.97 Ga (Schwarz-Schampera et al., 2009). Other examples include deposits in 3.3 Ga Mesoarchean rocks of the Dharwar Craton, India, however the deposit itself is undated (Deb, 2014), and the São Francisco Craton, Brazil in which a deposit is dated at 2.82 Ga (Vial et al., 2007). The most famous Mesoarchean gold deposit is the Witwatersrand deposit in the Kaapvaal Craton. The origin of this deposit is debated, with a general consensus agreeing a paleoplacer deposit, but some models suggest a hydrothermal origin (Goldfarb et al., 2001). Importantly the age of the host sediments match the ages of the Mesoarchean gold deposits to the north of the Kaapvaal Craton (Hunter and Stowe, 1997). This could make this deposit the only remnant of Mesoarchean lode gold systems (Goldfarb et al.,

2001), and could also provide one example of the widespread tectonic reworking of gold deposits during the Mesoarchean (Frimmel and Hennigh, 2015).

2.4.7. Summary of orogenic gold:

It is clear that granitoid emplacement plays an important role in the formation of orogenic gold deposits, however through the lack of unequivocal links between the two it is unlikely that it is the source of Archean orogenic gold. The type of granitoid emplacement related to orogenic gold deposits does not appear to be a controlling factor for gold deposition. For example in the Yilgarn craton the dominant plutons are granodiorite-granite-monzogranite, while in the Superior craton TTG plutons are related to the orogenic gold deposits (Goldfarb et al., 2001). This makes it seem unlikely that the mineralogy of the granitoid is important, however the constant temporal links suggest that they are vital as heat and fluid sources, as has been noted for the Barberton greenstone belt (e.g. Saager and Koppel, 1976, Jaguin et al., 2012). The presence of juvenile rocks and major shear zones in the vicinity of all orogenic gold deposits also highlights their importance in the process.

2.5. West African Craton, Reguibat Shield and Aouéouat Greenstone Belt

2.5.1. West African Craton:

The West African Craton is one of a number of Precambrian nuclei that forms the African continent (Derry, 1961). It is exposed at the surface in two major shields, the Leo Shield (also referred to as the Man Shield) in the south, and the Reguibat Shield in the north, both of which are composed of a western Archean domain and an eastern Paleoproterozoic domain. These two shields are separated by the expansive Taoudeni sedimentary basin, which is Proterozoic to Paleozoic in age, and are bounded on all sides by Pan-African and Variscan belts (Barth et al., 2002) (Figure 2.5.1a).

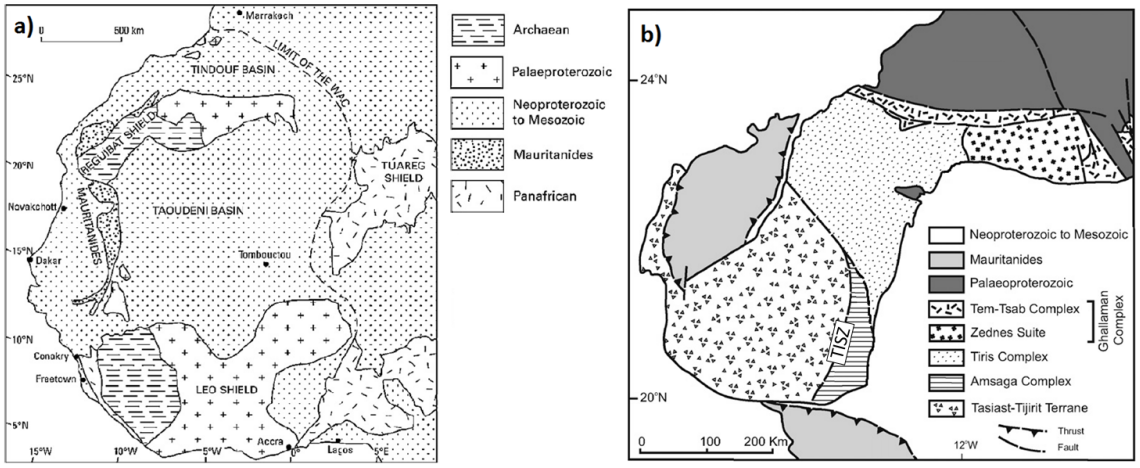


Figure 2.5.1: a) Geological map of the West African Craton, b) Geological map of the Reguibat Shield (modified fromSchofield et al., 2012).

Previous studies have attempted to make a connection between the formations in the Leo Shield and those of the Reguibat Shield (e.g. Thiéblemont et al., 2001, Schofield et al., 2012), however, with limited knowledge about these individual shields, and the large unexposed distance between them, any relationship theorised remains speculative. It is, however, probable that these shield areas are related in at least some aspects, and that they were once part of a much larger Archean terrane which formerly extended westward towards the Guyana Shield of South America (Morel, 1979). It is imperative that the various assemblages of the West African Craton and their relationships to each other are well defined before attempts are made to connect regions and processes across great unknown spaces (e.g. the Taoudeni Basin). There is however no doubt that younger large scale orogenies, post-Archean in age, affected the Leo Shield and the Reguibat Shield together, for example it is undisputed that both were affected by the Eburnean Orogeny at

~2.1Ga resulting in the formation of Birimian terranes (Boher et al., 1992) by which time it is likely the West African Craton was fully amalgamated (Schofield et al., 2012).

2.5.2. Reguibat Shield:

The Reguibat Shield, first identified by Menchikoff (1949), as already stated is comprised of an Archean western domain, and a Paleoproterozoic eastern domain (Figure 2.5.1). It is perhaps one of the most understudied regions of exposed Precambrian crust on Earth, and as recently as the early 1990s the geochronology was almost unknown. Since then several studies have been published from the region, but these are still few relative to most other shield areas on Earth. This section focuses on the Archean domain of the Reguibat Shield, and provides a review of the current state of knowledge of the area.

The Archean of the Reguibat Shield is characterised by granite-greenstone terranes. These terranes are dominated by older granitoid gneisses and migmatites which are infolded with supracrustal schist belts and intruded by younger plutonic intrusive bodies (Bea et al., 2013). The Reguibat Shield is bound on the northwest and south by the Mauritanides Belt. This is a Caledonian and Variscan fold-thrust belt consisting of a number of allochthonous terranes, many of which resemble Archean greenstone belts (Kolb et al., 2006, Meyer et al., 2006). The Mauritanides Belt lies unconformably on the West African Craton after final emplacement during the collision between Gondwana and Laurentia. On the southeast the Reguibat Shield is bound by a thrust zone separating the Archean basement from the overlying Taoudeni Basin (Sakellaris, 2008).

Research into the geological evolution of the Leo Shield has permitted rocks to be generally grouped into one of three age provinces; Leonian (~3.0 Ga), Liberian (~2.7 Ga) and Eburnean (~2.0 Ga) (Macfarlane and Institute of Geological, 1981). The first two of these terms tend not to be used very often in the Reguibat Shield for two apparent reasons. Firstly, it might imply that the one event affected the entire West African Craton without there being sufficient evidence for this, and secondly, the dispersal of terranes in the Reguibat Shield does not appear to follow a clear distribution relative to their age. This does not rule out the possibility of the co-evolution of parts of the Leo Shield with parts of the Reguibat Shield, and there are some strong similarities in ages recorded between the two. Examples of similarities between the Reguibat Shield and the Leo Shield include the Liberian event of the Leo Shield coinciding with possible movement on the Tâçarât-Inemmaûdene Shear Zone and the Ahmeyim Great Dyke of Mauritania (Schofield et al., 2012, Tait et al., 2013), the Eburnean orogeny affecting both shields (Boher et al., 1992), and

some strong similarities between the granite-greenstone stratigraphy of the western Reguibat Shield (Tasiast-Tijirit Terrane) and the granite-greenstone stratigraphy of the western Leo Shield (Rollinson, 1982, Rollinson, 1983, Rollinson, 1999), however, in the Reguibat Shield there are a number of geological events which do not fall into the classification used in the Leo Shield. To address this, a number of regional terranes have been established in the Reguibat Shield, generally divided by tectonic structures. These include from southwest to northeast: Tasiast-Tijirit Terrane, Tâçarât-Inemmaûdene Shear Zone, Amsaga Complex, Tiris Complex and Ghallaman Complex. A brief description along with a detailed geochronological review of each of these is presented below, along with a table of all Archean and Paleoproterozoic geochronological data from the Reguibat Shield (Table 2.5.1).

2.5.2.1. Tasiast-Tijirit Terrane:

The Tasiast-Tijirit Terrane lies in the southwest of the Reguibat Shield (Figures 2.5.1b, 2.5.2). It is composed of migmatitic gneisses, greenstone belts and voluminous TTG plutons, and so resembles a classic granite-greenstone terrane sequence. A description of the Tasiast-Tijirit Terrane is presented below as per Key et al. (2008). The migmatitic gneisses present in the Tasiast-Tijirit Terrane tectonically, and locally unconformably, underlie greenstone belt sequences and so preserve the complex tectonothermal history pre-dating deposition of the greenstone belts. These migmatitic gneisses are composed of a grey tonalitic-granodioritic gneiss host cut by at least four generations of felsic veins and minor mafic dykes. The greenstone belts of the Tasiast-Tijirit Terrane all comprise of interlayered mafic and ultramafic volcanic rocks, with greywackes as well as BIF either interbedded with the greenstones or confined in rift centres within them. The greenstone belts strike N-S to NNE-SSW, similar to gneisses and shear zones in the terrane, and their distribution can be seen in figure 2.5.2. Later plutonic magmatism postdates the volcanism and associated sedimentation recorded in the greenstone belts, both cutting across the fabrics of the migmatitic gneisses and intruding through greenstone successions. Some country rock xenoliths are common close to greenstone margins, and the plutons are locally foliated and cut by granitic veins. The modal composition of the TTG rocks is close to or on the tonalite-granodiorite boundary. A late pegmatitic granite intrudes rocks throughout the Tasiast-Tijirit Terrane as sheets and veins, and some late brittle deformation which strikes NE-SW to NNE-SSW, as well as E-W, has resulted in mafic dyke swarms and quartz-veins also forming in the region.

Terrane	Paper	Rock Lithology	U-Pb Age	Nd Model	Sm-Nd Isochron Age	Hf Model	Rb-Sr	K-Ar
Tasiast-Tijirit	Bonnici & Giraudon 1963	Unknown					2.84-2.34	
	Rocci et al. 1991	Unknown					2.84-2.34	
	Chardon 1996	TTG/Granite/Gneiss	3.00-2.90 (Pb-Pb ages)	3.10-3.04				
		Volcanic		3.60, 3.25, 3.05				
	Marutani et al. 2005	Low-K sericite from argillised zone						1852 ± 52
	Key et al. 2008	TTG/Granite/Gneiss	2933 ± 16, 2912 ± 35	3.08, 3.07		3.08, 3.03		
		Felsic Volcanic (Aouéouat)	2965 (Pb-Pb age)	3.00				
	Gärtner et al. 2013	Granite	3010 ± 8, 2935 ± 37, 2651 ± 21					
	Bea et al. 2013	TTG	3.00-2.90 (Unpublished data)					
		Syenite	2461 ± 7, 2449 ± 14	2.92-2.55			2466 ± 33	
	Montero et al. 2014	TTG/Granite/Gneiss	3029 ± 7, 3029 ± 8, 3022 ± 11, 2970 ± 20, 2952 ± 22, 2936 ± 24, 2925 ± 7, 2920 ± 6	3.06-2.92	2950 ± 230			
		Greywacke (Metasediment)	3025 ± 9 (Detrital)	3.40				
Amsaga	Auvrey et al. 1992	TTG/Granite/Gneiss	2715 ± 11					
		Gabbro Intrusion	2742 ± 7					
		Charnockite	2902 ± 8, 2834 ± 5					
	Potrel et al. 1994	TTG/Granite/Gneiss	2836 ± 14, 2751 ± 52	3.24-2.87			2831 ± 465, 2488 ± 130	
	Potrel et al. 1996	Orthogneiss	3515 ± 15 to 3422 ± 10	3.64				
		Paragneiss		3.88-3.48				
	Potrel et al. 1998	TTG/Granite/Gneiss	2726 ± 7	3.24-2.87			2265 ± 156	
		Gabbro		3.12	2706 ± 54			
		Charnockite	2986 ± 8, 2840 ± 9 (zircon rim)	3.23-3.03	3027 ± 164		2854 ± 104	
TISZ	Key et al. 2008	Gneiss	2954 ± 11	3.2		3.06		
Tiris	Vachette & Bronner 1975	Gneiss					2779 ± 83, 2706 ± 71	
	O'Connor et al. 2005	Granite	2.83-2.45 (including metamorphic ages (monazite))					
	Schofield et al. 2012	Granite	2948 ± 11, 2654 ± 8, 2487 ± 8, 2472 ± 6; 2691 ± 11, 2487 ± 8 (inheritence ages); 2482 ± 7 (metamorphic age(monazite))	2.90, 3.04, 3.14, 3.25				
Ghallaman (Temeimichat)	Schofield et al. 2006	Inherited zircons	2821 ± 45 (Inherited population from Eburnean gneiss)					
	Lahondère et al. 2003	TTG/Granite/Gneiss	3044 ± 5, 2915 ± 18, 2832 ± 4					
A-P Boundary (Eburnean)	Lahondère et al. 2003	TTG/Granite/Gneiss	2129 ± 6, 2073 ± 3, 2068 ± 6, 2059 ± 4					
	Schofield et al. 2006	TTG/Granite/Gneiss	2117 ± 36, 2093 ± 37, 2072 ± 98, 2071 ± 10, 2064 ± 12					
Mafic Dykes	Dosso et al. 1979	Dolerite Dykes					1609 ± 45	1750, 1610
	Tait et al. 2013	Ahmeyim Great Dyke (Basaltic)	2733 ± 2					

Table 2.5.1: Compilation of all known published Archean and Paleoproterozoic geochronological data from the Archean domain of the Reguibat Shield. Note: model ages are published in Ga; all other ages are published in Ma where available data exists.

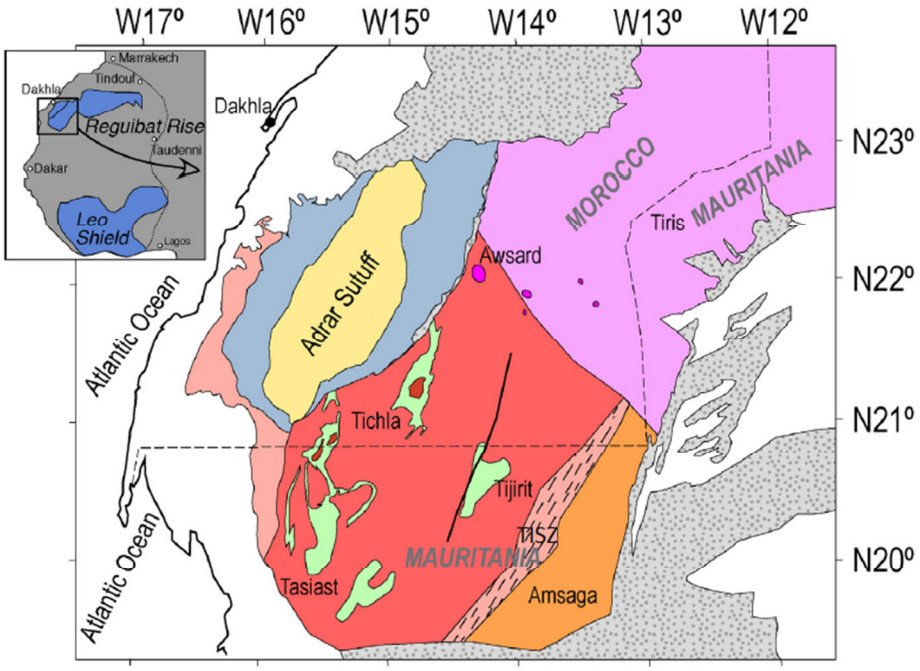


Figure 2.5.2: The distribution of greenstone belts (light green) in the Tasiast-Tijirit Terrane (red). Also highlighted are the late Asward syenite intrusions (pink). Map after Montero et al. (2014).

The oldest recorded magmatic zircons from the Tasiast-Tijirit Terrane are from a number of TTG and granitic rocks dated between ~3029 Ma and ~3022 Ma at its north-western margin (Montero et al., 2014). A 3010 ± 8 Ma granite (Gärtner et al., 2013), and a greenstone belt sedimentary rock with a dominant detrital zircon age population of ~3025 Ma (Montero et al., 2014) are also present in the north-western margin of the Tasiast-Tijirit Terrane. Although no crystallisation events older than ~3029 Ma are preserved in the Tasiast-Tijirit Terrane there is evidence for older crustal forming events being preserved in Nd model ages. Volcanic rocks from the Tasiast-Tijirit Terrane preserve Nd model ages of 3.60 Ga and 3.25 Ga (Chardon, 1996), and a greywacke from the Tichla Greenstone Belt gives a Nd model age of 3.40 Ga with a negative εNd of -1.3 (Montero et al., 2014). This suggests that the recycling of older crust played a part in the formation of these rocks.

The majority of rocks dated from the Tasiast-Tijirit Terrane prior to this study are gneiss, TTG and granite samples between ~2970 Ma and ~2912 Ma in age (Chardon, 1996, Key et al., 2008, Bea et al., 2013, Gärtner et al., 2013, Montero et al., 2014). One other lithology, a felsic volcanic rock from the Aouéouat greenstone belt, is dated at ~2965 Ma, with a Nd model age of 3.00 Ga (Key et al., 2008). All studied TTG rocks from the Tasiast-Tijirit Terrane have Nd model ages between 3.10 Ga and 2.92 Ga (Key et al., 2008, Montero et al., 2014), suggesting that new crust was formed in the Tasiast-Tijirit Terrane during this time period. Younger crystallisation ages are recorded in the far northwest of the Tasiast-Tijirit Terrane where the Reguibat Shield meets the Adrar Souttouf

Massif of the Mauritanides; a granite intrusion at 2651 ± 21 Ma (Gärtner et al., 2013) and the Asward syenite intrusions at 2461 ± 7 Ma and 2449 ± 14 Ma (Figures 2.5.1b 2.5.2) (Bea et al., 2013). There is some evidence for later tectonothermal events in the Tasiast-Tijirit Terrane seen in Rb-Sr whole rock and mineral ages of ~2840-2340 Ma (Bonnici and Giraudon, 1963, Rocci et al., 1991, Bea et al., 2013). The Rb-Sr ages however may be have been re-set, and with such little data it is difficult to link the intrusions < 2.9 Ga in age to any other rocks or events in the Tasiast-Tijirit Terrane. It is therefore likely that these intrusions are related to later tectonothermal events that partially affected the Tasiast-Tijirit terrane on its north-western margin.

Based on current knowledge, the Tasiast-Tijirit Terrane is almost solely formed by granite-greenstone formations between ~3029 Ma and ~2912 Ma in age. A combination of both recycling of older crust, some as old as 3.60 Ga, and juvenile input between 3.10-2.92 Ga was likely involved in the formation of the terrane. Although there is some evidence that later events have affected the region, these appear to be localised to the north-western margin, and are probably related to later cratonisation events (Gärtner et al., 2013, Bea et al., 2013, Montero et al., 2014). The lack of magmatism in the Tasiast-Tijirit Terrane post 2.91 Ga was highlighted by Montero et al. (2014), where it was suggested that this could be a result of the region being cratonised long before the surrounding Archean terranes of the Reguibat Shield.

2.5.2.2. Amsaga Complex:

The Amsaga Complex, also known as the Choum-Rag el Aboid Terrane (Key et al., 2008), is a relatively small terrane composed mainly of mafic, metasedimentary and migmatitic gneisses on the southeast of the Reguibat Shield (Figure 2.5.1b). It is host to the oldest known rocks in West Africa, with Paleoarchean U-Pb zircon crystallisation ages between ~3515 Ma and ~3422 Ma in an orthogneiss with a Nd model age of 3.64 Ga, as well as Nd model ages ranging from 3.88-3.48 Ga being found in a paragneiss (Potrel et al., 1996). Although there are old remnants of crust such as this found throughout the West African Craton, and further afield (e.g. the Nigerian Shield) these are rare (Barth et al., 2002), and it has been suggested that these sparse fragments could have once belonged to an early continental terrain which broke up and was incorporated in parts into separate younger continents (Kröner, 2001).

A large number of Meso-Neoarchean magmatic events are also recorded in the Amsaga Complex, responsible for forming the majority of rocks present in the region. The oldest of these is evidenced from a U-Pb zircon age of 2986 ± 8 Ma from a charnockite with a Sm-Nd isochron age of 3027 ± 164 Ma (Potrel et al., 1998). A second event is recorded by orthogneisses which have

been dated at 2834 ± 5 Ma and 2836 ± 14 Ma (Auvray et al., 1992, Potrel, 1994), and the rim of zircons from a charnockite dated at 2840 ± 9 Ma (Potrel et al., 1998). A third event is recorded by a number of granites and gabbros dating between ~2751 Ma and ~2715 Ma (Auvray et al., 1992, Potrel, 1994, Potrel et al., 1998). This last crystallisation event has certainly been, at least partially, derived from pre-existing crust as seen by both older Nd model ages (3.24-2.87 Ga) and negative εNd values. This event could be related to the latest stages of the Tâçarât-Inemmaûdene Shear Zone, for although the rocks cross-cut some shear fabrics, they are also sheared in parts themselves. All Meso-Neoarchean samples dated here show similar Nd model ages as seen elsewhere in the Reguibat Shield, within the range of 3.24 Ga and 2.87 Ga. No younger crustal events are preserved in the Amsaga Complex, however the terrane was affected during the Proterozoic as indicated by the re-setting of the Rb-Sr system between ~2500 Ma and ~2300 Ma (Potrel, 1994, Potrel et al., 1998).

2.5.2.3. Tâçarât-Inemmaûdene Shear Zone (TISZ):

The Tasiast-Tijirit Terrane and Amsaga Complex are classified as two separate terranes not only because they preserve evidence of being formed in different crustal settings, but also because they are separated by a major ductile shear zone; the Tâçarât-Inemmaûdene Shear Zone (TISZ) (Figures 2.5.1b, 2.5.2) (Key et al., 2008). This shear zone runs NNE to SSW, and does not penetrate into the Tiris Complex to the north or the Taoudeni Basin to the south.

A maximum age constraint is placed upon the TISZ by a 2954 ± 11 Ma granite gneiss present in its core (Key et al., 2008). A later 2726 ± 7 Ma granite form the margin of the Amsaga Complex (Potrel et al., 1998) is used to provide a minimum age for the shear zone as it cross-cuts shears splaying from its centre. This granite however is strongly sheared in places itself, which suggests either there was still some activity on the TISZ, or it was affected by late reactivation. The Ahmeyim Great Dyke of Mauritania provides a similar minimum age constraint (2733 ± 2 Ma) (Tait et al., 2013), as it runs sub-parallel to the shear zone, but is not affected by ductile deformation related to its movement.

2.5.2.4. Tiris Complex:

The Tiris Complex is the youngest of the major terranes comprising the Archean crust of the Reguibat Shield, situated to the northeast of the three terranes discussed above, and to the southwest of the Ghallaman Complex (Figure 2.5.1b). All dated samples from this complex are either granites or gneisses, and a number of ages come from inherited zircon populations. One

such granite sample has been dated as the oldest in the complex at 2948 ± 11 Ma (Schofield et al., 2012). Others span a wide age range and extend from the Archean into the Paleoproterozoic from ~2830-2450 Ma (O'Connor et al., 2005, Schofield et al., 2012). Nd model ages between 3.25 Ga and 2.90 Ga for these rocks however demonstrate they are sourced from recycling of older crustal material with no juvenile component apparent (Schofield et al., 2012). There is some evidence through Rb-Sr isochron ages in gneisses of a tectonothermal event between ~2780 Ma and ~2700 Ma (Vachette and Bronner, 1975, Schofield et al., 2012). The youngest rocks from the Tiris Complex, dated between 2.49 Ga and 2.45 Ga, are not seen elsewhere on the Reguibat Shield, and have been interpreted as late reactivation of older shear zones in the Tiris Complex (Schofield et al., 2012). A small allochthonous group of Paleoproterozoic rocks rest on the southeast of the Tiris Complex, known as the Ijil Complex (Bronner and Chauvel, 1979, Bronner and Fourno, 1992). This complex hosts significant BIF deposits mined for iron ore, Mauritania's largest industry.

2.5.2.5. Ghallaman Complex:

The Ghallaman Complex occupies the northwest of the Reguibat Shield Archean domain, including the entire contact with the Paleoproterozoic domain (Figure 2.5.1b). The Ghallaman Complex can be split into two sections; the Temmimichate-Tsabya Complex which forms a belt around the northern margin of the Archean domain, composed of ultramafic to mafic granulite facies igneous rocks, and the Zednes Suite, composed of TTG rocks and gneisses. Very few studies have been carried out on this region, and in particular the Temmimichate-Tsabya Complex, with no known geochronological data available from the area. Three ages have been defined from TTG rocks in the Zednes Suite; 3044 ± 5 Ma, 2915 ± 18 Ma, and 2832 ± 4 Ma (Lahondère, 2003). There is little else that can be said about this region other than the rocks of the Zednes Suite are Mesoarchean in age, though inferences have been made that the Temmimichate-Tsabya Complex is therefore also Mesoarchean in age (Schofield et al., 2006). Lahondère et al. (2003) suggest the Temmimichate-Tsabya Complex could be from an oceanic island-arc terrane, although the possibility exists that it could form part of the accretionary margin of the Paleoproterozoic Eburnean terrane (Schofield and Gillespie, 2007).

The Ghallaman Complex is separated from Paleoproterozoic rocks by a number of steeply dipping shear zones. Plutonic rocks and migmatites from these shear zones have been dated between ~2129 Ma and ~2059 Ma (Lahondère, 2003, Schofield et al., 2006), providing an age constraint for the timing of amalgamation between the two major domains of the WAC as part of the Eburnean Orogeny. One of these migmatite samples, dated at 2072 ± 98 Ma, is known to contain an inherited zircon population of 2821 ± 45 Ma (Schofield et al., 2006), consistent with ages obtained

from the basement of the Zednes Suite, however the nearest known exposure of the Zednes Suite is over 100km to the southeast. The Temmimichate-Tsabya Complex in exposed < 20km from this where this sample was collected, and could therefore be a more likely source for the inherited zircon population dated at 2821 ± 45 Ma. This could be used as an argument supporting a Mesoarchean age for the Temmimichate-Tsabya Complex.

2.5.2.6. Late dyke swarms:

Synonymous with the late granites of the Amsaga Complex, the Ahmeyim Great Dyke of Mauritania, up to 4km wide in places, intruded into the western Tasiast-Tijirit Terrane at 2733 ± 2 Ma (Tait et al., 2013). This has been attributed to the plumbing system of a Precambrian large igneous province. Similarly many later dyke swarms seen clearly from aeromagnetic imagery are present on the Reguibat Shield (Figure 2.5.3). Some of these have been dated, e.g. the doleritic dykes present in the Amsaga Terrane at 1.75-1.61 Ga (Dosso et al., 1979), and others are inferred to be Phanerozoic, related to the opening of the Atlantic Ocean (Gärtner et al., 2013, Tait et al., 2013). Most late dykes in the Reguibat Shield however remain undated.

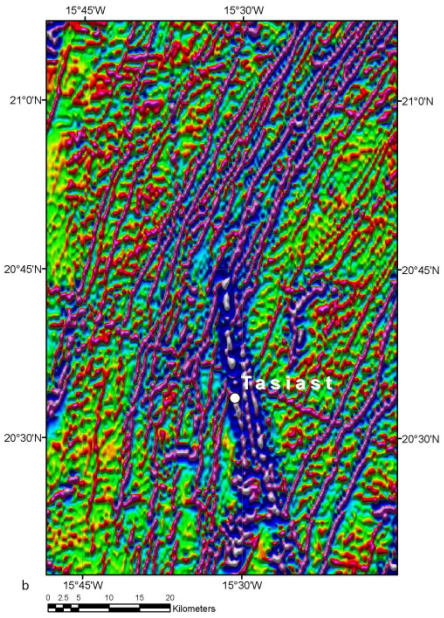


Figure 2.5.3: Aeromagnetic image of the southern Tasiast-Tijirit Terrane highlighting late dyke swarms (Heron et al., 2015).

2.5.2.7. Tectonic relationships of the Reguibat Shield:

The tectonic relationship between terranes in the Reguibat Shield that is most relevant to this project is that of the Tasiast-Tijirit Terrane and the Amsaga Complex, separated by the Tâçarât-Inemmaûdene Shear Zone. It is possible that the amalgamation of the Tasiast-Tijirit Terrane and

the Amsaga Complex has had a major effect on the formation of the Aouéouat greenstone belt and surrounding rocks. Two possible models for this event are discussed below, which will be expanded upon after the results of this project have been acquired.

1) Horizontal tectonics:

Key et al. (2008) suggest the TISZ represents a post-collisional suture between the Amsaga and Tasiast-Tijirit terranes, which were originally allochthonous. The 2726 ± 7 Ma partially sheared granite (Potrel et al., 1998) places a minimum constraint on the timing of amalgamation, while a maximum age is provided by the 2954 ± 11 Ma granite (Key et al., 2008) preserved in the core of the TISZ. Tait et al. (2013) describe the 2954 ± 11 Ma granite as syn-tectonic to constrain the time of amalgamation between the two terranes, and that this collision was preceded by calc-alkaline volcanism preserved in the Tasiast-Tijirit Terrane as greenstone belts, dated at ~2965 Ma (Key et al., 2008). The model of a ~2954 Ma amalgamation and associated greenstone belts at ~2965 Ma fits with a model of horizontal tectonics, in which the granite-greenstone sequences of the Tasiast-Tijirit Terrane represent the rocks formed above a subducting slab, probably in an oceanic

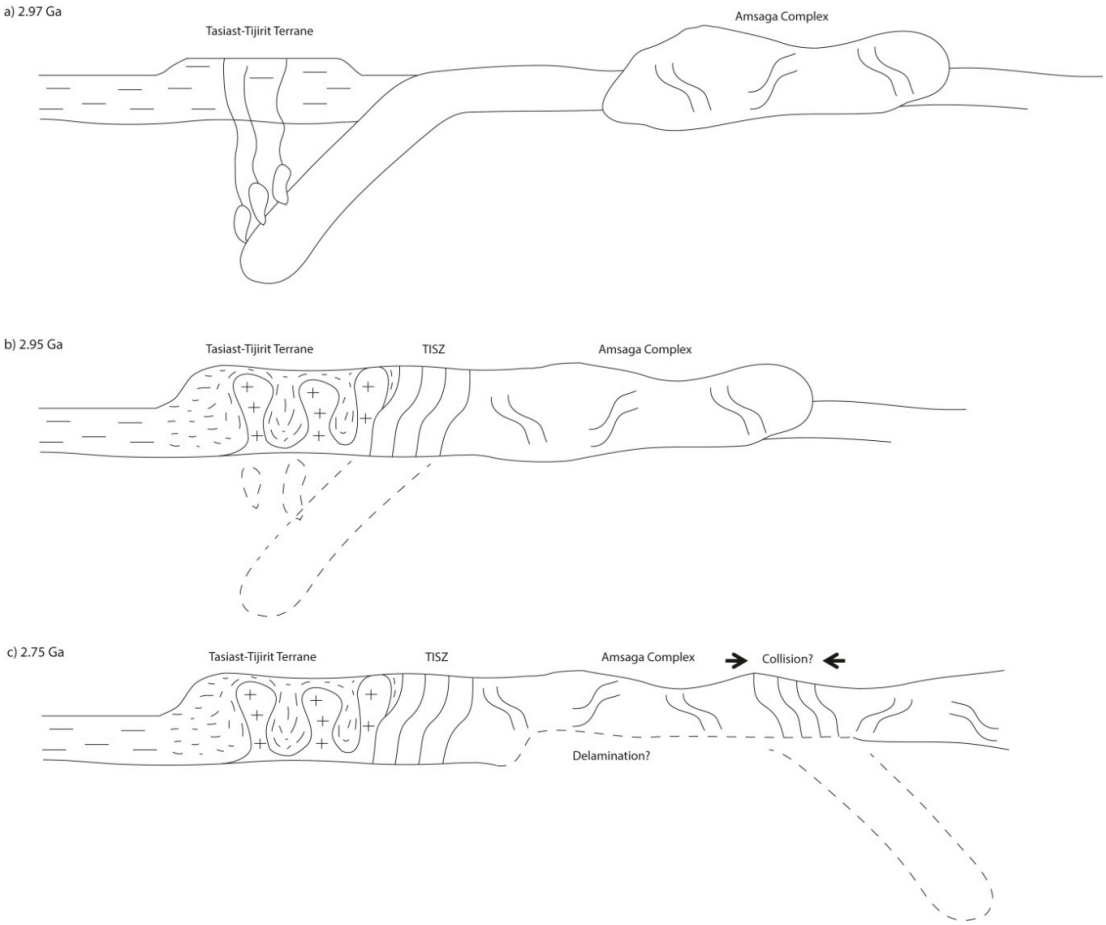


Figure 2.5.4: Sketch diagram of possible model for formation of the Tasiast-Tijirit Terrane through horizontal tectonics.

arc setting, forming around 2965 Ma (Figure 2.5.4a). This subduction may then have ceased ~2950 Ma with the collision of another island arc, or more likely micro-continent, of the Amsaga Complex, with the TISZ representing the suture zone between the Tasiast-Tijirit Terrane and the Amsaga Complex (Figure 2.5.4b). A later tectonothermal event then occurred at ~2840 Ma (ages recorded in the Amsaga Complex (Potrel, 1994, Potrel et al., 1998)), and a more significant granulite event resulted in crustal re-working and the formation of younger ~2751-2715 Ma granites (Auvray et al., 1992, Potrel, 1994, Potrel et al., 1998), possibly due to delamination, or a collisional event involving the Tiris Complex or another unexposed terrane (Figure 2.5.4c).

2) Vertical and horizontal tectonics:

A model of vertical tectonics for the Tasiast-Tijirit granite-greenstone terrane is preferred by numerous authors (e.g. Rocci et al., 1991, Potrel, 1994, Chardon, 1996, Schofield et al., 2012). This would involve vertical tectonics, or sagduction being the formation process of the initial granite-greenstone terrane between ~3029 Ma and ~2912 Ma (Figure 2.5.5a). Again here, the Tasiast-Tijirit Terrane would have formed as a separate terrane to the Amsaga Complex, in which there are very few rocks dated between ~3029 Ma and ~2912 Ma. Collision between these two terranes, with the TISZ representing the suture zone, could then have occurred at either ~2840

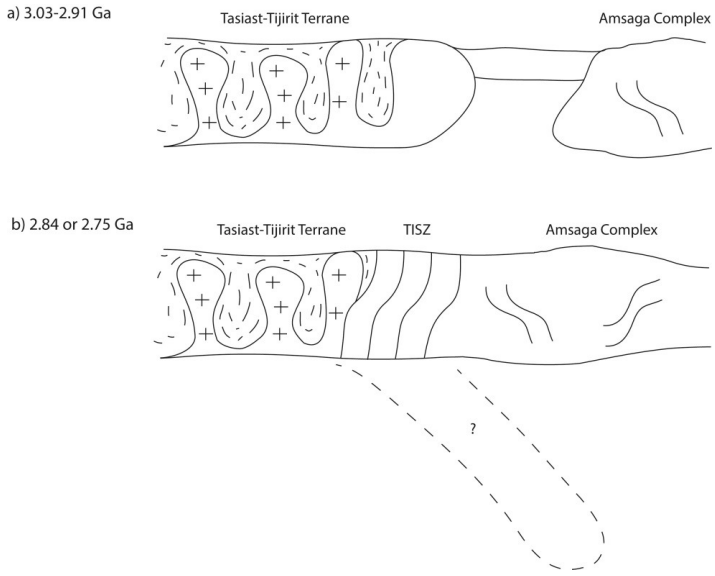


Figure 2.5.5: Sketch diagram of possible model for formation of the Tasiast-Tijirit Terrane through vertical and horizontal tectonics.

Ma (ages recorded in the Amsaga Complex (Potrel, 1994, Potrel et al., 1998)) or alternatively ~2730 Ma (the minimum age of amalgamation (Potrel et al., 1998, Tait et al., 2013)) resulting in

the granulite metamorphism and crustal re-working prevalent in the Amsaga Complex between ~2751 Ma and ~2715 Ma (Auvray et al., 1992, Potrel, 1994, Potrel et al., 1998) (Figure 2.5.5b). This model infers that vertical tectonics were the major tectonic process active in this region between 3.03 Ga and 2.91 Ga, but that horizontal plate tectonics were active by 2.75 Ga.

With both of these models being theoretically possible, additional geochronological and geochemical research may highlight the most appropriate model, or appropriate parts of these models.

There are no known crustal formation events later than 2715 ± 11 Ma (Auvray et al., 1992) within the three southern terranes (Tasiast-Tijirit Terrane, TISZ and Amsaga Complex) and so it appears that major tectonic events had ended by this time. Extensive areas of terrane margins however remain unexposed, and so unknown. The Reguibat Shield unconformably underlies the Proterozoic Taoudeni Basin (Key et al., 2008), and the Mauritanides Belt, known to have formed by crustal shortening during the Caledonian and Variscan Orogenies, has likely been finally thrust onto the Reguibat Shield at the early stages of the collision between Gondwana and Laurentia (325-300 Ma) (Martyn and Strickland, 2004).

Few studies have been published on the relationship between the Tiris Complex and the other Archean terranes. There is evidence that the three southern terranes are juxtaposed against the Tiris Complex along its south-western margin, with the contact again being characterised by ductile shear zones (Schofield et al., 2012). Other than one granite sample, all the dated lithologies in the Tiris Complex are younger than those of the Tasiast-Tijirit Terrane and much of the Amsaga Complex. Although few data are available, it is expected that the Tiris Complex was formed as a separate terrane before later amalgamation, particularly as the TISZ does not penetrate into the Tiris Complex. Rb-Sr ages between 2.78 Ga and 2.71 Ga in the Tiris Complex (Vachette and Bronner, 1975, Schofield et al., 2012), as well as the southern three terranes (e.g. Rocci et al., 1991, Potrel, 1994), suggest that by this time the complexes were amalgamated, or possibly were in the process of amalgamation leading to the re-setting of the Rb-Sr system at this time. The contact between the Tiris complex and the Ghallaman Complex is largely covered by superficial deposits, however there is some evidence that there is a structural contiguity between gneisses of the two terranes seen through common deformation fabrics (Schofield et al., 2012).

The contact between the Ghallaman Terrane and the Proterozoic domain of the Reguibat Shield as mentioned above is characterised by a number of steep shear zones, and records a history of collision during the Eburnean Orogeny at ~2.1 Ga (Lahondère, 2003, Schofield et al., 2006).

It is important to note that almost all crust forming events in the Reguibat Shield appear to have occurred between 3.2 Ga and 2.8 Ga. The majority of rocks that formed later than this have been sourced through the reworking of pre-existing crust, particularly during metamorphic events caused by the likely amalgamation of the different terranes that now constitute the shield. The only evidence of other crustal formation events, other than late dykes, are the older Nd model ages recorded in both the Tasiast-Tijirit Terrane and the Amsaga Complex up to 3.60 Ga. It is also worth noting that Foster (Foster and Piper, 1993) made reference to a granulite metamorphism event at 3.27 Ga affecting the Reguibat Shield, however this is loosely referred to with no supporting data and does not appear to be mentioned in any other publications.

The Reguibat Shield has been tectonically stable since ~1.7Ga (Schofield et al., 2006) with the only geological events since then being the intrusion of late dyke swarms, for example, related to the opening of the Central Atlantic Ocean (Tait et al., 2013).

2.5.3. Aouéouat greenstone belt and surrounding rocks:

This section discusses in detail the Aouéouat greenstone belt and surrounding rocks. The details of the different rock assemblages present in the area are sourced from various reports produced by Kinross Tasiast (Stuart, 2010, e.g. Sims, 2014). The Aouéouat greenstone belt is a ~75 km by 15 km north-south trending greenstone belt located in the western Tasiast-Tijirit Terrane and forms part of the Chami greenstone belt referred to in the literature (e.g. Key et al., 2008, Taylor et al., 2012). It is characterised by an ultramafic to felsic metavolcanic and metasedimentary succession with associated banded iron formations and intrusive units (Figure 2.5.6). The sedimentary packages mainly consist of greywackes and banded iron formations, while a subordinate amount of siltstones are also present in places. All rocks in the Aouéouat greenstone belt have undergone upper-greenschist to lower-amphibolite facies metamorphism, however for simplicity these rocks will often be referred to by their protolith name and without the prefix ‘meta’. A complex structural history is preserved in the Aouéouat greenstone belt which involves multiple deformation events resulting in isoclinal folding of the stratigraphy, as well as a number of later minor shear zones. The two major deformation events resulting in the folding recorded are an E-W compressional event, and a NW-SE compressional event. The shear zones are typically 0.5 m to 10 m thick, and are related to a thrust system involving a main basal thrust and a number of splays propagating from this thrust. As is seen throughout the Reguibat Shield, later cross cutting mafic dykes are present in the Aouéouat greenstone belt. These are typically < 5m wide.

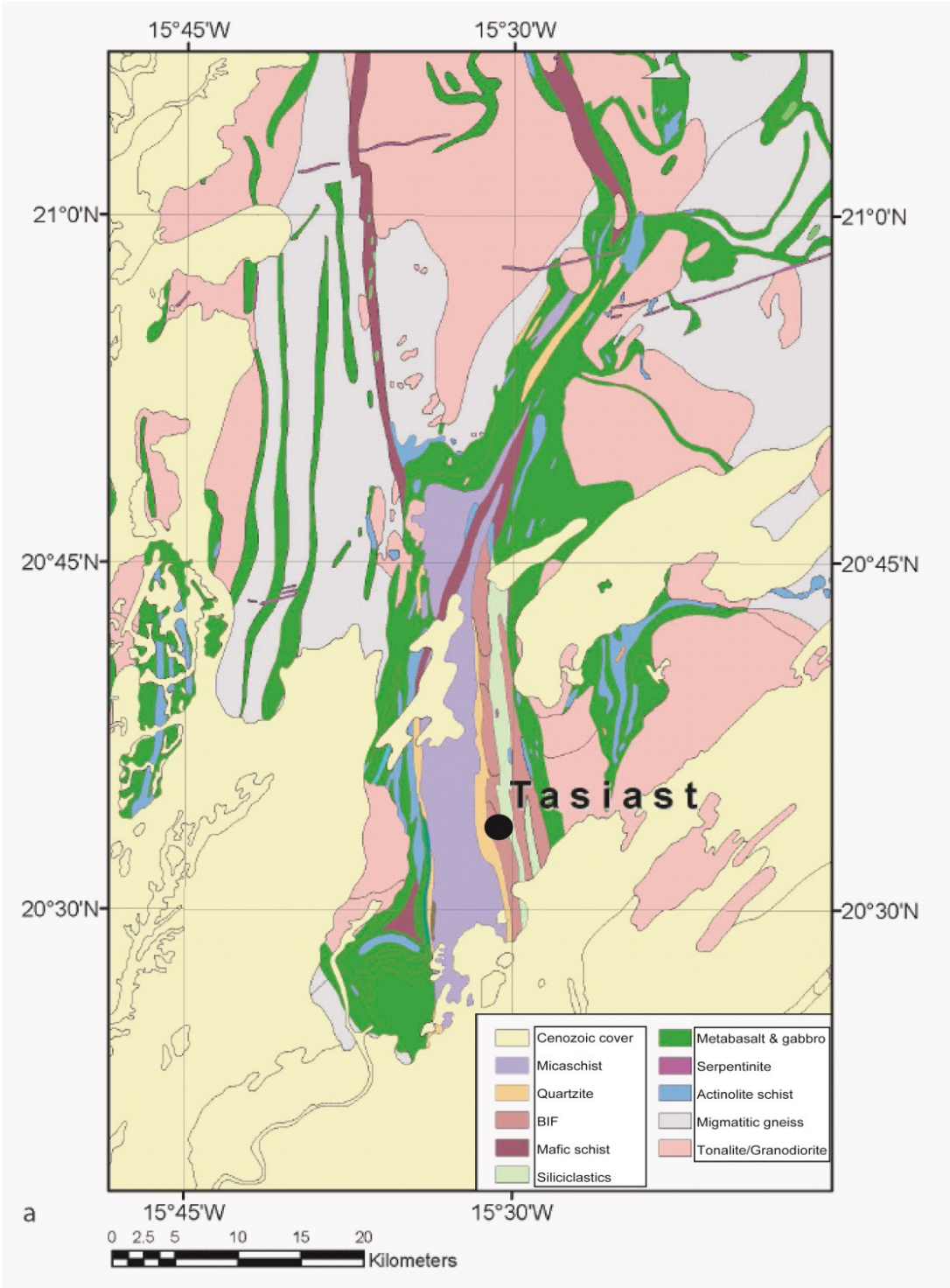


Figure 2.5.6: Geological map of the Aouéouat Greenstone Belt (Kinross Tasiast).

Three rock assemblages comprise the Aouéouat greenstone belt: the Temeimichat, Aouéouat and Tasiast assemblages. These are described in the following sections, and the relationship between these assemblages and the surrounding rocks can be seen in the map and cross section of figures 2.5.6 and 2.5.7.

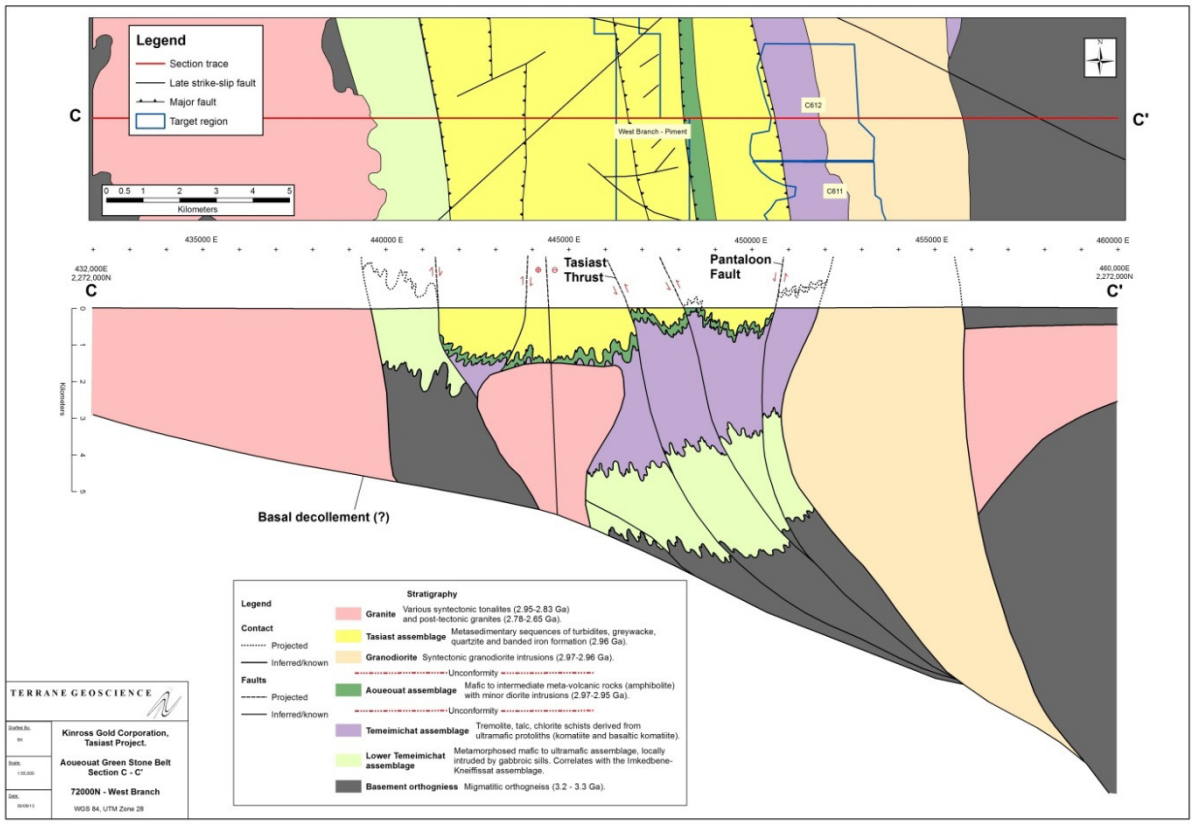


Figure 2.5.7: Cross section through the Aouéouat greenstone belt (Sims, 2014).

2.5.3.1. Temeimichat assemblage:

The Temeimichat assemblage is the lower of the three assemblages in the Aouéouat greenstone belt and is also the largest. It consists of ultramafic and mafic volcanic rocks, interpreted as being komatiite and basaltic komatiite flows, and unconformably overlies orthogneissic basement rocks.

2.5.3.2. Aouéouat assemblage:

The Aouéouat assemblage encompasses mafic to felsic volcanic rocks as well as some associated intrusive units, and unconformably overlies the Temeimichat assemblage. Mafic volcanic rocks, interpreted as being predominantly basaltic in nature, comprise the bulk of the Aouéouat assemblage. Intrusive diorite and quartz-diorite units are also present. The diorite and quartz-diorites are tentatively linked to the basalts, originating as fractionated dykes and sills emplaced during the eruption of the volcanic rocks. Overlying the mafic rocks is a thin and discontinuous felsic volcanic rock, classified as a felsite, which reaches a maximum thickness of 200m in places. This is an important unit with regards to gold mineralisation in the area, and is possibly sourced from pyroclastic flows or dacitic eruptions. A sample of felsite from the region was previously dated at ~2965 Ma as discussed in chapter 2.5.2.1 (Key et al., 2008), and although only three

zircons were available for this study, it is likely this is roughly the age of this lithology. The felsite forms the top of the Aouéouat assemblage, and is unconformably overlain by the sediments of the Tasiast assemblage.

2.5.3.3. Tasiast assemblage:

The Tasiast Assemblage consists of the sedimentary rocks of the Aouéouat greenstone belt that overlie the Aouéouat assemblage volcanic rocks. There are predominantly two rock types that form the Tasiast assemblage: banded iron formations and greywackes. The banded iron formations form the lower of the sedimentary units, and are composed of alternating iron mineral layers, mainly magnetite, and chert layers. The chert layers are not pure chert, and can contain feldspathic minerals and some thin sedimentary layers, and so it is not certain whether these rocks are pure hydrogenous banded-iron formations, or are reworked iron-rich clastic sediments that have been later metamorphosed. The former of these is more likely; however a siliciclastic source must have been in the vicinity to provide the additional material, either from exposed rocks or volcanic eruptions. The banded iron formations are interpreted to unconformably overlie the Aouéouat assemblage due to the presence of a conglomerate at the base of the Tasiast assemblage containing clasts of the felsite and mafic volcanics of the Aouéouat assemblage. Overlying the banded iron formations are siliciclastic sediments which make up most of the Tasiast assemblage. These are mainly greywackes, interpreted to have formed through turbiditic Bouma sequences, although other sedimentary facies are also present in minor amounts such as siltstones and conglomerates. Occasionally thin banded iron formations are interbedded with the sediments, presumably formed during periods of relative stability and quiescence in the source region of the greywackes.

2.5.3.4. Imkebdene-Kneffissat greenstone belt:

The Imkebdene-Kneffissat greenstone belt lies to the west of the Aouéouat greenstone belt. The only rocks exposed in this belt are ultramafic to mafic volcanic rocks. Although it is possible that this is an entirely separate greenstone belt, it is more likely that this correlates to the lower parts of the Temeimichat assemblage in the Aouéouat greenstone belt, and therefore represents the lower stratigraphy of the Aouéouat greenstone belt, structurally exposed by faulting.

2.5.3.5. TTG rocks:

Surrounding the Aouéouat and Imkebdene-Kneffissat greenstone belts are a number of TTG plutons (Figure 2.5.8). These are granodioritic in composition, and in many places are porphyritic in nature. Due to the relative unimportance of TTG plutons in gold mineralisation and its distribution, very little detail is known for these rocks. They are likely to be related to the TTG rocks of the Tasiast-Tijirit Terrane discussed earlier, and therefore to date between 2970 Ma and 2912 Ma.



Figure 2.5.8: Field photo of TTG intrusion (Sample TSUPB012).

2.5.3.6. Basement:

The remaining volumetrically significant lithology yet to be described is the orthogneissic basement. Similar to the TTG rocks, the orthogneissic basement is of little impact to the gold exploration programme in the Aouéouat greenstone belt. It is also not exposed in the immediate vicinity of the Aouéouat greenstone belt, and so little is known about the basement. Using the description by Key et al. (2008), the basement is formed by migmatitic gneisses of tonalitic composition cut by many felsic veins and mafic dykes, and unconformably underlies the greenstone belts. According to Tasiast reports it is exposed in the field to the west of the Imkebdene-Kneffissat greenstone belt and to the east of the Aouéouat greenstone belt (Figure 2.5.9).

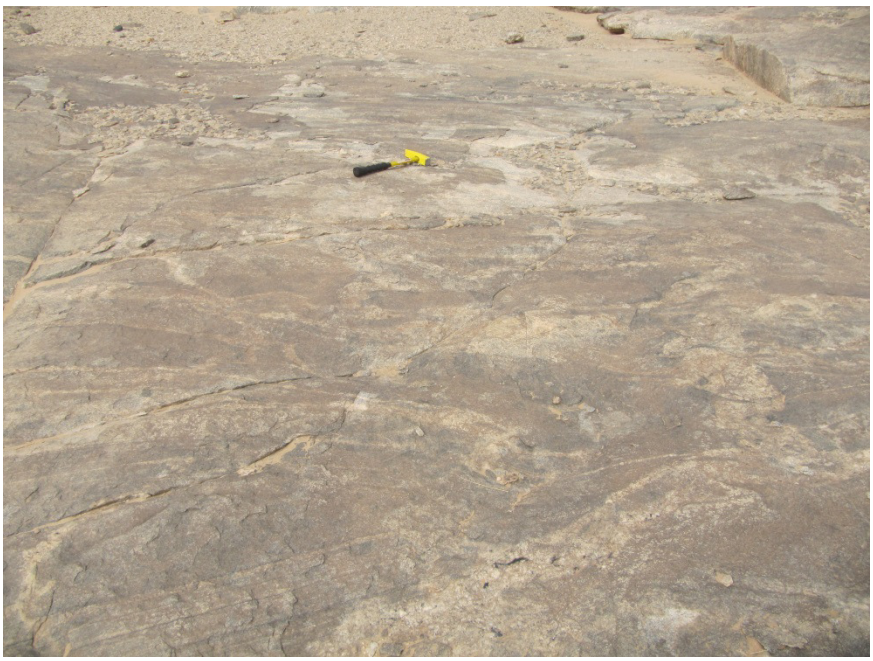


Figure 2.5.9: Field photo of orthogneiss basement.

2.5.4. Gold in the Aouéouat greenstone belt:

In comparison to Archean cratons worldwide, the Archean rocks of the West African Craton are largely devoid of gold mineralisation. Excluding some parts of the Guinea Rise in Sierra Leone, and the Tasiast deposit studied in this thesis, most known gold mineralisation in the West African Craton is hosted in Paleoproterozoic Birimian rocks (e.g. the world renowned Ashanti deposits in Ghana (Goldfarb et al., 2001)), related to the Eburnean Orogeny (Foster and Piper, 1993). In the Reguibat Shield there are few rocks of greenschist facies, which as discussed, are the most conducive to the formation and preservation of gold deposits. The apparent lack of gold deposits in the Reguibat Shield is therefore not surprising. This highlights the Tasiast deposit in rocks of a Mesoarchean age as an anomaly, as not only is it hosted in greenschist facies rocks, but it raises the possibility of the existence of an older Archean gold mineralisation event in the West African Craton.

The Aouéouat greenstone belt hosts the Tasiast gold deposit. This is a giant orogenic deposit, which was ranked as the 18th highest gold producing mine in the world in 2012 (NRH, 2012), and has current gold resource estimates of 12.8 million oz (Heron et al., 2015). Gold mineralisation in the Aouéouat greenstone belt is hosted in a network of quartz-carbonate veins and disseminated in the country rock and structures surrounding these. The quartz-carbonate veins themselves are typically < 20 cm in width, are complex in their nature continuously splaying into multiple smaller veins, and dip moderately to the east. The mineralisation zone associated with them can be found up to 20 m from the veins disseminated in strongly silicified country rock. There is a major

structural control to mineralisation distribution in the form of the Tasiast shear system which is composed of the Tasiast Thrust, and a number of shear zones interpreted to be splays propagating from it. The Tasiast shear system controls the distribution of gold deposits currently mined at Tasiast, namely the Piment and West Branch deposits (Figure 2.5.10), and has a known strike length of greater than 10 km and depths > 740 m. At the Tasiast Thrust, the older volcanic and intrusive rocks of the Aouéouat assemblage have been displaced to overlie the younger sedimentary successions of the Tasiast assemblage. The country rock in which mineralisation occurs is generally banded iron formation in the Piment deposit, and felsite in the West Branch deposit, although other targets have different host rocks, e.g. mafic volcanics and quartz diorites at the C6.7 target. This highlights that the mineralisation is only partially controlled by rock type, while the main controls are related to shear zones and quartz veins.

Mineralogically, the quartz-carbonate veins are generally > 95 % quartz and < 5 % calcite. Minor amounts of associated gold and sulphides are present in the veins, often accompanied by biotite and occasionally other minerals e.g. tourmaline and actinolite. The sulphides most commonly associated with the native gold are pyrite and pyrrhotite, which are both extensively disseminated in the country rocks and present in the quartz-veins. Occasionally mineralised zones associated with the quartz-carbonate veins can be > 20 cm in size (Figure 2.5.11).

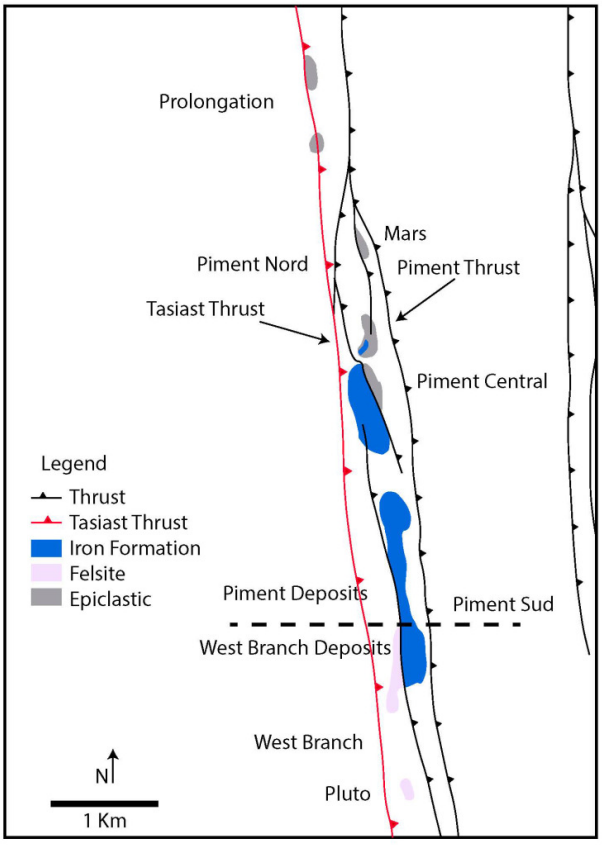


Figure 2.5.10: Location of main Tasiast deposits and their host rocks, as well as the main structural features (Stuart, 2010, Heron et al., 2015).

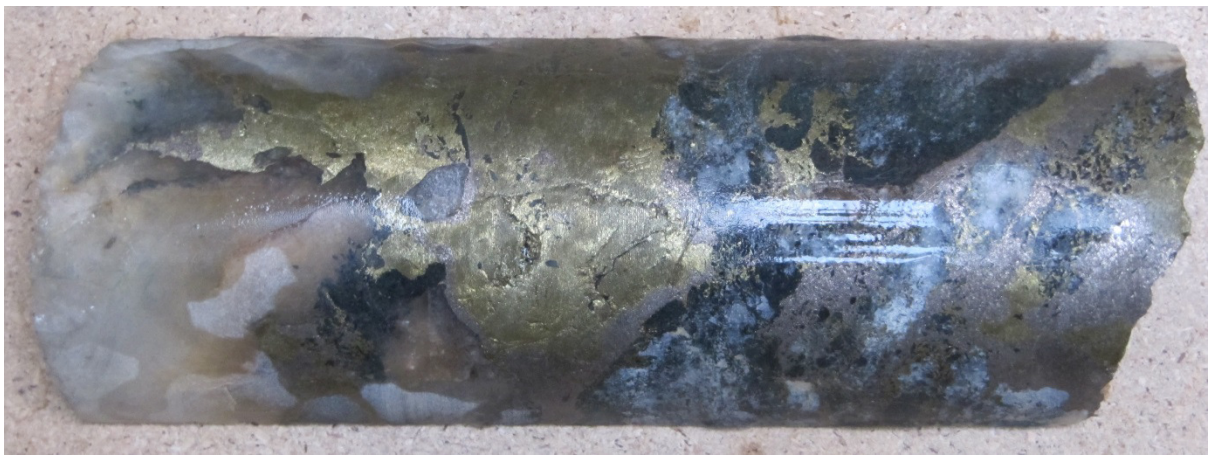


Figure 2.5.11: Drill core of quartz-carbonate vein showing extensive sulphide mineralisation (sample TSUPB017) (note drill core is 6cm in diameter).

It is not surprising that mineralisation is hosted within greenschist facies rocks and not amphibolites, as is seen in greenstone belt hosted gold deposits worldwide (Hunter and Stowe, 1997). There is some native gold present in amphibolites at Tasiast, but this is only located in the vicinity of shear zones which affect these rocks. Previous studies attempting to date the age of gold mineralisation in the Aouéouat greenstone belt have relied on K-Ar dating of low potassium sericite, which gave an age of 1852 ± 52 Ma from a surface exposure of a white argillised zone (Marutani, 2005).

Chapter 3: Methodology

3.1. Petrography:

Petrography was used initially at outcrop and hand sample scale in order to select representative samples of the relevant rock lithologies from the field to be studied for this project. After collection, polished thin sections of the rocks chosen for processing and analysis were made at the Department of Geology, Trinity College Dublin, and detailed petrography was carried out in order to further describe and classify these rocks. This was carried out using a Leica DM750P microscope, and thin section photomicrographs were imaged using a Leica DFC400 camera.

3.2. Fieldwork:

An initial set of 12 samples were collected by Kinross Tasiast, and shipped to Trinity College Dublin for mineral separation and U-Pb geochronology analysis. These were chosen to represent a wide range of lithologies present within and around the Aouéouat greenstone belt, and are referred to as 'Phase 1' samples for the purpose of analytical procedures. Following initial U-Pb zircon geochronology on these, a four week field session was undertaken to collect further samples for geochemistry, isotope analysis, and U-Pb geochronology.

The fieldwork was carried out on site at the Kinross Tasiast active mine in Mauritania. Initially the fieldwork was based around locating suitable lithologies from drill core log files and databases, followed by locating possible drill core sections from the core yard (Figure 3.1a). Upon location, these were inspected for petrography and quality (Figure 3.1b-d), before being accepted as usable core samples, or rejected. Accepted core was recorded and given a sample code, while alternatives were sought for rejected samples.

Following the collection of drill core samples, field samples were collected. Due to the deep weathering profile of the majority of rocks in the Aouéouat greenstone belt, field samples were restricted to TTG plutons surrounding the greenstone belt, and relatively resistant lithologies, including quartz-carbonate veins and banded iron formations from within the greenstone belt. Initial reconnaissance field trips were made to locate possible sites for suitable sample collection. These included traverses across the greenstone belt (W-E), traverses through field excavation trenches in the greenstone belt, and fieldwork out with the greenstone belt with an aim to locate quartz-carbonate veins, TTG plutons, and basement orthogneiss.



Figure 3.1: Field photos of; a) core yard, b) core shed, c) typical core storage box, d) core reference library.

Field exploration trenches were excavated in order to try and counteract the problems caused by both the deep lateritic profile (Figure 3.2a) and the extensive sand coverage in the Aouéouat greenstone belt. These have a depth of roughly 1.5-2.0 m, exposing the walls of the trench and the lithologies that they were comprised of (Figure 3.2b,d). The rocks were still deeply weathered, however the trenches were particularly useful for sampling quartz-carbonate veins, as these were generally the most resistant lithology of the rocks within the Aouéouat greenstone belt and so stood proud in the exploration trenches (Figure 3.2c).

Field reconnaissance with the aim of sampling orthogneiss basement rocks was unsuccessful, as all outcrops located within the boundary of the Kinross Tasiast exploration license were of TTG plutons (Figure 3.3a). In an attempt to solve this problem, samples were taken from slab shaped xenoliths hosted within TTG plutons (Figure 3.3b), with the possibility that these were xenoliths of basement orthogneiss that had been incorporated within the TTG rocks during their emplacement. Samples of banded iron formation were also collected from the field due to their relative resistance to weathering allowing exposures to remain where most other lithologies were absent.

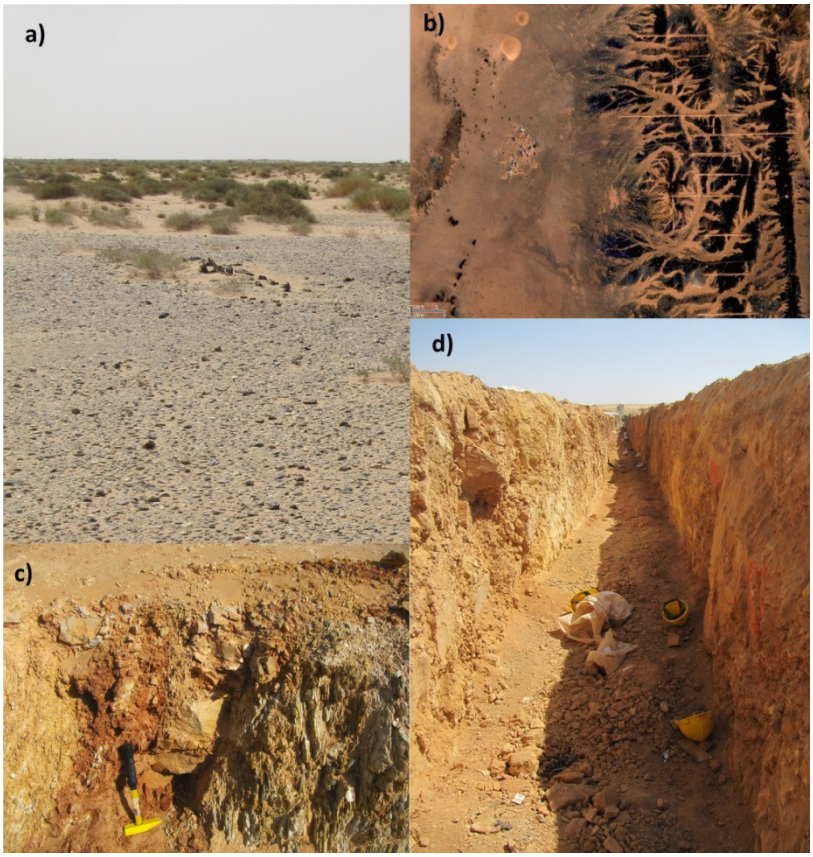


Figure 3.2: Field photos of; a) extensive laterite surface, b) satellite image of field exploration trenches, c) quartz-carbonate vein exposed in trench, d) field exploration trench.

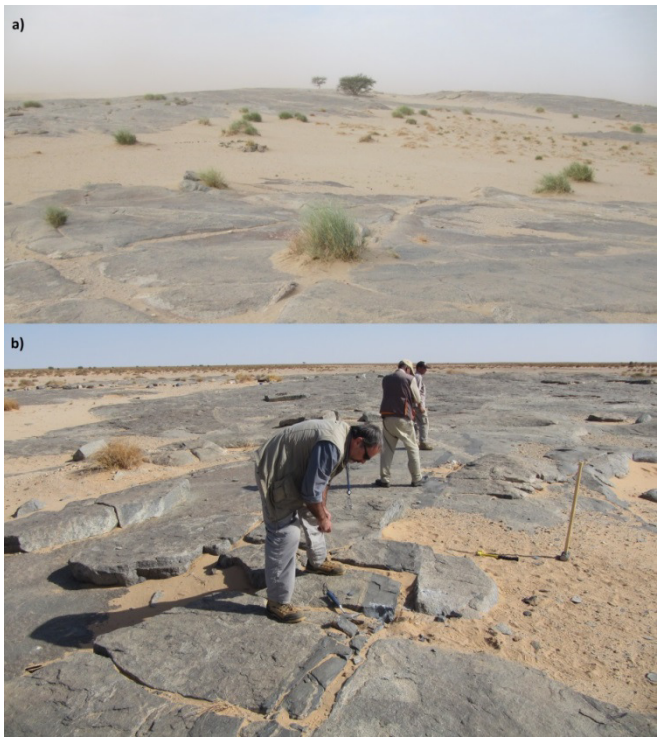


Figure 3.3: Field photos of; a) TTG exposure, b) slab shaped xenolith within TTG.

All of the samples collected from this field session, and any later additional samples are classed as 'Phase 2' samples for the purpose of analytical procedures. A full list of all samples collected for this project, along with their drill hole identifications, or field co-ordinates, is provided in appendix 2.

3.3. Sample processing and mineral separation:

All sample processing was carried out using the rock crushing and mineral separation facilities at the Department of Geology, Trinity College Dublin. Rock samples (a combination of drill core and surface samples) were cleaned, and split, with weathered surfaces being removed where possible. These were then crushed using a Retsch jaw crusher with tungsten carbide plates. Note that before sieving a representative sub-sample was retained for geochemical analysis. The split for geochemical analysis was pulverised to a powder in a Retsch agate mill to minimise metal contamination. The remaining material was sieved to separate the portion with a grain size < 300 µm which was then run on a Gemini water separation table to isolate the heavy mineral fraction. The heavy mineral fraction was subsequently passed over with a neodymium magnet to remove any magnetite and Fe-oxides, before being processed through a Frantz magnetic separator to remove the remaining magnetic fraction. The non-magnetic fraction was run through the heavy liquid methylene iodide which has a density of 3.32 g/cm^3. This resulted in the final mineral separate from which zircons could be hand-picked. For apatite, a further step included passing the final heavy mineral separate through the heavy liquid methylene iodide diluted with acetone to give a density of 2.7 g/cm^3. This resulted in a further mineral separate with a density between 2.70 g/cm^3 and 3.32 g/cm^3, from which apatite was hand-picked. Sulphides were hand-picked from the heavy mineral separate, and feldspars were hand-picked from the light mineral fraction collected from the water separation table. Detailed procedures for using the rock crushing and mineral separation equipment were written, and are included in appendix 3.

3.4. Analysis and data reduction:

This section outlines the analytical procedures used for the collection and production of all of the geochemical and isotopic data used in this study.

3.4.1. U-Pb dating:

Zircons were hand-picked under a binocular microscope and mounted in separate 25mm diameter

resin epoxy plugs, ground down to expose grain interiors and polished with 6µm and 1µm diamond paste. Where possible, 120-160 zircons were mounted for each sample, otherwise all available zircons were mounted (Figure 3.4).

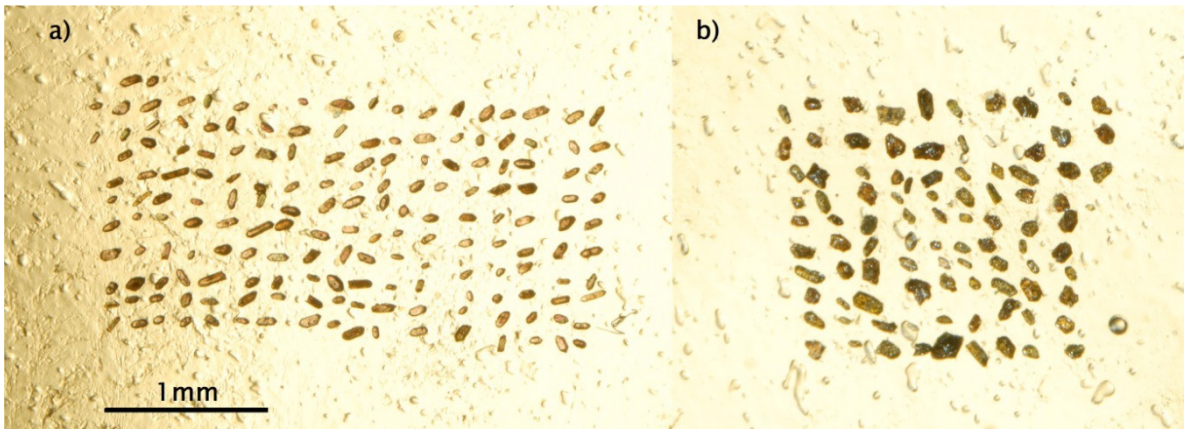


Figure 3.4: Images of zircons in 25mm polished pucks; a) TSUPB005, b) TSUPB011

Cathodoluminescence-imaging (CL-imaging) was carried out on all samples in order to better classify the morphology of the zircons, and to aid with the position of analyses spots so as to avoid damaged or metamict areas where possible (for Phase 2). Phase 1 CL-imaging was carried out at NERC Isotope Geosciences Laboratory (NIGL), Keyworth, England, retrospectively relative to U-Pb analysis. Phase 2 CL and BSE-imaging was carried out at the CMA, Trinity College Dublin, prior to U-Pb analysis. This allowed a differentiation to be made between igneous and hydrothermal zircon, as well as whether or not the zircon were igneous or detrital in nature. It is important to note however that zircon from a single rock and single age population can have widely varying morphologies, and zircon from widely different rock-types can have similar to identical morphologies with no systematic measurable differences (Hoskin and Schaltegger, 2003).

Phase 1 samples were analysed by LA-ICP-MS at the Mineral Exploration Research Centre, Laurentian University, using a Photon Machines 193 nm ArF Excimer laser with a spot size of 17 µm and a Thermo X Series II quadrupole ICP–MS. Phase 2 samples were analysed by LA-ICP-MS (Thermo Scientific iCAP Qs) at the Department of Geology, Trinity College Dublin using a Photon Machines 193 nm ArF Excimer laser equipped with a HeLex ablation cell. Nine isotopes (^{238}U, ^{232}Th, ^{208}Pb, ^{207}Pb, ^{206}Pb, $^{204}Pb/^{204}Hg$, ^{200}Hg, ^{91}Zr, ^{88}Sr) were acquired with a spot size of 30 µm. For analyses conducted at TCD the LA-ICP-MS system was tuned while ablating a line raster on NIST SRM 612 synthetic glass in order to obtain optimal sensitivity for Pb, Th and U, while keeping ThO^+/Th low and Th/U close to 1. ThO^+/Th and Th/U were typically < 0.002 and > 0.9, respectively. Full instrument set-up conditions are given in table 3.1.

	Laurentian	TCD
ICP Instrument model	Thermo X series II Q-ICP-MS	Thermo-Scientific iCAP-Qs (quadrupole)
Plasma RF power (W)	1500	1450
Plasma gas flow (lit/m)	0.7	0.7
Monitored masses	^{238}U, ^{232}Th, ^{209}Bi, ^{208}Pb, ^{207}Pb, ^{206}Pb, $^{204}Pb/^{204}Hg$, ^{202}Hg, ^{88}Sr	^{238}U, ^{232}Th, ^{208}Pb, ^{207}Pb, ^{206}Pb, $^{204}Pb/^{204}Hg$, ^{200}Hg, ^{91}Zr, ^{88}Sr
LA Instrument Model	Resonetics RESOlution M-50 193 nm ArF excimer	Photon Machines Analyte 193 nm ArF excimer
Fluence (J/cm2)	10.5	7
Repetition Rate (Hz)	5	5
Delay between analyses (seconds)	30	15
Ablation duration (seconds)	30	30
Carrier gas flow (lit/m)	0.60 (He), 0.74 (Ar), 0.006 (N_2)	0.70 (He), 0.006 (N_2)
Spot diameter (µm)	17	30

Table 3.1: Running conditions for ICP-MS and laser ablation at Laurentian University and Trinity College Dublin.

Zircon 91500 was used as the primary standard for all zircon U-Pb analyses. This is thought to have come from a syenite pegmatite near Kuehl Lake in Ontario, Canada, and is widely used as a reference standard due to its chemical and physical homogeneity, consisting of small chips separated from an original large crystal with a mass of 238g. The age of this standard is widely accepted at 1065 Ma (Wiedenbeck et al., 1995). The secondary standards used are Plešovice and Temora-2. Plešovice comes from a potassic granulite in the Bohemian Massif, Czech Republic and has an accepted TIMS weighted mean $^{206}Pb\,/\,^{238}U$ age of 337.13 ± 0.37 Ma (Sláma et al., 2008). Temora-2 is from a gabbroic diorite from New South Wales, Australia, with an accepted TIMS $^{206}Pb\,/\,^{238}U$ age of 416.75 ± 0.24 Ma (Black et al., 2003). The standard data from all of the U-Pb analyses carried out for this project are presented in figure 3.5. These are split into Phase 1 analyses, which were carried out in Laurentian University, and Phase 2 analyses, which were carried out in Trinity College Dublin. These are also presented as combined data, and give the following ages: 91500, 1062.9 ± 1.9 Ma; Plešovice, 337.2 ± 2.1 Ma; Temora-2, 416.6 ± 2.6 Ma. Of these, 91500 is the only standard which does not overlap within error, although it is only 0.2 Ma out with error. The two secondary standards give almost exactly the same age as the accepted TIMS age (both within 0.2 Ma), and therefore highlight the accuracy of the data attained for this project. Although CL-imaging was used to target the least damaged regions of non-standard zircon grains, the majority of zircons were relatively poor in quality resulting in varying degrees of discordance in the data. This is common in Archean zircons, and has been seen in other U-Pb zircon studies of the Reguibat Shield (Key et al., 2008, Schofield et al., 2012).

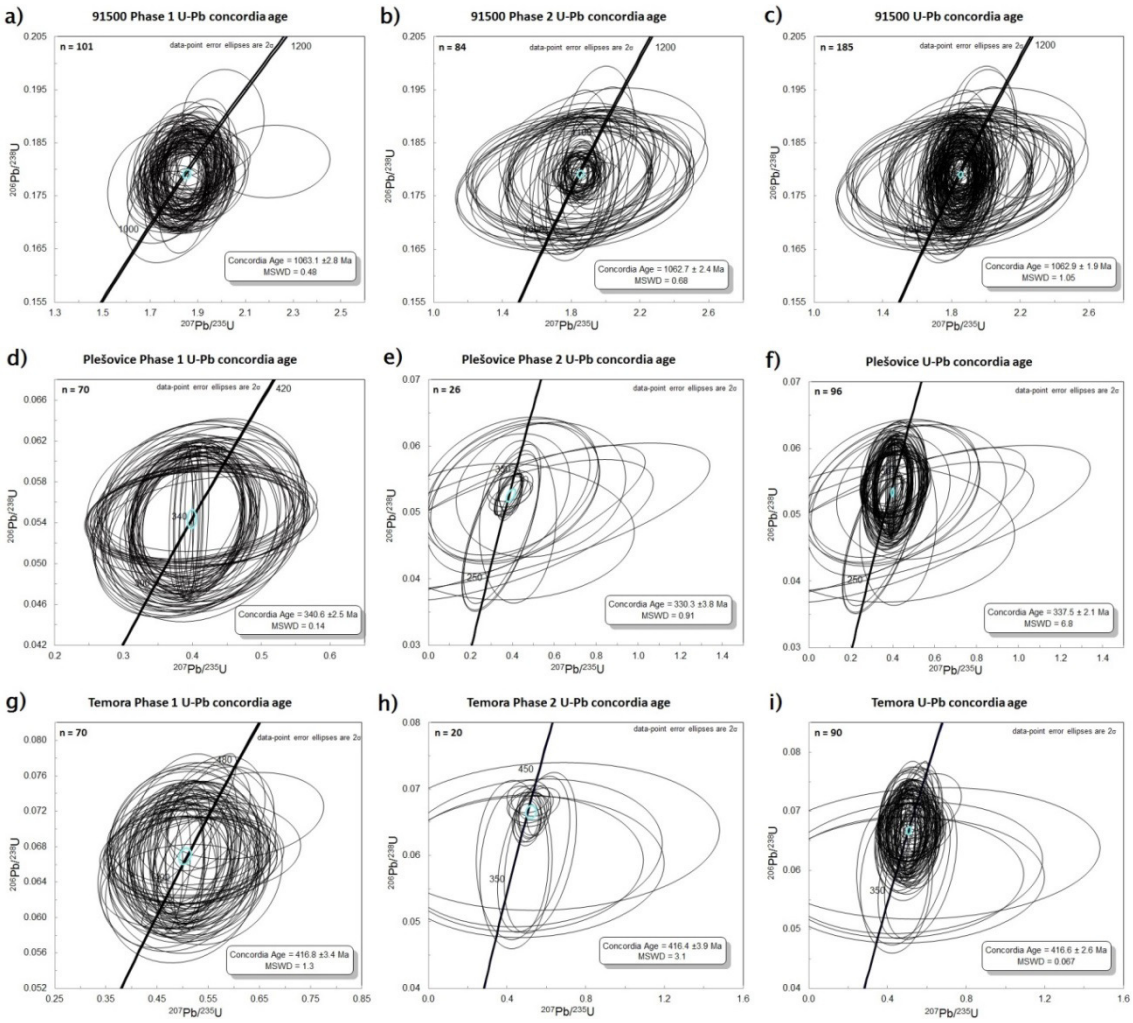


Figure 3.5: U-Pb Concordia plots of standard data; a) 91500 Phase 1, b) 91500 Phase 2, c) 91500 combined, d) Plešovice Phase 1, e) Plešovice Phase 2, f) Plešovice combined, g) Temora-2 Phase 1, h) Temora-2 Phase 2, i) Temora-2 combined.

All U-Pb zircon data reduction was performed using the Iolite software package (Paton et al., 2011) which operates within Igor Pro. Once raw data have been imported from the mass spectrometer software, Iolite uses several steps to process the data. These include 1) baseline corrections, 2) defining integrations for U–Pb primary reference materials, 3) calculating a down-hole U-Th-Pb fractionation correction, 4) defining integrations for secondary reference materials and unknowns and 5) applying a session-wide fractionation and instrumental drift corrections (Crowley et al., 2014). The VizualAge data reduction scheme within Iolite was also used to process the data (Petrus and Kamber, 2012). This has the capability of producing 'live Concordia' diagrams for visualising data while selecting integration intervals during data processing. Once the reduced data was exported from Iolite, Concordia plots, probability density plots and mean weighted average plots were generated using Isoplot, a geochronology add-in for Microsoft Excel (Ludwig, 2003). U-Pb zircon data are reported in Appendix 5.

Apatite crystals were hand-picked under a binocular microscope and mounted in 25mm diameter epoxy resin pucks, then ground and polished to expose the grain interiors. Apatite U-Pb data were all acquired at the Department of Geology, Trinity College Dublin using the same equipment and method as for the zircon U-Pb data above, with the following amendments. Eight isotopes (^{43}Ca, ^{202}Hg, ^{204}Pb, ^{206}Pb, ^{207}Pb, ^{208}Pb, ^{232}Th and ^{238}U) were acquired using a 36µm laser spot, a 5 Hz laser repetition rate and a fluence of 3.8 J/cm^2. A ~1 cm sized crystal of Madagascar apatite (Thomson et al., 2012) was used as the primary apatite reference material. This has yielded a weighted average ID-TIMS Concordia age of 473.5 ± 0.7 Ma, and is the reference material used in Cochrane et al. (2014). McClure Mountain collected from a syenite in Colorado, USA, was used as a secondary standard. McClure Mountain has a weighted mean ^{207}Pb/^{235}U crystallisation age of 523.5 ± 2.1 Ma, known from high-precision TIMS analyses (Schoene and Bowring, 2006, Chew, 2012). Over the course of analysis, the McClure Mountain apatite secondary standard yielded a weighted average ^{207}Pb-corrected age of 529.6 ± 2.5 Ma with an MSWD = 0.77. The ^{207}Pb-corrected age used an initial ^{207}Pb/^{206}Pb value of 0.88198, derived from an apatite ID-TIMS total U-Pb isochron (Schoene and Bowring, 2006).

The U-Pb apatite data were also reduced using the VizualAge data reduction scheme (Petrus and Kamber, 2012) through the freeware IOLITE package of Paton et al. (2011). The procedure was almost identical to that above, however a slightly different data reduction scheme was used to correct for common-Pb, which is incorporated into apatite during crystallisation, unlike with zircon. This was a ^{207}Pb-based correction method using a modified version of the VizualAge data reduction scheme (Chew et al., 2014). U-Pb apatite data are reported in Appendix 6.

3.4.2. Chemical Abrasion (CA) LA-ICP-MS:

Pb-loss has been recognized as a major factor limiting the accuracy of zircon age determinations (Mattinson, 2005), and over the years, various methods have been developed to deal with this, including the Wetherill Concordia diagram (Wetherill, 1956) and air abrasion techniques (Krogh, 1982). Chemical abrasion (CA) was specifically developed as a pre-treatment to eliminate or minimize Pb-loss in zircons prior to TIMS analysis (Mattinson, 2005), and has also been demonstrated to be effective for SIMS U-Pb zircon geochronology (Kryza et al., 2012). A part of this study aims to investigate if CA can be applied to LA-ICP-MS U-Pb zircon geochronology to reduce discordance. Although the technique has previously been applied to a small number of LA-ICP-MS U-Pb zircon studies (McConnell et al., 2009, Riggs et al., 2012, Riggs et al., 2013), it has not been rigorously assessed (Crowley et al., 2014). As part of this project a modified CA technique was tested by applying an annealing-leaching treatment to zircon reference materials and three

samples from the study area (TSUPB020 and TSUPB021; both greywackes, and TSUPB029; a TTG surface sample). Comparisons of data are made between the treated and un-treated zircons, presented in the results section, and the method is evaluated in the discussion as a possible pre-treatment utility prior to LA-ICP-MS analysis.

Samples were crushed and zircons separated by the same techniques as outlined above. Representative zircons were hand-picked under a binocular microscope, some of which were then thermally annealed at 850°C in quartz glass beakers for 60 hours. The annealed crystals were then ultrasonically washed in 4N HNO_3, rinsed in ultra-pure water (using a Milli-Q water purifier), then further washed in warm 4N HNO_3 prior to rinsing with ultra-pure water to remove surface contamination. The annealed and cleaned zircon fractions were then chemically abraded in 200µl 29N HF and 20µl 8N HNO_3 at 180°C in modified 1.5ml Teflon micro-centrifuge tubes in a Parr bomb for 12 hours. Following several cleaning steps in 3N HCl and ultra-pure water, treated and untreated zircons were mounted in separate epoxy pucks, and polished as described above.

The standards used for the CA-LA-ICP-MS were 91500, 91500CA, Penglai and PenglaiCA. The CA suffix indicates that these are samples which have undergone CA. 91500 was described above. The Penglai zircons are from an alkaline basalt from the northern Hainan Island of South China, and have an accepted TIMS age of 4.4 ± 0.1 Ma (Li et al., 2010). The analysis procedure is identical to that described above for the U-Pb zircon analysis. The data was processed twice, first using 91500 as the primary standard, and secondly using 91500CA as the primary standard. The results from the data processed using 91500CA as the primary standard are used, the reasons for which are discussed in chapter 5.6.1.

In addition to the CL imaging carried out on the chemically abraded zircons, post-analysis pit depths were also measured in order to compare the effect the CA process has on the ablation rates of the analyses. Pit depths were measured using white light interferometry on a MicroXAM microscope at the CMA, Trinity College Dublin.

3.4.3. Major element analysis:

Powders separated for major element geochemical analysis were dried in an oven at 105°C for 2 hours before being measured for loss on ignition (LOI) by igniting in a SNOL furnace at 1100°C for 1 hour. 200 mg of ignited sample powder was then melted in a furnace at 1100°C for 20 minutes with a lithium metaborate flux and transferred immediately to 100 mL of 5% HNO_3 loaded with Y as an internal standard. This solution was diluted and analysed for major elements at the

Department of Geology, Trinity College Dublin on a Spectro Arcos ICP-OES along with a collection of USGS rock standards. Data reduction (blank subtraction, internal standard and interference correction, calibration) was performed using the instrument software. Calibration lines were prepared from the USGS standards BHVO-1, BIR-1, AGV-2, and G-2 using the USGS recommended concentrations. Major element data are reported in Appendix 7.

3.4.4. Trace element analysis:

All trace element data were obtained in the Department of Geology, Trinity College Dublin using a method similar to that described in Babechuk et al. (2014). A 100 mg powder aliquot of all ultramafic to mafic samples were digested with a 2.5 mL HF plus 0.5 mL HNO_3 acid mixture in thoroughly cleaned sealed, screw-top Savillex Teflon beakers for 72 hrs at 160 °C with agitation at least once every 24 hours. For felsic samples or those known to contain zircon in their heavy mineral separates, 100 mg of powder was digested using the same acid mixture but in high-pressure Parr bombs in an oven at 190°C for 72 hours. Upon complete dissolution of all samples, the acid was dried down at 110°C to drive off SiF_4 and the residue was converted to nitrate form through addition of 2 aliquots of 1 ml HNO_3 with evaporation to incipient dryness between. The nitrate residue was dissolved in 100 g of 2% HNO_3 to yield a 1:1000 parts total dissolved solids stock solution. No undigested or other insoluble materials were observed for the samples. For trace element analysis, 0.08 g of stock solution was gravimetrically diluted to a total volume of 2 g (dilution factor of ~25,000) in a 2% HNO_3 solution containing a mixture of internal standards (^{6}Li, Rh, Re, Bi and ^{235}U). A total of 46 trace elements were analysed by quadrupole ICP-MS (Thermo Scientific iCap-Qs) following an experiment set-up described in Eggins et al. (1997) with modifications outlined by Kamber et al. (2003) and Kamber (2009). Analyses of samples (n = 15-25) were preceded by procedural blanks, two or more separate W-2 solutions for calibration, and quality control standards (USGS standards BIR-1, BHVO-1, BHVO-2, and AGV-2). After the procedural blanks, standards and unknowns were bracketed with a drift monitor solution spaced every 5-7 samples to externally correct for instrument drift remaining after internal standard correction.

Trace element data reduction (blank subtraction, drift correction, isobaric interference correction, and calibration) was performed offline and calibration of the corrected intensities used the preferred values for the W-2 standard reported by Babechuk et al. (2010). The values for the quality control standards agree well with values previously reported for the same powders (e.g. Kamber, 2009, Babechuk et al., 2010, Babechuk et al., 2015) on a Thermo xSeriesII and long-term averages reported from these studies indicate that the method reproducibility is better than 5%

for most elements and often between 1 and 2% for the elements key to this study (REE, HFSE). Trace element data are reported in Appendix 7.

3.4.5. Sm-Nd isotope analysis:

Neodymium isotope analyses were carried out on six volcanic rock samples of ultramafic to intermediate composition. These were conducted at the School of Geological Sciences, University College Dublin using the same method as Babechuk et al. (2015). After completion of the trace element analysis, the remaining stock solutions of the samples selected for isotope analysis were dried down and taken up in 2 mL of 1N HNO_3 for use in chromatography. The chromatographic procedure followed the methods of Pin et al. (1994) and Pin and Zalduegui (1997), whereby the solution was passed over TRU Spec resin to separate the REE and then flushed directly onto LN Spec resin to purify the Nd. Accuracy and external precision were monitored by repeated analysis of the La Jolla standard, which returned a mean $^{143}Nd/^{144}Nd$ of 0.5118423 ± 0.0000032 (2σ S.D., n = 6) during the experiments that is identical to the long term laboratory average with an external reproducibility of ± 0.00001010 ppm (2σ S.D., n = 25) and consistent with previous high precision work (e.g. Thirlwall, 1991). The Sm-Nd isotope data is presented in Appendix 7.

3.4.6. Pb-Pb isotope analysis:

Pb isotope analysis was carried out on plagioclase feldspars from TTG rocks, and pyrite from mineralised quartz-carbonate veins in order to attempt to compare the Pb isotope ratios between the two to study any possible link of fluid source from one of the TTG rocks and the hydrothermal fluids that crystallised as the veins. Plagioclase feldspars were initially analysed in situ on standard thin sections. This however was not successful, as in order to achieve a strong enough signal, the laser output was causing most grains to split from the section. Therefore, feldspars were hand-picked under a binocular microscope from the light mineral fraction of the mineral separation table, and mounted and polished in epoxy resin pucks in the same manner as zircons. Pyrite grains were also mounted in pucks, having been hand-picked from the same heavy mineral fraction as the zircon.

The samples were analysed for Pb isotopes by LA-ICP-MS (Thermo Scientific iCAP Qs) at the Department of Geology, Trinity College Dublin using a Photon Machines 193 nm ArF Excimer laser equipped with a HeLex ablation cell. The method used was similar to that described by Tyrrell et al. (2009) and Flowerdew et al. (2012). Nine isotopes (^{238}U, ^{232}Th, ^{208}Pb, ^{207}Pb, ^{206}Pb, ^{205}Tl, $^{204}Pb/^{204}Hg$, ^{203}Tl, ^{200}Hg) were acquired with a line raster using a spot diameter of 60μm. The

samples were rastered at 3µm/second and track lengths were typically 200µm long, however shorter lines were used on smaller grains, with ablation time varying between 25 and 70 seconds. The defining factor of the track lengths was the small grain size (< 200µm) for most of the grains analysed. The LA-ICP-MS system was tuned while ablating a line raster on NIST SRM 612 synthetic glass using the same setup as for the U-Pb dating described earlier. NIST SRM 612 synthetic glass was used as both the primary and secondary standard (different ablations), bracketed every three unknowns to correct for Tl based fractionation and verify the data reduction procedure. It has been shown that Pb isotope data can be collected from both feldspars and sulphides using laser ablation on non-matrix matched standards and there is no measurable fractionation of the ratios in doing so (Souders and Sylvester, 2010), although some studies prefer to use matrix matched standards (e.g. Halter et al., 2004, Sylvester, 2008). NIST SRM 612 has preferred Pb isotope ratio values of: $^{206}Pb/^{204}Pb$, 17.094 ± 0.0026; $^{207}Pb/^{204}Pb$, 15.510 ± 0.0036; $^{208}Pb/^{204}Pb$, 37.000 ± 0.0094 (Woodhead and Hergt, 2001). In this study, a total of 31 analyses of NIST SRM 612 as a secondary standard gave Pb isotope ratios of: $^{206}Pb/^{204}Pb$, 17.088 ± 0.1655; $^{207}Pb/^{204}Pb$, 15.506 ± 0.1471; $^{208}Pb/^{204}Pb$, 36.992 ± 0.3474. Data reduction was carried out using the freeware IOLITE package of Paton et al. (2011) and an associated Pb isotope data reduction scheme. The Pb isotope data is presented in Appendix 8.

Chapter 4: Results

4.1. Petrography:

In this section, each of the rocks collected for this thesis is described both in hand sample and thin section. Where multiple similar samples were collected, representative samples are described. Note that all drill core samples are 6cm in diameter. The aim of this section is to define the main petrographic features and to identify likely protoliths. As most rocks having undergone metamorphism, shearing and alteration in some cases protolith identification is somewhat subjective, with more than a single interpretation. The effects of these processes also removes the possibility of plotting the majority of samples on compositional based diagrams. As this chapter focus on protolith identification, details of metamorphic mineral assemblages (i.e. non-primary mineral assemblage) and pressure-temperature (P-T) inferences are not presented or discussed. It is also worth noting that samples are not orientated. Sample co-ordinates (drill collar site or field sample site) and target name (e.g. C6.2, C6.7) are presented in Appendix 2, and are shown on the map in figure 4.1.1.

4.1.1. Temeimichat assemblage (TSUPB023, TSUPB024, TSUPB033-TSUPB043):

The Temeimichat assemblage, consisting of ultramafic and mafic lithologies, most likely represents the lower stratigraphy of the Aouéouat greenstone belt, however the possibility remains that it is a separate greenstone belt entirely tectonically juxtaposed with the Aouéouat assemblage. Thirteen samples of diamond drill core were collected from four different targets covering an area of up to 40 km to represent this assemblage. Due to the consistency between the samples collected, four representative samples of these were chosen for petrographic description; two ultramafic schists, one from C6.2 and one from N2E; and two amphibolites, one from C6.2, and one from N2E.

TSUPB023:

TSUPB023 is a dark grey-green, to light grey-green, ultramafic tremolite-schist. The majority of the sample is composed of tremolite (70%), with surrounding chlorite (25%) (Figure 4.1.2b, 4.1.3a,b). The size of tremolite crystals changes throughout the rock across distinct boundaries, from all crystals < 1 x 0.5 mm (Figure 4.1.3a,b) in the darker layers of the rock, to large crystals, up to 4 x 1 mm which are visible in hand sample in the lighter parts of the rock (Figure 4.1.2b, 4.1.3d). The abrupt changes in tremolite crystal size are possibly due to these originally being from separate

komatiitic flows which crystallised at different rates. Although there is a preferred orientation to the tremolite crystals defining the schistosity of the rock, this is not the case for all crystals, suggesting there was some late static re-crystallisation. Chlorite fills the interstitial space between tremolite crystals, and follows the schistosity of the rock. Fe-oxide minerals are present throughout the sample, as is pyrite and a minor amount of pyrrhotite (Figure 4.1.3c). Late carbonate veins cross-cut through the rock (Figure 4.1.3d).

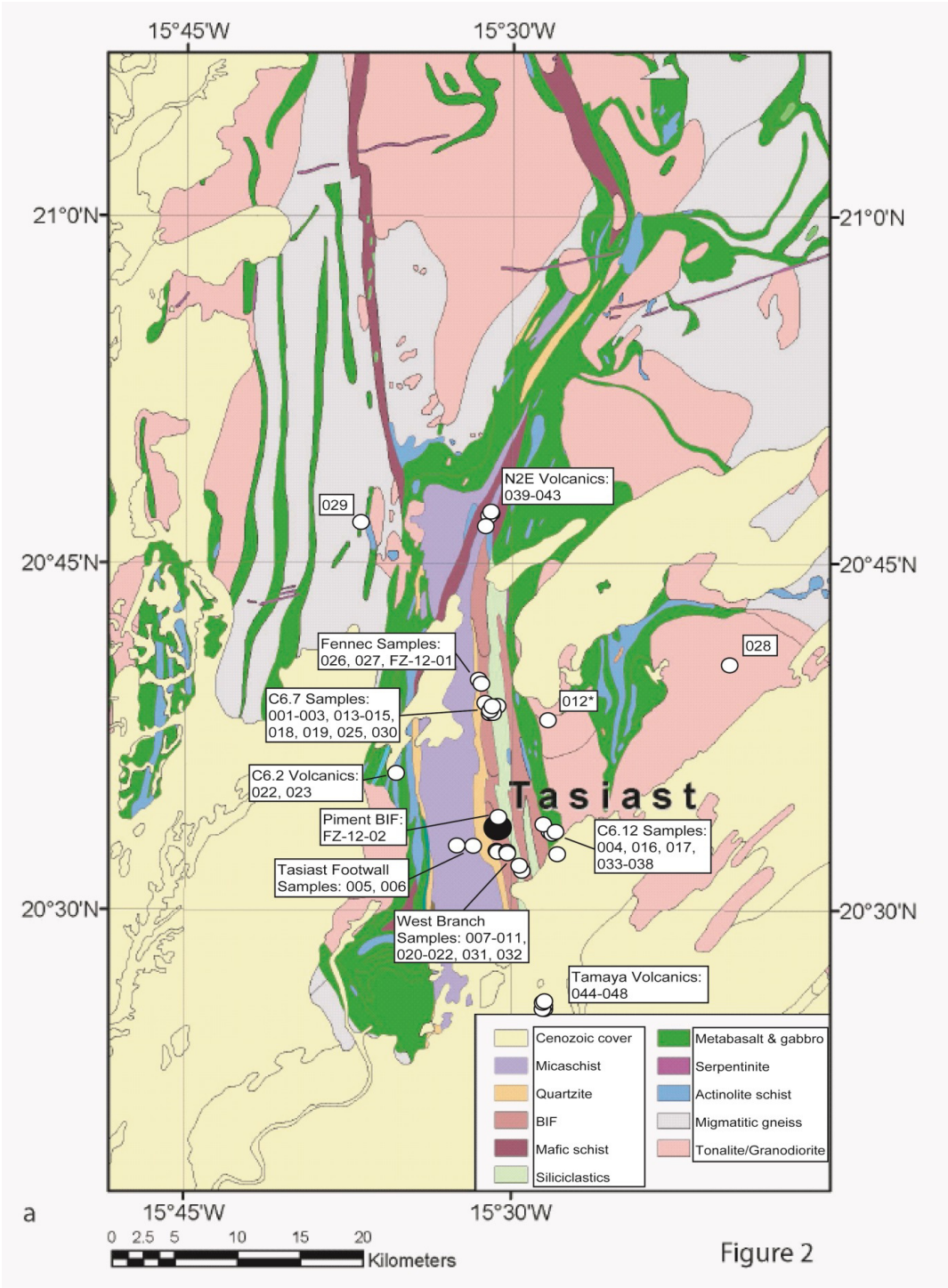


Figure 4.1.1: Geological map highlighting sample localities and target names (map sourced from Kinross Tasiast). Note an approximate location is given for sample TSUPB012.

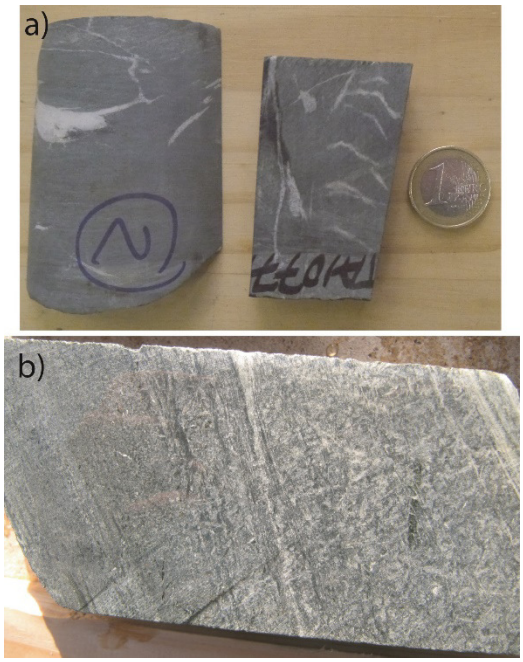


Figure 4.1.2: Hand sample photographs of Temeimichat assemblage; a) TSUPB039 showing fine grain size and quartz-filled shear structures, b) TSUPB023 showing differences in tremolite crystal size, schistosity and veining.

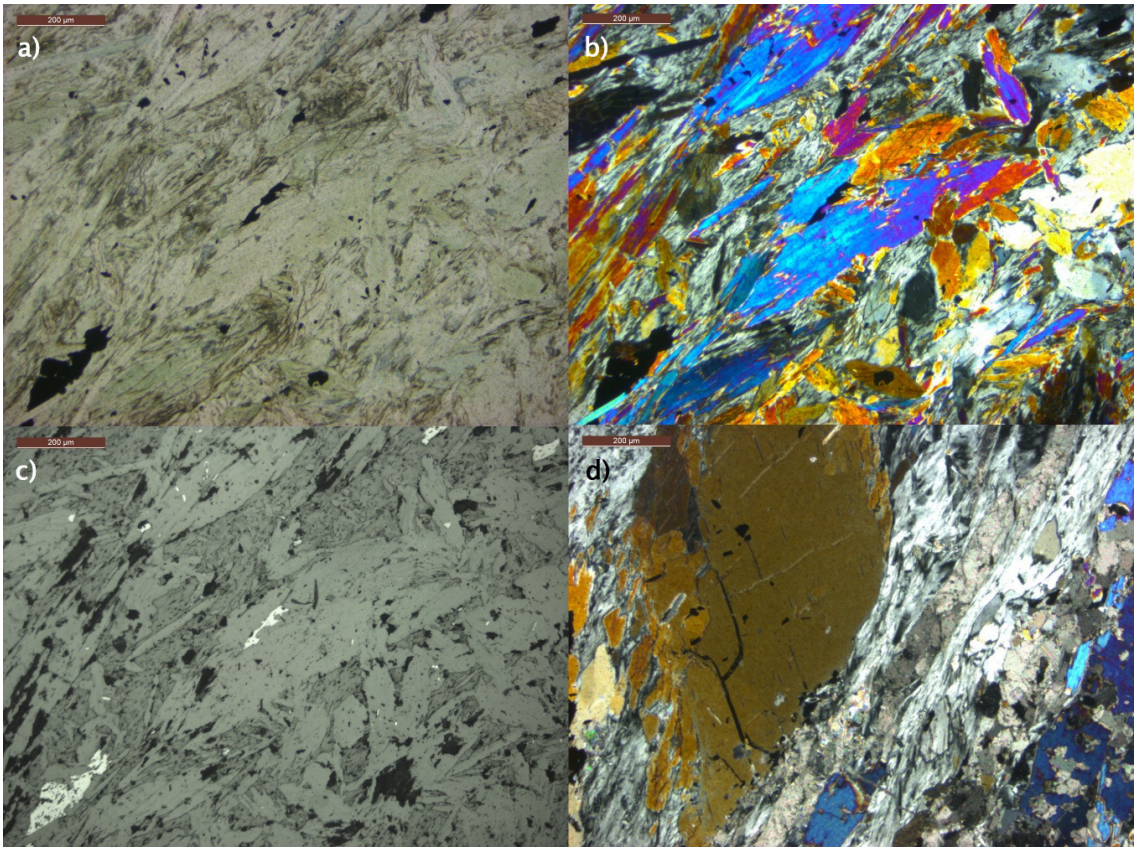


Figure 4.1.3: Representative photomicrographs of TSUPB023; a) PPL, b) XPL, c) reflected light, d) XPL view of large tremolite crystal, surrounding chlorite, and cross cutting carbonate-vein.

TSUPB042:

TSUPB042 is an ultramafic schist from N2E, and is similar in nature to TSUPB023. There are dark grey-green and light grey-green layers, with visible chlorite veins in the hand sample. There are also zones up to 5mm wide visible in the hand sample which have undergone silicification parallel to the schistosity of the rock. Tremolite crystals make up ~70% of the rock (Figure 4.1.4a,b), and most of the interstitial space is composed of chlorite (15%). Tremolite crystals reach up to 8mm in length, with size varying throughout the sample, the majority being < 1mm in length. Silicification and chloritisation are both visible in thin section (Figure 4.1.4a,b), as is substantial quartz-carbonate veining (Figure 4.1.4d). Fe-oxides take the form of magnetite, and pyrite is disseminated in small amounts throughout (Figure 4.1.4c); however the majority of sulphides in the sample are pyrrhotite, clearly visible in hand sample.

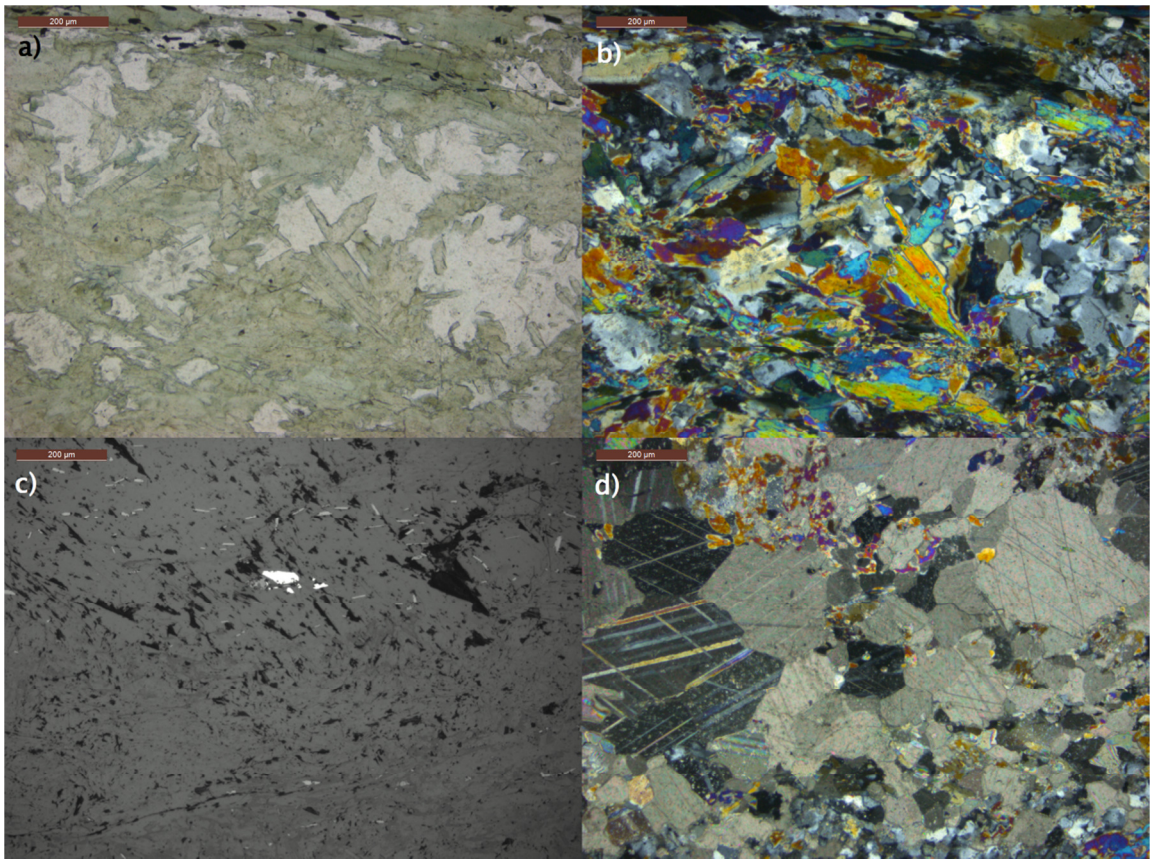


Figure 4.1.4: Representative photomicrographs of TSUPB042 including chlorite vein; a) PPL, b) XPL, c) reflected light highlighting pyrite and magnetite, d) XPL view of cross cutting quartz-carbonate-vein.

TSUPB024:

TSUPB024 is a dark grey-green amphibolite from C6.2. It is composed of ~80% hornblende crystals, generally < 0.4mm and randomly orientated, showing static re-crystallisation. The matrix

is composed of fine quartz and plagioclase (~20%) (Figure4.1.5a,b). Sulphides include pyrite and chalcopyrite disseminated in minor amounts throughout the sample (Figure4.1.5c).

TSUPB039:

TSUPB039 is a dark grey-green, very fine grained, strongly sheared amphibolite from N2E (Figure 4.1.2a). It is composed of > 90% hornblende crystals, which are generally < 0.1mm in length (Figure 4.1.5d). The hornblende crystals are consistently orientated, highlighting the strong shear-fabric this rock exhibits. The small volume of interstitial space is composed of a quartz-feldspar matrix. Fe-oxide minerals are present throughout the sample. A clear feature in hand sample is the large volume of quartz-veining, present both as extensive veins, and filling in shear structures (also seen in Figure 4.1.5d).

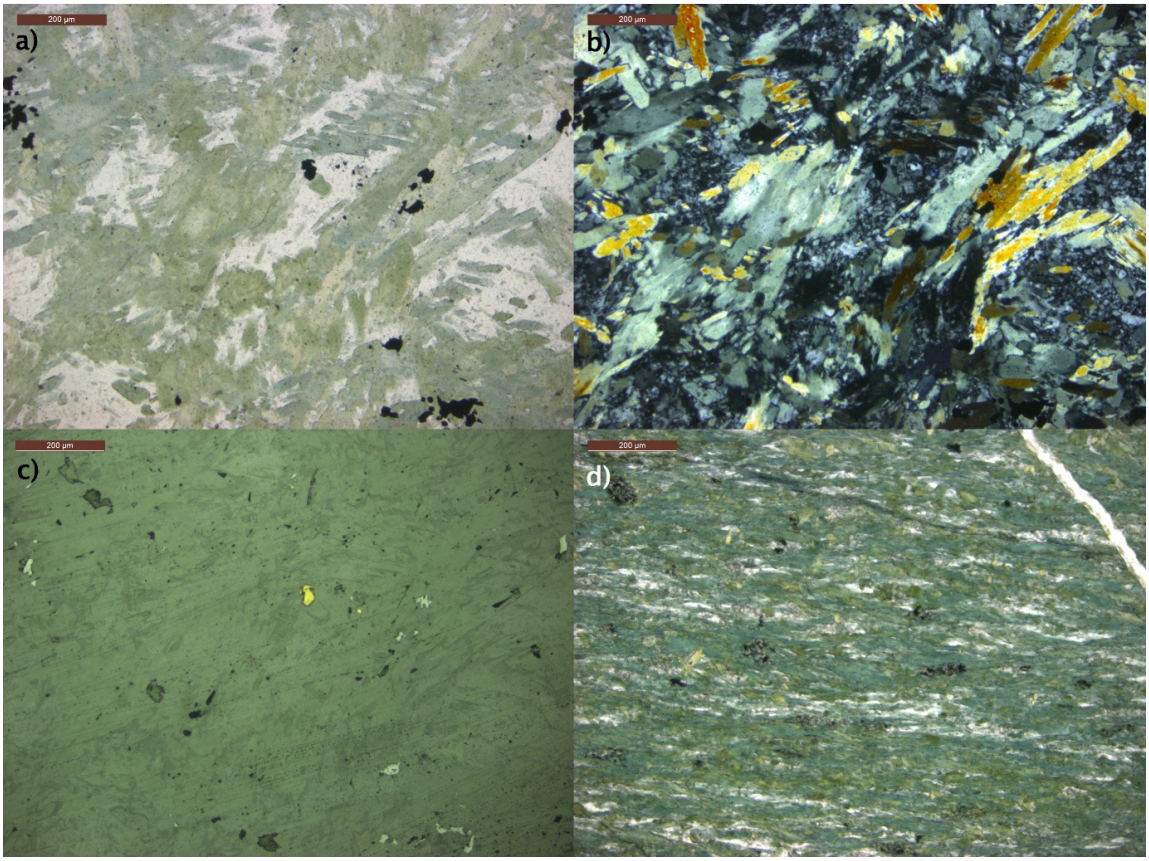


Figure 4.1.5: Representative photomicrographs of TSUPB024 and TSUPB039; a) TSUPB024 in PPL, b) TSUPB024 in XPL, c) TSUPB024 in reflected light, d) TSUPB039 in PPL including quartz-vein.

4.1.2. Aouéouat assemblage:

The Aouéouat assemblage consists of the mafic to felsic volcanic and plutonic rocks of the Aouéouat greenstone belt. Thirteen samples of diamond drill core were collected to represent

this assemblage, from four different targets. Two samples of TTG rocks were also collected from the Aouéouat assemblage; these are described along with the other TTG samples.

Aouéouat mafic-intermediate lithologies (TSUPB014, TSUPB018, TSUPB022, TSUPB044-TSUPB048):

Eight mafic rocks, all of which are amphibolites, were sampled from the Aouéouat assemblage. Three of these were chosen as representative samples; TSUPB014 and TSUPB018 from C6.7 and TSUPB022 from West Branch, and are discussed below.

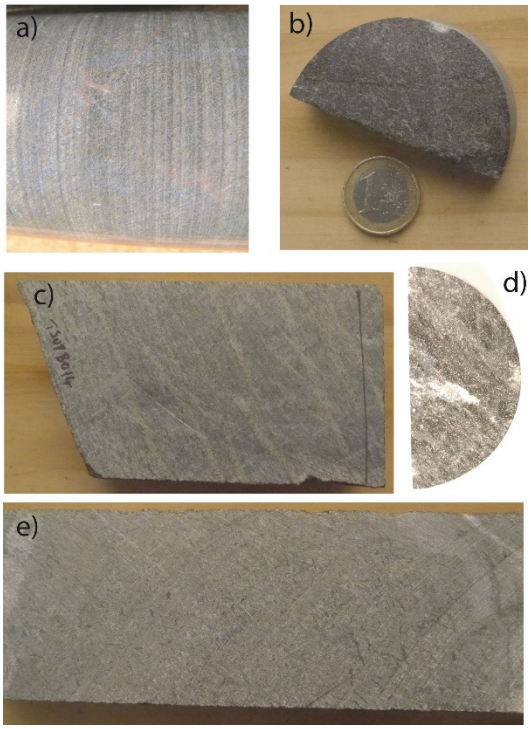


Figure 4.1.6: Hand sample photographs of Aouéouat assemblage; a) TSUPB013 showing schistosity, extensive pyrrhotite mineralisation, and blue quartz phenocrysts (note the vertical banding is from drilling, not the schistosity, b) TSUPB007 showing fine grain size, c) TSUPB014 showing schistosity and extensive chlorite veining, d) TSUPB009 showing schistosity, biotite, and quartz veining, e) TSUPB022 showing schistosity, late randomly oriented hornblende crystals, and quartz and carbonate veining.

All of the Aouéouat amphibolites are dark grey-green in colour, and show a strong schistosity. TSUPB022 has large visible hornblende crystals (up to 1 cm in length), randomly orientated. TSUPB014 also has visible hornblende crystals up to 1 cm in length; however these are less randomly orientated, and define the schistosity of the rock. TSUPB018 does not have visible hornblende crystals in hand sample. All three samples have visible quartz phenocrysts, which can

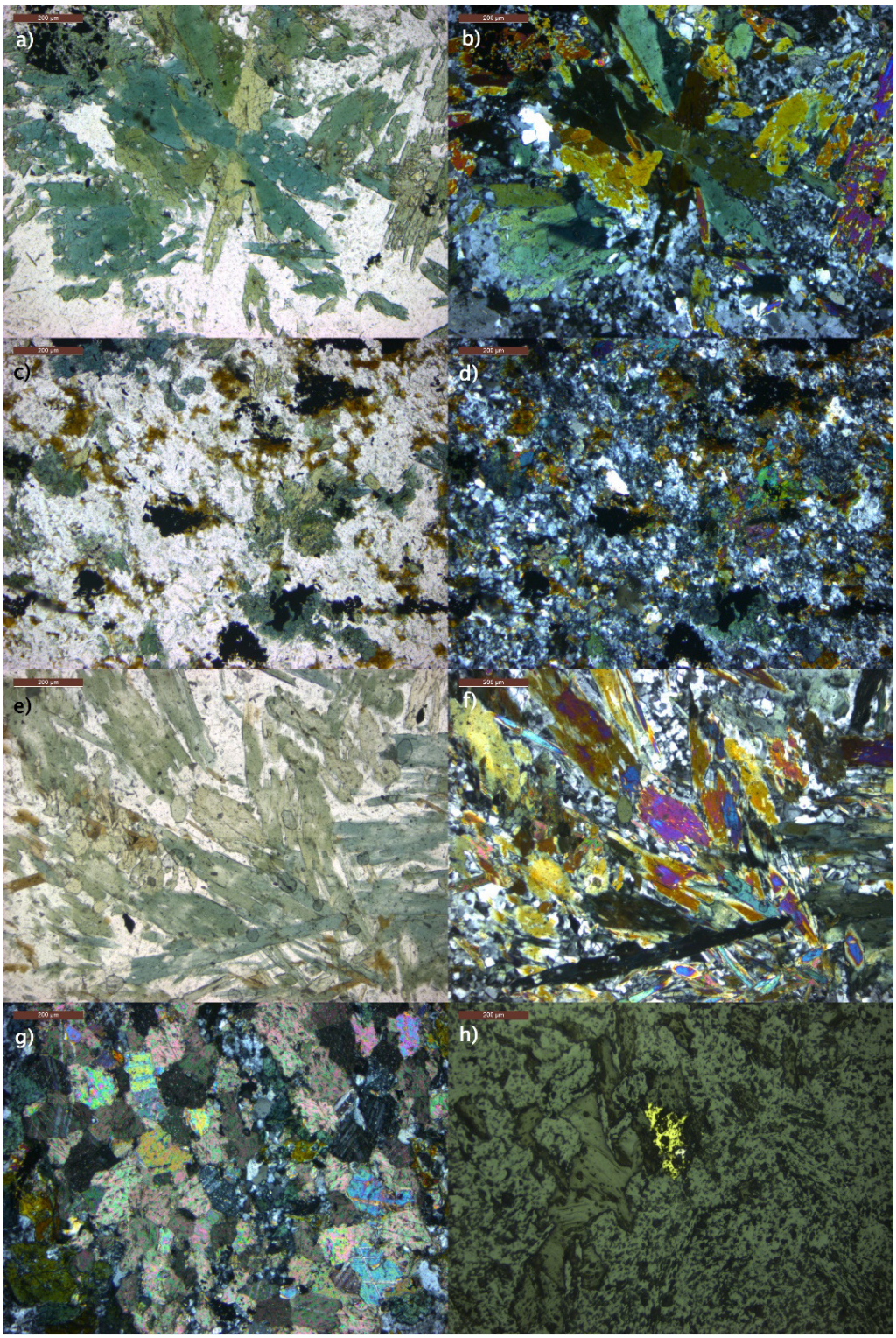


Figure 4.1.7: Representative photomicrographs of TSUPB014, TSUPB018 and TSUPB022; a) TSUPB014 in PPL, b) TSUPB014 in XPL, c) TSUPB018 in PPL, d) TSUPB018 in XPL, e) TSUPB022 in PPL, f) TSUPB022 in XPL, g) TSUPB014 showing carbonate vein, h) reflected light of TSUPB022 showing chalcopyrite.

be up to 2 mm in diameter in TSUPB014 and TSUPB022, and are < 1mm in TSUPB018. The strong schistosity of the samples is defined by hornblende and biotite (and includes Fe-oxides; formerly ilmenite), irrespective of the late randomly orientated hornblende. Quartz and chlorite veins are present throughout all of the samples, and associated pyrite and chalcopyrite are visible in hand

sample (Figure 4.1.6c,e). In thin section, all three samples are composed of hornblende, biotite, Fe-oxides and a matrix of quartz-feldspar (Figure 4.1.7a-f). As seen in the hand samples, TSUPB018 has the smallest hornblende crystals (< 1 mm), TSUPB014 has hornblendes up to 1 cm in length, and TSUPB022 > 1 cm. Similarly, TSUPB018 has the least amount of hornblende (~30%), while TSUPB014 is composed of ~40% and TSUPB022 ~60% hornblende. TSUPB018 and TSUPB022 have ~10% biotite, while TSUPB014 is devoid of any biotite, therefore when combined with the hornblende content it can be stated that TSUPB018 is the least mafic, and TSUPB022 the most mafic of these three samples. All samples contain Fe-oxides, as well as quartz, albite and carbonate veins (e.g. Figure 4.1.7g). Sulphide minerals include pyrite, chalcopyrite (Figure 4.1.7h) and pyrrhotite, though these are very sparse, and tend to be associated with the quartz and carbonate veins. The three samples are interpreted to represent basalts, which have undergone metamorphism and strong shearing. All samples have then undergone later static recrystallization of the hornblendes resulting in overprinting parts of the shear texture.

Aouéouat felsic volcanic (TSUPB007):

One felsic volcanic rock was sampled from West Branch within the Aouéouat assemblage, and is described below.

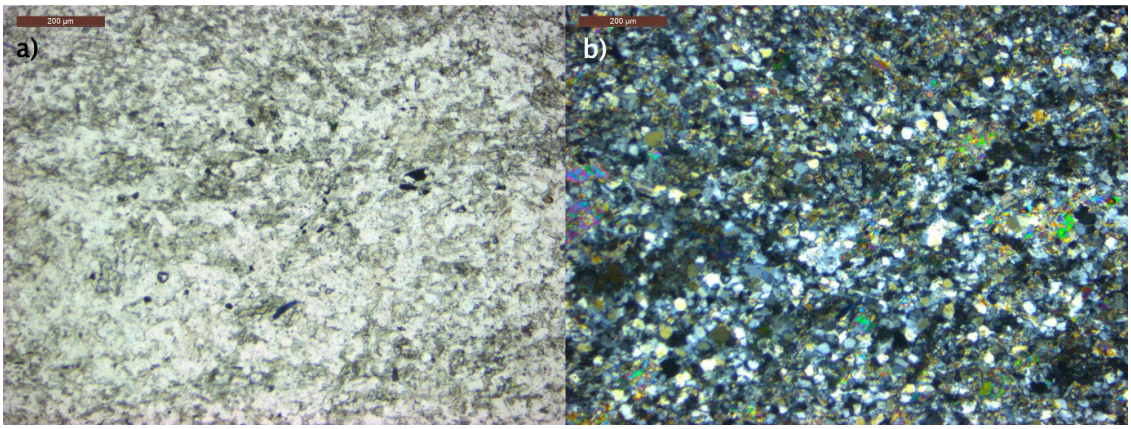


Figure 4.1.8: Photomicrographs of TSUPB007; a) PPL, b) XPL.

TSUPB007 alternates between dark grey and light grey bands, which are parallel to a strong schistosity. It is too fine grained to discern anything from hand sample (Figure 4.1.6b). In thin section, it is primarily composed of quartz and feldspar grains that are almost all < 40µm in size (Figure 4.1.8a,b). Quartz and feldspar constitute up ~80% of the rock, with the other common mineral being white mica, which composes ~10% with crystals up to 0.5mm in size. Quartz and feldspar phenocrysts up to 1mm in size are also distributed throughout the rock and account for ~5%, with quartz-veins common, and a very small amount of pyrrhotite disseminated throughout

the rock. The banding seen in hand sample appears to be caused by mica rich layers in the rock, as well as the thin quartz veins which are parallel to the schistosity. The protolith of this rock is probably a felsite; a very fine grained felsic volcanic rock.

Aouéouat quartz-diorites (TSUPB002, TSUPB013, TSUPB019):

A lithology regarded as one of the top priorities to study was the quartz-diorite unit present in the Aouéouat assemblage. This is due to its relationship with the gold hosting quartz-carbonate veins at target C6.7. Two representative thin sections from these samples, one from TSUPB002 and one from TSUPB013, are described below.

TSUPB013 is a quartz diorite, dark grey in colour, with quartz phenocrysts the most obvious feature in hand sample, appearing blue in colour (Figure 4.1.6a). In thin section, hornblende makes up ~40% of the rock, with no preferential crystal orientation (Figure 4.1.9a,b). The matrix, which comprises ~ 50% of the rock, is made up of fine grained quartz and feldspar. The final 10% is made up of quartz phenocrysts, up to 1 mm in size, Fe-oxides, and sulphides. The sulphides are pyrite and pyrrhotite, present together and extensively apparent in hand sample with mineralised zones > 5cm in length. TSUPB002 is light grey in colour, with an evident schistosity defined by biotite and Fe-oxides. Quartz phenocrysts are obvious throughout the sample, as is disseminated pyrite. There is also evidence for quartz and chlorite veining. In thin section the majority of the rock (~70%) is made of a fine quartz-feldspar matrix (Figure 4.1.9c). Both quartz and feldspar phenocrysts are abundant (~10%), with the feldspar phenocrysts showing signs of extensive sericitisation. The schistosity defined by extensive Fe-oxides and biotite (~15%), with pyrite and pyrrhotite also disseminated throughout the sample. Later chlorite, quartz and carbonate veins are all extensive within the sample (Figure 4.1.9d).

Although from the same quartz-diorite in the Aouéouat assemblage, there are large differences between the two samples. This appears to be due to TSUPB002 being an extensively sheared and altered version of TSUPB013, which has also resulted in the redistribution of minerals into mineral specific bands. TSUPB013 appears to have avoided any strong shearing and alteration and has kept its primary texture. It has however also been subject to strong mineralisation as seen by the large sulphide deposits.

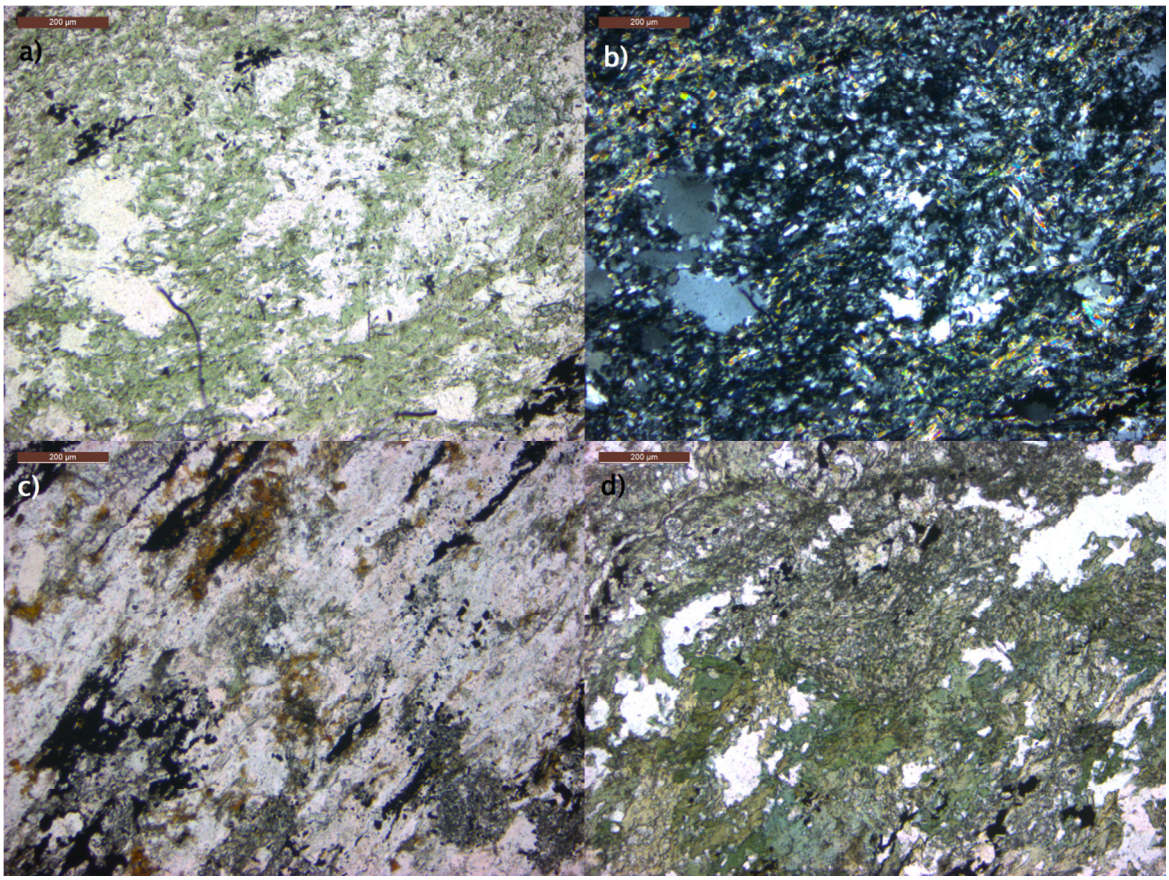


Figure 4.1.9: Representative photomicrographs of TSUPB013 and TSUPB002; a) TSUPB013 in PPL, b) TSUPB013 in XPL, c) TSUPB002 in PPL, d) TSUPB002 in PPL including chlorite, quartz, and carbonate veins.

Aouéouat diorite (TSUPB009):

One diorite was sampled from West Branch in the Aouéouat assemblage, and is described below.

TSUPB009 is a very dark, strongly sheared plutonic rock. In hand sample the most obvious features are garnets present throughout the rock, and the schistosity clearly defined by bands of biotite. Later quartz-veining is also present in the sample (Figure 4.1.6d). In thin section, the rock is clearly banded, with biotite layers alternating with layers of quartz and amphibole, which have been segregated and aligned during shearing (Figure 4.1.10a-d). The amphibole is a pale green hornblende, and constitutes ~10% of the rock. The biotite comprises ~15%, and quartz-feldspar ~65%. The schistosity is displaced around the garnets (< 5%), which have inclusions within them and are augened, showing that there was shearing during early stages of garnet growth, and active shearing after metamorphism and growth of garnets. Fe-oxides account for the final ~5% of the rock, with a very small amount of pyrrhotite also present, associated with quartz and chlorite veins. There is both later quartz-veining and carbonate present in the rock (~5%).

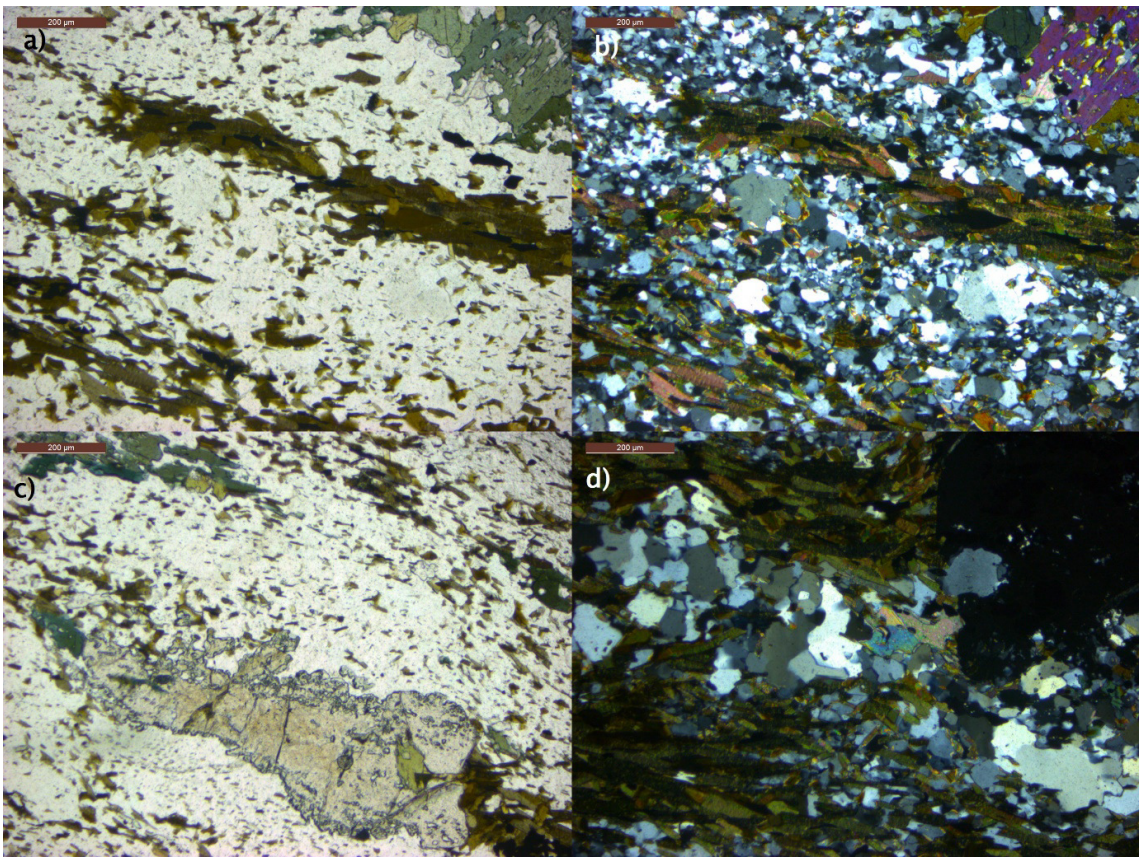


Figure 4.1.10: Representative photomicrographs of TSUPB009; a) PPL, b) XPL, c) garnet in PPL, d) garnet in XPL.

4.1.3. Tasiast assemblage:

The Tasiast assemblage consists of the sedimentary rocks that overlie the Aouéouat assemblage, and form the youngest stratigraphy of the Aouéouat greenstone belt. Seven samples of diamond drill core were collected to represent this assemblage, from three different targets; C6.7, Tasiast Foot Wall and West Branch.

C6.7 Sedimentary rocks (TSUPB001, TSUPB003):

Two sedimentary rocks were collected from C6.7, TSUPB001 and TSUPB003. In hand sample TSUPB001 appears as a fine grained grey rock, with strong schistosity picked out by dark minerals and chlorite veining. TSUPB003 on the other hand is a light green rock, with evident dark and light layering, and quartz and feldspar grains up to 1.5 mm in diameter (Figure 4.1.11a). In thin section, TSUPB001 contains abundant fine chlorite crystals (~15%) in a fine quartz-feldspar matrix (~65%) (Figure 4.1.12a-c). White mica also makes up a large proportion of the rock (~10%). There are relatively large grains of strained quartz, up to 0.5mm in diameter throughout the sample, a number of which are augened with the schistosity displaced around them. Along with the white

mica and chlorite, the schistosity is clearly picked out by the abundant Fe-oxides, which are flaky in nature and appear to be hematite (~5%), with chalcopyrite also present to a lesser extent (Figure 4.1.12d). TSUPB003 contains a lot more relatively large quartz and feldspar grains, up to 1mm in diameter, accounting for ~40% of the sample (Figure 4.1.13a-f). A number of the feldspars exhibit twinning, although most are partially altered to sericite (Figure 4.1.13b). These are in a matrix of mainly finer grained quartz and feldspar (~50%). Fine grained white mica layers occur between the coarse quartz-feldspar layers (Figure 4.1.13c-f), and chlorite and carbonate veins are present in the rock. Fe-oxides, pyrite and chalcopyrite are all present throughout this sample in minor amounts. In both rocks the schistosity is displaced around the large quartz and feldspar grains. Due to the presence of feldspar grains with original twinning, the lack of any apparent sorting, other than in the fine mica beds, and the presence of chlorite, these sediments appear to be locally derived, and not very mature. The mica layers were likely deposited as fine grained clay minerals which settled during a period of large sediment starvation, and therefore calmer conditions, before being later altered to mica.

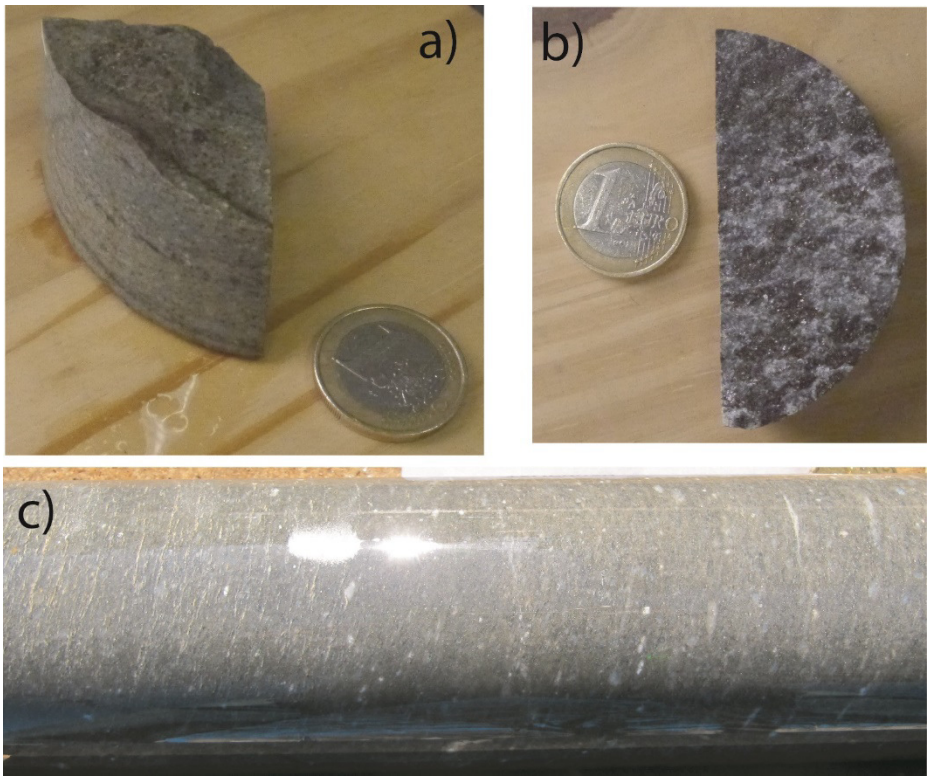


Figure 4.1.11: Hand sample photographs of Tasiast assemblage; a) TSUPB003 showing dark and light layering, and grains up to 1.5mm in diameter, b) TSUPB010 showing disc shaped biotite lenses, and fine grained matrix, c) TSUPB021 showing schistosity picked out by mica beds, and large quartz and feldspar grains.

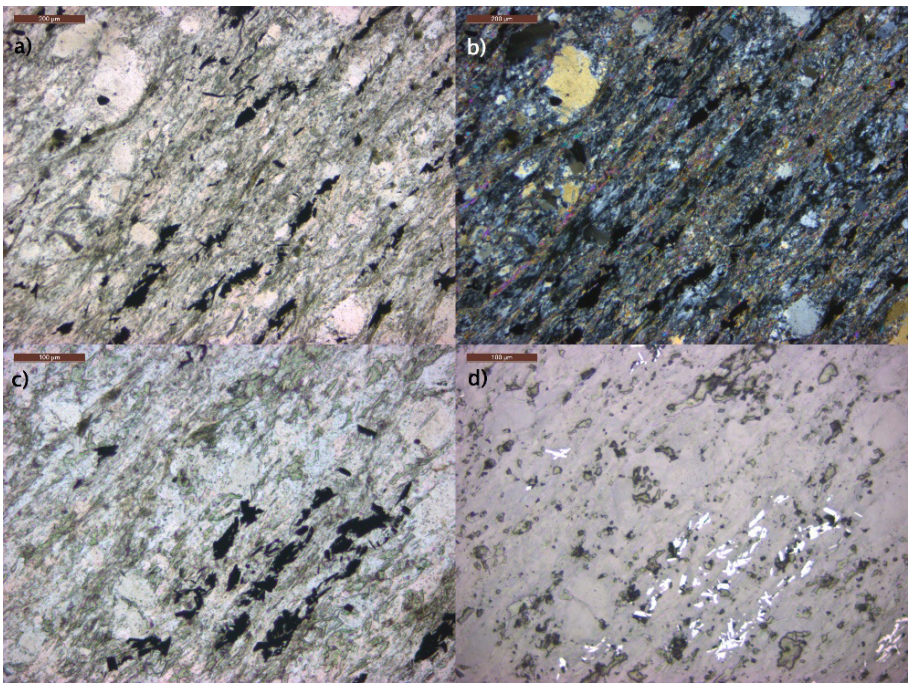


Figure 4.1.12: Representative photomicrographs of TSUPB001; a) PPL, b) XPL, c) PPL, d) reflected light.

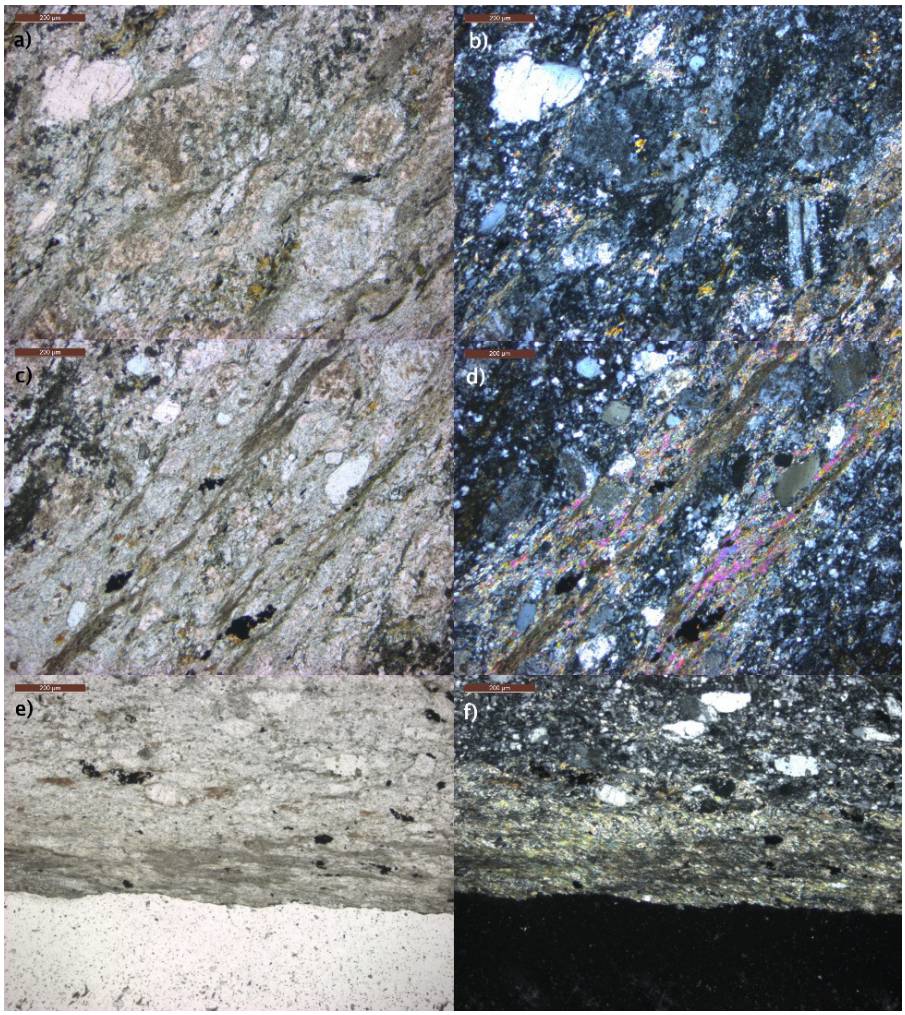


Figure 4.1.13: Representative photomicrographs of TSUPB003; a) PPL, b) XPL, c) PPL, d) XPL, e) mica bed in PPL, f) mica bed in XPL.

Tasiast Foot Wall Sediment (TSUPB005):

TSUPB005, collected from the Tasiast Foot Wall, is a light grey rock with schistosity and layering apparent in hand sample. Quartz grains up to 1mm in diameter are visible, as are quartz veins. In thin section, the rock is almost entirely composed of well sorted quartz and feldspar grains with a diameter of 50-100 µm, all of which have been altered or strained (Figure 4.1.14a,b). Biotite and minor chlorite make up ~5%, and define the schistosity of the rock. Quartz, carbonate and albite veins are all present in the sample (Figure 4.1.14c,d), along with rare associated pyrite. The sorting of the sample, and relative lack of mafic minerals indicates that this was likely a more mature and distal sourced sample with a different provenance than those from C6.7.

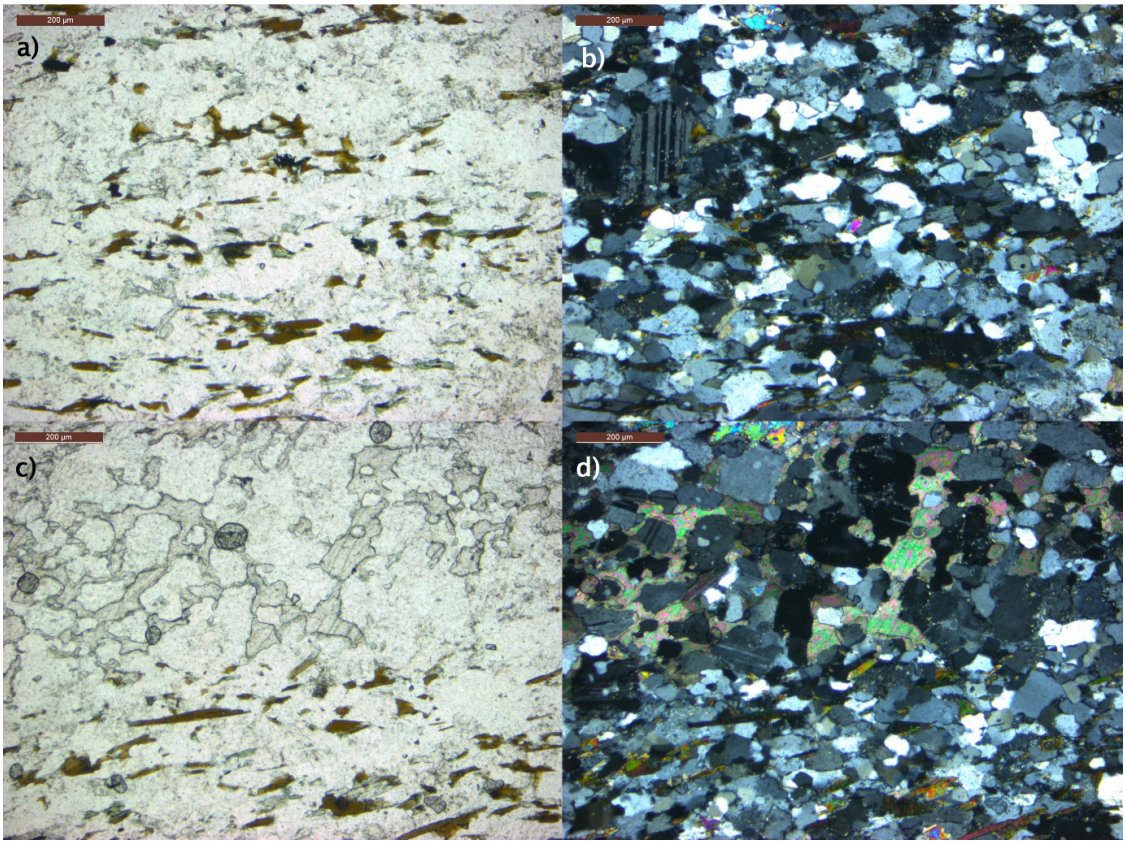


Figure 4.1.14: Representative photomicrographs of TSUPB005; a) PPL, b) XPL, c) PPL with carbonate and albite vein, d) XPL with carbonate and albite vein.

West Branch Sediments (TSUPB010, TSUPB011, TSUPB020, TSUPB021):

Four samples were collected from West Branch, 3 samples of greywacke, and one fine grained sediment. Two of the greywackes, TSUPB011 and TSUPB020 are from the hanging wall of the Tasiast Thrust, and one, TSUPB021 is from the foot wall. The fine grained sediment (TSUPB010) is from the Tasiast foot wall.

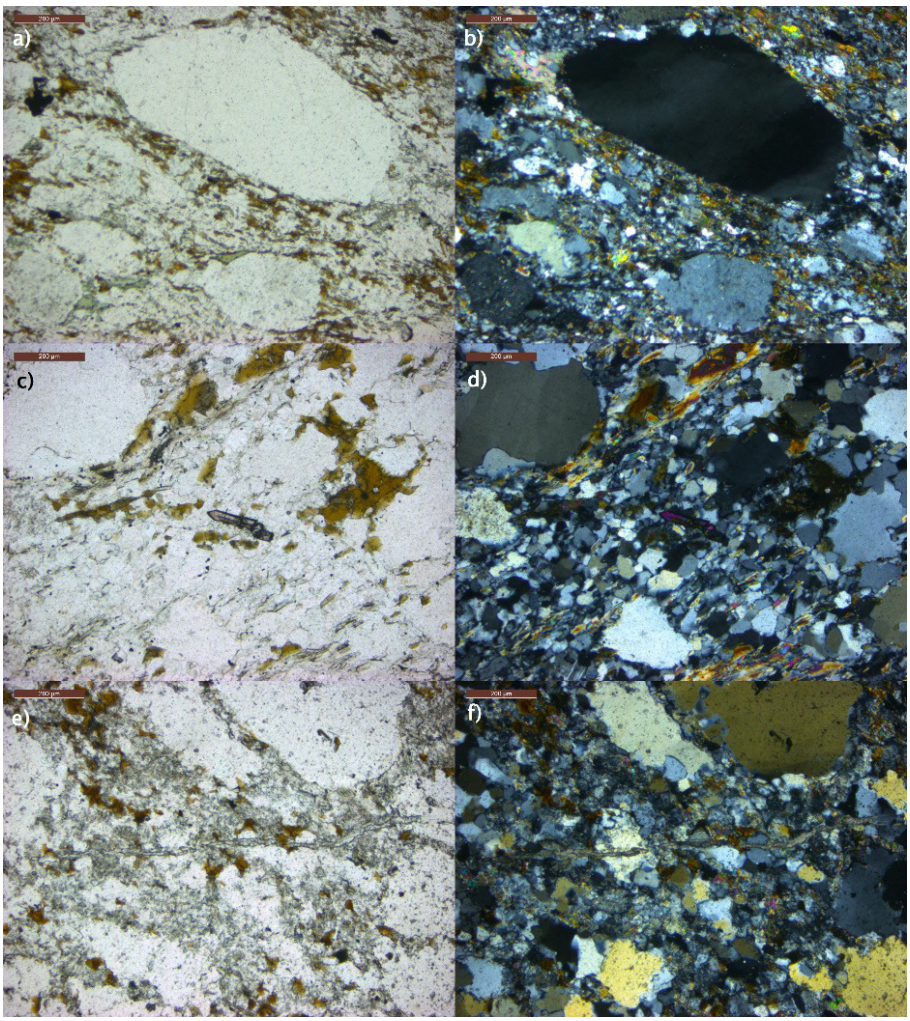


Figure 4.1.15: Representative photomicrographs of TSUPB011, TSUPB020 and TSUPB021; a) TSUPB011 in PPL, b) TSUPB011 in XPL, c) TSUPB020 in PPL, d) TSUPB020 in XPL, e) TSUPB021 in PPL, f) TSUPB021 in XPL.

TSUPB011, TSUPB020 and TSUPB021 are greywacke samples. In hand sample TSUPB020 and TSUPB021 are dark grey, with lighter quartz grains up to 4mm in diameter particularly evident in course grained beds within a majority of the medium-fine grained rock (Figure 4.1.11c). Schistosity is defined by thin mica layers. Later carbonate veins cross-cut the samples both parallel to and oblique to the schistosity. TSUPB011 is a very pale grey sample with no visible quartz or feldspar grains in hand sample, which appears to have undergone strong silicification. Biotite layers define the schistosity, but the rock appears massive. In thin section however, there is very little difference in general between all three samples (Figure 4.1.15a-f). The obvious feature is the large (up to 3mm) sub-rounded, strained quartz grains present in all of these samples. These are accompanied by sub-rounded feldspar grains, generally slightly smaller in size, though some are as large as the largest quartz grains. Very few feldspar grains show evidence of their original twinning in samples TSUPB011 and TSUPB020, with most having been altered extensively replaced by sericite. The majority of the three samples are composed of quartz and feldspar grains, with an average grain size of ~50µm. Biotite, and white mica are the most

common other minerals, making up < 10% of the rocks, with chlorite also present in minor amounts. Carbonate veins are present in all of the samples, as is pyrite. Pyrrhotite and chalcopyrite are present in TSUPB020 and TSUPB021. Due to the mature nature of these metasedimentary samples, and a small percentage of mafic minerals present, they are interpreted as greywackes, with either a fairly distal source, or a felsic source such as TTG rocks.

TSUPB010 is very fine grained and ~ 75% light grey and 25% black in colour. The very dark coloured mineral is biotite and forming in very thin sub-circular (< 1mm) patches up to ~1cm in diameter picking out the strong schistosity in the rock (Figure 4.1.11b). In thin section, the schistosity is clearly picked out by the large proportions of biotite (25%) and muscovite (25%) in the sample (Figure 4.1.16a,b). The remainder of the sample is composed of fine grained quartz (~50%). Very thin quartz-carbonate veins are also present in the sample, as is a small amount of pyrite.

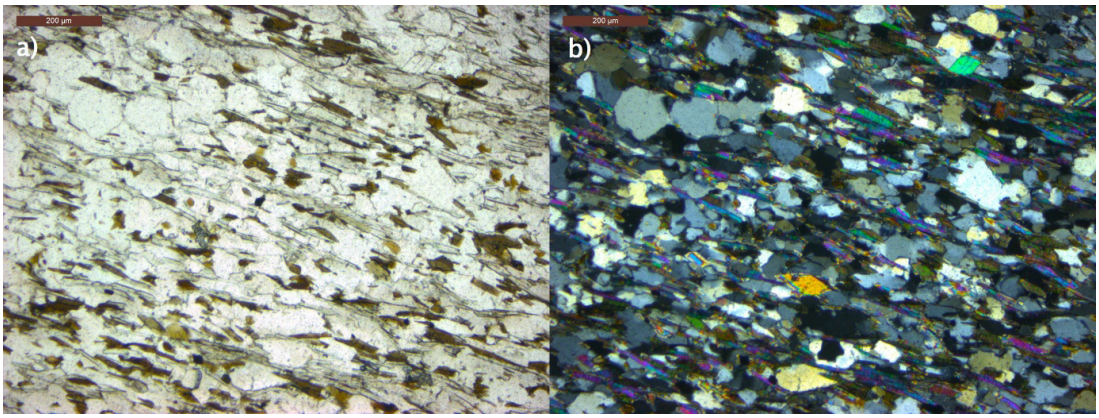


Figure 4.1.16: Representative photomicrographs of TSUPB010; a) PPL, b) XPL.

4.1.4. TTG Rocks:

Five TTG rocks were collected; two TTGs from the Aouéouat assemblage and three surface samples from the rocks surrounding the Aouéouat greenstone belt. Clasts of TTG were also recovered from a conglomerate in the Tasiast assemblage, which is also described here.

Aouéouat assemblage TTG rocks (TSUPB004, TSUPB008):

TSUPB004 is a coarse grained porphyritic plutonic rock from within the Aouéouat assemblage. In hand sample quartz and feldspar phenocrysts up to 0.5mm in diameter are present throughout the rock, the feldspar phenocrysts pale in colour and the quartz semi-transparent (Figure 4.1.17a). Large wavy biotite crystals are present, up to 3cm in length, and define the sheared fabric

apparent in the rock. In thin section, biotite crystals are most obvious feature, with the larger crystals defining the wavy shear fabric in the rock, as well as the smaller biotite crystals present throughout the sample wrapping around the quartz and feldspar phenocrysts which compose ~5% of the sample (Figure 4.1.18, figure 4.1.19a,b). The quartz phenocrysts (up to 0.5mm in length) also show shearing, and are strained, while the feldspars (up to 0.5mm in length) have kept their original shape, together accounting for ~ 50% of the rock. Some of the feldspars still show remnants of zoning and albite twinning, however most of the feldspars show signs of alteration to sericite (Figure 4.1.19b). The matrix of the rock is composed of fine quartz, feldspar and biotite crystals (~40% of the rock). The quartz-feldspar proportions are 37% quartz, 55% plagioclase and 8% K-feldspar, plotting on the tonalite-granodiorite boundary of the Q-A-P diagram (Figure 4.1.20). Carbonate and pyrite are both present throughout the rock, as well as albite veining, and some secondary clinopyroxene appears to have crystallised within the larger biotite crystals. The rock is a quartz-feldspar-biotite porphyry.

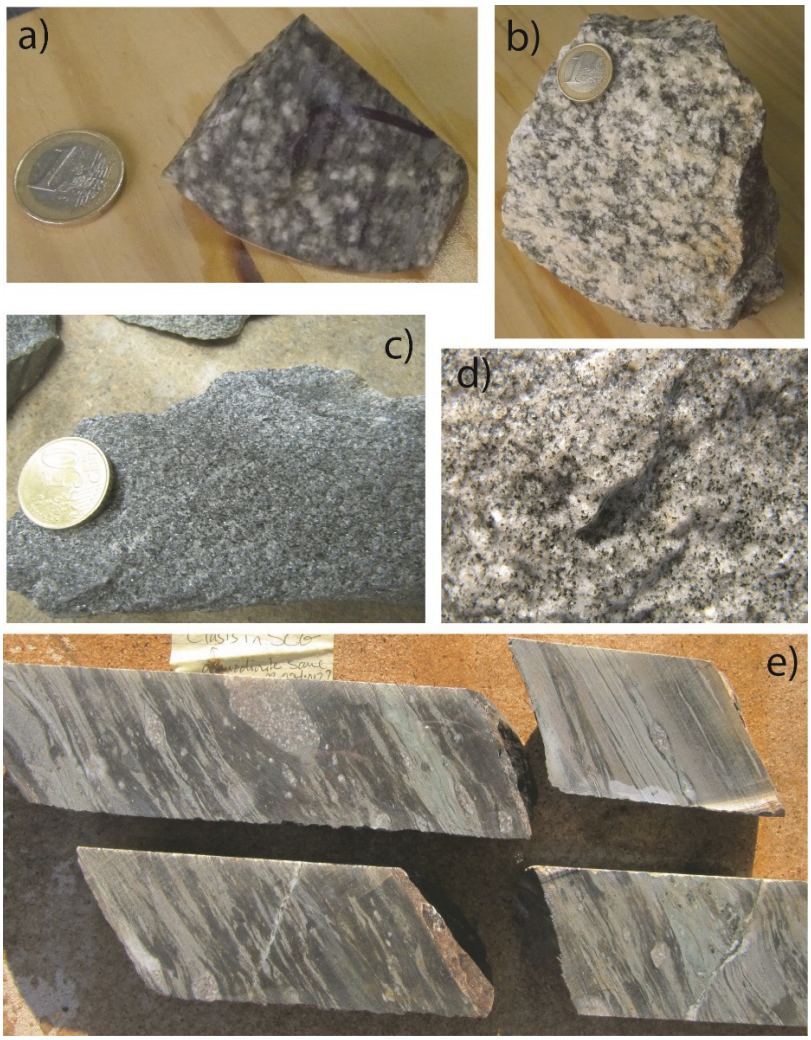


Figure 4.1.17: Hand sample photographs of TTG rocks; a) TSUPB004 showing porphyritic texture, and biotite picking out schistosity, b) TSUPB012, c) TSUPB028, d) TSUPB029, e) TSUPB030 showing clasts within a mylonitic matrix.

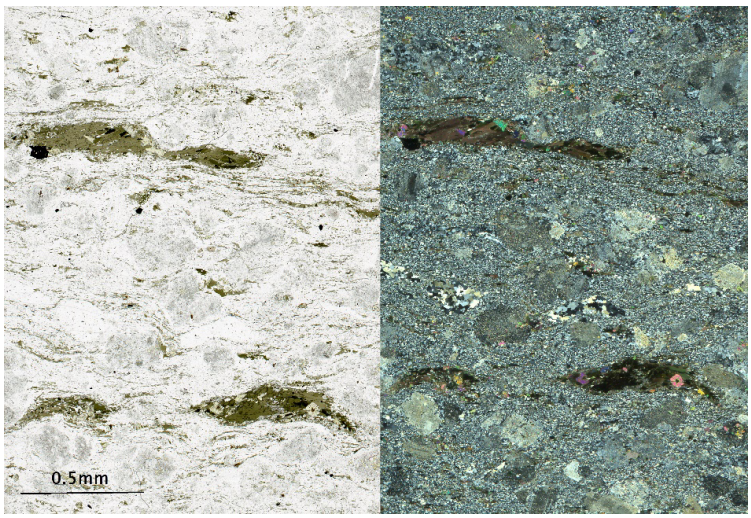


Figure 4.1.18: Large photomicrograph of TSUPB004.

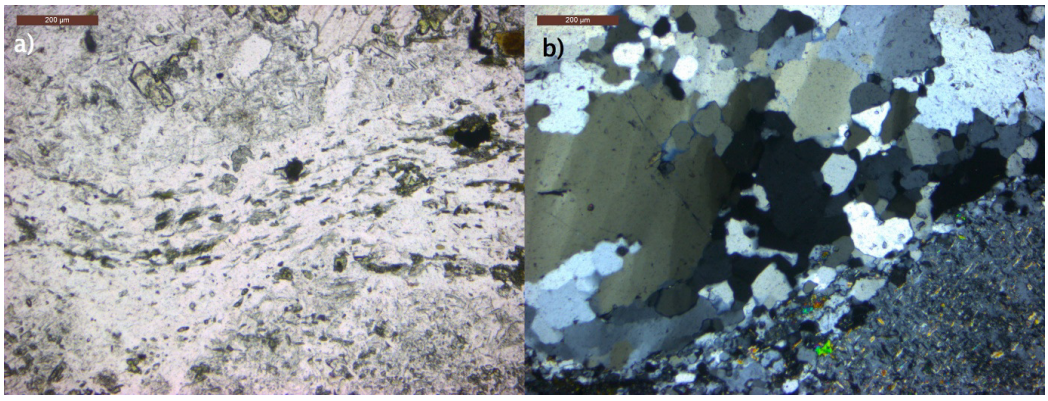


Figure 4.1.19: Photomicrographs of TSUPB004; a) PPL highlighting the shear fabric, b) XPL highlighting sericitisation of the feldspars adjacent to unaltered quartz.

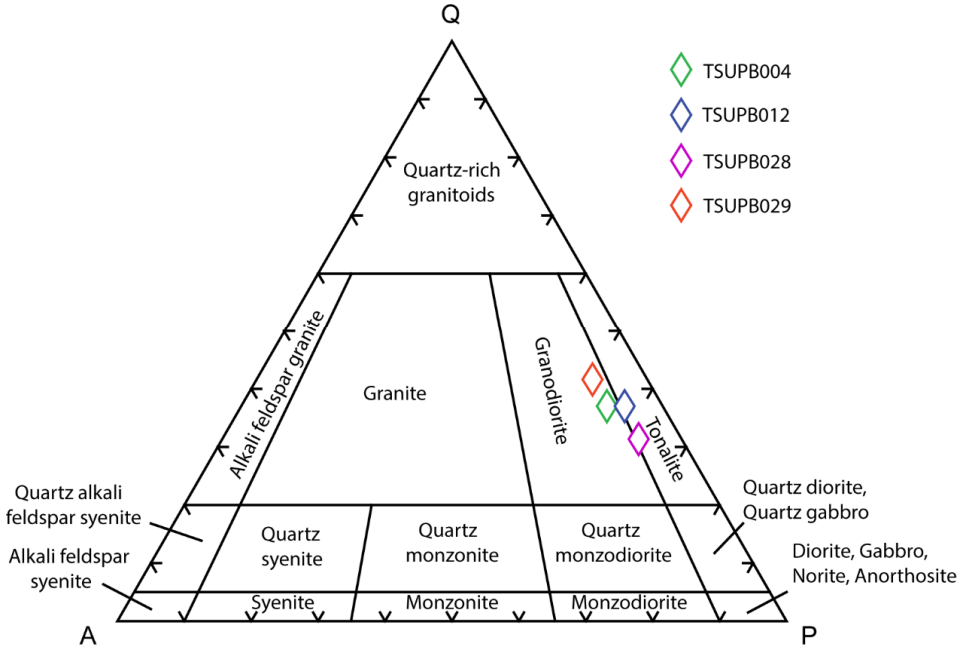


Figure 4.1.20: Quartz-Alkali feldspar-Plagioclase feldspar (Q-A-P) diagram of TTG rocks.

TSUPB008 is a fine grained plutonic rock from the Aouéouat assemblage. In hand sample it is dark grey, and sheared, however no minerals can be identified other than fine grained biotite. In thin section, it is clear that the majority of the sample is composed of fine grained (<100µm) quartz and feldspar (~80%) (Figure 4.1.21a,b). Biotite makes up ~15% and is concentrated in bands which have formed during metamorphism defining the schistosity of the sample. Fe-oxides as well as quartz and carbonate veining is common, along with associated sulphide minerals .These are primarily pyrrhotite, but also include pyrite and chalcopyrite.

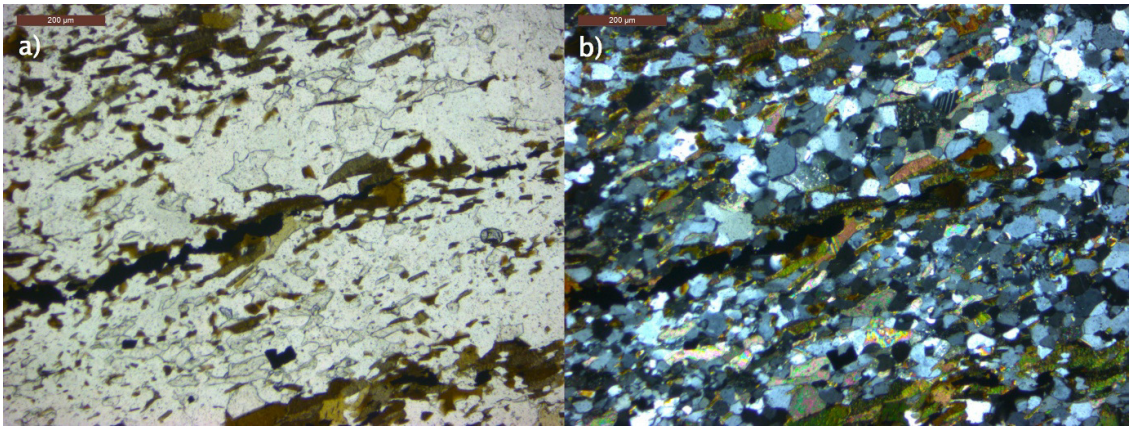


Figure 4.1.21: Representative photomicrographs of TSUPB008; a) PPL, b) XPL.

TTG plutons (TSUPB012, TSUPB028, TSUPB029):

TSUPB012 is a surface sample taken from a TTG pluton adjacent to the east side of the Aouéouat greenstone belt. In hand sample it is black and white in colour, and has a porphyritic texture, with white feldspar crystals up to 2cm in diameter, quartz crystals up to 1.5cm in diameter, and biotite crystals up to 2cm in length (Figure 4.1.17b). There is evidence of a shear fabric defined by the biotite, but it is not strong. In thin section the shear fabric is defined by the biotite, though not all biotite are aligned throughout the rock (Figure 4.1.22, figure 4.1.23a-d). The quartz and plagioclase phenocrysts are similar in size and the matrix is composed of quartz and feldspar crystals <0.5mm in size. The quartz-feldspar proportions are 37% quartz, 58% plagioclase and 5% K-feldspar, plotting in the tonalite field of the Q-A-P diagram (Figure 4.1.20). The rock is a quartz-feldspar-biotite porphyry, very similar in nature to TSUPB004, only less sheared and less altered, as seen by the low amount of sericitisation in the feldspars.

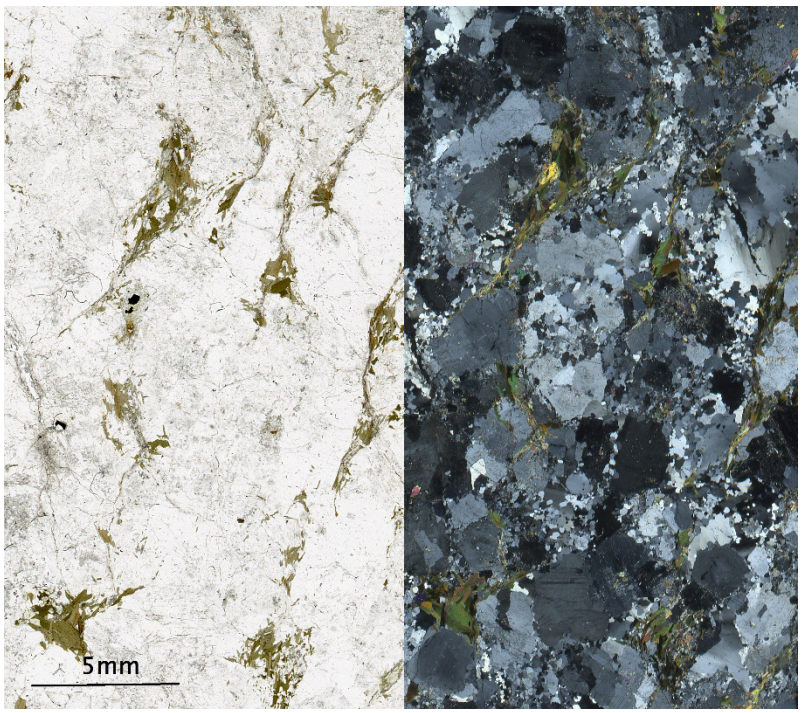


Figure 4.1.22: Large photomicrograph of TSUPB012.

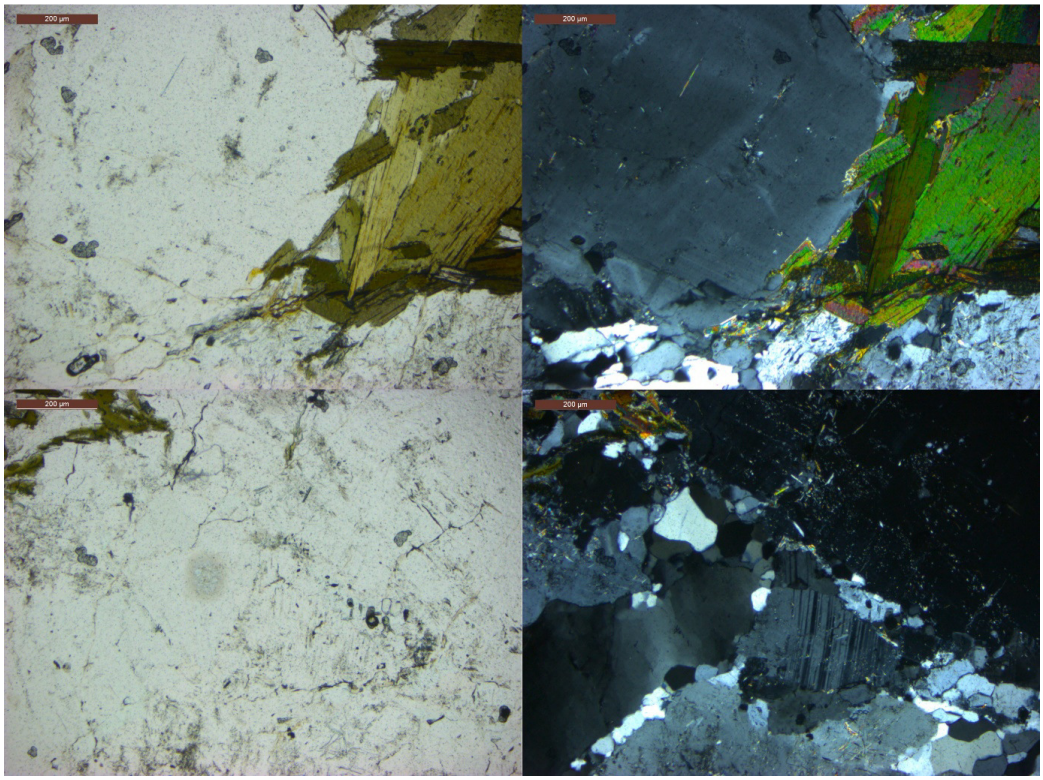


Figure 4.1.23: Photomicrographs of TSUPB012; a) PPL, b) XPL, c) PPL, d) XPL.

TSUPB028 is a fine grained grey plutonic rock, taken from a xenolith within a TTG pluton east of the Aouéouat greenstone belt. In hand sample it is clear that the biotite is aligned showing the rock has undergone shearing (Figure 4.1.17c). The other minerals apparent are quartz, feldspar and hornblende. In thin section, it is more difficult to see any evidence of shearing. All crystals are

< 300µm, with hornblende and biotite comprising ~15 % and ~5% of the sample respectively, suggesting a relatively mafic precursor magma (Figure 4.1.24, figure 4.1.25a,b). The quartz-feldspar proportions are 31% quartz, 63% plagioclase feldspar and 6% K-feldspar, with the feldspar showing very little sign of any alteration, making this sample tonalitic in composition (Figure 4.1.20). A minor amount of Fe-oxides are present, as well as muscovite.

TSUPB029 is a slightly coarser grained and lighter grey rock, taken from a xenolith within a TTG pluton west of the Imkebdene greenstone belt. In hand sample, again shearing is evident from the alignment of the biotite (Figure 4.1.17d). The majority of the rock is composed of quartz and feldspar, with muscovite also present. In thin section, the biotite clearly highlights that the rock is sheared, and makes up <5% of the rock (Figure 4.1.25a,b, figure 4.1.26). Quartz (~40%) and feldspar (~50%) make up the majority of the rock, with the feldspar showing small signs of alteration to sericite. Muscovite forms a minor constituent of the rock, as do garnets. The quartz-feldspar proportions are 42% quartz, 50% plagioclase feldspar and 8% K-feldspar, making this sample plot on the tonalite-granodiorite boundary (Figure 4.1.20).

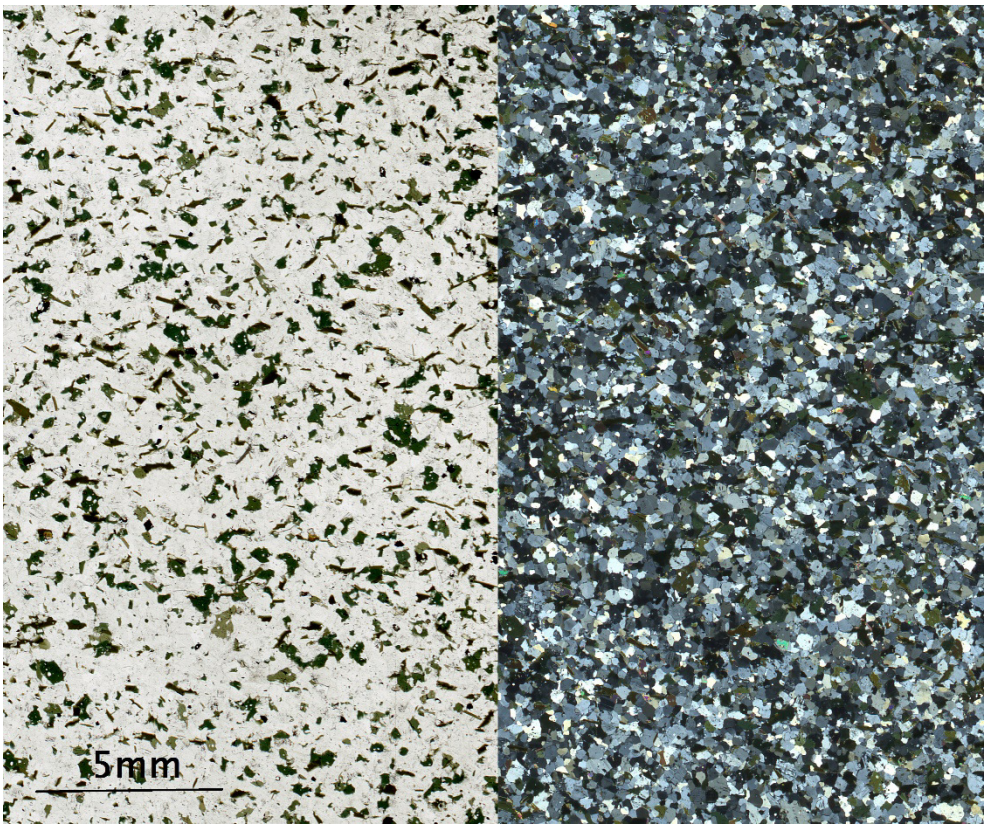


Figure 4.1.24: Large photomicrograph of TSUPB028.

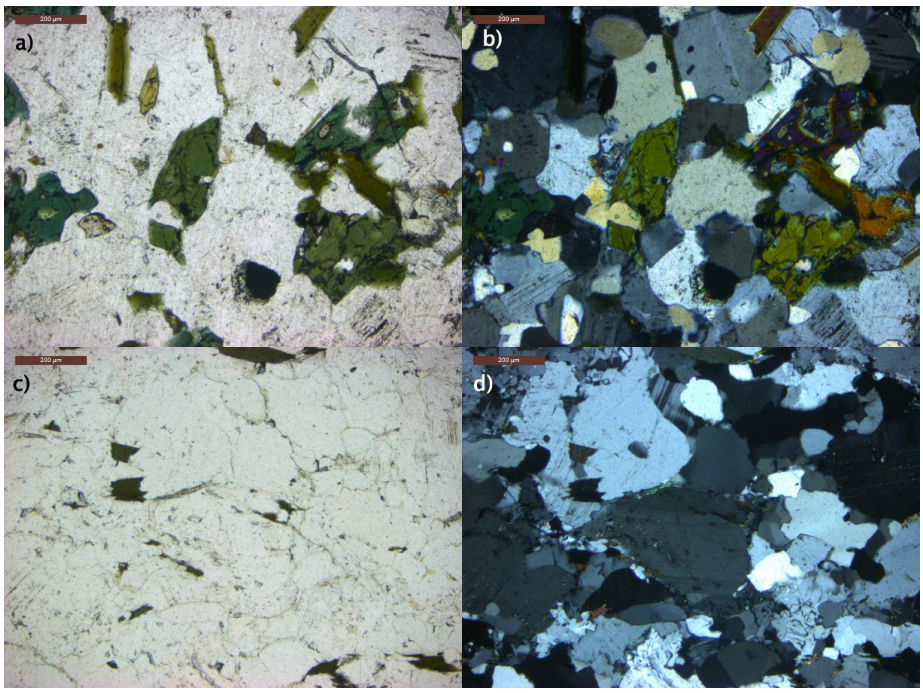


Figure 4.1.25: Photomicrographs of TSUPB028 and TSUPB029; a) TSUPB028 in PPL, b) TSUPB028 in XPL, c) TSUPB029 in PPL, d) TSUPB029 in XPL.

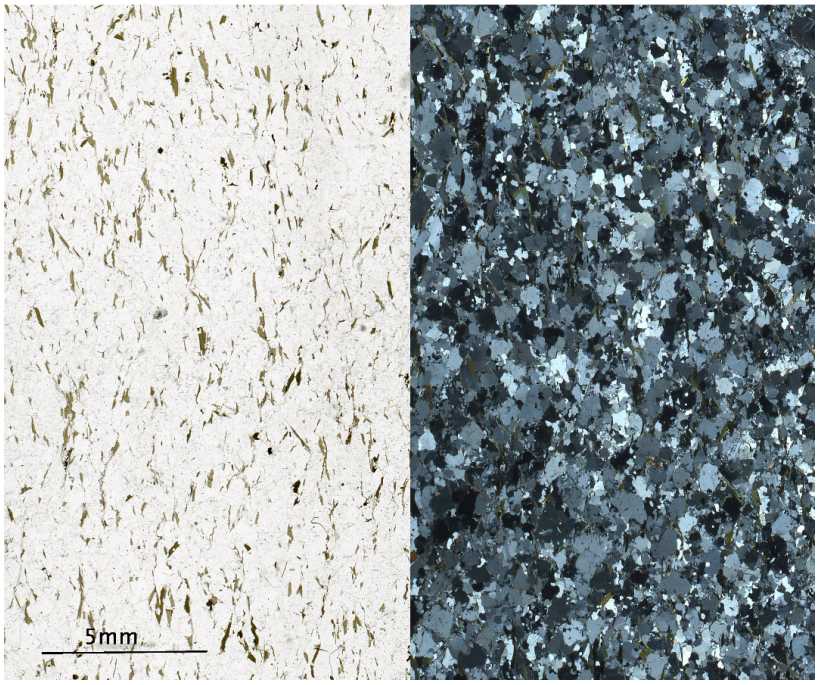


Figure 4.1.26: Large photomicrograph of TSUPB029.

TTG clasts in Tasiast assemblage:

Only a few metres below sample TSUPB003, from the base of the Tasiast assemblage, a conglomerate (TSUPB030) was sampled containing clasts of a TTG plutonic rock. In hand sample it appears that this sample is a mylonitic rock, with the matrix, which makes up > 95% of the

sample, being extremely fine grained, and both light green and black in colour (Figure 4.1.17e). The dark colour is likely an artefact of the fine grain size, and the green being the effect of chloritisation. There is abundant pyrrhotite, associated with quartz veining, present in the fine grained material, however only rare pyrrhotite is present within the clasts. The clasts, which range from single quartz grains > 2mm in diameter, to TTG clasts up to 5cm in length, are strongly sheared into relatively flat elongate discs. Quartz and feldspar phenocrysts are visible in the TTG > 4mm in diameter. In thin section, the matrix is very fine grained (< 30µm) and much of it has been altered by chloritisation (Figure 4.1.27). The TTG clasts are composed of quartz and feldspar phenocrysts, up to 3mm in length, in a matrix of quartz and feldspar; however they are strongly altered, with even the quartz showing signs of breaking down (Figure 4.1.28a-d). Chlorite and white mica are both present in the clasts, as secondary minerals. These are clasts of a TTG quartz-feldspar porphyry, hosted in a strongly sheared mylonite that was probably initially a conglomerate.

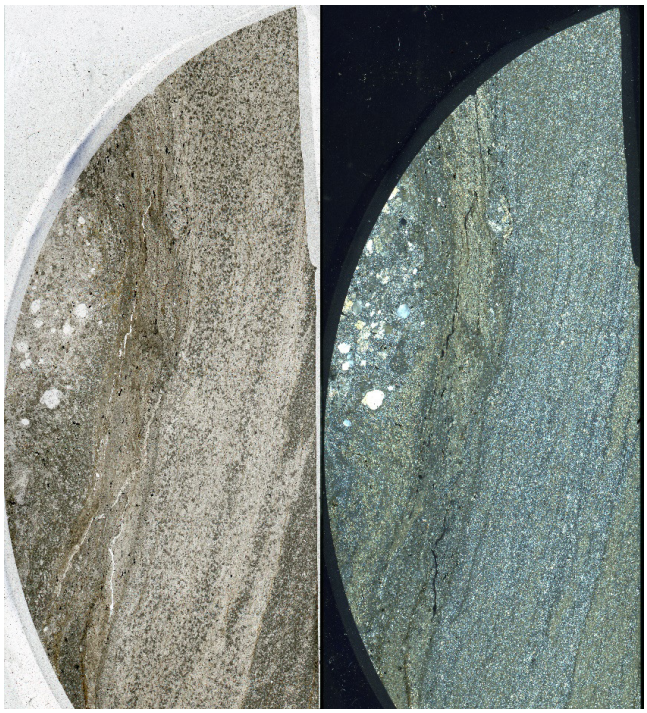


Figure 4.1.27: Large photomicrographs of TSUPB030.

4.1.5. Banded iron formation (FZ-12-01, FZ-12-02):

Two samples of BIF were collected from the Aouéouat greenstone belt; FZ-12-01 is a surface sample collected from a subcrop within the Fennec target, and FZ-12-02 is a drill core sample collected from the Piment target.

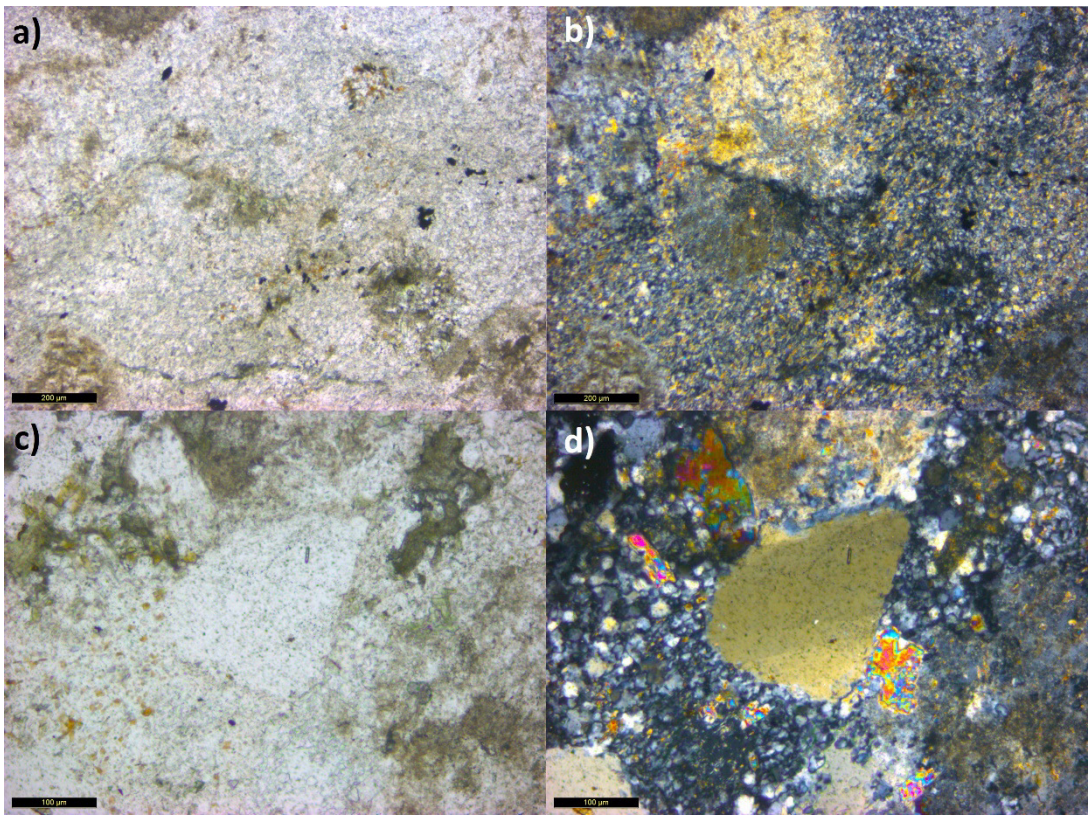


Figure 4.1.28: Photomicrographs of TSUPB030; a) PPL, b) XPL, c) PPL, d) XPL.

FZ-12-01 is dark in colour, with thin Fe-oxide bands which have weathered to orange, and show isoclinal folding. The silica, which appears black, makes up > 90% of the sample, and Fe-oxide < 10%, with no other minerals apparent. In thin section, the silica and Fe banding is clear, and there are small amounts of interstitial carbonate and white mica which have almost completely weathered out (Figure 4.1.30a,b).

FZ-12-02 is very different in nature from FZ-12-01. This sample alternates between thin black bands (silica) and thin brown bands (Fe-oxide) < 1cm (Figure 4.1.29). There are also some bands that are dark green in colour, and contain garnets up to 3mm in diameter, and thinner black bands which also contain numerous smaller garnets (~1mm in diameter). The sample is isoclinally folded with a strong schistosity parallel to the folding. It also contains some later ductile shear structures oblique to the main schistosity, as well as late brittle fractures which are infilled with carbonate. In thin section it becomes apparent that only ~50% of the rock is pure silica and Fe-oxide bands (Figure 4.1.30c,d). The large garnets are hosted in chlorite bands (Figure 4.1.30e,f,h), and the smaller garnets in predominantly chlorite bands, but with illite also present. The large garnets have abundant inclusions in their centre, and are near inclusion free at their margin, indicating their speed of growth slowed as the porphroyblasts formed. Garnets also show signs of deformation and alteration, with the large garnets having shear structures running through them, composed of chlorite (Figure 4.1.30h), and the smaller garnets appearing as ghost minerals

(Figure 4.1.30g), having undergone almost complete replacement by chlorite. Secondary tourmaline also appears to have formed throughout these bands. A number of layers between Fe-oxide bands are almost entirely composed of illite and others chlorite, while a number of bands have a combination of illite, chlorite and silica (Figure 4.1.30i). This highlights that this BIF sample contains a detrital component, which was likely a fine grained sediment deposited during its formation. Later formed quartz and carbonate veins persist throughout the sample (Figure 4.1.30j).



Figure 4.1.29: FZ-12-02 hand sample.

4.1.6. Pegmatite (TSUPB006):

The late pegmatite which is present throughout the study area did not appear to show any mineralogical variation between outcrops / drill core, and so a single representative sample of this, TSUPB006, was collected. In hand sample this is a pale coloured rock with large quartz and feldspar crystals > 5cm in diameter. There are abundant yellow-green muscovite crystals, up to 2cm in length, and small garnets, up to 2mm in diameter (Figure 4.1.31). In thin section, it is difficult to estimate the percentage of feldspar, which is perthitic in nature, relative to quartz due to the size of the crystals, however together they comprise > 95% of the rock (Figure 4.1.32a-d), and show some signs of sericite alteration. Muscovite and garnet make up the remaining ~5% of the rock (Figure 4.1.32e-h). The garnet crystals exhibit strong fracturing, with chlorite, quartz and white mica filling the cracks. Some small fractures throughout the rock also contain chlorite, white mica and quartz (Figure 4.1.32c,d).

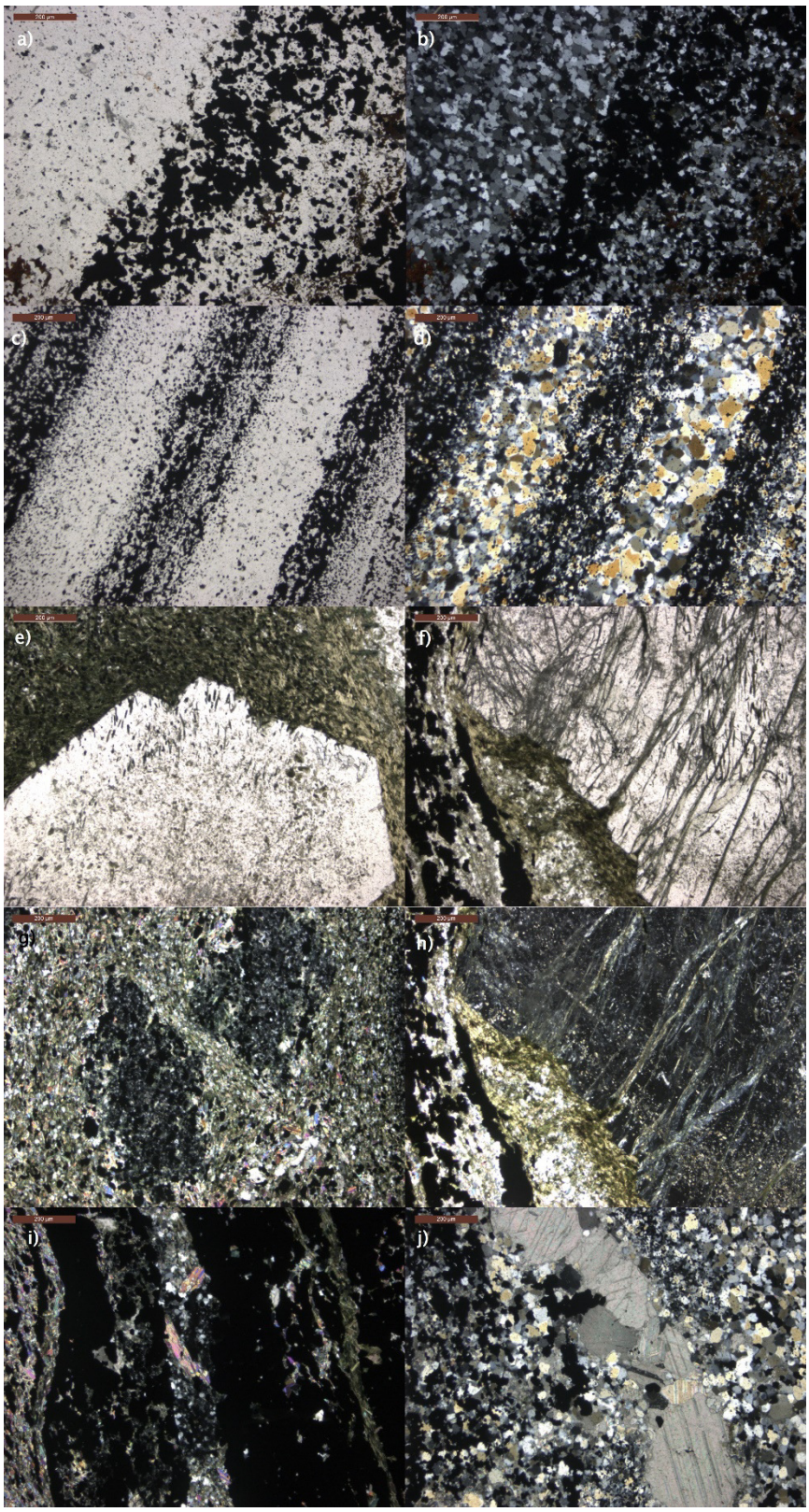


Figure 4.1.30: Photomicrographs of FZ-12-01 and FZ-12-02; a) FZ-12-01 in PPL, b) FZ-12-01 in XPL, c) FZ-12-02 in PPL, d) FZ-12-02 in XPL, e) FZ-12-02 in PPL showing garnet and chlorite, f) FZ-12-02 in PPL showing garnet chlorite and shearing, g) FZ-12-02 in XPL showing remnant garnets and chlorite, h) FZ-12-02 in XPL showing garnet, chlorite and shearing, i) FZ-12-02 in XPL showing chlorite, illite and carbonate, j) FZ-12-02 in XPL showing later quartz and carbonate veins.



Figure 4.1.31: Hand sample photographs of pegmatite.

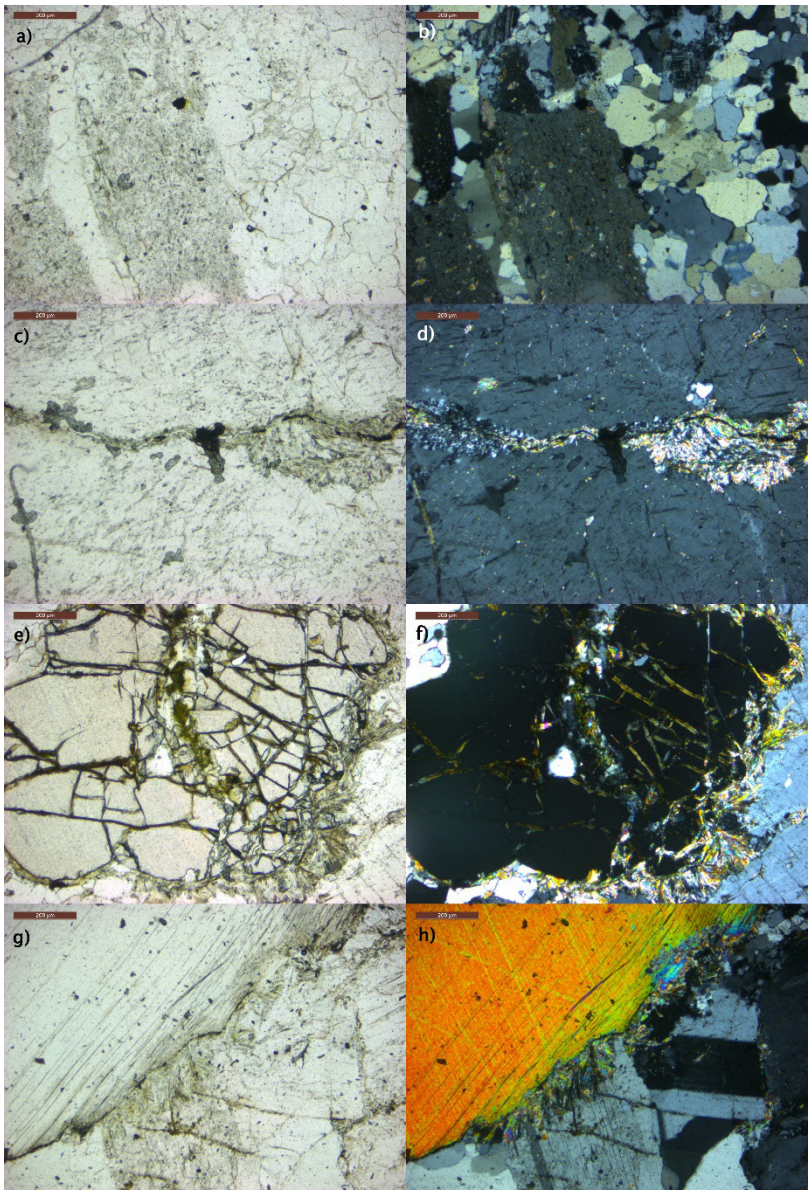


Figure 4.1.32: Photomicrographs of TSUPB006; a) PPL, b) XPL, c) PPL showing late veins, d) XPL showing late veins, e) PPL showing garnet, f) XPL showing garnet, g) PPL showing muscovite, h) XPL showing muscovite.

4.1.7. Quartz-carbonate veins (TSUPB015, TSUPB016, TSUPB027, TSUPB031, TSUPB032):

Although quartz-carbonate veins are present in the majority of the rocks studied as part of this project, these are generally < 1 cm wide. Throughout the Aouéouat greenstone belt there are numerous quartz-carbonate veins that are > 10 cm wide, and some can be up to 30 cm wide. These are a key lithology in regards to this project, as the quartz-carbonate veins are mineralised. The minerals associated with these veins include sulphides, biotite and tourmaline, however the most significant mineral they host is gold. Significantly not all of the quartz-carbonate veins in the Aouéouat greenstone belt carry gold, however it is some of these which have deposited the gold in the Aouéouat greenstone belt, and have resulted in its dissemination through surrounding rocks. One reason for studying these quartz-carbonate veins themselves is to try and discern any differences between the gold carrying veins and the veins which are largely devoid of gold. To achieve this quartz-carbonate veins were sampled from four different targets; three from drill core: C6.7, C6.12, and West Branch, and one surface sample: Fennec.

TSUPB015, from target C6.7, is pale grey-white in colour, with multiple veins and fractures < 1mm wide, and is hosted within amphibolite (Figure 4.1.33c). The veins and fractures are mostly aligned, probably caused during a late shearing event, up to 3mm thick, and are composed of carbonate, and some biotite mineralisation. Pyrite is visible in hand sample. In thin section, it is apparent that strained vein quartz comprises >97% of the sample. Thin carbonate veins dissect the sample, and fill in larger cavities in places (Figure 4.1.34a,b). There are also very thin biotite veins cutting the sample, and pyrite is the only sulphide present, associated with the carbonate veins.

TSUPB016, from C6.12, is a pale grey-white quartz vein, with multiple green-yellow thin veins and fractures < 1mm thick, and is hosted within amphibolite (Figure 4.1.33d). Pyrite is visible in hand sample. In thin section, >95% of the sample is quartz, and although slightly strained, the original crystal structure is still present, with crystals > 1cm (Figure 4.1.34c-e). Thin veins composed of carbonate and tourmaline cross cut the sample (Figure 4.1.34c,d), with a prevalent direction, probably related to late shearing, and also fill in some larger cavities in the rock (Figure 4.1.34e,f). Minor amounts of biotite and albite are also present, as is a small amount of pyrite, associated with the carbonate veins (Figure 4.1.34f).

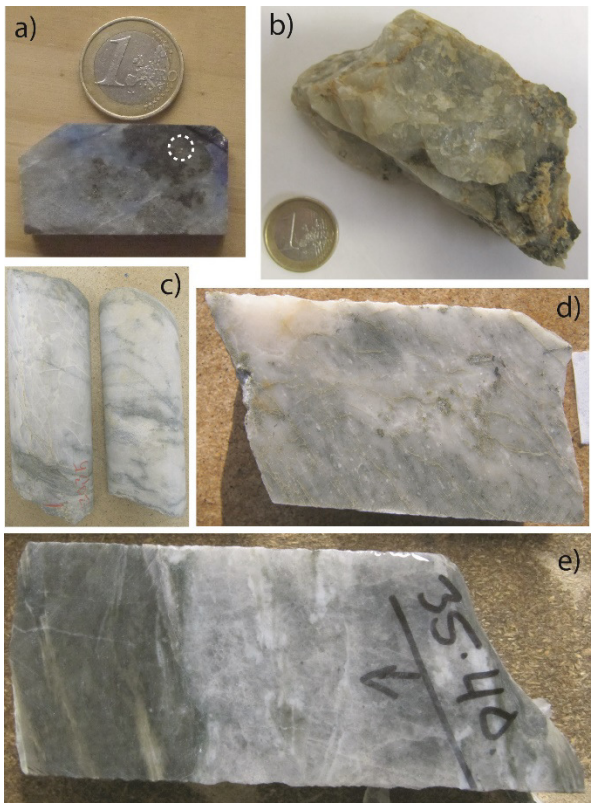


Figure 4.1.33: Hand sample photographs of quartz-veins; a) TSUPB031 showing biotite, pyrrhotite, and visible gold (circled), b) TSUPB026 (equivalent of TSUPB027) showing appearance of surface sample, c) TSUPB015 showing extensive thin carbonate and biotite veining, d) TSUPB016 showing extensive thin carbonate veining and cavity infilling, e) TSUPB032 showing thin carbonate veining and relationship to host rock.

TSUPB031 and TSUPB032 are both samples from the same quartz vein in West Branch, hosted within a diorite which is enveloped within a felsic volcanic rock. As with the other quartz-carbonate veins, these veins are light grey-white in colour (Figure 4.1.33e). There are multiple thin carbonate veins and fractures < 1mm thick, orientated in one dominant direction throughout the sample. The main difference between these samples and the C6.7 and C6.12 samples is the greater volume of mineralisation present, with both biotite and pyrrhotite common, and white mica, pyrite and gold also visible in hand specimen (Figure 4.1.35a). The mineralised zones are concentrated in clusters throughout the quartz vein, and are associated with the cross-cutting carbonate veins. In thin section, quartz accounts for > 95% of the rock, which is split about 50-50 between large quartz crystals, and strained quartz (Figure 4.1.35a,b,d). The rest of the sample is composed of carbonate and biotite mineralisation in veins, and infilling of larger cavities, as well as the associated sulphide minerals (pyrite, pyrrhotite), white mica and gold (Figure 4.1.35c).

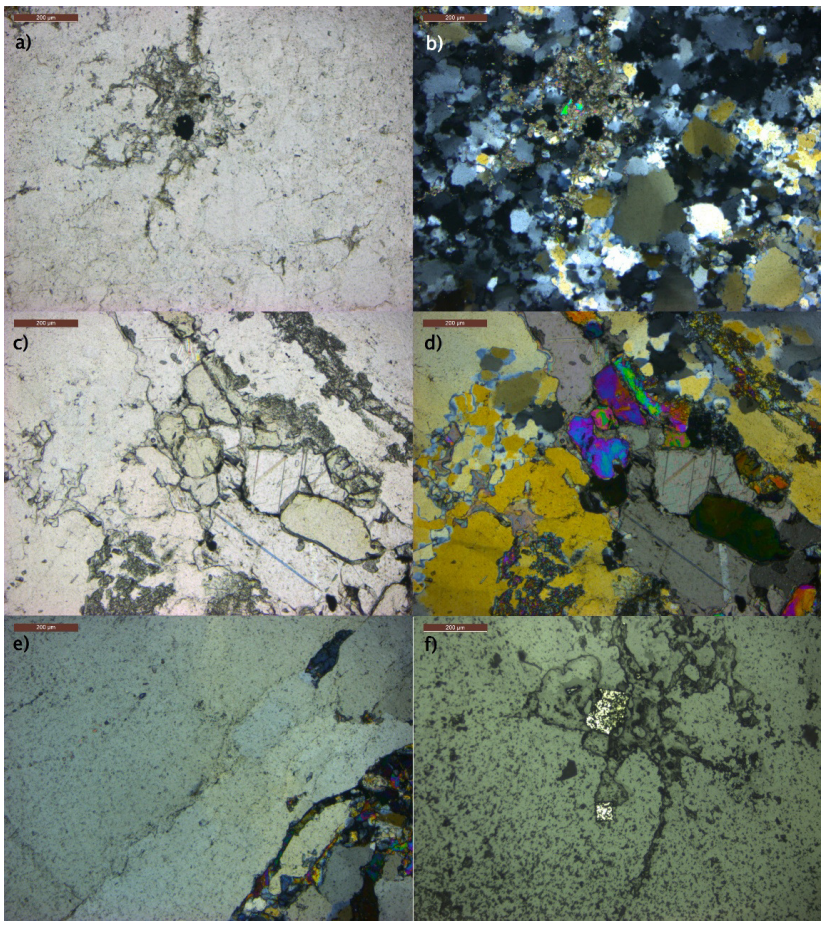


Figure 4.1.34: Photomicrographs of TSUPB015 and TSUPB016; a) TSUPB015 in PPL, b) TSUPB015 in XPL, c) TSUPB016 in PPL showing carbonate-tourmaline vein, d) TSUPB016 in XPL showing carbonate-tourmaline vein, e) TSUPB016 in XPL showing quartz crystal and carbonate-tourmaline filled cavity, f) TSUPB016 in reflected light showing pyrite in carbonate vein.

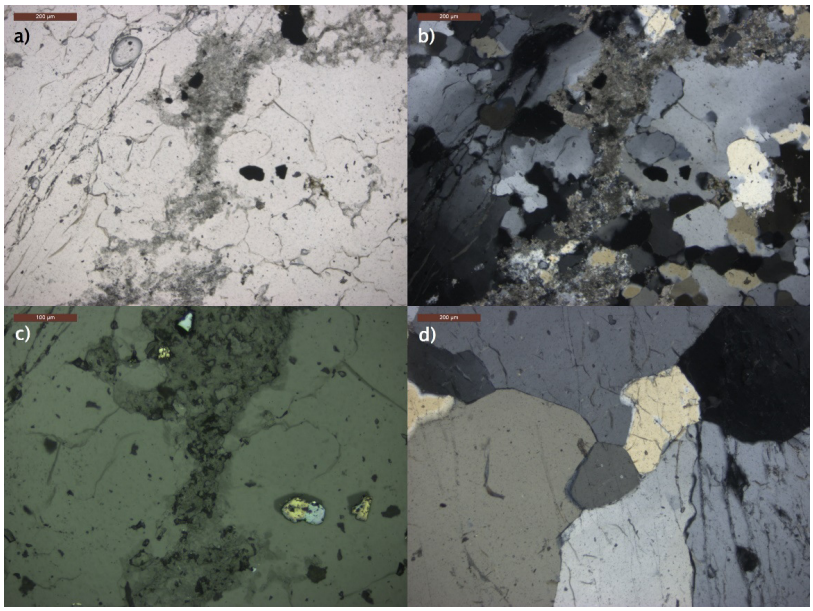


Figure 4.1.35: Photomicrographs of TSUPB031 and TSUPB032; a) TSUPB031 in PPL showing carbonate veins and fractures, b) TSUPB031 in XPL showing carbonate veins and fractures, c) TSUPB031 in reflected light showing pyrite and gold, d) TSUPB032 in XPL.

TSUPB027 was collected from an exploration trench in the Fennec target. Due to it being a surface sample, it is a dirty brown-grey rock with patches of clear vein quartz in amongst a network of other veins and host rock inclusions (Figure 4.1.33b). The quartz is light grey and translucent, making up ~45% of the rock, while the host rock is dark grey, with a strong foliation and also composes ~45% of the rock. At any contact between the quartz vein and the host rock the rocks is a light-brown colour, which is probably caused by silicification of the host rock, comprising the final ~10%. Thin carbonate veins are present throughout the quartz vein and host rock. It is not possible to identify any sulphides due to oxidation. In thin section, the vast majority of the vein quartz shows signs of strain. Chlorite, biotite, white mica and carbonate are all present in thin veins (< 1mm), which are also present throughout the host rock inclusions (Figure 4.1.36a,b). Within the host rock there are also veins of albite, quartz and white mica, which carry a large volume of sulphide minerals. Pore space is present where carbonate or sulphides have been weathered out, with no sulphides remaining in the thin section. Secondary minerals including chlorite, biotite and white mica are disseminated throughout the host rock, which obviously has a weaker structure than the vein quartz. The composition of the host rock is difficult to distinguish in hand sample or thin section due to the level of alteration it has undergone, and the volume of secondary minerals now formed. Around its margins silicification has overprinted any previous structure; however being sampled from an exploration trench allowed the host rock to be examined in the field. Although having undergone strong weathering and lateritisation, the host rock was identified as a meta-greywacke.

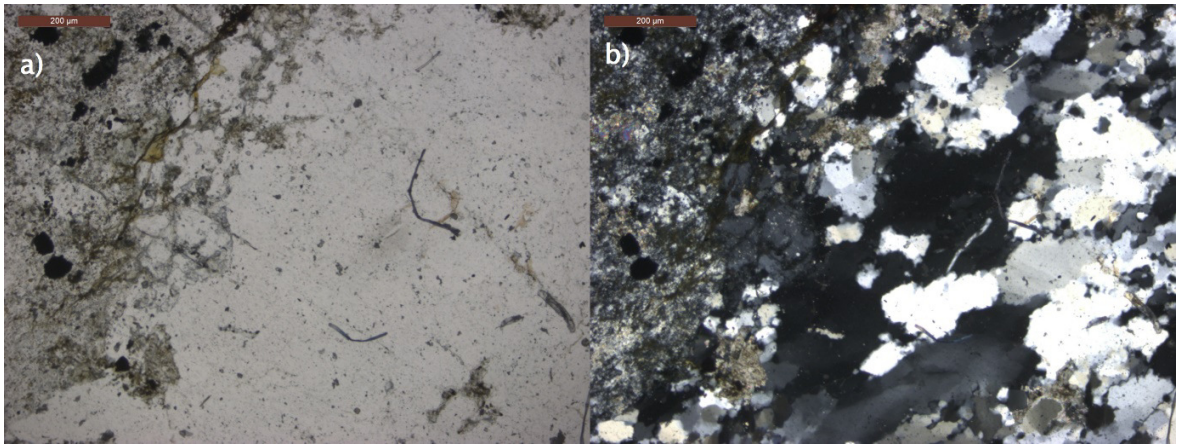


Figure 4.1.36: Photomicrographs of TSUPB027; a) PPL, b) XPL.

4.2. Geochronology:

Previous to this study, there was only one date available from the rocks within and around the Aouéouat greenstone belt, that of the ~2965 Ma felsic volcanic rock dated by Key et al. (2008). The primary aim of this study is to attempt to date the stratigraphy of the Aouéouat greenstone belt, and surrounding TTG plutons. This will also allow constraints to be placed on the ages of the tectonic activity, and mineralisation that the region underwent. The results from geochronology are presented below, by lithological assemblage, and in table 4.2.1.

4.2.1. Temeimichat assemblage:

Due to the ultramafic composition of the Temeimichat assemblage, it is very unlikely that these rocks contain any zircon, or any other datable mineral phases. This is a common issue when attempting to constrain the age of ultramafic sequences from greenstone belts worldwide, and places a large hindrance on constraining the timing of the early stages of greenstone belt formation. Two methods were attempted in order to date the Temeimichat assemblage; U-Pb zircon geochronology, and Sm-Nd isotope isochron dating.

One Temeimichat assemblage sample was chosen for U-Pb zircon geochronology (TSUPB023). This is an ultramafic tremolite-chlorite schist, interpreted to be a komatiite. This sample was chosen due to the presence of quartz and carbonate veining that cross-cut the sample, and the possibility that there were some original leucocratic zones in the sample. Although there was little expectation that there would be magmatic zircons in the komatiite, there was the possibility that inherited zircons would be present, sourced from the basement, or older more felsic flows from lower stratigraphy, which would help place a minimum age constraint on the assemblage. There was also the possibility that there were inherited zircons within the quartz-carbonate veins, which could also provide a maximum age, or if hydrothermal, could provide a minimum age the Temeimichat assemblage. Unfortunately no zircons were found in the rock and so this was not possible.

Two samples from the Temeimichat assemblage were analysed for Sm-Nd isotopes, TSUPB023 and TSUPB024. This was carried out as a pre-test for the possibility of analysing more samples to form a Sm-Nd isochron age. Although no further samples were analysed for Sm-Nd isotopes, and therefore no isochron age was calculated, it appears that the Temeimichat assemblage and the Aouéouat assemblage Sm-Nd ratios plot on separate isochrons, suggesting there is a difference in formation age between the two.

Table 4.2.1: Compilation of geochronological results, arranged by assemblage (rows) and geological event (columns).

Sample	HoleID	Target	Rock Code	Description	Hydrothermal Dates (Ma)	Interpretation	Granodiorite Dates (Ma)	Interpretation	Aouéouat Dates (Ma)	Interpretation	Young Basement Dates (Ma)	Interpretation	Old Basement Dates (Ma)	Interpretation	Other Dates (Ma)	Interpretation
Aouéouat Assemblage																
TSUPB007	TA05090RD	WB	FVC	Felsite	~2815	Hydrothermal			2990 ± 11	Magmatic Age			~3178; ~3196; ~3234	Old basement components		
TSUPB008	TA05090RD	WB	GGD	Granodiorite					2996 ± 8.2	Magmatic Age			~3219; 3293 ± 17	Old basement components		
TSUPB009	TA05090RD	WB	GDI	Diorite					3000 ± 66	Magmatic Age			3272 ± 14	Old basement components		
Tasiast Assemblage																
TSUPB020	TA05136RD	WB HW	SGW	Greywacke			~2953	Granodiorite Detrital	~2989	Aouéouat Detrital	~3047; ~3169	Young basement detrital	3170 - 3312	Old basement detrital		
TSUPB021	TA05136RD	WB FW	SGW	Greywacke			~2957	Granodiorite Detrital	~2992	Aouéouat Detrital	~3055	Young basement detrital	3209 - 3312	Old basement detrital		
TSUPB001	TA05227DD	C6.7	SAK	Greywacke	2848 ± 43	Hydrothermal							~3385; ~3510	Old basement components		
TSUPB003	TA05283DD	C6.7	SGW-SAK	Greywacke					2996 ± 12	Aouéouat Detrital						
TSUPB030	TA05283DD	C6.7	SGW/GDI	Granodiorite clasts							3059 ± 32	Young basement clasts				
TSUPB005	TA05291DD	TFW	SGW	Greywacke			2964 - 3074	Granodiorite Detrital	2964 - 3074	Aouéouat Detrital	2964 - 3074	Young basement detrital	~3112; ~3175	Old basement components		
TSUPB010	TA05155ARD	WB FW	SGW	Fine grained sediment	No zircon											
FZ-12-02	TA05192DD	Piment	BIM	Banded iron formation	No zircon											
Pegmatite																
TSUPB006	TA05293DD	TFW	GPG	Pegmatite											2766 ± 31	Magmatic Age
TSUPB011	TA05190DD	WB HW	SGW	Greywacke-Arkose											2765 ± 12	Hydrothermal (Pegmatite)
Granodiorites																
TSUPB004	TA05248DD	C6.12	GGD	Porphyritic granodiorite			2960 ± 9.4	Magmatic Age								
TSUPB012	Field		GGD	Porphyritic tonalite			2967 ± 11	Magmatic Age								
TSUPB028	463558/ 2286190		OGN	Tonalite			2943 ± 9.7	Magmatic Age								
TSUPB029	438741/ 2297645		OGN	Granodiorite	2830 ± 14	Hydrothermal Age (Quartz-vein)	2928 ± 5.5; 2974 ± 6.6	Magmatic/ Inheritance								
Quartz-veins																
TSUPB015	TA05261DD	C6.7	QVN	Quartz-carbonate vein	2819 ± 19	Hydrothermal Age	2946 ± 26	Granodiorite Inheritence			3037 ± 29	Young basement inheritence				
TSUPB016	TA05262DD	C6.12	QVN	Quartz-carbonate vein			2953 ± 11	Granodiorite Inheritance	2993 ± 20	Aouéouat Inheritance	3054 ± 53	Young basement inheritence				
TSUPB026	445849/ 2284695	Fennec	QVN	Quartz-carbonate vein	2839 ± 36; 2840 ± 35	Hydrothermal (Zircon / Apatite)	2958 ± 14	Granodiorite Inheritance								
TSUPB031	TA17106DD	WB	QVN	Quartz-carbonate vein	2840 ± 35	Hydrothermal (Apatite)										
TSUPB032	TA17113DD	WB	QVN	Quartz-carbonate vein	2840 ± 35	Hydrothermal (Apatite)										
TSUPB027	445930/ 2284698	Fennec	QVN	Quartz-carbonate vein	No zircon											
Quartz-diorites																
TSUPB002	TA05245DD	C6.7	GDI	Quartz-diorite	No zircon											
TSUPB013	TA15170DD	C6.7	GDI	Quartz-diorite	No zircon											
TSUPB019	TA05255DD	C6.7	GDI	Quartz-diorite	No zircon											
Temeimichat Assemblage																
TSUPB023	TA15056DD	C6.2	TTS	Ultramafic schist	No zircon											

4.2.2. Aouéouat assemblage:

Five samples were initially chosen from the Aouéouat assemblage for U-Pb geochronology. The results of these, along with subsequent additional samples from the Aouéouat assemblage are described below.

Aouéouat felsic volcanic (TSUPB007):

A single felsic volcanic rock collected from West Branch yielded ample zircon, from which 44 representative grains were analysed. CL-images of the zircons show oscillatory zoning in most indicating they are igneous in nature, with metamict cores present in some (Figure 4.2.1). Of the 44 zircon analyses, 24 were < 10% discordant, with three different age populations present (Figure 4.2.2a,b). The main population, accounting for 32 of the zircons, gives an upper-intercept age of 2990 ± 11 Ma (Figure 4.2.2c). This is interpreted to be the crystallisation age of the felsic volcanic rock. A similar age, though with a larger MSWD, of 2992 ± 8 Ma is given using a mean-weighted-average (MWA) plot of $^{207}Pb/^{206}Pb$ ages (Figure 4.2.2d). A small older population, interpreted to be inherited zircons, give $^{207}Pb/^{206}Pb$ ages of ~3178, 3196 and 3234 Ma. The only zircon < 10% discordant that is not contained within either of those two populations gives a $^{207}Pb/^{206}Pb$ age of 2815 Ma, which is interpreted to be a later hydrothermal age.

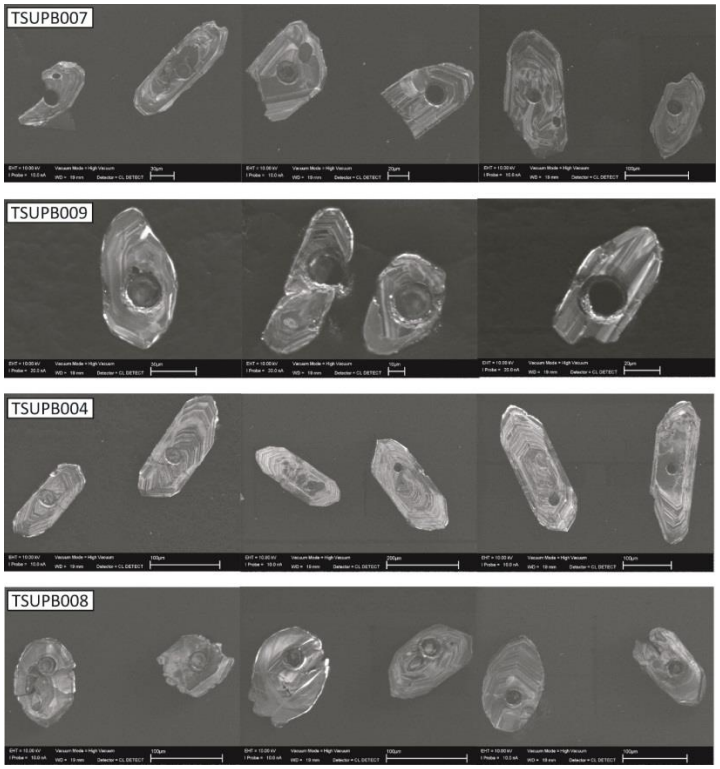


Figure 4.2.1: CL images of representative zircons from Aouéouat assemblage samples showing ablated pits from U-Pb dating.

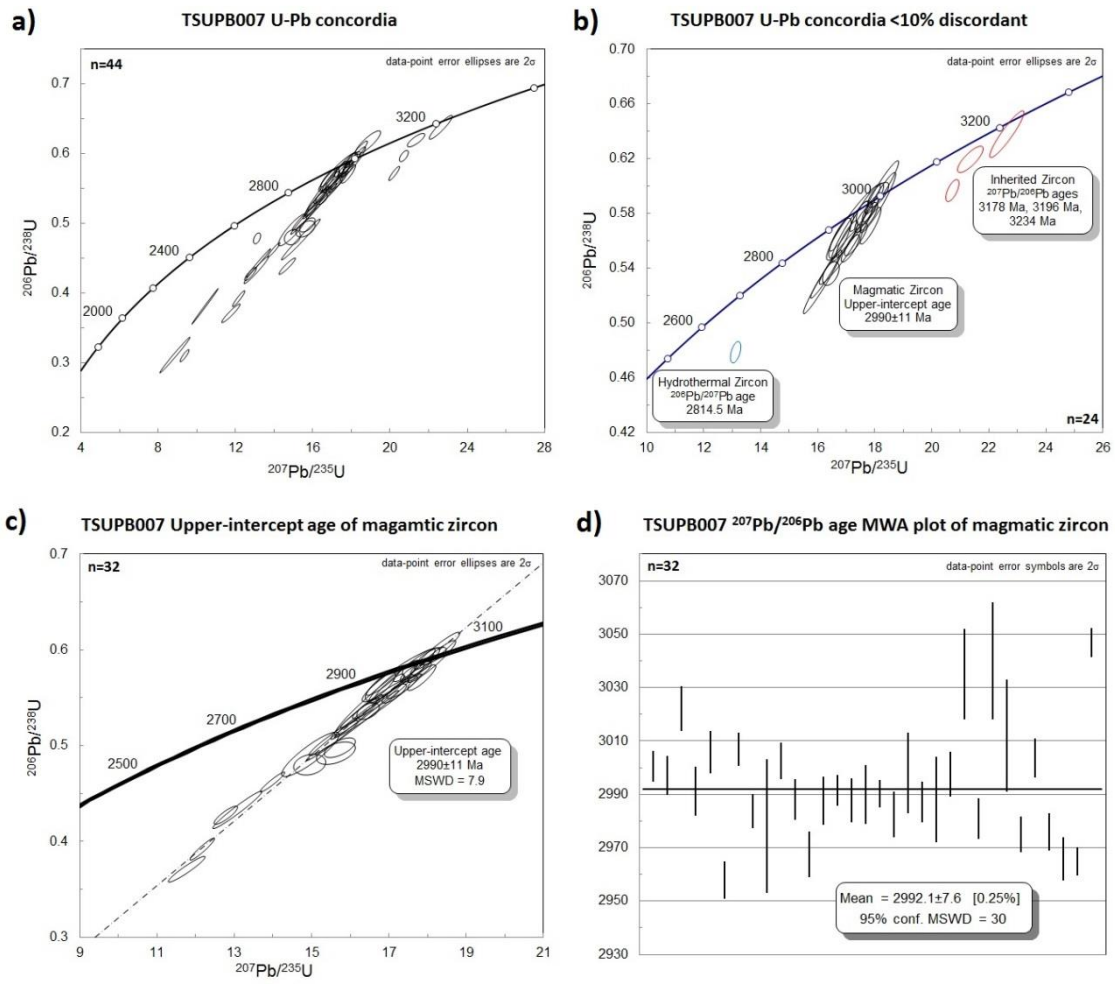


Figure 4.2.2: U-Pb geochronology plots of TSUPB007; a) U-Pb Concordia plot, b) U-Pb Concordia plot of analyses < 10% discordant, c) upper-intercept plot of magmatic population, d) $^{207}Pb/^{206}Pb$ age MWA plot of magmatic population.

Aouéouat quartz-diorites (TSUPB002, (+TSUPB013, TSUPB019)):

The quartz-diorite stratigraphy from C6.7 was one of the key lithologies targeted for U-Pb dating. This is due to it being the host rock for a number of the gold bearing quartz veins, and therefore also contains a lot of disseminated mineralisation within itself. Although dioritic in composition, the presence of quartz phenocrysts suggested that it could be possible to retrieve zircon from this lithology. Initially, TSUPB002 was processed; however no zircons were present in the sample. Subsequently, TSUPB013 was collected from the same lithology, but a different drill hole, leading to a similar result of zero zircon yield. The process was repeated for a third time with TSUPB019, and again no zircons were recovered, leading to the conclusion that this sample would remain undated.

Aouéouat diorite (TSUPB009):

The diorite sample collected from West Branch yielded a total of 8 zircons, 4 of which are < 10% discordant. The majority of the zircons show oscillatory zoning in CL-images, with most still exhibiting original crystal morphology, however some are metamict and some are sub-rounded. They are interpreted as being igneous in nature (Figure 4.2.1). Although the sample size is small, there appears to be two distinct age populations discernible (Figure 4.2.3a). The younger of these populations provides an upper-intercept age of 3000 ± 66 Ma, with an MSWD of 1.4 (Figure 4.2.3b) and is interpreted as the crystallisation age of the diorite. The older population gives an upper-intercept age of 3272 ± 14 Ma, with an MSWD of 1.4 (Figure 4.2.3c) which is interpreted to be an inherited population.

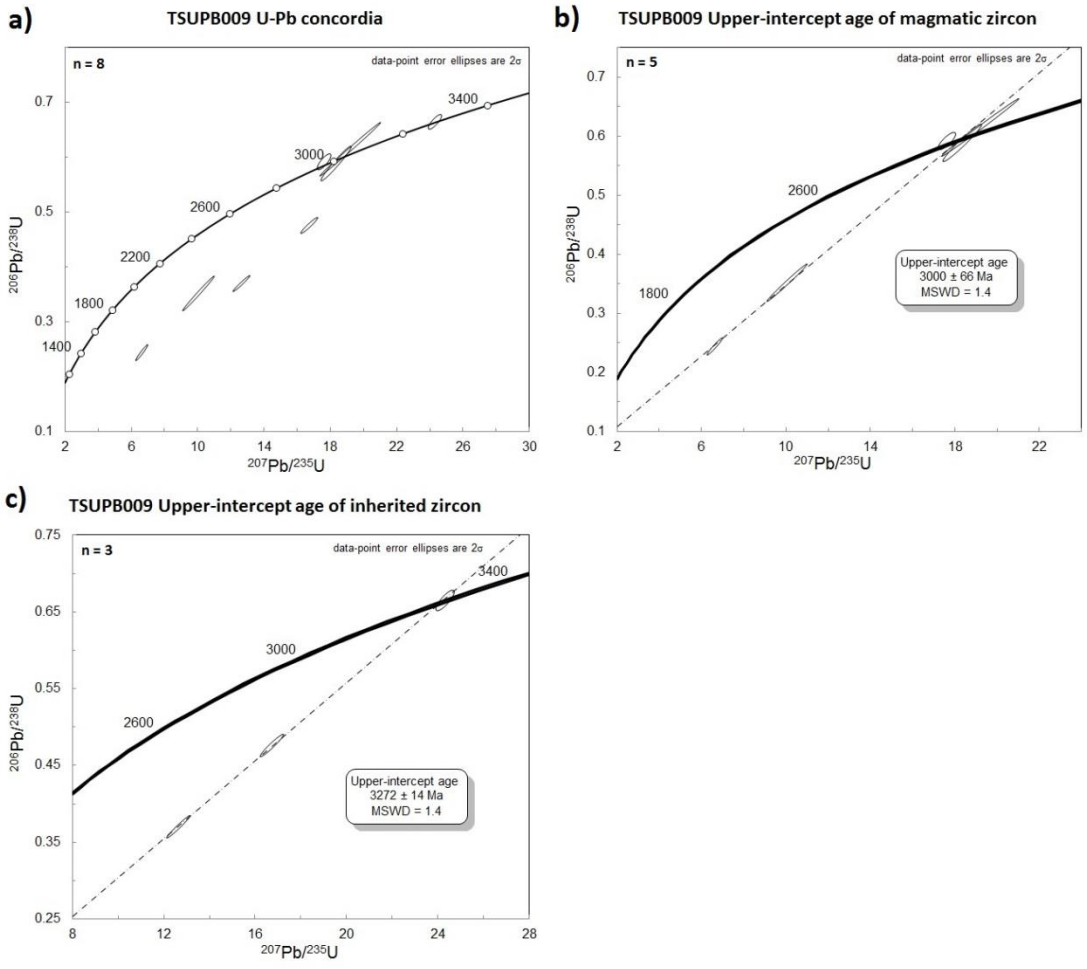


Figure 4.2.3: U-Pb geochronology plots of TSUPB009; a) U-Pb Concordia plot, b) Upper-intercept plot of magmatic population c) upper-intercept plot of inherited population.

Aouéouat TTG rocks (TSUPB004, TSUPB008):

Two TTG rocks were sampled from within the Aouéouat assemblage for U-Pb geochronology; the porphyritic granodiorite TSUPB004, and the strongly sheared and fine grained granodiorite TSUPB008.

TSUPB004 yielded ample zircon, from which 51 were analysed. CL-images of the zircon show they are all oscillatory zoned, with a clear crystal morphology, showing they are igneous zircons (Figure 4.2.1). Of the 51 zircons, only 5 are < 10% discordant, however there appears to be only one age population present (Figure 4.2.4a). An upper-intercept age of 2963 ± 19 Ma is calculated when all of the analyses are included, however this gives a very large MSWD of 40 (Figure 4.2.4b). By removing the analyses not within error of this intercept line, the MSWD is reduced to 6.3, with very little change in the upper-intercept age, to 2960 ± 9.4 Ma (Figure 4.2.4c). A $^{207}Pb/^{206}Pb$ age MWA plot of the 5 analyses < 10% discordant gives an age of 2956.8 ± 4.8 Ma, and an MSWD of 1.3; within error of the other methods (Figure 4.2.4d). This suggests that the sample has only one zircon age population, representing the age of crystallisation, the preferred age being 2960 ± 9.4 Ma.

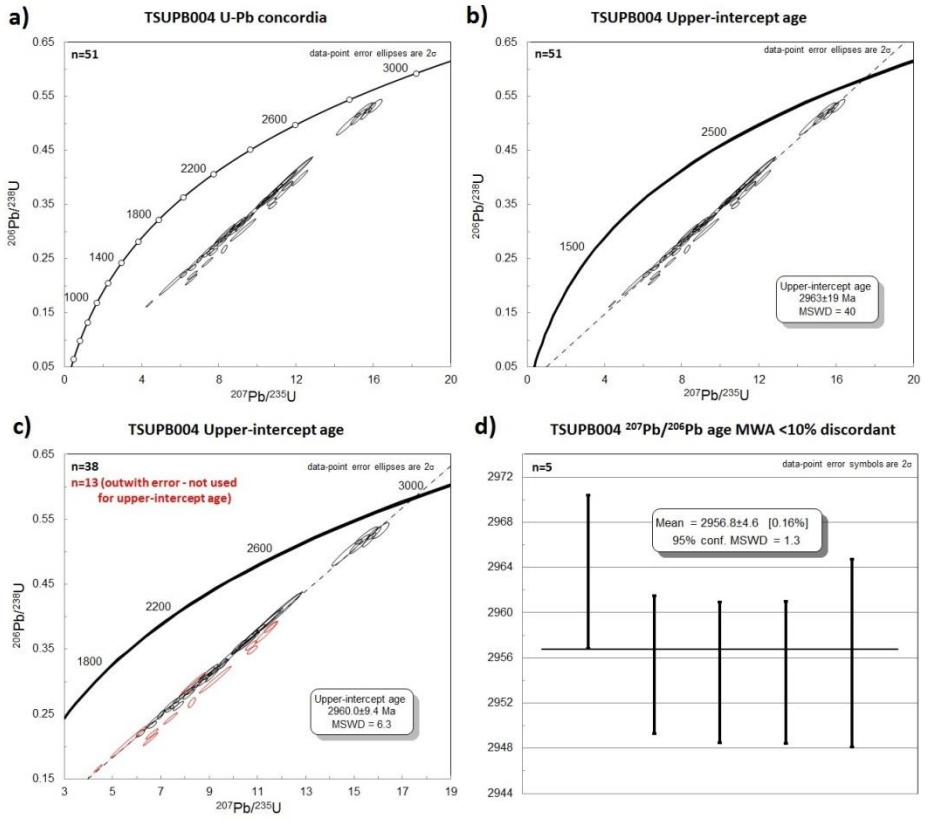


Figure 4.2.4: U-Pb geochronology plots of TSUPB004; a) U-Pb Concordia plot, b) upper-intercept plot of all zircons c) upper-intercept plot of zircons within error, d) $^{207}Pb/^{206}Pb$ age MWA plot of analyses < 10% discordant.

TSUPB008 also yielded ample zircon, with 38 being chosen for analysis. CL-images show a mixture of oscillatory zoned igneous crystals, some of which have their original morphology intact, and some of which appear rounded, as well as metamict zircons which appear sub-rounded in nature (Figure 4.2.1). Of the 38 zircons analysed, 18 are < 10% discordant, and appear to be from two separate age populations (Figure 4.2.5a,b). The younger of these <10% discordant populations gives an upper-intercept age of 2996 ± 8.2 Ma, interpreted to be the crystallisation age of the granodiorite (Figure 4.2.5c). The older of the two populations gives an upper-intercept age of 3293 ± 17 Ma, interpreted to be an inherited population (Figure 4.2.5d). There are a few analyses which do not fall within either of these populations. These could either be from inherited zircons younger than 3293 Ma, which is likely the case for the concordant analysis which gives a $^{207}Pb/^{206}Pb$ age of 3219 Ma, or could be an artefact of a mixing age between inherited zircon and magmatic zircon.

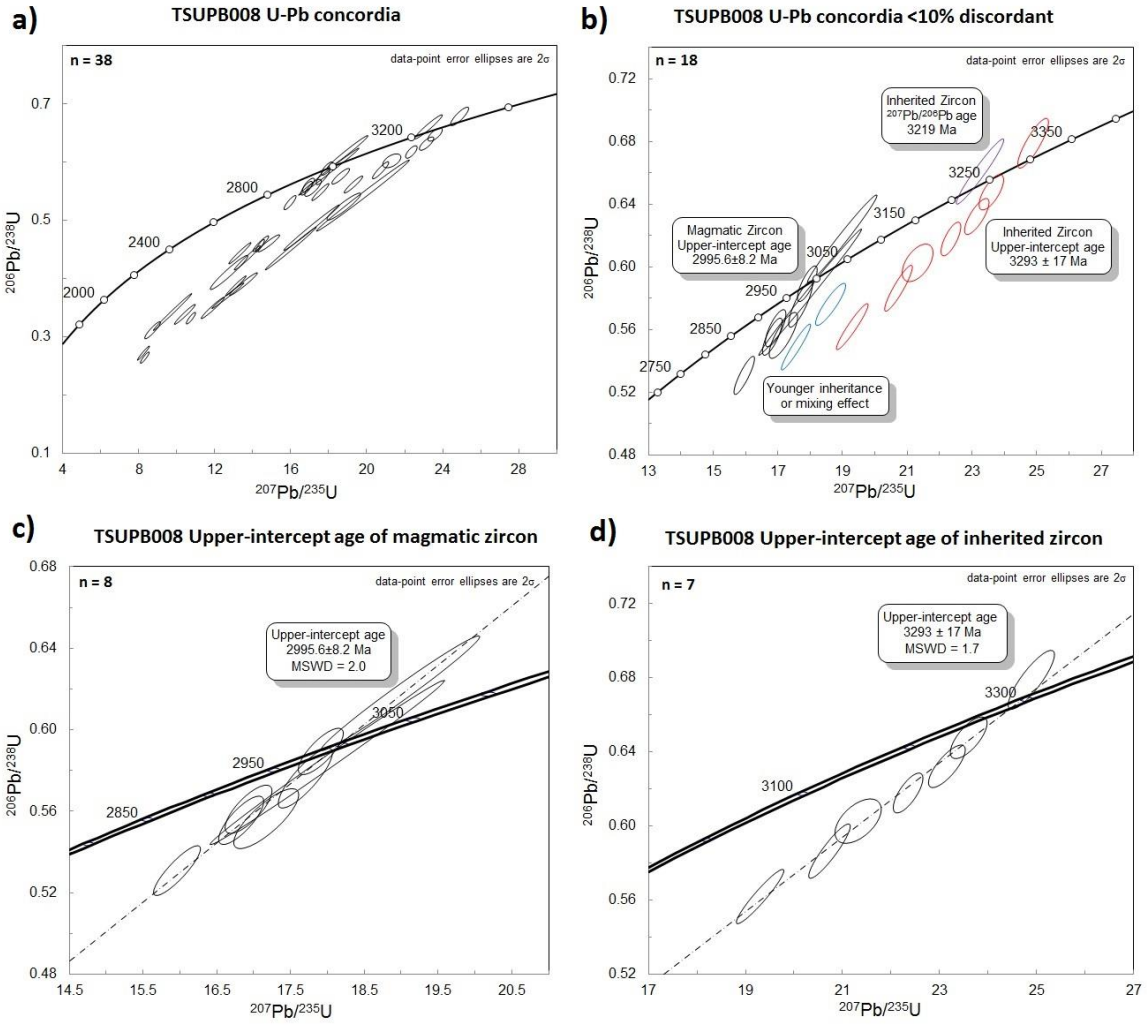


Figure 4.2.5: U-Pb geochronology plots of TSUPB008; a) U-Pb Concordia plot, b) U-Pb Concordia plot of analyses < 10% discordant, c) upper-intercept plot of magmatic population < 10% discordant, d). upper-intercept plot of inherited population < 10% discordant.

4.2.3. Tasiast assemblage:

Five sedimentary samples were initially chosen from the Tasiast assemblage for U-Pb geochronology, with an additional two samples processed as replacements for TSUPB010 and TSUPB011 which did not give the detrital data expected. These are described below.

TSUPB001, a sedimentary rock from C6.7, yielded 30 zircons, all of which were analysed. Ten of these gave meaningful data. CL-images show that most of the zircons are extremely metamict, and show signs of physical damage around their edges, with most sub-rounded in nature, consistent with being detrital grains in a (meta) sedimentary rock (Figure 4.2.6). A few zircons exhibit oscillatory zoning, highlighting an igneous provenance however with most grains it is impossible to discern any original internal features. There is a single zircon age population present in the sample, which gives an upper-intercept age of 2848 ± 43 Ma (Figure 4.2.7a,b). There are also two zircons, with $^{207}Pb/^{206}Pb$ ages of 3385 and 3510 Ma. These correspond to the zircons which still possess oscillatory zoning in the CL-images. The $^{207}Pb/^{206}Pb$ age probability density plot (PDP) highlights that there is a large range in the $^{207}Pb/^{206}Pb$ ages of the 2848 Ma zircon population (Figure 4.2.7c). Due to the metamict nature of the zircons seen in CL-imaging, and the young age when compared to the rest of the stratigraphy in the Aouéouat greenstone belt, this is interpreted to be a reset age. The cause of the resetting is interpreted to be a relatively late hydrothermal event with an age of ~2848 Ma.

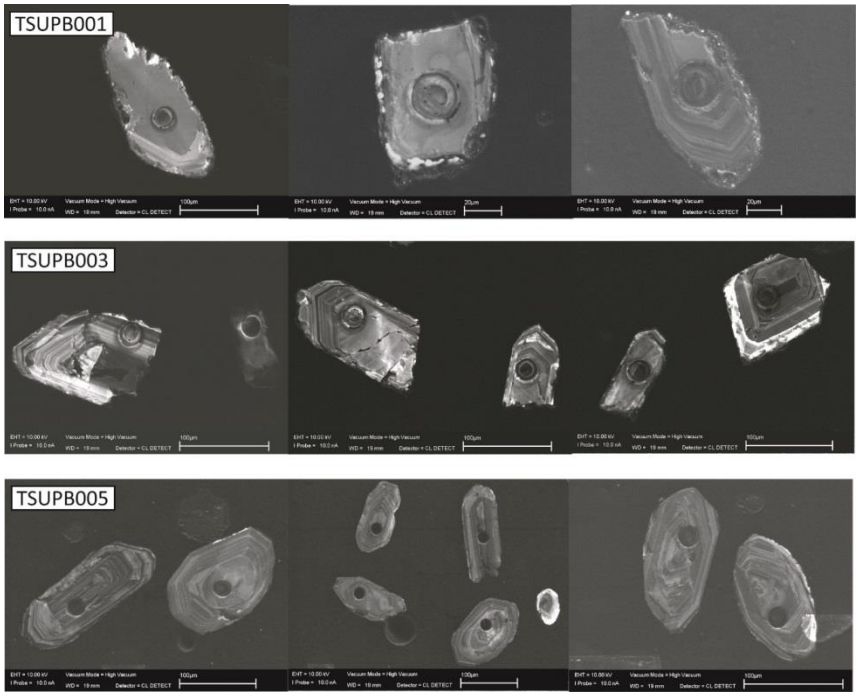


Figure 4.2.6: CL images of representative zircons from Tasiast assemblage samples (TSUPB001, TSUPB003, TSUPB005).

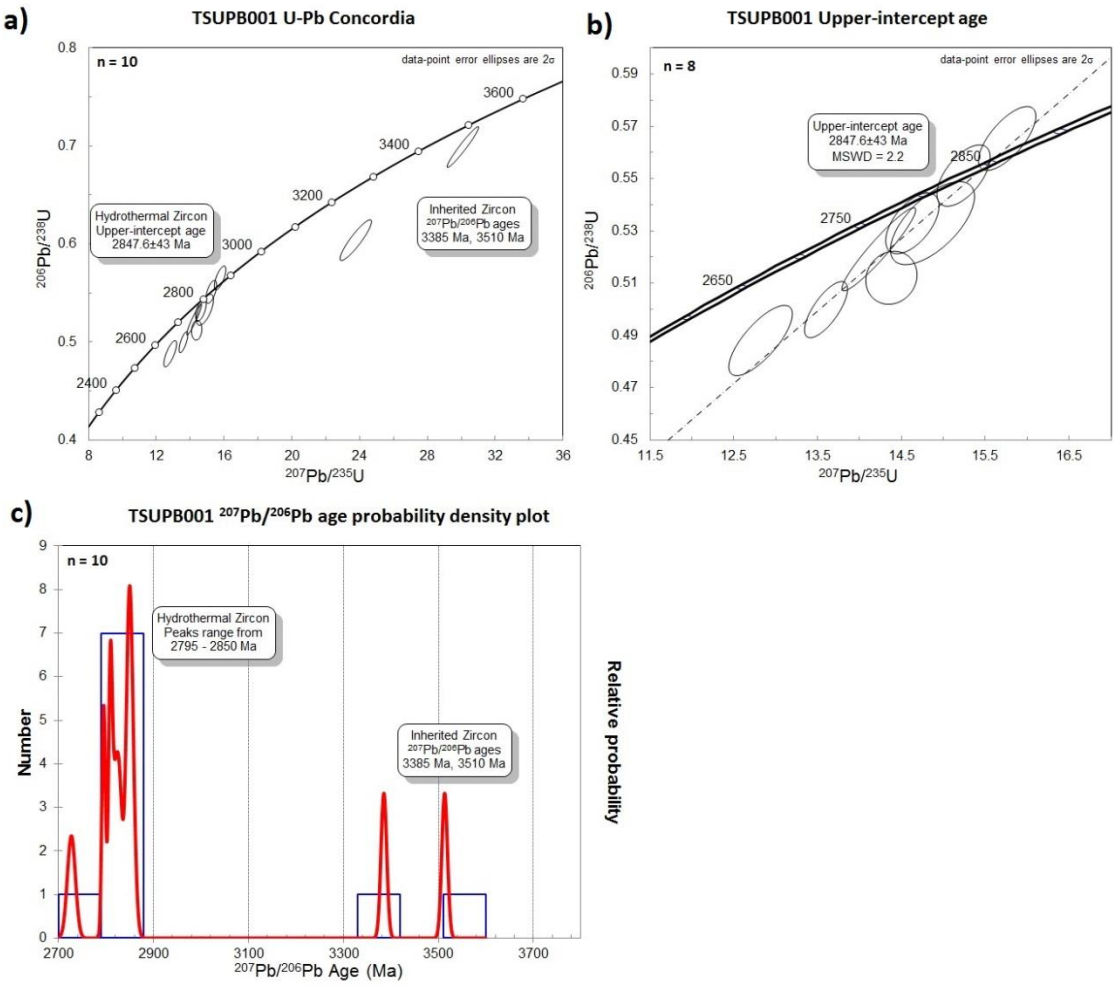


Figure 4.2.7: U-Pb geochronology plots of TSUPB001; a) U-Pb Concordia plot, b) upper-intercept plot of hydrothermal population, c) $^{207}Pb/^{206}Pb$ age PDP.

TSUPB003, a sedimentary rock from C6.7, yielded 25 zircons, 18 of which are < 10% discordant. CL-images show that almost all of the zircons have oscillatory zoning, and are sub-angular in nature; however they are all only broken fragments of zircons (Figure 4.2.6). This suggests they are sourced from an igneous rock and have been broken up during transport, however they have likely not travelled very far as they are sub-angular in nature. There is only one population of zircons present in the sample, the zircons of which are < 10% discordant give an upper-intercept age of 2996 ± 12 Ma (Figure 4.2.8a,b). This is interpreted to be a detrital population with a local source rock with an age of ~2996 Ma.

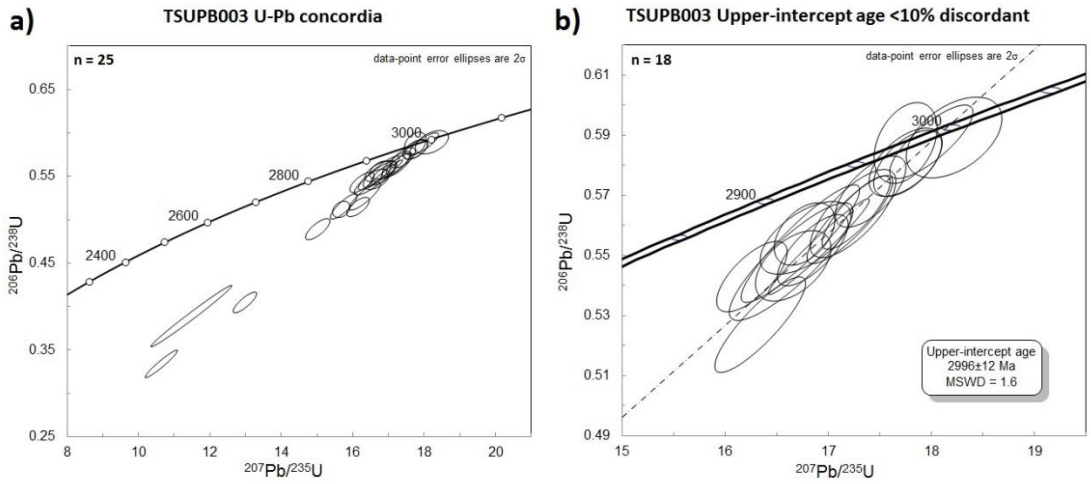


Figure 4.2.8: U-Pb geochronology plots of TSUPB003; a) U-Pb Concordia plot, b) upper-intercept plot of zircons < 10% discordant.

TSUPB005, a greywacke collected from the Tasiast Foot Wall, yielded ample zircons, 84 of which were analysed for age determination. CL-images show that the zircons are all sub-rounded, with the majority showing oscillatory zoning (Figure 4.2.6). A few of the zircons are metamict in nature. The zircons demonstrate a large range of ages, with no individual populations being discernible (Figure 4.2.9a,b). Plotting analyses < 10% discordant, the main $^{207}Pb/^{206}Pb$ age range in zircons is from 3074-2964 Ma (Figure 4.2.9d). It is possible to pick out some peaks in the PDP plot at 2985, 2999 and 3024 Ma, however it is unlikely that these are of any significance. There are three older concordant zircons, two of which have a $^{207}Pb/^{206}Pb$ age of 3112 Ma, and one of which has a $^{207}Pb/^{206}Pb$ age of 3175 Ma. There are a number of zircons with apparent younger ages giving $^{207}Pb/^{206}Pb$ ages between 2812 and 2910 Ma (Figure 4.2.9c). These ages are likely an artefact of Pb-loss, though could also have a hydrothermal age component. This sample is interpreted to contain a mixture of source rocks with crystallisation ages between 3074 and 2964 Ma. Due to the small number of older zircons, it is likely that these are from the rocks which formed the source of the main age population, occurring as inherited grains in the source rock lithologies.

Of the two samples initially collected to represent the sedimentary rocks from West Branch, TSUPB010 was chosen to represent the Tasiast Foot Wall. Upon further examination, this was discovered to be a very fine grained sediment, composed of ~50% mica minerals, and contained no zircons.

TSUPB011 was chosen to represent the Tasiast Hanging Wall from West Branch, and this sample yielded ample zircon. CL-imaging of these zircons however show that they are almost all dark with no apparent zoning, suggesting they are either hydrothermal in origin, or have been hydrothermally altered (Figure 4.2.10). They also show signs of physical damage (Figure 3.4). 85

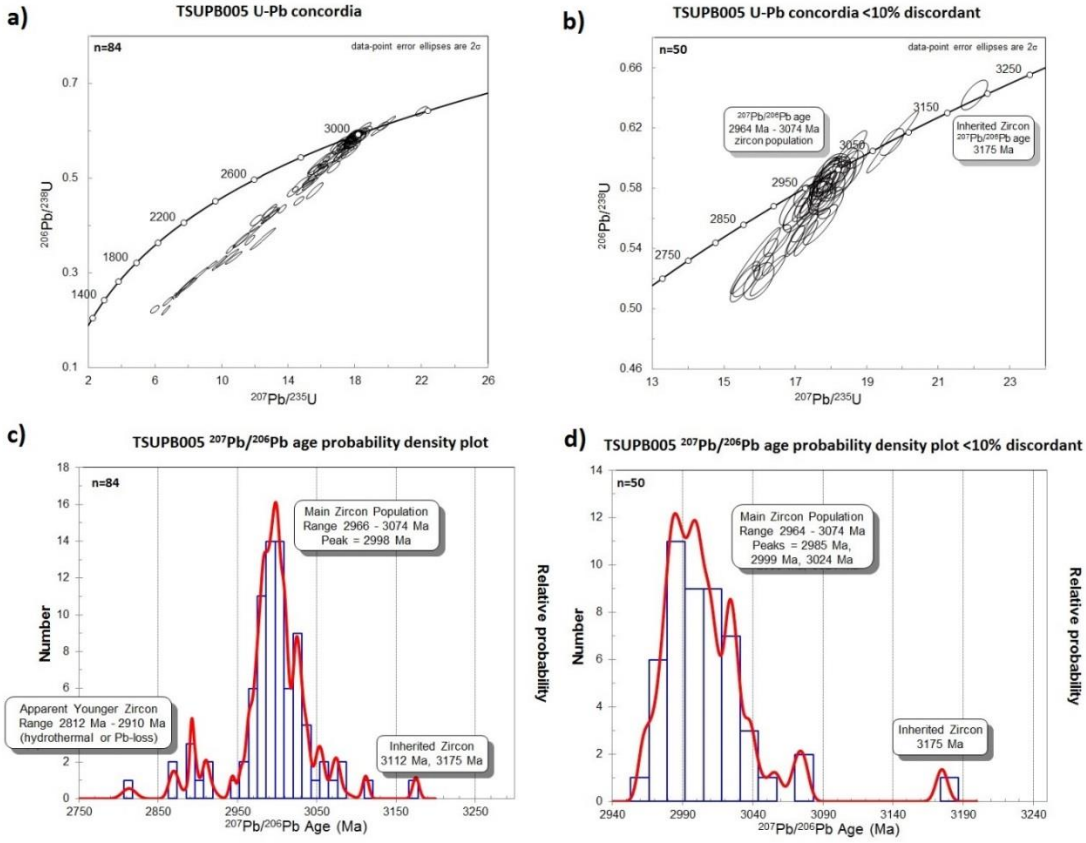


Figure 4.2.9: U-Pb geochronology plots of TSUPB005; a) U-Pb Concordia plot, b) U-Pb Concordia plot of zircons < 10% discordant, c) $^{207}Pb/^{206}Pb$ age PDP, d) $^{207}Pb/^{206}Pb$ age PDP of zircons < 10% discordant.

zircons were analysed for U-Pb geochronology, 50 of which are < 10% discordant. The analyses have large errors, and appear to cover a large range of ages, from ~ 2900 – 2500 Ma, something which is not an artefact of discordant analyses (Figure 4.2.11a-b). Using only the analyses < 10% discordant, an upper-intercept age of 2764 ± 12 Ma is calculated after removing three analyses which fall out with the error of an initial upper-intercept age (Figure 4.2.11c). This is almost identical to the $^{207}Pb/^{206}Pb$ MWA age of 2765.7 ± 9.8 Ma calculated when four analyses were rejected (Figure 4.2.11d). Although it is not normal practice to use single population calculations such as upper-intercept ages or MWA ages for a detrital population with a large range in $^{207}Pb/^{206}Pb$ ages, here it is interpreted that the zircons are giving a hydrothermal or alteration age, and the large range in $^{207}Pb/^{206}Pb$ ages is due to the different degrees of re-setting each of the individual zircons have undergone. Therefore the best calculation for the age of this hydrothermal or alteration event is through a single population calculation. The preferred interpretation for this rock is therefore that it is a greywacke in which all of the zircons have been altered by a hydrothermal event at 2765 ± 12 Ma. It is also worth noting here the anonymously low uranium content of these zircons, with an average of 33ppm for all 85 analyses, suggests that the uranium was leached out during the alteration event.

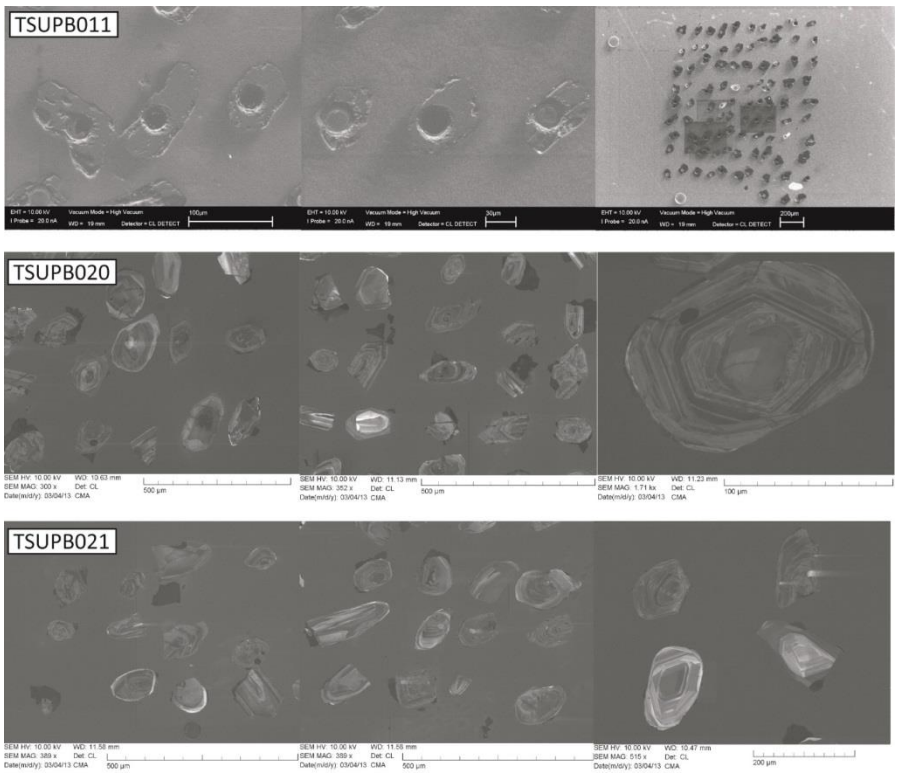


Figure 4.2.10: CL images of representative zircons from Tasiast assemblage samples (TSUPB011, TSUPB020, TSUPB021).

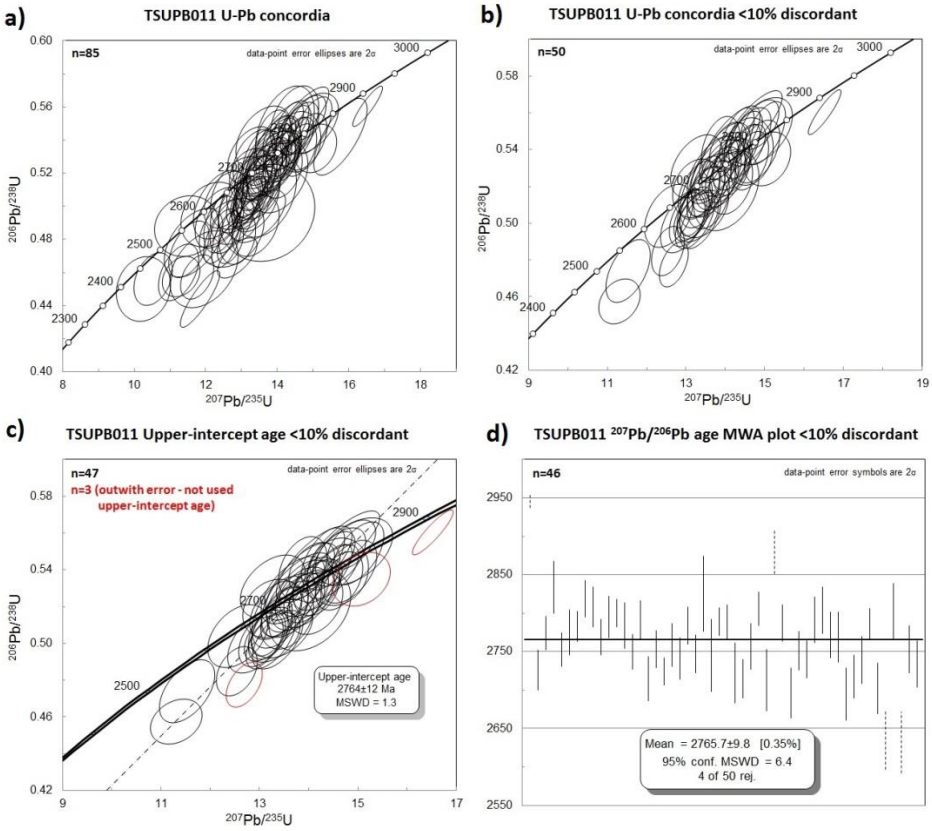


Figure 4.2.11: U-Pb geochronology plots of TSUPB011; a) U-Pb Concordia plot, b) U-Pb Concordia plot of zircons < 10% discordant, c) upper-intercept plot of zircons < 10% discordant, d) $^{207}Pb/^{206}Pb$ age MWA plot of zircons < 10% discordant.

TSUPB020 was collected from the same lithology as TSUPB011, to represent the Tasiast Hanging Wall from West Branch, and yielded ample zircon. CL-images show that zircons from this sample are sub-rounded, with many broken or cracked. A few however still have their original entire crystal morphology (Figure 4.2.10). There is a mixture of oscillatory zoned zircons and metamict zircons, suggesting more than one source for this rock. 70 zircons were analysed for U-Pb geochronology, 34 of which are < 10% discordant and cover an age range of ~3350 Ma to ~2940 Ma (Figure 4.2.12a,b). The younger detrital zircons are highlighted in figure 4.2.12c, with one age population at ~2940 Ma, and concordant zircons with $^{207}Pb/^{206}Pb$ ages of 3001 Ma and 3051 Ma. An older population have a range of $^{207}Pb/^{206}Pb$ ages between 3238 and 3288 Ma, giving an upper intercept age of 3265 ± 14 Ma (Figure 4.2.12d). The $^{207}Pb/^{206}Pb$ age PDP of analyses < 10% discordant gives similar age peaks, with a younger population ranging from 3051 – 2942 Ma, and highlights peaks of 2961 – 2942 Ma, 3002 Ma, and 3051 – 3043 Ma (Figure 4.2.12f). The range of the older zircon population is from 3356 – 3231 Ma, with a peak at 3259 Ma, and there are also two small peaks at 3120 Ma and 3164 Ma (Figure 4.2.12f). The $^{207}Pb/^{206}Pb$ age PDP of all analyses shows a very similar age distribution, however also has a number of younger peaks, which are likely an artefact of Pb-loss (Figure 4.2.12e).

TSUPB021 was collected from the same stratigraphy as TSUPB010, to represent the Tasiast Footwall from West Branch and yielded ample zircon. CL-images of this sample are almost identical to those of TSUPB020, containing sub-rounded and broken zircons, with a mixture of oscillatory zoned and metamict zircons making up the population (Figure 4.2.10). 82 representative zircons were chosen for analysis, 54 of which are < 10% discordant. These show a very similar age distribution as TSUPB020, with $^{207}Pb/^{206}Pb$ ages from a younger population ranging from 3050 – 2956 Ma, and an older population ranging from 3290 – 3236 Ma (Figure 4.2.13a-d). The $^{207}Pb/^{206}Pb$ age PDP of analyses < 10% discordant has peaks in the younger population at 2908 Ma, 2974 – 2960 Ma, 3014 Ma and 3050 Ma (Figure 4.2.13f). The older population consists of a large peak between 3309 and 3240 Ma, with the highest peak at 3251 Ma (Figure 4.2.13f). Again the $^{207}Pb/^{206}Pb$ age PDP of all analyses has a number of smaller younger peaks, which are attributed to Pb-loss (Figure 4.2.13e).

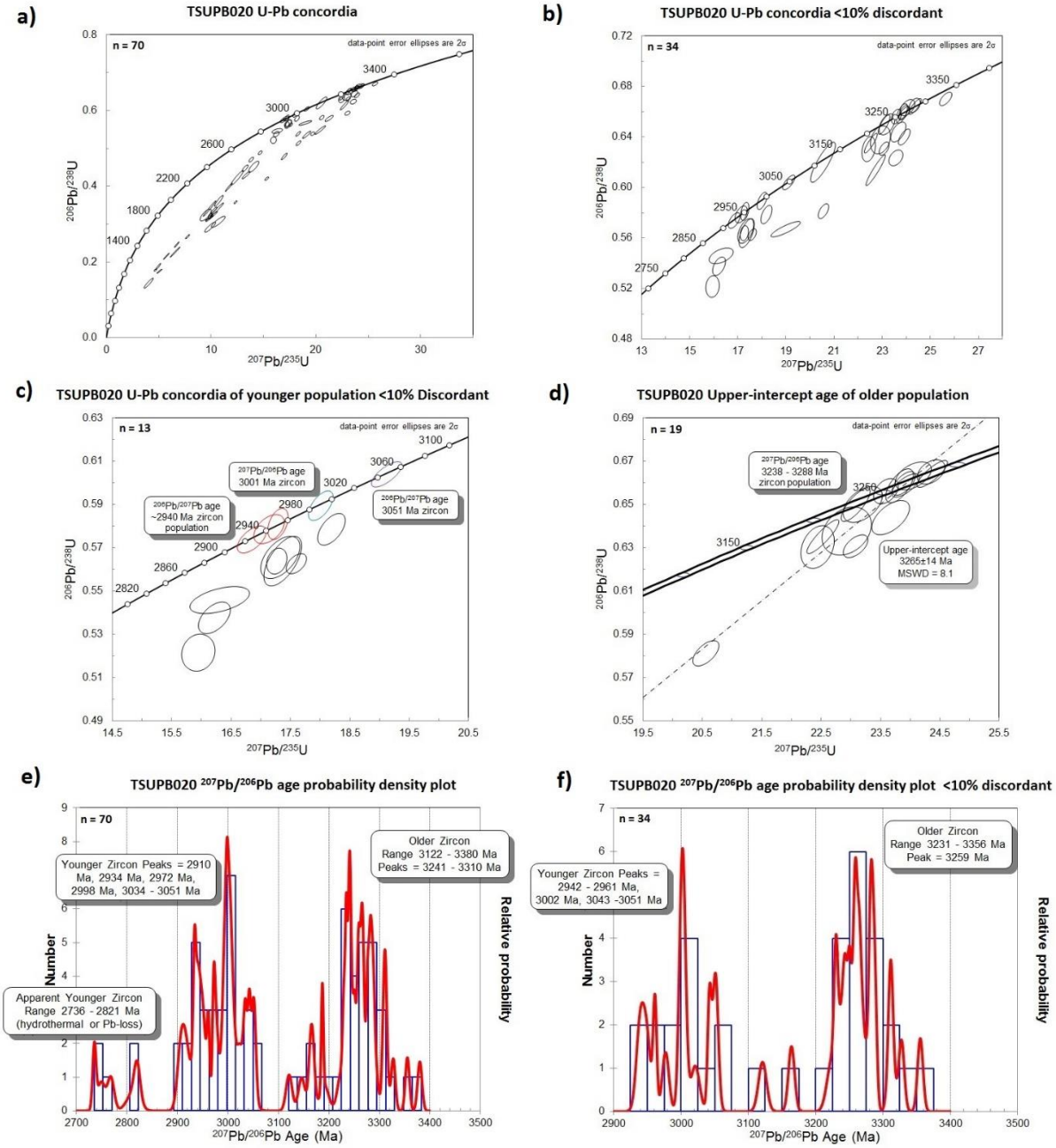


Figure 4.2.12: U-Pb geochronology plots of TSUPB020; a) U-Pb Concordia plot, b) U-Pb Concordia plot of zircons < 10% discordant, c) U-Pb Concordia plot of younger population < 10% discordant, d) upper-intercept plot of older population < 10% discordant, e) $^{207}Pb/^{206}Pb$ age PDP, f) $^{207}Pb/^{206}Pb$ age PDP of zircons < 10% discordant.

TSUPB020 and TSUPB021 were both chosen as samples to test Chemical Abrasion prior to LA-ICP-MS analysis. This was due in part to the large zircon yield obtained from these samples, and in part due to the range in different age populations present within the sample. This would allow the effect on different age populations to be tested, and to observe whether some populations were preferentially removed in their entirety. CL-images of the two treated samples show the physical effect the Chemical Abrasion had on the zircons, with most of the remaining zircons having

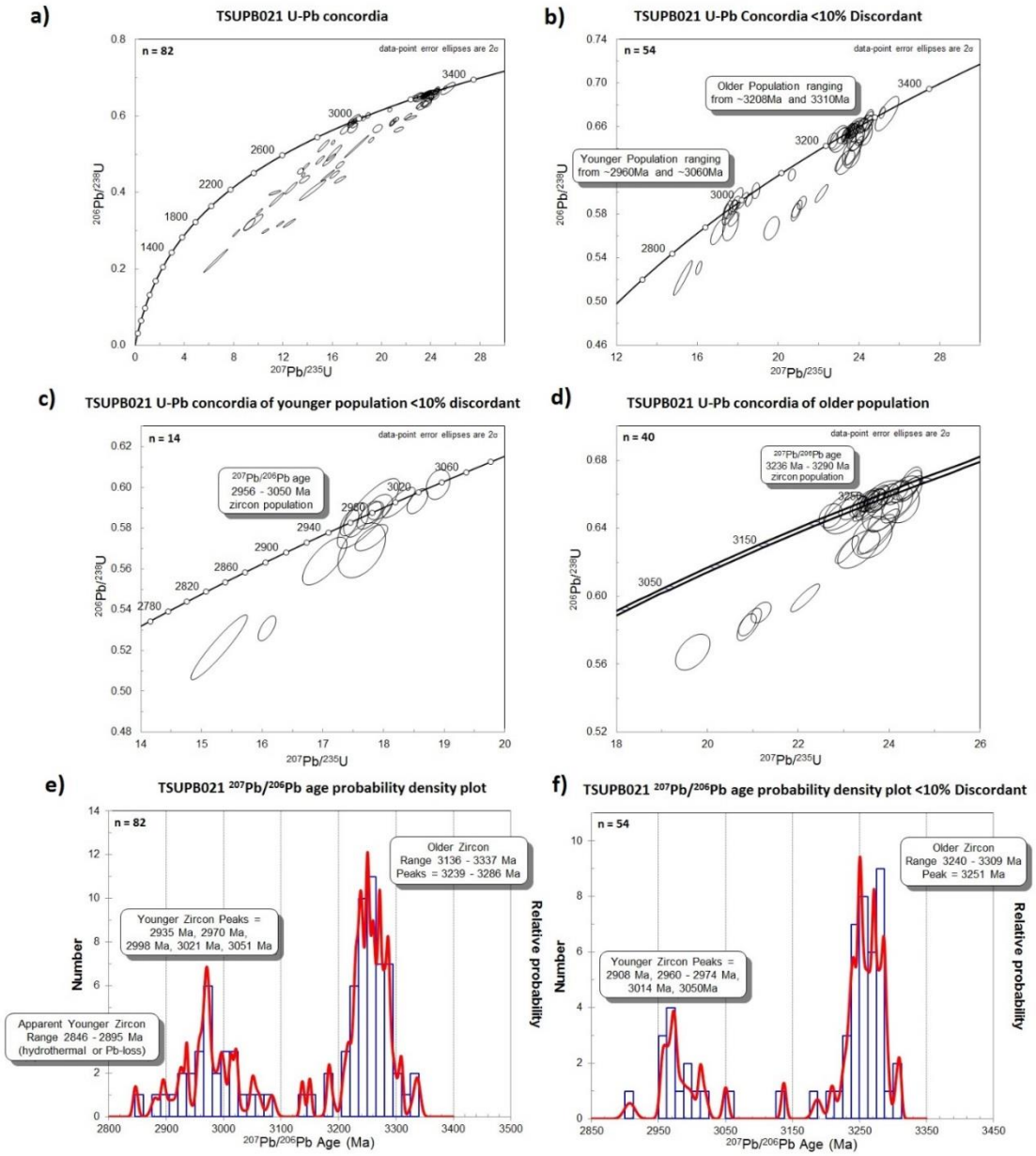


Figure 4.2.13: U-Pb geochronology plots of TSUPB021; a) U-Pb Concordia plot, b) U-Pb Concordia plot of zircons < 10% discordant, c) U-Pb Concordia plot of younger population < 10% discordant, d) U-Pb Concordia plot of older population < 10% discordant, e) $^{207}Pb/^{206}Pb$ age PDP, f) $^{207}Pb/^{206}Pb$ age PDP of zircons < 10% discordant.

portions dissolved from them (Figure 4.2.14). A number of zircons were dissolved completely during the process. Of the remaining zircons, 32 were chosen from TSUPB020, and 64 chosen from TSUPB021. Of these, only one zircon from TSUPB020, and two from TSUPB021 were > 10% discordant, highlighting how effective a technique chemical abrasion is at removing discordant grains prior to analysis. The results of TSUPB020CA are very similar to TSUPB020, with $^{207}Pb/^{206}Pb$ age peaks at 2955 Ma, 2990 Ma and 3047 Ma representing the younger detrital zircons, and a range of 3312 – 3170 Ma covering the older population (Figure 4.2.15a,c,e). Likewise with TSUPB021CA, the peaks are 2957 Ma, 2992 Ma, and 3055 Ma in the younger detrital zircons, and

a range of 3312 – 3209 Ma covering the older population (Figure 4.2.15b,d,f). When compared directly, the $^{207}Pb/^{206}Pb$ age PDP peaks of TSUPB020 and TSUPB020CA match well (Figure 4.2.16a,b). The CA peaks are more defined, with less scatter, and all young ages from TSUPB020 are absent from TSUPB020CA showing that these were from the most damaged zircon grains, and were likely an effect of Pb-loss and not a young population. The one difference in the data is that the chemically abraded population places a larger emphasis on a peak at 3170 Ma, to the younger end of the older population. This is possibly due to the relatively small sample size of 34 for a detrital sample. The $^{207}Pb/^{206}Pb$ age PDP peaks of TSUPB021 and TSUPB021CA match very well, with the only differences being that the very young ages removed, and the peaks being more defined (Figure 4.2.16c,d).

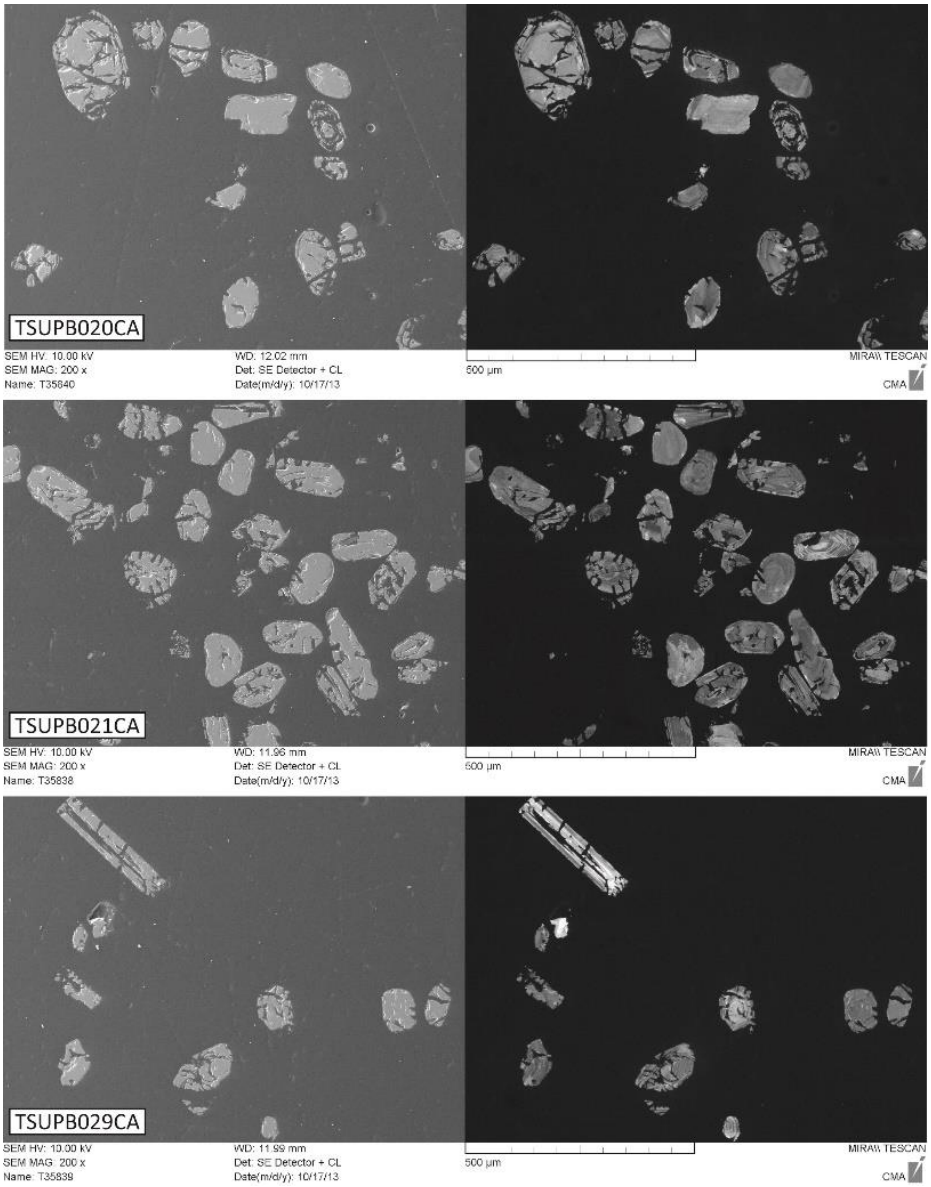


Figure 4.2.14: CL images of chemically abraded zircons.

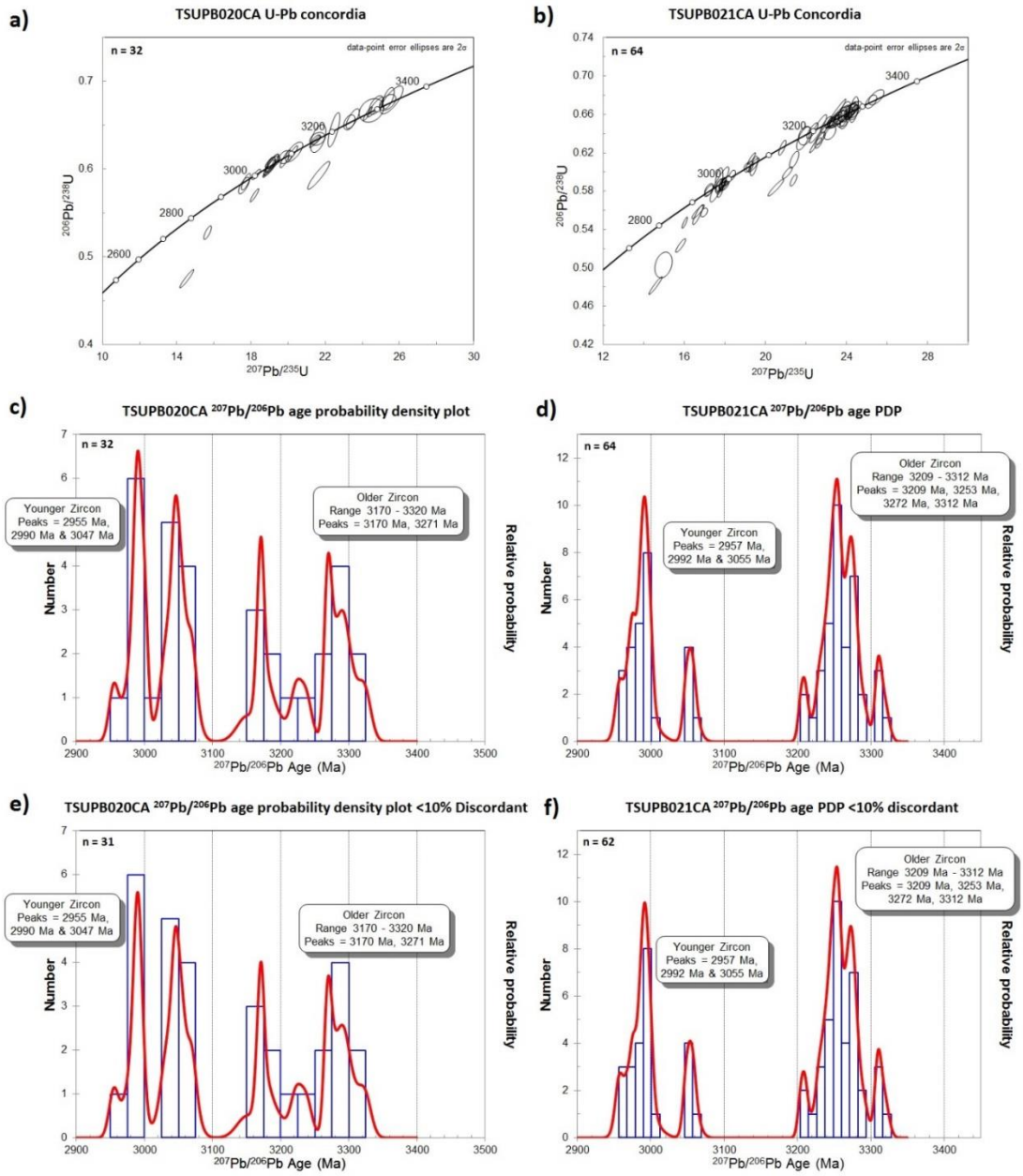


Figure 4.2.15: U-Pb geochronology plots of TSUPB020CA and TSUPB021CA; a) U-Pb Concordia plot of TSUPB020CA, b) U-Pb Concordia plot TSUPB021CA, c) $^{207}Pb/^{206}Pb$ age PDP of TSUPB020CA, d) $^{207}Pb/^{206}Pb$ age PDP of TSUPB021CA, e) $^{207}Pb/^{206}Pb$ age PDP of TSUPB020CA <10% discordant, f) $^{207}Pb/^{206}Pb$ age PDP of TSUPB021CA < 10% discordant.

Due to the greater definition of the $^{207}Pb/^{206}Pb$ age PDP peaks of the chemically abraded samples, with no apparent bias in sampling other than possibly in the older population of TSUPB020, these are the results that will be used to interpret the greywackes from West Branch. The first observation is that the two samples have a very similar distribution of detrital zircons, and although sampled from either side of the Tasiast Thrust, most likely represent the same stratigraphy. There is evidently a large range of lithologies being sourced for these rocks, with an older terrane likely being the source for the zircons < 3170 Ma. The younger zircons, between

2955 Ma and 3055 Ma in age most likely have a different source, which is probably the stratigraphy of the Aouéouat greenstone belt itself. The range of sources suggests that the sedimentary rocks from West Branch probably had a more distal source region than those of C6.7.

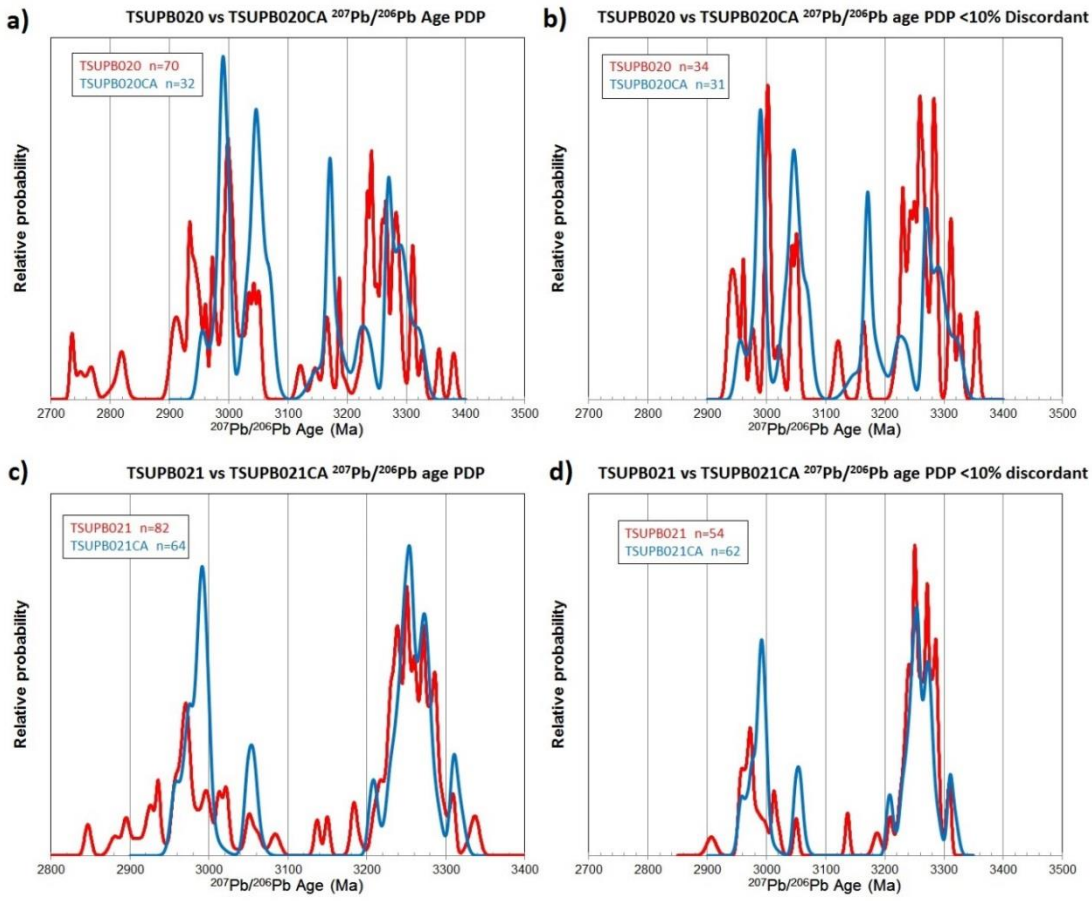


Figure 4.2.16: Comparison of $^{207}Pb/^{206}Pb$ age PDPs between untreated and chemically abraded samples of TSUPB020 and TSUPB021 ; a) TSUPB020 vs TSUPB020CA, b) TSUPB020 vs TSUPB020CA of zircons < 10% discordant, c) TSUPB021 vs TSUPB021CA, d) TSUPB021 vs TSUPB021CA of zircons < 10% discordant.

4.2.4. TTG rocks:

Six TTG rock samples were chosen for U-Pb geochronology. Of these, the two collected as part of the Aouéouat assemblage have already been described above. Three of the remaining samples are surface samples collected from TTG plutons surrounding the Aouéouat greenstone belt, and the fourth is of TTG clasts contained in a conglomerate from the base of the Tasiast Assemblage.

TSUPB012 was sampled from the granodiorite pluton adjacent to the east side of the Aouéouat greenstone belt and yielded ample zircon. CL-images show all of these zircons have oscillatory zoning, and an original euhedral crystal morphology (Figure 4.2.17). Thirty-nine analyses were carried out on this sample, 7 of which are < 10% discordant, and all of the analyses appear to

belong to one zircon population (Figure 4.2.18a). An upper-intercept age of 2967 ± 11 Ma was calculated using all analyses (Figure 4.2.18b), and of 2979 ± 10 Ma using only the analyses < 10% discordant (Figure 4.2.18c). A $^{207}Pb/^{206}Pb$ age MWA plot of only the analyses < 10% discordant gives an age of 2968.9 ± 8.5 Ma (Figure 4.2.18d). Although all of these ages are within error, there is a 12 Ma difference between them. The preferred age for this sample is 2967 ± 11 Ma, as although it has the largest MSWD, it uses all of the analyses, which appear to be from a single population, and is almost identical to the $^{207}Pb/^{206}Pb$ age MWA plot of analyses < 10% discordant. This is interpreted to be the crystallisation age of the rock.

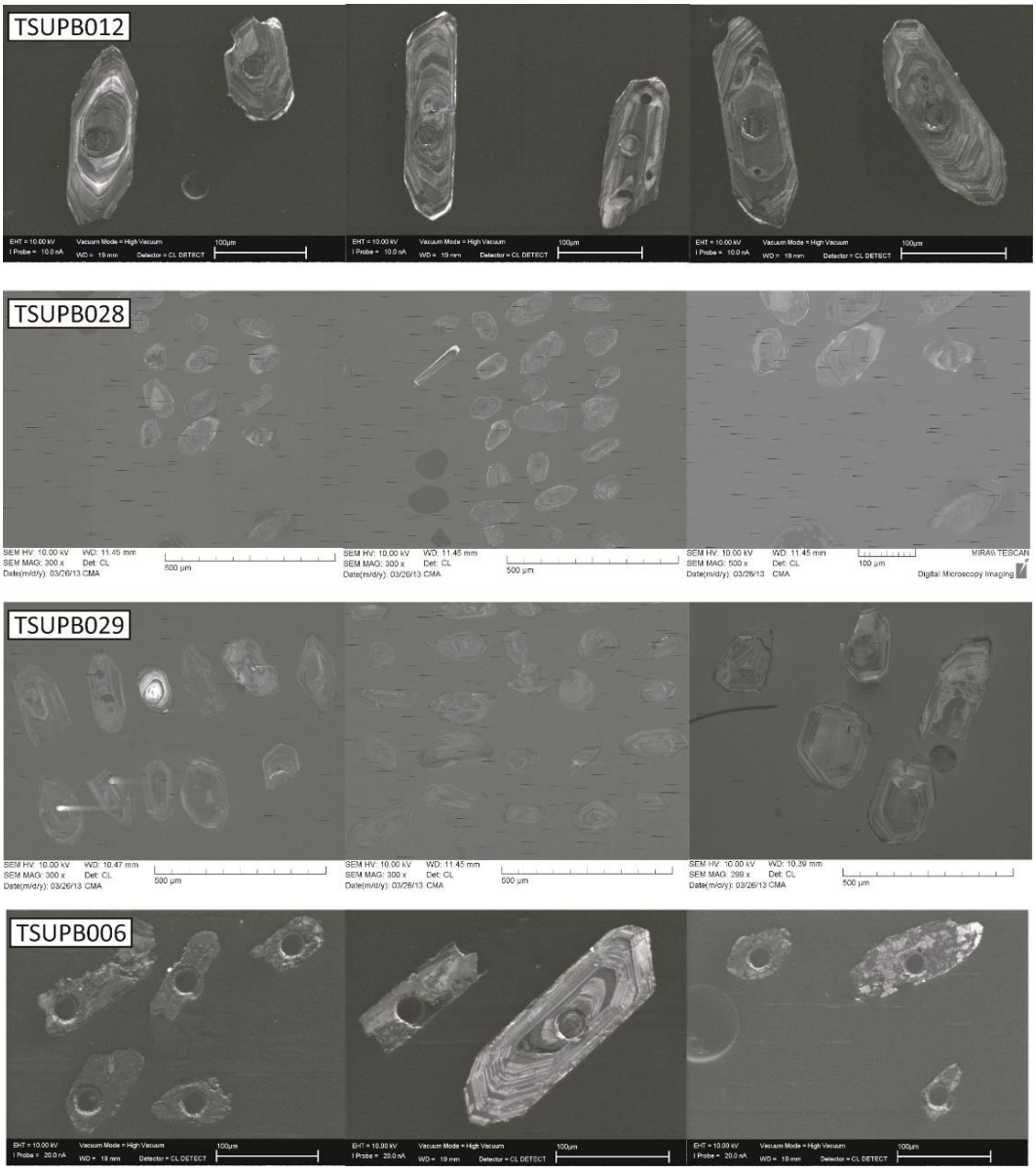


Figure 4.2.17: CL images of representative zircons from TTG rocks and pegmatite.

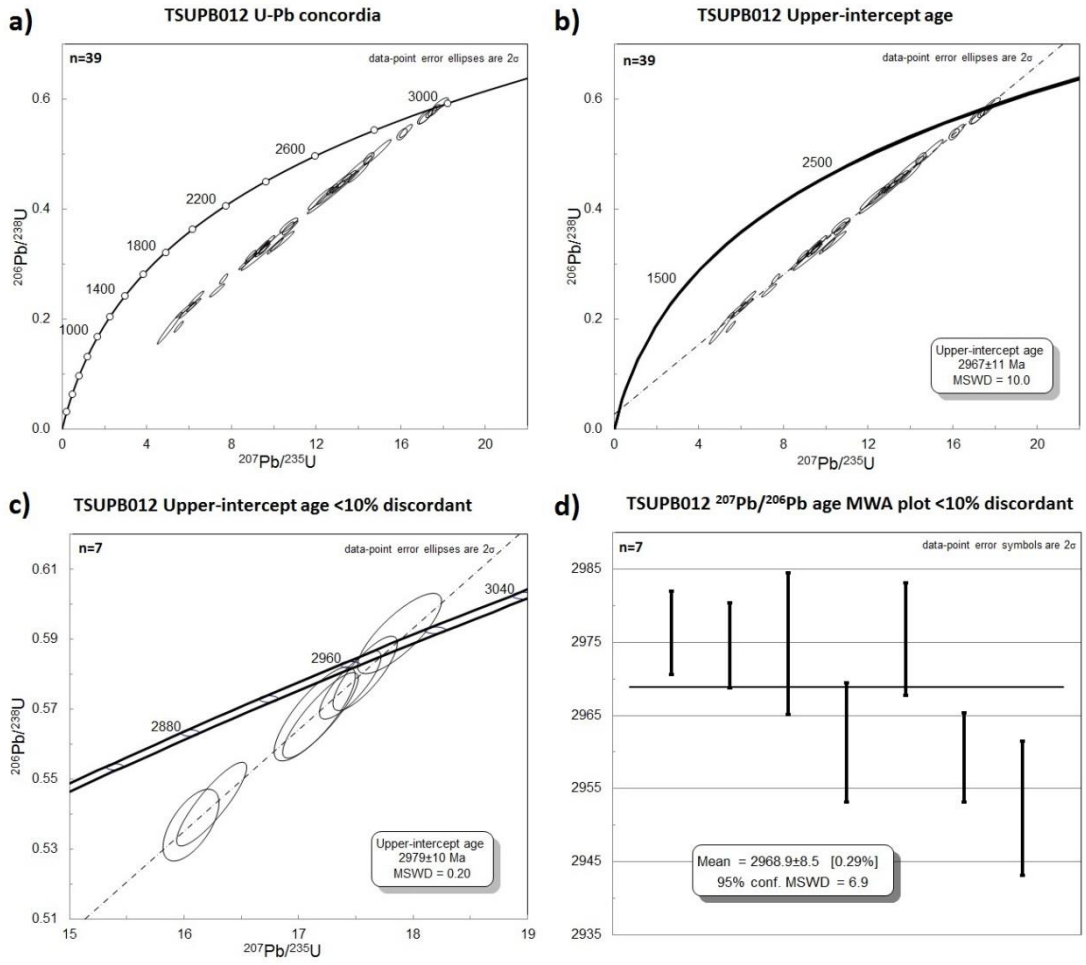


Figure 4.2.18: U-Pb geochronology plots of TSUPB012; a) U-Pb Concordia plot, b) Upper-intercept plot, c) upper-intercept plot of zircons < 10% discordant, d) $^{207}Pb/^{206}Pb$ age MWA plot of zircons < 10% discordant.

TSUPB028 and TSUPB029 were sampled from east of the Aouéouat greenstone belt, and west of the Imkebdene greenstone belt respectively. These samples were initially planned to represent the orthogneissic basement to the east and west of the Aouéouat greenstone belt and the surrounding TTG plutons. On reaching the extremities of accessible outcrop, it became apparent that the exposed rocks were almost certainly still TTG plutons. To give the greatest possible chance of sampling a rock representative of the basement, these two samples were taken from slab shaped xenoliths from within TTG plutons, leaving the possibility that these were xenoliths of basement rock encompassed within the TTG plutons.

TSUPB028 returned a yield of 32 zircons, only 10 of which provided usable data. CL-images show the zircon to all be oscillatory zoned, and sub-rounded in nature (Figure 4.2.17). Only four of the analyses are < 10% discordant, and the small zircon yield and scatter of the data make it difficult to get an accurate age for this rock (Figure 4.2.19a). An upper-intercept age of 2945 ± 49 Ma is calculated when using all analyses (Figure 4.2.19b), however when removing any outliers a younger age of 2896 ± 10 Ma is calculated. A $^{207}Pb/^{206}Pb$ age MWA plot of all analyses bar one

gives an age of 2933 ± 9 Ma, with the one relatively young $^{207}Pb/^{206}Pb$ age being 2830 Ma (Figure 4.2.19c). A $^{207}Pb/^{206}Pb$ age MWA plot of only the analyses < 10% discordant gives an age of 2943 ± 9.7 Ma, with an MSWD of 1.3 (Figure 4.2.19d). The younger age could be due to Pb-loss; however it could also possibly be due to a hydrothermal event, which may be affecting the other zircons in the sample. The preferred age for this sample is the one calculated from the $^{207}Pb/^{206}Pb$ ages < 10% discordant, of 2943 ± 9.7 Ma.

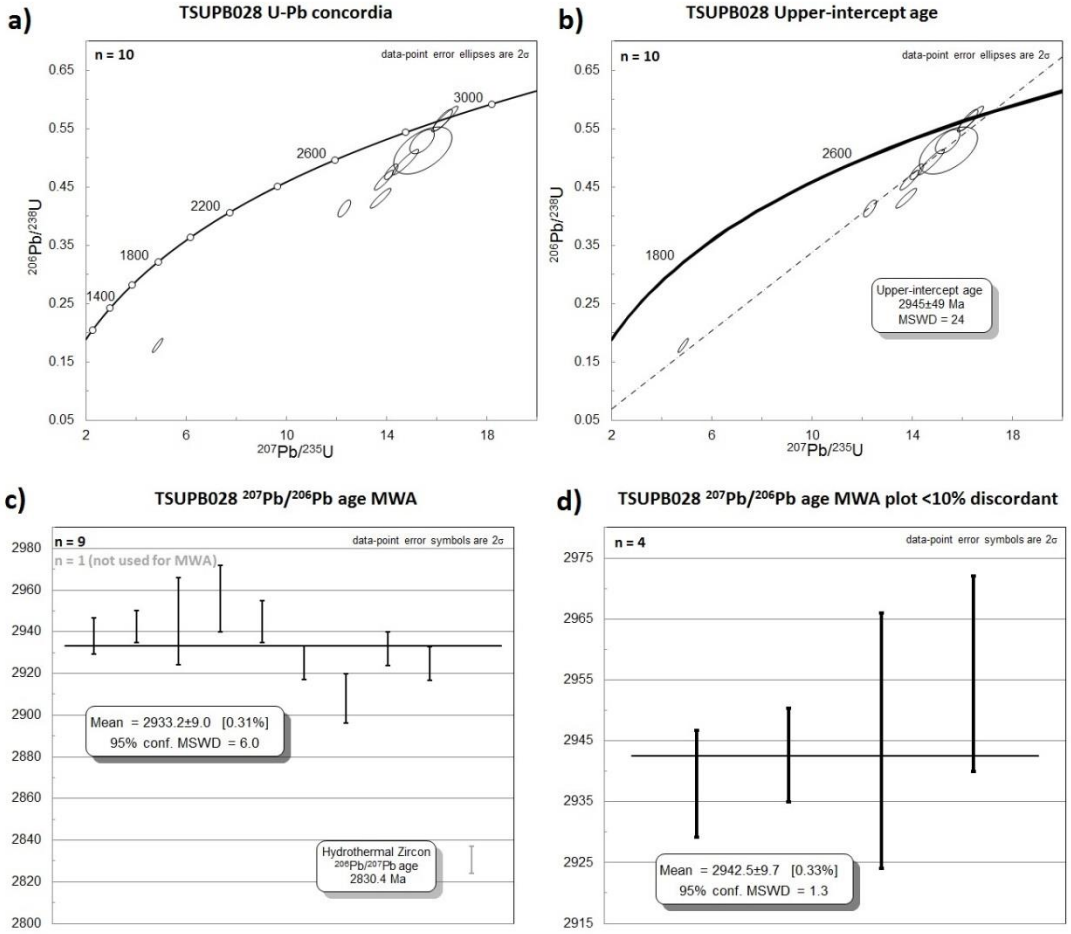


Figure 4.2.19: U-Pb geochronology plots of TSUPB028; a) U-Pb Concordia plot, b) upper-intercept plot, c) $^{207}Pb/^{206}Pb$ age MWA plot, d) $^{207}Pb/^{206}Pb$ age MWA plot of zircons < 10% discordant.

TSUPB029 yielded ample zircon, 84 of which were chosen for analysis. CL-images show that most of the zircons exhibit oscillatory zoning (Figure 4.2.17), however a number are either metamict, or contain metamict zones within them. Of the 84 analyses, a large number contain very large errors, and show strong signs of Pb-loss and common-Pb (Figure 4.2.20a). 21 of the analyses are < 10% discordant, and range in age from ~2800 Ma to ~3050 Ma (Figure 4.2.20c). The younger age population of these gives a Concordia age of 2830 ± 14 Ma (Figure 4.2.20d), and by taking only the analyses from this age population with a low error (< 0.4 $^{207}Pb/^{235}U$ 2SE) irrespective of discordance, an upper-intercept age of 2831 ± 18 Ma is calculated (Figure 4.2.20b). Due to the

large range of ages, as well as the effects of Pb-loss and common-Pb, the data from TSUPB029 is also presented on PDPs (Figure 4.2.20e,f). From these we can see that the same profile is present in both plots, with the difference being that by taking only the analyses < 10% discordant the youngest ages, which are an effect of Pb-loss are removed, as are the oldest ages, which are an effect of common-Pb. Both plots have the same highest peak at 2932 Ma and 2933 Ma. The younger range from 2857 – 2823 Ma is representative of the ages calculated as above for this population, and the older range, from 3046 – 2983 could either be an older population, or could be an artefact of elevated common-Pb.

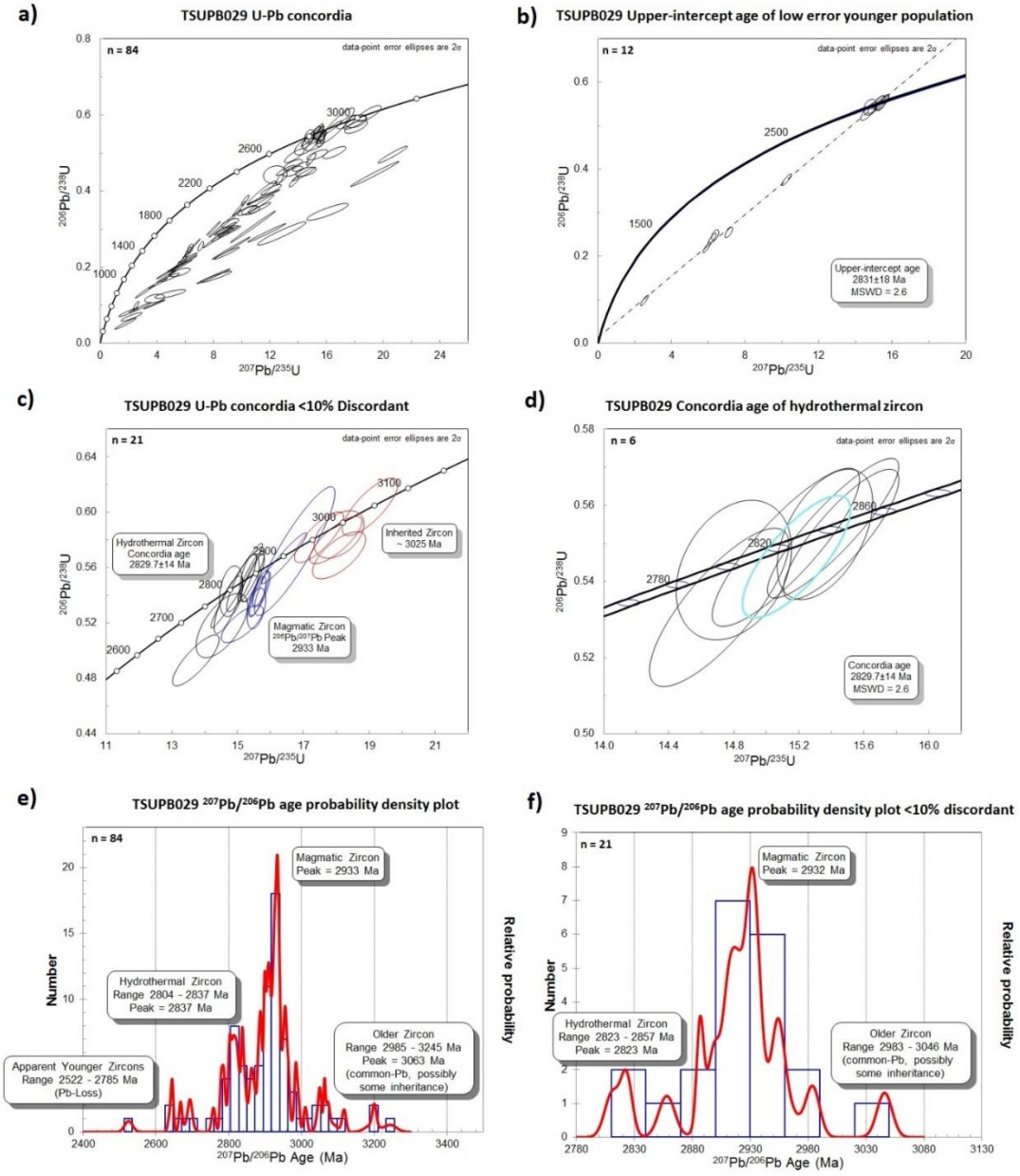


Figure 4.2.20: U-Pb geochronology plots of TSUPB029; a) U-Pb Concordia plot, b) upper-intercept plot of low-error young population, c) U-Pb Concordia plot of zircons < 10% discordant, d) U-Pb Concordia age of young population, e) $^{207}Pb/^{206}Pb$ age PDP, f) $^{207}Pb/^{206}Pb$ age PDP of zircons < 10% discordant.

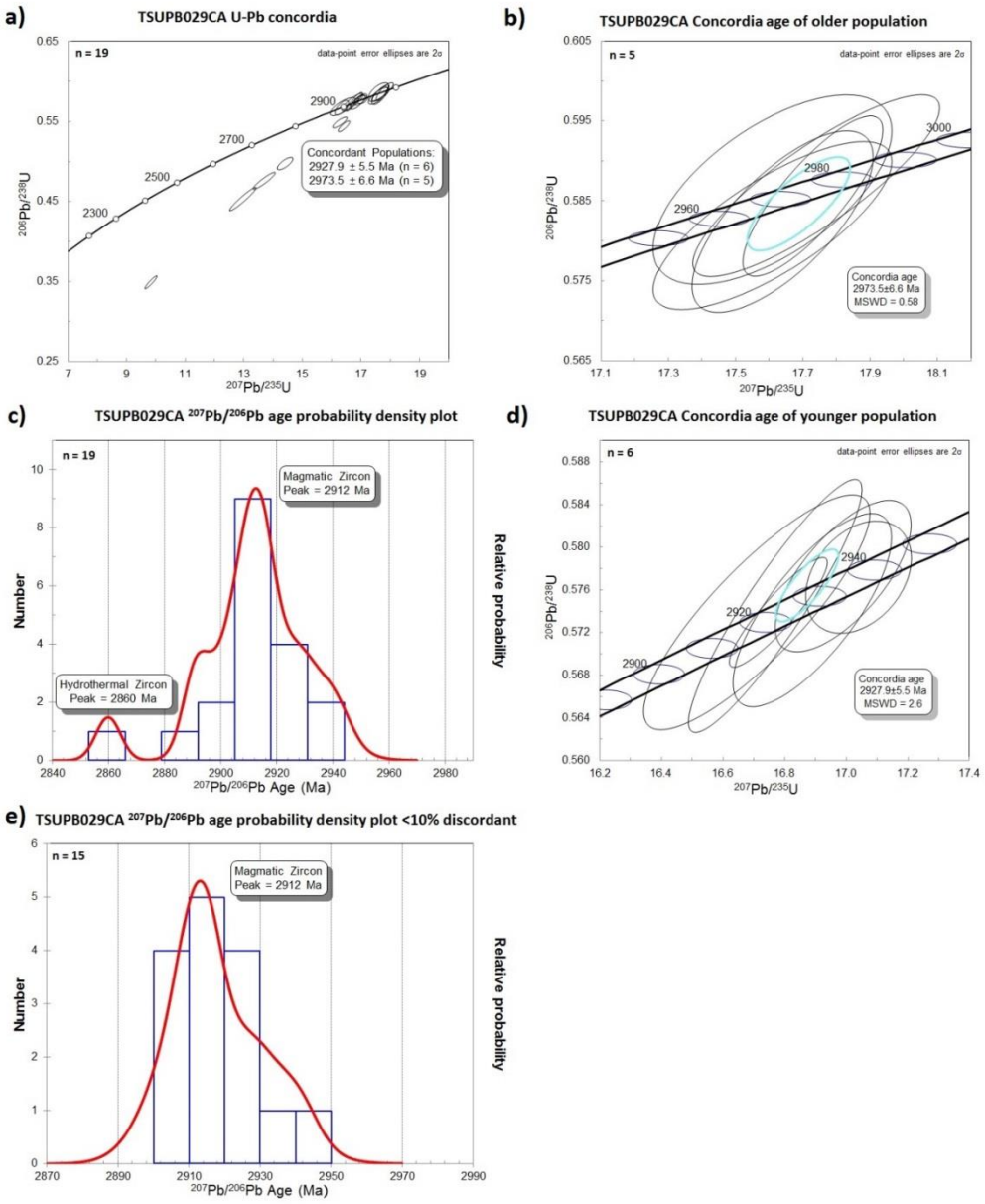


Figure 4.2.21: U-Pb geochronology plots of TSUPB029CA; a) U-Pb Concordia plot of TSUPB029CA, b) U-Pb Concordia age of older population, c) $^{207}Pb/^{206}Pb$ age PDP, d) U-Pb Concordia age of younger population, e) $^{207}Pb/^{206}Pb$ age PDP of zircons <10% discordant.

Due to the ample yield of zircon recovered from TSUPB029, as well as the apparent multiple age populations, strong Pb-loss, and common-Pb effects, this sample was also chosen to test Chemical Abrasion prior to LA-ICP-MS analysis. A large proportion (~75%) of the sample which was treated by Chemical Abrasion was completely dissolved, and it is clear from the CL-images of TSUPB029CA that all of the zircons were dissolved to some degree (Figure 4.2.14). This left very few zircons suitable for analysis; however it was possible to complete 19 analyses on the remaining zircons. Of the 19 analyses, 15 are < 10% discordant (Figure 4.2.21a). Five of these allow a Concordia age of 2974 ± 6.6 Ma to be calculated (Figure 4.2.21b), and six allow a Concordia age of 2928 ± 5.5 Ma to be calculated (Figure 4.2.21d). PDPs both show a $^{207}Pb/^{206}Pb$ age peak at 2912 Ma, with the 4

zircons that are > 10% discordant being the youngest four (Figure 4.2.21c,e). The youngest of these, with a $^{207}Pb/^{206}Pb$ age of 2860 Ma is close to the age of the young population in the untreated sample. When compared directly, the main $^{207}Pb/^{206}Pb$ age PDP peaks of TSUPB029 and TSUPB029CA match fairly well, although TSUPB029CA gives an age ~20 Ma younger (Figure 4.2.22a,b). It is clear however that almost all of the younger and older analyses are missing from TSUPB029CA having been removed during Chemical Abrasion.

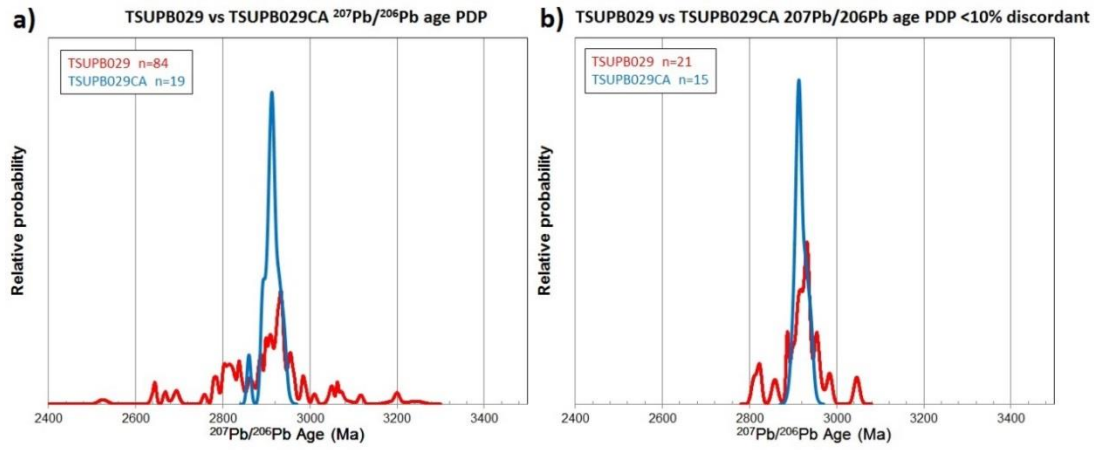


Figure 4.2.22: Comparison of $^{207}Pb/^{206}Pb$ age PDPs between untreated and chemically abraded samples of TSUPB029; a) TSUPB029 vs TSUPB029CA, b) TSUPB029 vs TSUPB029CA of zircons < 10% discordant.

TSUPB029 shows some of the problems when applying Chemical Abrasion to zircons before LA-ICP-MS analysis, but also some of the benefits. Chemical Abrasion has succeeded in removing all of the zircons that have been affected by Pb-loss and Common-Pb; however in this instance it appears to have also removed a real younger population of zircons almost entirely. This is almost certainly not an artefact of sample bias, as < 100 zircons were chemically abraded before analysis. Something that appears to have resulted from the chemical abrasion though is that two older concordant populations are now discernible that were not evident in the pre-treatment population. This shows the benefit of combining both untreated as well as Chemically Abraded zircons when analysing complex samples. Therefore by using the combined data, the interpretation is that TSUPB029 has a crystallisation age of 2928 ± 5.5 Ma, with an older inherited population of 2974 ± 6.6 Ma. The rock has since undergone some form of alteration event at 2830 ± 14 Ma that has fully re-set some zircons, and has possibly caused some of the extreme Pb-loss and elevated common-Pb seen in the sample. However it is possible that the Pb-loss and elevated common-Pb could also be due to recent surface weathering effects.

TSUPB030 consists of a conglomerate, or mylonite which contains a number of TTG clasts within it. Due to the small size of these, and likelihood of losing a large percentage of them through rock crushing and sample processing, six thin sections were taken through the largest of the clasts. These were carefully searched for zircons to be analysed by in-situ LA-ICP-MS. Two zircons were found, only one of which was large enough to be ablated (Figure 4.2.23a,b). Two analyses were carried out on the zircon (Figure 4.2.24a). These give a $^{207}Pb/^{206}Pb$ age MWA of 3059 ± 32 Ma (Figure 4.2.24b), which is interpreted to be the crystallisation age of the TTG rock which sourced the clasts at the base of the Tasiast assemblage.

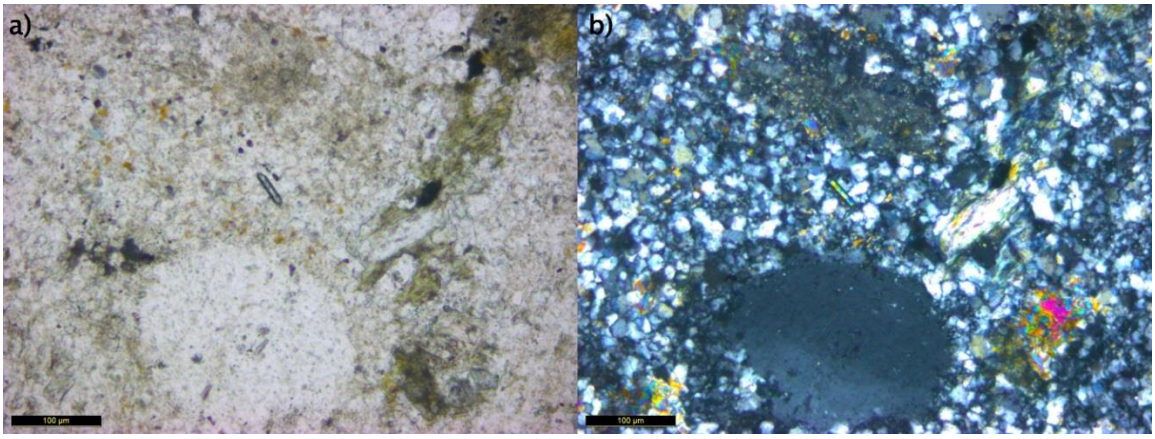


Figure 4.2.23: Thin section photomicrograph of zircon in TSUPB030; a) PPL, b) XPL.

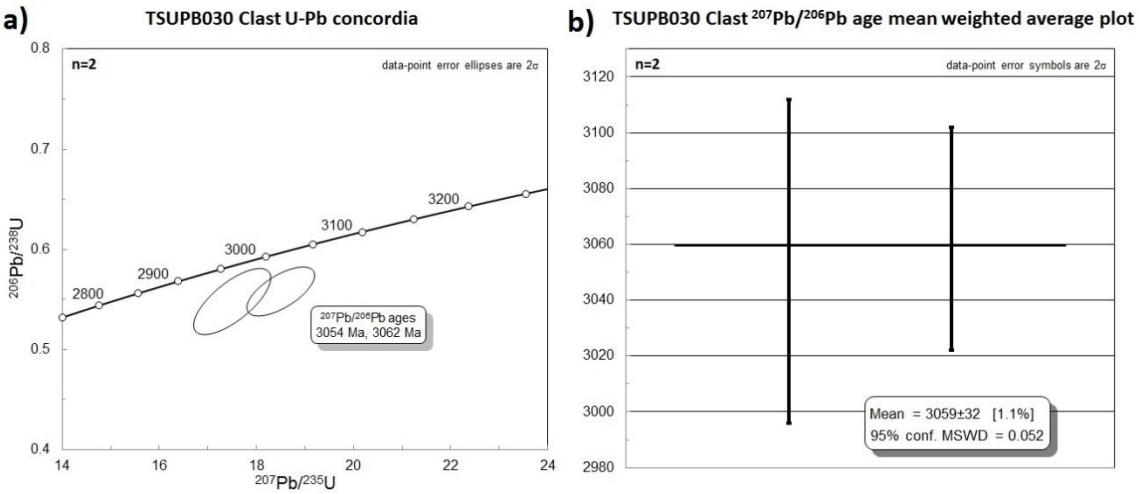


Figure 4.2.24: U-Pb geochronology plots of TSUPB030; a) U-Pb Concordia plot, b) $^{207}Pb/^{206}Pb$ age MWA plot.

4.2.5. Banded iron formation:

Seeing as petrographic analysis of two BIF samples revealed that they contain a significant detrital component, these were targeted with the aim of constraining the deposition age of the BIF deposits in the Aouéouat greenstone belt. FZ-12-02 was chosen to be processed for U-Pb zircon

geochronology due to the abundance of detrital material within this sample. This left the possibility that some of the detrital material may have been sourced from a local volcanic eruption, which if containing zircons would place a fairly tight constraint on the deposition of the BIF. Unfortunately no zircons were recovered from this sample, leaving the BIF units undated.

4.2.6. Pegmatite:

The late pegmatite, which cross-cuts the Aouéouat greenstone belt and surrounding plutons, was processed for U-Pb zircon geochronology. This sample yielded 44 zircons, 34 of which gave usable data. CL-images show that the zircons display their original crystal shape, however only a few exhibit oscillatory zoning (Figure 4.2.17). Most of the zircons are completely metamict and dark with no zoning present at all. This suggests that they likely have high U contents, which was confirmed by analysis, with an average U value of 5316ppm for 34 analyses. Due to the poor quality of the zircons, the analyses have very large errors, and almost all show strong Pb-loss effects (Figure 4.2.25a). It was however possible to plot an upper-intercept line through all of the analyses, which gives an age of 2766 ± 31 Ma (Figure 4.2.25b). Although the error is quite large, the pegmatite is clearly younger than any of the other stratigraphy in the Aouéouat greenstone belt or surrounding TTG rocks, with the age of pegmatite formation interpreted to be 2766 ± 31 Ma.

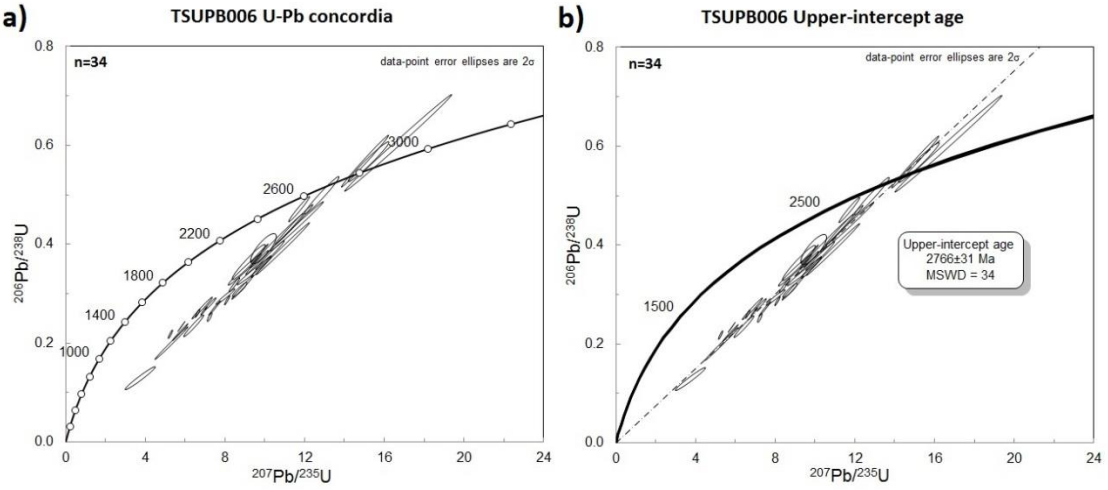


Figure 4.2.25: U-Pb geochronology plots of TSUPB006; a) U-Pb Concordia plot, b) upper-intercept plot.

4.2.7. Quartz-carbonate veins:

In the Aouéouat greenstone belt the quartz-carbonate veins host the gold mineralisation. Samples of this lithology were therefore taken from four vein systems in four different targets. Three of

these vein systems carry gold; C6.7, Fennec and West Branch, while C6.12 is barren of gold. The aim of sampling these veins was primarily to date the age of gold mineralisation, while also attempting to test if there is a temporal difference between gold bearing veins and veins barren of gold.

TSUPB015 was sampled from C6.7 and yielded 43 zircons. CL-images of the zircons show oscillatory zoning in most indicating they are igneous in nature, with metamict cores present in some (Figure 4.2.26). The zircons are therefore almost certainly xenocrystic. A number of zircons possess an extremely thin (<10 µm) overgrowth seen by the dark CL rim surrounding the zircon on all sides, interpreted as hydrothermal in origin. Of the 43 zircon analyses, 15 were <10 % discordant (Figure 4.2.27a,b). Concordia ages of populations aged 3037 ± 29 Ma and 2946 ± 26 Ma were calculated (Figure 4.2.27c,d). A further two analyses overlapping with Concordia were obtained from this sample, with Concordia ages of 2819 ± 19 and 2695 ± 18 Ma, the latter of which is attributed to Pb-loss. The two concordant populations of 3037 ± 29 Ma and 2946 ± 26 Ma are interpreted to be inherited zircons sourced from rocks which the quartz veins have passed through. The concordant analysis at 2819 ± 19 is possibly a hydrothermal age associated with the quartz vein.

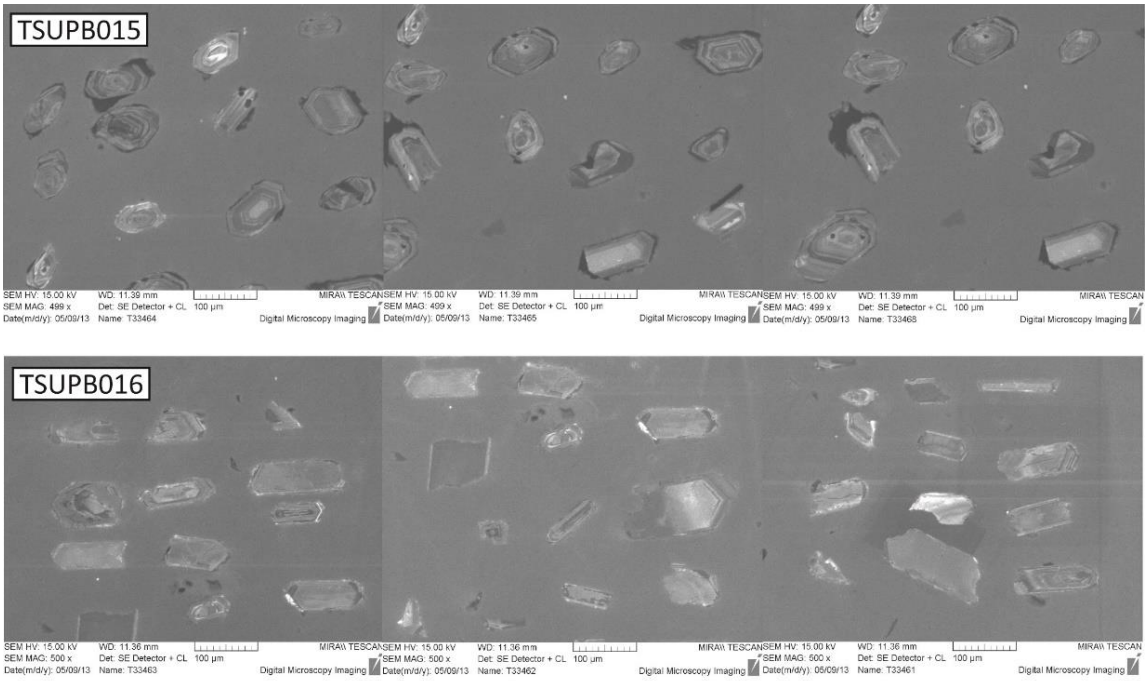


Figure 4.2.26: CL images of representative zircons from quartz-carbonate veins (TSUPB015, TSUPB016).

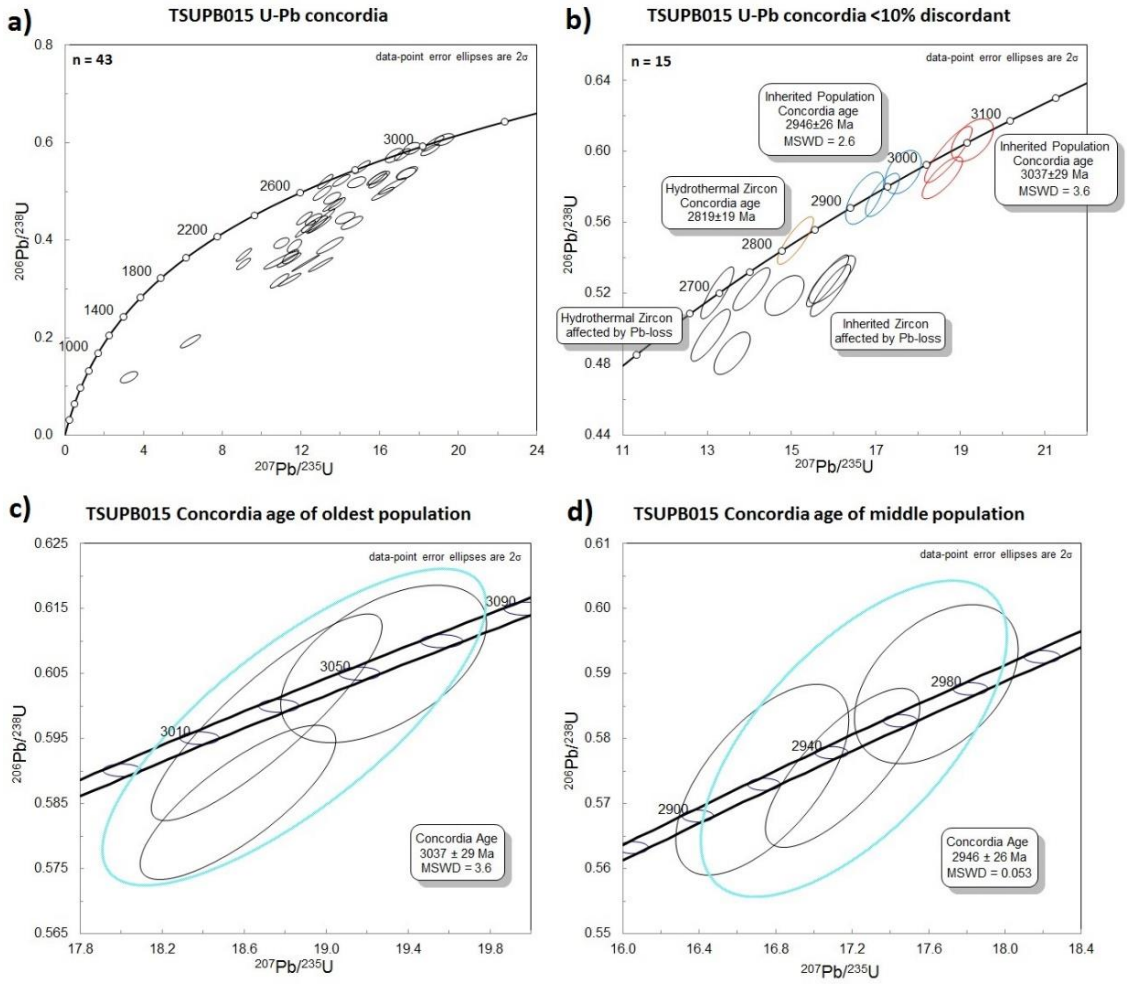


Figure 4.2.27: U-Pb geochronology plots of TSUPB015; a) U-Pb Concordia plot, b) U-Pb Concordia plot of zircons < 10% discordant, c) Concordia age of oldest population, d) Concordia age of middle population.

TSUPB016 is a quartz-carbonate vein devoid of gold from C6.12 and yielded 48 zircons. CL-images show oscillatory zoning again with some metamict cores indicating these too are xenocrystic, however none show evidence of hydrothermal overgrowths (Figure 4.2.26). This is confirmed by the U-Pb data, with the 14 analyses <10 % discordant containing one concordant population at 2953 ± 11 Ma (Figure 4.2.28a,b,e), and a total range of $^{207}Pb/^{206}Pb$ ages of 3060 – 2943 Ma (Figure 4.2.28f). There are also possibly two other populations present, calculated by upper-intercept ages of 3054 ± 53 Ma and 2993 ± 20 Ma (Figure 4.2.28c,d). The interpretation of this sample is that it contains inherited zircons, sourced from rocks which are between 3060 and 2943 Ma in age, suggesting the quartz veins have passed through rocks of this age before crystallisation.

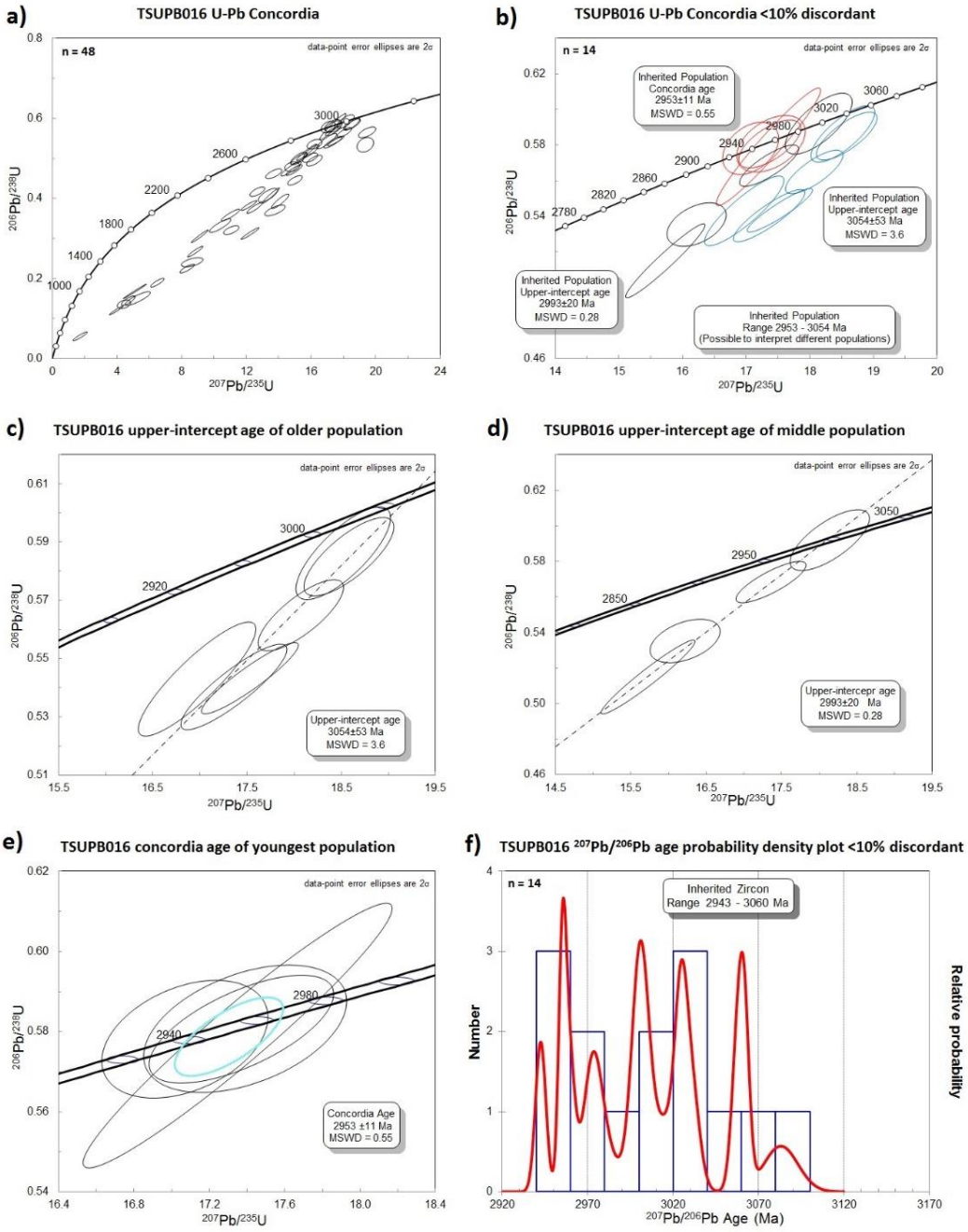


Figure 4.2.28: U-Pb geochronology plots of TSUPB016; a) U-Pb Concordia plot, b) U-Pb Concordia plot of zircons < 10% discordant, c) upper-intercept plot of older population, d) upper-intercept plot of middle population, e) Concordia age of youngest population, f) $^{207}Pb/^{206}Pb$ age PDP of zircons < 10% discordant.

TSUPB027 was sampled from an exploration trench in Fennec, returning a rock chip assay of 317 g/t gold, and was therefore prioritised for U-Pb zircon analysis. This sample however yielded no zircon (although a small volume of gold was recovered from the heavy mineral fraction (Appendix 4)), and so a secondary quartz-vein sampled from the same exploration trench in Fennec, TSUPB026, was processed, yielding ample zircon. CL-images show igneous zircon with oscillatory zoning, some with more complex zoning, and a number possessing cores, suggesting they are xenocrystic (Figure 4.2.29). All zircons from this sample had an obvious, generally <10 µ thick,

overgrowth which is interpreted as hydrothermal in origin, of which an initial set of 104 were analysed (Figure 4.2.30a). Analysis of the interior parts of these zircons produced and age population with an upper-intercept age of 2950 ± 11 Ma (Figure 4.2.30b), with six zircons < 10% discordant giving an upper intercept age of 2958 Ma ± 14 Ma (Figure 4.2.30c). A Concordia age of 2963 ± 10 Ma (Figure 4.2.30d) and the peak in $^{207}Pb/^{206}Pb$ ages < 10% discordant of 2961 Ma are both almost identical to the upper intercept age of zircons < 10% discordant, but with a larger MSWD, and therefore the preferred age of the xenocrystic zircons is 2958 Ma ± 14 Ma.

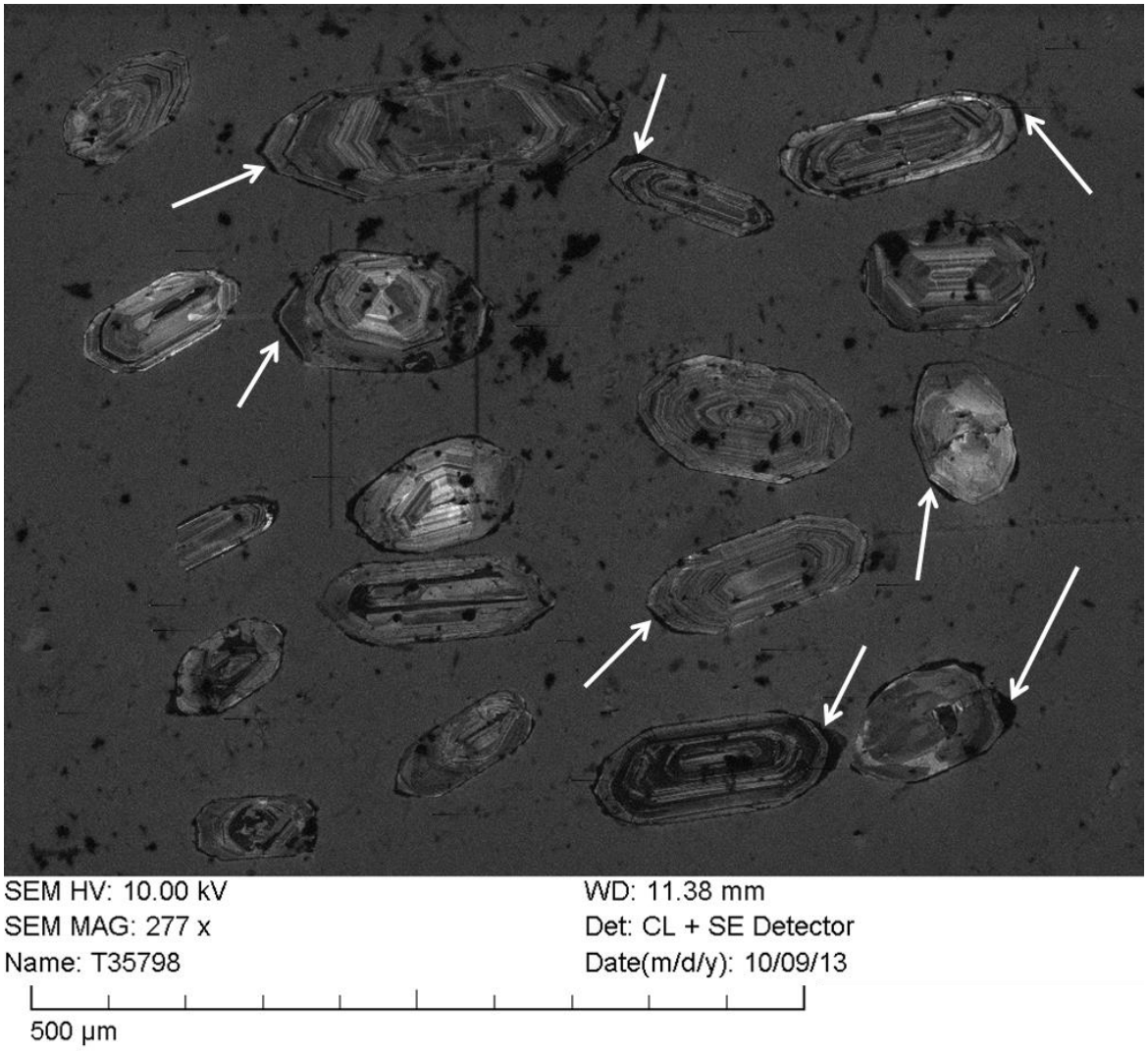


Figure 4.2.29: CL images of TSUPB026 highlighting hydrothermal overgrowths.

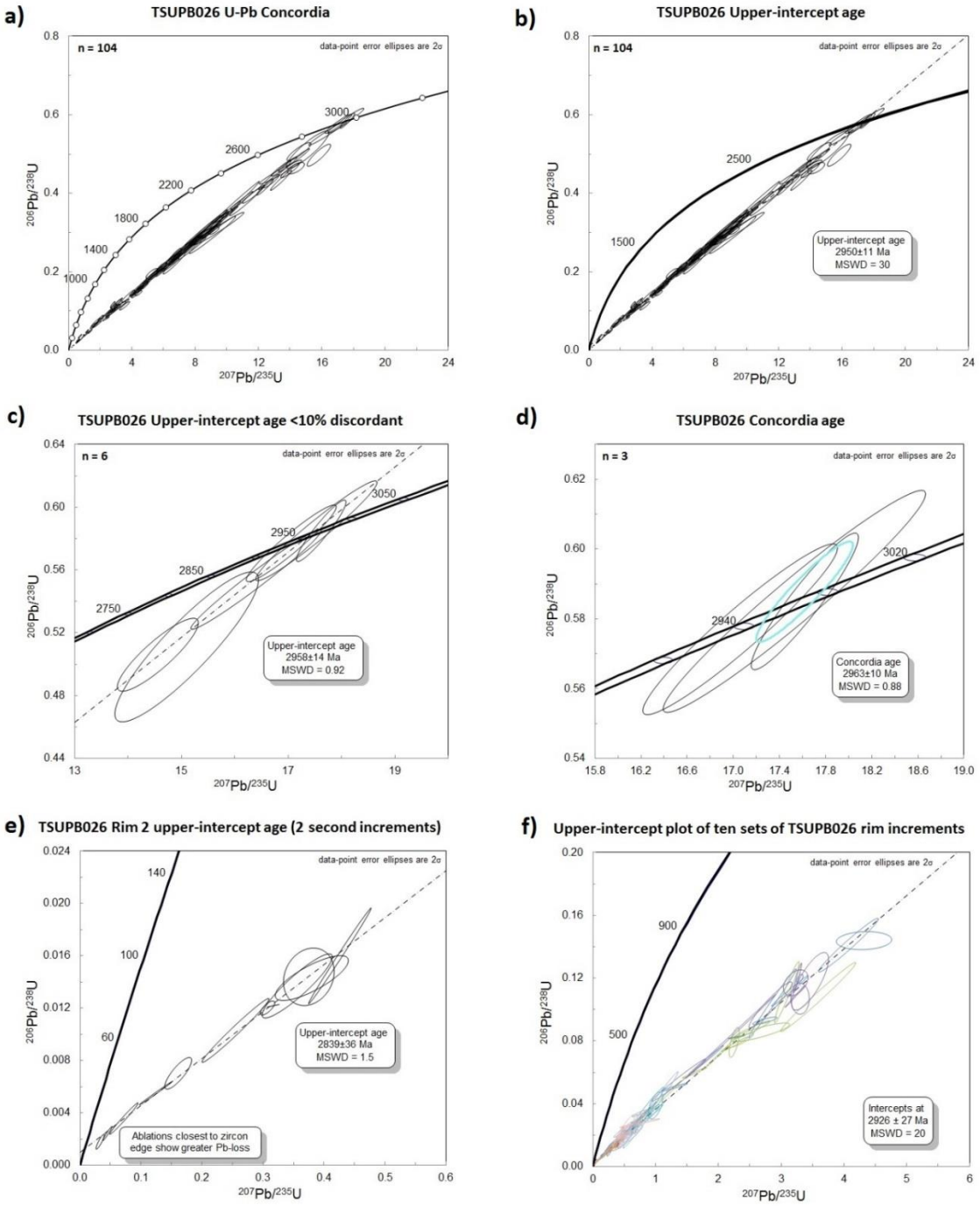


Figure 4.2.30: U-Pb geochronology plots of TSUPB026; a) U-Pb Concordia plot, b) upper-intercept plot c) upper-intercept plot of zircons < 10% discordant, d) Concordia age, e) $^{207}Pb/^{206}Pb$ age PDP of zircons < 10% discordant, f) upper-intercept plot of hydrothermal overgrowth.

Due to the ubiquitous presence of hydrothermal overgrowths on the zircons extracted from this sample, a second set of ten zircons were hand-picked, pre-treated in dilute HNO_3, and mounted directly on double sided sticky tape without polishing. The exterior crystal faces were then ablated in two-second increments in an attempt to sample only the hydrothermal overgrowths. Five of the ten analyses exhibited extreme Pb-loss resulting in errors >140 Ma, which was not unexpected, since the rim of a zircon is the most likely part of a crystal to be affected by Pb-loss

(Krogh, 1982). This can also be seen here as the integrations from closest to the zircon edge show the greater Pb-loss. Three analyses did not produce any meaningful data and one sample gave a similar age to those obtained above, highlighting the lack of an overgrowth. This left one analysis providing usable data. An upper-intercept age of the two-second increments gave an age of 2839 ± 36 Ma (Figure 4.2.30e). It is worth noting that the lower intercept is close to zero and there is no overlap with the Concordia curve, and so no significance is placed on the lower intercept age. Another point worth noting is that when all of the rim increments are included and a Discordia line plotted, the age returned is 2926 ± 27 Ma (Figure 4.2.30f). This is close to the crystallisation ages of the zircon, though slightly younger due to the inclusion of the hydrothermal rims resulting in a slight mixing age being returned.

The interpretation for this sample is that the xenocrystic zircons are all sourced from a rock with an age of 2958 Ma ± 14 Ma. All of these zircons have a hydrothermal overgrowth dated at 2839 ± 36 Ma. This is interpreted to be the age of the quartz-vein forming hydrothermal event.

TSUPB031 and TSUPB032 were both collected from the active gold mine in West Branch. Neither of these however yielded any zircon for dating.

On completion of the U-Pb zircon geochronology, the interpretation of the quartz-veins in the Aouéouat greenstone belt is that the ages between ~3060 and 2945 Ma obtained from three of the quartz veins are interpreted as xenocrystic inherited zircons from neighbouring country rocks, or from deeper unexposed rock, and so provide a window on the ages of rocks present in the Aouéouat stratigraphy. The 2839 ± 36 Ma age obtained from the hydrothermal overgrowth from the Fennec sample is within error of a concordant age obtained from C6.7 (2819 ± 19 Ma). The dated vein is of a known visible gold bearing generation, suggesting this is the mineralisation age of the Tasiast gold deposit.

In an attempt to confirm the hydrothermal age of the quartz-veins, further work was undertaken to separate apatite crystals for U-Pb apatite geochronology. Apatite was recovered from all of the samples described above, and was analysed for all samples other than TSUPB027, for which TSUPB026 is the equivalent rock specimen.

Apatite from TSUPB026 (Fennec) and TSUPB016 (C6.12) both show scatter on Tera-Wasserburg Concordia due to partial resetting of the U-Pb system by post-crystallisation thermal events (Figure 4.2.31a). These data are therefore difficult to interpret in calculating a U-Pb age. TSUPB015 (C6.7) does not show much scatter on a Tera-Wasserburg Concordia allowing the

calculation of a U-Pb lower-intercept age of 2835 ± 190 Ma; however the large age uncertainty is a result of all but three of the apatite crystals containing very low uranium resulting in a low spread of $^{238}U/^{206}Pb$ ratios (Figure 4.2.31b). TSUPB031 (West Branch) shows a large spread in $^{238}U/^{206}Pb$ ratios allowing the calculation of a lower-intercept age of 2793 ± 69 Ma (Figure 4.2.31c). TSUPB032 (West Branch) shows the least scatter on Tera-Wasserburg Concordia as well as the greatest spread in $^{238}U/^{206}Pb$ ratios resulting in it having the lowest error lower-intercept age of the three samples, which is 2853 ± 41 Ma (Figure 4.2.31d).

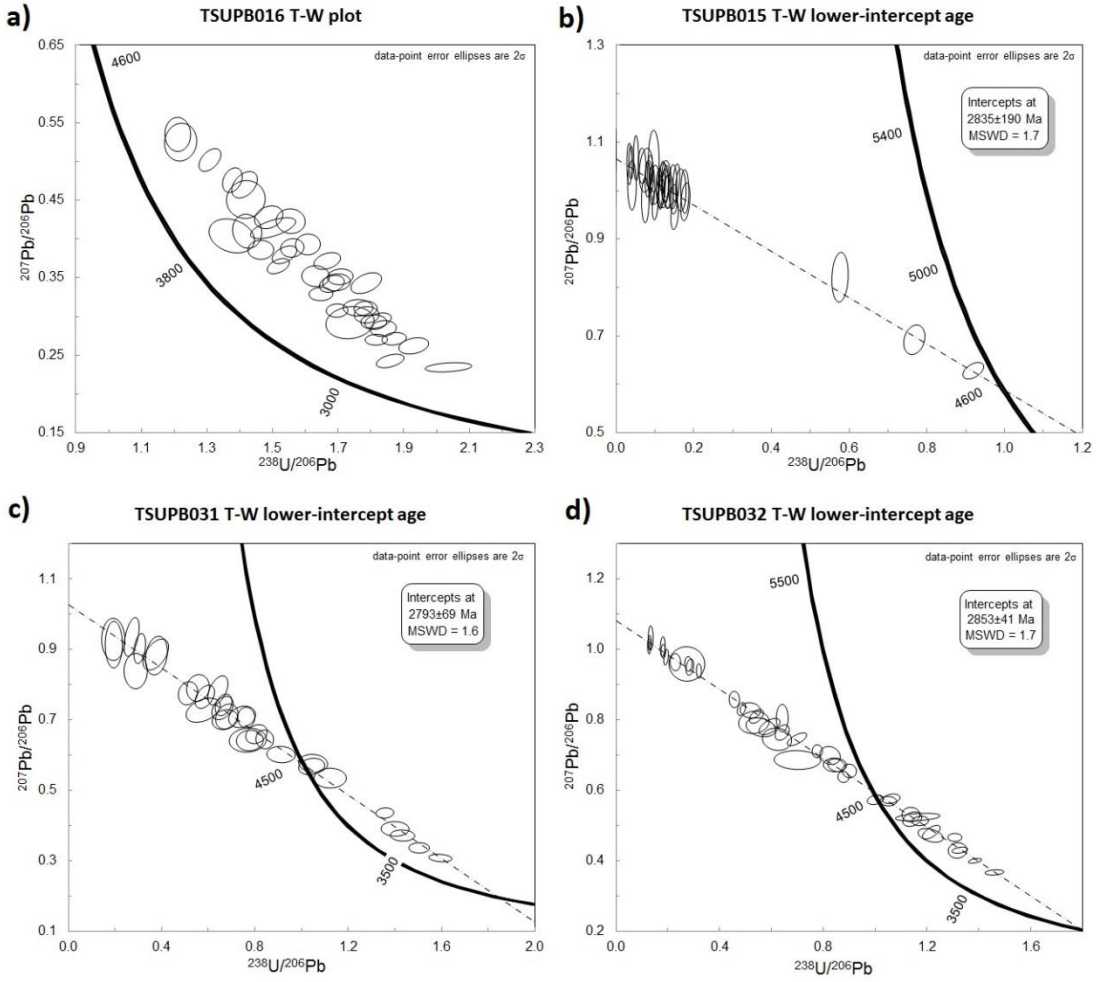


Figure 4.2.31: U-Pb apatite geochronology Tera-Wasserburg plots; a) TSUPB026, b) TSUPB015, c) TSUPB031, d) TSUPB032.

All three of these samples are likely sourced from the same quartz-vein system that carries the gold in the Aouéouat greenstone belt, and they all produce apatite U-Pb ages within error of one other. For this reason the three samples have been combined in one plot to calculate the age of this hydrothermal event. The result is a lower-intercept age of 2840 ± 35 Ma (Figure 4.2.32). This age is in agreement with the U-Pb zircon date obtained from the hydrothermal rim in TSUPB026

(Fennec), and is interpreted as the age of the hydrothermal mineralisation age of the Tasiast gold deposit.

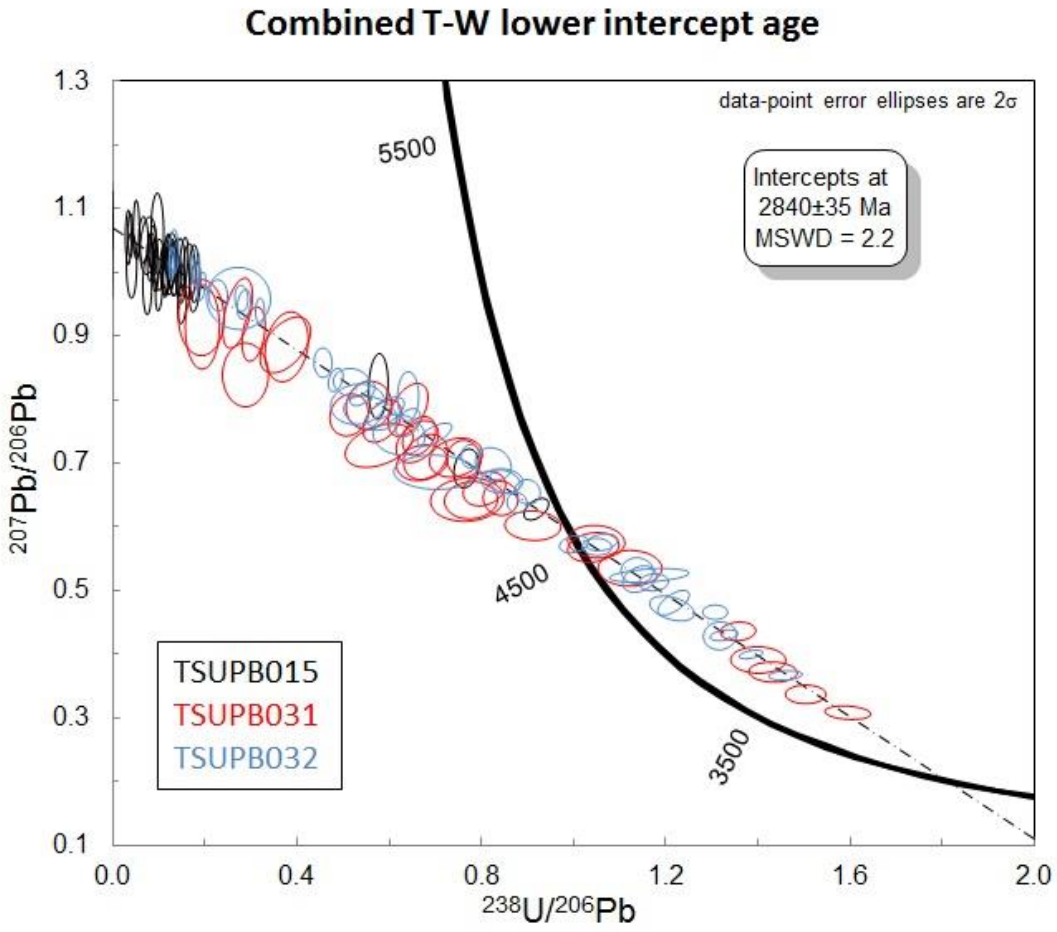


Figure 4.2.32: U-Pb apatite geochronology Tera-Wasserburg plot of combined mineralised quartz-veins.

4.3. Geochemistry:

A total of 34 samples were analysed for major and trace element geochemistry, covering all representative lithologies studied in this project other than the quartz-carbonate veins. These are: 1) eight ultramafic-mafic volcanic samples from the Temeimichat assemblage; 2) eleven samples from the Aouéouat assemblage, subdivided into: mafic-intermediate volcanic and plutonic rocks, and one felsic volcanic rock; 3) seven sedimentary samples from the Tasiast assemblage; 4) six TTG samples from the Aouéouat greenstone belt and surrounding plutons; 5) one sample of banded iron formation; 6) the late pegmatite which is present throughout the region. The results of these are presented below. Unless otherwise stated, all trace and REE plots and ratios are normalised to primitive mantle values after McDonough and Sun (1995). Chondrite normalised ratios are normalised to values after McDonough and Sun (1995), and upper continental crustal average is normalised to MuQ after Kamber et al. (2005). Trace element anomalies are calculated as follows:

Eu anomaly = $(Eu_N/(Gd_N*Sm_N))^{1/2}$
Nb anomaly = $(Nb_N/(La_N*Th_N))^{1/2}$
Sr anomaly = $(Sr_N/(Nd_N*Pr_N))^{1/2}$
Ti anomaly = $(Ti_N/(Tb_N*Sm_N))^{1/2}$

4.3.1. Element mobility:

A challenge when studying Archean rocks is that samples can be affected by metamorphism and/or hydrothermal alteration. In tropical regions there is also the added impact of surface rocks being strongly weathered (Kazimoto and Ikingura, 2014). As a first-pass test to determine the extent to which samples selected for geochemical analysis have been affected by these processes, two plots are presented here for the rocks in and around the Aouéouat greenstone belt. The first of these is the Chemical Index of Alteration (CIA) plot (Nesbitt and Young, 1982) (Figure 4.3.1a). Most unaltered igneous rocks have a CIA value between 35 and 50, depending on mafic content, and during weathering will shift towards the Al_2O_3 apex depending on the extent of alteration due to the Al being insoluble and generally immobile, while Ca, Na and K are mobile. The Temeimichat assemblage volcanic rocks all have a CIA value of between 28 and 39, which conform to the values presented by Nesbitt & Young (1982) for unweathered and unaltered basaltic rocks (30-45). CIA values for the Aouéouat assemblage volcanics range between 41 and 51, suggesting a number of these samples have undergone some alteration, which is not surprising as these are the rocks which host the gold mineralisation sourced from a hydrothermal event. Unaltered and

unweathered granitoids generally have a CIA of between 45 and 55 (Nesbitt and Young, 1982), which encompasses all of the TTG rocks here with the exception of TSUPB008, which has a CIA value of 57. This sample is a strongly sheared granodiorite from within the Aouéouat assemblage and therefore has probably also undergone significant alteration, as have the Aouéouat assemblage diorites, in particular TSUPB013, which has the highest CIA value of all samples at 71. The CIA values of the Tasiast assemblage sedimentary rocks will depend on their source composition in addition to the degree of weathering they underwent at their source. All of the Tasiast assemblage sedimentary rocks plot near to the range of unweathered and unaltered basaltic or granitoid rocks except TSUPB001, which has a CIA value of 63. This sample, from C6.7, could have been subject to more weathering at source, however it has certainly been affected by hydrothermal alteration during the gold mineralisation event, and so the high CIA value is not unexpected. A further method used to determine alteration is loss on ignition (LOI). LOI is increased by intrusive alteration (e.g. late carbonate veinlets), as well as chlorite formation and seafloor alteration. Previous studies have used an LOI of 3.5% as a cut-off point for using samples demonstrating an unperturbed geochemical signal (Kazimoto and Ikingura, 2014). The only samples here which have an LOI > 3.5% are the four ultramafic schists, in which it is common to have greater LOI values due to the almost complete alteration of these rocks to chlorite and tremolite.

Due to the inevitable alteration of greenstone belt lithologies, it is common to focus on immobile elements (e.g. REE, HFSE). It is also important however, to show that these elements are also not affected by seafloor alteration, or weathering during exposure. Babechuk & Kamber (2011) showed that by plotting incompatible element ratios versus loss on ignition (LOI) the effects of alteration, metamorphism and weathering on incompatible element mobility could be evaluated. Here Nb/Th is plotted against LOI (Figure 4.3.1b), and highlights both that Nb/Th ratios are relatively constant over a large range in LOI, and that there are no apparent trends between the two. This is also the case for other ratios used later (e.g. REE ratios). These plots highlight that there appears to be no correlation between degree of alteration, and incompatible element ratio values, and also that the only samples to have undergone any notable degree of alteration are those from the zones of hydrothermal mineralisation in the Aouéouat greenstone belt. These are the sedimentary rock sample TSUPB001, the granodiorite sample TSUPB008, and the quartz-diorite sample TSUPB013. The geochemistry of the rocks studied here, other than the three Aouéouat assemblage samples mentioned above, is therefore regarded as a suitable indicator of the original chemistry of the rocks in this study.

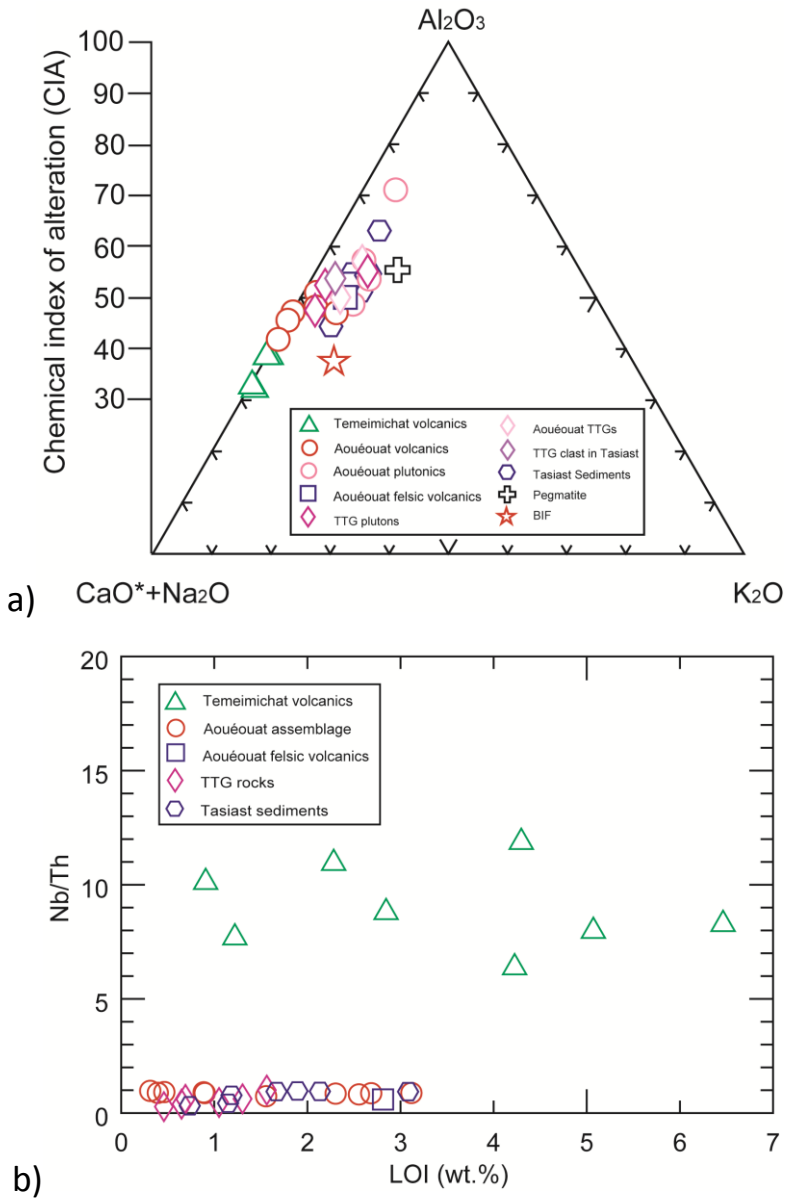


Figure 4.3.1: a) Chemical Index of Alteration plot (Nesbitt and Young, 1982), b) Nb/Th versus LOI plot (Babechuk and Kamber, 2011).

4.3.2. Temeimichat assemblage:

The Temeimichat assemblage samples are divided into two categories; komatiites and basaltic komatiites. The komatiites have SiO_2 values between 43.0 and 46.5 wt%, while the basaltic komatiites contain up to 51.2 wt% SiO_2. Similarly the komatiites have slightly less Al_2O_3 wt %; up to 11.5 wt%, as opposed to 15.0 wt% in the basaltic komatiites. MgO values range from 12.4 to 21.0 wt% in the komatiites, but are all <9.4 wt% in the basaltic komatiites. The five komatiite samples, all of which now occur as tremolite schists, plot in the komatiite field of the Jensen plot (Jensen, 1976) (Figure 4.3.6d), and all but one classify as komatiites using the trace element ratio decision tree from Mukherjee & Gupta (2008) (Figure 4.3.2). The only exception is TSUPB034,

which has a slightly higher Al/Ti_{PM} ratio, and so could be classified as a low-Th high-Mg basalt, as komatiites have a mantle-like Al/Ti_{PM} ratio, and so a deviation from 1 results in a non-komatiitic classification (Barnes et al., 2014). The komattites can also be sub-classified as Monroe type komatiites, showing close to chondritic Al_2O_3/TiO_2 and Gd/Yb ratios (Arndt, 1994). The three basaltic komatiite samples, all of which now occur as amphibolites, plot in the basaltic komatiite field of the Jensen plot (Figure 4.3.6d), and as low-Th basaltic komatiites using the decision tree from Mukherjee & Gupta (2008) (Figure 4.3.2).

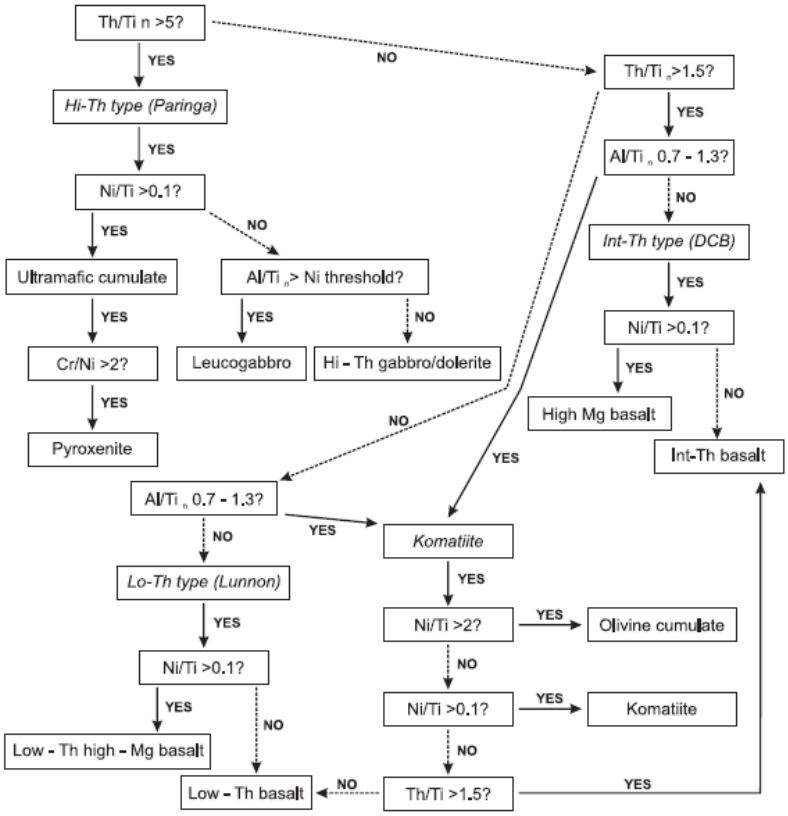


Figure 4.3.2: Decision tree for geochemical classification of mafic and ultramafic rocks based on trace element ratios (Mukherjee and Gupta, 2008).

The most striking geochemical feature that persists through all samples of the Temeimichat assemblage is the characteristic LREE-depletion (La_n/Sm_n = 0.43-0.76) and relatively flat MREE-HREE profiles (Gd_n/Yb_n = 0.95-1.18). These rocks also have elevated Cr and Ni (247-3077 ppm), small positive and negative Nb anomalies (0.77-1.24), positive Sr anomalies (1.41-2.77) (not including TSUPB034 (0.41)), negative Zr anomalies, and smooth REE profiles other than very slightly positive and negative Eu anomalies (0.82-1.12) (Figure 4.3.3). All of these features are typical, of Archean komatiites (e.g. Hanski et al., 2001, Chaudhuri et al., 2015) and low-Th Archean basalts (e.g. Kerrich et al., 1999, Barnes et al., 2012) respectively. Trace and REE plots of the Temeimichat assemblage clearly highlight the LREE-depleted signatures (La_n/Yb_n = 0.34-0.82). This persists across the Aouéouat greenstone belt irrespective of which target the sample was

collected from, highlighting the spatial extent of the Temeimichat assemblage. The LREE depleted patterns are restricted to this assemblage alone, indicating that a unique source and/or environment contributed towards its formation. The nature of this source will be discussed in conjunction with data from the Aouéouat assemblage later in this chapter.

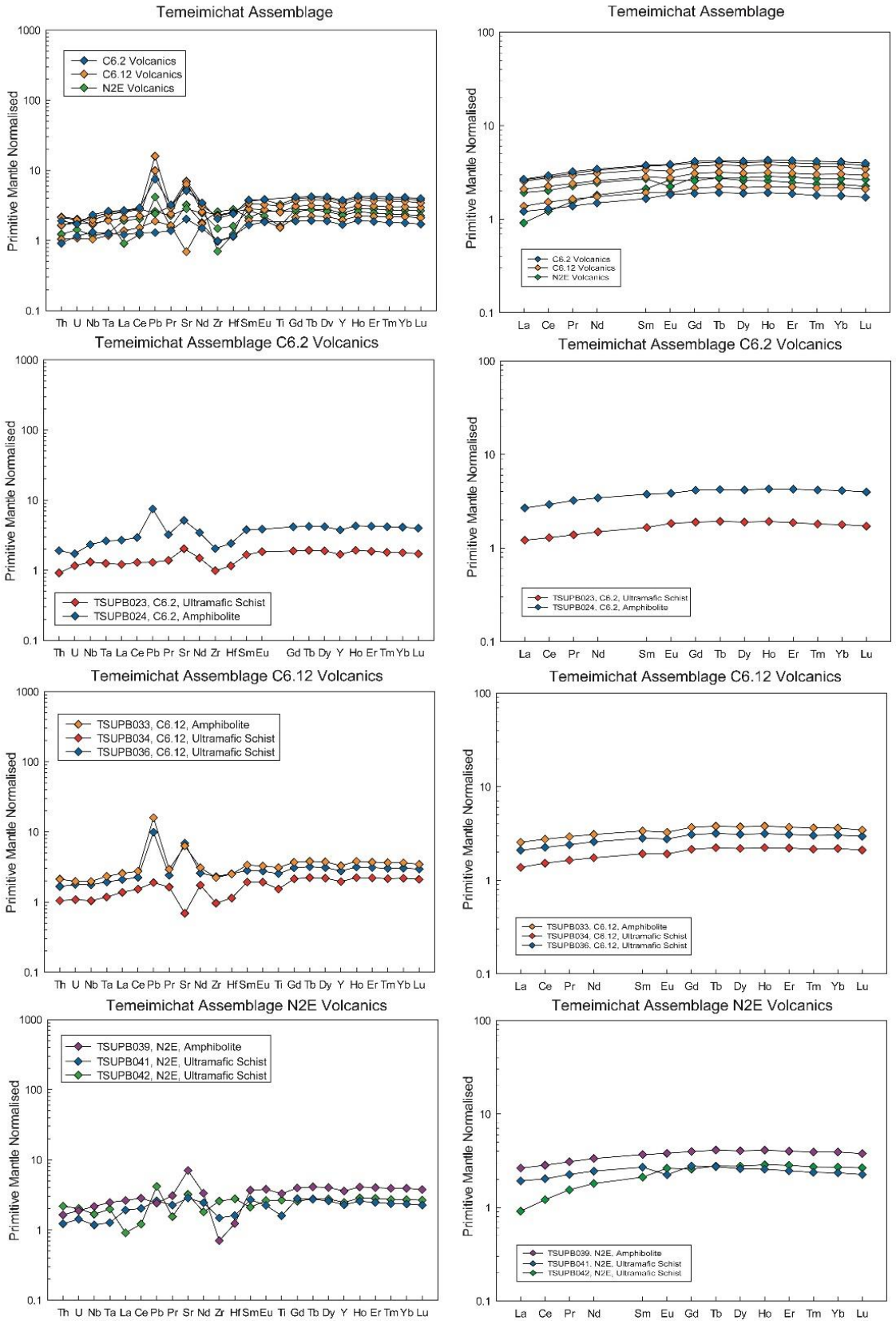


Figure 4.3.3: Temeimichat Trace and REE plots.

4.3.3. Aouéouat assemblage:

Geochemically, there is little difference between the trace element profiles and ratios of the mafic-intermediate volcanic rocks and mafic-intermediate plutonic rocks, and therefore these are described here together. The volcanic rocks, all of which now occur as amphibolites, have SiO_2 values of between 50.2 and 57.2 wt% other than one quartz-amphibolite from Tamaya (TSUPB047) with 64.8 wt% SiO_2. The plutonic rocks consist of one diorite, with SiO_2 of 58.7 wt%, and three quartz-diorites with SiO_2 values between 60.2 and 65.7 wt%. It should be noted that the rocks in the Aouéouat greenstone belt have undergone varying degrees of silicification which have affected their SiO_2 values, and can be seen in figure 4.3.6b (discussed later). Al_2O_3 values are all within the range of 12.5 to 16.5 wt%, again other than the quartz-amphibolite which has only 9.5 wt% Al_2O_3. The plutonic rocks all have <2.8 wt% MgO, while the volcanics have up to 8.5 wt% MgO.

Trace and REE profiles of the Aouéouat assemblage (Figure 4.3.4) show that all of the mafic to intermediate samples from the Aouéouat assemblage have almost identical patterns, with the only exception being one amphibolite (TSUPB022) which has lower concentrations of trace elements. The REE profiles are all slightly LREE-enriched (La_n/Yb_n = 3.1-6.1) with slightly flatter MREE-HREE profiles (Gd_n/Yb_n = 0.99-1.45) than LREE profiles (La_n/Sm_n = 2.68-3.52), and are smooth other than some slightly negative Eu anomalies (> 0.86). Trace element profiles show Th and U enrichment, and negative Nb (0.16-0.19), Ta, Sr (0.19-0.6) (not including TSUPB022 (1.12)) and Ti (0.65-0.88) anomalies. The large negative Sr anomalies could be related to the breakdown of plagioclase to sericite (and loss of Sr) in the samples more susceptible to alteration (Potrel, 1997).

One felsic volcanic rock from the Aouéouat assemblage was analysed for major and trace element geochemistry. Two granodiorites were also sampled from the Aouéouat assemblage, and are included and briefly discussed here, however more detail is presented on these and along with the other TTG rocks later. The three samples have SiO_2 values between 70.6 and 71.9 wt%, and Al_2O_3 values between 14.4 and 16.3 wt%. MgO is <1.6 wt% in all of the felsic rocks. Trace and REE profiles of the Aouéouat felsic rocks (Figure 4.3.5) show they are strongly LREE-enriched (La_n/Yb_n = 22-41), and again have smooth REE profiles other than small negative Eu anomalies (0.88-0.90). As with the Aouéouat mafic-intermediate rocks, the trace element profiles show Th and U enrichment, and negative Nb (0.08-0.13), Ta and Ti (0.29-0.38) anomalies, with both positive and negative Sr anomalies (0.61-1.91).

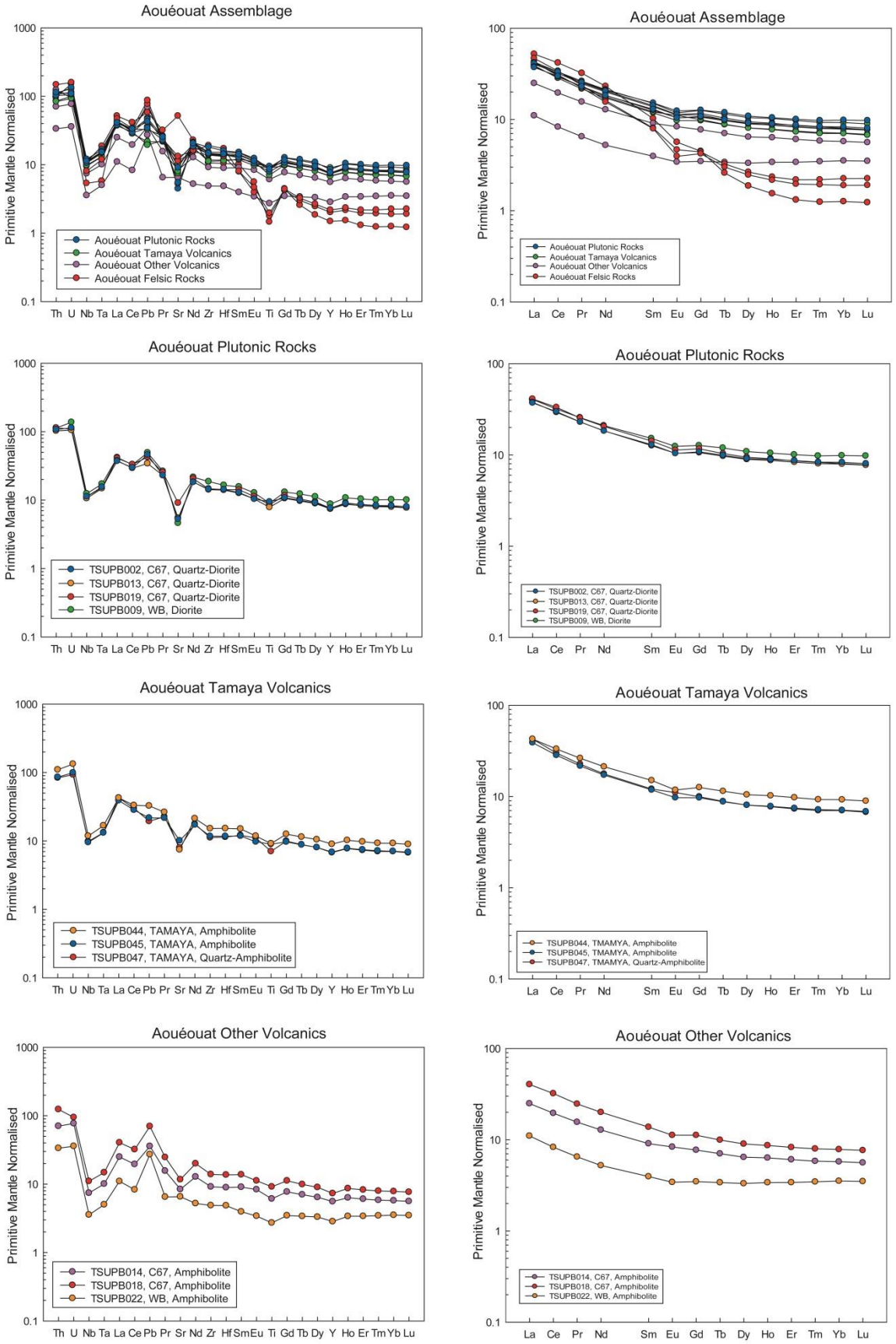


Figure 4.3.4: Aouéouat Mafic to Intermediate Trace and REE plots.

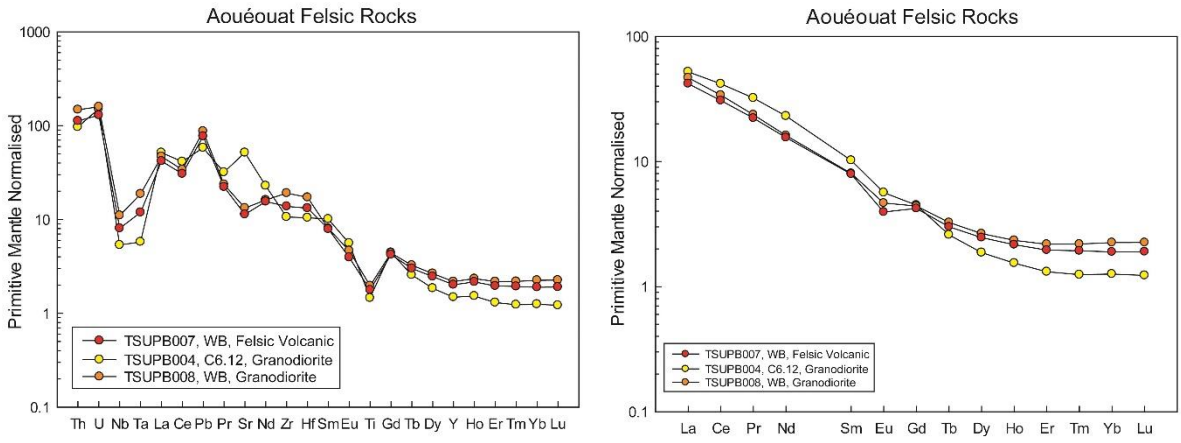


Figure 4.3.5: Aouéouat Felsic Trace and REE plots.

4.3.4. Aouéouat greenstone belt volcanic and plutonic rocks:

Having briefly described the geochemistry of the rocks of the Temeimichat and Aouéouat assemblages in their respective groupings above, detailed results are best presented with all of the rocks together using trace element ratio plots, which are presented below.

The rocks of the Aouéouat greenstone belt can be grouped into the three main categories described above, i.e. the ultramafic-mafic Temeimichat assemblage, the mafic-intermediate Aouéouat assemblage rocks, and the felsic rocks of the Aouéouat assemblage. Two volcanic discrimination plots developed by Winchester and Floyd (1977) are presented in order to classify the rocks. These both highlight the different compositions between the rock assemblages by using trace element and major element ratios. The first of these is the Zr/TiO_2 versus Nb/Y incompatible element ratio plot (Figure 4.3.6a) in which the Temeimichat assemblage volcanics plot in the sub-alkaline basalt field, the Aouéouat assemblage mafic-intermediate rocks plot in the andesite/basalt field, and the Aouéouat felsic rocks plot along the boundary between rhyodacite/dacite and trachyandesite fields. The second, and similar plot is Zr/TiO_2 plotted against SiO_2 (Figure 4.3.6b). In this diagram it can be seen that, particularly in the Aouéouat assemblage, a number of the samples plot in fields with high SiO_2 values compared to what is expected from the incompatible element ratio diagram. This is partially because in the case of the quartz-diorites there are large quartz phenocrysts present; however the main reason is that many rocks in the Aouéouat greenstone belt have undergone silicification related to the late hydrothermal activity. These two factors have shifted a number of the samples upwards on this plot, however, several samples fall in identical fields in both plots, indicating that they were less, or unaffected by silicification. This emphasises the necessity to use immobile elements for classification purposes.

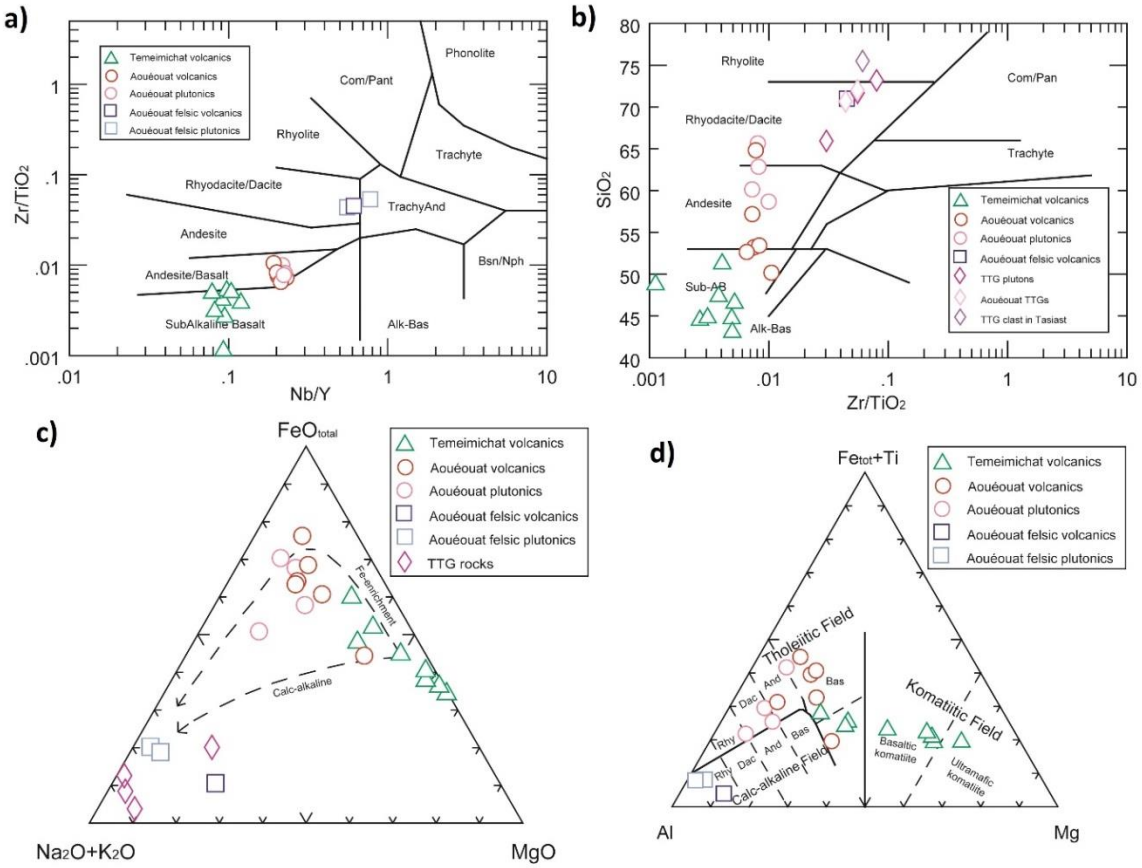


Figure 4.3.6: a) Zr/TiO_2 versus Nb/Y incompatible element ratio plot (Winchester and Floyd, 1977), b) SiO_2 versus Zr/TiO_2 ratio plot (Winchester and Floyd, 1977), c) AMF classification diagram showing example trends of tholeiitic and calc-alkaline magma series (trends plotted after Reimink et al., 2014), d) Jensen cation plot of volcanic rocks (Jensen, 1976).

All of the mafic-intermediate rocks in the Aouéouat greenstone belt, as well as the mafic rocks from the Temeimichat assemblage, plot within classification fields consistent with their petrographic descriptions. Two further rock differentiation diagrams are the AMF diagram (Figure 4.3.6c) and the Jensen cation plot (Figure 4.3.6d). In each of these plots the Temeimichat assemblage and Aouéouat assemblage rocks follow a tholeiitic trend (i.e. Fe-enrichment), where most of the Aouéouat assemblage volcanics plot in the high-Fe tholeiite field. The Jensen cation plot is particularly useful for these rocks, as it both distinguishes komatiites from basalts, and uses elements which exhibit greater stability during low-grade metamorphism and metasomatism (Rollinson, 1993), as seen in the CIA plot earlier.

Figure 4.3.7 visually highlights the major element composition (wt%) of the rocks, plotted against Mg # (Mg number). Mg# is a way of expressing the ratio of Mg to Fe in a rock, and can be used as a proxy for degree of fractionation, whereas MgO alone cannot as it ceases to vary in plagioclase-saturated systems (Barnes et al., 2012). Both SiO_2 and TiO_2 show negative correlations across all

rocks, while Al_2O_3 shows a strong negative correlation in the Temeimichat assemblage, but no correlation in the Aouéouat assemblage. There is no correlation between FeO and Mg#. The two assemblages can be distinguished solely on Mg #, which is expected from their petrography. The only anomaly is one of the Aouéouat assemblage amphibolites (TSUPB022) which has a relatively high Mg# when compared to the rest of the Aouéouat assemblage. The major element vs Mg# plots show that there is a large range in major element values within the assemblages; however the values are not exceptional when compared to other Archean ultramafic-intermediate rocks (e.g. Ketchum et al., 2013, Liu et al., 2014, Barnes et al., 2014).

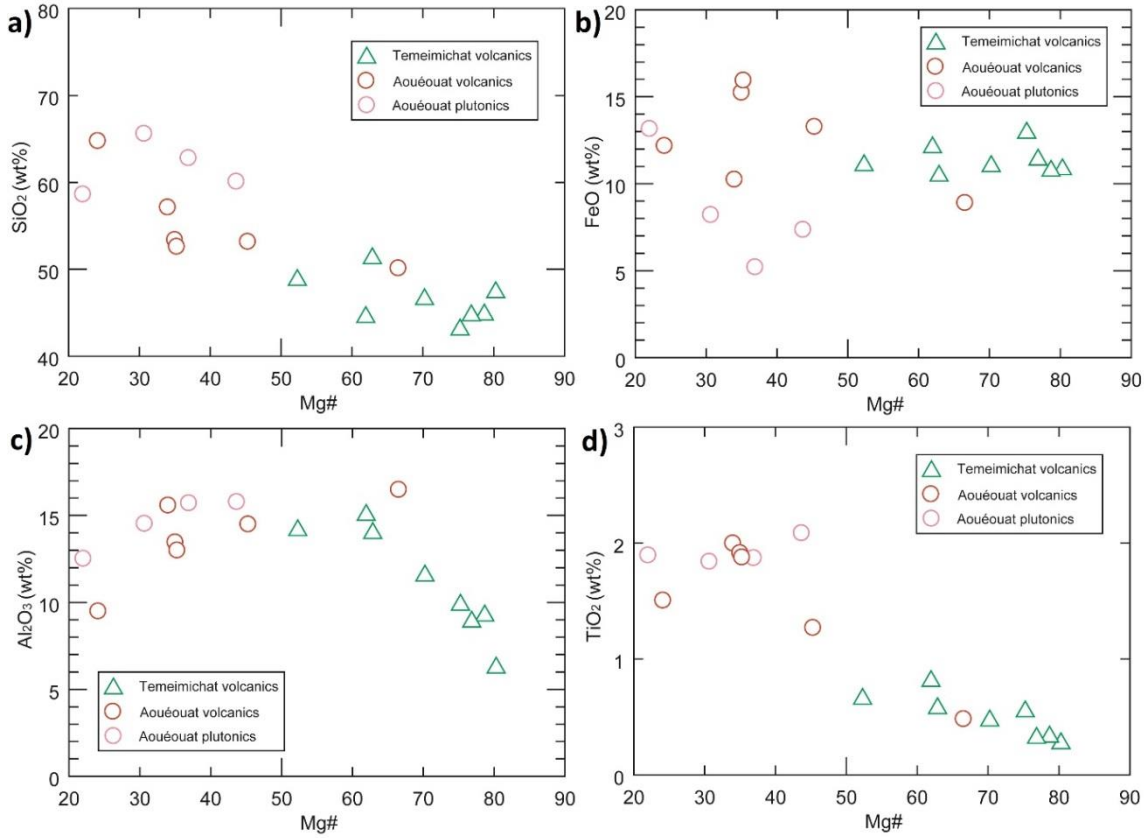


Figure 4.3.7: Mg # bivariate plots, a) SiO_2 (wt%), b) FeO (wt%), c) Al_2O_3 (wt%), d) TiO_2 (wt%). (Mg# calculated using an estimated $(Fe^{2+}/(Fe^{2+} + Fe^{3+}))$ ratio of 0.85 (Luttinen and Furnes, 2000, Philipp et al., 2001).

Having distinguished the groupings of the Aouéouat assemblage rocks and their geochemical characteristics, the next step is to establish possible sources (e.g. mantle, crustal components) and depth, as well as possible tectonic environments (e.g. oceanic plateau, island arc) of their formation, to aid in explaining the differences between them. The uncertainties related to Mesoarchean tectonics were discussed at length in Chapter 2.3, and these need to be taken into account when using tectonic discrimination diagrams to classify Mesoarchean rocks. Although the diagrams may therefore not be indicative of the exact tectonic processes involved here, they are nonetheless a useful aid to both discriminate between samples, and elucidate processes affecting

source composition, which in turn will aid in constraining applicable tectonic models. One important trace element proxy that can be used to distinguish between environments for oceanic basalts is the Th-Nb proxy (Pearce, 2008). The behaviour of Th and Nb differs during partial melting, with Th being preferentially released from subducting slabs into the overlying mantle wedge, or from the melting of hydrous mafic material at depth (i.e. at the base of an over thickened volcanic pile) while Nb is retained in the source rock. Th is also enriched in the continental lithosphere, along with LREE, and so can be preferentially added to a melt relative to Nb through crustal assimilation (i.e. a crustal component to the melt) or crustal contamination during the eruption of basaltic volcanics through pre-existing crust. Therefore one of, or a combination of crustal assimilation and crustal contamination can result in an increased Th/Nb ratio (Condie, 2003, Pearce, 2008). In all samples from the Aouéouat assemblage, Th is enriched, with values ranging from 2-9 ppm, but generally >6.5, relative to typical tholeiitic basalt contents of <2 ppm (Van Der Zander et al., 2010) and even average Archean upper crust of 5.7 ppm (Taylor, 1985). The array of between present day NMORB and OIB is shown on the Th-Nb proxy diagram (Figure 4.3.8a), and any deviation to higher Th/Yb values indicates either a crustal component through contamination upon ascent of the magma, or through subduction (i.e. assimilation of subducted crust in the source). Pearce (2008) presented a representative set of Archean oceanic greenstones in order to deduce an Archean mantle average to be included in this plot. It was concluded that the Archean MORB-OIB array was similar to that of the present day suggesting that by the Archean the primitive mantle had already separated into Archean continental crust and Archean mantle during the Hadean. All samples from the Temeimichat assemblage (Th/Nb = 0.08-0.18) plot very close to the Archean mantle average as calculated by Pearce (2008), suggesting that they represent uncontaminated mantle derived basalts, similar in composition to oceanic basalts (Figure 4.3.8a). The Aouéouat assemblage samples (Th/Nb = 1.03-1.36) however plot together above the mantle array, indicating that there is a crustal component involved in these rocks, either through a subduction related crustal assimilation, or through crustal contamination (Figure 4.3.8a). As would be expected, the Aouéouat felsic rocks (Th/Nb = 1.68) plot very close to the Archean felsic average as defined by Pearce (2008) (Figure 4.3.8a). Puchtel et al. (2009) plotted data from a number of Archean greenstones along with modern day island-arc and oceanic plateau basalts, and showed that the Archean greenstones plot with the modern day oceanic plateau basalts, and distinct from the island-arc basalts. The Temeimichat assemblage similarly plots with the other Archean greenstone belts and close to the modern day oceanic plateau data. The Aouéouat assemblage shows higher LREE-enrichment than modern day island arc basalts included in the plot, however still plots within range of these samples. In order to differentiate between a crustal contamination source and the melting of a subducted slab, Bedard et al. (2013) demonstrated that if the source of the high-Th but low-Nb was a combination of a

depleted source and melting of the subducted slab then an array parallel to the mantle array would be apparent in the trace element ratios, and that if crustal contamination was the factor then the arrays would be oblique. In the samples studied here however, the samples plot within a confined field and it is not possible to define a clear array (Figure 4.3.8a). That is unless the source for the Aouéouat assemblage is the same as that of the Temeimichat assemblage, which would infer that the source of the high-Th low-Nb was crustal contamination, which is one possible model, however it cannot be ruled out that there are two separate sources for these assemblages.

A number of other trace element ratio discrimination plots have been formed based upon the same principles as those just described. A plot of Th/Nb vs La/Sm (Piercey et al., 2002) again uses these two ratios to indicate whether the samples have been sourced from the mantle, or have a degree of crustal contamination/assimilation incorporated. In this diagram the Temeimichat assemblage plots in the tholeiitic field, while the Aouéouat assemblage plots in the calc alkaline field, and closer to average continental crust ratios (Figure 4.3.8b), again indicating there is likely a crustal component involved in the Aouéouat assemblage. I has been suggested that by plotting normalised ratios of Sm/Yb_{CH} vs Nb/Th_{PM}, signatures independent of REE fractionation become apparent (Polat, 2009, Lodge et al., 2014). In this plot the Temeimichat assemblage shows near chondritic Sm/Yb, and also near primitive mantle Nb/Th for some of the samples, however there is a larger range of Nb/Th ratios most of which suggest an affinity similar to oceanic plateaus (Figure 4.3.8d). The Aouéouat assemblage however has lower Nb/Th, as either the Nb has been retained during their formation (possibly in a subduction setting), or Th has been added through crustal contamination.

A further trace element ratio discrimination plot presented for the Aouéouat greenstone belt volcanics is Th/Yb vs Zr/Y as developed by Ross and Bédard (2009) (Figure 4.3.8b). These ratios differentiate between magmas of different affinities, as an alternative to the AMF diagram. The Temeimichat assemblage clearly plots in the tholeiitic field as expected; however the mafic-intermediate rocks of the Aouéouat assemblage plot just inside the calc-alkaline field. This is in contrast to both the AMF diagram and the Jensen cation plot presented above, and suggests that it could in fact be a crustal contamination signature that is causing this assemblage to have higher Th/Yb and Zr/Y ratios than would be expected for what appear to be tholeiitic basalts.

The Zr/Y vs Zr diagram is commonly used for modern day basalts in order to distinguish their tectonic environment (Pearce and Norry, 1979). Here the Aouéouat assemblage rocks plot just within the field of within-plate basalt field, though are on the boundary between a continental arc

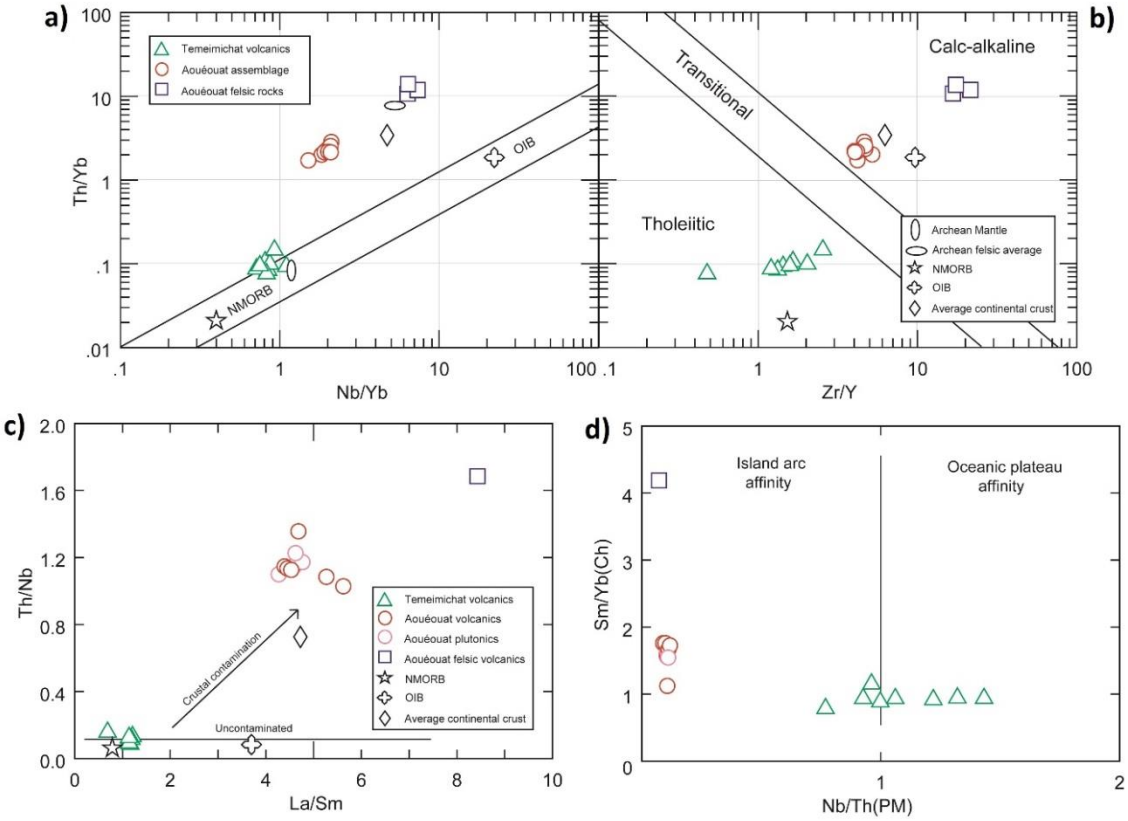


Figure 4.3.8: a) Th-Nb proxy diagram of Th/Yb vs Nb/Yb (Pearce, 2008), b) Th/Yb vs Zr/Y discrimination diagram (Ross and Bédard, 2009), c) Th/Nb vs La/Sm discrimination diagram (Piercey et al., 2002), d) Sm/Yb_{CH} vs Nb/Th_{PM} showing arc-like signatures vs oceanic signatures. Representative values are shown for: NMORB (Workman and Hart, 2005), OIB (Sun and McDonough, 1989), Average Continental Crust (MUQ) (Kamber et al., 2005), Archean Mantle and Archean Felsic Average (both Pearce, 2008).

and oceanic arc setting using the model developed by Pearce (1983) (Figure 4.3.9a). Some of the Temeimichat assemblage samples plot within the volcanic-arc basalts field, however others do not plot in the field of any tectonic setting, which suggests that this diagram is not applicable to these rocks, other than to demonstrate that the Aouéouat assemblage possesses a "continental lithospheric" signature and the Temeimichat assemblage possesses an "oceanic signature". On the Ti-V discrimination diagram for basalts (Shervais, 1982) the Aouéouat assemblage plots close to the field of oceanic-island and alkali-basalt (Figure 4.3.9b). The Temeimichat assemblage plots fully within the arc-tholeiite field again showing the lack of any continental lithospheric component to its chemistry. The final discrimination plot presented for the Aouéouat and Temeimichat assemblages is Th/Ti_{PM} vs Al/Ti_{PM} (Figure 4.3.9c) (Barnes et al., 2012). Here relatively high Th compared to Ti is evident, and also relatively high Ti compared to Al in the Aouéouat assemblage. Neither of these ratios are close to that of the primitive mantle, which highlights the relatively large abundance of Th and Ti respectively, probably through some form of crustal input, however relative to other trace elements it is apparent that Ti is relatively depleted in the

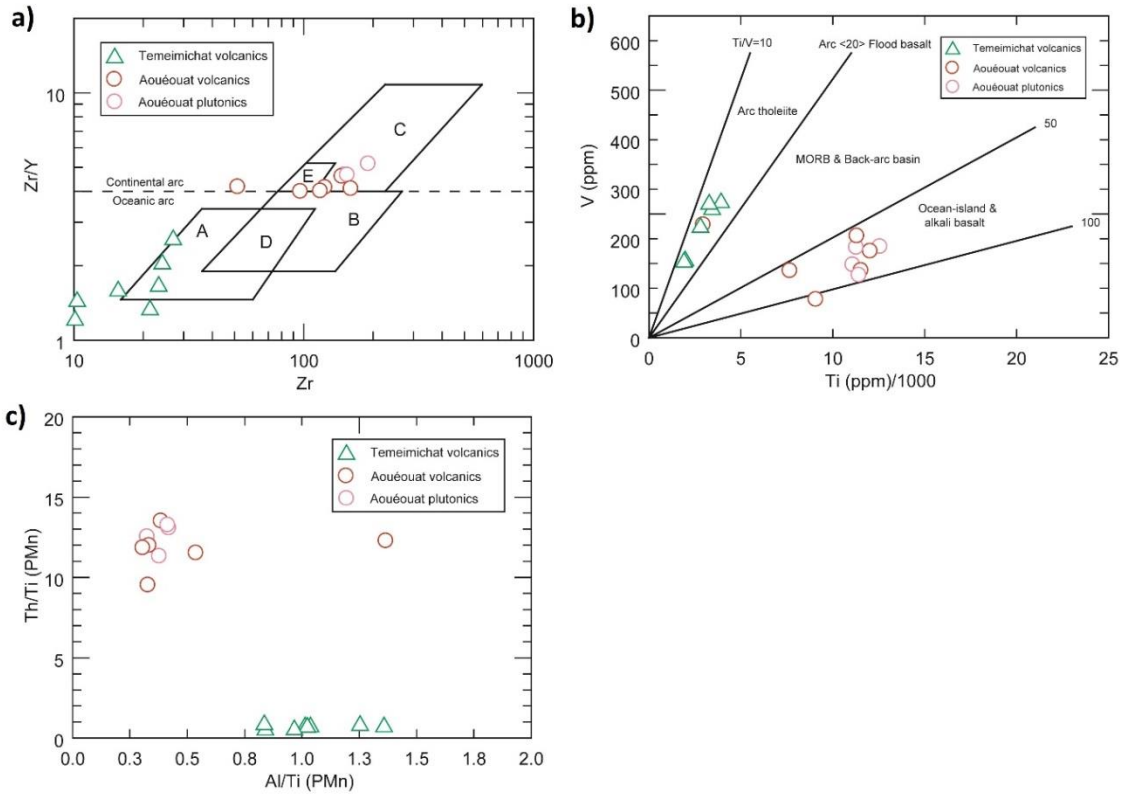


Figure 4.3.9: a) Zr/Y vs Zr discrimination diagram for tectonic setting, the fields are; A: volcanic-arc basalts, B: MORB, C: within-plate basalts, D: MORB and volcanic-arc basalts, E: MORB and within-plate basalts (Pearce and Norry, 1979), continental-arc and oceanic-arc fields are also highlighted, however there is some overlap close to the boundary (Pearce, 1983), b) Ti-V discrimination diagram for tectonic setting (Shervais, 1982), c) Th/Ti_{PM} vs Al/Ti_{PM} discrimination plot, also used to compare to primitive mantle ratios (Barnes et al., 2012), primitive mantle normalised using McDonough and Sun (1995).

Aouéouat assemblage, so this apparent low Al/Ti ratio could be due to Al depletion (Figure 4.3.4). This geochemical feature may be explained by the existence of a residual Ti-rich mineral in the source, (e.g. rutile or ilmenite). The Temeimichat assemblage ratios however plot close to primitive mantle in both cases, other than a slight deviation in Al/Ti_{PM}. These Al/Ti_{PM} differences could be explained by slightly different mantle melting depths for the Temeimichat assemblage. A similar scenario was demonstrated by Robin-Popieul et al. (2012) for the Barberton komatiites where it was modelled that Al-depleted samples were extracted at greater depths at which a large proportion of melt (30–40%) was retained in the source and the residue contained a high proportion of residual garnet (15%), while the Al-enriched samples were extracted at shallower crustal depths associated with the exhaustion of residual garnet. Note however that although the Temeimichat assemblage samples are described here as slightly Al-depleted and slightly Al-enriched, the difference between the Al/Ti_{PM} ratios are not significant, as both groups classify as Al-undepleted rocks. This range is typical in extensive sequences of Archean tholeiites reported in

greenstone belts elsewhere, including the Abitibi greenstone belt and the Kalgoorlie Terrane (Kerrich et al., 1999, Barnes et al., 2012). Therefore although not extracted from a vast range of different mantle melting depths, a difference in mantle melting depths could be inferred as a possible reason for the range of Al/Ti_{PM} ratios here.

4.3.4.1. Nd isotopes:

Two samples from the Temeimichat assemblage (one komatiite and one basaltic komatiite), and four samples from the Aouéouat assemblage (three amphibolites and one quartz-diorite) were analysed for Nd-isotopes (Figure 4.3.10). Although the Aouéouat assemblage has been dated at ~3.0 Ga, no dates were acquired for the Temeimichat assemblage, and so the assumption has been made here that the Temeimichat assemblage was emplaced shortly before the Aouéouat assemblage. The possibility remains however that the Temeimichat assemblage is older, and although it could be up to 3.3 Ga, this is unlikely. εNd is the measure of the deviation of a sample from the expected value of a sample of that age from CHUR (DePaolo and Wasserburg, 1976). Samples from each assemblage plot within distinct groups of εNd values. The Temeimichat assemblage has $\varepsilon Nd_{(3.0Ga)}$ values of +3.57 and +2.74, plotting very close to the depleted mantle curve. The Aouéouat assemblage has $\varepsilon Nd_{(3.0Ga)}$ values close to zero, ranging from -1.09 to +0.41. If the Temeimichat assemblage was as old as 3.3Ga, the $\varepsilon Nd_{(3.3Ga)}$ values are +2.76 and +2.06 which does not greatly alter the εNd position relative to the depleted mantle curve. This suggests that the Temeimichat assemblage was sourced directly from a depleted mantle reservoir. The Aouéouat assemblage however has T_{DM} ages between 3.3 and 3.2 Ga, and so was either extracted from the depleted mantle at this time, or has assimilated older crust.

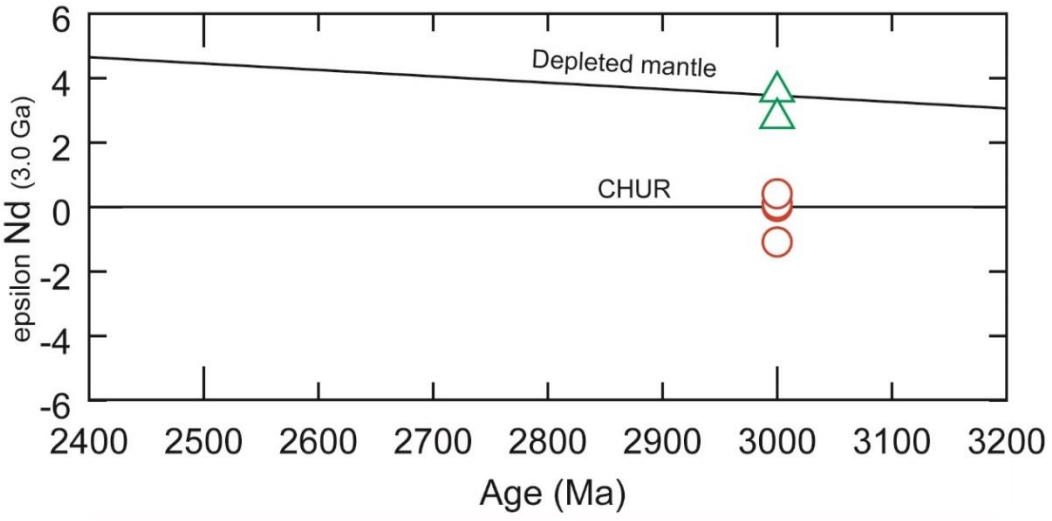


Figure 4.3.10: $\varepsilon Nd_{(T)}$ values of Temeimichat assemblage samples (green triangles) and Aouéouat assemblage samples (red circles) with depleted mantle evolution curve and CHUR evolution curve from DePaolo (1976).

4.3.5. Tasiast assemblage:

The Tasiast assemblage sedimentary rocks were collected from three separate targets (C6.7, WB and TFW). Due to the differences in nature between individual samples, they are often described below by their sample code. The C6.7 samples are TSUPB001 and TSUPB003, the TFW (Tasiast footwall) sample is TSUPB005, and four samples were collected from WB (West Branch); TSUPB010, TSUPB011, TSUPB020 and TSUPB021.

The C6.7 and TFW sedimentary rocks have SiO_2 values between 64.6 and 69.4 wt%, while the WB greywackes have SiO_2 values between 76.1 and 80.0 wt%. This difference in SiO_2 values could be an effect of the more mature nature of the WB greywackes due to the physical robustness of quartz increasing the relative SiO_2 content, or it could be an effect of a difference in source rock composition, with the C6.7 sediments having a less evolved volcanic source, while the varied source of the WB samples contain a lot of TTG derived clastic material. The fine grained sediment has a low SiO_2 value of 50.8 wt% due to it containing a large proportion of clay minerals. Al_2O_3 values are between 16.4 and 17.0 wt% for the less mature sediments, and lower, between 11.8 and 14.1 wt% for the more mature sediments. The difference seen here in Al_2O_3 values is likely due to Al-rich micas being deposited as fine grained sediments, or forming as the alteration products of clay minerals, evidence of which is seen in that TSUPB010, the fine grained sediment, has the highest Al_2O_3 value, of 18.5 wt%. MgO values are <0.4 wt% in all of the distal sediments, and between 1.0 and 2.4 wt% in the locally sourced sediments. It is worth noting that TSUPB001 has one of the highest TiO_2 values, 2.0 wt%, of all the samples analysed for this study, and is > 3 times greater than all of the other clastic sediments. Although Ti is classified as an immobile element, there is evidence that it can be deposited by hydrothermal fluids in Ti rich minerals (e.g titanite) (Giere, 1990). Although a hydrothermal origin is one possibility for the high Ti content, titanite is not observed in TSUPB001, therefore a more likely explanation for the high TiO_2 value in TSUPB001 is that this is an artefact of source rock geochemistry.

Geochemically, the trace and REE plots show little variance between relatively mature and relatively immature sediments the local and distal source regions, with all of the samples having a LREE-enriched profile (TSUPB001 and TSUPB010 La_n/Yb_n = 5-6, all others La_n/Yb_n = 17-41) with negative Eu (0.71-0.97), Ti (0.28-0.82) and Y anomalies (Figure 4.3.11). Other than the fine grained sediment, which has a less pronounced LREE-enriched profile (La_n/Sm_n = 3.01) than the clastic sediments (La_n/Sm_n = 3.15-7.41), the differences in trace element profiles are caused by alteration of the samples. TSUPB001 has a less pronounced LREE-enriched profile (La_n/Sm_n = 2.88), with a relatively higher abundance of HREE than the other sediments. This could be due to the sample

showing signs of strong hydrothermal alteration; however it more likely represents the original geochemistry, as it is possibly a reworked ash bed as opposed to a clastic sediment, resulting in almost an identical profile to the volcanic rocks from the Aouéouat assemblage. TSUPB011 shows the opposite trend, with a steeper LREE-enriched profile (La_n/Sm_n = 5.98), and has a lower abundance of the HREE. This sample has been heavily altered by a nearby pegmatite, and would otherwise be expected to plot identically to TSUPB020 due to sample location and petrography. It is possible that the pegmatitic fluids have stripped the sample of a number of trace and rare earth elements. The negative Eu anomalies are stronger in the WB unaltered greywackes (0.71-0.72) than the unaltered locally sourced sediments (0.91-0.93), which can be a sign of a more evolved source rock (e.g. Rollinson, 1993, McLennan et al., 1993), and is most likely the reason here.

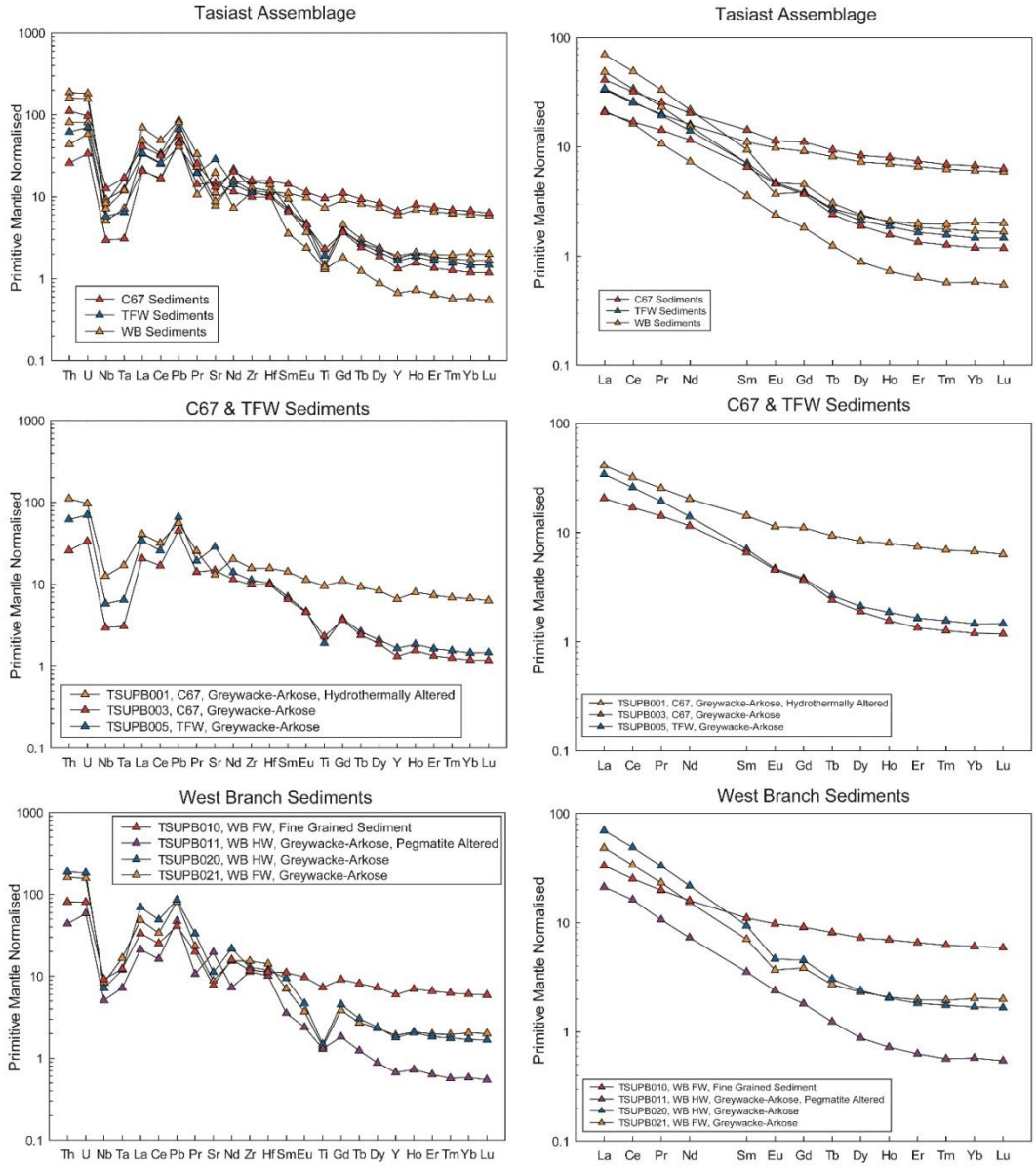


Figure 4.3.11: Aouéouat Felsic Trace and REE plots.

Two trace element ratio plots are presented to discriminate between the source composition, and the depositional environment of Tasiast assemblage sedimentary rocks. The first of these is the Th/Sc vs Zr/Sc diagram (McLennan et al., 1993) (Figure 4.3.12a). These elements are used due to immobile nature in surface conditions and weathering, and so preserve the source rock chemistry (Taylor, 1985). Due to Zr and Th being common in heavy minerals such as zircon and titanite, which are concentrated during sediment recycling, this allows the correlation of these elements with more mature or distal sediments (Bagas et al., 2008). The two ratios can also reveal compositional heterogeneity in the provenance if the samples show Th/Sc and Zr/Sc values along the trend from mantle to upper continental crust compositions (McLennan et al., 1993). Both of these factors are apparent in the Tasiast sediments presented here. Firstly the more mature the sediment, the further to the top right of the diagram it plots, confirming that the WB sediments are more mature and the C6.7 sediments are not as mature and/or as reworked. Secondly, the two sediments from C6.7 plot towards the bottom left, highlighting that their provenance was more primitive in its nature, while the WB sediments plot in the upper continental crust field, highlighting that their provenance was of a continental crustal nature. The second plot is the Ti/Zr vs La/Sc diagram, which is used to discriminate between compositions of sandstone and different tectonic environments, i.e. oceanic island arc, continental island arc, active continental margin, and passive margin environments (Bhatia and Crook, 1986) (Figure 4.3.12b). This plot suggests that in comparison to modern sediments, the more mature WB greywackes are equivalent to a passive margin sediment, the TFW sample equivalent to a modern day active continental margin sediment, and the C6.7 samples equivalent to a modern day island arc sediment. Note here that TSUPB010 only plots in the oceanic island arc field due to the lack of siliciclastic material in its fine grained composition. TSUPB003 has a particularly high Cr/Th ratio, of 33.6, relative to the average upper continental crust value of 5.8 (Kamber et al., 2005). Even when comparing the Cr/Th ratio of TSUPB003 to the early Archean (>3.5 Ga) continental crustal ratio of Condie (1993) of 29.6, it is still high. This again suggests a more mafic or ultramafic source, while the distal sediments have Cr/Th ratios between 4.5 and 7.6, close to the crustal average, and TSUPB001 has a low ratio of 2.1, due to its low Cr content, possibly related to hydrothermal activity.

Finally, in the major element provenance discrimination diagram of Ohta (2008), we see the same trend in the sedimentary rocks, from a mafic-intermediate provenance in the locally derived sediment towards a felsic source for the more mature sediments (Figure 4.3.13). Again TSUPB010 is only plotting in the mafic provenance field due to the geochemical composition obtained from the micaceous minerals which have formed as a result of the original fine grained clay minerals present in the sediment.

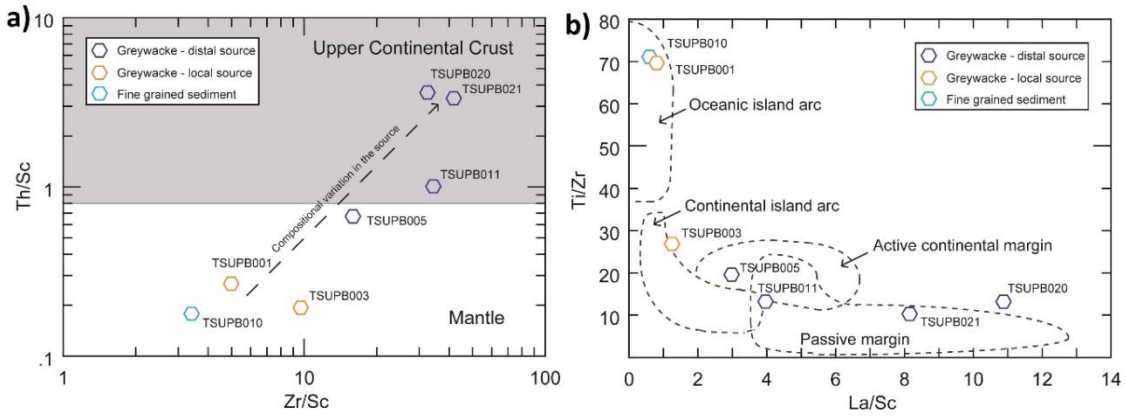


Figure 4.3.12: a) Th/Sc vs Zr/Sc diagram highlighting the difference in provenance composition and extent of sedimentary recycling (McLennan et al., 1993), b) Ti/Zr vs La/Sc diagram highlighting tectonic environment of sediment deposition (Bhatia and Crook, 1986, modified by Bahlburg, 1998).

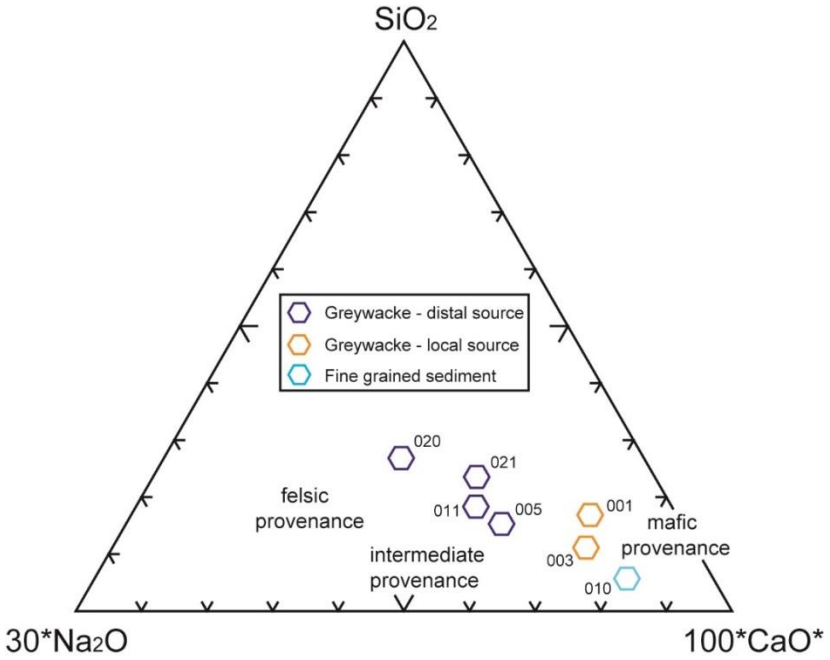


Figure 4.3.13: SiO_2-Na_2O-CaO* diagram highlighting sediment provenance (Ohta, 2008).

4.3.6. TTG rocks:

Three of these are surface samples from TTG plutons, two are drill core samples of granodiorites from within the Aouéouat assemblage (and have been partially discussed elsewhere), and one sample is of a granodiorite clast separated from a sediment at the base of the Tasiast assemblage.

The Aouéouat assemblage granodiorites have SiO_2 values of between 70 and 72 wt%, as does the granodiorite adjacent to the greenstone belt, which is very close to the Archean TTG average of 70.2 SiO_2 wt% (Drummond et al., 1996). TSUPB029 has a slightly higher SiO_2 content of 73 wt%,

consistent with the higher percentage of quartz in this sample, while the granodiorite clast has an SiO_2 value of 75 wt%. TSUPB028 has a lower SiO_2 content, of 66 wt%, which is expected as it is more mafic, containing a larger percentage of hornblende than the other samples. Al_2O_3 values are between 15 and 16 wt% for all samples other than the clast which has 14 wt%. MgO values are <1 wt% for all samples other than the slightly more mafic TSUPB028 which has 2 wt% MgO. The major element geochemistry of all samples classifies them as TTGs according to the parameters defined by Martin (1994), and can all, other than the clast, be sub-classified again as high-Al TTGs, the most common type of Archean TTG (Barker and Arth, 1976, Martin, 1994). These are characterised by elevated Sr and Eu and low Yb and Y contents, strongly fractionated REE patterns ((La/Yb)N up to 150) and high Sr/Y ratios, interpreted as reflecting the presence of garnet and amphibole as well as the lack of any influence by plagioclase, either as residual or fractionating phase (Martin et al., 2005).

Excluding the clast, trace and REE profiles of the TTG rocks are all similar in nature with only some minor differences (Figure 4.3.14). Not much emphasis will be placed on the data from the clast here, and it is worth noting that the sample from West of Imkebdene (TSUPB029) has been affected by a later hydrothermal event. All profiles are LREE-enriched (La_n/Yb_n = 19-51, TSUPB029 = 81), and show negative Nb and Ta anomalies, as are seen in TTG trace element profiles throughout the Archean. There are small negative Ce anomalies in the field samples, most likely due to modern oxidative weathering, however there is also a negative Ce anomaly in the TTG clast. The sediment from which the TTG clasts were extracted is extremely sheared, and lies very close to the base of the Tasiast assemblage, and so this anomaly is probably caused by later oxidative fluids passing along the shear zone. The shear zone may also explain the high SiO_2 content of the clast, with silicification possibly having affected this rock. Unlike the majority of samples analysed, there are only very small negative Eu anomalies, and only in some of the TTG samples. The hydrothermal alteration of TSUPB029 does not appear to have had any major effect on the REE content, other than possibly on Eu. Plotted against the average REE contents of Archean TTG rocks, there are no significant differences apparent other than the negative Ce anomalies already discussed (Figure 4.3.15).

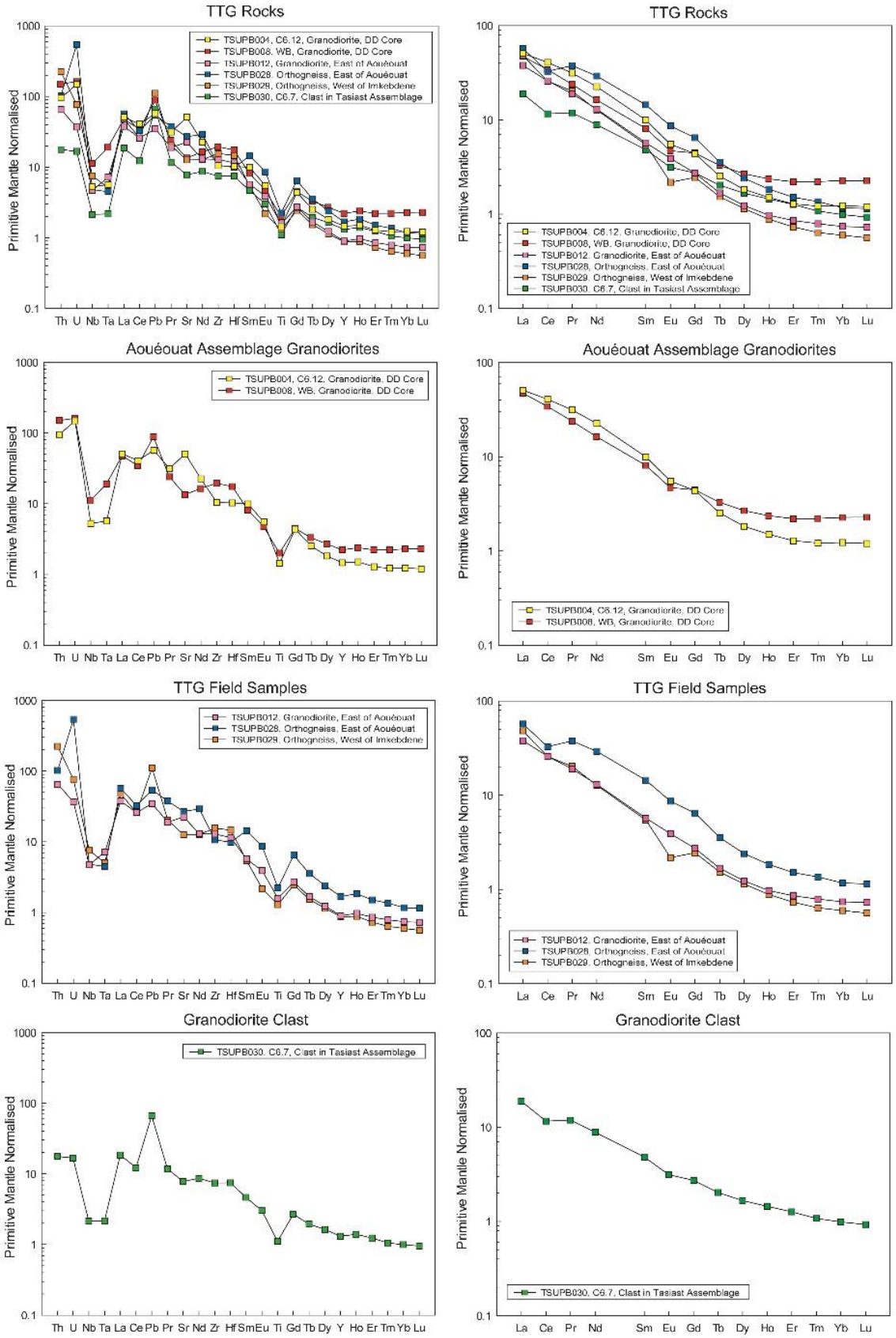


Figure 4.3.14: TTG trace and REE plots.

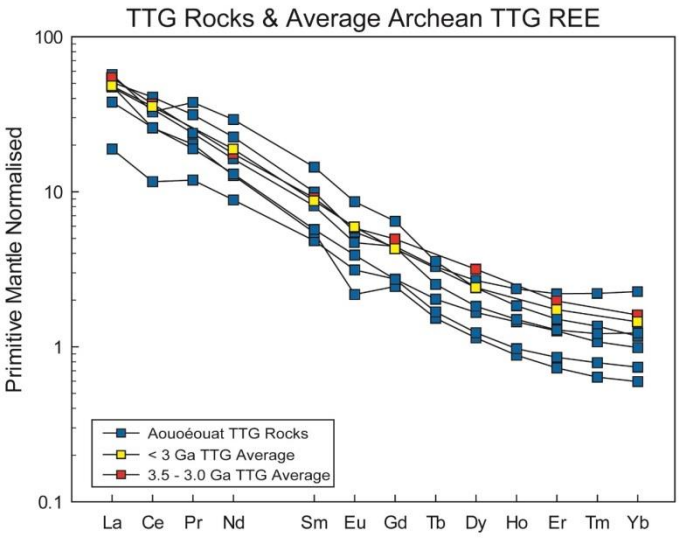


Figure 4.3.15: TTG REE plot of Aouéouat TTG rocks with two Archean average REE profiles also plotted. Archean average values from Martin et al. (2005).

Nb/Ta ratios range between 10 and 16, i.e. sub-chondritic, for the Aouéouat granodiorites and TSUPB012, the pluton adjacent to the greenstone belt. A higher Nb/Ta ratio of 19 (higher than chondritic) is recorded for the orthogneiss east of Aouéouat, and a much larger ratio of 27 for the orthogneiss West of Imkebdene, possibly affected by late hydrothermal alteration (Figure 4.3.16a). The significance of the Nb/Ta ratio is that a low ratio reflects preferential transport of Ta over Nb during processes such as slab dehydration, however if the slab was melted during subduction then a chondritic, or higher than chondritic Nb/Ta ratio would be expected (Kamber et al., 2002).

A difference between Archean TTG rocks and post-Archean granitoids is that Archean TTG rocks are characterised by high La/Yb ratios at relatively low Yb contents, while post-Archean granitoids have low La/Yb ratios and high Yb contents, i.e. Archean TTG rocks are more depleted in HREE (Martin, 1986). A plot of La/Yb_{CN} vs Yb_{CN} can be used to highlight this. It was suggested that the difference in HREE contents between Archean TTG rocks and post-Archean was caused by partial melting of the slab contributing towards the source of Archean TTGs, while post Archean granitoids were sourced from the melting of the mantle wedge (Martin, 1986), however Kamber et al. (2002) showed that adakites do not have as strong HREE-depletion as Archean TTGs, and plot within the post Archean granitoid field (including the area which overlaps with Archean TTG rocks). All of the samples analysed here plot within the Archean TTG field, only TSUPB008 plots in the area which overlaps with the post Archean granitoids field (Figure 4.3.16b). This is not unexpected due to the rocks being Archean in age and petrography classifying them as tonalitic/granodioritic in composition, however this again confirms that the granitoid rocks within and around the Aouéouat greenstone belt are typical Archean TTG rocks.

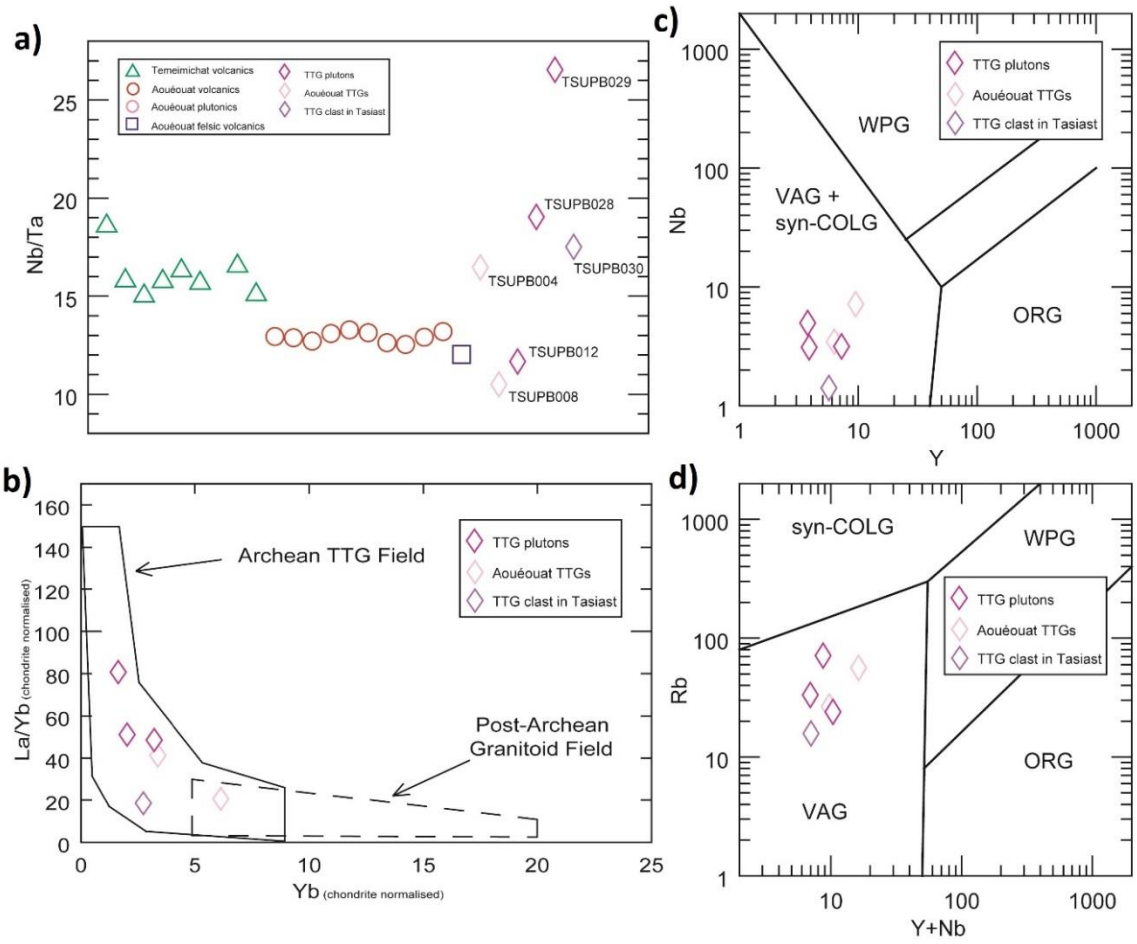


Figure 4.3.16: a) Nb/Ta ratio plot. Ratios for reference: NMORB – 17.65 (Sun and McDonough, 1989), CHUR – 17.65 (McDonough and Sun, 1995), Average Continental Crust – 13.69 (Kamber et al., 2005). b) Plot of La/Yb_{CN} vs Yb_{CN} (Martin, 1986), Chondrite normalised using McDonough and Sun (1995). c) Nb-Y discrimination diagram classifying granitoids according to their tectonic setting; VAG: volcanic-arc granitoids, syn-COLG: syn-collisional granitoids, WPG: within-plate granitoids, ORG: Ocean-ridge granitoids (Pearce et al., 1984). d) Rb-(Y+Nb) discrimination diagram (Pearce et al., 1984), abbreviations as before.

Two further discrimination plots are presented here in order to discuss the tectonic setting of the TTG rocks. These are the Nb-Y discrimination diagram, and the Rb-(Y+Nb) discrimination diagram (Pearce et al., 1984). The Nb-Y diagram plots all of the samples within the volcanic-arc and syn-collisional field (Figure 4.3.16c). The Rb-(Y+Nb) diagram further distinguishes between these two environments, with all samples plotting within the volcanic-arc field (Figure 4.3.16d). The likely tectonic environments in which the Aouéouat assemblage was formed according to the trace element plots presented above, i.e. rocks of an island-arc affinity, match this proposal for the TTG rocks according to the diagrams used here.

It should be noted that the TTG samples were primarily collected for representative geochronology, hence the low sample size covering only a tiny proportion of the Aouéouat

greenstone belt and surrounding region. It was stated by Kamber et al. (2002) that there is very large variability in TTG rock chemistry through the possibility of multiple melt sources and assimilation events, as well as the heterogeneity of hand specimens even within a relatively small outcrop, and therefore taking average values is more representative. A large sample size of TTG rocks was not possible here, and hence these samples may not be fully representative of the TTG geochemistry of the region, however they do cover a range of TTG rocks spatially, petrographically and geochemically.

4.3.7. Banded iron formation:

The banded iron formation was sampled from the Piment deposit. This was processed in its entirety, without micro-sampling of individual bands, and gave an SiO_2 content of 35.6 wt%, and an Fe_2O_3 content of 59.5 wt %, with the total combined SiO_2 and Fe_2O_3 making up > 95% of the rock. Al_2O_3 accounts for 1.5 wt%, K_2O 0.4% and Na_2O was below the detection limit. Alexander et al. (2009) showed that an Al_2O_3 content > 0.5 wt% in BIFs is indicative of a significant volume of detrital material within the sample. These elements are therefore almost certainly enriched in the illite, chlorite and garnet rich layers present in the rock. The REE profile shows a LREE-enriched pattern with a relatively high positive Eu anomaly (1.34) (Figure 4.3.17), representative of Algoma-type BIF and associated with local volcanic activity (Huston and Logan, 2004). The Y/Ho ratio is relatively low, at 33.9, and the trace element pattern shows negative Nb (0.13), Ta, Sr (0.54), Zr, Hf, and Ti (0.21) anomalies. The petrography, as well as the high Al_2O_3 content, highlights the detrital component of this sample which is therefore included in all of the trace element ratios that can be calculated. The relatively low Y/Ho ratio is therefore likely a mixed

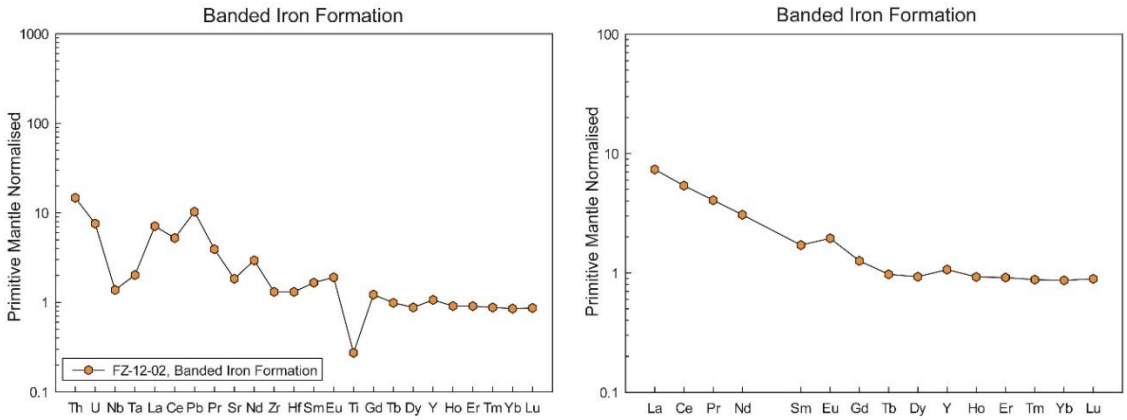


Figure 4.3.17: BIF trace and REE plots.

signature between a seawater signature contained within the silica and Fe-oxide bands (typically ~2 times higher than crustal ratios, ~60-70 (Nozaki et al., 1997)), and a crustal signature contained within the detrital material (Y/Ho_{MuQ}=26.1). The Y/Ho value of 33.9 is comparable to Y/Ho values

obtained by Alexander et al. (2009) in samples with significant Al_2O_3 content. Elements such as Th, Nb and Zr, which are insoluble in seawater, are also enriched by a factor of 10 when compared to other Archean chemical sediments (Bolhar et al., 2004), another indication that the trace element signatures of FZ-12-02 are strongly influenced by a detrital component.

4.2.7. Pegmatite:

The late stage pegmatite found throughout the Aouéouat greenstone belt and surrounding rocks has an SiO_2 value of 74.4 wt% and an Al_2O_3 value of 15.7 wt%. Ti, Fe and Mg contents are all below detection limit, and it has the highest K_2O content of all rocks analysed, at 3.5 wt%, due to the large percentage of K-feldspar in the rock. The REE profile is slightly U-shaped, and unlike the other magmatic rocks analysed, is irregular and not smooth, with a large negative Eu anomaly (0.04) (Figure 4.3.18). The irregular REE profile is due to the 'lanthanide tetrad effect', which is commonly seen in highly evolved magmatic systems. The non-chondritic ratios of Y/Ho (31.8) and Zr/Hf (16.1) are also indicative of processes other than CHARAC-behaviour (charge and radius controlled) being responsible for the distribution of REEs in the sample (Bau, 1996). The Y/Ho and Zr/Hf ratios of TSUPB006 are similar to those of the high silica granitoids of Erzgebirge, Germany (Förster and Tischendorf, 1994). These are interpreted to be transitional melts between pure silica melts and aqueous fluids, which is possibly also the case for the pegmatite TSUPB006. In the trace element profile, there are negative Sr (0.24) and Ti (0.02) anomalies, again indicative that this is a highly evolved melt with plagioclase and titanium-oxides remaining in the restite, and positive U, Pb, Zr and Hf anomalies, possibly causing a large volume of high-U zircon. It is the only sample from out with the Temeimichat assemblage without a negative Nb anomaly.

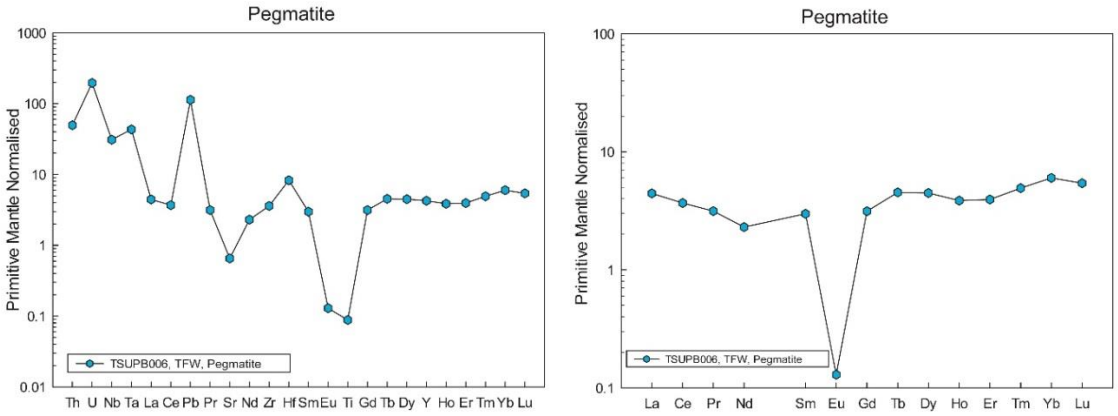


Figure 4.3.18: Pegmatite trace and REE plots.

4.4. Pb Isotopes:

In order to further study the Tasiast deposit mineralisation event, Pb isotope analysis was carried out on sulphides from mineralised quartz-veins, and feldspars from TTG rocks. There were three aims to this experiment: 1) to examine if Quadrupole-LA-ICP-MS is a viable method for measuring Pb isotopes, 2) to determine if there is a difference between the Pb isotope composition of sulphides from different quartz-carbonate veins, and therefore mineral deposits, in order to elucidate if there were multiple hydrothermal events, 3) to determine if there are any possible genetic links between the mineralisation events and surrounding TTG rocks.

Upon collection of the data, a number of issues were raised from this experiment. Due to the method used for data collection being Q-LA-ICP-MS, the errors are significant in size (2-3 orders of magnitude greater than the accepted multi-collector TIMS values (Woodhead and Hergt, 2001), 1-2 orders of magnitude greater than errors collected using multi-collector LA-ICP-MS (Tyrrell et al., 2009)); however the standard data are within error of the accepted values (see Chapter 3.4.6). This highlights that with a large enough sample size, Pb isotope data collected from Q-LA-ICP-MS can be accurate, but is less precise than TIMS or multi-collector LA-ICP-MS methods. The TTG rocks contain only small amounts of K-feldspar, which is the preferred feldspar for Pb isotope studies due it accepting a higher amount of initial Pb (Doe and Tilling, 1967). This resulted in plagioclase feldspar being used to represent the TTG rocks as part of this study. It has been shown that plagioclase can be used to measure Pb isotopes (Souders and Sylvester, 2010) and so should not pose problems with distinguishing populations, however the resultant relatively high proportion of radiogenic Pb in plagioclase feldspars removes the possibility of plotting the samples on a Pb-growth curve in order to calculate crystallisation ages. Pyrite was used to represent the mineralisation event due to its abundance in the mineral separates, and crystal quality, however it largely excludes Pb during formation. The few Pb isotope data points retrieved from the pyrite are therefore probably sourced from small galena inclusions within the pyrite crystals.

Pb isotope data were acquired from four quartz-carbonate vein pyrite separates and five TTG rock plagioclase separates. $^{207}Pb/^{204}Pb$ vs $^{206}Pb/^{204}Pb$ and $^{208}Pb/^{204}Pb$ vs $^{206}Pb/^{204}Pb$ plots are presented in figure 4.4.1a,b, in which pyrite Pb isotope ratios are presented as error crosses, and plagioclase Pb isotope ratios are presented as envelopes which encompass all analysis and associated errors. The quartz-vein samples collected from the field (TSUPB026 & TSUPB027) did not contain any sulphides that were usable due to surface weathering effects, and the TTG clast (TSUPB030) was split into two distinct populations, though this may not be significant.

Without over-interpreting these data, there are a few clear results apparent. TSUPB016 does not overlap with any of the other quartz-carbonate veins, all of which plot within error of each other, suggesting that TSUPB016 formed from a different hydrothermal event than the other quartz-carbonate veins. This is significant in that TSUPB016 is the only quartz-carbonate vein studied as part of this project that is largely barren of gold mineralisation. Little information can be interpreted from the TTG rocks other than TSUPB028 is distinct from TSUPB004 and TSUPB012. Interestingly the TTG rocks TSUPB029 and TSUPB030_2 overlap with the sulphides from TSUPB031 and TSUPB032 (Figure 4.4.1c,d). This suggests that there is a possible link between these samples, in that either the emplacement of TSUPB029 and/or TSUPB030 had some influence on the hydrothermal mineralisation event, or that the hydrothermal event may have affected these TTG rocks. This is discussed in more detail in Chapter 5.2.

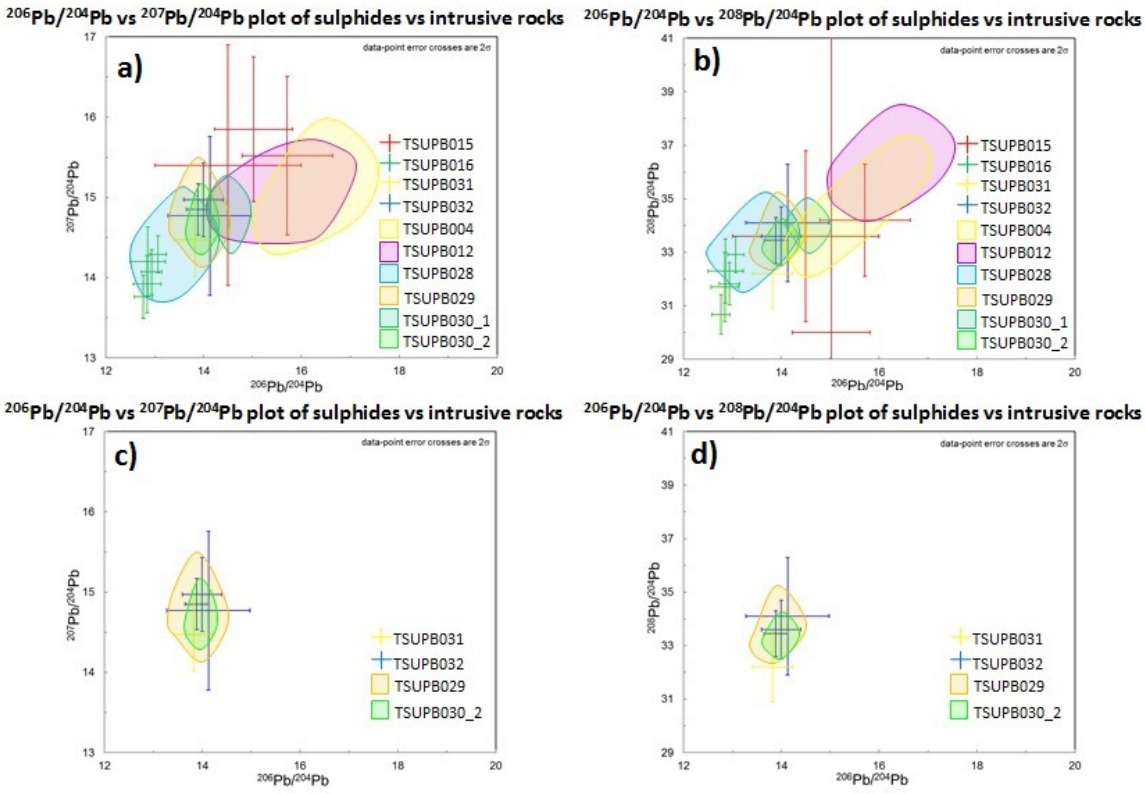


Figure 4.4.1: Pb-Pb isotope plots of pyrite hosted in quartz-veins and feldspars from TTG rocks; a) $^{207}Pb/^{204}Pb$ vs $^{206}Pb/^{204}Pb$ plot of all samples, b) $^{208}Pb/^{204}Pb$ vs $^{206}Pb/^{204}Pb$ plot of all samples, c) $^{207}Pb/^{204}Pb$ vs $^{206}Pb/^{204}Pb$ plot of overlapping samples, d) $^{208}Pb/^{204}Pb$ vs $^{206}Pb/^{204}Pb$ plot of overlapping samples.

Chapter 5: Discussion:

5.1. The Aouéouat greenstone belt and associated rocks:

Petrography, geochemistry and geochronology of representative lithologies from the Aouéouat greenstone belt and associated rocks have been presented in chapter 4. Here these results will be discussed for each of the rock assemblages, along with the processes and environments that could have contributed towards their formation and evolution.

5.1.1. Temeimichat assemblage:

The petrography of the Temeimichat assemblage allows the classification of tremolite schists and amphibolites as the two lithologies that are interbedded together to make up this rock package. The tremolite schists are ultramafic, and are classified as komatiites by multiple geochemical classification schemes (Figures 4.3.2 and 4.3.6). The amphibolites are mafic in composition (> 80% hornblende) and are classified as basaltic komatiites. The striking geochemical characteristic of the Temeimichat assemblage is the consistent LREE depleted signature. Both major and trace element ratios show that this assemblage is tholeiitic in nature, and plots on the mantle array, with Th/Nb ratios close to that of the Archean mantle average as calculated by Pearce (2008). Sm-Nd isotope analysis plot very close to the depleted mantle curve, irrelevant of whether the rocks are close to 3.0 Ga in age, or between 3.3 Ga and 3.2 Ga in age. These data are typical of other Archean komatiites and basaltic komatiites (Barnes et al., 2012, Chaudhuri et al., 2015), and suggest that the rocks are sourced directly from the depleted Archean mantle. There are no apparent signs through either geochemistry or mineral inheritance of any contamination or crustal assimilation involved in their composition. The basaltic komatiites are all classified as low-Th basaltic komatiites using the decision tree from Mukherjee & Gupta (2008) (Figure 4.3.2), and Monroe type komatiites after Arndt (1994). The Low-Th basalt group is the Archean analogue of Phanerozoic LIP basalts, and can be confidently interpreted as the product of a mantle plume or plumes and associated with continental breakup (Barnes et al., 2012). Interbedding of the tremolite schists and amphibolites suggests the protoliths were erupted as either komatiites or komatiitic basalts depending on the degree of mantle melting involved in the genesis of separate melt batches, or due to fractional crystallisation of the source melt, eventually erupting as individual flows. The petrography of the komatiites being predominantly chlorite, with the later crystallisation of tremolite crystals is not unique, with a likely model being that the chlorite was formed by seafloor hydrothermal alteration, with later re-crystallization caused by the regional metamorphism and deformation of the greenstone belt (Rollinson, 1999). All samples from the

Temeimichat assemblage show evidence of a complex history including seawater alteration, greenschist metamorphism, and shearing, in some cases accompanied or followed by an episode of static re-crystallisation.

Although no age data were recovered for any rocks from the Temeimichat assemblage, there is a close association between the Temeimichat assemblage and the Aouéouat assemblage. These two assemblages are separated by an unconformity, and the Temeimichat assemblage possibly represents the lower stratigraphy of the Aouéouat assemblage. Therefore with the Aouéouat assemblage having been dated at 3000 Ma to 2990 Ma, it is probable that the Temeimichat assemblage is not significantly older than this. The most likely environment for formation of the Temeimichat assemblage given the geochemical, petrographic and age evidence is a mantle plume derived Archean oceanic plateau. Deducing the nature of the rocks on which it was deposited is more of a challenge. The presence of a proximal 3.3 Ga to 3.2 Ga basement is very likely, however no signs of this were found in the Temeimichat assemblage itself. It is possible that the Temeimichat assemblage was ensialic in nature, being deposited on this basement, with an absence of contamination being achieved through insulation in feeder pipes resulting in the rocks here retaining their source geochemical signature. A preferred interpretation is that the presence of a mantle plume resulted in a rifting event in the gneissic basement, and subsequently the Temeimichat assemblage was deposited in the rift basin (Figure 5.1.1).

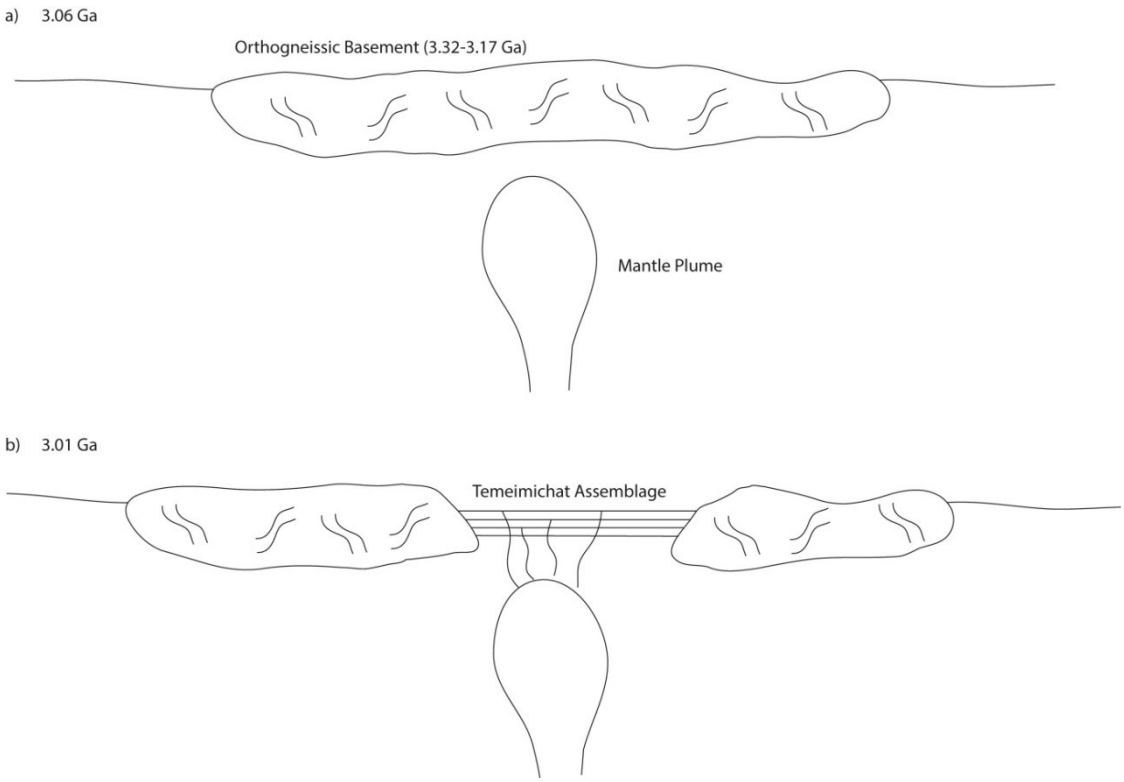


Figure 5.1.1: Sketch of preferred model for Temeimichat assemblage formation environment.

5.1.2. Aouéouat assemblage:

A number of different lithologies are present in the Aouéouat assemblage. A large proportion of the analysed samples are amphibolites, with varying degrees of hornblende content (~30-60%). These are classified as mafic to intermediate volcanic rocks, and were likely erupted as basalts or basaltic andesites depending on individual composition. One felsic volcanic rock was also sampled. It is difficult to classify the original nature of the felsic volcanic rock due to later alteration and metamorphism, but it was likely either a dacite or rhyolite, or a felsic volcanic tuff. Most of the plutonic rocks are quartz-dioritic to dioritic in composition. These were probably emplaced as dykes or sills, related to the feeder system of the volcanic rocks. All of the Aouéouat assemblage rocks have undergone a complex alteration, metamorphic and shearing history. Some rocks have been more affected by these processes than others, seen clearly by the different states of the quartz-diorite samples, likely linked to the proximity of local shear zones. Late static re-crystallisation has also affected a number of these samples, while others have kept their strongly sheared fabric in its entirety.

Crystallisation ages of three samples have allowed the Aouéouat assemblage to be dated to between 3000 Ma and 2990 Ma. One of these samples is a highly sheared TTG rock, probably a granodiorite, also emplaced as a localised intrusion related to the feeder system of the volcanic rocks. A relatively unaltered tonalite-granodiorite sampled from the Aouéouat assemblage gives an age of 2960 Ma. Due to its petrography and age being similar to those of TTG plutons bordering the Aouéouat greenstone belt, this is interpreted to be a later intrusion associated with the emplacement of the TTG plutons (Figure 5.1.2).

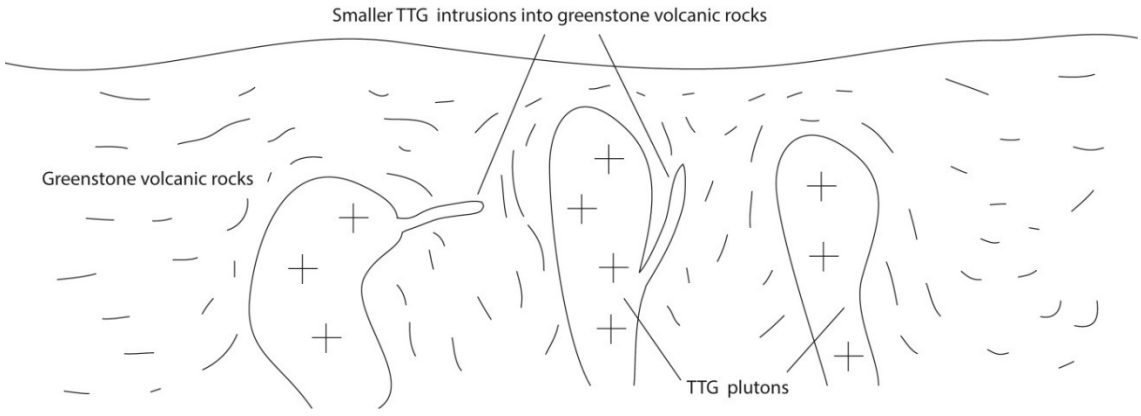


Figure 5.1.2: Sketch of interpretation for small younger TTG rocks within the Aouéouat greenstone belt stratigraphy.

The mafic to intermediate volcanic and plutonic rocks of the Aouéouat assemblage all follow a tholeiitic trend, are slightly LREE enriched, and have high Th/Nb ratios. Trace element ratios (including Th/Nb) suggest these rocks contain a crustal component, with values close to those of average continental crust. Supporting the notion of a crustal-derived component in the Aouéouat assemblage rocks, is the fact that a number of inherited zircons have been found in the samples from this assemblage which range in age from 3293 Ma to 3178 Ma. This crustal component could be derived by crustal contamination during their passage through continental crust, or alternatively could signify a crustal component at source due to subduction. Geochemical signatures such as those observed in the Aouéouat assemblage lithologies are often attributed to an 'arc signature' in Archean greenstone belts, due to similarities with geochemical signatures obtained from modern day island arcs.

Four samples from the Aouéouat assemblage were analysed for Sm-Nd isotopes. These indicate the Aouéouat assemblage was not directly sourced from depleted mantle, with Nd model ages calculated between 3.27 Ga and 3.17 Ga. The significance of these Nd isotope data suggests the Aouéouat assemblage was either extracted from depleted mantle between 3.27 Ga and 3.17 Ga, or has assimilated crust that was extracted from the mantle between 3.27 Ga and 3.17 Ga, or earlier. The possibility of the formation of the Aouéouat assemblage being through fractional crystallisation is highly unlikely for a number of reasons, including: a lack of gabbro and peridotite members suggesting that the source is the partial melt of a mafic rock, that there is no significant enrichment of potassium in any lithologies which would have occurred during fractional crystallisation, and that there is relative LREE enrichment, likely due to the presence of a garnet bearing restite.

What is certain, as documented by the presence of xenocrystic zircons, and diagnostic trace element ratios (e.g. Th/Nb, La/Sm) and Nd isotopes ($\varepsilon Nd_{3.0Ga}$ = 0.41 to -1.09), is that the Aouéouat assemblage contains an older crustal component, and is not sourced directly from the mantle. It is not clear however, as is the case for almost all Archean greenstone belts, whether the reason for this crustal component is due to subduction, or later-stage crustal contamination. Note that Pearce (2008) states that other methods to obtain a crustal signature in Archean basalts include mantle re-fertilisation through delamination and later element mobility during metamorphism, however these can almost certainly be ruled out here due to the presence of inherited xenocrystic zircons. It is likely, no matter what the mechanism for producing the Aouéouat assemblage was, that it was erupted through a Paleoarchean sialic crust and not within a juvenile ocean or oceanic-arc environment. The only other plausible method to achieve such a strong crustal signature

would be the subduction and melting of either orthogneissic basement itself, or sediments associated with subduction.

Importantly, all of the above data from the Aouéouat assemblage distinguishes it clearly from the Temeimichat assemblage, upon which it unconformably lies. There are three viable mechanisms by which the Aouéouat assemblage could have been formed; 1) subduction, 2) vertical tectonics, 3) mantle plume. These three models are presented below, in which a key point that must be incorporated into any model is that there is no crustal component to the Temeimichat assemblage, but that there has to be a crustal component of at least 3.2 Ga in the Aouéouat assemblage.

1) If the driving force behind the formation of the Aouéouat assemblage was subduction, then presumably the subducting plate was driven beneath the Temeimichat assemblage, resulting in the Aouéouat assemblage being erupted through it and deposited on top. Due to the presence of an older crustal component, this requires that either the arc signature was obtained from melting of the downgoing slab (Figure 5.1.3a), or that the Temeimichat assemblage was deposited on, or tectonically associated with a gneissic basement from which the crustal contamination could have been sourced (Figure 5.1.3b).

2) If the formation of the Aouéouat assemblage was through vertical tectonics, somehow there has to be a mechanism by which the Temeimichat assemblage is closely associated with a gneissic basement in order to source the older crustal component. One way in which this could have been achieved, is if the Temeimichat assemblage was initially erupted onto the gneissic basement. Vertical tectonics and 'sagduction' due to the overburden of the Temeimichat assemblage could then have resulted in the partial melting of the underlying gneissic basement, which became the source, at least in part, of the Aouéouat assemblage (Figure 5.1.3c).

3) An alternative, and more plausible scenario in relation to the discussion on the Temeimichat assemblage above, is that the Temeimichat assemblage, sourced from a hot Archean mantle plume, initiated rifting in an established continent, within which the Temeimichat assemblage was deposited. The relative migration of the mantle plume subsequently resulted in the melt passing through the orthogneissic basement en route to eruption (Figure 5.1.3d).

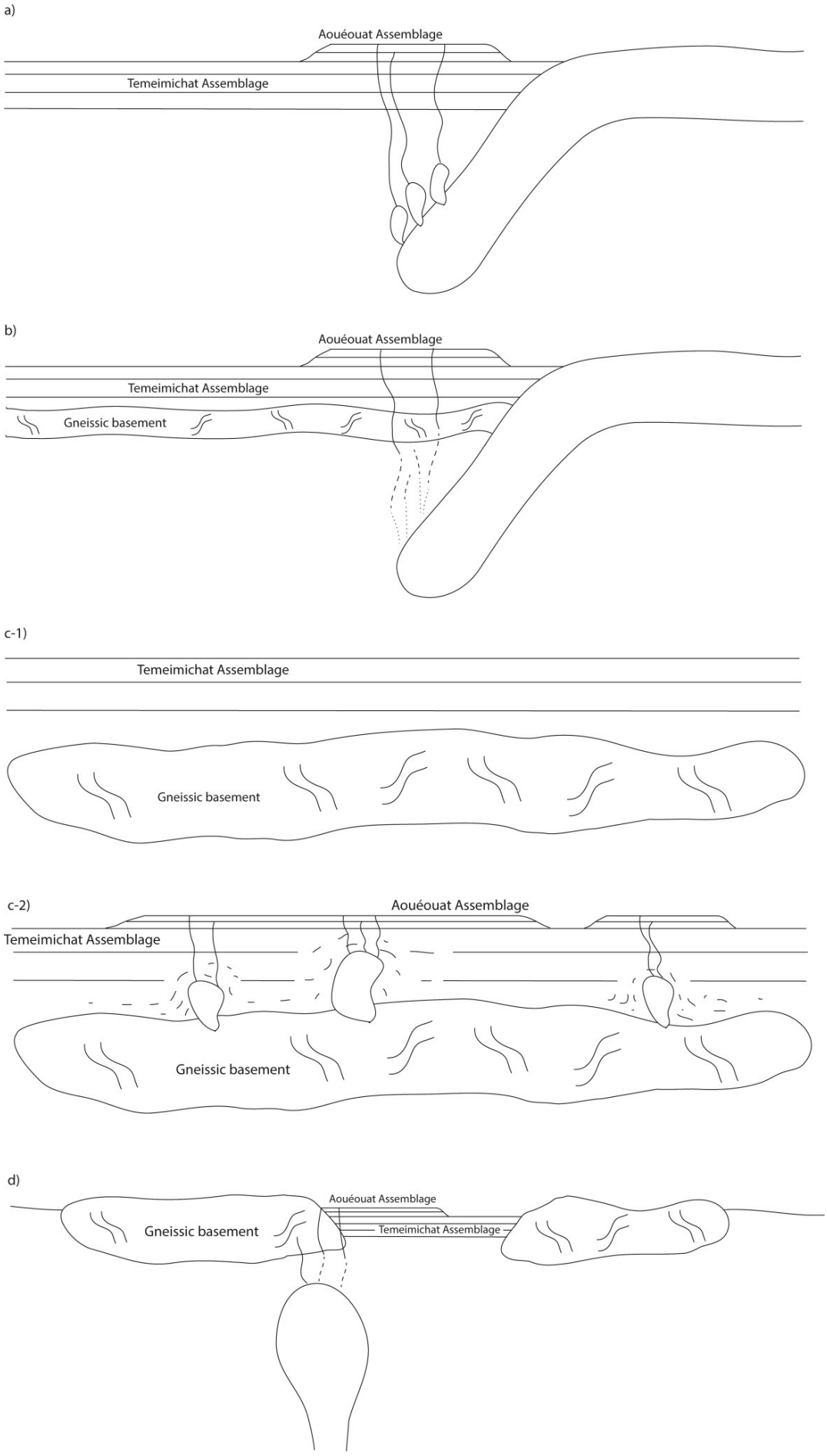


Figure 5.1.3: Sketch of possible models for Aouéouat assemblage formation environment.

5.1.3. Tasiast assemblage:

The petrography, geochronology and geochemistry of the Tasiast assemblage allows the general distinction of three different groups of sedimentary rocks, all of which have undergone later metamorphism and shearing. The first are the C6.7 sedimentary rocks, which petrographically appear to have originally been greywackes, and are relatively immature in nature with a mafic component. Major element contents and trace element ratios support this interpretation, suggesting their source rocks have more of a mantle derived signature than a continental crustal one, and that the sediments came from a relatively local source (Figures 4.3.12, 4.3.13). One of the samples from C6.7 (TSUPB003) has a single detrital age population of 2996 Ma, which suggests that it was sourced directly from the Aouéouat assemblage, and is probably a reworked crystal tuff. It is possible that the second sample (TSUPB001) was also solely sourced from the Aouéouat assemblage, however the detrital zircon have all been overprinted by a younger hydrothermal event other than two extremely old inheritance ages (3385 Ma and 3510 Ma). The nature of TSUPB001 makes it difficult to distinguish between being a relatively primitive sediment and an altered fine grained igneous rock. It is possible therefore that this is simply a reworked ash fall from a volcanic bed. These sediments make up the oldest stratigraphy of the Tasiast assemblage, with TSUPB003 being collected from ~8 m above the base of the sedimentary units. It is worth also mentioning TSUPB030, the rock from which the TTG clasts were dated. This sample was collected from the base of the Tasiast assemblage, only 6 m from TSUPB003. One of the TTG clasts from this sample was dated at 3059 Ma, which is not recorded at all in the overlying sediment. This means that during the initial stages of sediment deposition, an exposed TTG was eroded into the basin, possibly from rift flanks, or local highs in topography. This source was then not subsequently utilised as a source for overlying sediments. This is seen in other greenstone belts, for example in the East Pilbara Craton, detritus from much older surrounding rocks or from eroded TTG domes is seen in the basal sandstones which are largely composed of sediments from the younger volcanic cycles (Van Kranendonk et al., 2007a). Although classified as a conglomerate, it is possible that this sample is in fact a mylonite from a shear zone that has been active along the contact between the Aouéouat assemblage and the Tasiast assemblage. An alternative explanation for the lack of evidence for this TTG in the overlying sediment is that it could have been incorporated into the shear zone from elsewhere, which would negate the need for it to be exposed as an initial local TTG source.

The sedimentary rocks from the TFW and West Branch can also be classified as having originally been greywackes, however these have a greater degree of sorting, and are more evolved with a higher SiO_2 content and fewer mafic minerals. This petrographic evidence, along with trace

element ratios (e.g. Th/Sc, Ti/Zr), suggest these rocks have a more distal source, with the two unaltered West Branch samples (TSUPB020 and TSUPB021) being the most mature sedimentary rocks from the Tasiast assemblage. Detrital zircon geochronology adds support to this interpretation. The TFW sample (TSUPB005) is sourced from a range of rocks with ages between 3074 Ma and 2964 Ma. These are interpreted as being the TTG plutons which surround the Aouéouat greenstone belt, the Aouéouat assemblage, and an unaccounted for younger basement component, which is also seen in the conglomerate. There is also one zircon with an older age of 3175 Ma, which is interpreted to be a detrital zircon of igneous origin, with an inherited core. The unaltered West Branch sedimentary rocks have the same populations present, however these are distinguishable from one another, and correspond to the three source rocks named above, i.e. the TTG plutons which surround the Aouéouat greenstone belt, the Aouéouat assemblage, and an unaccounted for younger basement component. In addition to these populations, > 50% of the detrital zircons from the unaltered West Branch sedimentary rocks belong to a population of older detrital zircons between 3320 Ma and 3170 Ma. These are interpreted to have been sourced from an older orthogneissic basement. This interpretation of a basement contribution to the sediment provenance is also supported by the presence of inherited zircons seen in the Aouéouat assemblage. The most likely explanation for this latter population being present in these rocks is that they have a more distal source, which has reached the extent of exposed orthogneissic basement. Another possibility is that the erosion and uplift leading to deposition of the older sediments has exposed the gneissic basement, which can now also be utilised as a source. Therefore it may not necessarily be only a distal component to the diversity of the sediments, but could be due to the available exposed rocks in the region.

Finally, TSUPB010, also collected from West Branch is a fine grained sediment, composed of ~50% mica, interpreted to represent original deposition of fine grained clay minerals. It is likely that this sample is either from the top of a Bouma sequence associated with the West Branch greywackes, or was deposited during a period of relative quiescence in the region.

As seen from the above discussion, the oldest component of the Tasiast assemblage appears to be composed of locally derived sediments, and over time progressively younger strata utilise more distal sources resulting in a greater range of source rocks and a higher degree of sorting. Two models in which this could be possible are: 1) the closing of a rift basin in which the Temeimichat and Aouéouat volcanic rocks were deposited has brought more diverse lithologies within source range, or 2) the formation of basins and topographic highs resulted in the combined effects of gradual exposure and erosion of lower stratigraphy, i.e. Temeimichat and Aouéouat volcanics,

followed by TTG rocks, followed by gneissic basement rocks, as well as more distal source rocks being raised in topographic highs allowing for erosion.

5.1.4. TTG rocks:

A number of TTG rocks closely spatially associated with the Aouéouat greenstone belt were sampled. A strongly sheared TTG rock from within the Aouéouat assemblage (TSUPB008) was dated at ~2996 Ma, and has been classified as part of the Aouéouat assemblage. A TTG clast (TSUPB030) from the base of the Tasiast assemblage has been classified along with the Tasiast assemblage. TSUPB004 and TSUPB012 are both porphyritic TTG rocks that plot close to or on the tonalite-granodiorite boundary on the QAP diagram (Figure 4.1.20). TSUPB012 was sampled from the TTG pluton adjacent to the Aouéouat greenstone belt, while TSUPB004 was sampled from within the Aouéouat assemblage. The petrography and geochronology of TSUPB004 suggest that it is a later intrusion into the Aouéouat assemblage, associated with the TTG plutons and not the Aouéouat assemblage itself (Figure 4.2.4). The ages of these two samples are within error of each other (2960 ± 9 Ma and 2967 ± 11 Ma) and geochemically and petrographically they are very similar in nature, with TSUPB004 showing signs of slightly stronger shearing than the other due to it being sampled from within the Aouéouat greenstone belt. There is very little difference in the major element geochemistry between the two samples, with some geochemical differences (i.e. concentrations of FeO and K_2O) which may be accounted for by surface weathering of TSUPB012. Therefore it is possible that these two samples are in fact from the same TTG pluton which has intruded into the Aouéouat greenstone belt. If they are from different TTG plutons, which remains possible due to the differences in some trace element ratios, they are almost certainly linked by being part of the same large scale intrusion event that is associated with the Aouéouat greenstone belt. However some differences can be expected when sampling TTG rocks due to their heterogeneity (Kamber et al., 2002) as discussed in chapter 4.3.6.

TSUPB028 and TSUPB029 were both sampled from further afield relative to the greenstone belt in an attempt to date the orthogneissic basement. These show minor shear fabrics. TSUPB028, from the east of the Aouéouat greenstone belt is tonalitic in composition, and probably had a mafic component to its source melt resulting in it having the highest Mg and Fe content of the TTG rocks sampled for this project, which is visibly seen with hornblende and biotite crystals accounting for ~20% of the rocks composition. TSUPB029 is slightly coarser grained, and plots close to the tonalite-granodiorite boundary on the QAP diagram (Figure 4.1.20). It is clear that these samples do not represent the gneissic basement, as is seen by their geochronology. TSUPB028 has a crystallisation age of 2933 Ma. TSUPB029 has a slightly more complicated history,

with three age populations. Two of these are at 2974 Ma and 2928 Ma one of which is probably a crystallisation age. A possible interpretation for TSUPB029 is that the younger age of 2928 Ma is the crystallisation age of this rock, which has assimilated an older rock in its melt. The older rock had a crystallisation age of 2974 ±7 Ma, and is probably an older TTG rock from the region. This theory is also backed up by the extent of xenoliths of different TTG rocks contained within the plutons from which these samples were collected (Figure 2.5.9). The third event to affect TSUPB029 is a hydrothermal event at ~2830 Ma, which will be discussed in detail in chapter 5.2.

To summarise the Aouéouat TTG rocks, there was a period of TTG plutonism from ~2970-2960 Ma, which is 20-30 Myrs later than the crystallisation of the greenstone belt volcanics. There is also evidence of a second period of TTG plutonism at ~2940-2920 Ma. There are further detrital and inheritance ages that have been attributed to TTG plutons between 2960 Ma and 2940 Ma, though these have less precise data, and could be attributed to either of the two TTG plutonic events already mentioned. Due to the small number of TTG rocks sampled for dating, it is possible that there was either continuous, or punctuated TTG plutonism over the entire time span of 2970-2920 Ma. This however cannot be deduced from the data available.

TTG rocks associated with the Aouéouat greenstone belt are typical of those seen in granite-greenstone terranes worldwide, in that they surround the greenstone belt, and occupy a much larger spatial extent than the greenstone volcanic rocks and sedimentary rocks of the region. They also have the same geochemical characteristics of Archean TTG rocks, including strongly fractionated REE profiles, elevated Sr and Eu and high Sr/Y. It was concluded in chapter 2.3 that these TTG rocks require melting of hydrated mafic rocks at depth, with multiple possible models for the formation of the TTG plutons in Archean granite-greenstone terranes also being discussed. The two most common models used to explain TTG rock formation in granite-greenstone terranes those associated with either subduction, or vertical tectonics. Due to the extensive discussion on TTG rock formation in chapter 2.3.5 these are only briefly discussed here.

If the TTG rocks were formed due to active subduction, it would also possibly be expected to see associated volcanic rocks with these ages, and likewise if the Aouéouat assemblage was formed as a result of subduction, it would possibly be expected to observe TTG rocks associated with this assemblage. Neither of these two scenarios are evident, which is not to say they do not, or did not at one point exist. The relatively small number of sampled TTG plutons in this study cannot be used to represent all of the TTG rocks in the region, and younger volcanic rocks could have been eroded away completely, or exist in unexposed greenstone belts. The assumption made from detrital zircons in the Tasiast assemblage is that all of the zircons dated between 2980 Ma and

2900 Ma are associated with TTG rocks, due to these being the only rocks known of this age. Some of the detrital zircons could however be sourced from volcanic rocks of this age that once existed, or have not been sampled.

If the TTG rocks associated with the Aouéouat assemblage were formed through vertical tectonics, it would be required that the process of sagduction was long-lasting, with multiple phases of new TTG plutons rising over ~50 Myrs. Extended periods of TTG plutonism are seen in other Archean cratons which have had vertical tectonics proposed as a viable tectonic model (e.g. Pilbara (Collins et al., 1998), and Superior cratons (Benn and Moyen, 2008)). A vertical tectonic model for the formation of the TTG rocks associated with the Aouéouat assemblage can incorporate models for both the Temeimichat assemblage and the Aouéouat assemblage which were discussed in chapters 5.1.1 and 5.1.2., and so this is a viable mechanism under which the TTG rocks associated with the Aouéouat assemblage could have been formed.

Alternate models that can explain periods of TTG plutonism are tectonic events such as basin formation during transtensional rifting of the volcanic rocks, or early stages of inversion of a basin which was generated during a rifting event, however these are unlikely to extent over time periods as long as 50 Myrs as is the case in the Aouéouat greenstone belt. Delamination of the root zones of the volcanic stratigraphy may also have allowed formation of the TTG rocks, with multiple delamination events being required to account for the 50 Myr timespan of TTG rock forming events. Although any of these latter scenarios could possibly fit with models which incorporate the Temeimichat, Aouéouat and Tasiast assemblages, the preferred model is that of vertical tectonics resulting in the partial convective overturn of the Temeimichat and Aouéouat assemblage greenstone belt volcanic rocks. This is due to the lack of association between TTG rocks and volcanic equivalents, as well as the extent of TTG rocks which are present throughout the Tasiast-Tijirit Terrane. This is discussed in greater detail in chapter 5.3 in relation to data already published on TTG rocks from the Tasiast-Tijirit Terrane.

5.1.5. Banded iron formation:

The two BIF samples collected for this project were located in the Tasiast assemblage, and are Algoma-type BIF associated with local volcanic or hydrothermal activity. FZ-12-01 is a relatively pure BIF sample, composed of silica and Fe-oxides, with some later carbonate veining affecting the rock. FZ-12-02 has some bands which are relatively pure, however a large proportion of the bands contain either chlorite, illite, and/or garnet, and the sample has also been affected by late carbonate veining. The petrography, along with the geochemical data, highlights there was a

significant volume of detrital material within at least some of the BIF in the Aouéouat greenstone belt, and therefore the basin in which they were deposited was not too distal from a terrestrial source, and almost certainly not the open ocean. Although undated, both samples are clearly isoclinally folded, showing they were affected by the same deformation events that affected the rest of the Aouéouat greenstone belt and so the deposition of BIF of the Aouéouat greenstone belt certainly predate these deformation events. Their depositional environment is likely associated with that of the Tasiast assemblage clastic sedimentary rocks, however the BIF were either deposited during periods of low to no clastic sedimentary input, or were deposited further from a terrestrial source than the Tasiast assemblage clastic sedimentary rocks.

5.1.6. Pegmatite:

The pegmatite, dated at ~2766 Ma represents the youngest rock identified in the area, and is > 150 Ma younger than the TTG intrusions. The geochemical data suggests that this is crystallised from a highly evolved magma, and possibly formed from a transitional melt between pure silica and aqueous fluids. Local hydrothermal alteration associated with the pegmatite event has resulted in the complete re-setting of zircon U-Pb ages in surrounding rocks, as is seen in one of the Tasiast sedimentary rocks (TSUPB011). It also appears to have resulted in the redistribution of mobile elements within the rocks.

As the pegmatite is younger than, and cross-cuts all other lithologies, it highlights that there was still magmatic activity on a regional scale after the formation of the Aouéouat greenstone belt and the surrounding TTG plutons. It is a highly evolved melt, possibly derived from the partial melting of peraluminous rocks at depth. It is not however possible to expand on its tectonic origin without incorporating the geology of the Reguibat Shield as a whole.

5.1.7. Quartz-carbonate veins:

The quartz-carbonate veins are composed of a combination of strained quartz and relatively large (> 1 cm) unaltered quartz crystals. They are all cross-cut by narrow carbonate veins, which appears to be where any mineralisation is concentrated. The quartz-carbonate veins from West Branch, C6.7 and Fennec contain pyrrhotite and biotite in relatively large volumes (generally up to 5% total), along with some relatively minor pyrite. The veins from C6.12 contain tourmaline, and pyrite. The difference in mineralogy of the quartz veins is important, as the veins containing tourmaline are largely devoid of gold, whereas the veins which do not contain tourmaline, and are probably a different generation of quartz veins, host the gold which is mined at Tasiast. The

carbonate veins appear to have a preferred alignment, which along with the presence of strained quartz highlights that these have been affected, at least in part, by shearing, though not to the same extent as the volcanic and sedimentary rocks which form the Aouéouat greenstone belt.

The age of the mineralised quartz-carbonate veins has been dated by U-Pb apatite dating to ~2840 Ma, and is confirmed by the age of hydrothermal zircon which has crystallised as rims around xenocrystic zircons. The xenocrystic zircon ages are consistent with being sourced from the Aouéouat greenstone belt and surrounding TTG plutons. In addition to the gold-bearing mineralised quartz-carbonate veins, an age of ~2840 Ma for this hydrothermal event is also found in a number of other lithologies within and around the Aouéouat greenstone belt. These are: an almost fully re-set sedimentary rock from the Tasiast assemblage (TSUPB001), a partially re-set TTG rock from west of the Imkebdene belt (TSUPB029), and a single concordant zircon from the felsic volcanic rock of the Aouéouat assemblage (TSUPB007). This highlights that gold was deposited by a hydrothermal event which was extensive in nature throughout the Aouéouat greenstone belt, and also possibly affected the surrounding TTG plutons as seen in TSUPB029. A further very interesting inference from the U-Pb apatite data is that the quartz veins, and therefore likely most of the rocks in the region other than those affected by the late pegmatite event or the younger mafic dyke swarms, have not been heated above ~450°C since ~2840 Ma. This has greater implications for the Reguibat Shield and the West African Craton as a whole.

5.2. Gold in the Aouéouat greenstone belt:

One of the primary aims of this project was to study the gold mineralisation at Tasiast in order to further the understanding of its origin and history. The top priority in regards to this was to date the hydrothermal event that concentrated and deposited the gold in the Aouéouat greenstone belt, with any significant mineral component that could be used as a tracer associated with the gold also studied. This should in turn aid with future gold exploration in the region as well as add valuable information to the global database of Archean gold mineralisation worldwide.

It can be stated at the outset of this discussion that the Tasiast gold deposit is certainly an Archean orogenic gold deposit as defined by Groves et al. (1998). The mineralisation at the Tasiast deposit is primarily controlled by the quartz-carbonate veins which carry the gold. Their presence is structurally controlled, focussed in splays off of the main Tasiast thrust which runs N-S through the Aouéouat greenstone belt. The two major deposits that are currently being mined at Tasiast are the West Branch deposit, and the Piment deposit, hosted primarily in the quartz diorites of the Aouéouat assemblage, and metasedimentary rocks of the Tasiast assemblage respectively. In addition to these, a number of further potential deposits in the Aouéouat greenstone belt are currently being explored. There are different generations of quartz-carbonate veins present in the Aouéouat greenstone belt, most of which are syn-tectonic. There is also a compositional difference to the veins which carry gold, and the veins which do not, with tourmaline bearing veins being largely devoid of gold, while those which carry the gold all contain pyrrhotite, pyrite and biotite.

Previous studies attempting to date mineralisation at Tasiast relied on K–Ar dating of low potassium sericite, which gave an age of 1.9 Ga from a white argillised zone at the surface (Marutani, 2005). In the nearby Guelb Moghrein copper deposit of the Mauritanides, distinct morphological types of hydrothermal monazite and xenotime were dated at 2492 ± 9 and 1742 ± 12 Ma respectively (Meyer et al., 2006), highlighting that Paleoproterozoic remobilisation may be a possibility in this part of the Reguibat Shield. Therefore prior to this study a Paleoproterozoic age of mineralisation for the Tasiast deposit was the favoured interpretation (e.g. Marutani, 2005, Taylor et al., 2012). These ages however do not seem to correlate with significant tectonic or magmatic activity in the Tasiast-Tijirit Terrane. Other than these, there have been no previous attempts to directly date mineralisation at the Tasiast deposit, or other deposits in the neighbouring region. For this study, dating of the gold mineralisation event was achieved through a combination of U-Pb zircon and U-Pb apatite geochronology. This resulted in a final accepted

age of 2840 ± 35 Ma. Further details on the quartz-carbonate veins and gold mineralisation can be found in Heron et al. (2015), published as part of this thesis in Appendix 9.

Although one of the main problems in understanding orogenic gold deposits relates to the timing of mineralisation (Groves, 2003, Sarma et al., 2011), this has been successfully accomplished here. The dating of the Tasiast gold deposit has established that it is Mesoarchean in age, and therefore one of the oldest known gold deposits worldwide. It does not correlate with other well-known major gold deposits; it clearly predates the significant Neoarchean period of orogenic gold deposition (2.8-2.5 Ga) (Doyle et al., 2015), and predates the major peak (~2.65 Ma) by almost 200 Myrs. Neither is it as old as the oldest orogenic gold deposits in the Pilbara or Kaapvaal Craton, dated at 3.4 Ga and 3.0 Ga respectively (Neumayr et al., 1998, Schwarz-Schampera et al., 2009). One orogenic gold deposit with an age of 2.82 ± 0.05 Ga is known of, from the São Francisco Craton in Brazil (Vial et al., 2007). Although similar in age to the Tasiast deposit, there is little worth in attempting to link the two of these deposits due to the complex tectonic history that would need to be inferred in doing so. As can be seen from figure 5.2.1, there are very few dated orogenic gold deposits as old as the Tasiast deposit. It is worth briefly mentioning here that this gold deposit is unique within the West African Craton where all of the documented orogenic gold deposits are associated with Eburnean tectonics and date to ~2.1 Ga (Goldfarb et al., 2001).

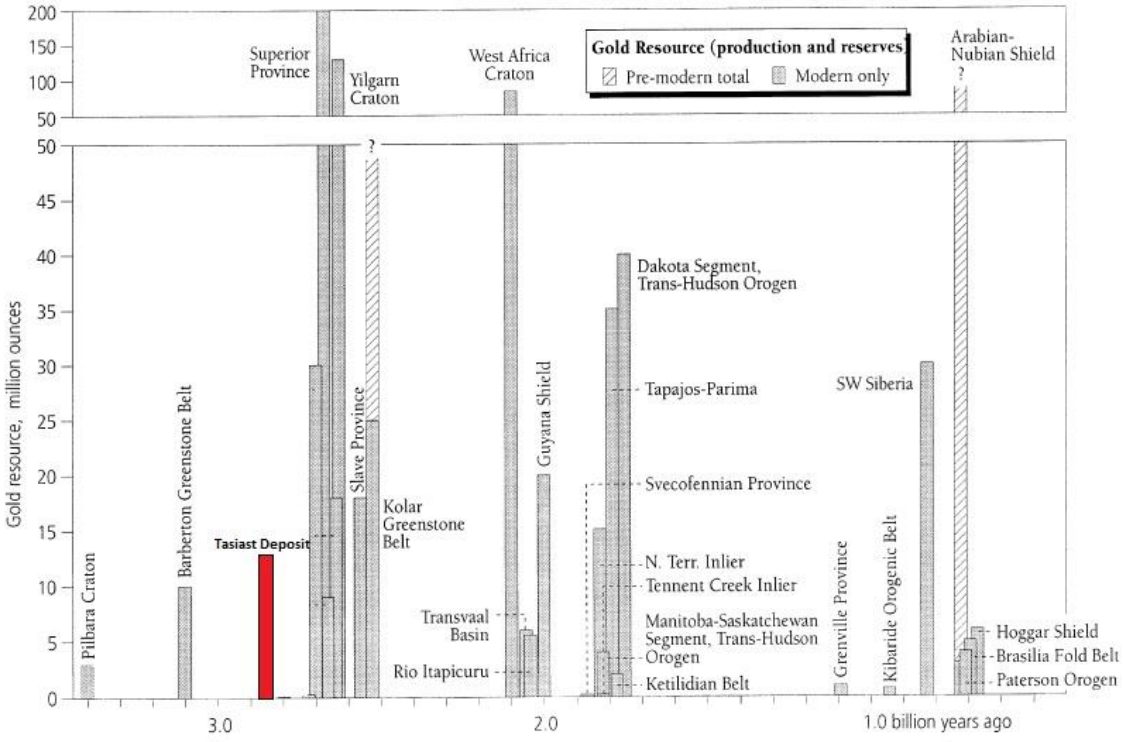


Figure 5.2.1: Gold production vs. best approximation for the age of gold vein formation for Precambrian orogenic gold deposits. Note the Tasiast deposit is highlighted in red, and values are correct as of December 31, 2014, taken from Heron et al. (2015). Figure modified after Goldfarb et al. (2001).

The major Neoarchean orogenic gold deposits are commonly linked to global supercontinent assembly, and the accompanying preservational bias effects that may exist with this. It is therefore possible that the Tasiast deposit may be an artefact of an early continental collision event associated with the assembly of the Neoarchean supercontinent Superia (Bleeker, 2003).

There is a strong link between giant gold deposits and the proximity of juvenile crust, with evidence from this suggesting that the juvenile material acts as the source of the gold. It is also suggested that orogenic gold deposits do not form after cratonisation (Mole et al., 2013). The gold mineralisation at Tasiast is deposited in the Aouéouat and Tasiast assemblages, which are located directly above the Temeimichat assemblage. The Temeimichat assemblage is juvenile in nature, and so this is a strong candidate to be the source of the gold at the Tasiast deposit. Bierlein et al. (2006) made the observation that there is a temporal link between the age of the juvenile rocks and the age of gold mineralisation. In the Aouéouat greenstone belt, the best estimate of this age gap is ~160 Myrs, assuming that the Temeimichat assemblage is ~3000 Ma old, which importantly is also a minimum age gap. The largest Neoarchean giant deposits which contain resources > 100 million oz. gold have a time gap < 100 Ma between the emplacement of the juvenile crust and the gold mineralisation. The time gap associated with the Tasiast deposit is more similar to that at the Barberton greenstone belt and the Southern Cross deposit in the Yilgarn Craton of ~150 Myrs (De Ronde et al., 1991, Mole et al., 2013), both of which are also smaller in size than the largest Neoarchean deposits. This backs up the observations made by Bierlein et al. (2006), that orogenic gold deposits are defined by both the close proximity of juvenile rocks, and the time gap between the emplacement of these and the hydrothermal mineralisation event.

A significant inference from the data here in relation to the Reguibat Shield, is that the thick SCLM keel that underlies the West African Craton was probably formed around or after, but not before 2840 Ma, the timing of gold mineralisation, at least in this location. 2840 Ma may also correspond to an orogenic event associated with continental collision between two terranes in the Reguibat Shield. The Tasiast Thrust, which runs N-S through the Aouéouat greenstone belt is possibly a relatively small second order structure high in the crust that has acted as the final trap for the gold, and the model of Zibra et al. (2014) suggests that there is likely a large scale shear zone deeper in the crust. In this case, the shear zone would have been active ~2840 Ma. As discussed earlier, many of these large scale shear structures that have been linked to orogenic gold deposits are interpreted as ancient suture zones between continents and imply active subduction (Blewett et al., 2010). This is obviously a possible model for the source of the gold at Tasiast, but does not necessarily link the Aouéouat greenstone belt to any form of active subduction, and the location of the gold here is not directly associated with a large scale suture zone itself, but more likely due

to the greenstone belt representing the rheologically weakest section of the upper crust within which compressive tectonic displacement could be accommodated. Therefore the active tectonics which resulted in the formation of the Aouéouat greenstone belt and surrounding TTG plutons need not be, and likely are not associated directly with the active tectonics that drove the gold mineralisation event at Tasiast 80-100 Myrs later.

The hydrothermal event associated with gold mineralisation, as mentioned above, affects many of the lithologies present in the Aouéouat greenstone belt and surrounding rocks. The feldspar and sulphide Pb-Pb isotope study carried out for this project links the gold mineralisation event to one of the TTG rocks sampled from the area (TSUPB029). The nature of the gold mineralisation however is orogenic, and it is very unlikely that TSUPB029 played any role as a compositional or heat source for the gold mineralisation. Interestingly this TTG sample contains a large proportion of zircons with ages reset to the age of the gold mineralisation event. This highlights that the match in Pb-Pb isotope signatures are significant, and not a coincidence, however it is likely that the hydrothermal event re-set the feldspar Pb isotope signature of the TTG rock, and not that the mineralisation inherited the Pb isotope signature from the TTG rock.

As has been discussed above, it appears that no evidence has been derived from this project to suggest that the source of the gold mineralisation is magmatic, and no clear links have been made between any of the TTG rocks and the gold mineralisation which could support a magmatic origin. The large temporal gap between crystallisation ages of the TTG rocks in the region and the age of gold mineralisation implies that these are not linked in any way, although it has been mentioned that the sample size of TTG rocks studied for this project is too small to rule out this possibility completely. Further definitions for intrusion related deposits include ‘comparatively restricted zones of hydrothermal alteration within granitoids’ and ‘a continental tectonic setting well inboard of inferred or recognized convergent plate boundaries’ (Groves, 2003), neither of which appear to be the case at the Tasiast deposit. There is the need for a heat source to activate the hydrothermal fluids, and in this case, if present, a magmatic source for this heat may have remained deep within the crust as suggested by Ridley et al. (2000), and hence cannot be sampled. It is likely that the source of gold is from the nearby juvenile rocks (Temeimichat assemblage), and this has probably been mobilised by a relatively large scale compressional tectonic event and the metamorphic fluids and shear structures associated with this, with or without associated magmatism.

5.3. Reguibat Shield discussion and proposed model:

This project represents one of, if not the, largest and most detailed studies carried out on rocks of the Reguibat Shield, and in particular the Tasiast-Tijirit Terrane. To begin with, the results of this project will be discussed with regards to previous knowledge of the Tasiast-Tijirit Terrane, before expanding to the wider context of the Reguibat Shield, and the West African Craton as a whole. A model will then be proposed for the formation of the Aouéouat greenstone belt and surrounding TTG rocks with reference to the Tasiast-Tijirit Terrane and other Reguibat Shield terranes.

5.3.1. Tasiast-Tijirit Terrane:

The Aouéouat greenstone belt and surrounding TTG rocks make up a part of the Tasiast-Tijirit Terrane, and are consistent with previous descriptions of the terrane as it has been described in the literature (e.g. Chardon, 1996, Key et al., 2008); resembling a classic granite-greenstone terrane sequence. The migmatitic gneisses present in the Tasiast-Tijirit Terrane do not outcrop in the area under Kinross Tasiast's exploration license, however these have been discussed by Key et al. (2008). Here they are described as tectonically, and locally unconformably, underlying greenstone belt sequences and so preserve the complex tectonothermal history pre-dating formation of these greenstone belts. They are composed of a grey tonalitic gneiss host cut by at least four generations of felsic veins and minor metamorphosed mafic dykes. These minor intrusions are differentiated from later plutonic magmatism. As part of this project the migmatitic gneisses have been referred to as an 'orthogneiss', however this was never located in the field due to the restrictions of the exploration license relating to this project. Although not sampled itself, significant evidence was found for this orthogneiss in the analysed rocks, including inherited zircons from the Aouéouat assemblage, a significant population of detrital zircons from the Tasiast assemblage, and relatively old Nd-model ages for the Aouéouat assemblage volcanic rocks. These combined data suggest the orthogneissic basement of the Tasiast-Tijirit terrane is composed of rocks with a range of ages between 3320 Ma and 3170 Ma, and represent the oldest crystallisation ages recorded in the Tasiast-Tijirit Terrane, excluding two inheritance ages of 3385 Ma and 3510 Ma sampled from the Aouéouat assemblage, which are interpreted to represent minor older components of the orthogneiss. Although no outcrops of the orthogneiss were located as part of this project, through the fieldwork descriptions of Key et al. (2008), it may be that it is exposed in places within the Tasiast-Tijirit Terrane. A further observation made by Key et al. (2008) is that a number of small amphibolite units are found within the gneissic basement interpreted as older greenstone belt remnants. Until sampled and dated however, there is no solid evidence of the orthogneissic basement being present at the modern day surface at all in the

Tasiast-Tijirit Terrane, and it may be that the migmatitic nature of the TTG rocks is being interpreted as older gneissic basement. The lack of exposure of a gneissic basement which is evidenced through inherited zircons is also seen in other greenstone belts, e.g. the East Pilbara Craton and the Abitibi greenstone belt (Kamber, 2015). One possibility for the lack of exposed basement rocks in the Tasiast-Tijirit Terrane, is that almost the entire basement was re-melted, similar to that modelled by van Kranendonk et al. (2007b) (Appendix 1c) for the East Pilbara Craton. In this case only the edge of the rising plutons would have remained un-melted, and representative of the original basement. This would also have been among the first of the TTG lithologies to become exposed and therefore eroded, explaining its extensive presence in the Tasiast assemblage, as well as the relative lack of modern day exposure (hence it not having been located in the field). Reasons against this being a possibility are that the TTG rocks contain younger Nd model ages than the age of the basement, suggesting the source of the TTG rocks is the greenstone volcanics and not the basement itself. It is almost certain that a basement orthogneiss aged between 3320 Ma and 3170 Ma is present within the Tasiast-Tijirit Terrane, and it is certain that rocks of this age did exist prior to the formation of the Aouéouat greenstone belt.

The oldest rocks previously recorded from the Tasiast-Tijirit Terrane are TTG and granitic rocks aged between 3031 Ma and 3010 Ma (Gärtner et al., 2013, Montero et al., 2014). Rocks of this age were not sampled as part of this project, however detrital zircon populations within error of this age are present within the Tasiast assemblage. Of particular note here is the zircon within the probable conglomerate hosted TTG clast that was dated at 3059 ± 32 Ma. The presence of TTG rocks as old as 3031 Ma indicates there was plutonic activity at this time, and so it is possible that the detrital zircons dated as part of this project were sourced from exposed TTG plutons of this age. Significantly, rocks of this age from the literature also include a detrital age population of 3027 Ma collected from a greenstone belt sedimentary rock from the northwest of the Tasiast-Tijirit Terrane (Montero et al., 2014). This detrital age was achieved through an upper-intercept age calculation, which is unlikely to be accurately representative of the zircons from the sampled sedimentary rock. The $^{207}Pb/^{206}Pb$ ages of the analysed zircons range between 2989 Ma and 3051 Ma, however a minimum age constraint is placed by a cross cutting TTG intrusion dated at 3010 Ma. Therefore a range of ages between 3051 Ma and 3010 Ma are likely to be representative, and not dissimilar to ages recorded in some of the Tasiast assemblage samples.

Due to the presence of rocks dated between 3010 Ma and 3031 Ma (and possibly 3051 Ma, or older in the Aouéouat greenstone belt region) being older than the Aouéouat greenstone belt volcanics, rocks of this age in the Aouéouat greenstone belt have been referred to as a 'younger basement component' in this project. Other studies in the region however suggest that the rocks

of this age are TTG and granitic plutons, and so perhaps are related to granite-greenstone terranes older than the Aouéouat greenstone belt. Current evidence for granite-greenstone terranes of this age is limited to Nd model ages between 3.1 Ga and 3.0 Ga from a variety of rocks from the Tasiast-Tijirit Terrane (Chardon, 1996, Key et al., 2008, Montero et al., 2014). This does not mean that rocks must have been formed at this time, only that their source was extracted from the depleted mantle at this time. However, seeing as the rocks which were emplaced as the Temeimichat assemblage close to 3.0 Ga are juvenile, it is possible that this may also have been the case for the other 3.1-3.0 Ga model ages from the region.

An alternative possibility, which would be compatible with the observed evolution of the Temeimichat assemblage, is that the 3.1-3.0 Ga TTG rocks were formed during the early stages of rifting associated with a mantle plume event, in which the sialic crust was partially melted before complete rupture and extrusion of the Temeimichat assemblage. This could also explain clasts of TTG rocks of this age in the lowest stratigraphy of the Tasiast assemblage, having a relatively proximal location in comparison to the orthogneiss basement. No matter what their emplacement method was, it appears that these rocks were exposed during the early stages of deposition of the Tasiast assemblage, as they almost certainly constituted a component of the earliest recorded rocks to be eroded and redeposited in the Tasiast assemblage.

One previous attempt has been made to date Aouéouat greenstone belt volcanism; by Key et al. (2008). This was a felsic volcanic rock, from which only three zircons were recovered from a total of 50kg of sample, one of which was datable. The small zircon yield is not surprising given the lack of zircons in a number of samples processed as part of this project. Key et al. (2008) reported a $^{207}Pb/^{206}Pb$ age of ~2965 Ma for the single datable zircon, and as it was sub-concordant, it was interpreted as a minimum age. Given the felsic volcanic nature of this rock, it could almost certainly be assumed to originate from the Aouéouat assemblage, and the 'minimum age' of ~2965 Ma could more accurately lie between 3000 Ma and 2990 Ma. Interestingly however, a Nd model age of 3.0 Ga was calculated for this felsic volcanic rock which conflicts with the 3.3-3.2 Ga Nd model ages calculated from the Aouéouat assemblage in this project. Two possible ways of explaining these data are: 1) the felsic volcanic rock analysed by Key et al. (2008) was in fact from the Temeimichat assemblage due to the similar Nd model ages, suggesting that the Temeimichat assemblage was in fact formed close to 3000 Ma given the age of the zircons analysed, or 2) the felsic volcanic rock was somehow insulated from crustal contamination which has affected all other rocks analysed from the Aouéouat assemblage. The possibility suggested by Key et al. (2008) that the zircons are inherited would seem unlikely given the relatively young Nd model age suggesting the rock has been derived directly from the depleted mantle. Further information,

such as exact location and trace element geochemistry of the sample would be necessary in order to more definitively constrain its origin.

The majority of rocks dated from the Tasiast-Tijirit Terrane prior to this study are gneissic, TTG and granite samples between 2970 Ma and 2911 Ma in age (Chardon, 1996, Key et al., 2008, Bea et al., 2013, Gärtner et al., 2013, Montero et al., 2014). Although Montero et al. (2014) state that the northwest region of the Tasiast-Tijirit Terrane studied for their project *"is fundamentally different from the Tasiast-Tirijit and Tiris terranes, and that the Mauritanian terrane division is not applicable here"*, it appears that all of the rocks analysed by Montero et al. (2014) are consistent with all other Tasiast-Tijirit terrane TTG rocks. The ages from all of the above projects from this terrane correlate well with the dates obtained from the TTG rocks as part of this study, and combined with this study these ages suggest that there was active plutonism over the entire range of 60 Mrys, from 2970 Ma to 2911 Ma. It is therefore likely that the possibility of two distinct periods of TTG plutonism resulting in the ages collected as a part of this project is an artefact of sample selection and quantity, and not representative of the Tasiast-Tijirit Terrane as a whole. Some of the few geochemical data currently published from the Reguibat Shield are from Tasiast-Tijirit Terrane TTG rocks. These existing geochemical data are in agreement with the major element geochemistry presented as part of this project and the modal composition of TTG rocks from this terrane being close to or on the tonalite-granodiorite boundary. SiO_2 contents and total alkali contents are also within the same range of 65.8-77.5% and 5.8-9.1% respectively (Pitfield et al., 2005). Major element data are the only geochemical data that appear to be publicly available from this study, which was part of a French/Mauritanian mapping programme for exploration purposes, and so no other geochemical data can be compared between the Aouéouat greenstone belt and surrounding TTG rocks and other lithologies form the Tasiast-Tijirit Terrane.

Although previously mentioned in the literature as being widespread in the Tasiast-Tijirit Terrane (Key et al., 2008), the age of ~2766 Ma for the late pegmatite presented here is the first age constraint for this event. It is noteworthy that intrusion of these pegmatites appears to be a unique event in the Tasiast-Tijirit Terrane, in that no other ages within error of this have been detected. Furthermore, there are no signs in the Aouéouat greenstone belt and surrounding rocks of the two younger ages of ~2651 and ~2461 Ma recorded in the west of the Tasiast-Tijirit Terrane (Gärtner et al., 2013, Bea et al., 2013), suggesting the presence of later tectonothermal events that only affected the western margin of the terrane.

Previous Nd and Hf isotope model ages from the Tasiast-Tijirit Terrane are predominantly confined to between 3.10 Ga and 2.95 Ga. These model ages are possibly linked to the same

depleted mantle melting events as those represented by the Temeimichat assemblage, with the uncertainty of model ages being relatively large, as well as their being uncertainty of the true age of the Temeimichat assemblage. There are a number of other greenstone belts associated with the Aouéouat greenstone belt, all encompassed within the "Chami greenstone belt", and it is likely that these have been formed over the same broad time period. With almost all previously published model ages from the Tasiast-Tijirit Terrane being between 3.10 Ga and 2.95 Ga, it is significant that the only samples from the Aouéouat greenstone belt to yield Nd model ages overlapping with this range are those from the Temeimichat assemblage. All other Nd model ages from the Aouéouat greenstone belt come from the Aouéouat assemblage, and are between 3.27 Ga and 3.17 Ga, signifying an older crustal component. Using Nd model ages, Chardon (Chardon, 1996) also found that felsic volcanic rocks of the Tasiast-Tijirit Terrane contained an older crustal component, while Montero et al. (2014) found only one Nd model age > 3.1 Ga, in a greenstone belt metasediment. Due to all published Nd model ages from TTG rocks in the Tasiast-Tijirit Terrane being < 3.1 Ga, and the apparent similarity between rocks throughout the Tasiast-Tijirit Terrane, it would suggest there is a strong possibility that the TTG rocks surrounding the Aouéouat greenstone belt also have Nd model ages < 3.1 Ga. This theory is also aided by the fact that Archaean TTG suites tend to show little evidence for a crustal prehistory (Berger and Rollinson, 1997). Future Nd isotope studies of TTG rocks around the Aouéouat would add strength to, or reject this theory. If it is the case that the TTG rocks do have Nd model ages < 3.1 Ga, this would require that there is little or no older basement component to the TTG rocks, and it is likely that the TTG rocks are all sourced from juvenile rocks associated with the mantle plume event < 3.1 Ga, i.e. the Temeimichat assemblage greenstone belt volcanics, and their equivalents which may have been extensive throughout the Tasiast-Tijirit Terrane at the time of TTG rock formation. Therefore it is possible that a vast amount of the Tasiast-Tijirit Terrane was formed through reworking of juvenile rocks equivalent to the Temeimichat assemblage, and not an older 3.3-3.2 Ga basement. Paleoarchean Nd model ages of 3.25 Ga, 3.40 Ga and 3.60 Ga are also recorded in felsic volcanic rocks and greenstone belt metasedimentary rocks from the Tasiast-Tijirit Terrane (Chardon, 1996, Montero et al., 2014). It is noteworthy that the 3.25 Ga model age from a felsic volcanic rock matches the Nd model age obtained for one of the volcanic rocks from the Aouéouat assemblage, suggesting that the two may be linked, possibly through the same event. The two Nd model ages > 3.3 Ga have not been detected during this study, however two U-Pb zircon ages recorded from sample TSUPB001 in the Tasiast assemblage (3510 Ma, 3385 Ma) are likely inherited from an older basement component within the dominant 3.3-3.2 Ga basement, and are compatible with the Nd model ages > 3.3 Ga from the literature. A model linking juvenile magmatic events, and the Nd model ages and U-Pb ages of the rock assemblages in and around the Aouéouat greenstone belt, is presented in figure 5.3.1.

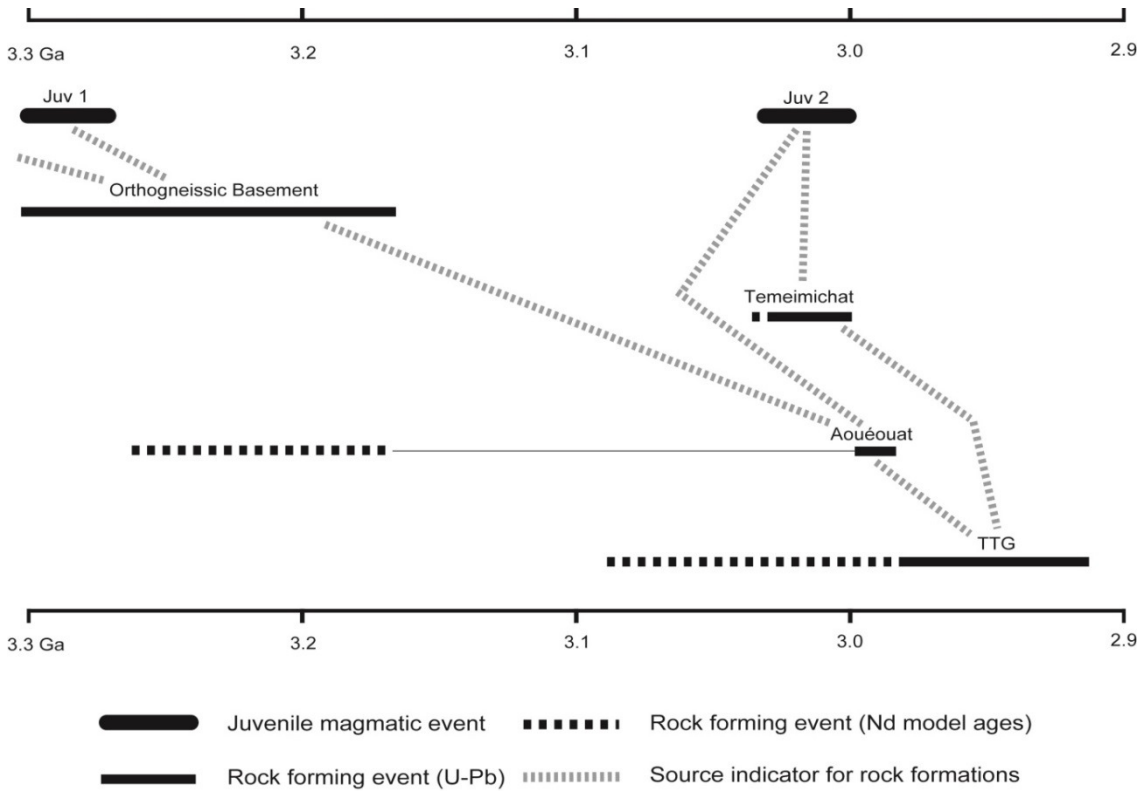


Figure 5.3.1: Schematic diagram indicating which juvenile magmatic events contributed towards the formation of the rock assemblages in and around the Aouéouat greenstone belt using Nd model ages and U-Pb ages.

Evidence for the 2840 Ma hydrothermal event that deposited the gold in the Aouéouat greenstone belt has only been recorded once in the literature, through Rb-Sr ages published by Rocci et al. (1991), which give a range of 2.84-2.34 Ga. It is likely that the 2840 Ma hydrothermal event was the last major event to affect the Aouéouat greenstone belt due to the preservation of the U-Pb apatite ages in the quartz-carbonate veins. The Rb-Sr whole rock and single mineral isotope system has a similar closure temperature to U-Pb in apatite, with a maximum of ~500°C (Purdy and Jäger, 1976, Del Moro et al., 1982), therefore according to currently available data, the Aouéouat greenstone belt matches the oldest known part of the Tasiast-Tijirit Terrane having not been a part of any major tectonothermal event since 2840 Ma.

5.3.2. Reguibat Shield:

The Amsaga Complex, discussed in chapter 2.5.2.2, is host to the two oldest known U-Pb zircon ages from the Reguibat Shield; 3515 Ma and 3422 Ma (Potrel et al., 1996). These were interpreted as inherited zircons, and it was suggested that they could have been sourced from old remnants of an early crust that was broken up and incorporated into separate younger continents (Kröner,

2001, Barth et al., 2002). Two similar ages from the Aouéouat greenstone belt can now be added to the inventory of Paleoarchean ages known from the Reguibat Shield; 3510 Ma and 3385 Ma. There is no additional evidence to suggest an alternative geological hypothesis than that already stated. These Paleoarchean inherited ages which represent vestiges of an earlier formed crust are also used to explain the very old (> 3.4 Ga) Nd model ages found in the Tasiast-Tijirit Terrane as well as an Eoarchean Nd model age (3.64 Ga) from the Amsaga Complex (Potrel, 1994).

There is no definitive physical evidence of exposed gneissic basement in any of the terranes comprising the Reguibat Shield. The strongest geochemical evidence for the presence of an older chemically evolved basement comes from the detrital and inherited zircons of the Tasiast and Aouéouat assemblages in this study, dated between 3320 Ma and 3170 Ma. Nd model ages from this study and that of Chardon (1996) provide further geochemical evidence for presence of a pre-existing basement of ~3320-3170 Ma. Aside from the Tasiast-Tijirit Terrane, the only evidence for a possible gneissic basement in other terranes in the Reguibat Shield comes from Nd model ages in the Amsaga Complex, the TISZ, and the Tiris Complex. The Nd model ages from these terranes indicates a basement aged between 3.25 Ga and 3.10 Ga exists as a component in the formation of the plutonic rocks. Whether the same basement is present as a component in each of these terranes is unknown. A reference is made to this time period by Foster (1993) in which a 3.27 Ga granulite metamorphism event in the Reguibat Shield is referred to, which correlates well with the peak of detrital zircons in the Tasiast assemblage greywackes. In the study by Foster (1993) however, there is no mention of where this information was sourced, and there is no apparent evidence of an event of this age in other literature.

The only evidence in the Reguibat shield for rocks of the same age as the Aouéouat (and probably Temeimichat) assemblage are Nd model ages. These are found both in the Amsaga Complex and the Tiris Complex. No further evidence is seen, although this is not unexpected as greenstone belts are either not present or unexposed in these two terranes, and the Temmimichate-Tsabya Complex of the Ghallaman Complex which does contain greenstones is undated. The Zednes Suite of the Ghallaman Complex has a TTG rock dated at 3044 Ma (Lahondère, 2003), which is the only example of an exposed TTG rock this old in the Reguibat Shield. It is difficult however to use this in any way as evidence for TTG rocks of this age being present in the Aouéouat greenstone belt, as evidenced by detrital zircons and the TTG clasts, due to the large distance between these two Terranes.

As stated earlier, it appears that most TTG rocks were emplaced in the Tasiast-Tijirit Terrane over a 60 Myr period between ~2970 Ma and ~2910 Ma. Rocks of this age however are not seen

elsewhere in the Reguibat Shield other than an augen granite gneiss from within the TISZ dated at 2954 Ma (Key et al., 2008) which was possibly originally part of the Tasiast-Tijirit Terrane, and a granitic rock from the Ghallaman complex dated at 2915 Ma (Lahondère, 2003). The Amsaga Complex plutonic rocks formed between 2902 Ma and 2706 Ma, the Tiris Complex between ~2830 Ma and ~2450 Ma, and the remaining few dated samples from the Ghallaman Complex between 2840 Ma and 2820 Ma. This highlights that the Reguibat Shield terranes have undergone a different crystallisation history than one another, with the Tasiast-Tijirit Terrane appearing to become largely stable earlier than other terranes in the shield. Key et al. (2008) link the major element geochemical compositions of the Amsaga Terrane TTG rocks with those of the Tasiast-Tijirit Terrane as being very similar, however state that a number of lithologies including the charnockites, and massive quartzofeldspathic gneisses are noticeable by their absence. The difference in lithologies as well as an age gap between the crystallisation ages of the Amsaga Complex and Tasiast-Tijirit Terrane plutonic rocks makes it difficult to link these two together, and it is most likely that these were formed as different terranes, at least during the early part of their history.

Evidence of the ~2840 Ma hydrothermal event that deposited the gold in the Aouéouat greenstone belt is found elsewhere in the Reguibat Shield. The most convincing evidence is a 2840 Ma hydrothermal rim on a zircon from a Charnockite in the Amsaga Complex (Potrel et al., 1998). There is also a TTG rock dated at ~2836 Ma in the Amsaga Complex (Potrel, 1994). Although this could be a hydrothermal overprint age as was the case for TSUPB029, it is currently defined as a crystallisation age. If linked together, this would suggest that the Amsaga Complex and the Tasiast-Tijirit Terrane were both affected by this same hydrothermal event. Although these may have already been adjoined, this is evidence that they were almost certainly amalgamated by 2840 Ma. Interestingly, a TTG sample from the Ghallaman complex is dated at 2832 Ma and inherited zircons probably also sourced from this complex are dated at 2821 Ma (Lahondère, 2003, Schofield et al., 2006). The Ghallaman Complex, although the furthest Reguibat Shield terrane from the Tasiast-Tijirit Terrane, appears to be the most similar in age and nature, containing remnant greenstone belt lithologies, and ages that match those from events recorded in the Aouéouat greenstone belt and surrounding rocks. Whether or not there is any significance to this is impossible to say, however it may be that these have shared a similar history throughout their existence.

The final major event to affect the Aouéouat greenstone belt is the late hydrothermal pegmatite event dated at 2766 ± 31 Ma. This pegmatite appears to be widespread in the Tasiast-Tijirit Terrane. The rocks which can be clearly associated with this are the 2726 Ma granite from the

margin of the Amsaga complex (Potrel et al., 1998), which incidentally was thought to be the first evidence of crustal reworking recorded in the Tasiast-Tijirit Terrane, though this is now known not to be the case, and the Ahmeyim Great Dyke of Mauritania which has been dated at 2733 Ma (Tait et al., 2013). These both appear to be affected by some relatively minor late movement of the Tâçarât-Inemmaûdene Shear Zone, highlighting that it was still active at this time, and may have contributed towards the pegmatite formation. Although the Ahmeyim Great Dyke of Mauritania is proposed to be part of the plumbing system of a Precambrian large igneous province (Tait et al., 2013), there is no evidence for the large igneous province itself. Either way, there was certainly some nearby tectonic activity at the time as seen by emplacement of the Ahmeyim Great Dyke of Mauritania itself which may be associated with pegmatites in the Aouéouat greenstone belt. There are a large number of TTG rocks dated between 2751 Ma and 2706 Ma from the Amsaga Complex (Auvray et al., 1992, Potrel, 1994, Potrel et al., 1998), and also some in the Tiris Complex (Vachette and Bronner, 1975, O'Connor et al., 2005, Schofield et al., 2012). It has been proposed in this study that at least the Amsaga Complex and Tasiast-Tijirit Terrane were amalgamated by this time, and so alternatively the late pegmatite of the Tasiast-Tijirit Terrane could be a product of the magmatism recorded in the Amsaga Complex, and unassociated with the TISZ or the Ahmeyim Great Dyke of Mauritania.

5.3.3. West African Craton:

The difficulties in relating rocks and tectonothermal events over large distances were mentioned in chapter 2.5.1, however similarities and possible links can still be discussed with a view to establishing if any possible connections can be made. Data from the Guinea Rise in the Leo Shield suggest that accretion in the southern part of the West African Craton may have begun around 3300-3200 Ma, with a high grade orthogneiss in this region being dated to 3244 Ma (Kouamelan et al., 1997, Bering, 1998, Thiéblemont et al., 2001). There is also evidence in the Leo Shield for older inherited zircons > 3400 Ma in these rocks, and TTG rocks containing xenoliths of pre-existing crust (Barth et al., 2002). The 3244 Ma orthogneiss from the Guinea Rise could be the only current evidence for surface exposure of the orthogneiss basement that may be exposed in the Tasiast-Tijirit Terrane, and the crust forming event of this age as seen by Nd-Model ages. Further to this, there is evidence of this sialic crust being present during the later stages of deposition of the greenstone belt stratigraphy in the western Leo Shield, similar to what is seen in the Aouéouat greenstone belt (Rollinson, 1983). The major Leonian event (~3.0Ga) of the Leo Shield could be the equivalent of the extrusion of the greenstones and formation of the TTG rocks in the Tasiast-Tijirit Terrane, which was evidently a large scale tectonothermal event, dated as part of this project. The ~2840 Ma hydrothermal, and possibly orogenic event also co-exists with a

surprising number of events further afield than the Reguibat Shield. The North Zaire Massive (now Congo), Angola, and the Tanzanian Shield all have major granitic bodies that formed at ~2840 Ma (Foster and Piper, 1993). It is also known that gold mineralisation from the São Francisco craton of Brazil is dated at 2.82 Ga (Vial et al., 2007). There is evidence for this event having affected much of the Reguibat Shield, and there is also evidence for dominant overprinting of this age in the Leo Shield (Thiéblemont et al., 2001). Although these may not all be directly related, it at least highlights that there was extensive tectonothermal, and probably orogenic activity present during this time period of the Archean. The Liberian event (~2.7 Ga) of the Leo Shield overlaps with the late pegmatite, possible movement on the Tâçarât-Inemmaûdene Shear Zone and the Ahmeyim Great Dyke of Mauritania, as well as a number of rocks dated from the Amsaga Complex and Tiris Complex. It has been proposed before, using less examples, that this is evidence for coeval tectonothermal events from 3.0-2.7 Ga affecting both the Reguibat Shield and Leo Shield together (Schofield et al., 2012), and the similar rock sequences in each shield and the most recent evidence (e.g. Tait et al., 2013, Montero et al., 2014, this study) would appear to strengthen this theory. It is already accepted that the Eburnean orogeny (~2.0 Ga) affected both shields, by which time the West African Craton was fully amalgamated (Boher et al., 1992, Schofield et al., 2012). The final event worth mentioning that appears to have affected much of the West African Craton is the Central Atlantic Magmatic Province at ~200 Ma (e.g. Gärtner et al., 2013, Tait et al., 2013). This event is recorded by lower intercept U-Pb zircon ages caused by Pb-loss. Although lower intercept ages were not able to be calculated for this project, it is likely that this event did have an effect on all samples analysed.

5.3.4. Tectonic model:

In proposing a model for the formation of the Aouéouat greenstone belt and surrounding TTG rocks, many factors, and lines of evidence need to be taken into account. These include primarily the petrography, geochronology and geochemistry of this project, however any applicable model must also be able to fit with data already published on the rocks from the Tasiast-Tijirit Terrane, and the Reguibat Shield as a whole. Some aspects of any proposed model will be more clear cut than others, and it will be discussed below how probable each of the steps of the proposed model are, along with viable alternatives. The preferred model is presented in Figure 5.3.1.

It is clear that there was a Paleo-Mesoarchean crust composed of rocks between 3320 Ma and 3170 Ma in age present before the formation of any of the Aouéouat greenstone belt rocks, which was probably orthogneissic in nature, and also contained some Eoarchean components. The presence of a mantle plume then signalled the start of activity that led to the formation of the

Temeimichat assemblage (Figure 5.3.1a). Using Nd-model ages and the evidence for TTG rocks being emplaced ~3.06 Ga, this may have commenced sometime soon after 3.10 Ga, however the Temeimichat assemblage was probably emplaced closer to 3.01 Ga. The favoured model is that thermal and mechanical erosion due to an impinging mantle plume contributed to a rifting event in the orthogneissic basement, and juvenile rocks were emplaced as a large igneous province in the resulting basin (Figure 5.3.1b). It is possible however that the large igneous province could have been extruded onto the basement without major rifting, or it could have been extruded as an oceanic plateau in the vicinity of continental crust and the gneissic basement rock.

Any proposed model then becomes more difficult to constrain with regards extrusion of the Aouéouat assemblage between 3000 Ma and 2990 Ma. The Aouéouat assemblage clearly features a crustal component, which includes at least some of the orthogneissic basement as seen through Nd model ages and inherited zircons, and so must have been erupted through this pre-existing basement. This could have been possible if a rift basin had begun to re-close bringing the orthogneiss and the Temeimichat assemblage close to one another, and the relative migration of the mantle plume head may have shifted to below the basement allowing crustal contamination of the volcanic rocks being emplaced. It would be easier to explain this event if the Temeimichat assemblage was ensialic, however there is no evidence in any Temeimichat rocks of a crustal component, suggesting it was not deposited on the orthogneissic basement. If the Temeimichat assemblage was initially extruded close to continental crust, it could also be the relative migration of the plume head alone to below the adjacent continental crust that has created the crustal signature in these rocks. It is difficult to envisage a model involving subduction that can incorporate a basement component while also extruding the Aouéouat assemblage on top of the Temeimichat assemblage, unless it is the gneissic basement itself that is being subducted which given Mesoarchean geodynamics is highly unlikely. If subduction was the dominant process responsible for producing the observed crustal signature it would therefore also need to occur contemporaneously with the Temeimichat assemblage being deposited on to gneissic basement. The simplest model is therefore presented as the favoured model, in that the relative migration of the mantle plume resulted in melt passing through the orthogneissic basement en route to eruption (Figure 5.3.1c).

The next event in the formation of the Aouéouat greenstone belt and surrounding rocks is that of the TTG plutonism. There was a detailed discussion in chapter 2.3.5 as to whether vertical or horizontal tectonics are responsible for the formation of TTG rocks and granite-greenstone geology. From this discussion it is clear that it can be argued that both are viable mechanisms for producing granite-greenstone terranes. It is worth noting that there is very little evidence

worldwide that can support the theory that subduction was active and widespread during the Mesoarchean, and so if no strong evidence for subduction exists here then it would be the less favoured model. Field evidence in the Tasiast-Tijirit Terrane appears to show a predominance of steeply plunging mineral lineations within greenstone belts (Rocci et al., 1991, Chardon, 1996, Schofield et al., 2012, Sims, 2014) and concentric fabrics from within TTG domes (Schofield et al., 2012). There is however no strong geochemical evidence from this study that can predominantly favour either vertical tectonics or horizontal tectonics. The favoured models for formation of the Aouéouat and Temeimichat assemblages discussed in chapter 5.1 do not involve subduction and when brought together it therefore fits that the preferred model for the TTG rock emplacement around the Aouéouat greenstone belt, and the Tasiast-Tijirit Terrane as a whole, is that vertical tectonics were responsible. This would have involved partial convective overturn of the crust, caused by the build-up of a large plateau of greenstone volcanic rocks (the Temeimichat and Aouéouat assemblages). The initiation of such an event would have been due to the crust becoming unstable, and partial melting occurring at its base resulting in the formation of TTG plutons. This may have been initiated by crustal delamination, which would concur with migration of the mantle plume away from the base of a large igneous province resulting in its cooling and instability. The TTG plutons were then emplaced into the greenstone volcanic rocks, resulting in the dome-and-keel structure of greenstone belts and TTG plutonic rocks (Figure 5.3.1d). This probably occurred over the 60 Myr timespan of ~2970 Ma until ~2910 Ma. A combination of the relative extent of convective overturn and melting, and the relative exposure level today has resulted in the greenstone belts only being exposed in the west of the Tasiast-Tijirit Terrane. Although it cannot be disproven that subduction had a role to play in the formation of the Tasiast-Tijirit Terrane TTG rocks, there are reasons to prefer a vertical tectonic model. Subduction would have to have occurred beneath the mantle plume related Temeimichat assemblage, and involved partial melting of crustal rocks. Both of these are possible as explained in chapter 5.1, however volcanism would likely be expected as part of a subduction related sequence, and there is no evidence for coeval volcanism and TTG rock emplacement, with up to 20 Myrs between the youngest volcanic rock and the oldest TTG rock associated with this event.

Continuing on from the preferred model described above, the subsequent event is deposition of the Tasiast assemblage sedimentary rocks. The emplacement and rise of TTG rocks within the large igneous province would begin to cause displacement in the rocks at the surface. Initially it appears that some pre-existing ‘younger basement’, or older TTG rock aged ~3060 Ma was exposed at the surface as this was the first lithology to be eroded and deposited, possibly from newly formed rift flanks. Other possible geological models are however viable, e.g. the rock interpreted as a basal conglomerate to the Tasiast assemblage may in fact be a mylonite within a

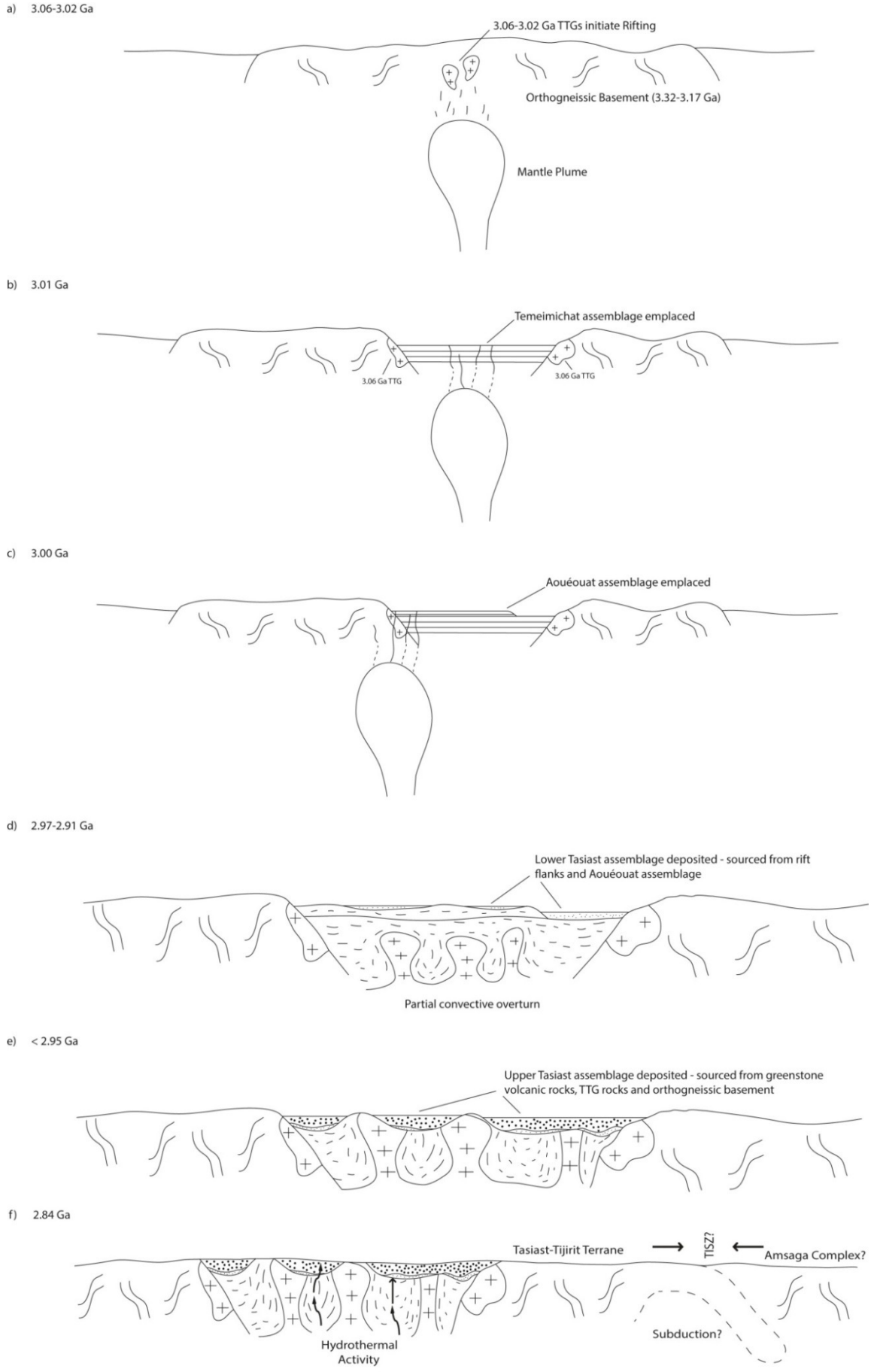
minor shear zone. If this rock is a mylonite and not a conglomerate it would remove the presence of a detrital ~3060 Ma TTG rock component from the base of the Tasiast deposit, resulting in the lowest stratigraphy of the Tasiast assemblage being that of a locally derived volcanic sediment. The current interpretation however remains that the Tasiast assemblage contains a basal conglomerate. Deposition of local volcanic rocks, which involve the Aouéouat assemblage, and possibly Temeimichat assemblage volcanic rocks then follows (Figure 5.3.1d). These locally derived sediments highlight there was not extensive topography or wide reaching catchment areas at the time, or that there were no other rocks exposed at the surface. It is also possible that these locally derived sediments could have been deposited any time between extrusion of the Aouéouat assemblage and exposure of the TTG rocks, and therefore may completely predate any deformation caused by TTG emplacement. After deposition of the locally derived sedimentary rocks there is a gradual decrease in the age of the youngest detrital zircon contained in the sediment with stratigraphic height. This could either be due to specific source region, or could be due to the gradual erosion and exposure of the TTG plutons, which almost certainly formed topographic highs or intervening rift basins to form within which the Tasiast assemblage was deposited (Figure 5.3.1e). The younger Tasiast assemblage sedimentary rocks cannot have been deposited prior to 2955 Ma, the age of the youngest detrital zircon. These were likely deposited soon after TTG emplacement, particularly if the driving force of the creation of topographic highs and/or intervening rift basins was the TTG magmatism, however the minimum age constraint of the sediments is 2840 Ma, the age of the following hydrothermal event. A further interesting point is that at some stage the orthogneissic basement becomes a source rock for the Tasiast assemblage. This could either be through erosional exhumation exposing the basement rock, or through the basement rock becoming exposed on topographic highs due to regional tectonic exhumation, resulting in this rock being deposited in the basin. It is probably a combination of the two.

The next major event to affect the region is the ~2840 Ma hydrothermal event. As discussed in chapter 5.2, this is most likely the result of an orogenic event, and either continent-continent collision or continent-arc/plateau collision. This event is recorded in both the Tasiast-Tijirit Terrane and the Amsaga Complex, as well as there being evidence of it affecting the Leo Shield. It is unknown what terranes were involved in this continent-continent collision or continent-arc/plateau collision event. The most obvious explanation is that it may have been associated with the event that created the TISZ and also brought the Tasiast-Tijirit Terrane and the Amsaga Complex together (Figure 5.3.1f), however these terranes may already have been amalgamated by this time. Alternatively a currently unexposed separate terrane may have collided with the Tasiast-Tijirit Terrane causing this deformational and associated hydrothermal event at ~2840.

The significance of this orogenic event is that the hydrothermal activity associated with it liberated and deposited the gold in the Aouéouat greenstone belt. It is also probable that this event caused the inversion of pre-existing rift basins and associated deformation of the Aouéouat greenstone belt, and it may have signalled initiation of the Neoarchean supercontinent of Superia/Sclavia. This orogenic event therefore may also have resulted in the formation of significant gold deposits in any other neighbouring regions that also contain low-grade juvenile volcanic rocks and suitable host structures, with the implication that gold occurrence at ~2840 Ma may be more extensive than previously realised.

Events later than ~2840 Ma are difficult to constrain using data from this project within the Tasiast-Tijirit Terrane. The final Archean event recorded in the terrane is the ~2766 Ma pegmatite event. Although only recorded in the Tasiast-Tijirit Terrane as a hydrothermal pegmatite event, rocks of this age are widespread in both the Amsaga Complex and the Tiris Complex. This suggests that at this time a tectonic event affected both of these regions, however had a minimal effect on the more distal Tasiast-Tijirit Terrane. The western edge of the Tasiast-Tijirit Terrane underwent some form of tectonothermal event, presumably associated with an outboard terrane in the late Neoarchean, before the major Eburnean Orogeny combined the Archean and Proterozoic domains of the Reguibat Shield at ~2.0 Ga, although this did not appear to affect the Tasiast-Tijirit Terrane. Some later mafic dyke swarms cross-cut the Tasiast-Tijirit Terrane and are both Proterozoic and Phanerozoic in age. The final event that has been recorded in the Tasiast-Tijirit Terrane is the opening of the Mid-Atlantic Ocean at ~200 Ma. This event is restricted to being recorded by causing Pb-loss in some minerals, for example zircon.

Figure 5.3.1: Diagrammatic sketch of events in the formation of the Aouéouat greenstone belt: a) development of a mantle plume ~3.06 Ga initiates rifting of orthogneissic basement and the emplacement of some TTG plutons, b) extrusion of the Temeimichat assemblage as a large igneous province within the rift basin at ~3.01 Ga, c) relative migration of the mantle plume allows a basement component to be incorporated in the extrusion of the Aouéouat assemblage at ~3.00 Ga, d) partial convective overturn initiated by crustal delamination results in the formation of TTG rocks between 2.97 Ga and 2.91 Ga and the sagduction of volcanic rocks between these at the same time as the first locally derived sedimentary rocks are deposited in small initial rift basins, e) larger rift basins are developed in which the main Tasiast assemblage rocks are deposited <2.95 Ga, f) collision between the Tasiast-Tijirit Terrane and an outboard terrane, possibly the Amsaga Complex, at 2.84 Ga create the orogenic event which mobilises and deposits gold in the Aouéouat greenstone belt.


a) 3.06-3.02 Ga
3.06-3.02 Ga TTGs initiate Rifting
Orthogneissic Basement (3.32-3.17 Ga)
Mantle Plume
b) 3.01 Ga
Temeimichat assemblage emplaced
3.06 Ga TTG
3.06 Ga TTG
c) 3.00 Ga
Aouéouat assemblage emplaced
d) 2.97-2.91 Ga
Lower Tasiast assemblage deposited - sourced from rift flanks and Aouéouat assemblage
Partial convective overturn
e) < 2.95 Ga
Upper Tasiast assemblage deposited - sourced from greenstone volcanic rocks, TTG rocks and orthogneissic basement
f) 2.84 Ga
Tasiast-Tijirit Terrane
TTSZ?
Amsaga Complex?
Hydrothermal Activity
Subduction?

5.4. Crustal, mantle and tectonic evolution:

5.4.1. Crustal evolution:

The topic of crustal evolution was discussed in detail in chapter 2.2.1, where significance of the timing of crustal formation, and the different ways in which it can be modelled were deliberated. The West African Craton is one of the two Archean cratons worldwide where the lithospheric thickness has reached > 300km, with the other being the Siberian Craton (Artemieva and Mooney, 2001) (Figure 2.1.1). The significance of this particularly thick lithosphere is not presently known, however it does indicate that there were some differences in crustal evolution processes of the West African Craton when compared to most other Archean cratons worldwide. It was discussed in chapter 2.5 that few geological studies on the rocks of the West African Craton relative to most Archean cratons worldwide exist, and in particular very few studies have focussed on the rocks of the Reguibat Shield. This study on the Aouéouat greenstone belt in the Reguibat Shield has provided both new U-Pb zircon geochronology, and Nd isotope data for the region. Both of these data sets can add to the global database used to develop crustal evolution models.

5.4.1.1. Detrital zircon:

The most common method for modelling crustal evolution is using the detrital zircon record. This study sampled a total of five sedimentary rocks from the Tasiast assemblage which provided detrital zircon ages. Combined probability density plots of these samples are presented in figure 5.4.1. The shortcomings of using detrital zircons as a method of modelling crustal evolution were discussed in chapter 2.2.1.2. Data here highlight on a small scale some of these problems. One issue is that a much larger sample size was analysed for the West Branch greywacke samples, which account for 248 of the 367 analyses, than for the C6.7 or Tasiast Footwall samples. This automatically biases the detrital ages recorded towards the age populations contained within the West Branch rocks. A second issue is that the two samples collected from C6.7 are interpreted as being sedimentary rocks with a proximal volcanic rock source. These two sedimentary rocks make up a relatively small proportion of the Tasiast assemblage as a whole, yet due to their significance they represent 40% of the rocks sampled for detrital zircon data, though only 10% of the analyses. It is unlikely however that these rocks comprise as much as 10% of the Tasiast assemblage rocks as a whole, and so the combined detrital age population will be biased towards the ages contained within these rocks. The two biasing factors seen here do not even touch on the large scale issues of age biasing such as preservation versus destruction associated with their tectonic setting. They do though highlight other biases, in that certain ‘geologically interesting’ rocks will

always be over-represented in the detrital zircon record, and that it is impossible to collect a true proportional age distribution of the sedimentary rocks that are analysed. Nonetheless the detrital zircon data collected as part of this project provides interesting information with regards contributing to the global detrital zircon record.

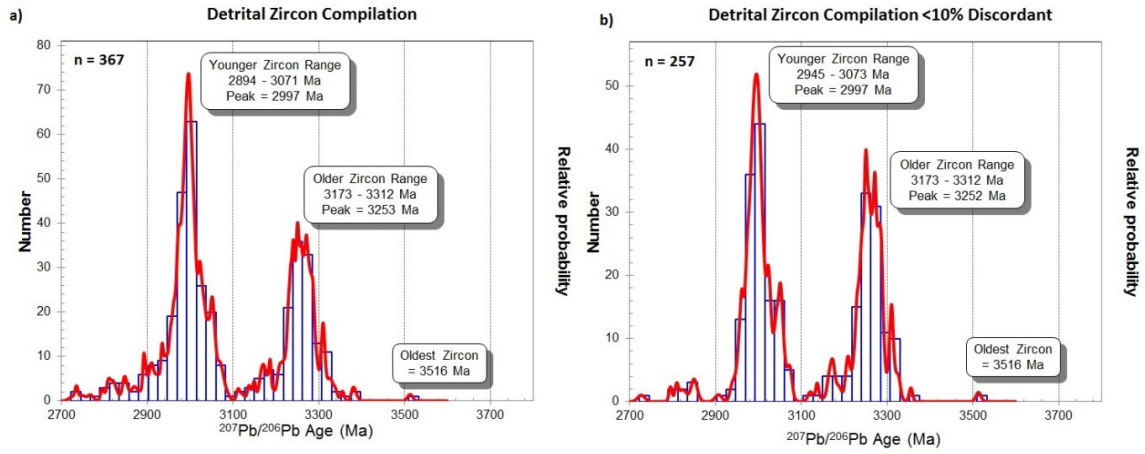


Figure 5.4.1: Probability density plots of detrital zircon analyses; a) all analyses combined, b) all analyses < 10% discordant combined.

The first point to note regarding the zircon populations presented here (Figure 5.4.1) is the difference between the plot showing all analyses and the plot showing only analyses < 10% discordant. There are a total of 90 analyses that are > 10% discordant, and therefore removed from the second plot, however there is almost no difference in age peaks between the two plots other than at the youngest end of the spectrum. These young ages have been explained elsewhere as being an effect of two factors: 1) hydrothermal overprinting from the hydrothermal event dated at ~2840 Ma and a mixing effect between this event and the crystallisation age of the zircon, and 2) Pb-loss resulting in larger errors of more damaged zircons. It is therefore suitable to use the plot of zircons < 10% discordant as a representative, though not proportionately representative (as was discussed above), sample of the ages of detrital zircons in the Aouéouat greenstone belt. There are two main age populations represented: one between 3312 Ma and 3173 Ma, and one between 3073 Ma and 2945 Ma, with peaks at 3252 Ma and 2997 Ma. These are highlighted on the global detrital zircon record after Voice et al. (2011) in figure 5.4.2. This record uses analyses < 5% discordant, which would limit analyses from this study to 187. If the 187 detrital ages from this study < 5% discordant are included in the model, there would be a ~0.2% increase in the number of data points used. These would not produce any significant changes and do not appear to overlap with any existing significant or discernible age peaks. If using only the analyses included from African rocks however, there would be a 3.7% increase in data points included, with the peaks coinciding with a peak currently seen in the African detrital

zircon record (inset in figure 5.4.2). The detrital zircon data presented as part of this project therefore match the ages of detrital zircon populations found on the African continent. Detrital zircon populations aged between 3312 Ma and 2945 Ma are also found on the Antarctic, Australian and North American continents, however of these continents only Antarctica features detrital zircons of this age as a relatively significant proportion, but this may be biased due to the lack of surface rock exposure (Voice et al., 2011).

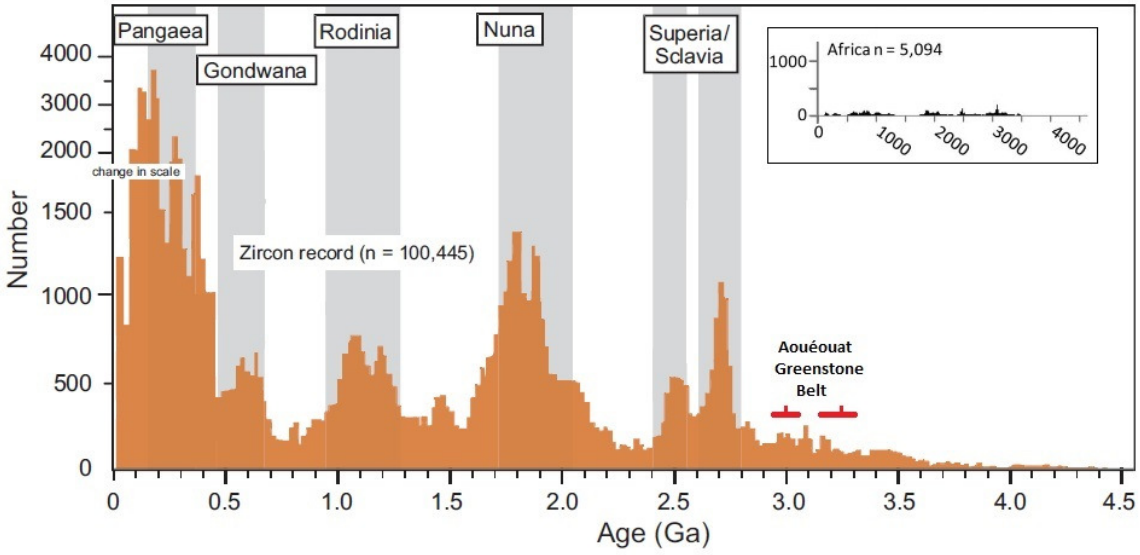


Figure 5.4.2: Figure 2.2.3 modified to highlight the detrital zircon ages from this study, and an inset of African detrital zircon populations (modified from Voice et al. (2011) and Cawood et al. (Cawood et al., 2013)).

If suitable for use as a proxy for crustal formation, the detrital zircon data from both this project, and the combined data from Voice et al. (2011), suggest that a crustal formation event occurred between 3.3 Ga and 2.9 Ga which contributed towards the rocks that constitute the modern day African continent, as well as on the Antarctic, Australian and North American continents. Data of this age collected from the African continent however, including that from this project, make up a significant proportion of the African detrital zircon record. It has been stated that older source rocks are underrepresented in the detrital zircon record (Allègre and Rousseau, 1984). Africa may be an example of where the detrital zircon record has not been flooded by zircons from younger supercontinent formation events, which has allowed the significance of the age peak between 3.3 Ga and 2.9 Ga to be discerned. Whether or not this age peak is related to crustal formation, or a supercontinent event resulting in preservational bias (possibly Vaalbara (de Kock et al., 2009) or Ur (Rogers, 1996)) cannot be deduced. Importantly, when combined with the global detrital zircon database, there is little significance attributed to this age period again highlighting a problem with using detrital zircon U-Pb ages as a proxy for crustal formation.

5.4.1.2. Alternative isotope systems:

Methods using alternative isotopic systems to model crustal evolution were discussed in chapter 2.2.1.3, where it was concluded that the best results are provided when using multiple isotopic systems in tandem. Collecting data from multiple isotopic systems from detrital zircons (i.e. Hf, O) was out with the scope of this project, and so whole rock Sm-Nd isotopes were analysed for six samples; two samples from the Temeimichat assemblage, and four samples from the Aouéouat assemblage. Nd model ages were calculated for these (depleted mantle model ages calculated assuming crystallisation at 3.0 Ga). The Temeimichat assemblage Nd model ages are 2.95 Ga and 3.01 Ga, and the Aouéouat assemblage Nd model ages range from 3.17 Ga to 3.27 Ga. The Temeimichat assemblage rocks are interpreted to be derived directly from the depleted mantle. They also unconformably underlie the 3.00-2.99 Ga Aouéouat assemblage, and so the Nd model age of 3.01 Ga is probably closer to the actual depleted mantle extraction age. A Nd model age of 3.01 Ga is also in agreement with previous Nd model ages from the Tasiast-Tijirit Terrane which lie between 3.10 Ga and 2.95 Ga. These Nd model ages, along with the geochemistry highlighting the depleted nature of the rocks, suggests that the Temeimichat assemblage rocks are juvenile in nature, and therefore direct examples of crustal growth at ~ 3.01 Ga. It appears that the majority of rocks from the Tasiast-Tijirit Terrane were created from crust formed at this time, although most of these are the product of the re-melting of the juvenile rocks between 2.97 Ga and 2.91 Ga and now exist as TTG rocks. Prior to this project only one Nd model age within the range of 3.17 Ga and 3.27 Ga had been obtained from rocks in the Tasiast-Tijirit Terrane (Chardon, 1996). It is clear however that the Aouéouat Assemblage rocks also have Nd model ages which match this age. The Aouéouat assemblage rocks provide an example of how Nd model ages alone cannot be used as a proxy for crustal formation, as these model ages could be an artefact of the mixture of different source rocks contributing towards their formation. In the model proposed in chapter 5.3.4, the Aouéouat assemblage formed through mantle plume derived volcanics being contaminated by an orthogneissic basement en route to emplacement. If this is the case, the Nd model ages calculated here for the Aouéouat assemblage would be a mixture between ~3.00 Ga (the age of the Aouéouat assemblage rocks) and the Nd model ages contained within the orthogneiss. It is therefore likely that the Nd model ages for the Aouéouat assemblage rocks represent a minimum age for the crustal formation of the rocks which have contributed towards their source.

By combining the detrital zircon record from the Tasiast assemblage with the Nd isotope record of the Aouéouat assemblage, it could be suggested that the orthogneissic basement which presumably provided the large older detrital zircon population of 3.17-3.31 Ga represents a

crustal growth event, which is also seen in the Nd isotope model ages. This is assuming that the orthogneissic basement represents a crustal growth, which as discussed earlier may not be the case as this could be an artefact of preservation. This would therefore be an ideal situation in which to combine Hf isotope data from the zircons of this age population with the data already collected, as this could elucidate whether or not these zircons represent new crust, or older recycled crust. As it stands it can only be stated that a crustal formation event in the Tasiast-Tijirit Terrane occurred at, or prior to, ~3.27 Ga, which either formed or contributed towards the orthogneissic basement, which in turn contributed towards the Aouéouat assemblage. A second crustal formation event then occurred between 3.10 Ga and 3.00 Ga which formed the Temeimichat assemblage, which in turn contributed towards the TTG plutons (Figure 5.3.1). One further point worth noting, is that the large range in Nd model ages of the TTG plutons in the literature (3.10-2.95 Ga), which is higher than that of the proposed Temeimichat assemblage Nd model ages, and therefore mantle plume event, may be due to relatively small volumes of the Aouéouat assemblage being assimilated in the TTG melt. It is therefore not necessary to invoke a mantle plume event of up to 100 Myrs to account for this large range in TTG rock Nd model ages, and the Temeimichat mantle plume event may have been a much shorter lived event.

5.4.1.3. Crustal evolution summary:

The link between crustal evolution and supercontinent formation is often made, and it was discussed briefly above that there could be evidence in the Aouéouat greenstone belt for an old supercontinent event, e.g. Vaalbara or Ur. This however can only be speculation, and there is no strong evidence for the crustal formation events recorded in the Aouéouat greenstone belt alone relating to supercontinent formation. It is also clear that the older the rock is, the more difficult it is to attribute crustal formation ages to supercontinent events due to the lack of physical evidence and data available. There is evidence for two crustal growth events in the Aouéouat greenstone belt, one at ~3.27 Ga, and one at ~3.01 Ga. It was proposed that preservational bias was less likely to be a factor when studying rocks < 2.90 Ga due to the lack of evidence for supercontinent formation (Hawkesworth et al., 2010), and so perhaps the detrital zircon record in the Aouéouat greenstone belt is a close approximation to crustal formation ages. By combining the detrital zircon record and the Nd isotope method for the Aouéouat greenstone belt rocks however, it is clear that a number of the detrital zircon ages, in particular those derived from the TTG rocks, are not representative of crustal formation, and so it is therefore not the case that the detrital zircon record can be used alone to derive a crustal formation model for rocks < 2.90 Ga, at least in terms of the West African Craton.

5.4.2. Mantle evolution:

Intrinsically linked to crustal evolution is the concept of mantle depletion, and one of the major finds of this project is that the Temeimichat assemblage was likely sourced directly from a depleted mantle reservoir. This is similar in nature to modern day oceanic crust, however the model proposed as part of this project for the formation of the Temeimichat assemblage is that the driving factor was the presence of a mantle plume as opposed to plate tectonics. The discussion in chapter 2.2.2 touched on models for the timing of the creation of the depleted mantle, and therefore the melt extraction which led to the formation of new crust, and it was stated that there are very few Archean greenstone belts with HFSE ratios similar to MORB, i.e. a depleted signature (Condie and Benn, 2006). The Temeimichat assemblage provides us with a relatively rare example of an uncontaminated Archean rock sequence sourced from a depleted mantle reservoir. Pearce (2008) stated that geochemical studies of uncontaminated Archean basalts could help to resolve questions mantle evolution, as they are largely free of the complexities associated with interactions of the SCLM and continental crust. This could be extremely useful when it comes to calculating depleted mantle evolution lines. It is known that depleted mantle evolution lines are not perfectly accurate, yet they are used to calculate whether or not a rock was sourced from a depleted mantle reservoir (Babechuk and Kamber, 2011, Kamber, 2015). Kamber (2015) suggests that geochemical data on unaltered rocks with a demonstrable depleted mantle origin should be collated and made available to the geochemical community in order to improve depleted mantle evolution lines, which will both aid in calculating accurate model ages and help to constrain when continental crust was generated. Figure 4.3.10 showed that the εNd value for one of the Temeimichat assemblage samples plots above the depleted mantle evolution curve of DePaolo & Wasserburg (1976), highlighting exactly what was discussed above; that there is a need to update and improve depleted mantle evolution lines by using newly gathered data . The strong depleted signature of the Temeimichat assemblage is also seen in its Nb/Th ratios. Kamber (2011) presented a figure highlighting the Nb/Th ratios for the depleted mantle through time, and when the Nb/Th ratios of the Temeimichat assemblage are plotted with these it is clear that they show a more depleted signature, plotting higher than the depleted mantle evolution curve which these data are used to create (Figure 5.4.3). The significance of the data collected from the Temeimichat assemblage is that at 3.0 Ga, the Temeimichat assemblage was extracted from a depleted mantle reservoir which was more depleted than the currently modelled depleted mantle. There are two ways in which this can be explained. The first is that the depleted mantle evolution curve is not accurate for the Mesoarchean, and in fact the depleted mantle was more depleted, at least at ~3.0 Ga, than the mantle evolution curve suggests. This could have knock-on consequences for crustal evolution

models which use the depleted mantle as a factor in their calculations, as it would suggest that there had been a greater degree of crustal extraction earlier in the Earth's history. The second explanation could be that the Temeimichat assemblage was extracted from a depleted mantle reservoir which was more depleted than the global average depleted mantle. If the case, this would suggest the mantle was composed of isolated, heterogeneous reservoirs, and agrees with the findings in parts of the Pilbara Craton that suggest small isolated reservoirs of depleted mantle contributed to the greenstones there (Van Kranendonk et al., 2007a). If the case, it may be that the depleted mantle evolution curve is an accurate 'average depleted mantle evolution curve', but that it will not always be accurate in every instance due to heterogeneous mantle reservoirs. Either way, it is clear that depleted mantle evolution curves are not accurate for all rocks, and it is concurred with Kamber (2015) here, that a greater geochemical database of rocks with a depleted mantle origin would help to improve this situation by facilitating the production of updated models.

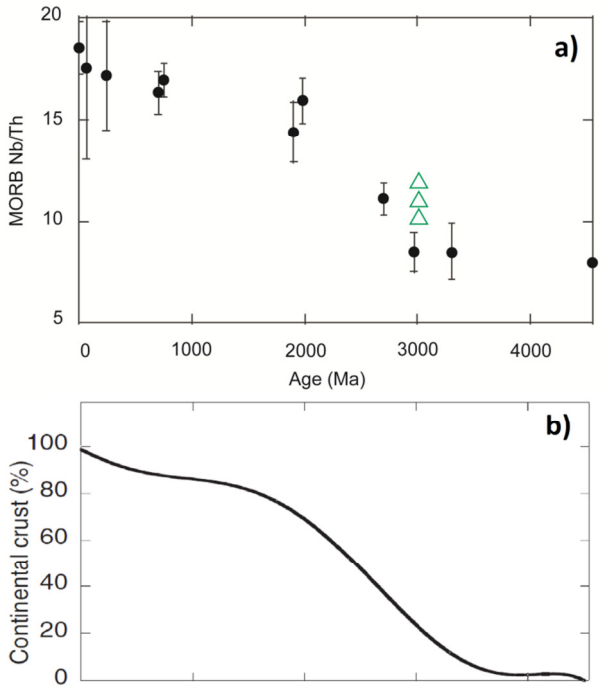


Figure 5.4.3: Temporal evolution trends for; a) Nb/Th ratios in the depleted mantle, with Temeimichat assemblage ratios plotted as green triangles, b) continental crust mass estimated using the Nb/Th ratios from 'a)' as well as Pb-isotope systematics. Modified from Kamber (2011).

5.4.3. Plate tectonic evolution:

In chapter 2.3 it was discussed that perhaps the greatest debate that exists in early Earth geology pertains to which crustal processes were responsible for the formation of granite-greenstone terranes. This debate generally focuses on two end members; horizontal tectonics, which is

largely driven by subduction, and vertical tectonics, which is largely driven by gravitational instability within the crust. It is generally accepted that the horizontal tectonics of the Wilson cycle (1966) is active on modern day Earth, and that the rock record suggests that it is unlikely this process was widely active on the earliest Earth (i.e. pre-Mesoarchean). A second aspect to the debate of early Earth tectonics relates to the timing of the onset of modern day tectonics. Arguments for and against modern day tectonics being active during the Hadean and Eoarchean were presented in chapter 2.3.3, including studies from the Nuvvuagittuq belt in Canada (O'Neil et al., 2012, Turner et al., 2014) and the Isua greenstone belt in Greenland (Bédard et al., 2013, Furnes et al., 2014). From these it appears that more evidence needs to be presented to provide a compelling argument that horizontal tectonics were active during the Hadean and Eoarchean eras. Arguably more evidence is also needed to support active horizontal tectonics during the Paleoarchean, with little evidence present in rocks of this age that is not also used to infer horizontal tectonic models in Eoarchean rocks. During the Mesoarchean however, there is a stronger case for active horizontal tectonics, as this is when the first large scale geological evidence as opposed to only the geochemical evidence and small scale geological evidence available for the older rocks. This includes the proposed subduction related suture zone which combines the West Pilbara Superterrane with the East Pilbara Terrane at ~3.09-3.07 Ga (Van Kranendonk et al., 2007b) and numerous structures, interpreted to be subduction-related, in the Kaapvaal Craton dated between 3.23 Ga and 3.08 Ga (Moyen et al., 2006). Interestingly, these events occurred shortly before the Aouéouat greenstone belt was formed, however there are still numerous studies of rocks younger than the Aouéouat greenstone belt which advocate vertical tectonics as the active mechanism by which granite-greenstone terranes were formed, e.g. the Abitibi greenstone belt which formed between 2760 Ma and 2670 Ma (Benn, 2006, Kamber, 2015). At least two separate recent studies have highlighted 3.0 Ga as the time for widespread subduction initiation. The first of these is Shirey and Richardson (2011) who note that ~3.0 Ga is when the first eclogite inclusions are found in diamonds, and although other mechanisms are possible to transport mafic rocks to a great enough depth to form eclogite, subduction is the easiest and therefore most likely solution. The second study is that of the model for crustal evolution through time by Dhuime et al. (2012) (Figure 2.2.5); their model proposes an inflection at 3.0 Ga when there appears to be a decrease in the rate of crustal growth. It is suggested by Dhuime et al. (2012) that rather than a decrease in the rate of crustal formation, this could represent the onset of a means by which crust was destroyed at an increased rate, i.e. subduction. The timing of these models coincides directly with the formation of the Aouéouat greenstone belt, and although there may be no direct significance to their coincidence, it is possible that the Aouéouat greenstone belt and surrounding TTG rocks could have experienced some subduction related process in their formation. It was concluded in chapter 2.3.6 that the

evidence points towards a Meso-Neoarchean time for the onset of modern day plate tectonics. One possible model for the onset of subduction which could apply to the Aouéouat greenstone belt is that presented by Gerya et al. (2015) in which mantle plumes drive the onset of subduction and horizontal tectonics. Should subduction have been a driving force behind the formation of the Aouéouat greenstone belt, it would need a model in which subduction coincides with a mantle plume, which the model of Gerya et al. (2015) provides. In this case, it could be that that the Aouéouat greenstone belt and surrounding TTG rocks preserve an example of subduction initiation during the Mesoarchean, the timing of which coincides with the models presented by Dhuime et al. (2012) and Shirey and Richardson (2011) of subduction initiation at ~3.0 Ga. The preferred model for the formation of the Aouéouat greenstone belt, presented in chapter 5.3.4, involves vertical tectonics and not subduction, however the possible ways in which subduction could have been the driving force were discussed, and so it cannot be ruled out that the Aouéouat greenstone belt does preserve evidence for Mesoarchean subduction. Whether or not the Aouéouat greenstone belt was formed through horizontal or vertical tectonics, it is clearly placed at a significant time in the Earth's history with regards to tectonic models. This study of the Aouéouat greenstone belt can therefore certainly add valuable information to the debate on what tectonic mechanisms were active during the Mesoarchean, and more precisely at ~3.0 Ga. From the studies discussed here, it is clear that both horizontal tectonics and vertical tectonics could have played a part in the formation of the Aouéouat greenstone belt with evidence existing for the possibility of both tectonic systems being active at this time.

Two of the topics which are at the forefront of the debate with regards to plate tectonic evolution, and were discussed in detail in chapter 2.3.5, are the arc signature of TTG rocks, and greenstone belt volcanic rocks representing modern day ophiolites. These will now be discussed in relation to the Aouéouat greenstone belt and surrounding TTG rocks. It is clear from the geochemistry of the TTG rocks in the Aouéouat greenstone belt that they exhibit the geochemical characteristics of the so called 'arc' signature, i.e. have a strongly fractionated REE profile, being enriched in LILE but not in HFSE, similar to that of modern day adakites. It is generally agreed that in order to create this geochemical signature, hydrated mafic rocks must be melted at depths great enough to allow the formation of a residual garnet bearing restite. This is therefore also most likely the case for the TTG rocks associated with the Aouéouat greenstone belt. The debate is ongoing however between the method of melting the hydrous mafic rock being through subduction, and subsequent melting of the subducted slab, or through melting at the base of an over thickened volcanic pile, i.e. a LIP. It is not possible to definitively apply one of these two models to the formation of the TTG rocks associated with the Aouéouat greenstone belt through geochemistry, and in particular the arc signature alone. This is currently the case for all granite-

greenstone terranes worldwide. Some authors continue to use this arc signature as evidence for subduction being the driving factor (e.g. Wang et al., 2004, Furnes et al., 2014) however more targeted geochemical studies appear to be highlighting small differences between TTG rocks and modern day adakites, for example La/Yb_{CN} vs Yb_{CN} (Figure 4.3.16b) (Martin, 1986, Kamber et al., 2002), suggesting that TTG rocks could not have been formed through 'conventional' subduction-related melting.

It was noted in chapter 2.3.5 that if greenstone belt volcanic rocks are representative of modern day ophiolites, this would be strong evidence for subduction being present throughout the Archean as the driving factor to obduct oceanic crust onto continental crust. As is the case for the majority, if not all Archean greenstone belts, there is no evidence in the Aouéouat greenstone belt of tectonised upper mantle harzburgite, with the ultramafic rocks being komatiitic flow volcanics. There is also no evidence for layered gabbro, or sheeted dyke complexes in the Aouéouat greenstone belt. The Temeimichat assemblage was seen to plot on the mantle array and shows no sign of crustal contamination, similar to modern day NMORB (Figure 4.3.8). There is no strong evidence that the Temeimichat assemblage is ensialic in origin, leaving the possibility open that it formed as oceanic crust. This however leaves the same debate as is seen in the literature as to whether or not greenstone volcanic rocks represent modern day ophiolites, with there being no apparent evidence from the Aouéouat greenstone belt that can stand against any of the arguments currently proposed by either side of the debate. Continuing on from the discussion presented in chapter 2.3.5, it can therefore be stated that there is no evidence in the Aouéouat greenstone belt that can be used to define it as an Archean equivalent of a modern day ophiolite. A more plausible tectonic setting of a LIP within an oceanic setting was presented in chapter 2.3.5 which fits the geological evidence available.

It was mentioned briefly above that the Temeimichat assemblage rocks possess a geochemical signature that could indicate formation at either a mid-ocean ridge setting or an oceanic plateau setting. Either of these are plausible environments, however by inference, a mid-ocean ridge setting would imply that modern day horizontal tectonics were underway, or at least a precursor to modern day horizontal tectonics was. Again, due to there being possible environments that could be active in both horizontal tectonic models and vertical tectonic models, these data alone do not support one over the other. There is no evidence in the Aouéouat greenstone belt of an ancient suture zone related directly to this region. There are many second and third order shear zones and faults present in the Aouéouat greenstone belt, for example the Tasiast Thrust, which are important with regards to gold mineralisation. These are almost certainly related to a large scale tectonic structure, however this is not exposed, or has not been located, and so cannot be

used to infer an ancient suture zone. The TISZ is the most likely feature in the Reguibat Shield to represent an ancient suture zone, and is discussed elsewhere (e.g. chapter 2.5.2.3 and 5.3.2), however this is almost certainly younger than the Aouéouat greenstone belt (although it is possible that the TISZ could be an older structure which was later reactivated). If this does represent a subduction related suture zone, the maximum age of which could be 2954 Ma (Key et al., 2008), there is no evidence to suggest is was in existence at the same time as the formation of the Aouéouat greenstone belt, however horizontal tectonics could have played a part in the later development of the region around the Aouéouat greenstone belt.

5.4.3.1. Plate tectonic evolution summary:

With regards to TTG rocks representing modern day adakites, the current evidence appears to highlight some geochemical differences between the two rock types. These geochemical differences suggest that subduction and the melting of the downgoing slab would not have been a viable source for the production of TTG rocks (Kramers, 1988, Nutman et al., 1999, Kamber et al., 2002), and these differences are also seen in the TTG rocks associated with the Aouéouat greenstone belt. It appears that the most viable alternative model for creating TTG rocks is that of the melting of an over thickened, hydrated mafic volcanic pile at depth. The major issue with this model is the difficulty in transporting enough water to depth in order to produce the volumes of TTG rocks that are formed in granite-greenstone terranes (Arndt, 2013). This is an issue that could be addressed in the future by modelling the conditions within an over thickened volcanic pile of hydrated mafic rocks, e.g. an oceanic plateau, in order to assess the feasibility of this setting as a viable source for TTG rock formation. With regards to greenstone volcanic rocks versus modern day ophiolites, there does not appear to be any evidence to suggest that the Aouéouat greenstone belt represents an obducted ophiolitic sequence. As well as this, there appears to be little direct structural evidence in the Aouéouat greenstone belt that would suggest a subduction setting was involved in its formation, although this evidence is generally only seen in large scale geophysical studies.

The preferred tectonic setting for the formation of the specific assemblages of the Aouéouat greenstone belt and surrounding TTG plutons that relate to the above discussion is that the Temeimichat assemblage was formed above a mantle plume, similar to a modern day oceanic plateau, and the TTG rocks were produced by the melting of this LIP at depth, and a vertical tectonic system resulting in partial convective overturn. The is not to say that subduction was not active at 3.0 Ga, only that there does not appear to be any strong evidence available within the

Aouéouat greenstone belt and surrounding TTG rocks that horizontal tectonics were the driving force behind their formation.

5.5. Comparison of the Aouéouat greenstone belt with Archean greenstone belts worldwide:

In this section the pertinent features of the Aouéouat greenstone belt and surrounding rocks will be compared to features from well-known granite-greenstone terranes worldwide. This will begin by introducing a number of granite-greenstone terranes, or greenstone belts, each of which will then be discussed in relation the Aouéouat greenstone belt with regards to any similarities of differences in their evolution. The location of the Archean cratons in which the discussed terranes are found can be seen in figure 2.1.2.

In chapter 4.2 it was demonstrated that the intermediate to felsic volcanic rocks of the Aouéouat assemblage formed between 3000 Ma and 2990 Ma, and it is probable that the ultramafic to mafic rocks of the Temeimichat assemblage formed only slightly earlier. This classifies the Aouéouat greenstone belt as Mesoarchean in age, and as one of the oldest known greenstone belts in the world. Well studied older greenstone belts, or granite-greenstone terranes, include the Isua greenstone belt (3.9-3.8 Ga), the East Pilbara Craton (3.5-3.2 Ga), and the Barberton greenstone belt (3.5-3.3 Ga). The Isua greenstone belt has been extensively studied due to it being the oldest known relatively well preserved and exposed greenstone belt, and one of the ongoing debates is regarding the tectonic processes involved in its formation (i.e. horizontal or vertical tectonics) (e.g. Nutman et al., 2007a, Friend and Nutman, 2010, Furnes et al., 2014). The East Pilbara Craton and the Barberton greenstone belt (part of the Kaapvaal Craton) are similar in age to one another, and it has been proposed that these were once part of the Vaalbara supercontinent (Cheney, 1996, de Kock et al., 2009). The East Pilbara Craton and Barberton greenstone belt have been extensively studied in relation to the mode of formation of granite-greenstone terranes, not only because of their age, but their size, and quality of exposure and preservation (e.g. de Wit, 1991, Collins et al., 1998, Moyen et al., 2006, Van Kranendonk et al., 2007a). The two regions also play host to a number of gold deposits (e.g. the McPhees and Iron Stirrup deposits in East Pilbara Craton (Baker et al., 2002), and the Sheba and Fairview deposits in Barberton greenstone belt (Agangi et al., 2014)). Granite-greenstone terranes which are known to have formed at or around the same time as the Aouéouat greenstone belt include a number of greenstone belt terranes from southwest Greenland dated between 3.07 Ga and 2.97 Ga (Polat et al., 2008, Ordóñez-Calderón et al., 2011, Polat et al., 2011, Szilas et al., 2013), the Koolyanobbing greenstone belt in the Yilgarn Craton (Angerer et al., 2013) and the Olondo greenstone belt in the Siberian Craton (Puchtel et al., 2004) both of which are dated at 3.00 Ga. The Belingwe greenstone belt of the Zimbabwe craton is slightly younger having been formed between 2.9 Ga and 2.7 Ga (Bolhar et al., 2003). Collectively, these named granite-greenstone belts are the best studied such terranes which are Mesoarchean in age. Two Neoarchean greenstone belts will also

be discussed due to their significance in granite-greenstone terrane debates; the 2.7-2.6 Ga Abitibi greenstone belt from the Superior Craton (Kerrich et al., 1998, Benn and Moyen, 2008) and the 2.7 Ga Kalgoorlie greenstone belt of the Yilgarn Craton (Barley et al., 2008, Barnes et al., 2012). A broad list encompassing close to half of the known global greenstone belts compiled by Furnes et al. (2015) in which they are ordered by age, can be used for reference.

5.5.1. East Pilbara Craton:

The East Pilbara Craton provides the strongest evidence of any granite-greenstone terrane worldwide of vertical tectonics. This is seen clearly in aerial photography where the light coloured and ovoid (due to the present day erosive surface) TTG bodies are enveloped by darker, linear greenstones (Figure 2.1.4). The same exposure levels are not seen in the Tasiast-Tijirit Terrane, however a number of studies have recorded vertical lineations within greenstone belts of the region (Rocci et al., 1991, Chardon, 1996, Schofield et al., 2012, Sims, 2014) highlighting that the tectonic history may be similar, with a greater degree of late deformation, and possibly a different exposure level resulting in the lack of clear dome-and-keel stratigraphy being present in the Tasiast-Tijirit Terrane. Although there are clear structural differences between the East Pilbara Terrane and the Aouéouat greenstone belt and surrounding TTG rocks, there are a number of similarities between the two regions. The Temeimichat assemblage greenstone belt volcanic rocks are almost certainly plume derived volcanics, while the Aouéouat assemblage volcanic rocks are also interpreted as being plume derived. The greenstone belt volcanic rocks of the East Pilbara Craton are also interpreted as plume derived volcanics, exhibiting similar geochemical LREE depletion in all komatiitic and basaltic komatiitic rocks other than a few rocks from the upper stratigraphy (e.g. in the Kelly or Sulphur Springs groups) (Van Kranendonk and Pirajno, 2004, Van Kranendonk et al., 2007a). These LREE enriched samples from the upper stratigraphy of the East Pilbara Craton greenstone volcanic rocks are interpreted as being plume derived volcanic rocks which have undergone increasing degrees of crustal contamination, similar to the crustal contamination exhibited in the Aouéouat assemblage which overlies the Temeimichat assemblage. The TTG rocks associated with the East Pilbara Craton are interpreted as being the product of large scale melting of these plume related volcanic rocks, again an interpretation which has been put forward in chapter 5.1.4 for the TTG rocks associated with the Aouéouat greenstone belt. A further similarity between the Aouéouat greenstone belt and the East Pilbara Craton is the extensive presence of inherited and detrital zircons from both volcanic and sedimentary rocks which are older than any dated supracrustal rocks, providing evidence of an older basement which is no longer exposed (Van Kranendonk et al., 2007b). The combination of these similarities between the Aouéouat greenstone belt and the East Pilbara Craton suggest that the East Pilbara

Terrane could be used as a reasonable proxy for the Aouéouat greenstone belt and surrounding TTG rocks, possibly extending to the entire Tasiast-Tijirit Terrane.

5.5.2. Barberton greenstone belt:

The Barberton greenstone belt on the Kaapvaal Craton as mentioned above has been linked to the East Pilbara Terrane for a number of reasons. There is less clear evidence for vertical tectonics being active in the Barberton greenstone belt however, with the debate as to its method of formation ongoing. The greenstone belt sequences of the Barberton greenstone belt have been interpreted as 15-21km thick , with the volcanic Onverwacht group being > 15km thick alone (Viljoen and Viljoen, 1969, Lowe and Byerly, 2007). This was therefore interpreted as being a LIP similar to that of an oceanic plateau, however other studies argue that this sequence has been thickened through isoclinal folding (de Wit, 1982) or that it is composed of an imbricated tectonic stack of multiple rock complexes (Furnes et al., 2011), the latter of which suggests a horizontal tectonic model for the formation of the Barberton greenstone belt. The Aouéouat greenstone belt is not as well exposed as the Barberton greenstone belt, and in general the rocks in the Aouéouat greenstone belt have undergone a greater degree of metamorphism and alteration. It is clear that the Aouéouat greenstone belt volcanic rocks are isoclinally folded in places, however it is not possible to determine the effect this has had on apparent thickening. Due to the fact that the Aouéouat greenstone belt has not been tilted, the thickness of the stratigraphy could only be determined by drilling, or possibly interpreted through geophysical studies. Currently a combination of drilling and geophysical studies suggests the Aouéouat greenstone belt could be < 5km thick (Figure 2.5.7), though as mentioned this is without the possible effect of apparent thickening being taken into account (Sims, 2014). The general stratigraphy of the Barberton greenstone belt and the Aouéouat greenstone belt is similar, in that it follows a typical greenstone belt model as was discussed in chapter 2.1. One of the significant coincidences between the Barberton greenstone belt and the Aouéouat greenstone belt is the presence of major orogenic gold deposits of a Mesoarchean age. This also poses a possibility that these two terranes were formed in a similar environment. There is an important distinction made with regards to the Aouéouat greenstone belt in that the gold mineralisation event was not the same as the granite-greenstone terrane forming event. This is also the case for the Barberton greenstone belt, and so the question here is whether the gold forming events were similar in nature. Both gold mineralisation events mark one of the final deformation events recorded the regions, and both have a < 100 Myr gap between greenstone belt formation and gold mineralisation, which may attribute towards their relatively small size when compared to the Neoarchean giant deposits (Bierlein et al., 2006). The exact nature of the event which drove the

gold mineralisation is unclear in both instances, with continental collision of an outboard terrane in the respective region being one possibility, and delamination of the SCLM being another. Until the tectonic model which led to gold mineralisation is known for both regions, and for orogenic gold deposits in general, it is not possible to ascertain whether or not the Barberton greenstone belt and the Aouéouat greenstone belt are analogous of one another with relation to their Mesoarchean orogenic gold deposits.

5.5.3. Greenstone belts ~3.0 Ga in age:

The vast majority of studies on the greenstone belts in the southwest of Greenland are focussed around the debate on whether greenstone belts represent modern day ophiolites, and are therefore evidence for Archean subduction. One of these greenstone belts, the Isua greenstone belt, was discussed in chapter 2.3.3.2, with arguments presented both for and against it being associated with horizontal tectonics and subduction. The younger greenstone belts from this region however, including the Ivisaartoq-Ujarassuit greenstone, the Storø greenstone belt and the Fiskenæsset greenstone belt have not been as extensively studied. Being the closest studied greenstone belts in age to the Aouéouat greenstone belt, the studies of the southwest Greenland greenstone belts are discussed in here relation to this project. The Storø greenstone belt preserves evidence for the tectonic imbrication of a mafic crust, with the accretion process occurring between 2960 Ma and 2600 Ma (Ordóñez-Calderón et al., 2011). The geochemistry of the Storø greenstone belt is comparable to that of subduction related volcanic rocks, and there is no evidence of crustal contamination (Ordóñez-Calderón et al., 2011). The Ivisaartoq-Ujarassuit and the Fiskenæsset greenstone belts contain volcanic rocks both with and without an arc signature, similar to the Aouéouat greenstone belt; however there are also boninites present in the Ivisaartoq-Ujarassuit greenstone belt pointing towards a subduction setting (Polat et al., 2011), and there is no field evidence or isotopic evidence to support crustal contamination as a source of the arc signature (Polat et al., 2010). These greenstone belts of southwest Greenland highlight there was a strong possibility that horizontal tectonics and subduction were active at ~3.0 Ga, and may therefore also have been the driving force behind formation of the Aouéouat greenstone belt. There appears however to be both tectonic (thrust-stacking) and geochemical (boninite signatures) evidence for subduction present in the greenstone belts of southwest Greenland that is not present in the Aouéouat greenstone belt and surrounding rocks. This may be due to some lithologies being unsampled or a lack of preservation of original structures in the Aouéouat greenstone belt, however although having formed at roughly the same time in Earth history, currently the southwest Greenland greenstone belts are not interpreted as being reasonable analogues for the Aouéouat greenstone belt.

The Koolyanobbing greenstone belt of the Yilgarn Craton, dated at 3.00 Ga, shows a number of similarities to the Aouéouat greenstone belt. It is interpreted to contain plume derived komatiites and tholeiitic basalts, some of which have not been affected by crustal contamination, and some of which do show signs of crustal contamination. Similar to the Aouéouat greenstone belt, the volcanic rocks of the Koolyanobbing greenstone belt have been interpreted to have possibly erupted in a rift basin, with the crustal contamination being sourced from the rift flanks (Angerer et al., 2013). One difference between the two greenstone belts however is that rocks with boninitic affinity have been found in the Koolyanobbing greenstone belt and are interpreted as evidence for subduction being active at the time. It therefore may be that the contamination is coming from a nearby oceanic arc complex and not rift flanks, and that a mantle plume led to the eruption of the Koolyanobbing greenstone belt volcanics in a setting similar to a modern day-like forearc convergent margin (Angerer et al., 2013). An arc setting was discussed as a possible model for the Aouéouat greenstone belt in chapter 5.1, however arc settings appear to be a recurring model for Archean greenstone belts, with the coincidence of a subduction zone and a mantle plume being necessary to explain the concurrence of these rock types. Until recently it would appear that the coincidence of a mantle plume and a subduction zone is a rather complicated model to be so commonly required to explain granite-greenstone terranes, with more simple models being provided as alternatives, though without the inferred subduction. This complex model may however may have been addressed by the model presented by Gerya at al. (2015) in which subduction is initiated by a mantle plume. No rocks with a boninitic signature have been sampled in the Aouéouat greenstone belt. If rocks with a boninitic signature do exist in the Aouéouat greenstone belt, and were to be sampled, this could lead to alternate models being proposed for the formation of the Aouéouat greenstone belt. The presence of boninitic rocks in the Aouéouat greenstone belt however it is thought to be unlikely due to the extensive sampling of the Aouéouat greenstone belt lithologies chosen for this project. The Olondo greenstone belt in the Siberian Craton is interpreted to represent an ophiolitic sequence, similar to the greenstone belts of southwest Greenland, with evidence of ultramafic plutonic rocks and boninitic rocks, neither of which are seen in the Aouéouat greenstone belt (Puchtel et al., 2004). The Olondo greenstone belt is therefore not interpreted as analogous of the Aouéouat greenstone belt.

5.5.4. Kalgoorlie Terrane and Abitibi greenstone belt:

The two major Neoarchean greenstone belts mentioned were the Kalgoorlie Terrane of the Yilgarn Craton and the Abitibi greenstone belt of the Superior Craton. Although Neoarchean in age, a time when there appears to be a stronger argument for horizontal tectonics and active

subduction, both of these regions are the subject of debate, with horizontal tectonic models as well as vertical tectonic models proposed (Kerrich et al., 1998, Barley et al., 2008, Benn and Moyen, 2008, Barnes et al., 2012). The Abitibi greenstone belt is another region within which the stratigraphy has been tilted and so a cross sectional area is exposed. Two opposing models proposed for the Abitibi greenstone belt are similar to those proposed for the Barberton greenstone belt in that 1) the Abitibi greenstone belt is composed of a series of tectonically juxtaposed sections of oceanic crust resulting from arc-continent accretion (Ludden et al., 1986, Kimura et al., 1993), and 2) the Abitibi greenstone belt is composed of one single tectonic terrane which probably formed as an oceanic plateau (Ayer et al., 2002, Benn, 2006). Geochemically, the Kalgoorlie Terrane is composed of similar lithologies to the Abitibi greenstone belt (Barnes et al., 2012). It also shows many similarities to the Temeimichat assemblage of the Aouéouat greenstone belt. The similar lithologies have been interpreted as analogues of modern day plume basalts associated with LIPs, though these are not necessarily oceanic plateau basalts, but instead may represent early stages of rift openings (e.g. as in the opening of the North Atlantic (Fitton et al., 1997, Barnes et al., 2012)). Although more recent developments have suggested that subduction did not play a part in the formation of the Kalgoorlie Terrane, the majority of studies on the greenstone belts of the Yilgarn Craton argue that they are composed of distinct tectonostratigraphic terranes juxtaposed during subduction and accretion (Swager et al., 1992, Barley et al., 2008). With regards to gold mineralisation, it is clear that source and/or preservation and/or tectonics changed at some point between the Mesoarchean and the Neoarchean resulting in Neoarchean cratons containing more significant gold deposits than Mesoarchean cratons. This is clearly seen in figure 5.2.1 by the significant elevation in the amount of available gold resources found within the Superior and Yilgarn Cratons at ~2.65 Ga (Goldfarb et al., 2001) compared to those available from older cratons. Often this increase in gold deposits contained within Neoarchean cratons is attributed to the development of horizontal tectonics and subduction related orogenic events leading to an increase in gold mineralisation at this time. The development of horizontal tectonics may however not be the reason, with some studies (e.g. Ayer et al., 2002, Barnes et al., 2012) appearing to suggest a non-subduction related tectonic regime for the major Neoarchean gold producing regions. It is still unclear as to what the active tectonic regime was that led to the formation of the greenstone belts of the Superior and Yilgarn cratons. It is clear however that there is a reasonable possibility that vertical tectonics were still active during the Neoarchean.

5.5.5. Summary of greenstone belt comparisons:

The West Pilbara Terrane is interpreted as being similar to that of the Aouéouat greenstone belt, as well as being similar to the Barberton greenstone belt. It is therefore likely that these were all formed under an analogous tectonic regime, however a definitive model cannot be confirmed. The Barberton greenstone belt has been extensively studied over the past four decades, and there is still no consensus on the method of its formation even with the high quality and extent of its exposure and relative lack of alteration. The Aouéouat greenstone belt however has poor surface exposure, and this is the only study to date on its origin and evolution. Studies on the greenstone belts of southwest Greenland, many of which are similar in age to the Aouéouat greenstone belt, do not appear to be analogous to the Aouéouat greenstone belt due to the strong evidence for subduction contained within these rocks that are not observed in the Aouéouat greenstone belt (e.g. boninites and an absence of crustal contamination). This may however be due to the small number of studies carried out on these two regions.

Extensive studies on the major Neoarchean cratons highlight that even at this time it is not understood whether horizontal or vertical tectonics were the driving factor behind the formation of granite-greenstone terranes, with strong arguments being presented for both. A definitive answer cannot be provided with regards to the mode of formation of the Aouéouat greenstone belt, however data presented as part of this project points towards a mantle plume and vertical tectonics being the driving forces behind the formation of the Aouéouat greenstone belt and surrounding TTG rocks. The data presented as part of this project add valuable information to the debate on granite-greenstone terrane formation, both temporally and spatially filling gaps in the record of the petrography, geochronology and geochemistry of granite-greenstone terranes.

5.6. Methodology discussion:

While this project was ongoing, a new geochemical facility was established at the Department of Geology, Trinity College Dublin. The setup of a new geochemical facility resulted in this project being a part of developing 'routine' protocols for major and trace element analysis, and for U-Pb geochronological studies. As well as the more routine geochemical and isotopic studies which were developed, two specific analytical methods were developed and tested: 1) a major test was carried out with respect to using chemical abrasion (CA) as a pre-treatment step to U-Pb zircon LA-ICP-MS geochronology, and 2) analysing Pb isotopes by in-situ Quadropole (Q) LA-ICP-MS of feldspars and pyrite. These are discussed below.

5.6.1. Chemical Abrasion (CA) LA-ICP-MS:

Pb-loss has been recognized as a major factor limiting the accuracy of zircon age determinations (Mattinson, 2005), and over the years various approaches have been developed to deal with this, including the Wetherill Concordia diagram (Wetherill, 1956) and air abrasion techniques (Krogh, 1982). Pb-loss affects U-Pb zircon analyses at all scales, whether the whole grain is analysed (e.g. TIMS), or only a small portion of the grain is analysed (e.g. SIMS). CA was specifically developed as a pre-treatment to eliminate or minimize Pb-loss in zircons prior to TIMS analysis (Mattinson, 2005), and has also been demonstrated to be effective for SIMS U-Pb zircon geochronology (Kryza et al., 2012). A part of this study aims to investigate if CA can be applied to LA-ICP-MS U-Pb zircon geochronology to reduce discordance, with a particular focus on the effect it has on Archean zircons, detrital populations, and samples with a complex age history. Although the technique has previously been applied to a small number of LA-ICP-MS U-Pb zircon studies (McConnell et al., 2009, Riggs et al., 2012, Riggs et al., 2013), it had not yet been rigorously assessed (Crowley et al., 2014). The protocols involved in the CA technique are detailed in chapter 3.4.2.

Two zircon standards were treated with (CA); 91500 and Penglai. U-Pb analyses were carried out on both the chemically abraded standards, and untreated versions of these standards. The depth of ablation pits in these samples were also measured using white light interferometry with an aim to understand if the CA processes had any effect on ablation rates. It was found that the pre-treatment did indeed have an effect on ablation rates, with the CA zircons yielding shallower pits, and the untreated zircons displayed a greater degree of laser-induced elemental fractionation effects (Figure 5.6.1). The disparity in down-hole fractionation is likely depth dependant, which illustrates that primary reference materials should be chemically abraded when analysing CA unknowns. It is still possible however that reference materials and unknowns will respond

differently to the treatment, resulting in differing down-hole fractionation of U-Pb and Th-Pb. Accurate measurement and comparison of ablation depths may help to minimise any mismatch between the down-hole fractionation of reference materials and unknown samples (Crowley et al., 2014). As a result of this test, all analyses carried out on CA zircons in this project used CA 91500 (91500CA) as the primary standard.

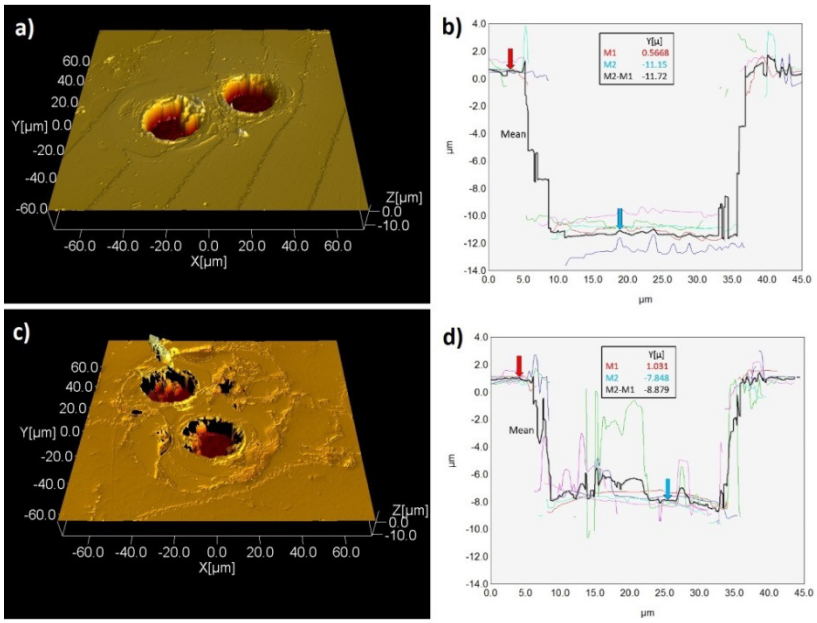


Figure 5.6.1: Ablation pit profiles from sample TSUPB021; a) 3D view of untreated zircons, b) cross-sectional view of untreated zircons, c) 3D view of chemically abraded zircons, d) cross-sectional view of chemically abraded zircons.

CA was applied to a subset of three samples from this project as a pre-treatment; two greywackes from West Branch (TSUPB020 and TSUPB021) and one TTG surface sample (TSUPB029). The physical effect CA had on the zircons is seen clearly in figure 4.2.14, in which all grains exhibit some signs of partial dissolution. In sample TSUPB029, which had the greatest Pb-loss induced discordance of the three treated samples in the untreated subset (Figure 4.2.20a), ~75% of the zircons were completely dissolved during CA. This suggests that the portions of zircons which remain yield the least discordant analyses, an observation which is supported by the fact that only eight analyses from the three samples (115 analyses in total) were > 10% discordant. This highlights that CA is extremely effective in removing discordant grains, and discordant zones within grains prior to analysis by LA-ICP-MS, with only the least discordant zircons surviving the CA process. The benefits of this are that a smaller number of analyses can be carried out on each sample, with the knowledge that the analyses that are carried out are more likely to have minimal discordance and produce more statistically valid data. This is preferable to carrying out a vast number of analyses with a large proportion being unusable when calculating an age for the

sample, thus saving on valuable instrument time and costly resources. The effects of CA are particularly useful with Archean zircons, as often the majority of Archean zircons are discordant in nature due to Pb-loss with a relatively large proportion of the analyses being unusable (e.g. Key et al., 2008, Schofield et al., 2012). It was seen in chapter 4.2.3 that CA did not show any signs of preferentially dissolving one particular detrital population, with the results of both greywacke samples producing the same ages both with and without the CA pre-treatment (Figure 4.2.16). The results from these samples were in fact improved post CA due to the removal of analyses which had been affected by Pb-loss, and the appearance of more defined age peaks which are associated with different source lithologies.

TSUPB029 showed signs of stronger Pb-loss and common Pb-effects pre CA, and this resulted in a much smaller proportion of the grains which underwent CA surviving the effects of dissolution. A problem which was exhibited in this sample is that one population of zircons, interpreted to be hydrothermal in nature, was completely dissolved. Had this sample only been analysed post CA, then this zircon population would have been completely omitted from the results. At the same time however, two distinct concordant zircon populations were defined post CA that were not distinguishable pre-treatment.

The results of this study highlight both advantages and concerns with regards to the use of CA on zircons prior to LA-ICP-MS. Both instrument time, and therefore costs can be reduced due to the pre-removal of discordant grains, or zones within grains. The higher degree of concordance also results in more precise age data being acquired. The distinction of multiple concordant age populations may be achieved where previously only one age population was interpreted due to the removal of less concordant grains between these populations. Concerns however exist that it is possible to remove entire zircon populations during the CA process. This is particularly apparent with high-U zircons, where grains with U concentrations higher than ~1100 ppm were removed during CA, seen when comparing treated and untreated analyses. This resulted in the complete removal of the hydrothermal population form TSUPB029, and although it did not affect the greywacke samples, it could in theory bias detrital studies through the removal of specific zircon populations. This study therefore shows the benefit of combining both untreated as well as CA zircons when analysing complex samples. When analysing non-complex samples CA is recommended due to the removal of discordant grains before analysis, which could prove particularly useful for studies on Archean rocks due to the discordant nature of Archean zircons, however CA should not be used alone on complex samples due to the possibility of preferentially dissolving entire age populations prior to analysis. Details of this study have been published, and are available in Appendix 10.

5.6.2. Pb-Pb isotope analysis using Q-LA-ICP-MS:

A minor aspect of this study examined if Quadropole (Q)-LA-ICP-MS is a viable method for measuring Pb isotopes. Pb isotopes are most commonly, and successfully analysed using the multi-collector TIMS method (Woodhead and Hergt, 2001), however it has been shown that laser ablation is also a viable method when combined with a multi-collector ICP-MS (Tyrrell et al., 2009, Souders and Sylvester, 2010). Woodhead et al. (2009) tested Q-LA-ICP-MS and the pitfalls and benefits discovered in this study were discussed in chapter 3.4.6.

The results of this study highlighted that the errors for the standard analyses on NIST612 are significant in size (2-3 orders of magnitude greater than the accepted multi-collector TIMS values (Woodhead and Hergt, 2001), 1-2 orders of magnitude greater than errors collected using multi-collector LA-ICP-MS (Tyrrell et al., 2009)); however the standard data are within error of the accepted values (see Chapter 3.4.6). There were problems with using in-situ laser ablation on thin section slides, as in order to achieve a strong enough signal the higher laser output resulted in most of the feldspar grains splitting from the section. This resulted in feldspars being hand-picked and mounted in pucks, similar to the pyrite. Problems were also encountered in acquiring high enough Pb counts from the pyrite analyses, although the only solution to this is to use alternate minerals, or analyse a higher sample size with the prospect of ablating more galena inclusions within the pyrite.

Although only run as an initial test, some interesting results were found. The first of these is that the hydrothermally altered TTG rock possesses a similar Pb isotope signature to the pyrites from the mineralised quartz veins, providing further evidence that this TTG rock was affected by the gold mineralisation event at Tasiast. It was also discernible that pyrite from the gold bearing quartz-carbonate veins have a distinct Pb isotope signature from the pyrite hosted in the gold-barren quartz-carbonate veins. It is expected that with a higher number of analyses this data could be more constrained, and statistically significant. The results from this study therefore highlight that low resolution, however usable Pb isotope data can be collected using Q-LA-ICP-MS. Importantly however, the standard data collected from this study highlight that with a large enough sample size, Pb isotope data collected from Q-LA-ICP-MS can be accurate, but is clearly less precise than TIMS or multi-collector LA-ICP-MS methods. Depending on the quality and precision of the Pb-isotope data needed for a specific purpose, Q-LA-ICP-MS may therefore become a preferred method for the collection of Pb isotope due to the greater instrument availability and lower costs associated with this method.

5.7. Future studies:

The results of this project have added a vast amount of data and knowledge to the relatively understudied Tasiast-Tijirit Terrane, and allowed a model to be proposed for the formation and evolution of the region, and in particular the Aouéouat greenstone belt. It is clear however that there are still many areas of uncertainty in relation to the geological history of the region, and this project has raised a number of questions that have still to be answered. The most pertinent questions are discussed here, with a short outline of future studies that could be undertaken to address them.

5.7.1. Isotope studies:

One of the major findings of this thesis is that the Temeimichat assemblage was sourced from a depleted mantle reservoir, and signals a period of juvenile crustal formation. It was discussed in chapter 5.4.2 that there is a need to add data to, and evaluate, current models for the evolution of the depleted mantle, and that in order to achieve this, a greater geochemical database of rocks with a depleted mantle origin should be developed (Babechuk and Kamber, 2011, Kamber, 2015). Neodymium isotopes were analysed on two samples from the Temeimichat assemblage as part of this study, and showed that at least part of the Temeimichat assemblage appears to be more depleted than the depleted mantle evolution curve of DePaolo & Wasserburg (1976) at its time of extrusion (Figure 4.3.10). The Temeimichat assemblage therefore provides a valuable example of a Mesoarchean rock assemblage that could add to this geochemical database, and aid in developing updated depleted mantle evolution curves. Such updated mantle evolution curves could have a major impact on all models in this area of research. In order to achieve this, an expanded isotope study of the Temeimichat assemblage could be carried out, analysing Nd, Pb and Hf isotopes of the juvenile, uncontaminated rocks. A suite of samples have already been collected from the Temeimichat assemblage, a number of which have been analysed for major and trace element data (Appendix 7), and would provide a suitable starting point for future Nd, Pb and Hf isotope studies.

One of the assumptions made in the model for formation of the Tasiast-Tijirit Terrane (Figure 5.3.1), is that the TTG rocks surrounding the Aouéouat greenstone belt were created through reworking of the juvenile Temeimichat assemblage. The basis for this assumption is that all previous Nd model ages published from TTG rocks in the Tasiast-Tijirit Terrane are < 3.1 Ga, similar to those of the Temeimichat assemblage, and therefore they do not appear to contain a significant older component. This contrasts with the volcanic rocks of the Aouéouat assemblage

which have Nd model ages > 3.1 Ga. Although a reasonable assumption is to estimate that TTG rocks surrounding the Aouéouat greenstone belt feature the same Nd isotope signatures as the TTG rocks of the Tasiast-Tijirit Terrane, this could be confirmed by carrying out a Nd isotope study focussed on the TTG rocks surrounding the Aouéouat greenstone belt. The result of this would be to add strength, or question the model that the vast majority of the Tasiast-Tijirit Terrane is composed of TTG rocks derived through the reworking of a large igneous province.

In addition to carrying out whole rock Pb isotope analysis on the Temeimichat assemblage, this study highlighted that there are benefits to studying the Pb isotope ratios of sulphide minerals associated with mineralisation events, as well as the Pb isotope ratios of feldspars from TTG rocks. It was concluded in chapter 5.2 that it is likely that the Pb isotope signature of the feldspars in sample TSUPB029 have been reset by the main mineralising hydrothermal event, resulting in similar values. It was also concluded that it is unlikely that the gold mineralisation event in the Aouéouat greenstone belt was sourced from TTG intrusions. Although the Pb isotope data collected as part of this project was minimal, it is clear that the quartz-carbonate veins which host gold have a distinct Pb isotope signature from those which are barren of gold (Figure 4.4.1). Future studies may therefore benefit in focussing on the Pb isotopes of sulphide minerals of different quartz-carbonate veins in order to discern which veins are part of the suite of gold hosting veins, and those which are not. The Q-LA-ICP-MS study carried out as part of this project highlighted that unless a large number of analyses are carried out on a mineral (e.g. pyrite); the data acquired is quite low precision. It would therefore be recommended that any future study attempting to determine the Pb isotope signatures of quartz-carbonate veins in the Aouéouat greenstone belt use a multi-collector ICP-MS. This is not to say that quadrupole analyses of Pb isotopes are not useful, in that as seen in this study the presence of different generations of sulphides were clearly discerned using the relatively quick and cheap method of Q-LA-ICP-MS. Studies such as this highlight projects worth refining with a more detailed and focussed study, as is the case here.

5.7.2. TTG rocks and orthogneissic basement:

With this study focussing on the stratigraphy of the Aouéouat greenstone belt, only one sample was collected form a surrounding TTG pluton (TSUPB012), which was dated at 2967 ± 11 Ma. A further two TTG intrusions were inadvertently selected for geochronology in an attempt to sample the orthogneissic basement, as well as a TTG intrusion into the Aouéouat greenstone belt stratigraphy, all of which lie within the age range of TTG rocks of the Tasiast-Tijirit Terrane of between ~2970 Ma and ~2910 Ma. It was stated in chapter 4.3.6 that there is a very large

variability in TTG rock chemistry through the possibility of multiple melt sources and assimilation events, as well as the heterogeneity of hand specimens even within a relatively small outcrop (Kamber et al., 2002), and that the samples analysed as part of this project are unlikely to be fully representative of the TTG rocks in the region. Further to this, the only detailed studies into the TTG rocks of the Tasiast-Tijirit Terrane have been at the margins of the region, and related to the relationships with neighbouring terranes (Key et al., 2008, Bea et al., 2013, Gärtner et al., 2013, Montero et al., 2014). This leaves scope for a more detailed study into the TTG rocks associated with the greenstone belts of the Tasiast-Tijirit Terrane, which could involve mapping of the different generations of TTG plutons, as well as both geochronological and isotope studies of the rocks. The geochronological studies would aid in confirming whether or not there was continuous TTG formation from ~2970-2910 Ma, or whether this was punctuated by discrete pulses of TTG plutonism. The isotope studies, as discussed above would help to elucidate whether the TTG rocks are solely derived from the reworking of a juvenile LIP. All of these data would be valuable in developing the current model presented for the formation of the Tasiast-Tijirit Terrane.

A particularly interesting finding in this project is that one of the TTG rocks sampled (TSUPB029) appears to have been altered by the same hydrothermal event that has deposited the gold in the Aouéouat greenstone belt at ~2840 Ma. This sample is also linked to the mineralisation event through similar Pb isotope signatures. It has been proposed in this thesis the TTG rocks have been affected by the hydrothermal event, and not that the TTG rock emplacement drove the hydrothermal mineralisation event; however a TTG source does remain a possibility. It is clear that either way, the gold mineralisation event is linked to at least some TTG rocks, and a more expansive study of the TTG rocks surrounding the Aouéouat greenstone belt may elucidate this link, and could lead to the discovery of further rocks that have been affected by the hydrothermal event at ~2840 Ma, and possibly lead to the discovery of new gold deposits.

A further important aspect of a more detailed study into the TTG rocks of the Tasiast-Tijirit Terrane would be to possibly confirm the presence of an orthogneissic basement in the region. It is clear that this was not sampled as part of this project for reasons discussed in chapter 5.1, however it certainly was exposed at the time the Tasiast assemblage was deposited (Figure 4.2.15). The presence of exposed orthogneissic basement of a similar age has been documented in the geological similar western Leo Shield (Kouamelan et al., 1997, Bering, 1998, Thiéblemont et al., 2001), and exposed orthogneissic basement in the Tasiast-Tijirit Terrane was described by Key et al. (2008). Although what was described by Key et al. (2008) may in fact be the migmatitic texture of the TTG plutons sampled as part of this project (Figure 2.5.9), there is enough evidence

to suggest that the orthogneissic basement is exposed somewhere in the Tasiast-Tijirit Terrane, and sampling these rocks should be a priority of any future study into the TTG rocks of this region.

5.7.3. Additional geochronology:

Although this study was successful in dating the majority of the stratigraphy in the Aouéouat greenstone belt, there are some lithologies which remain undated. The most significant of these is the ultramafic to mafic rocks of the Temeimichat assemblage. The difficulties in dating ultramafic to mafic greenstone belt volcanic rocks are not unique to this study, and were discussed in chapter 2.1. It is possible that further Sm-Nd isotope studies may allow the calculation of a Sm-Nd isochron age for the Temeimichat assemblage, with only two Sm-Nd isotope analyses being carried out on this assemblage in this project, however there does not appear to be a large range of Sm-Nd ratios present in the trace element geochemistry of these samples, and a Sm-Nd isochron age calculation may still prove difficult to achieve. The lack of a crustal signature in any of the Temeimichat assemblage rocks removes the possibility of inherited zircons being used to place an age constraint on the timing of the Temeimichat assemblage, and so although further studies could possibly add a tighter constraint to the currently preferred age of close to 3.01 Ga, it appears unlikely that the Temeimichat assemblage will be accurately dated until further methods are developed to date ultramafic to mafic rocks.

A further lithology that proved undatable in this project was the quartz-diorite of the Aouéouat assemblage which hosts the gold mineralisation at West Branch. This lithology is devoid of zircon, however U-Pb apatite ages proved to be successful in dating the quartz-carbonate veins. It may therefore be possible to separate apatite from the least altered quartz-diorite sample (i.e. least likely to have hydrothermally reset U-Pb apatite ages) in order to date the crystallisation age of this lithology. If the quartz-diorite of the Aouéouat assemblage however remains undated, the age constraint for the formation of the Aouéouat assemblage of 3000 Ma to 2990 Ma almost certainly applies here.

5.7.4. Banded iron formation:

One major aspect of greenstone belts that was only touched upon as a part of this project is that of banded iron formations. As discussed in chapter 4.2.5, an attempt was made to date one banded iron formation (FZ-12-02) from the Aouéouat greenstone belt due to it containing a relatively large proportion of detrital material, possible sourced through ash falls. This would have aided in constraining the timing of deposition for the Tasiast assemblage if successful. One of the

major uses of banded iron formations in Archean (and Proterozoic) studies however is that of reconstructing paleo environmental conditions; in particular seawater geochemistry (Bolhar et al., 2004, Bekker et al., 2010). In order to achieve this, trace element geochemistry would need to be carried out on single chert horizons, which would contain the trace element signature of the seawater from which they precipitated. As with other possible studies discussed above, this would aid greatly in the development of the tectonic model for formation of the Tasiast-Tijirit Terrane. In particular, it could help elucidate the type of basin in which the Tasiast assemblage, and likely the entire Aouéouat greenstone belt was deposited in, whether that be a closed basin (e.g. an intra-continental pull-apart basin), or in the open ocean (e.g. oceanic plateau). As well as adding to the model of the Tasiast-Tijirit Terrane, significant banded iron formations are present in the Ijil Complex, allochthonous to the Tiris Complex (Bronner and Chauvel, 1979, Bronner and Fourno, 1992) and stromatolites are present in the Atar Group, part of the Taoudeni basin to the southwest of the Tasiast-Tijirit Terrane (Fairchild et al., 1990, Kah et al., 2009). Geochemical studies of these banded iron formations and stromatolites would also contribute to an improved understanding of global environmental changes over geological timescales with a specific application to the Archean and Proterozoic, and would also almost certainly provide data for both before and after the globally significant great oxygenation event.

Chapter 6: Conclusion

The Aouéouat greenstone belt is composed of three major stratigraphic packages; the Temeimichat assemblage, the Aouéouat assemblage, and the Tasiast assemblage, and is surrounded by TTG plutonic rocks on all sides. The Temeimichat assemblage is juvenile in nature, composed of mantle plume derived ultramafic to mafic komatiite and basaltic komatiites. It was likely extruded into a rift basin at ~3.01 Ga which was formed due to the break-up of a 3.32-3.17 Ga pre-existing continental crust due to the anomalous heat produced by the presence of the mantle plume. The Aouéouat assemblage, composed of mafic to felsic volcanic rocks, unconformably overlies the Temeimichat assemblage, having been extruded between 3.00 Ga and 2.99 Ga. This rock sequence contains a crustal component, which was likely attained by eruption of these volcanic rocks through the pre-existing basement. Following formation of the greenstone belt volcanic rocks, extensive melting at the base of the LIP resulted in partial convective overturn and extensive production of TTG rocks from 2.97-2.91 Ga. Displacement in the crust caused by emplacement of TTG rocks resulted in initially locally derived sediments being deposited through the erosion of the greenstone belt volcanic rocks to form the base of the Tasiast assemblage. Eventually sediments sourced from a greater range of lithologies and distances were deposited, including sediments derived from the exposure and erosion of the TTG rocks themselves, and erosion of proximal gneissic basement. Banded iron formations were deposited during periods of tectonic quiescence with minimal sedimentary input. An orogenic event caused by collision of an outboard terrane, possibly the Amsaga Complex, occurred at ~2.84 Ga. This event resulted in the reactivation of faults and shear zones in the Aouéouat greenstone belt which were likely initially formed during partial convective overturn of the terrane. A hydrothermal event at ~2.84 Ga utilized these faults and shear zones as fluid pathways, liberated gold from the juvenile Temeimichat assemblage, and deposited gold in the overlying Aouéouat and Tasiast assemblages, forming the Tasiast gold deposit. The final Archean event to affect the region is a ~2.76 Ga tectonothermal event which resulted in the emplacement of pegmatitic rocks. Evidence for a tectonothermal event of this age is also seen in the Amsaga Complex, through the emplacement of the Ahmeyim Great Dyke of Mauritania, and possibly some late movement on the Tâçarât-Inemmaûdene Shear Zone, however the cause of this event is unknown. This interpretation for the formation of the Aouéouat greenstone belt and surrounding rocks is inferred to be the case for the entire Tasiast-Tijirit Terrane of the Reguibat Shield. A similar evolution to that of the Tasiast-Tijirit Terrane may have occurred in the rocks of the Guinea Rise of the Leo Shield, signifying a possible co-existence of some terranes of the Leo and Reguibat Shields since > 3.3 Ga.

The ~2.84 Ga Tasiast gold deposit is one of few Archean orogenic gold deposits which predates the major global period of Neoarchean gold deposition. It is also the first known Archean orogenic gold deposit of the West African Craton, adding valuable data to both the temporal and spatial evolution of orogenic gold deposits worldwide. The extensive presence of a ~2.84 Ga tectonothermal event in rocks of the Reguibat Shield, and those further afield, highlights there is potential for further major gold deposits of this age to be discovered should the appropriate lithological and structural conditions be present.

Two episodes of crustal growth are recorded in the Aouéouat greenstone belt, one at ~3.27 Ga, and one at ~3.01 Ga. The ~3.27 Ga crustal growth event likely resulted in the formation of the orthogneissic basement, and is recorded in both whole rock Nd model ages and detrital zircon data. Rocks from this earlier crustal growth episode also contributed to formation of the Aouéouat assemblage. The crustal growth episode at ~3.01 Ga is recorded in the first stage juvenile rocks of the Temeimichat assemblage. A large proportion of crust formed in this episode of crustal growth was re-melted and crystallised as TTG rocks of the Tasiast-Tijirit Terrane.

According to current models for depleted mantle evolution, Nd isotopes and trace element ratios suggest that the Temeimichat assemblage was derived from a mantle reservoir which was depleted to a greater extent than that of the depleted mantle. This could highlight one of two possibilities; that the Temeimichat assemblage was derived from an isolated mantle reservoir which has undergone extensive previous melt extraction, or that current models for depleted mantle evolution are not accurate. It is clear from this thesis that current depleted mantle evolution models are not applicable to all studies. With such a large number of crustal and mantle evolution studies relying on the current models for the depleted mantle, there is a clear necessity to develop updated models for the evolution of the depleted mantle. Due to the geochemical and isotopic signatures the Temeimichat assemblage contains, these would be suitable rocks for inclusion in the development for improved depleted mantle evolution models.

The evolution of modern day like plate tectonics remains a hotly debated topic. Evidence from the Aouéouat greenstone belt suggests that vertical tectonics, i.e. partial convective overturn and sagduction, were still active between 3.0 Ga and 2.9 Ga, with the driving force behind the formation of the Aouéouat greenstone belt volcanic rocks being the development of a mantle plume, and its subsequent relative migration. It is possible, that by ~2.84 Ga, horizontal tectonics and subduction had developed in the region, resulting in the orogenic event which led to gold mineralisation in the Aouéouat greenstone belt. Other tectonic mechanisms for this ~2.84 Ga event however remain a possibility.

From an analytical perspective, there is an evident issue with age determinations for Archean zircons in that major Pb-loss is often an issue which impedes calculation of robust ages. Chemical abrasion as a pretreatment for LA-ICP-MS was developed as part of this study and contributed to the first publication demonstrating this utility. The technique proved to be successful in minimizing discordance for LA-ICP analysis, resulting in a more accurate definition of age populations acquired through a smaller number of analyses. Chemical abrasion is recommended as a procedure prior to analyzing Archean zircons; however for complex samples (i.e. those with multiple age populations, or hydrothermal overprinting) it is most effective when used in tandem with untreated zircons in order to reduce the possibility of completely removing individual high-U zircon populations, and for samples with a small zircon yield it is discouraged. U-Pb apatite geochronology also proved to be a successful technique as a part of this research, constraining an age of 2840 ± 35 Ma for the hydrothermal event which resulted in the gold mineralisation of the Tasiast deposit. This represents one of the oldest known U-Pb apatite ages, while also highlighting that no major regional tectonothermal events have affected the Aouéouat greenstone belt since ~2.84 Ga.

References:

AGANGI, A., HOFMANN, A. & PRZYBYŁOWICZ, W. 2014. Trace element zoning of sulfides and quartz at Sheba and Fairview gold mines: Clues to Mesoarchean mineralisation in the Barberton Greenstone Belt, South Africa. *Ore Geology Reviews,* 56**,** 94-114.

ALEXANDER, B. W., BAU, M. & ANDERSSON, P. 2009. Neodymium isotopes in Archean seawater and implications for the marine Nd cycle in Earth's early oceans. *Earth and Planetary Science Letters,* 283**,** 144-155.

ALLÈGRE, C. J. & ROUSSEAU, D. 1984. The growth of the continent through geological time studied by Nd isotope analysis of shales. *Earth and Planetary Science Letters,* 67**,** 19-34.

ANDRES, M., BLICHERT-TOFT, J. & SCHILLING, J.-G. 2004. Nature of the depleted upper mantle beneath the Atlantic: evidence from Hf isotopes in normal mid-ocean ridge basalts from 79°N to 55°S. *Earth and Planetary Science Letters,* 225**,** 89-103.

ANGERER, T., KERRICH, R. & HAGEMANN, S. G. 2013. Geochemistry of a komatiitic, boninitic, and tholeiitic basalt association in the Mesoarchean Koolyanobbing greenstone belt, Southern Cross Domain, Yilgarn craton: Implications for mantle sources and geodynamic setting of banded iron formation. *Precambrian Research,* 224**,** 110-128.

ANHAEUSSER, C. R. 2014. Archaean greenstone belts and associated granitic rocks – A review. *Journal of African Earth Sciences,* 100**,** 684-732.

ARMSTRONG, R. L. & HARMON, R. S. 1981. Radiogenic Isotopes: The Case for Crustal Recycling on a Near-Steady-State No-Continental-Growth Earth [and Discussion]. *Philosophical Transactions of the Royal Society of London A: Mathematical, Physical and Engineering Sciences,* 301**,** 443-472.

ARNDT, N. T. 1994. Archaean komatiites. In: Condie K.C. (ed) Archaean crustal evolution. *Developments in Precambrian geology,* 11**,** 11-44.

ARNDT, N. T. 2013. The Formation and Evolution of the Continental Crust. *Geochemical Perspectives,* 2**,** 405-405.

ARNDT, N. T. & JENNER, G. A. 1986. Crustally contaminated komatiites and basalts from Kambalda, Western Australia. *Chemical Geology,* 56**,** 229-255.

ARNDT, N. T., LESHER, M. & BARNES, S. 2008. Komatiite.

ARNE, D. C., BIERLIN, F. P., MORGAN, J. W. & STEIN, H. J. 2001. Re-Os dating of sulfides associated with gold mineralization in Central Victoria, Australia. *Economic Geology,* 96**,** 1455-1459.

ARTEMIEVA, I. M. & MOONEY, W. D. 2001. Thermal thickness and evolution of Precambrian lithosphere: A global study. *Journal of Geophysical Research,* 106.

AUVRAY, B., PEUCAT, J. J., POTREL, A., BURG, J. P., CARUBA, C., DARS, R. & LO, K. 1992. New radiometric data on the Archean of the Reguibat Rise (Amsaga, Mauritania). *Comptes Rendus De L Academie Des Sciences Serie Ii,* 315**,** 63-70.

AYER, J., AMELIN, Y., CORFU, F., KAMO, S., KETCHUM, J., KWOK, K. & TROWELL, N. 2002. Evolution of the southern Abitibi greenstone belt based on U–Pb geochronology: autochthonous volcanic construction followed by plutonism, regional deformation and sedimentation. *Precambrian Research,* 115**,** 63-95.

BABECHUK, M. G. & KAMBER, B. S. 2011. An estimate of 1.9 Ga mantle depletion using the high-field-strength elements and Nd–Pb isotopes of ocean floor basalts, Flin Flon Belt, Canada. *Precambrian Research,* 189**,** 114-139.

BABECHUK, M. G., KAMBER, B. S., GREIG, A., CANIL, D. & KODOLÁNYI, J. 2010. The behaviour of tungsten during mantle melting revisited with implications for planetary differentiation time scales. *Geochimica et Cosmochimica Acta,* 74**,** 1448-1470.

BABECHUK, M. G., WIDDOWSON, M. & KAMBER, B. S. 2014. Quantifying chemical weathering intensity and trace element release from two contrasting basalt profiles, Deccan Traps, India. *Chemical Geology,* 363**,** 56-75.

BABECHUK, M. G., WIDDOWSON, M., MURPHY, M. & KAMBER, B. S. 2015. A combined Y/Ho, high field strength element (HFSE) and Nd isotope perspective on basalt weathering, Deccan Traps, India. *Chemical Geology,* 396**,** 25-41.

BAGAS, L., BIERLEIN, F. P., BODORKOS, S. & NELSON, D. R. 2008. Tectonic setting, evolution and orogenic gold potential of the late Mesoarchaean Mosquito Creek Basin, North Pilbara Craton, Western Australia. *Precambrian Research,* 160**,** 227-244.

BAHLBURG, H. 1998. The geochemistry and provenance of Ordovician turbidites in the Argentine Puna. *Geological Society, London, Special Publications,* 142**,** 127-142.

BAKER, D. E. L., SECCOMBE, P. K. & COLLINS, W. J. 2002. Structural History and Timing of Gold Mineralization in the Northern East Strelley Belt, Pilbara Craton, Western Australia. *Economic Geology,* 97**,** 775-786.

BARKER, F. & ARTH, J. G. 1976. Generation of trondhjemitic-tonalitic liquids and Archean bimodal trondhjemite-basalt suites. *Geology,* 4**,** 596-600.

BARLEY, M. E., BROWN, S. J. A., KRAPEŽ, B. & KOSITCIN, N. 2008. Physical volcanology and geochemistry of a Late Archaean volcanic arc: Kurnalpi and Gindalbie Terranes, Eastern Goldfields Superterrane, Western Australia. *Precambrian Research,* 161**,** 53-76.

BARLEY, M. E., EISENLOHR, B. N., GROVES, D. I., PERRING, C. S. & VEARNCOMBE, J. R. 1989. Late Archean convergent margin tectonics and gold mineralization: A new look at the Norseman-Wiluna Belt, Western Australia. *Geology,* 17**,** 826-829.

BARNES, S. J., FISHER, L. A., ANAND, R. & UEMOTO, T. 2014. Mapping bedrock lithologies through in situ regolith using retained element ratios: a case study from the Agnew-Lawlers area, Western Australia. *Australian Journal of Earth Sciences,* 61**,** 269-285.

BARNES, S. J., VAN KRANENDONK, M. J. & SONNTAG, I. 2012. Geochemistry and tectonic setting of basalts from the Eastern Goldfields Superterrane. *Australian Journal of Earth Sciences,* 59**,** 707-735.

BARRIE, C. T., LUDDEN, J. N. & GREEN, T. H. 1993. Geochemistry of volcanic rocks associated with Cu-Zn and Ni-Cu deposits in the Abitibi Subprovince. *Economic Geology,* 88**,** 1341-1358.

BARTH, M. G., RUDNICK, R. L., CARLSON, R. W., HORN, I. & MCDONOUGH, W. F. 2002. Re・Os and U・Pb geochronological constraints on the eclogite–tonalite connection in the Archean Man Shield, West Africa. *Precambrian Research,* 118**,** 267-283.

BAU, M. 1996. Controls on the fractionation of isovalent trace elements in magmatic and aqueous systems: evidence from Y/Ho, Zr/Hf, and lanthanide tetrad effect. *Contributions to Mineralogy and Petrology,* 123**,** 323-333.

BEA, F., MONTERO, P., HAISSEN, F. & EL ARCHI, A. 2013. 2.46 Ga kalsilite and nepheline syenites from the Awsard pluton, Reguibat Rise of the West African Craton, Morocco. Generation of extremely K-rich magmas at the Archean–Proterozoic transition. *Precambrian Research,* 224**,** 242-254.

BECKER, T. W. & FACCENNA, C. 2011. Mantle conveyor beneath the Tethyan collisional belt. *Earth and Planetary Science Letters,* 310**,** 453-461.

BÉDARD, J. H. 2006. A catalytic delamination-driven model for coupled genesis of Archaean crust and sub-continental lithospheric mantle. *Geochimica et Cosmochimica Acta,* 70**,** 1188-1214.

BÉDARD, J. H., HARRIS, L. B. & THURSTON, P. C. 2013. The hunting of the snArc. *Precambrian Research,* 229**,** 20-48.

BEGG, G. C., HRONSKY, J. A. M., ARNDT, N. T., GRIFFIN, W. L., O'REILLY, S. Y. & HAYWARD, N. 2010. Lithospheric, Cratonic, and Geodynamic Setting of Ni-Cu-PGE Sulfide Deposits. *Economic Geology,* 105**,** 1057-1070.

BEINTEMA, K. A. 2003. Geodynamic evolution of the West and Central Pilbara Craton in Western Australia : a mid-Archaean active continental margin. *Geologica Ultraiectina,* 232**,** 1-248.

BEKKER, A., SLACK, J. F., PLANAVSKY, N., KRAPEŽ, B., HOFMANN, A., KONHAUSER, K. O. & ROUXEL, O. J. 2010. Iron Formation: The Sedimentary Product of a Complex Interplay among Mantle, Tectonic, Oceanic, and Biospheric Processes. *Economic Geology,* 105**,** 467-508.

BELL, E. A., HARRISON, T. M., KOHL, I. E. & YOUNG, E. D. 2014. Eoarchean crustal evolution of the Jack Hills zircon source and loss of Hadean crust. *Geochimica et Cosmochimica Acta,* 146**,** 27-42.

BENN, K. 2004. Late Archaean Kenogamissi complex, Abitibi Subprovince, Ontario, Canada: doming, folding and deformation-assisted melt remobilisation during syntectonic batholith emplacement. *Geological Society of America Special Papers,* 389**,** 297-307.

BENN, K. 2006. Tectonic delamination of the lower crust during Late Archean collision of the Abitibi–Opatica and Pontiac Terranes, Superior Province, Canada. *Archean Geodynamics and Environments***,** 267-282.

BENN, K., KAMBER, B., XA & S 2009. In Situ U/Pb Granulite‐Hosted Zircon Dates, Kapuskasing Structural Zone, Ontario: A Late Archean Large Igneous Province (LIP) as a Substrate for Juvenile Crust. *The Journal of Geology,* 117**,** 519-541.

BENN, K. & MOYEN, J.-F. 2008. The Late Archean Abitibi-Opatica terrane, Superior Province: A modified oceanic plateau. *Geological Society of America Special Papers,* 440**,** 173-197.

BENNETT, V. 2003. Compositional evolution of the mantle. *Treatise on geochemistry,* 2**,** 568.

BERGER, M. & ROLLINSON, H. 1997. Isotopic and geochemical evidence for crust-mantle interaction during late Archaean crustal growth. *Geochimica et Cosmochimica Acta,* 61**,** 4809-4829.

BERING, D. 1998. *Évaluation de l'inventaire des ressources minérales de Guinée*, Bundesanstalt für Geowissenschaften und Rohstoffe.

BHATIA, M. R. & CROOK, K. A. 1986. Trace element characteristics of graywackes and tectonic setting discrimination of sedimentary basins. *Contributions to mineralogy and petrology,* 92**,** 181-193.

BIERLEIN, F., GROVES, D., GOLDFARB, R. & DUBÉ, B. 2006. Lithospheric controls on the formation of provinces hosting giant orogenic gold deposits. *Mineralium Deposita,* 40**,** 874-886.

BLACK, L. P., KAMO, S. L., ALLEN, C. M., ALEINIKOFF, J. N., DAVIS, D. W., KORSCH, R. J. & FOUDOULIS, C. 2003. TEMORA 1: a new zircon standard for Phanerozoic U–Pb geochronology. *Chemical Geology,* 200**,** 155-170.

BLEEKER, W. 2002. Archaean tectonics: a review, with illustrations from the Slave craton. *Geological Society, London, Special Publications,* 199**,** 151-181.

BLEEKER, W. 2003. The late Archean record: a puzzle in ca. 35 pieces. *Lithos,* 71**,** 99-134.

BLEEKER, W. & HALL, B. 2007. The Slave Craton: geological and metallogenic evolution. *In:* GOODFELLOW, W. D. (ed.) *Mineral Resources of Canada: A Synthesis of Major Deposit-types, District Metallogeny, the Evolution of Geological Provinces, and Exploration Methods.* Geological Survey of Canada Special Publication.

BLEWETT, R. S., HENSON, P. A., ROY, I. G., CHAMPION, D. C. & CASSIDY, K. F. 2010. Scale-integrated architecture of a world-class gold mineral system: The Archaean eastern Yilgarn Craton, Western Australia. *Precambrian Research,* 183**,** 230-250.

BOHER, M., ABOUCHAMI, W., MICHARD, A., ALBAREDE, F. & ARNDT, N. T. 1992. Crustal growth in West Africa at 2.1 Ga. *Journal of Geophysical Research: Solid Earth,* 97**,** 345-369.

BOILY, M., LECLAIR, A., MAURICE, C., BÉDARD, J. H. & DAVID, J. 2009. Paleo- to Mesoarchean basement recycling and terrane definition in the Northeastern Superior Province, Québec, Canada. *Precambrian Research,* 168**,** 23-44.

BOLHAR, R., KAMBER, B. S., MOORBATH, S., FEDO, C. M. & WHITEHOUSE, M. J. 2004. Characterisation of early Archaean chemical sediments by trace element signatures. *Earth and Planetary Science Letters,* 222**,** 43-60.

BOLHAR, R., WOODHEAD, J. D. & HERGT, J. M. 2003. Continental setting inferred for emplacement of the 2.9–2.7 Ga Belingwe Greenstone Belt, Zimbabwe. *Geology,* 31**,** 295-298.

BONNICI, J. & GIRAUDON, R. 1963. Le groupe du Tasiast, nouvelle unité lithostratigraphique du socle antécambrien de la Mauritanie occidentale. *Bulletin de la Société Géologique de France,* 5**,** 1118-1123.

BOUHALLIER, H., CHARDON, D. & CHOUKROUNE, P. 1995. Strain patterns in Archaean dome-and-basin structures: The Dharwar craton (Karnataka, South India). *Earth and Planetary Science Letters,* 135**,** 57-75.

BOURDON, E., EISSEN, J.-P., MONZIER, M., ROBIN, C., MARTIN, H., COTTEN, J. & HALL, M. L. 2002. Adakite-like lavas from Antisana Volcano (Ecuador): evidence for slab melt metasomatism beneath Andean Northern Volcanic Zone. *Journal of Petrology,* 43**,** 199-217.

BOWRING, S., WILLIAMS, I. & COMPSTON, W. 1989. 3.96 Ga gneisses from the Slave province, Northwest Territories, Canada. *Geology,* 17**,** 971-975.

BRONNER, G. & CHAUVEL, J. 1979. Precambrian banded iron-formations of the Ijil Group (Kediat Ijil, Reguibat Shield, Mauritania). *Economic Geology,* 74**,** 77-94.

BRONNER, G. & FOURNO, J. 1992. Audio-magnetotelluric investigation of allochthonous iron formations in the Archaean Reguibat shield (Mauritania): structural and mining implications. *Journal of African Earth Sciences (and the Middle East),* 15**,** 341-351.

BROWN, M. 2006. Duality of thermal regimes is the distinctive characteristic of plate tectonics since the Neoarchean. *Geology,* 34**,** 961-964.

BROWN, S., FLETCHER, I., STEIN, H., SNEE, L. & GROVES, D. 2002. Geochronological constraints on pre-, syn-, and postmineralization events at the world-class Cleo gold deposit, Eastern Goldfields Province, Western Australia. *Economic Geology,* 97**,** 541-559.

CAMPBELL, I. H. & ALLEN, C. M. 2008. Formation of supercontinents linked to increases in atmospheric oxygen. *Nature Geosci,* 1**,** 554-558.

CASSIDY, K., CHAMPION, D., MCNAUGHTON, N., FLETCHER, I., WHITAKER, A., BASTRAKOVA, I. & BUDD, A. 2002. Characterisation and metallogenic significance of Archaean granitoids of the Yilgarn Craton, Western Australia. *Minerals and Energy Research Institute of Western Australia (MERIWA), Report***,** 514.

CASSIDY, K. F., GROVES, D. I. & MCNAUGHTON, N. J. 1998. Late-Archean granitoid-hosted lode-gold deposits, Yilgarn Craton, Western Australia: deposit characteristics, crustal architecture and implications for ore genesis. *Ore Geology Reviews,* 13**,** 65-102.

CATES, N. L., ZIEGLER, K., SCHMITT, A. K. & MOJZSIS, S. J. 2013. Reduced, reused and recycled: detrital zircons define a maximum age for the Eoarchean (ca. 3750–3780Ma) Nuvvuagittuq Supracrustal Belt, Québec (Canada). *Earth and Planetary Science Letters,* 362**,** 283-293.

CAWOOD, P. A. & HAWKESWORTH, C. J. 2013. Temporal relations between mineral deposits and global tectonic cycles. *Geological Society, London, Special Publications,* 393.

CAWOOD, P. A., HAWKESWORTH, C. J. & DHUIME, B. 2013. The continental record and the generation of continental crust. *Geological Society of America Bulletin,* 125**,** 14-32.

CAWOOD, P. A., KRONER, A. & PISAREVSKY, S. 2006. Precambrian plate tectonics: criteria and evidence. *GSA today,* 16**,** 4.

CHAMPION, D. & SMITHIES, R. Archaean granites. Magmas to Mineralisation: The Ishihara Symposium. Geoscience, Australia, 2003. 19-24.

CHARDON, D. 1996. *Les déformations continentales archéennes: exemples naturels et modélisation thermomecanique.* Université Rennes 1.

CHARDON, D., GAPAIS, D. & CAGNARD, F. 2009. Flow of ultra-hot orogens: A view from the Precambrian, clues for the Phanerozoic. *Tectonophysics,* 477**,** 105-118.

CHAUDHURI, T., MAZUMDER, R. & ARIMA, M. 2015. Petrography and geochemistry of Mesoarchaean komatiites from the eastern Iron Ore belt, Singhbhum craton, India, and its similarity with 'Barberton type komatiite'. *Journal of African Earth Sciences,* 101**,** 135-147.

CHENEY, E. 1996. Sequence stratigraphy and plate tectonic significance of the Transvaal succession of southern Africa and its equivalent in Western Australia. *Precambrian Research,* 79**,** 3-24.

CHEW, D. M., DONELICK, R.A. 2012. Combined Apatite Fission Track and U–Pb Dating by LA–ICPMS and Future Trends in Apatite Provenance Analysis. *In:* SYLVESTER, P. (ed.) *Quantitative Mineralogy and Microanalysis of Sediments and Sedimentary Rocks.* Mineralogical Association of Canada.

CHEW, D. M., PETRUS, J. A. & KAMBER, B. S. 2014. U–Pb LA–ICPMS dating using accessory mineral standards with variable common Pb. *Chemical Geology,* 363**,** 185-199.

CHUNG, S.-L., LIU, D., JI, J., CHU, M.-F., LEE, H.-Y., WEN, D.-J., LO, C.-H., LEE, T.-Y., QIAN, Q. & ZHANG, Q. 2003. Adakites from continental collision zones: melting of thickened lower crust beneath southern Tibet. *Geology,* 31**,** 1021-1024.

CLIFT, P. D. 2010. Enhanced global continental erosion and exhumation driven by Oligo-Miocene climate change. *Geophysical Research Letters,* 37.

COCHRANE, R., SPIKINGS, R. A., CHEW, D., WOTZLAW, J.-F., CHIARADIA, M., TYRRELL, S., SCHALTEGGER, U. & VAN DER LELIJ, R. 2014. High temperature (> 350 C) thermochronology and mechanisms of Pb loss in apatite. *Geochimica et Cosmochimica Acta,* 127**,** 39-56.

COLLINS, W. J., VAN KRANENDONK, M. J. & TEYSSIER, C. 1998. Partial convective overturn of Archaean crust in the east Pilbara Craton, Western Australia: driving mechanisms and tectonic implications. *Journal of Structural Geology,* 20**,** 1405-1424.

COMPSTON, W. T. & PIDGEON, R. 1986. Jack Hills, evidence of more very old detrital zircons in Western Australia. *Nature,* 321**,** 766-769.

CONDIE, K. C. 1981. Archean greenstone belts. *In:* KENT, C. C. (ed.) *Developments in Precambrian Geology.* Elsevier.

CONDIE, K. C. 1993. Chemical composition and evolution of the upper continental crust: contrasting results from surface samples and shales. *Chemical geology,* 104**,** 1-37.

CONDIE, K. C. 2000. Episodic continental growth models: afterthoughts and extensions. *Tectonophysics,* 322**,** 153-162.

CONDIE, K. C. 2001. *Mantle plumes and their record in Earth history*, Cambridge University Press.

CONDIE, K. C. 2003. Incompatible element ratios in oceanic basalts and komatiites: tracking deep mantle sources and continental growth rates with time. *Geochemistry, Geophysics, Geosystems,* 4**,** 1-28.

CONDIE, K. C. 2004. Supercontinents and superplume events: distinguishing signals in the geologic record. *Physics of the Earth and Planetary Interiors,* 146**,** 319-332.

CONDIE, K. C. 2005. High field strength element ratios in Archean basalts: a window to evolving sources of mantle plumes? *Lithos,* 79**,** 491-504.

CONDIE, K. C. & ASTER, R. C. 2010. Episodic zircon age spectra of orogenic granitoids: the supercontinent connection and continental growth. *Precambrian Research,* 180**,** 227-236.

CONDIE, K. C., BELOUSOVA, E., GRIFFIN, W. & SIRCOMBE, K. N. 2009. Granitoid events in space and time: constraints from igneous and detrital zircon age spectra. *Gondwana Research,* 15**,** 228-242.

CONDIE, K. C. & BENN, K. 2006. Archean geodynamics: similar to or different from modern geodynamics? *Archean Geodynamics and Environments***,** 47-59.

CONNOLLY, B. D., PUCHTEL, I. S., WALKER, R. J., AREVALO, R., PICCOLI, P. M., BYERLY, G., ROBIN-POPIEUL, C. & ARNDT, N. 2011. Highly siderophile element systematics of the 3.3 Ga Weltevreden komatiites, South Africa: implications for early Earth history. *Earth and Planetary Science Letters,* 311**,** 253-263.

CROWLEY, Q. G., HERON, K., RIGGS, N., KAMBER, B., CHEW, D., MCCONNELL, B. & BENN, K. 2014. Chemical Abrasion Applied to LA-ICP-MS U–Pb Zircon Geochronology. *Minerals,* 4**,** 503-518.

CROWLEY, Q. G., KEY, R. & NOBLE, S. R. 2015. High-precision U–Pb dating of complex zircon from the Lewisian Gneiss Complex of Scotland using an incremental CA-ID-TIMS approach. *Gondwana Research*.

CZARNOTA, K., BLEWETT, R. & GOSCOMBE, B. 2010. Predictive mineral discovery in the eastern Yilgarn Craton, Western Australia: an example of district scale targeting of an orogenic gold mineral system. *Precambrian Research,* 183**,** 356-377.

DAVIES, G. F. 1992. On the emergence of plate tectonics. *Geology,* 20**,** 963-966.

DAVIES, G. F. 1993. Cooling the core and mantle by plume and plate flows. *Geophysical Journal International,* 115**,** 132-146.

DAVIES, G. F. 1995. Penetration of plates and plumes through the mantle transition zone. *Earth and Planetary Science Letters,* 133**,** 507-516.

DAVIES, G. F. 2007. Controls on density stratification in the early mantle. *Geochemistry, Geophysics, Geosystems,* 8.

DAVIES, G. F. 2008. Episodic layering of the early mantle by the 'basalt barrier'mechanism. *Earth and Planetary Science Letters,* 275**,** 382-392.

DAVIS, W. J., JONES, A. G., BLEEKER, W. & GRÜTTER, H. 2003. Lithosphere development in the Slave craton: a linked crustal and mantle perspective. *Lithos,* 71**,** 575-589.

DE KOCK, M. O., EVANS, D. A. & BEUKES, N. J. 2009. Validating the existence of Vaalbara in the Neoarchean. *Precambrian Research,* 174**,** 145-154.

DE RONDE, C., KAMO, S., DAVIS, D., DE WIT, M. & SPOONER, E. 1991. Field, geochemical and U-Pb isotopic constraints from hypabyssal felsic intrusions within the Barberton greenstone belt, South Africa: Implications for tectonics and the timing of gold mineralization. *Precambrian Research,* 49**,** 261-280.

DE RONDE, C. E. J. & DE WIT, M. J. 1994. Tectonic history of the Barberton greenstone belt, South Africa: 490 million years of Archean crustal evolution. *Tectonics,* 13**,** 983-1005.

DE WIT, M. & THIART, C. 2005. Metallogenic fingerprints of Archaean cratons. *Geological Society, London, Special Publications,* 248**,** 59-70.

DE WIT, M. J. 1982. Gliding and overthrust nappe tectonics in the Barberton Greenstone Belt. *Journal of Structural Geology,* 4**,** 117-136.

DE WIT, M. J. 1991. Archaean greenstone belt tectonism and basin development: some insights from the Barberton and Pietersburg greenstone belts, Kaapvaal Craton, South Africa. *Journal of African Earth Sciences (and the Middle East),* 13**,** 45-63.

DE WIT, M. J. & ASHWAL, L. D. 1997. *Greenstone belts,* Oxford, Clarendon Press.

DE WIT, M. J. & HART, R. A. 1993. Earth's earliest continental lithosphere, hydrothermal flux and crustal recycling. *Lithos,* 30**,** 309-335.

DEB, M. 2014. Precambrian geodynamics and metallogeny of the Indian shield. *Ore Geology Reviews,* 57**,** 1-28.

DEFANT, M. J. & DRUMMOND, M. S. 1990. Derivation of some modern arc magmas by melting of young subducted lithosphere. *Nature,* 347**,** 662-665.

DEL MORO, A., PUXEDDU, M., DI BROZOLO, F. R. & VILLA, I. 1982. Rb-Sr and K-Ar ages on minerals at temperatures of 300–400 C from deep wells in the Larderello geothermal field (Italy). *Contributions to Mineralogy and Petrology,* 81**,** 340-349.

DEPAOLO, D. J. 1981. Neodymium isotopes in the Colorado Front Range and crust-mantle evolution in the Proterozoic. *Nature,* 291**,** 193-196.

DEPAOLO, D. J. & WASSERBURG, G. J. 1976. Nd isotopic variations and petrogenetic models. *Geophysical Research Letters,* 3**,** 249-252.

DERRY, D. R. 1961. Economic aspects of Archean-Proterozoic boundaries. *Economic Geology,* 56**,** 635-647.

DESROCHERS, J.-P., HUBERT, C., LUDDEN, J. N. & PILOTE, P. 1993. Accretion of Archean oceanic plateau fragments in the Abitibi, greenstone belt, Canada. *Geology,* 21**,** 451-454.

DHUIME, B., HAWKESWORTH, C. J., CAWOOD, P. A. & STOREY, C. D. 2012. A change in the geodynamics of continental growth 3 billion years ago. *Science,* 335**,** 1334-1336.

DILEK, Y. & FURNES, H. 2011. Ophiolite genesis and global tectonics: Geochemical and tectonic fingerprinting of ancient oceanic lithosphere. *Geological Society of America Bulletin,* 123**,** 387-411.

DILEK, Y. & POLAT, A. 2008. Suprasubduction zone ophiolites and Archean tectonics. *Geology,* 36**,** 431-432.

DIMARCO, M. J. & LOWE, D. R. 1989. Stratigraphy and sedimentology of an early Archean felsic volcanic sequence, eastern Pilbara Block, Western Australia, with special reference to the Duffer Formation and implications for crustal evolution. *Precambrian Research,* 44**,** 147-169.

DOE, B. & TILLING, R. 1967. Distribution of lead between coexisting K-feldspar and plagioclase. *American Mineralogist,* 52**,** 805-&.

DOSSO, L., VIDAL, P., SICHLER, B. & BONIFAY, A. 1979. Age précambrien de dolérites de la Dorsale Réguibat (Mauritanie). *Comptes rendus Académie des sciences de Paris,* 288**,** 739-742.

DOUBLIER, M. P., THÉBAUD, N., WINGATE, M. T. D., ROMANO, S. S., KIRKLAND, C. L., GESSNER, K., MOLE, D. R. & EVANS, N. 2014. Structure and timing of Neoarchean gold mineralization in the Southern Cross district (Yilgarn Craton, Western Australia) suggest leading role of late Low-Ca I-type granite intrusions. *Journal of Structural Geology,* 67, Part B**,** 205-221.

DOYLE, M. G., FLETCHER, I. R., FOSTER, J., LARGE, R. R., MATHUR, R., MCNAUGHTON, N. J., MEFFRE, S., MUHLING, J. R., PHILLIPS, D. & RASMUSSEN, B. 2015. Geochronological

Constraints on the Tropicana Gold Deposit and Albany-Fraser Orogen, Western Australia. *Economic Geology,* 110**,** 355-386.

DRISCOLL, N. W., HOGG, J. R., CHRISTIE-BLICK, N. & KARNER, G. D. 1995. Extensional tectonics in the Jeanne d'Arc Basin, offshore Newfoundland: implications for the timing of break-up between Grand Banks and Iberia. *Geological Society, London, Special Publications,* 90**,** 1-28.

DRUMMOND, M. S. & DEFANT, M. J. 1990. A model for Trondhjemite-Tonalite-Dacite Genesis and crustal growth via slab melting: Archean to modern comparisons. *Journal of Geophysical Research: Solid Earth,* 95**,** 21503-21521.

DRUMMOND, M. S., DEFANT, M. J. & KEPEZHINSKAS, P. K. 1996. Petrogenesis of slab-derived trondhjemite–tonalite-dacite/adakite magmas. *Geological Society of America Special Papers,* 315**,** 205-215.

DUPRÉ, B. & ARNDT, N. 1990. Pb isotopic compositions of Archean komatiites and sulfides. *Chemical geology,* 85**,** 35-56.

DUPRÉ, B., CHAUVEL, C. & ARNDT, N. T. 1984. Pb and Nd isotopic study of two Archean komatiitic flows from Alexo, Ontario. *Geochimica et Cosmochimica Acta,* 48**,** 1965-1972.

EGGINS, S. M., WOODHEAD, J. D., KINSLEY, L. P. J., MORTIMER, G. E., SYLVESTER, P., MCCULLOCH, M. T., HERGT, J. M. & HANDLER, M. R. 1997. A simple method for the precise determination of ≥ 40 trace elements in geological samples by ICPMS using enriched isotope internal standardisation. *Chemical Geology,* 134**,** 311-326.

ERIKSSON, K. 1980. Transitional sedimentation styles in the Moodies and Fig Tree Groups, Barberton mountain land, South Africa: evidence favouring an Archean continental margin. *Precambrian Research,* 12**,** 141-160.

FAIRCHILD, I., MARSHALL, J. & BERTRAND-SARFATI, J. 1990. Stratigraphic shifts in carbon isotopes from Proterozoic stromatolitic carbonates (Mauritania): influences of primary mineralogy and diagenesis. *American Journal of Science,* 290**,** 46-79.

FARQUHAR, J., WING, B. A., MCKEEGAN, K. D., HARRIS, J. W., CARTIGNY, P. & THIEMENS, M. H. 2002. Mass-Independent Sulfur of Inclusions in Diamond and Sulfur Recycling on Early Earth. *Science,* 298**,** 2369-2372.

FENG, R. & KERRICH, R. 1992. Geodynamic evolution of the southern Abitibi and Pontiac terranes: evidence from geochemistry of granitoid magma series (2700–2630 Ma). *Canadian Journal of Earth Sciences,* 29**,** 2266-2286.

FITTON, J., SAUNDERS, A., NORRY, M., HARDARSON, B. & TAYLOR, R. 1997. Thermal and chemical structure of the Iceland plume. *Earth and Planetary Science Letters,* 153**,** 197-208.

FLOWERDEW, M. J., MILLAR, I. L., VAUGHAN, A. P. M., HORSTWOOD, M. S. A. & FANNING, C. M. 2006. The source of granitic gneisses and migmatites in the Antarctic Peninsula: a combined U–Pb SHRIMP and laser ablation Hf isotope study of complex zircons. *Contributions to Mineralogy and Petrology,* 151**,** 751-768.

FLOWERDEW, M. J., TYRRELL, S., RILEY, T. R., WHITEHOUSE, M. J., MULVANEY, R., LEAT, P. T. & MARSCHALL, H. R. 2012. Distinguishing East and West Antarctic sediment sources using the Pb isotope composition of detrital K-feldspar. *Chemical Geology,* 292–293**,** 88-102.

FÖRSTER, H. & TISCHENDORF, G. 1994. The western Erzgebirge-Vogtland granites: Implications to the Hercynian magmatism in the Erzgebirge-Fichtelgebirge anticlinorium. *Metallogeny of Collisional Orogens***,** 35-48.

FORSYTH, D. & UYEDA, S. 1975. On the relative importance of the driving forces of plate motion. *Geophysical Journal International,* 43**,** 163-200.

FOSTER, R. & PIPER, D. 1993. Archaean lode gold deposits in Africa: Crustal setting, metallogenesis and cratonization. *Ore Geology Reviews,* 8**,** 303-347.

FOWLER, M. & ROLLINSON, H. 2012. Phanerozoic sanukitoids from Caledonian Scotland: implications for Archean subduction. *Geology,* 40**,** 1079-1082.

FRANÇOIS, C., PHILIPPOT, P., REY, P. & RUBATTO, D. 2014. Burial and exhumation during Archean sagduction in the east Pilbara granite-greenstone terrane. *Earth and Planetary Science Letters,* 396**,** 235-251.

FREI, R., POLAT, A. & MEIBOM, A. 2004. The Hadean upper mantle conundrum: evidence for source depletion and enrichment from Sm-Nd, Re-Os, and Pb isotopic compositions in 3.71 Gy boninite-like metabasalts from the Isua Supracrustal Belt, Greenland. *Geochimica et cosmochimica acta,* 68**,** 1645-1660.

FRIEND, C. R. L. & NUTMAN, A. P. 2010. Eoarchean ophiolites? New evidence for the debate on the Isua supracrustal belt, southern West Greenland. *American Journal of Science,* 310**,** 826-861.

FRIMMEL, H. E. 2008. Earth's continental crustal gold endowment. *Earth and Planetary Science Letters,* 267**,** 45-55.

FRIMMEL, H. E. & HENNIGH, Q. 2015. First whiffs of atmospheric oxygen triggered onset of crustal gold cycle. *Mineralium Deposita,* 50**,** 5-23.

FURNES, H., DE WIT, M. & DILEK, Y. 2014. Four billion years of ophiolites reveal secular trends in oceanic crust formation. *Geoscience Frontiers,* 5**,** 571-603.

FURNES, H., DE WIT, M., STAUDIGEL, H., ROSING, M. & MUEHLENBACHS, K. 2007. A vestige of Earth's oldest ophiolite. *science,* 315**,** 1704-1707.

FURNES, H., DE WIT, M. J., ROBINS, B. & SANDSTÅ, N. R. 2011. Volcanic evolution of the upper Onverwacht Suite, Barberton greenstone belt, South Africa. *Precambrian Research,* 186**,** 28-50.

FURNES, H., DILEK, Y. & DE WIT, M. 2015. Precambrian greenstone sequences represent different ophiolite types. *Gondwana Research,* 27**,** 649-685.

FYFE, W. & KERRICH, R. 1985. Fluids and thrusting. *Chemical Geology,* 49**,** 353-362.

GAO, Y., HOU, Z., KAMBER, B. S., WEI, R., MENG, X. & ZHAO, R. 2007. Adakite-like porphyries from the southern Tibetan continental collision zones: evidence for slab melt metasomatism. *Contributions to Mineralogy and Petrology,* 153**,** 105-120.

GAPAIS, D., CAGNARD, F., GUEYDAN, F., BARBEY, P. & BALLEVRE, M. 2009. Mountain building and exhumation processes through time: inferences from nature and models. *Terra Nova,* 21**,** 188-194.

GAPAIS, D., JAGUIN, J., CAGNARD, F. & BOULVAIS, P. 2014. Pop-down tectonics, fluid channelling and ore deposits within ancient hot orogens. *Tectonophysics,* 618**,** 102-106.

GAROFALO, P. S. & RIDLEY, J. R. 2014. Gold-transporting hydrothermal fluids in the Earth's crust: an introduction. *Geological Society, London, Special Publications,* 402.

GÄRTNER, A., VILLENEUVE, M., LINNEMANN, U., EL ARCHI, A. & BELLON, H. 2013. An exotic terrane of Laurussian affinity in the Mauritanides and Souttoufides (Moroccan Sahara). *Gondwana Research,* 24**,** 687-699.

GERYA, T., STERN, R., BAES, M., SOBOLEV, S. & WHATTAM, S. 2015. Plate tectonics on the Earth triggered by plume-induced subduction initiation. *Nature,* 527**,** 221-225.

GIERE, R. 1990. Hydrothermal mobility of Ti, Zr and REE: examples from the Bergell and Adamello contact aureoles (Italy). *Terra Nova,* 2**,** 60-67.

GOLDFARB, R. J., GROVES, D. I. & GARDOLL, S. 2001. Orogenic gold and geologic time: a global synthesis. *Ore Geology Reviews,* 18**,** 1-75.

GOODWIN, A. M. 1977. Archean basin-craton complexes and the growth of Precambrian shields. *Canadian Journal of Earth Sciences,* 14**,** 2737-2759.

GOODWIN, A. M. 1996. *Principles of Precambrian geology*, Academic Press.

GRIFFIN, W., PEARSON, N., BELOUSOVA, E., JACKSON, S., VAN ACHTERBERGH, E., O'REILLY, S. Y. & SHEE, S. 2000. The Hf isotope composition of cratonic mantle: LAM-MC-ICPMS analysis of zircon megacrysts in kimberlites. *Geochimica et Cosmochimica Acta,* 64**,** 133-147.

GRIFFIN, W. L., WANG, X., JACKSON, S. E., PEARSON, N. J., O'REILLY, S. Y., XU, X. & ZHOU, X. 2002. Zircon chemistry and magma mixing, SE China: In-situ analysis of Hf isotopes, Tonglu and Pingtan igneous complexes. *Lithos,* 61**,** 237-269.

GROVES, D. I. 1993. The crustal continuum model for late-Archaean lode-gold deposits of the Yilgarn Block, Western Australia. *Mineralium deposita,* 28**,** 366-374.

GROVES, D. I., CONDIE, K. C., GOLDFARB, R. J., HRONSKY, J. M. A. & VIELREICHER, R. M. 2005. 100th Anniversary Special Paper: Secular Changes in Global Tectonic Processes and Their

Influence on the Temporal Distribution of Gold-Bearing Mineral Deposits. *Economic Geology,* 100**,** 203-224.

GROVES, D. I., GOLDFARB, R. J., GEBRE-MARIAM, M., HAGEMANN, S. G. & ROBERT, F. 1998. Orogenic gold deposits: A proposed classification in the context of their crustal distribution and relationship to other gold deposit types. *Ore Geology Reviews,* 13**,** 7-27.

GROVES, D. I., GOLDFARB, R.J., ROBERT, F. & HART, C.J.R. 2003. Gold deposits in metamorphic belts: overview of current understanding, outstanding problems, future research, and exploration significance. *Economic Geology,* 98**,** 1-29.

HALTER, W. E., PETTKE, T. & HEINRICH, C. A. 2004. Laser-ablation ICP-MS analysis of silicate and sulfide melt inclusions in an andesitic complex I: analytical approach and data evaluation. *Contributions to Mineralogy and Petrology,* 147**,** 385-396.

HAMILTON, W. B. 2011. Plate tectonics began in Neoproterozoic time, and plumes from deep mantle have never operated. *Lithos,* 123**,** 1-20.

HANSKI, E., HUHMA, H., RASTAS, P. & KAMENETSKY, V. S. 2001. The Palaeoproterozoic Komatiite–Picrite Association of Finnish Lapland. *Journal of Petrology,* 42**,** 855-876.

HARGRAVES, R. B. 1986. Faster spreading or greater ridge length in the Archean? *Geology,* 14**,** 750-752.

HARRISON, T. M., BLICHERT-TOFT, J., MÜLLER, W., ALBAREDE, F., HOLDEN, P. & MOJZSIS, S. J. 2005. Heterogeneous Hadean Hafnium: Evidence of Continental Crust at 4.4 to 4.5 Ga. *Science,* 310**,** 1947-1950.

HARRY, D. L. & GREEN, N. L. 1999. Slab dehydration and basalt petrogenesis in subduction systems involving very young oceanic lithosphere. *Chemical Geology,* 160**,** 309-333.

HAWKESWORTH, C. J., CAWOOD, P. & DHUIME, B. 2013. Continental growth and the crustal record. *Tectonophysics,* 609**,** 651-660.

HAWKESWORTH, C. J., DHUIME, B., PIETRANIK, A. B., CAWOOD, P. A., KEMP, A. I. S. & STOREY, C. D. 2010. The generation and evolution of the continental crust. *Journal of the Geological Society,* 167**,** 229-248.

HAWKESWORTH, C. J. & KEMP, A. I. S. 2006. Evolution of the continental crust. *Nature,* 443**,** 811-817.

HELMSTAEDT, H., AND SCHULZE, D. 1989. Southern African kimberlites and their mantle sample: Implications for Archean tectonics and lithosphere evolution. *In:* ROSS, J. (ed.) *Kimberlites and Related Rocks.* Geological Society of Australia Special Publication.

HERON, K., JESSELL, M., BENN, K., HARRIS, E. & CROWLEY, Q. G. 2015. The Tasiast deposit, Mauritania. *Ore Geology Reviews*.

HERZBERG, C., CONDIE, K. & KORENAGA, J. 2010. Thermal history of the Earth and its petrological expression. *Earth and Planetary Science Letters,* 292**,** 79-88.

HICKMAN, A. H. 2004. Two contrasting granite–greenstone terranes in the Pilbara Craton, Australia: evidence for vertical and horizontal tectonic regimes prior to 2900 Ma. *Precambrian Research,* 131**,** 153-172.

HOFMANN, A., BOLHAR, R., ORBERGER, B. & FOUCHER, F. 2013. Cherts of the Barberton greenstone belt, South Africa: petrology and trace-element geochemistry of 3.5 to 3.3 Ga old silicified volcaniclastic sediments. *South African Journal of Geology,* 116**,** 297-322.

HOFMANN, A. W. 1988. Chemical differentiation of the Earth: the relationship between mantle, continental crust, and oceanic crust. *Earth and Planetary Science Letters,* 90**,** 297-314.

HOLLAND, H. D. 1984. *The chemical evolution of the atmosphere and oceans*, Princeton University Press.

HOLLAND, H. D. 2005. 100th Anniversary Special Paper: Sedimentary Mineral Deposits and the Evolution of Earth's Near-Surface Environments. *Economic Geology,* 100**,** 1489-1509.

HOSKIN, P. W. O. & SCHALTEGGER, U. 2003. The Composition of Zircon and Igneous and Metamorphic Petrogenesis. *Reviews in Mineralogy and Geochemistry,* 53**,** 27-62.

HUNTER, D. & STOWE, C. 1997. A historial review of the origin, composition, and setting of Archaean greenstone belts (pre-1980). *OXFORD MONOGRAPHS ON GEOLOGY AND GEOPHYSICS,* 35**,** 5-30.

HUSTON, D. L. & LOGAN, G. A. 2004. Barite, BIFs and bugs: evidence for the evolution of the Earth's early hydrosphere. *Earth and Planetary Science Letters,* 220**,** 41-55.

HUTTON, J. 1788. X. Theory of the Earth; or an Investigation of the Laws observable in the Composition, Dissolution, and Restoration of Land upon the Globe. *Transactions of the Royal Society of Edinburgh,* 1**,** 209-304.

HYNES, A. 2013. How feasible was subduction in the Archean? *Canadian Journal of Earth Sciences,* 51**,** 286-296.

JACOBSEN, S. B. & WASSERBURG, G. 1979. Nd and Sr isotopic study of the Bay of Islands ophiolite complex and the evolution of the source of midocean ridge basalts. *Journal of Geophysical Research B,* 84**,** 7429-7445.

JAGUIN, J., POUJOL, M., BOULVAIS, P., ROBB, L. J. & PAQUETTE, J. L. 2012. Metallogeny of precious and base metal mineralization in the Murchison Greenstone Belt, South Africa: indications from U–Pb and Pb–Pb geochronology. *Mineralium Deposita,* 47**,** 739-747.

JENKIN, G. R. T., LUSTY, P. A. J., MCDONALD, I., SMITH, M. P., BOYCE, A. J. & WILKINSON, J. J. 2014. Ore deposits in an evolving Earth: an introduction. *Geological Society, London, Special Publications,* 393.

JENSEN, L. S. 1976. A new cation plot for classifying subalkalic volcanic rocks. *Ontario Division of Mines Miscellaneous Paper,* 66.

JOHNSON, T. E., BROWN, M., KAUS, B. J. P. & VANTONGEREN, J. A. 2014. Delamination and recycling of Archaean crust caused by gravitational instabilities. *Nature Geosci,* 7**,** 47-52.

JORDAN, T. H. 1988. Structure and formation of the continental tectosphere, in Oceanic and continental lithosphere; similarities and differences. *In:* MENZIES, M. A., COX, K.G. (ed.) *Journal of Petrology, Special Lithosphere Issue.*

KAH, L. C., BARTLEY, J. K. & STAGNER, A. F. 2009. Reinterpreting a Proterozoic Enigma: Conophyton-Jacutophyton Stromatolites of the Mesoproterozoic Atar Group, Mauritania. *Perspectives in Carbonate Geology.* John Wiley & Sons, Ltd.

KAMBER, B. S. 2009. Geochemical fingerprinting: 40 years of analytical development and real world applications. *Applied Geochemistry,* 24**,** 1074-1086.

KAMBER, B. S. 2010. Archean mafic–ultramafic volcanic landmasses and their effect on ocean–atmosphere chemistry. *Chemical Geology,* 274**,** 19-28.

KAMBER, B. S. 2011. Geochemistry and Secular Geochemical Evolution of the Earth's Mantle and Lower Crust. *Frontiers in Geochemistry.* John Wiley & Sons, Ltd.

KAMBER, B. S. 2015. The evolving nature of terrestrial crust from the Hadean, through the Archaean, into the Proterozoic. *Precambrian Research,* 258**,** 48-82.

KAMBER, B. S., BOLHAR, R. & WEBB, G. E. 2004. Geochemistry of late Archaean stromatolites from Zimbabwe: evidence for microbial life in restricted epicontinental seas. *Precambrian Research,* 132**,** 379-399.

KAMBER, B. S. & COLLERSON, K. D. 1999. Origin of ocean island basalts: A new model based on lead and helium isotope systematics. *Journal of Geophysical Research: Solid Earth,* 104**,** 25479-25491.

KAMBER, B. S., EWART, A., COLLERSON, K. D., BRUCE, M. C. & MCDONALD, G. D. 2002. Fluid-mobile trace element constraints on the role of slab melting and implications for Archaean crustal growth models. *Contributions to Mineralogy and Petrology,* 144**,** 38-56.

KAMBER, B. S., GREIG, A. & COLLERSON, K. D. 2005a. A new estimate for the composition of weathered young upper continental crust from alluvial sediments, Queensland, Australia. *Geochimica et Cosmochimica Acta,* 69**,** 1041-1058.

KAMBER, B. S., GREIG, A., SCHOENBERG, R. & COLLERSON, K. D. 2003. A refined solution to Earth's hidden niobium: implications for evolution of continental crust and mode of core formation. *Precambrian Research,* 126**,** 289-308.

KAMBER, B. S., WHITEHOUSE, M. J., BOLHAR, R. & MOORBATH, S. 2005b. Volcanic resurfacing and the early terrestrial crust: Zircon U–Pb and REE constraints from the Isua Greenstone Belt, southern West Greenland. *Earth and Planetary Science Letters,* 240**,** 276-290.

KAZIMOTO, E. O. & IKINGURA, J. R. 2014. Trace element geochemistry and petrogenesis of the granitoids and high-K andesite hosting gold mineralisation in the Archean Musoma-Mara Greenstone Belt, Tanzania. *Journal of African Earth Sciences,* 91**,** 66-78.

KENT, R. W. & FITTON, J. G. 2000. Mantle Sources and Melting Dynamics in the British Palaeogene Igneous Province. *Journal of Petrology,* 41**,** 1023-1040.

KERR, A. 2003. Oceanic plateaus. *Treatise on geochemistry,* 3**,** 537-565.

KERRICH, R. & CASSIDY, K. F. 1994. Temporal relationships of lode gold mineralization to accretion, magmatism, metamorphism and deformation — Archean to present: A review. *Ore Geology Reviews,* 9**,** 263-310.

KERRICH, R., POLAT, A., WYMAN, D. & HOLLINGS, P. 1999. Trace element systematics of Mg-, to Fe-tholeiitic basalt suites of the Superior Province: implications for Archean mantle reservoirs and greenstone belt genesis. *Lithos,* 46**,** 163-187.

KERRICH, R., WYMAN, D., FAN, J. & BLEEKER, W. 1998. Boninite series: low Ti-tholeiite associations from the 2.7 Ga Abitibi greenstone belt. *Earth and Planetary Science Letters,* 164**,** 303-316.

KETCHUM, K. Y., HEAMAN, L. M., BENNETT, G. & HUGHES, D. J. 2013. Age, petrogenesis and tectonic setting of the Thessalon volcanic rocks, Huronian Supergroup, Canada. *Precambrian Research,* 233**,** 144-172.

KEY, R. M., LOUGHLIN, S. C., GILLESPIE, M., DEL RIO, M., HORSTWOOD, M. S. A., CROWLEY, Q. G., DARBYSHIRE, D. P. F., PITFIELD, P. E. J. & HENNEY, P. J. 2008. Two Mesoarchaean terranes in the Reguibat shield of NW Mauritania. *Geological Society, London, Special Publications,* 297**,** 33-52.

KHANNA, T. C., BIZIMIS, M., MANIKYAMBA, C., YOGODZINSKI, G. M., BALARAM, V., PRACHITI, P. K. & RAJU, K. 2011. Pb-isotope systematics of metavolcanic rocks from ~2.7 Ga Penakacherla greenstone belt, eastern Dharwar craton, India. *8th International Symposium on Gondwana to Asia.***,** 26-27.

KHANNA, T. C., BIZIMIS, M., YOGODZINSKI, G. M. & MALLICK, S. 2014. Hafnium–neodymium isotope systematics of the 2.7 Ga Gadwal greenstone terrane, Eastern Dharwar craton, India: Implications for the evolution of the Archean depleted mantle. *Geochimica et Cosmochimica Acta,* 127**,** 10-24.

KIMURA, G., LUDDEN, J. N., DESROCHERS, J. P. & HORI, R. 1993. The evolving earthA model of ocean-crust accretion for the Superior province, Canada. *Lithos,* 30**,** 337-355.

KLOPPENBURG, A., WHITE, S. H. & ZEGERS, T. E. 2001. Structural evolution of the Warrawoona Greenstone Belt and adjoining granitoid complexes, Pilbara Craton, Australia: implications for Archaean tectonic processes. *Precambrian Research,* 112**,** 107-147.

KOLB, J., SAKELLARIS, G. & MEYER, F. M. 2006. Controls on hydrothermal Fe oxide–Cu–Au–Co mineralization at the Guelb Moghrein deposit, Akjoujt area, Mauritania. *Mineralium Deposita,* 41**,** 68-81.

KOMIYA, T., MARUYAMA, S., MASUDA, T., NOHDA, S., HAYASHI, M. & OKAMOTO, K. 1999. Plate Tectonics at 3.8-3.7 Ga: Field Evidence from the Isua Accretionary Complex, Southern West Greenland. *J Geol,* 107**,** 515-554.

KOUAMELAN, A. N., DELOR, C. & PEUCAT, J. J. 1997. Geochronological evidence for reworking of Archean terrains during the Early Proterozoic (2.1 Ga) in the western Cote d'Ivoire (Man Rise-West African Craton). *Precambrian Research,* 86**,** 177-199.

KRAMERS, J. D. 1988. An open-system fractional crystallization model for very early continental crust formation. *Precambrian Research,* 38**,** 281-295.

KRAMERS, J. D. & TOLSTIKHIN, I. N. 1997. Two terrestrial lead isotope paradoxes, forward transport modelling, core formation and the history of the continental crust. *Chemical Geology,* 139**,** 75-110.

KROGH, T. E. 1982. Improved accuracy of U-Pb zircon ages by the creation of more concordant systems using an air abrasion technique. *Geochimica et Cosmochimica Acta,* 46**,** 637-649.

KRÖNER, A. E., B. N. PIDGEON, R. T. 2001. The Oldest Rocks in West Africa: SHRIMP Zircon Age for Early Archean Migmatitic Orthogneiss at Kaduna, Northern Nigeria. *The Journal of Geology,* 109**,** 399-406.

KRYZA, R., CROWLEY, Q. G., LARIONOV, A., PIN, C., OBERC-DZIEDZIC, T. & MOCHNACKA, K. 2012. Chemical abrasion applied to SHRIMP zircon geochronology: An example from the Variscan Karkonosze Granite (Sudetes, SW Poland). *Gondwana Research,* 21**,** 757-767.

KUSKY, T. M. 2004. Precambrian ophiolites and related rocks. *Developments in Precambrian geology,* 13**,** 772.

KUSKY, T. M. & KIDD, W. S. F. 1992. Remnants of an Archean oceanic plateau, Belingwe greenstone belt, Zimbabwe. *Geology,* 20**,** 43-46.

LAHONDÈRE, D., THIÉBLEMONT, D., GOUJOU, J.-C., ROGER, J., MOUSSINE-POUCHKINE, A., LE MÉTOUR, J., COCHERIE, A., GUERROT, C. 2003. Notice explicative des cartes géologiques et gîtologiques à 1/200 000 et 1/500 000 du Nord de la Mauritanie. *DMG, Ministe`re des Mines et de l'Industrie, Nouakchott.,* 1.

LANGMUIR, C. H., BENDER, J. F., BENCE, A. E., HANSON, G. N. & TAYLOR, S. R. 1977. Petrogenesis of basalts from the FAMOUS area: Mid-Atlantic Ridge. *Earth and Planetary Science Letters,* 36**,** 133-156.

LEE, C.-T. A., LUFFI, P. & CHIN, E. J. 2011. Building and Destroying Continental Mantle. *Annual Review of Earth and Planetary Sciences,* 39**,** 59-90.

LENARDIC, A., MORESI, L. N. & MÜHLHAUS, H. 2003. Longevity and stability of cratonic lithosphere: Insights from numerical simulations of coupled mantle convection and continental tectonics. *Journal of Geophysical Research: Solid Earth,* 108**,** n/a-n/a.

LI, X.-H., LONG, W.-G., LI, Q.-L., LIU, Y., ZHENG, Y.-F., YANG, Y.-H., CHAMBERLAIN, K. R., WAN, D.-F., GUO, C.-H., WANG, X.-C. & TAO, H. 2010. Penglai Zircon Megacrysts: A Potential New Working Reference Material for Microbeam Determination of Hf–O Isotopes and U–Pb Age. *Geostandards and Geoanalytical Research,* 34**,** 117-134.

LI, Z. X., BOGDANOVA, S. V., COLLINS, A. S., DAVIDSON, A., DE WAELE, B., ERNST, R. E., FITZSIMONS, I. C. W., FUCK, R. A., GLADKOCHUB, D. P., JACOBS, J., KARLSTROM, K. E., LU, S., NATAPOV, L. M., PEASE, V., PISAREVSKY, S. A., THRANE, K. & VERNIKOVSKY, V. 2008. Assembly, configuration, and break-up history of Rodinia: A synthesis. *Precambrian Research,* 160**,** 179-210.

LIU, L., ZHANG, L. & DAI, Y. 2014. Formation age and genesis of the banded iron formations from the Guyang Greenstone Belt, Western North China Craton. *Ore Geology Reviews,* 63**,** 388-404.

LODGE, R. W. D., GIBSON, H. L., STOTT, G. M., FRANKLIN, J. M. & HAMILTON, M. A. 2014. Geodynamic Reconstruction of the Winston Lake Greenstone Belt and VMS Deposits: New Trace Element Geochemistry and U-Pb Geochronology. *Economic Geology,* 109**,** 1291-1313.

LOWE, D. R. & BYERLY, G. R. 2007. Chapter 5.3 An Overview of the Geology of the Barberton Greenstone Belt and Vicinity: Implications for Early Crustal Development. *In:* MARTIN J. VAN KRANENDONK, R. H. S. & VICKIE, C. B. (eds.) *Developments in Precambrian Geology.* Elsevier.

LUDDEN, J., HUBERT, C. & GARIÉPY, C. 1986. The tectonic evolution of the Abitibi greenstone belt of Canada. *Geological Magazine,* 123**,** 153-166.

LUDDEN, J. & HYNES, A. 2000. The Lithoprobe Abitibi-Grenville transect: two billion years of crust formation and recycling in the Precambrian Shield of Canada. *Canadian Journal of Earth Sciences,* 37**,** 459-476.

LUDWIG, K. R. 2003. User's Manual for Isoplot 3.00 : a Geochronological Toolkit for Microsoft Excel.

LUSTY, P. A. J. & GUNN, A. G. 2014. Challenges to global mineral resource security and options for future supply. *Geological Society, London, Special Publications,* 393.

LUTTINEN, A. V. & FURNES, H. 2000. Flood Basalts of Vestfjella: Jurassic Magmatism Across an Archaean–Proterozoic Lithospheric Boundary in Dronning Maud Land, Antarctica. *Journal of Petrology,* 41**,** 1271-1305.

MA, X., FAN, H.-R., SANTOSH, M. & GUO, J. 2014. Chronology and geochemistry of Neoarchean BIF-type iron deposits in the Yinshan Block, North China Craton: Implications for oceanic ridge subduction. *Ore Geology Reviews,* 63**,** 405-417.

MACDOUGALL, J. D. 1988. *Continental flood basalts*, Springer Science & Business Media.
MACFARLANE, A. & INSTITUTE OF GEOLOGICAL, S. 1981. *The Geology and mineral resources of northern Sierra Leone,* London, H.M.S.O.
MACGREGOR, A. M. Some milestones in the Precambrian of Southern Rhodesia. Proceedings of the Geological Society of South Africa, 1951. 27-71.
MAHONEY, J. J. & COFFIN, M. F. 1997. *Large igneous provinces: continental, oceanic, and planetary flood volcanism*, American Geophysical Union.
MANIKYAMBA, C. & KERRICH, R. 2012. Eastern Dharwar Craton, India: Continental lithosphere growth by accretion of diverse plume and arc terranes. *Geoscience Frontiers,* 3**,** 225-240.
MANIKYAMBA, C., NAQVI, S. M., SUBBA RAO, D. V., RAM MOHAN, M., KHANNA, T. C., RAO, T. G. & REDDY, G. L. N. 2005. Boninites from the Neoarchaean Gadwal Greenstone belt, Eastern Dharwar Craton, India: implications for Archaean subduction processes. *Earth and Planetary Science Letters,* 230**,** 65-83.
MARCHI, S., BOTTKE, W. F., ELKINS-TANTON, L. T., BIERHAUS, M., WUENNEMANN, K., MORBIDELLI, A. & KRING, D. A. 2014. Widespread mixing and burial of Earth's Hadean crust by asteroid impacts. *Nature,* 511**,** 578-582.
MARESCHAL, J.-C. & WEST, G. F. 1980. A model for Archean tectonism. Part 2. Numerical models of vertical tectonism in greenstone belts. *Canadian Journal of Earth Sciences,* 17**,** 60-71.
MARTIN, H. 1986. Effect of steeper Archean geothermal gradient on geochemistry of subduction-zone magmas. *Geology,* 14**,** 753-756.
MARTIN, H. 1994. The Archean grey gneisses and the genesis of continental crust. *Archean crustal evolution,* 11**,** 205-259.
MARTIN, H., MOYEN, J.-F. & RAPP, R. 2009. The sanukitoid series: magmatism at the Archaean–Proterozoic transition. *Earth and Environmental Science Transactions of the Royal Society of Edinburgh,* 100**,** 15-33.
MARTIN, H., SMITHIES, R. H., RAPP, R., MOYEN, J. F. & CHAMPION, D. 2005. An overview of adakite, tonalite–trondhjemite–granodiorite (TTG), and sanukitoid: relationships and some implications for crustal evolution. *Lithos,* 79**,** 1-24.
MARTYN, J. & STRICKLAND, C. 2004. Stratigraphy, structure and mineralisation of the Akjoujt area, Mauritania. *Journal of African Earth Sciences,* 38**,** 489-503.
MARUTANI, M., HIGASHIHARA, M., WATANABE, Y., MURAKAMI, H., KOJIMA, G., DIOUMASSI, B. 2005. Metallic ore deposits in the Islamic Republic of Mauritania. *Resour. Geol.,* 55**,** 59-70.
MATTINSON, J. M. 2005. Zircon U–Pb chemical abrasion ("CA-TIMS") method: Combined annealing and multi-step partial dissolution analysis for improved precision and accuracy of zircon ages. *Chemical Geology***,** 47-66.
MCCONNELL, B., RIGGS, N. & CROWLEY, Q. G. 2009. Detrital zircon provenance and Ordovician terrane amalgamation, western Ireland. *Journal of the Geological Society,* 166**,** 473-484.
MCDONOUGH, W. F. & SUN, S. S. 1995. The composition of the Earth. *Chemical Geology,* 120**,** 223-253.
MCKENZIE, D. & BICKLE, M. J. 1988. The Volume and Composition of Melt Generated by Extension of the Lithosphere. *Journal of Petrology,* 29**,** 625-679.
MCLENNAN, S. M. 1988. Recycling of the continental crust. *Pure and applied geophysics,* 128**,** 683-724.
MCLENNAN, S. M., HEMMING, S., MCDANIEL, D. K. & HANSON, G. N. 1993. Geochemical approaches to sedimentation, provenance, and tectonics. *Geological Society of America Special Papers,* 284**,** 21-40.
MCLENNAN, S. M. & TAYLOR, S. R. 1991. Sedimentary Rocks and Crustal Evolution: Tectonic Setting and Secular Trends. *The Journal of Geology,* 99**,** 1-21.
MENCHIKOFF, N. 1949. *Quelques traits de l'histoire géologique du Sahara occidental*, Paris : s.n.
MEYER, M. F., KOLB, J., SAKELLARIS, G. A. & GERDES, A. 2006. New ages from the Mauritanides Belt: recognition of Archean IOCG mineralization at Guelb Moghrein, Mauritania. *Terra Nova,* 18**,** 345-352.
MOLE, D. R., FIORENTINI, M. L., CASSIDY, K. F., KIRKLAND, C. L., THEBAUD, N., MCCUAIG, T. C., DOUBLIER, M. P., DUURING, P., ROMANO, S. S., MAAS, R., BELOUSOVA, E. A., BARNES, S.

J. & MILLER, J. 2013. Crustal evolution, intra-cratonic architecture and the metallogeny of an Archaean craton. *Geological Society, London, Special Publications,* 393.

MONTERO, P., HAISSEN, F., EL ARCHI, A., RJIMATI, E. & BEA, F. 2014. Timing of Archean crust formation and cratonization in the Awsard-Tichla zone of the NW Reguibat Rise, West African Craton: A SHRIMP, Nd–Sr isotopes, and geochemical reconnaissance study. *Precambrian Research,* 242**,** 112-137.

MOONEY, W. D., LASKE, G. & MASTERS, T. G. 1998. CRUST 5.1: A global crustal model at 5° × 5°. *Journal of Geophysical Research: Solid Earth,* 103**,** 727-747.

MOORBATH, S., WELKE, H. & GALE, N. H. 1969. The significance of lead isotope studies in ancient, high-grade metamorphic basement complexes, as exemplified by the Lewisian rocks of Northwest Scotland. *Earth and Planetary Science Letters,* 6**,** 245-256.

MOREL, S. W. 1979. The geology and mineral resources of Sierra Leone. *Economic Geology,* 74**,** 1563-1576.

MOYEN, J.-F. 2011. The composite Archaean grey gneisses: Petrological significance, and evidence for a non-unique tectonic setting for Archaean crustal growth. *Lithos,* 123**,** 21-36.

MOYEN, J.-F., STEVENS, G. & KISTERS, A. 2006. Record of mid-Archaean subduction from metamorphism in the Barberton terrain, South Africa. *Nature,* 442**,** 559-562.

MOYEN, J.-F., STEVENS, G., KISTERS, A. F. M. & BELCHER, R. W. 2007. Chapter 5.6 TTG Plutons of the Barberton Granitoid-Greenstone Terrain, South Africa. *In:* MARTIN J. VAN KRANENDONK, R. H. S. & VICKIE, C. B. (eds.) *Developments in Precambrian Geology.* Elsevier.

MOYEN, J.-F. & VAN HUNEN, J. 2012. Short-term episodicity of Archaean plate tectonics. *Geology,* 40**,** 451-454.

MOYEN, J. F. & STEVENS, G. 2006. Experimental constraints on TTG petrogenesis: implications for Archean geodynamics. *Archean geodynamics and environments***,** 149-175.

MUKHERJEE, P. K. & GUPTA, P. K. 2008. Arbitrary scaling in ISOCON method of geochemical mass balance: an evaluation of the graphical approach. *Geochemical Journal,* 42**,** 247-253.

MUKHOPADHYAY, J., CROWLEY, Q. G., GHOSH, S., GHOSH, G., CHAKRABARTI, K., MISRA, B., HERON, K. & BOSE, S. 2014. Oxygenation of the Archean atmosphere: New paleosol constraints from eastern India. *Geology*.

NAGEL, T. J., HOFFMANN, J. E. & MÜNKER, C. 2012. Generation of Eoarchean tonalite-trondhjemite-granodiorite series from thickened mafic arc crust. *Geology*.

NAQVI, S. M. & HUSSAIN, S. M. 1979. Geochemistry of metaanorthosites from a greenstone belt in Karnataka, India. *Canadian Journal of Earth Sciences,* 16**,** 1254-1264.

NEAL, C. R., MAHONEY, J.J., KROENKE, L.W., DUNCAN, R.A., PETTERSON, M.G. 1997. The Ontong Java Plateau. *In:* MAHONEY, J. J., COFFIN, M.F. (ed.) *Large Igneaous Provinces: Continental, Oceanic, and Planetary Flood Volcanism.* American Geophysical Union, Geophysical Monograph.

NEBEL, O., RAPP, R. P. & YAXLEY, G. M. 2014. The role of detrital zircons in Hadean crustal research. *Lithos,* 190–191**,** 313-327.

NESBITT, H. W. & YOUNG, G. M. 1982. Early Proterozoic climates and plate motions inferred from major element chemistry of lutites. *Nature,* 299**,** 715-717.

NEUMAYR, P., RIDLEY, J. R., MCNAUGHTON, N. J., KINNY, P. D., BARLEY, M. E. & GROVES, D. I. 1998. Timing of gold mineralization in the Mt York district, Pilgangoora greenstone belt, and implications for the tectonic and metamorphic evolution of an area linking the western and eastern Pilbara Craton. *Precambrian Research,* 88**,** 249-265.

NOZAKI, Y., ZHANG, J. & AMAKAWA, H. 1997. The fractionation between Y and Ho in the marine environment. *Earth and Planetary Science Letters,* 148**,** 329-340.

NRH 2012. National Resource Holdings Global Gold Mines and Deposit Ranking 2012.

NRH 2013. National Resource Holdings Global 2013 Gold Mine and Deposit Rankings.

NUTMAN, A. P., BENNETT, C. V., FRIEND, L. C. R. & NORMAN, D. M. 1999. Meta-igneous (non-gneissic) tonalites and quartz-diorites from an extensive ca. 3800 Ma terrain south of the Isua supracrustal belt, southern West Greenland: constraints on early crust formation. *Contributions to Mineralogy and Petrology,* 137**,** 364-388.

NUTMAN, A. P., BENNETT, V. C., FRIEND, C. R. L., HORIE, K. & HIDAKA, H. 2007a. ~3,850 Ma tonalites in the Nuuk region, Greenland: geochemistry and their reworking within an Eoarchaean gneiss complex. *Contributions to Mineralogy and Petrology,* 154**,** 385-408.

NUTMAN, A. P., FRIEND, C. R. L., HORIE, K. & HIDAKA, H. 2007b. Chapter 3.3 The Itsaq Gneiss Complex of Southern West Greenland and the Construction of Eoarchaean Crust at Convergent Plate Boundaries. *In:* MARTIN J. VAN KRANENDONK, R. H. S. & VICKIE, C. B. (eds.) *Developments in Precambrian Geology.* Elsevier.

O'CONNOR, E. A., PITFIELD, P. E. J., SCHOFIELD, D. I., COATS, S., WATERS, C., POWELL, J., FORD, J., CLARKE, S. & GILLESPIE, M. 2005. Notice explicative des cartes ge´ologiques et gıˆtologiques a` 1/200000 et 1/500000 du Nord-Ouest de la Mauritanie. *DMG, Ministe`re des Mines et de l'Industrie, Nouakchott.*

O'NEIL, J., CARLSON, R. W., PAQUETTE, J.-L. & FRANCIS, D. 2012. Formation age and metamorphic history of the Nuvvuagittuq Greenstone Belt. *Precambrian Research,* 220–221**,** 23-44.

O'NEILL, C., LENARDIC, A., MORESI, L., TORSVIK, T. H. & LEE, C. T. A. 2007. Episodic Precambrian subduction. *Earth and Planetary Science Letters,* 262**,** 552-562.

OHTA, T. 2008. Measuring and adjusting the weathering and hydraulic sorting effects for rigorous provenance analysis of sedimentary rocks: a case study from the Jurassic Ashikita Group, south-west Japan. *Sedimentology,* 55**,** 1687-1701.

ORDÓÑEZ-CALDERÓN, J. C., POLAT, A., FRYER, B. J. & GAGNON, J. E. 2011. Field and geochemical characteristics of Mesoarchean to Neoarchean volcanic rocks in the Storø greenstone belt, SW Greenland: Evidence for accretion of intra-oceanic volcanic arcs. *Precambrian Research,* 184**,** 24-42.

PALIN, R. M. & WHITE, R. W. 2016. Emergence of blueschists on Earth linked to secular changes in oceanic crust composition. *Nature Geosci,* 9**,** 60-64.

PARK, R. G. 1995. Palaeoproterozoic Laurentia-Baltica relationships: a view from the Lewisian. *Geological Society, London, Special Publications,* 95**,** 211-224.

PARMAN, S. W. & GROVE, T. L. 2004. Petrology and Geochemistry of Barberton Komatiites and Basaltic Komatiites: Evidence of Archean Fore-Arc Magmatism. *Developments in Precambrian Geology.* Elsevier.

PATCHETT, P. J., KOUVO, O., HEDGE, C. E. & TATSUMOTO, M. 1982. Evolution of continental crust and mantle heterogeneity: evidence from Hf isotopes. *Contributions to Mineralogy and Petrology,* 78**,** 279-297.

PATON, C., HELLSTROM, J., PAUL, B., WOODHEAD, J. & HERGT, J. 2011. Iolite: Freeware for the visualisation and processing of mass spectrometric data. *Journal of Analytical Atomic Spectrometry,* 26**,** 2508-2518.

PE-PIPER, G., PIPER, D. J. W., JANSA, L. F. & DE JONGE, A. 2007. Early Cretaceous opening of the North Atlantic Ocean: Implications of the petrology and tectonic setting of the Fogo Seamounts off the SW Grand Banks, Newfoundland. *Geological Society of America Bulletin,* 119**,** 712-724.

PEARCE, J. A. 1983. Role of the sub-continental lithosphere in magma genesis at active continental margins.

PEARCE, J. A. 2008. Geochemical fingerprinting of oceanic basalts with applications to ophiolite classification and the search for Archean oceanic crust. *Lithos,* 100**,** 14-48.

PEARCE, J. A., HARRIS, N. B. W. & TINDLE, A. G. 1984. Trace Element Discrimination Diagrams for the Tectonic Interpretation of Granitic Rocks. *Journal of Petrology,* 25**,** 956-983.

PEARCE, J. A. & NORRY, M. J. 1979. Petrogenetic implications of Ti, Zr, Y, and Nb variations in volcanic rocks. *Contributions to mineralogy and petrology,* 69**,** 33-47.

PEARSON, D. G. 1999. The age of continental roots. *Lithos,* 48**,** 171-194.

PELTONEN, P., KONTINEN, A. & HUHMA, H. 1996. Petrology and Geochemistry of Metabasalts from the 1.95 Ga Jormua Ophiolite, Northeastern Finland. *Journal of Petrology,* 37**,** 1359-1383.

PETRUS, J. A. & KAMBER, B. S. 2012. VizualAge: A Novel Approach to Laser Ablation ICP-MS U-Pb Geochronology Data Reduction. *Geostandards and Geoanalytical Research,* 36**,** 247-270.

PHILIPP, H., ECKHARDT, J.-D. & PUCHELT, H. 2001. Platinum-Group Elements (PGE) in Basalts of the Seaward-Dipping Reflector Sequence, SE Greenland Coast. *Journal of Petrology,* 42**,** 407-432.

PHILLIPS, G. Australian and global setting for gold in 2013. Proceedings World Gold, 2013. 15-21.

PIERCEY, S. J., MORTENSEN, J. K., MURPHY, D. C., PARADIS, S. & CREASER, R. A. 2002. Geochemistry and tectonic significance of alkalic mafic magmatism in the Yukon–Tanana terrane, Finlayson Lake region, Yukon. *Canadian Journal of Earth Sciences,* 39**,** 1729-1744.

PIN, C., BRIOT, D., BASSIN, C. & POITRASSON, F. 1994. Concomitant separation of strontium and samarium-neodymium for isotopic analysis in silicate samples, based on specific extraction chromatography. *Analytica Chimica Acta,* 298**,** 209-217.

PIN, C. & ZALDUEGUI, J. S. 1997. Sequential separation of light rare-earth elements, thorium and uranium by miniaturized extraction chromatography: Application to isotopic analyses of silicate rocks. *Analytica Chimica Acta,* 339**,** 79-89.

PITFIELD, P. E. J., KEY, R. M., WATERS, C. N., HAWKINS, M. P. H., SCHOFIELD, D. I., LOUGHLIN, S. C. & BARNES, R. P. 2005. Notice explicative des cartes ge´ologiques et gıˆtologiques au 1/200 000 et 1/500 000 du Sud de la Mauritanie. *DMG, Ministe`re des Mines et de l'Industrie, Nouakchott, Mauritania.*

POLAT, A. 2009. The geochemistry of Neoarchean (ca. 2700 Ma) tholeiitic basalts, transitional to alkaline basalts, and gabbros, Wawa Subprovince, Canada: Implications for petrogenetic and geodynamic processes. *Precambrian Research,* 168**,** 83-105.

POLAT, A., APPEL, P. W. U. & FRYER, B. J. 2011. An overview of the geochemistry of Eoarchean to Mesoarchean ultramafic to mafic volcanic rocks, SW Greenland: Implications for mantle depletion and petrogenetic processes at subduction zones in the early Earth. *Gondwana Research,* 20**,** 255-283.

POLAT, A., FREI, R., APPEL, P. W. U., DILEK, Y., FRYER, B., ORDÓÑEZ-CALDERÓN, J. C. & YANG, Z. 2008. The origin and compositions of Mesoarchean oceanic crust: Evidence from the 3075 Ma Ivisaartoq greenstone belt, SW Greenland. *Lithos,* 100**,** 293-321.

POLAT, A., FREI, R., SCHERSTÉN, A. & APPEL, P. W. U. 2010. New age (ca. 2970 Ma), mantle source composition and geodynamic constraints on the Archean Fiskenæsset anorthosite complex, SW Greenland. *Chemical Geology,* 277**,** 1-20.

POLAT, A. & KERRICH, R. 2001. Geodynamic processes, continental growth, and mantle evolution recorded in late Archean greenstone belts of the southern Superior Province, Canada. *Precambrian Research,* 112**,** 5-25.

POLAT, A., LI, J., FRYER, B., KUSKY, T., GAGNON, J. & ZHANG, S. 2006. Geochemical characteristics of the Neoarchean (2800–2700 Ma) Taishan greenstone belt, North China Craton: Evidence for plume–craton interaction. *Chemical Geology,* 230**,** 60-87.

POTREL, A. 1994. *Evolution tectono-métamorphique d'un segment de croûte continentale archéenne. Exemple de l'Amsaga (R.I. Mauritanie), Dorsale Réguibat (Craton Ouest Africain).* Université Rennes 1.

POTREL, A. 1997. Geochemistry of the Amsaga Area Orthogneisses (Archean Reguibat Rise, Mauritania). *Revista Brasileira de Geociências,* 27**,** 211-218.

POTREL, A., PEUCAT, J. J. & FANNING, C. M. 1998. Archean crustal evolution of the West African Craton: example of the Amsaga Area (Reguibat Rise). U・Pb and Sm・Nd evidence for crustal growth and recycling. *Precambrian Research,* 90**,** 107-117.

POTREL, A., PEUCAT, J. J., FANNING, C. M., AUVRAY, B., BURG, J. P. & CARUBA, C. 1996. 3.5 Ga old terranes in the West African Craton, Mauritania. *Journal of the Geological Society,* 153**,** 507-510.

POUPINET, G. & SHAPIRO, N. M. 2009. Worldwide distribution of ages of the continental lithosphere derived from a global seismic tomographic model. *Lithos,* 109**,** 125-130.

POWELL, C. M., LI, Z. X., MCELHINNY, M. W., MEERT, J. G. & PARK, J. K. 1993. Paleomagnetic constraints on timing of the Neoproterozoic breakup of Rodinia and the Cambrian formation of Gondwana. *Geology,* 21**,** 889-892.

POWELL, R., WILL, T. & PHILLIPS, G. 1991. Metamorphism in Archaean greenstone belts: calculated fluid compositions and implications for gold mineralization. *Journal of Metamorphic Geology,* 9**,** 141-150.

PUCHTEL, I. S., BRANDON, A. D. & HUMAYUN, M. 2004. Precise Pt–Re–Os isotope systematics of the mantle from 2.7-Ga komatiites. *Earth and Planetary Science Letters,* 224**,** 157-174.

PUCHTEL, I. S., WALKER, R. J., ANHAEUSSER, C. R. & GRUAU, G. 2009. Re–Os isotope systematics and HSE abundances of the 3.5 Ga Schapenburg komatiites, South Africa: Hydrous melting or prolonged survival of primordial heterogeneities in the mantle? *Chemical Geology,* 262**,** 355-369.

PURDY, J. W. & JÄGER, E. 1976. *K-Ar ages on rock-forming minerals from the Central Alps*, Università di Padova.

QIU, Y. & MCNAUGHTON, N. J. 1999. Source of Pb in orogenic lode-gold mineralisation: Pb isotope constraints from deep crustal rocks from the southwestern Archaean Yilgarn Craton, Australia. *Mineralium Deposita,* 34**,** 366-381.

REIMINK, J. R., CHACKO, T., STERN, R. A. & HEAMAN, L. M. 2014. Earth[rsquor]s earliest evolved crust generated in an Iceland-like setting. *Nature Geosci,* 7**,** 529-533.

REY, P. F., PHILIPPOT, P. & THÉBAUD, N. 2003. Contribution of mantle plumes, crustal thickening and greenstone blanketing to the 2.75–2.65 Ga global crisis. *Precambrian Research,* 127**,** 43-60.

RIDLEY, J. R., DIAMOND, L.W. 2000. Fluid chemistry of orogenic lode-gold deposits and implications for genetic models. *In:* HAGEMANN, S. G., BROWN, P.E. (ed.) *Gold in 2000.* Reviews in economic geology: Society of Economic Geologists.

RIGGS, N. R., BARTH, A. P., GONZÁLEZ-LEÓN, C. M., JACOBSON, C. E., WOODEN, J. L., HOWELL, E. R. & WALKER, J. D. 2012. Provenance of Upper Triassic strata in southwestern North America as suggested by isotopic analysis and chemistry of zircon crystals. *Geological Society of America Special Papers,* 487**,** 13-36.

RIGGS, N. R., REYNOLDS, S. J., LINDNER, P. J., HOWELL, E. R., BARTH, A. P., PARKER, W. G. & WALKER, J. D. 2013. The Early Mesozoic Cordilleran arc and Late Triassic paleotopography: The detrital record in Upper Triassic sedimentary successions on and off the Colorado Plateau. *Geosphere,* 9**,** 602-613.

ROBERT, F. 1996. Quartz-carbonate vein gold. *Eckstrand, Ž*.

ROBERT, F., SHEAHAN, P. & GREEN, S. B. 1991. *Greenstone gold and crustal evolution: Nuna Conference volume*, Geological Assn of Canada.

ROBERTS, N. M. W. & SPENCER, C. J. 2014. The zircon archive of continent formation through time. *Geological Society, London, Special Publications,* 389.

ROBERTS, N. M. W., VAN KRANENDONK, M. J., PARMAN, S. & CLIFT, P. D. 2014. Continent formation through time. *Geological Society, London, Special Publications,* 389.

ROBIN-POPIEUL, C. C. M., ARNDT, N. T., CHAUVEL, C., BYERLY, G. R., SOBOLEV, A. V. & WILSON, A. 2012. A New Model for Barberton Komatiites: Deep Critical Melting with High Melt Retention. *Journal of Petrology*.

ROBINSON, P. T., MALPAS, J., DILEK, Y. & ZHOU, M. 2008. The significance of sheeted dike complexes in ophiolites. *GSA Today,* 18**,** 4-10.

ROCCI, G., BRONNER, G. & DESCHAMPS, M. 1991. Crystalline basement of the West African craton. *The West African orogens and circum-Atlantic correlatives.* Springer.

ROGERS, J. J. W. 1996. A History of Continents in the past Three Billion Years. *The Journal of Geology,* 104**,** 91-107.

ROLLINSON, H. R. 1982. P-T conditions in coeval greenstone belts and granulites from the Archaean of Sierra Leone. *Earth and Planetary Science Letters,* 59**,** 177-191.

ROLLINSON, H. R. 1983. The geochemistry of mafic and ultramafic from the Archaean greenstone belts of Sierra Leone. *Mineralogical Magazine,* 47**,** 267-280.

ROLLINSON, H. R. 1993. Using geochemical data: evaluation, presentation, interpretation.

ROLLINSON, H. R. 1997. Eclogite xenoliths in west African kimberlites as residues from Archaean granitoid crust formation. *Nature,* 389**,** 173-176.

ROLLINSON, H. R. 1999. Petrology and geochemistry of metamorphosed komatiites and basalts from the Sula Mountains greenstone belt, Sierra Leone. *Contributions to Mineralogy and Petrology,* 134**,** 86-101.

ROLLINSON, H. R. 2007. Recognising early Archaean mantle: a reappraisal. *Contributions to Mineralogy and Petrology,* 154**,** 241-252.

ROLLINSON, H. R. 2009. New models for the genesis of plagiogranites in the Oman ophiolite. *Lithos,* 112**,** 603-614.

ROLLINSON, H. R. 2010. Coupled evolution of Archean continental crust and subcontinental lithospheric mantle. *Geology,* 38**,** 1083-1086.

ROLLINSON, H. R. & TARNEY, J. 2005. Adakites—the key to understanding LILE depletion in granulites. *Lithos,* 79**,** 61-81.

ROLLINSON, H. R. & WINDLEY, B. F. 1980. An archaean granulite-grade tonalite-trondhjemite-granite suite from scourie, NW Scotland: Geochemistry and origin. *Contributions to Mineralogy and Petrology,* 72**,** 265-281.

ROSS, P.-S. & BÉDARD, J. H. 2009. Magmatic affinity of modern and ancient subalkaline volcanic rocks determined from trace-element discriminant diagrams. *Canadian Journal of Earth Sciences,* 46**,** 823-839.

ROY, A. S., A. ; JEYAKUMAR, S. ; AGGRAWAL, S. K. ; EBIHARA, M. 2002. Sm-Nd age and mantle source characteristics of the Dhanjori volcanic rocks, Eastern India. *Geochemical Journal,* 36**,** 503-518.

SAAGER, R. & KOPPEL, V. 1976. Lead isotopes and trace elements from sulfides of Archean greenstone belts in South Africa; a contribution to the knowledge of the oldest known mineralizations. *Economic Geology,* 71**,** 44-57.

SAKELLARIS, G. A., MEYER, F.M. 2008. A Metamorphic Origin of the Guelb Moghrein Fe Oxide-Copper-Gold-Cobalt Deposit, Mauritania. *XIII All-Russian conference on thermobarogeochemistry in conjunction with IV APIFIS symposium*.

SANISLAV, I. V., WORMALD, R. J., DIRKS, P. H. G. M., BLENKINSOP, T. G., SALAMBA, L. & JOSEPH, D. 2014. Zircon U–Pb ages and Lu–Hf isotope systematics from late-tectonic granites, Geita Greenstone Belt: Implications for crustal growth of the Tanzania Craton. *Precambrian Research,* 242**,** 187-204.

SARMA, D. S., FLETCHER, I., RASMUSSEN, B., MCNAUGHTON, N., MOHAN, M. R. & GROVES, D. 2011. Archaean gold mineralization synchronous with late cratonization of the Western Dharwar Craton, India: 2.52 Ga U–Pb ages of hydrothermal monazite and xenotime in gold deposits. *Mineralium Deposita,* 46**,** 273-288.

SAUNDERS, A. D., FITTON, J. G., KERR, A. C., NORRY, M. J. & KENT, R. W. 2013. The North Atlantic Igneous Province. *Large Igneous Provinces: Continental, Oceanic, and Planetary Flood Volcanism.* American Geophysical Union.

SCHOENE, B. & BOWRING, S. A. 2006. U–Pb systematics of the McClure Mountain syenite: thermochronological constraints on the age of the 40Ar/39Ar standard MMhb. *Contributions to Mineralogy and Petrology,* 151**,** 615-630.

SCHOFIELD, D. I. & GILLESPIE, M. R. 2007. A tectonic interpretation of “Eburnean terrane” outliers in the Reguibat Shield, Mauritania. *Journal of African Earth Sciences,* 49**,** 179-186.

SCHOFIELD, D. I., HORSTWOOD, M. S. A., PITFIELD, P. E. J., CROWLEY, Q. G., WILKINSON, A. F. & SIDATY, H. C. O. 2006. Timing and kinematics of Eburnean tectonics in the central Reguibat Shield, Mauritania. *Journal of the Geological Society,* 163**,** 549-560.

SCHOFIELD, D. I., HORSTWOOD, M. S. A., PITFIELD, P. E. J., GILLESPIE, M., DARBYSHIRE, F., O’CONNOR, E. A. & ABDOULOYE, T. B. 2012. U–Pb dating and Sm–Nd isotopic analysis of granitic rocks from the Tiris Complex: New constaints on key events in the evolution of the Reguibat Shield, Mauritania. *Precambrian Research,* 204–205**,** 1-11.

SCHOPF, J. W., KUDRYAVTSEV, A. B., CZAJA, A. D. & TRIPATHI, A. B. 2007. Evidence of Archean life: Stromatolites and microfossils. *Precambrian Research,* 158**,** 141-155.

SCHWARZ-SCHAMPERA, U., TERBLANCHE, H. & OBERTHÜR, T. 2009. Volcanic-hosted massive sulfide deposits in the Murchison greenstone belt, South Africa. *Mineralium Deposita,* 45**,** 113-145.

SHERVAIS, J. W. 1982. Ti-V plots and the petrogenesis of modern and ophiolitic lavas. *Earth and Planetary Science Letters,* 59**,** 101-118.

SHIREY, S. B., KAMBER, B. S., WHITEHOUSE, M. J., MUELLER, P. A. & BASU, A. R. 2008. A review of the isotopic and trace element evidence for mantle and crustal processes in the Hadean and Archean: Implications for the onset of plate tectonic subduction. *Geological Society of America Special Papers,* 440**,** 1-29.

SHIREY, S. B. & RICHARDSON, S. H. 2011. Start of the Wilson Cycle at 3 Ga Shown by Diamonds from Subcontinental Mantle. *Science,* 333**,** 434-436.

SILLITOE, R. 1991. Intrusion-related gold deposits. *Gold metallogeny and exploration.* Springer.

SIMS, J. 2014. Tasiast Project Mauritania National Instrument 43-101 Technical Report, Prepared for Kinross Gold Corporation.

SLÁMA, J., KOŠLER, J., CONDON, D. J., CROWLEY, J. L., GERDES, A., HANCHAR, J. M., HORSTWOOD, M. S. A., MORRIS, G. A., NASDALA, L., NORBERG, N., SCHALTEGGER, U., SCHOENE, B., TUBRETT, M. N. & WHITEHOUSE, M. J. 2008. Plešovice zircon — A new natural reference material for U–Pb and Hf isotopic microanalysis. *Chemical Geology,* 249**,** 1-35.

SLEEP, N. H. & WINDLEY, B. F. 1982. Archean Plate Tectonics: Constraints and Inferences. *The Journal of Geology,* 90**,** 363-379.

SMITHIES, R. H. 2000. The Archaean tonalite–trondhjemite–granodiorite (TTG) series is not an analogue of Cenozoic adakite. *Earth and Planetary Science Letters,* 182**,** 115-125.

SMITHIES, R. H., CHAMPION, D. C. & CASSIDY, K. F. 2003. Formation of Earth's early Archaean continental crust. *Precambrian Research,* 127**,** 89-101.

SMITHIES, R. H., CHAMPION, D. C., VAN KRANENDONK, M. J., HOWARD, H. M. & HICKMAN, A. H. 2005. Modern-style subduction processes in the Mesoarchaean: Geochemical evidence from the 3.12 Ga Whundo intra-oceanic arc. *Earth and Planetary Science Letters,* 231**,** 221-237.

SOUDERS, A. K. & SYLVESTER, P. J. 2010. Accuracy and precision of non-matrix-matched calibration for lead isotope ratio measurements of lead-poor minerals by LA-MC-ICPMS. *Journal of Analytical Atomic Spectrometry,* 25**,** 975-988.

STEIN, M. & HOFMANN, A. W. 1994. Mantle plumes and episodic crustal growth. *Nature,* 372**,** 63-68.

STERN, C. R. 2011. Subduction erosion: Rates, mechanisms, and its role in arc magmatism and the evolution of the continental crust and mantle. *Gondwana Research,* 20**,** 284-308.

STERN, C. R. & KILIAN, R. 1996. Role of the subducted slab, mantle wedge and continental crust in the generation of adakites from the Andean Austral Volcanic Zone. *Contributions to mineralogy and petrology,* 123**,** 263-281.

STERN, R. J. 2005. Evidence from ophiolites, blueschists, and ultrahigh-pressure metamorphic terranes that the modern episode of subduction tectonics began in Neoproterozoic time. *Geology,* 33**,** 557-560.

STERN, R. J. & SCHOLL, D. W. 2010. Yin and yang of continental crust creation and destruction by plate tectonic processes. *International Geology Review,* 52**,** 1-31.

STUART, H. 2010. Technical Report on the Tasiast Gold Mine Islamic Republic of Mauritania for Red Back Mining Inc.: unpublished technical report prepared for Red BackMining Inc., effective date 6 September 2010. 104.

SUGITANI, K., GREY, K., ALLWOOD, A., NAGAOKA, T., MIMURA, K., MINAMI, M., MARSHALL, C. P., VAN KRANENDONK, M. J. & WALTER, M. R. 2007. Diverse microstructures from Archaean chert from the Mount Goldsworthy–Mount Grant area, Pilbara Craton, Western Australia: Microfossils, dubiofossils, or pseudofossils? *Precambrian Research,* 158**,** 228-262.

SUN, S.-S. & MCDONOUGH, W. F. 1989. Chemical and isotopic systematics of oceanic basalts: implications for mantle composition and processes. *Geological Society, London, Special Publications,* 42**,** 313-345.

SWAGER, C., WITT, W., GRIFFIN, T., AHMAT, A., HUNTER, W., MCGOLDRICK, P. & WYCHE, S. 1992. Late Archaean granite-greenstones of the Kalgoorlie Terrane, Yilgarn Craton, Western Australia. *The Archaean: terrains, processes and metallogeny,* 22**,** 107-122.

SYLVESTER, P. J. 2008. *Matrix effects in Laser Ablation-ICP-MS*.

SZILAS, K., VAN HINSBERG, V. J., KISTERS, A. F. M., HOFFMANN, J. E., WINDLEY, B. F., KOKFELT, T. F., SCHERSTÉN, A., FREI, R., ROSING, M. T. & MÜNKER, C. 2013. Remnants of arc-related Mesoarchaean oceanic crust in the Tartoq Group of SW Greenland. *Gondwana Research,* 23**,** 436-451.

TAIT, J., STRAATHOF, G., SÖDERLUND, U., ERNST, R. E., KEY, R., JOWITT, S. M., LO, K., DAHMADA, M. E. M. & N'DIAYE, O. 2013. The Ahmeyim Great Dyke of Mauritania: A newly dated Archaean intrusion. *Lithos,* 174**,** 323-332.

TATSUMI, Y. 2005. The subduction factory: how it operates in the evolving Earth. *GSA today,* 15**,** 4-10.

TAYLOR, C. D., ANDERSON, E. D., BRADLEY, D. C., BEAUDOIN, G., COSCA, M. A., EPPINGER, R. G., FERNETTE, G. L., FINN, C. A., FRIEDEL, M. J., GILES, S. A., GOLDFARB, R. J., HORTON, J. D., LEE, G. K., MARSH, E. E., MAUK, J. L., MOTTS, H. A., OULD EL JOUD, M. Y., OULD-SOUEIDATT, S., OULD-TALEB-MOHAMED, A. & ROCKWELL, B. W. 2012. Mauritania: A Greenfields Exploration Opportunity in Northwestern Africa. *SEG Newsletter*.

TAYLOR, R. N., NESBITT, R. W., VIDAL, P., HARMON, R. S., AUVRAY, B. & CROUDACE, I. W. 1994. Mineralogy, chemistry, and genesis of the boninite series volcanics, Chichijima, Bonin Islands, Japan. *Journal of Petrology,* 35**,** 577-617.

TAYLOR, S. R., MCLENNAN, S.M. 1985. *The continental crust: Its composition and evolution*, Blackwell Scientific Pub.

THIÉBLEMONT, D., DELOR, C., COCHERIE, A., LAFON, J. M., GOUJOU, J. C., BALDÉ, A., BAH, M., SANÉ, H. & MARK FANNING, C. 2001. A 3.5 Ga granite–gneiss basement in Guinea: further evidence for early archean accretion within the West African Craton. *Precambrian Research,* 108**,** 179-194.

THIRLWALL, M. F. 1991. Long-term reproducibility of multicollector Sr and Nd isotope ratio analysis. *Chemical Geology,* 94**,** 85-104.

THOMSON, S. N., GEHRELS, G. E., RUIZ, J. & BUCHWALDT, R. 2012. Routine low-damage apatite U-Pb dating using laser ablation–multicollector–ICPMS. *Geochemistry, Geophysics, Geosystems,* 13.

THURSTON, P. C. 2002. Autochthonous development of Superior Province greenstone belts? *Precambrian Research,* 115**,** 11-36.

TOLSTIKHIN, I. N., KRAMERS, J. D. & HOFMANN, A. W. 2006. A chemical Earth model with whole mantle convection: The importance of a core–mantle boundary layer (D") and its early formation. *Chemical Geology,* 226**,** 79-99.

TOMKINS, A. G. 2013. On the source of orogenic gold. *Geology,* 41**,** 1255-1256.

TOMLINSON, K. Y. & CONDIE, K. C. 2001. Archean mantle plumes: Evidence from greenstone belt geochemistry. *Geological Society of America Special Papers,* 352**,** 341-357.

TOMLINSON, K. Y., DAVIS, D. W., STONE, D. & HART, T. R. 2003. U–Pb age and Nd isotopic evidence for Archean terrane development and crustal recycling in the south-central Wabigoon subprovince, Canada. *Contributions to Mineralogy and Petrology,* 144**,** 684-702.

TREMBLAY, A. 2001. Postmineralization Faults in the Beaufor Gold Deposit, Abitibi Greenstone Belt, Canada: Geometry, Origin, and Tectonic Implications for the Val-d'Or Mining District. *Economic Geology,* 96**,** 509-524.

TURNER, S., RUSHMER, T., REAGAN, M. & MOYEN, J.-F. 2014. Heading down early on? Start of subduction on Earth. *Geology*.

TYRRELL, S., LELEU, S., SOUDERS, A. K., HAUGHTON, P. D. W. & DALY, J. S. 2009. K-feldspar sand-grain provenance in the Triassic, west of Shetland: distinguishing first-cycle and recycled sediment sources? *Geological Journal,* 44**,** 692-710.

VACHETTE, M. & BRONNER, G. 1975. Âges radiométriques Rb・Sr de 2900 et 2700 Ma, des séries précambriennes de l'Amsaga et du Tiris, Dorsale Réguibat (Mauritanie). *Trav. Lab. Sci. Terre, Marseille (France), B,* 11**,** 147-148.

VALLEY, J. W. 2003. Oxygen Isotopes in Zircon. *Reviews in Mineralogy and Geochemistry,* 53**,** 343-385.

VAN DER ZANDER, I., SINTON, J. M. & MAHONEY, J. J. 2010. Late Shield-Stage Silicic Magmatism at Wai‘anae Volcano: Evidence for Hydrous Crustal Melting in Hawaiian Volcanoes. *Journal of Petrology,* 51**,** 671-701.

VAN HUNEN, J. & MOYEN, J. F. 2012. Archean Subduction: Fact or Fiction? *Annual Review of Earth and Planetary Sciences, Vol 40,* 40**,** 195-219.

VAN HUNEN, J. & VAN DEN BERG, A. P. 2008. Plate tectonics on the early Earth: Limitations imposed by strength and buoyancy of subducted lithosphere. *Lithos,* 103**,** 217-235.

VAN HUNEN, J., VAN DEN BERG, A. P. & VLAAR, N. J. 2004. Various mechanisms to induce present-day shallow flat subduction and implications for the younger Earth: a numerical parameter study. *Physics of the Earth and Planetary Interiors,* 146**,** 179-194.

VAN KRANENDONK, M. J. 2011. Onset of Plate Tectonics. *Science,* 333**,** 413-414.

VAN KRANENDONK, M. J., COLLINS, W. J., HICKMAN, A. & PAWLEY, M. J. 2004. Critical tests of vertical vs. horizontal tectonic models for the Archaean East Pilbara Granite–Greenstone Terrane, Pilbara Craton, Western Australia. *Precambrian Research,* 131**,** 173-211.

VAN KRANENDONK, M. J., HICKMAN, A. H. & SMITHIES, R. H. 2007a. The East Pilbara Terrane of the Pilbara Craton, Western Australia: Formation of a continental nucleus through repeated mantle plume magmatism. *Earth’s Oldest Rocks. Developments in Precambrian Geology,* 15**,** 307-337.

VAN KRANENDONK, M. J., HUGH SMITHIES, R., HICKMAN, A. H. & CHAMPION, D. C. 2007b. Review: secular tectonic evolution of Archean continental crust: interplay between horizontal and vertical processes in the formation of the Pilbara Craton, Australia. *Terra Nova,* 19**,** 1-38.

VAN KRANENDONK, M. J., HUGH SMITHIES, R., HICKMAN, A. H., WINGATE, M. T. D. & BODORKOS, S. 2010. Evidence for Mesoarchean (~3.2 Ga) rifting of the Pilbara Craton: The missing link in an early Precambrian Wilson cycle. *Precambrian Research,* 177**,** 145-161.

VAN KRANENDONK, M. J., KRÖNER, A., HEGNER, E. & CONNELLY, J. 2009. Age, lithology and structural evolution of the c. 3.53 Ga Theespruit Formation in the Tjakastad area, southwestern Barberton Greenstone Belt, South Africa, with implications for Archaean tectonics. *Chemical Geology,* 261**,** 115-139.

VAN KRANENDONK, M. J. & PIRAJNO, F. 2004. Geochemistry of metabasalts and hydrothermal alteration zones associated with c. 3.45 Ga chert and barite deposits: implications for the geological setting of the Warrawoona Group, Pilbara Craton, Australia. *Geochemistry: Exploration, Environment, Analysis,* 4**,** 253-278.

VAN THIENEN, P., VLAAR, N. J. & VAN DEN BERG, A. P. 2004. Plate tectonics on the terrestrial planets. *Physics of the Earth and Planetary Interiors,* 142**,** 61-74.

VEEVERS, J. J. 2004. Gondwanaland from 650–500 Ma assembly through 320 Ma merger in Pangea to 185–100 Ma breakup: supercontinental tectonics via stratigraphy and radiometric dating. *Earth-Science Reviews,* 68**,** 1-132.

VIAL, D. S., DEWITT, E., LOBATO, L. M. & THORMAN, C. H. 2007. The geology of the Morro Velho gold deposit in the Archean Rio das Velhas greenstone belt, Quadrilátero Ferrífero, Brazil. *Ore Geology Reviews,* 32**,** 511-542.

VILJOEN, M. & VILJOEN, R. P. 1969. An introduction to the geology of the Barberton granite-greenstone terrain. *Geological Society of South Africa Special Publication,* 2**,** 9-28.

VLAAR, N. J., VAN KEKEN, P. E. & VAN DEN BERG, A. P. 1994. Cooling of the earth in the Archaean: Consequences of pressure-release melting in a hotter mantle. *Earth and Planetary Science Letters,* 121**,** 1-18.

VOICE, P. J., KOWALEWSKI, M. & ERIKSSON, K. A. 2011. Quantifying the Timing and Rate of Crustal Evolution: Global Compilation of Radiometrically Dated Detrital Zircon Grains. *The Journal of Geology,* 119**,** 109-126.

WANG, Z., WILDE, S. A., WANG, K. & YU, L. 2004. A MORB-arc basalt–adakite association in the 2.5 Ga Wutai greenstone belt: late Archean magmatism and crustal growth in the North China Craton. *Precambrian Research,* 131**,** 323-343.

WEST, I. & WEST, J. 2007. The ophiolite succession of the Troodos Mountains of Cyprus , shown schematically.

WETHERILL, G. W. 1956. Discordant uranium-lead ages, I. *Eos, Transactions American Geophysical Union,* 37**,** 320-326.

WIDOM, E., CARLSON, R. W., GILL, J. B. & SCHMINCKE, H. U. 1997. Th–Sr–Nd–Pb isotope and trace element evidence for the origin of the São Miguel, Azores, enriched mantle source. *Chemical Geology,* 140**,** 49-68.

WIEDENBECK, M., ALLÉ, P., CORFU, F., GRIFFIN, W. L., MEIER, M., OBERLI, F., QUADT, A. V., RODDICK, J. C. & SPIEGEL, W. 1995. Three natural zircon standards for U-Th-Pb, Lu-Hf, trace element and REE analyses. *Geostandards Newsletter,* 19**,** 1-23.

WILLBOLD, M., HEGNER, E., STRACKE, A. & ROCHOLL, A. 2009. Continental geochemical signatures in dacites from Iceland and implications for models of early Archaean crust formation. *Earth and Planetary Science Letters,* 279**,** 44-52.

WILSON, J. T. 1966. Did the Atlantic Close and then Re-Open? *Nature,* 211**,** 676-681.

WINCHESTER, J. A. & FLOYD, P. A. 1977. Geochemical discrimination of different magma series and their differentiation products using immobile elements. *Chemical Geology,* 20**,** 325-343.

WOODHEAD, J. D., HERGT, J., MEFFRE, S., LARGE, R. R., DANYUSHEVSKY, L. & GILBERT, S. 2009. In situ Pb-isotope analysis of pyrite by laser ablation (multi-collector and quadrupole) ICPMS. *Chemical Geology,* 262**,** 344-354.

WOODHEAD, J. D. & HERGT, J. M. 2001. Strontium, Neodymium and Lead Isotope Analyses of NIST Glass Certified Reference Materials: SRM 610, 612, 614. *Geostandards Newsletter,* 25**,** 261-266.

WORKMAN, R. K. & HART, S. R. 2005. Major and trace element composition of the depleted MORB mantle (DMM). *Earth and Planetary Science Letters,* 231**,** 53-72.

WYCHE, S., KIRKLAND, C. L., RIGANTI, A., PAWLEY, M. J., BELOUSOVA, E. & WINGATE, M. T. D. 2012. Isotopic constraints on stratigraphy in the central and eastern Yilgarn Craton, Western Australia. *Australian Journal of Earth Sciences,* 59**,** 657-670.

WYMAN, D. & KERRICH, R. 1988. Alkaline magmatism, major structures, and gold deposits; implications for greenstone belt gold metallogeny. *Economic Geology,* 83**,** 454-461.

XUE, Y., CAMPBELL, I., IRELAND, T. R., HOLDEN, P. & ARMSTRONG, R. 2013. No mass-independent sulfur isotope fractionation in auriferous fluids supports a magmatic origin for Archean gold deposits. *Geology,* 41**,** 791-794.

YARDLEY, B. W. D. & CLEVERLEY, J. S. 2013. The role of metamorphic fluids in the formation of ore deposits. *Geological Society, London, Special Publications,* 393.

YIN, A. & HARRISON, T. M. 2000. Geologic Evolution of the Himalayan-Tibetan Orogen. *Annual Review of Earth and Planetary Sciences,* 28**,** 211-280.

YOGODZINSKI, G. M., LEES, J. M., CHURIKOVA, T. G., DORENDORF, F., WOERNER, G. & VOLYNETS, O. N. 2001. Geochemical evidence for the melting of subducting oceanic lithosphere at plate edges. *Nature,* 409**,** 500-4.

ZEGERS, T. E., DE WIT, M., DANN & WHITE 1998. Vaalbara, Earth's oldest assembled continent? A combined structural, geochronological, and palaeomagnetic test. *Terra Nova,* 10**,** 250-259.

ZEGERS, T. E. & VAN KEKEN, P. E. 2001. Middle Archean continent formation by crustal delamination. *Geology,* 29**,** 1083-1086.

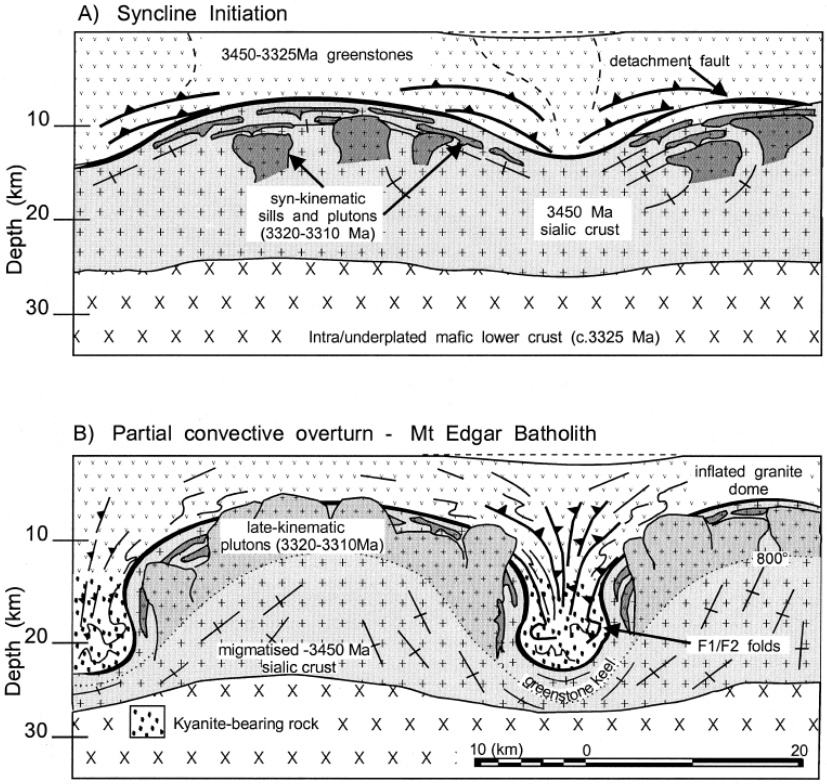
ZEGERS, T. E., WHITE, S. H., DE KEIJZER, M. & DIRKS, P. 1996. Extensional structures during deposition of the 3460 Ma Warrawoona Group in the eastern Pilbara Craton, Western Australia. *Precambrian Research,* 80**,** 89-105.

ZHOU, X., LIN, S. AND ANDERSON, S.D. 2013. Stratigraphic and structural setting of gold deposits in the vicinity of the Central Manitoba mine, Rice Lake greenstone belt, southeastern Manitoba. *Report of Activities 2013.* Manitoba Mineral Resources, Manitoba Geological Survey.

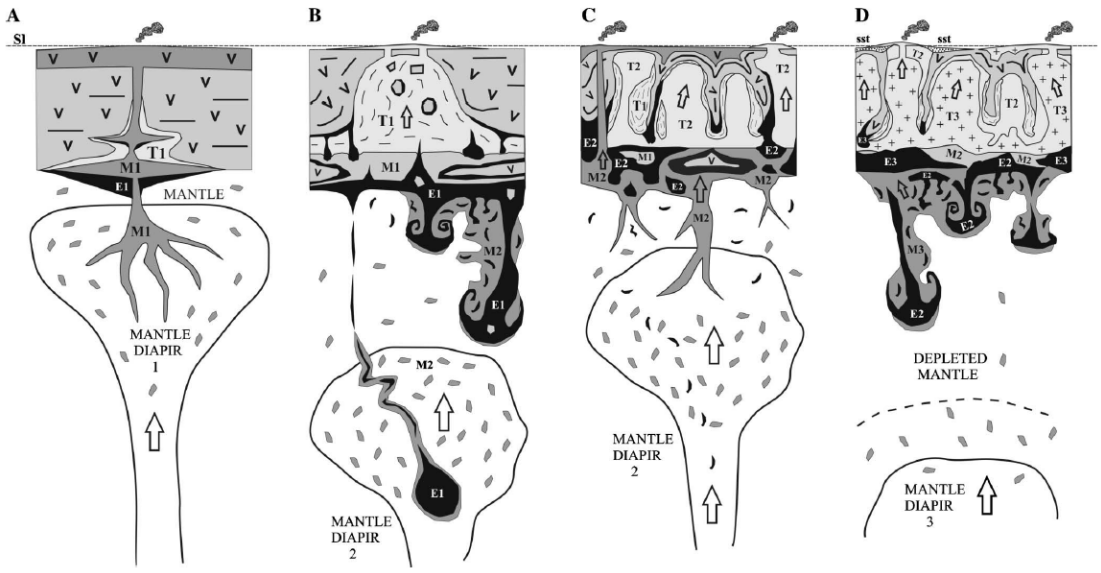
ZIBRA, I., GESSNER, K., SMITHIES, H. R. & PETERNELL, M. 2014. On shearing, magmatism and regional deformation in Neoarchean granite-greenstone systems: Insights from the Yilgarn Craton. *Journal of Structural Geology,* 67, Part B**,** 253-267.

Appendices:

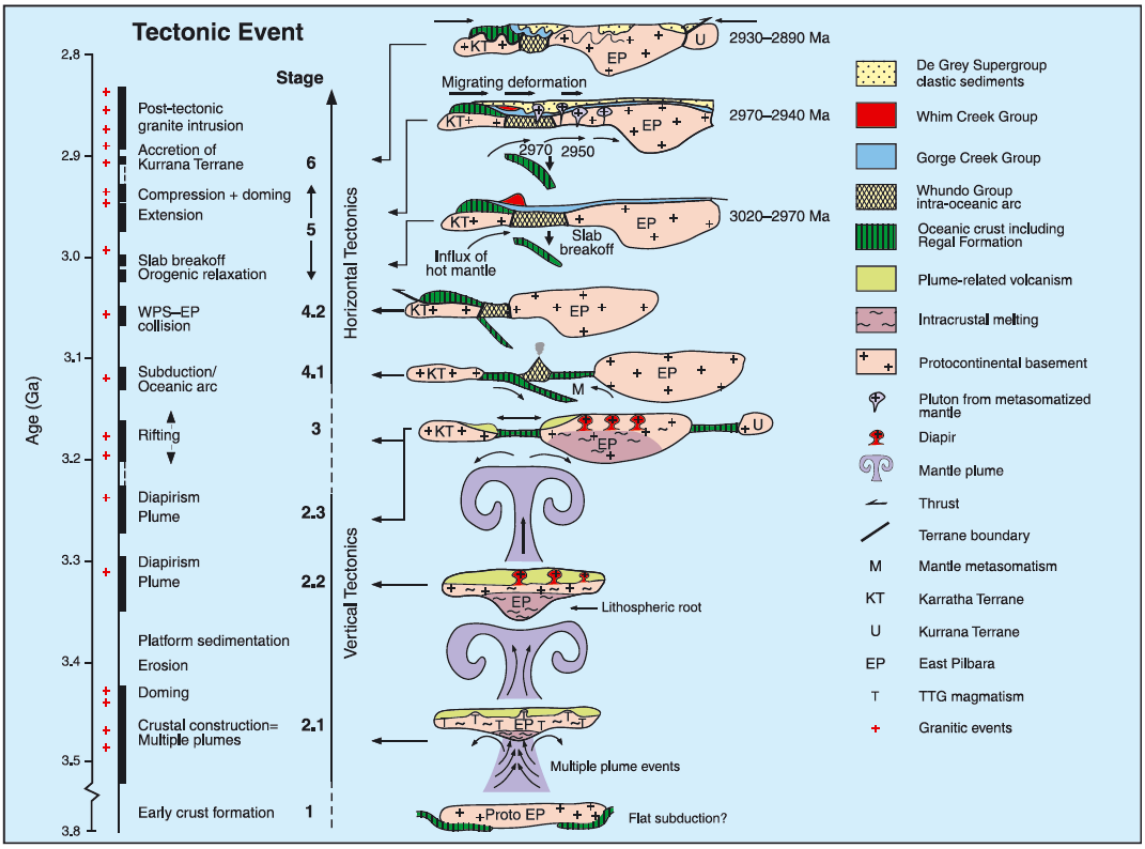
Appendix 1: Models incorporating vertical tectonics



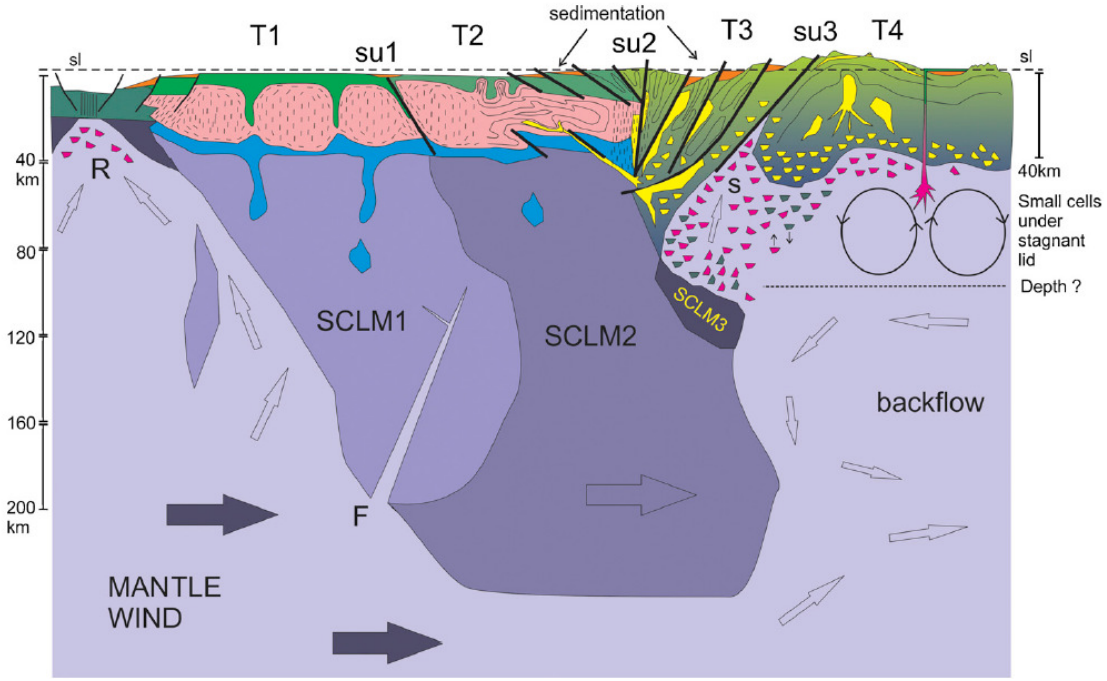
1a: Model of partial convective overturn in East Pilbara Craton (Collins et al., 1998).



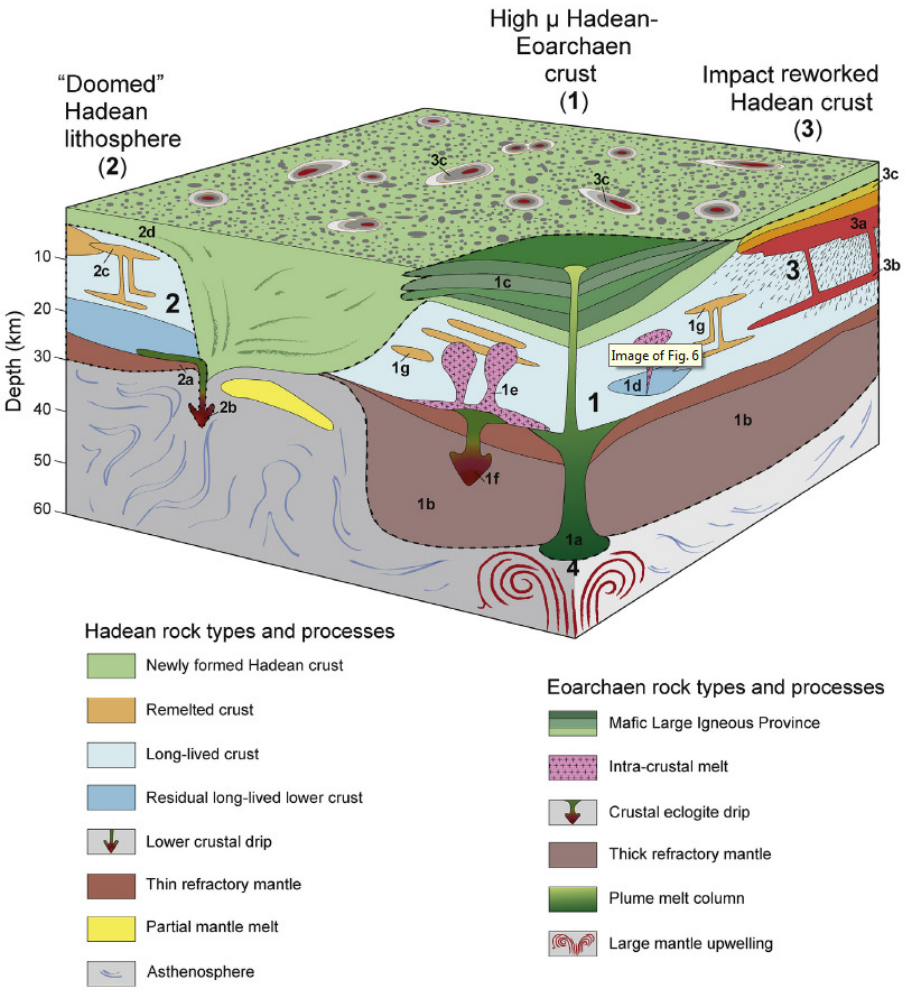
1b: Model of partial convective overturn (Bédard, 2006).



1c: Tectonic evolution of the Pilbara Craton involving partial convective overturn in East Pilbara Craton, suggesting a Mesoarchean age for the onset of horizontal tectonics (Van Kranendonk et al., 2007b).



1d: Model showing a number of terranes that have evolved and amalgamated without subduction (Bédard et al., 2013).



1e: Model of lithospheric processes operating across the Hadean-Archean boundary (Kamber, 2015).

Appendix 2: Table of samples.

Sample	HoleID	Target	From (m)	To (m)	Northing (Collar)	Easting (Collar)	Assemblage	Rock classification
TSUPB001	TA05227DD	C6.7	81.5	82.5	2283024	446683	Tasiast	Greywacke
TSUPB002	TA05245DD	C6.7	340.5	341.2	2282615	446498	Aouéouat	Quartz-diorite
TSUPB003	TA05283DD	C6.7	20.2	20.5	2283218	446250	Tasiast	Greywacke
TSUPB004	TA05248DD	C6.12	296.8	298.3	2273000	451100	TTG	Porphyritic granodiorite
TSUPB005	TA05291DD	TFW	81.7	82.6	2271806	445290	Tasiast	Greywacke
TSUPB006	TA05293DD	TFW	277.0	277.8	2271809	444101	Pegmatite	Pegmatite
TSUPB007	TA05090RD	WB	548.5	548.8	2271261	447722	Aouéouat	Felsite
TSUPB008	TA05090RD	WB	618.6	618.9	2271261	447722	TTG	Granodiorite
TSUPB009	TA05090RD	WB	656.8	657.0	2271261	447722	Aouéouat	Diorite
TSUPB010	TA05155ARD	WB-HW	1235.8	1236.0	2270261	448589	Tasiast	Fine grained sediment
TSUPB011	TA05190DD	WB-FW	516.0	516.3	2269911	448695	Tasiast	Greywacke
TSUPB012	Field sample	n/a	n/a	n/a	n/a	n/a	TTG	Porphyritic tonalite
TSUPB013	TA15170DD	C6.7	95.1	96.1	2282366	446701	Aouéouat	Quartz-diorite
TSUPB014	TA15094DD	C6.7	315.0	315.3	2283015	446900	Aouéouat	Amphibolite
TSUPB015	TA05261DD	C6.7	129.0	132.0	2282415	446500	Quartz vein	Quartz-carbonate vein
TSUPB016	TA05262DD	C6.12	442.4	442.7	2273596	450250	Quartz vein	Quartz-carbonate vein
TSUPB017	TA05248DD	C6.12	329.6	329.8	2273000	451100	Quartz vein	Quartz-carbonate vein
TSUPB018	TA05255DD	C6.7	300.8	301.2	2282815	446500	Aouéouat	Amphibolite
TSUPB019	TA05255DD	C6.7	202.9	203.9	2282815	446500	Aouéouat	Quartz-diorite
TSUPB020	TA05136RD	WB-HW	218.7	219.2	2271421	447755	Tasiast	Greywacke
TSUPB021	TA05136RD	WB-FW	792.0	793.0	2271421	447755	Tasiast	Greywacke
TSUPB022	TA05190DD	WB	268.1	268.6	2269911	448695	Aouéouat	Amphibolite
TSUPB023	TA15056DD	C6.2	213.0	214.1	2277774	439819	Temeimichat	Ultramafic schist
TSUPB024	TA15056DD	C6.2	117.7	118.2	2277774	439819	Temeimichat	Amphibolite
TSUPB025	Field sample	C6.7	n/a	n/a	2282432	446622	Quartz vein	Quartz-carbonate vein
TSUPB026	Field sample	Fennec	n/a	n/a	2284695	445849	Quartz vein	Quartz-carbonate vein
TSUPB027	Field sample	Fennec	n/a	n/a	2284698	445930	Quartz vein	Quartz-carbonate vein
TSUPB028	Field sample	n/a	n/a	n/a	2286190	463558	TTG	Tonalite
TSUPB029	Field sample	n/a	n/a	n/a	2297645	438741	TTG	Granodiorite
TSUPB030	TA05283DD	C6.7	26.1	26.5	2283218	446250	TTG	Granodiorite clasts
TSUPB031	TA17106DD	WB	86.35 & 87.0	86.45 & 87.25	2271411	447000	Quartz vein	Quartz-carbonate vein
TSUPB032	TA17113DD	WB	35.4	37.0	2271525	446927	Quartz vein	Quartz-carbonate vein
TSUPB033	TA05249DD	C6.12	250.0	250.3	2272800	450900	Temeimichat	Amphibolite
TSUPB034	TA05249DD	C6.12	338.7	339.0	2272800	450900	Temeimichat	Ultramafic schist
TSUPB035	TA05254DD	C6.12	329.6	329.9	2273000	450700	Temeimichat	Amphibolite
TSUPB036	TA05254DD	C6.12	415.9	416.2	2273000	450700	Temeimichat	Ultramafic schist
TSUPB037	TA05268DD	C6.12	164.1	164.4	2271200	451300	Temeimichat	Ultramafic schist
TSUPB038	TA05268DD	C6.12	321.0	321.3	2271200	451300	Temeimichat	Amphibolite
TSUPB039	TA10771RD	N2E	199.0	119.3	2298300	446606	Temeimichat	Amphibolite
TSUPB040	TA16013DD	N2E	222.6	222.9	2297200	446209	Temeimichat	Amphibolite
TSUPB041	TA16013DD	N2E	160.5	160.8	2297200	446209	Temeimichat	Ultramafic schist
TSUPB042	TA12678DD	N2E	396.0	396.3	2298001	446304	Temeimichat	Ultramafic schist
TSUPB043	TA13215RD	N2E	184.0	184.3	2298197	446607	Temeimichat	Amphibolite
TSUPB044	TA12084RD	Tamaya	137.3	137.6	2259599	450328	Aouéouat	Amphibolite
TSUPB045	TA17116DD	Tamaya	66.6	66.9	2259474	450219	Aouéouat	Amphibolite
TSUPB046	TA17121DD	Tamaya	54.3	54.6	2259074	450264	Aouéouat	Amphibolite
TSUPB047	TA17131DD	Tamaya	92.0	92.3	2259200	450295	Aouéouat	Quartz-amphibolite
TSUPB048	TA17148DD	Tamaya	72.0	72.3	2259000	450300	Aouéouat	Quartz-amphibolite
FZ-12-01	Field sample	Fennec	n/a	n/a	2285005	445599	Tasiast	Banded iron formation
FZ-12-02	TA05192DD	Piment	98.7	98.8	2274325	446919	Tasiast	Banded iron formation

Appendix 3: Instructions for using the rock crushing and mineral separation equipment at the Department of Geology, Trinity College Dublin.

Instructions for using rock crushing and mineral separation facilities at Trinity College Dublin

Below are instructions for using the rock crushing and mineral separation facilities at Trinity College Dublin. Note that these are general instructions, and each individual user may develop certain methods to suit their own needs. These instructions are not an alternative to being trained on how to use the machines by one of the responsible staff members (David Chew, Quentin Crowley, Robbie Goodhue, Neil Kearney) which must be completed before using any piece of equipment; however, they provide a useful reference for users post-training.

Cleaning the machinery and all associated equipment and rooms is extremely important. If you are not concerned with the contamination of your own samples then that is your choice and you can clean appropriately during your time using the facilities, however all machines and equipment must be thoroughly cleaned before being left for the next user.

Any issues with faulty or damaged equipment, or the cleanliness of the facilities must be brought up with Neil Kearney.

All users must sign the sign in sheet before using the facilities.

Relevant safety equipment must be worn for all facilities.

Rock Splitter:

Safety equipment: Ear protectors, safety glasses.

1) Check the rock splitter is clean. Place your sample centred on the lower blade. Check the upper blade is centred. Use the pump to raise the plate, and when near the top move your sample to where you want it split and raise the plate one final bit until your sample is held in place between the two blades.

2) Close the lid. Continue to use the pump, and eventually you will feel the hydraulics taking over and the machine easily pumps without resistance. Continue to pump until you hear the rock fully split.

3) Release the pressure and lower the plate by pushing the black lever beside the pump to the right. Carefully raise the lid and collect your sample.

4) Repeat until your sample is split as required.

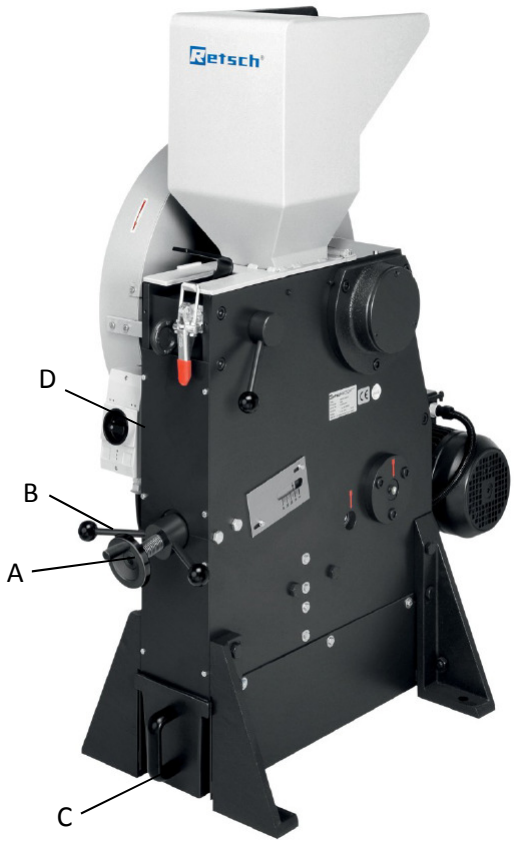
5) Clean the rock splitter.

Cleaning the rock splitter:

1) Use a small brush to clean the plate, the blades, and lift the plate brushing beneath and behind it – it's heavy so be careful not to drop it. Also brush around the base inside the splitter clearing it of

any rock dust or chips. Brush everything onto the floor, and use a large brush and pan to clean this up when finished.

Retsch Jaw Crusher:



Safety equipment: Ear protectors, safety glasses, dust mask.

1) Sign in on the sheet outside the rock crushing room.

2) Check the machine is turned off at the wall and at the machine.

3) Check the Jaw Crusher and worktop are clean. If dirty in any way follow the cleaning instructions below, and if unreasonably dirty report this to either the previous user, or to Neil Kearney.

4) Adjust the gap between the plates by turning the adjustor wheel (A) at the front of the machine and monitoring the size of the gap visually by looking into the crusher, and also on the number dial to the side of the machine. ~20 on the dial is usually a good place to start, however note that this can be reset manually so do not rely solely on this before your first run. Secure the plates in place using the locking nut (B).

5) Clamp the hopper in place, and place the collection drawer (C) in its slot.

6) Turn on the air extraction fan, and adjust it to face the crusher as close as possible.

7) Turn the machine on at the wall, and start it using the switch on the crusher.

8) Drop some of your split rocks into the funnel; you will hear when they are crushed. After a few are crushed, shake the drawer to level out what has been processed. If you have a large sample to get through, you will need to empty the drawer at least once into a sample bag before continuing with your crushing.

   Note: If one of your rocks does jam, turn off the machine and open the funnel. Remove it by hand if possible, if not then you will have to move the plates apart to loosen it. When removed do not try to crush it again, it will need to be split first using the Rock Splitter before the smaller pieces can be processed.

   Note: If your sample volume is small, you will be better off putting the sample between the plates without using the funnel. Then clamp the funnel in place before turning the machine on. This will reduce the volume of sample lost, and also make cleaning the funnel afterwards easier.

9) Turn off the crusher, and leave to settle for a minute before emptying your crushed fraction into a sample bag. Open the funnel and check that no large rocks have jammed. Adjust the plates closer together, maybe to about 5 on the dial (this is both user and sample dependant), tighten, close the funnel and replace the drawer.

10) Turn on the machine, and tip some of your crushed fraction into the funnel. Do not fill the crushing chamber more than two-thirds full (i.e. don't tip in more than about a quarter of a standard sample bag at a time), or debris may be forced behind the moving plate, damaging the crusher. When you hear that this is crushed, repeat until finished. Remember every so often to shake the drawer, and to empty it into a bag if it is getting full.

11) Repeat steps 8 and 9, but adjust the plates closer together. Make sure you can still see some daylight between the plates before tightening. If they are too close your sample will struggle to get through and you will shred some of the tungsten carbide plates themselves into your sample.

12) When your entire sample has been crushed and bagged, make sure the bags are labelled, and then clean the Jaw Crusher.

Cleaning the jaw crusher:

1) Clear away your sample, and turn off the Jaw Crusher at the wall. Keep the air extraction fan on.

2) Open the funnel and vacuum inside as much as possible, around the outside of the funnel, and around the top of the opening into the plates.

3) Remove the front plate of the crusher. To do this you will need to hold the handle with your left hand while removing the pin with your right. **Be careful as it is extremely heavy**. When the pin is removed you will be able to lift the plate and rest it on the machine, before then using both hands to remove it fully and sit on the side bench. You will have been shown how to do this during your training. If in doubt ask someone to carry out this step for you.

4) Vacuum any visible surface inside the machine, the removed plate, and the drawer. Places easily missed are: 1) the screw above where the drawer sits, 2) the lip on which the drawer sits, 3) the gap beneath the fixed plate and 4) the two overflow areas, one front and one back. Finally vacuum the outside surfaces, and the floor.

5) Turn on the air gun, and when it has built up enough pressure, use it to blow clean inside the funnel, on top of, down the sides of, and below the fixed plate, the screw above the drawer and the lips on which the drawer sits.

6) Now use alcohol and paper towel to clean every inside surface from top to bottom. You will need to wipe every surface at least twice, and if still dirty wipe again until clean. Remember to also clean the removable plate and the drawer.

   *** Do not use water on the machine at any time, as it will cause it to rust and will make the next sample stick inside the crushing chamber***

7) Replace the removable plate, clean the worktop, and leave the drawer face down on the worktop. Place some paper towel over the gap between the blades to prevent dust from settling in the machine.
8) Turn off the extractor fan. If it is your final sample, sweep or vacuum the floor, and give it a mop before leaving, as well as vacuum any other flat surface in the room which has gathered dust.

Sieve:

Safety equipment: Ear protectors, safety glasses, dust mask.

1) Clean the worktop, then remove the 3 parts of the sieve from the machine and give a wipe with alcohol. Also wipe down the surface of the machine, and the clamps. Check there are no grains from previous samples in stuck in the sieve gauze. If there are then remove them using the wire brush or the awl, and let the person who used it before you know they are not cleaning it properly. Be careful not to apply too much force to the sieve mesh as you may rip it.

2) Centre the collecting tray of the sieve on the machine and place the 300µm sieve on top. Tip some of your sample into the 300µm sieve (usually ~¼ of a sample bag will suffice).

3) Put the lid on top of the sieve (currently the lid is the 150µm sieve). Clamp the lid on, making sure only the rubber from the clamp is making contact with the lid, and tighten.

4) Aim the extraction fan towards the sieve and turn on.

5) Turn on the machine by turning the dial. ~5 minutes should be enough, but it depends on the sample size you have put in, so give it a visual check to judge whether or not it is fully separated.

6) Transfer the < 300µm fraction into a labelled bag, and the < 300µm fraction into a labelled bag.

7) Repeat until your entire sample has been sieved.

Cleaning the sieve:

1) Vacuum the sieves and collecting tray, the machine, the clamp and the bench.

2) Use the wire brush to brush the underside of the sieve to try and remove as many grains as possible from the gauze.

3) Use the awl to individually remove any grains that have remained in the sieve.

4) Use alcohol to clean the sieves, the machine and the clamps, wiping at least twice, or until clean. Note the rubber will always appear dirty even when clean.

5) Return the sieves when finished onto the machine.

Gemini Mineral Separation Table:

Safety equipment: Ear protectors, dust mask.

Unattached equipment:
1 x Funnel
1 x Chute
2 x Large Tubs
3 x Small Tubs

1) Sign in on the sheet outside the room.

2) Check that the middle tube is in the case (as it drips), and open the safety valve to the water supply. The safety valve is located directly through the wall from the socket the separation table is connected to in the wet lab. It is the red lever in the corner above the sink, and in line with the fire blanket. Horizontal is off, and vertical is on.

3) Rinse the 5 tubs in the sink, and wipe the funnel and chute with alcohol. Check the tubes are in the cases then run the water on the table for a minute giving it a wipe without the tubs in place. Check the base of the tubes and also the top of the cases which hold them have been wiped clean of any sediment.

4) Place the tubs in their cases and the tubes in their respective tubs. Hook the chute into place on its holder, and push the funnel fully down through its slot.

5) Fully open the water supply to the table by opening the valve connected to the pipe. Switch on the table at the wall and start it by pressing the green button. Start the feeder by switching it on at the wall, the back of the power box, and turning the dial to roughly 50.

6) Loosen the rock powder in the bag by shaking it then pour into the funnel, making sure it slides down the inside of the funnel like a landslide. This will help to prevent it caking together and blocking. Don't put too much in at once, roughly until the top of the 'landslide' is about 10cm from the base of the funnel. If your sample cakes and blocks the funnel repeatedly, consider washing it in a gold pan first to remove the fines (note the sample will then have to be dried afterwards before you can try it on the shaking table again).

7) Adjust the dial until there is a steady flow of the sample onto the table. It's not possible to be perfect here, as the flow rate will change. Each sample will also be different from one another depending on its composition. It is best to judge the flow by looking at the table, if far too much sediment is being forced over the channels into the first tube it is probably too fast, and if there is only a narrow stream of sediment being forced into the first tube it is probably too slow. When happy enough with the flow it can be left to run by itself.

8) Check after 10 or 15 minutes to see how it is running, and that the funnel has not blocked. If blocked, tap the funnel until it falls through. If the sample has nearly or completely run through top it up. It is usually best to top up before it has run through as this will keep the same flow rate

and reduce the chance of an entire new batch blocking. It can take longer for a sample to run through depending on your flow rate, so judge how long it is taking and return to check accordingly. Also check for any major leakage on each return. There is a high chance of some water being on the floor when you return. Do not worry about this; (unless it is extreme, in which case, stop the feeder first before stopping the table and the water and solving the leak) mop it up each time to stop it spreading too much. 3-4 mop-loads are not uncommon.

9) When your final batch has run through, use the end of a spoon to tap the funnel and chute to release any remaining sample. Scrape through any sample that has gathered in the funnel attached to the table. Leave the table running for a minute or so after this. You can then stop the table, and after another minute or so stop the water flow. Turn off the water at the safety valve and turn off the feeder and table at the wall. Leave the sediment in the tubs for a few minutes to settle. (This time can be used to clean the funnel and chute as described in step 3 below).

10) Take 2 clean tubs from above the oven outside the room, and give them a wipe down with alcohol. Label them with your sample code and 'H' or 'L' for your heavies and lights.

11) Without disturbing the sediment too much, take one of the large gray tubs of light minerals from its case, and tip most of the water down the sink. Use a small amount of water to swirl the sample into suspension and tip into its labelled tub. This will have to be repeated a few times to get all of the sample transferred. If the tub fills with water, leave to settle while doing the same with the white tubs of heavy minerals. Once settled tip any water down the sink, and when completed place the tubs in the oven outside the room at 60 - 80°C (which should already be pre-set). If you have a large sample you will need to use more than two tubs.

12) The table can now be cleaned.

Cleaning the mineral separation table:

1) Clean the worktop using a wet paper towel.

2) Rinse out the 5 tubs and give a wipe with paper towel until clean of any sediment. No need to dry these.

3) Rinse the funnel and chute in the sink using paper towel. Dry completely with paper towel and then give both a clean with alcohol before sitting them on the worktop.

4) Replace the 5 tubes in their cases, and turn on the water at the safety valve and then the table. Work from the top to the bottom of the table, giving everything at least 2 wipes with wet and then dry paper towel. Generally in the order: Feeder, funnel (inside and outside), supporting beams (painted green), table and water valves, tubes, casing. While doing this have the table on and running so any sediment is deposited in the cases. When cleaned the tubs can be placed on the table to drain, and the water safety valve turned off.

5) If it is your final sample you have just run, give the electricity casing (white plastic ledge running around the room) a clean with wet and dry paper towel, as well as the paper towel holder and any other surface that has gathered dust.

6) Mop the floor.

Bagging the sample:

1) The samples will generally dry out in the oven overnight. If particularly large then it could take several days.

2) When dry turn off the oven and transfer the samples into labelled bags.

3) Clean out the tubs with water, dry them, and then wipe with alcohol also removing your sample code.

Frantz Magnetic Separator:

1) Assemble the feeder, chute and collector (the method of this will have been shown during training).

2) Before moving the feeder into place, angle the magnetic separator. The downward slope is adjusted using the screw behind the machine, suggested to be at an angle of 20°. The tilt of the chute is adjusted using the wheel to the right of the machine, suggested to be 10°. The angles you set will depend on what you are separating, with the above angles only suggestions.

3) On a separate table (not metal), lay out an A4 piece of paper. On this lay out an A5 piece of paper with a small fold on one of the long edges. Use a spoon to spread out some of your heavy mineral separate on the A5 piece of paper. Turn a small sample bag inside out, and place it over the neodymium magnet. Run this over your sample without touching it to remove the most magnetic minerals from it. This will help to prevent these minerals from blocking the magnetic separator. Lay this on the A4 piece of paper, the magnetic minerals will stay on the sample bag, held by the magnetic force.

4) Turn on the magnetic separator, and set it to run at 0.5 Amps. Using the A5 piece of paper, which now has your sample on it, pour your sample into the funnel, being careful not to overflow. Adjust the rate of the feeder until you are happy that it is processing your sample fast enough, but is able to process everything before the split in the chute.

5) While this is running, prepare your next batch using the neodymium magnet on the A5 paper.

6) Note here, that occasionally the magnetic separator can block if there is a large volume of magnetic minerals present. If you see this happening, turn off the machine. Move the collection tubs temporarily so that the magnetic one collects from both chutes. Set the magnetic separator to 0 Amps and run it for a few seconds. All of the blocked magnetic minerals will flow into your magnetic fraction. Replace the tubs and continue as normal at 0.5 Amps.

7) This can be continued until your sample is complete. You will need to empty the processed sample into labelled sample bags (M@0.5A and NM@0.5A) every so often so prevent them from overflowing. You will notice that the more magnetic the fraction, the darker it will be. When you have used the neodymium magnet for the last of your sample, you can carefully, and above paper, turn the sample bag inside out while still in contact with the magnet to collect all of this fraction in that sample bag. Note that if the sample is very magnetic, this bag may need to be replaced a few times due to the volume of magnetic minerals coating it.

8) Be aware that the electromagnet can get very hot, especially at higher currents. This is a potential fire risk. **The magnetic separator must never be left running unattended overnight**. Check on it roughly every hour while it is running.

9) When complete, set the magnetic separator to 1.0 Amps. Chop a small corner off of the sample bag which holds your non-magnetic fraction from 0.5 Amps, and either pour from this directly into the funnel, or onto the A5 paper and then into the funnel. As above, the processed sample will need to be bagged at regular intervals to prevent overflow (M@1.0A and NM@1.0A).

10) When complete, bag and label your sample, and clean the machine. Note 0.5 and 1.0 Amps are only suggestions, and depending what mineral you are separating and other factors will result in you choosing different cut-offs.

Cleaning the Frantz magnetic separator:

1) Remove all of the components of the machine. Blow clean all of the small components using compressed air one at a time and place them in the component tub when clean. After all of the small components have been cleaned, place the lid on the tub

*** Note never use water on the magnetic separator or any of its components***

2) Blow clean the chute and its cover, and wipe with dry paper towel.

3) Blow clean the entire machine from top to bottom.

4) Wipe the metal table, and the table you used for your sample with a damp cloth and then dry them.

5) If this was your final sample, leave the components in the tub on the table ready for the next user, otherwise re-assemble the machine and run your next sample.

Heavy Liquid Separation:

Safety equipment: Gloves, safety glasses, lab coat.

1) Set up the separating funnel in the clamp stand, with two funnels below held above two beakers, and the valve in place (note two samples can be set up and run at once if needed). Place filter paper in the two funnels.

2) If your target mineral has density >3.3 (e.g., zircon), select the density 3.3 heavy liquid (methylene iodide, MI) from the cupboard below the fume hood. If targeting a mineral <3.3 (e.g., apatite), then select the density 2.7 MI. Always check the density of the 2.7 MI before use, using the large measuring cylinder and the hydrometer. If density too low, add 3.3 MI as necessary; if density too high, dilute with acetone as necessary.

3) With the separating funnel placed above one of the funnels with filter paper, pour heavy liquid into the separatory funnel making sure the valve is closed. Do not use more MI than you need for the size of the sample you are separating.

4) Set the bottle of MI to the side with a funnel and filter paper in it.

5) Pour your sample into the separating funnel and carefully swirl until all of your sample is in suspension. Leave to settle.

6) When settled, swirl your sample again until it is all in suspension. Repeat this for at least a third time, more if it is a large sample.

7) When settled for the final time, open the valve allowing the heavy separate and MI to flow into the filter paper. Close the valve before any of the light fraction reaches the valve.

8) Move the separating funnel over the second funnel, and release the light fraction into the filter paper. Rinse the separatory funnel with acetone until all of your sample has passed through.

9) Before using any acetone on the heavy fraction, you can replace the pure undiluted MI from the beaker into the MI bottle passing it through filter paper. Do not pour any MI that has been mixed with acetone back into the bottle.

10) Rinse both the heavy and light fractions with acetone until it appears that only acetone is passing through the filter paper.

11) Pour all of the acetone, and any MI/acetone mix into the large salvage bottles to the side (the acetone will evaporate and the MI can be recovered from these at a later date).

12) If only running one or two samples, these can be left in the funnels to dry overnight, otherwise place the filter paper with samples on a labelled piece of paper or foil in the fume cupboard. If only a small volume of sample is contained in the filter paper, use a paper-clip to seal this to avoid any chance of losing your mineral separates.

13) Clean the equipment, and return to collect your samples the following morning.

Cleaning the heavy liquid equipment:

1) Any piece of equipment that has been used must be rinsed with acetone (to recover any MI) in the fume cupboard, allowing the acetone to collect in a beaker. All of this acetone should then be poured into the large MI/acetone salvage bottles to the side.

2) Once rinsed with acetone, and dry, the equipment (separatory funnels, valves, funnels, beakers) should be cleaned with warm water in the sink, and dried with paper towel. The separatory funnels can be left in the fume cupboard to dry overnight, as can any other wet equipment.

3) Wipe down the fume cupboard, and make sure any samples you leave to dry are clearly labelled.

Retsch Planetary Ball Mill:

Safety equipment: Safety glasses.

Unattached equipment:
1 x case
1 x lid
6 x balls
1 x large rubber washer

1) Give everything a wipe using alcohol and paper towel to check they are clean. If particularly dirty follow the cleaning instructions below, and let the person who used it before you know they are not cleaning it properly.

2) Place a maximum of 5 heaped spatulas (or equivalent) of your whole rock sample into the case with the 6 balls and place the lid.

3) Place the case in the machine and clamp in place. To clamp, lift the red stopper and turn the handle with the 3 legs hooked in. Make sure the 3 legs are hooked in, and the clamp is on the centre of the case. When tight let go of the red stopper, and tighten until it locks in place. If there is little to no resistance then raise the red stopper and tighten some more.

4) Close the lid and set the mill to run at 500 rpm for 4 minutes (note that this time can be set to longer depending on the sample, and how well it is milling). Turn the knob to move up or down an option or value, and press to select. Press the start button to begin the milling.

5) If you hear a loud banging when the machine has started up, stop it and tighten the clamp, checking it is centred on the case, then restart.

6) When the machine has finished, remove the clamp by raising the red stopper and un-tightening. Take the case back to the bench, and remove the balls using the spatula. Depending on the hardness of the minerals, there will be a few small rock chips left. These cannot be discarded as this will most likely bias your sample. These should be removed using a spatula and broken down using a mortar and pestle. Transfer the powder to a sample bag and carefully feel for any chips that were missed, and remove them to be broken down in the same way.

7) A second load of about 5 spatulas of the whole rock sample can then be processed for 4 minutes along with the broken down chips. If there were a lot of chips left from the first load use slightly less whole rock in the second load. There should be very few if any chips left the second time. If there are, check to see if they are heterogeneous rock chips or homogeneous looking minerals. If only a couple of heterogeneous rock chips they can be discarded. If there are a number of them, or they are homogeneous minerals then use the mortar and pestle to crush them, and mill them for 2 minutes with only one spatula of whole rock sample.

Cleaning the ball mill:

1) Use something with a point, but not sharp (so as not to cause any damage) to remove the rubber washer from the lid. There is a small gap in the lid next to the washer for this purpose.

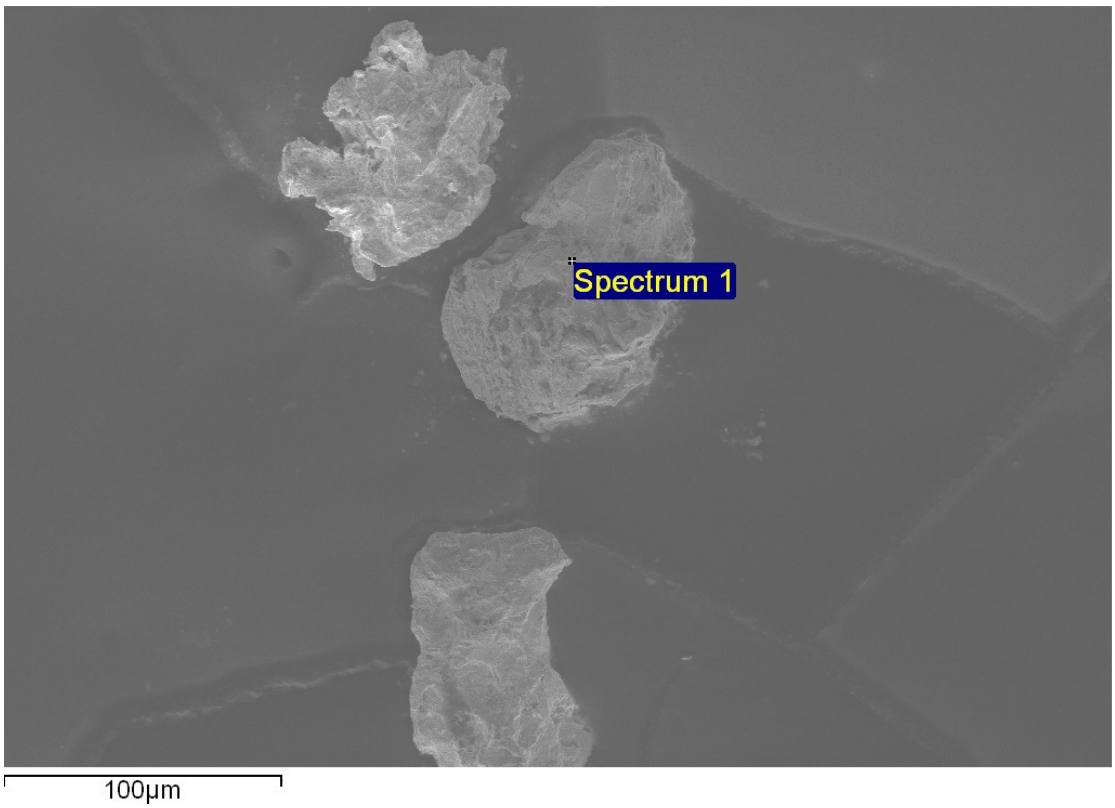
2) Run everything under a cold tap, rubbing off any powder with your fingers or wet paper towel, and sit them on a clean paper towel. **Note this step must be immediately followed by steps 3 and 4.**

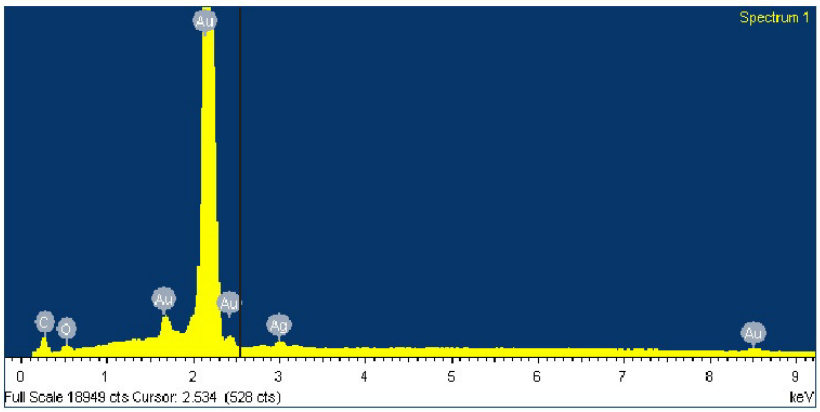
3) Clean the area of the bench where you were working before and place a dry paper towel here. Dry all of the parts, placing them on the clean paper towel when dry.

4) Use alcohol to clean all of the parts once more, and then replace the rubber washer. **This must be done immediately following steps 2 and 3 to prevent corrosion. Under no circumstances can any components be left wet.**

5) Note that clay-rich samples may require you to add sand (rich in quartz) to the mill after steps 1-4 to completely clean the mill. For this step, add the 6 balls, an equivalent heap of sand to your sample and mill for 30 seconds. Remaining clays should be liberated by the quartz. Repeat cleaning steps 1 through 4 after milling the sand.

Appendix 4: Energy-dispersive X-ray spectroscopy (EDS) spectra of gold separated from TSUPB027.





Appendix 5: U-Pb zircon data table.

		Ratios								Age (Ma)						
Analysis	U ppm	Th/U	$^{207}Pb/^{235}U$	Err 2SE abs	$^{206}Pb/^{238}U$	Err 2SE abs	Rho	$^{207}Pb/^{206}Pb$	Err 2SE abs	$^{207}Pb/^{235}U$	Err 2SE abs	$^{206}Pb/^{238}U$	Err 2SE abs	$^{207}Pb/^{206}Pb$	Err 2SE abs	% Disc
Plešovice_1	898	0.10	0.41	0.11	0.0526	0.0068	0.21	0.0568	0.0033	301.1	110.0	296.6	59.0	282.0	22.0	5.5
Plešovice_2	469	0.09	0.39	0.07	0.0530	0.0058	0.24	0.0537	0.0022	309.6	380.0	296.8	52.0	379.0	43.0	7.7
Plešovice_3	992	0.11	0.39	0.11	0.0530	0.0068	0.21	0.0526	0.0033	298.8	110.0	297.5	61.0	301.0	24.0	5.1
Plešovice_4	699	0.09	0.39	0.11	0.0531	0.0068	0.31	0.0535	0.0033	322.7	420.0	298.2	53.0	399.0	25.0	4.7
Plešovice_5	787	0.10	0.39	0.11	0.0532	0.0068	0.16	0.0528	0.0033	305.9	110.0	304.0	61.0	354.0	30.0	4.9
Plešovice_6	995	0.10	0.39	0.07	0.0533	0.0049	0.24	0.0514	0.0023	359	100.0	305.9	62.0	720.0	120.0	5.9
Plešovice_7	566	0.10	0.39	0.07	0.0534	0.0059	0.19	0.0516	0.0020	311.8	410.0	308.3	56.0	422.0	22.0	7.3
Plešovice_8	578	0.09	0.39	0.07	0.0534	0.0059	0.19	0.0532	0.0022	357.9	530.0	310.5	56.0	347.0	22.0	7.2
Plešovice_9	371	0.08	0.39	0.01	0.0535	0.0058	0.04	0.0535	0.0023	289.6	210.0	322.8	53.0	58.0	12.0	7.3
Plešovice_10	418	0.09	0.40	0.01	0.0535	0.0058	0.27	0.0544	0.0022	348.1	38.0	328.6	16.0	482.0	21.0	6.9
Plešovice_11	1038	0.11	0.40	0.11	0.0536	0.0068	0.21	0.0538	0.0034	329.9	34.0	329.6	19.0	336.0	27.0	5.7
Plešovice_12	577	0.09	0.40	0.12	0.0536	0.0069	0.07	0.0537	0.0033	336.6	62.0	329.8	12.0	390.0	18.0	4.6
Plešovice_13	577	0.09	0.39	0.07	0.0537	0.0059	0.18	0.0537	0.0022	327.6	40.0	330.3	16.0	310.0	30.0	7.4
Plešovice_14	451	0.09	0.39	0.07	0.0537	0.0058	0.27	0.0524	0.0022	333.5	40.0	330.5	16.0	347.0	24.0	7.5
Plešovice_15	878	0.09	0.40	0.08	0.0537	0.0049	0.09	0.0533	0.0023	350.3	82.0	330.6	42.0	500.0	34.0	5.5
Plešovice_16	592	0.09	0.40	0.08	0.0537	0.0049	0.41	0.0536	0.0023	327.0	40.0	331.3	16.0	300.0	21.0	4.9
Plešovice_17	430	0.09	0.39	0.01	0.0537	0.0058	0.10	0.0534	0.0021	329.9	40.0	331.3	16.0	322.0	21.0	6.9
Plešovice_18	478	0.08	0.41	0.07	0.0537	0.0059	0.10	0.0537	0.0025	325.3	39.0	331.5	16.0	269.0	19.0	8.5
Plešovice_19	566	0.09	0.42	0.12	0.0537	0.0069	0.37	0.0550	0.0033	341.6	250.0	332.4	53.0	381.0	14.0	5.1
Plešovice_20	590	0.09	0.41	0.13	0.0538	0.0039	0.34	0.0544	0.0037	332.0	49.0	332.7	36.0	382.0	40.0	5.6
Plešovice_21	673	0.10	0.41	0.11	0.0538	0.0069	0.20	0.0553	0.0033	334.1	83.0	332.9	42.0	346.0	34.0	5.2
Plešovice_22	606	0.09	0.40	0.07	0.0538	0.0058	0.26	0.0545	0.0019	336.2	82.0	333.4	42.0	343.0	30.0	5.8
Plešovice_23	725	0.10	0.41	0.11	0.0539	0.0069	0.20	0.0547	0.0034	334.4	230.0	333.7	52.0	327.0	18.0	5.2
Plešovice_24	732	0.11	0.40	0.12	0.0541	0.0068	0.30	0.0535	0.0034	330.8	65.0	333.8	12.0	320.0	24.0	5.9
Plešovice_25	470	0.09	0.41	0.07	0.0541	0.0060	0.16	0.0560	0.0023	332.7	83.0	334.1	42.0	320.0	30.0	7.9
Plešovice_26	799	0.10	0.39	0.07	0.0541	0.0058	0.05	0.0529	0.0021	330.6	54.0	334.7	30.0	296.0	32.0	6.8
Plešovice_27	603	0.09	0.41	0.07	0.0541	0.0059	0.20	0.0544	0.0024	334.9	33.0	334.7	18.0	358.0	31.0	7.9
Plešovice_28	746	0.09	0.40	0.11	0.0542	0.0069	0.08	0.0535	0.0033	329.9	49.0	335.2	36.0	363.0	36.0	4.9
Plešovice_29	717	0.10	0.42	0.08	0.0542	0.0050	0.13	0.0553	0.0025	336.0	46.0	335.3	36.0	363.0	38.0	6.2
Plešovice_30	798	0.10	0.40	0.08	0.0542	0.0049	0.17	0.0542	0.0025	435.3	220.0	335.7	51.0	999.0	27.0	5.9
Plešovice_31	529	0.09	0.39	0.07	0.0542	0.0059	0.13	0.0522	0.0022	330.9	260.0	335.9	55.0	312.0	17.0	7.5
Plešovice_32	547	0.09	0.40	0.07	0.0542	0.0059	0.09	0.0524	0.0024	334.0	10.0	336.0	36.0	378.0	40.0	7.9
Plešovice_33	609	0.09	0.39	0.12	0.0543	0.0069	0.02	0.0533	0.0035	336.5	9.7	336.1	36.0	376.0	41.0	6.4
Plešovice_34	752	0.10	0.40	0.13	0.0543	0.0039	0.11	0.0537	0.0036	342.8	81.0	336.6	42.0	374.0	34.0	5.0
Plešovice_35	522	0.09	0.39	0.07	0.0543	0.0059	0.18	0.0518	0.0019	343.3	85.0	336.6	42.0	378.0	34.0	7.1
Plešovice_36	613	0.09	0.41	0.13	0.0543	0.0038	0.10	0.0544	0.0037	335	34.0	336.9	18.0	326.0	37.0	5.2
Plešovice_37	664	0.10	0.40	0.13	0.0543	0.0039	0.12	0.0540	0.0037	338.9	50.0	337.0	36.0	366.0	34.0	5.6
Plešovice_38	500	0.09	0.40	0.01	0.0544	0.0059	0.16	0.0539	0.0020	334.0	49.0	337.2	35.0	335.0	35.0	6.3
Plešovice_39	633	0.09	0.39	0.07	0.0544	0.0058	0.07	0.0533	0.0021	343.5	54.0	337.3	30.0	402.0	39.0	7.3
Plešovice_40	818	0.11	0.40	0.07	0.0544	0.0058	0.20	0.0531	0.0018	341.3	54.0	337.3	30.0	381.0	33.0	6.0
Plešovice_41	832	0.10	0.40	0.01	0.0544	0.0059	0.10	0.0537	0.0019	331.1	8.8	337.3	36.0	392.0	40.0	5.8
Plešovice_42	571	0.09	0.40	0.07	0.0545	0.0049	0.07	0.0527	0.0023	348.0	48.0	337.3	36.0	425.0	45.0	5.6
Plešovice_43	489	0.09	0.40	0.07	0.0545	0.0060	0.05	0.0535	0.0023	353.2	83.0	337.4	42.0	438.0	34.0	8.0
Plešovice_44	575	0.09	0.40	0.07	0.0545	0.0049	0.02	0.0536	0.0022	349.4	89.0	337.5	24.0	399.0	39.0	4.6
Plešovice_45	480	0.09	0.41	0.13	0.0545	0.0039	0.11	0.0547	0.0037	351.3	80.0	337.9	42.0	439.0	36.0	5.4
Plešovice_46	948	0.11	0.41	0.01	0.0546	0.0059	0.37	0.0546	0.0017	343.9	47.0	337.9	36.0	390.0	35.0	5.1
Plešovice_47	646	0.09	0.41	0.08	0.0547	0.0049	0.24	0.0537	0.0023	343.8	240.0	338.2	51.0	418.0	14.0	5.5
Plešovice_48	717	0.10	0.41	0.12	0.0547	0.0071	0.28	0.0557	0.0034	346.2	82.0	338.3	42.0	382.0	35.0	5.8
Plešovice_49	643	0.12	0.40	0.12	0.0547	0.0038	0.27	0.0528	0.0036	337.0	64.0	339.1	12.0	349.0	24.0	5.2
Plešovice_50	407	0.09	0.38	0.01	0.0547	0.0059	0.34	0.0514	0.0022	342.8	83.0	339.4	42.0	376.0	38.0	7.2
Plešovice_51	674	0.10	0.42	0.13	0.0547	0.0039	0.02	0.0558	0.0037	351.0	50.0	339.5	37.0	472.0	41.0	5.8

		Ratios								Age (Ma)						
Analysis	U ppm	Th/U	$^{207}Pb/^{235}U$	Err 2SE abs	$^{206}Pb/^{238}U$	Err 2SE abs	Rho	$^{207}Pb/^{206}Pb$	Err 2SE abs	$^{207}Pb/^{235}U$	Err 2SE abs	$^{206}Pb/^{238}U$	Err 2SE abs	$^{207}Pb/^{206}Pb$	Err 2SE abs	% Disc
Plešovice_52	580	0.09	0.39	0.08	0.0547	0.0049	0.00	0.0518	0.0025	334.2	47.0	339.5	35.0	344.0	37.0	6.5
Plešovice_53	445	0.09	0.40	0.07	0.0547	0.0058	0.14	0.0539	0.0026	347.0	48.0	339.7	36.0	420.0	46.0	9.1
Plešovice_54	800	0.10	0.42	0.13	0.0548	0.0039	0.18	0.0551	0.0036	343.5	83.0	339.9	42.0	363.0	27.0	5.0
Plešovice_55	693	0.10	0.42	0.12	0.0548	0.0070	0.14	0.0556	0.0036	352.6	53.0	339.9	30.0	419.0	37.0	6.9
Plešovice_56	513	0.09	0.39	0.08	0.0548	0.0050	0.23	0.0520	0.0026	340.5	56.0	340.0	30.0	420.0	40.0	7.4
Plešovice_57	791	0.11	0.39	0.07	0.0548	0.0058	0.25	0.0522	0.0018	334.0	49.0	340.1	36.0	378.0	45.0	6.1
Plešovice_58	518	0.08	0.42	0.12	0.0550	0.0071	0.02	0.0553	0.0035	339.0	52.0	340.5	36.0	404.0	42.0	5.9
Plešovice_59	1010	0.10	0.42	0.13	0.0550	0.0039	0.25	0.0553	0.0036	337.9	83.0	340.6	42.0	366.0	42.0	5.5
Plešovice_60	790	0.10	0.39	0.07	0.0550	0.0058	0.38	0.0524	0.0020	342.8	92.0	340.7	24.0	374.0	35.0	6.8
Plešovice_61	708	0.09	0.41	0.13	0.0550	0.0039	0.25	0.0529	0.0036	333.1	49.0	341.0	36.0	336.0	39.0	4.7
Plešovice_62	527	0.10	0.41	0.13	0.0550	0.0039	0.20	0.0536	0.0038	347.9	87.0	341.1	24.0	368.0	37.0	6.5
Plešovice_63	725	0.11	0.41	0.12	0.0551	0.0038	0.25	0.0541	0.0035	345.5	94.0	341.1	24.0	368.0	35.0	4.4
Plešovice_64	674	0.10	0.40	0.12	0.0551	0.0038	0.23	0.0526	0.0036	337.7	8.8	341.3	36.0	380.0	45.0	5.1
Plešovice_65	635	0.09	0.41	0.08	0.0551	0.0049	0.35	0.0533	0.0022	336.4	48.0	341.3	36.0	378.0	39.0	4.4
Plešovice_66	583	0.09	0.41	0.12	0.0553	0.0071	0.19	0.0533	0.0033	337.3	48.0	341.4	36.0	349.0	33.0	5.1
Plešovice_67	453	0.09	0.40	0.07	0.0553	0.0058	0.02	0.0532	0.0026	342.3	8.1	341.5	36.0	350.0	36.0	8.8
Plešovice_68	947	0.17	0.42	0.12	0.0556	0.0068	0.06	0.0543	0.0032	341.1	53.0	342.0	30.0	341.0	36.0	4.5
Plešovice_69	624	0.09	0.41	0.12	0.0556	0.0070	0.27	0.0539	0.0035	341.0	50.0	342.0	36.0	455.0	38.0	6.4
Plešovice_70	723	0.12	0.41	0.12	0.0558	0.0038	0.12	0.0536	0.0036	343.5	54.0	342.2	30.0	324.0	29.0	5.2
Plešovice_71	898	0.15	0.33	0.28	0.0514	0.0086	0.36	0.0466	0.0110	348.6	91.0	342.3	24.0	379.0	36.0	6.2
Plešovice_72	1748	0.18	0.40	0.34	0.0529	0.0087	0.31	0.0544	0.0130	349.7	6.9	342.6	36.0	379.0	28.0	2.3
Plešovice_73	737	0.14	0.39	0.31	0.0531	0.0084	0.39	0.0530	0.0130	346.0	53.0	343.1	30.0	377.0	34.0	2.1
Plešovice_74	871	0.18	0.54	0.33	0.0535	0.0083	0.17	0.0722	0.0130	350.8	84.0	343.2	43.0	436.0	36.0	15.2
Plešovice_75	693	0.10	0.39	0.35	0.0535	0.0089	0.27	0.0524	0.0130	339.4	90.0	343.2	23.0	316.0	27.0	2.4
Plešovice_76	902	0.10	0.40	0.33	0.0539	0.0084	0.34	0.0552	0.0130	328.0	11.0	343.2	36.0	325.0	41.0	1.9
Plešovice_77	838	0.11	0.41	0.05	0.0523	0.0026	0.86	0.0569	0.0026	358.5	91.0	343.4	24.0	460.0	34.0	3.5
Plešovice_78	792	0.11	0.38	0.05	0.0528	0.0026	0.79	0.0517	0.0026	337.5	53.0	343.5	30.0	344.0	43.0	2.7
Plešovice_79	788	0.11	0.38	0.05	0.0527	0.0026	0.71	0.0521	0.0025	343.0	48.0	343.5	36.0	421.0	40.0	2.2
Plešovice_80	791	0.11	0.39	0.05	0.0526	0.0026	0.72	0.0533	0.0026	354.0	92.0	343.7	24.0	417.0	24.0	2.7
Plešovice_81	816	0.11	0.38	0.05	0.0526	0.0026	0.53	0.0521	0.0027	355.0	84.0	344.0	43.0	456.0	43.0	3.3
Plešovice_82	816	0.11	0.38	0.06	0.0527	0.0026	0.76	0.0528	0.0026	336.0	55.0	344.0	30.0	355.0	45.0	2.7
Plešovice_83	1624	0.14	0.39	0.09	0.0540	0.0019	0.33	0.0535	0.0040	336.6	47.0	344.0	35.0	329.0	31.0	2.7
Plešovice_84	2842	0.23	0.39	0.09	0.0525	0.0019	0.60	0.0545	0.0040	351.3	84.0	344.9	43.0	416.0	41.0	2.6
Plešovice_85	2337	0.17	0.38	0.09	0.0531	0.0019	0.19	0.0529	0.0040	356.5	90.0	344.9	24.0	417.0	33.0	2.8
Plešovice_86	666	0.12	0.38	0.05	0.0525	0.0030	0.51	0.0535	0.0020	337.0	48.0	344.9	36.0	335.0	37.0	2.7
Plešovice_87	458	0.11	0.39	0.05	0.0536	0.0030	0.14	0.0528	0.0023	345.4	91.0	345.1	24.0	333.0	30.0	4.4
Plešovice_88	447	0.11	0.39	0.05	0.0533	0.0030	0.15	0.0536	0.0021	346.0	91.0	345.2	24.0	393.0	43.0	3.5
Plešovice_89	2669	0.12	0.43	0.15	0.0486	0.0100	0.11	0.0638	0.0042	353.1	88.0	345.6	23.0	389.0	24.0	9.4
Plešovice_90	2089	0.12	0.35	0.15	0.0483	0.0098	0.69	0.0533	0.0010	340.3	89.0	345.6	23.0	313.0	28.0	3.1
Plešovice_91	2256	0.11	0.34	0.15	0.0472	0.0099	0.65	0.0524	0.0009	345.8	54.0	346.0	30.0	369.0	26.0	2.6
Plešovice_92	2184	0.11	0.35	0.15	0.0471	0.0096	0.68	0.0517	0.0008	347.1	85.0	347.2	43.0	364.0	32.0	2.6
Plešovice_93	2118	0.10	0.36	0.55	0.0490	0.0091	0.77	0.0552	0.0110	342.0	49.0	347.2	36.0	399.0	43.0	3.0
Plešovice_94	1033	0.09	0.42	0.75	0.0493	0.0091	0.69	0.0536	0.0110	356.7	80.0	348.7	42.0	382.0	26.0	7.7
Plešovice_95	2024	0.11	0.37	0.57	0.0474	0.0087	0.66	0.0551	0.0110	348.2	84.0	349.0	43.0	406.0	34.0	4.8
Plešovice_96	2283	0.12	0.36	0.51	0.0471	0.0084	0.00	0.0542	0.0110	347.6	90.0	350.2	23.0	364.0	31.0	4.7
Temora_1	91	0.32	0.50	0.12	0.0632	0.0068	0.12	0.0558	0.0049	373.0	100.0	364.7	61.0	509.0	63.0	12.7
Temora_2	74	0.35	0.50	0.13	0.0635	0.0039	0.13	0.0559	0.0054	411	380.0	365.3	53.0	570.0	40.0	14.0
Temora_3	147	0.55	0.50	0.12	0.0644	0.0069	0.03	0.0571	0.0042	391	350.0	368.5	51.0	493.0	35.0	10.2
Temora_4	106	0.28	0.48	0.12	0.0646	0.0069	0.09	0.0546	0.0042	360.0	110.0	371.6	60.0	362.0	56.0	9.7
Temora_5	70	0.37	0.48	0.07	0.0650	0.0059	0.04	0.0531	0.0041	439.0	100.0	376.9	58.0	741.0	97.0	13.3
Temora_6	214	0.57	0.49	0.12	0.0650	0.0069	0.24	0.0545	0.0041	458.0	94.0	378.1	60.0	899.0	62.0	8.5
Temora_7	148	0.47	0.54	0.07	0.0651	0.0059	0.33	0.0591	0.0031	421	370.0	378.1	55.0	799.0	44.0	9.5

		Ratios								Age (Ma)						
Analysis	U ppm	Th/U	$^{207}Pb/^{235}U$	Err 2SE abs	$^{206}Pb/^{238}U$	Err 2SE abs	Rho	$^{207}Pb/^{206}Pb$	Err 2SE abs	$^{207}Pb/^{235}U$	Err 2SE abs	$^{206}Pb/^{238}U$	Err 2SE abs	$^{207}Pb/^{206}Pb$	Err 2SE abs	% Disc
Temora_8	117	0.52	0.49	0.08	0.0653	0.0050	0.10	0.0544	0.0042	485	460.0	393.1	55.0	395.0	52.0	13.3
Temora_9	233	0.34	0.50	0.08	0.0653	0.0050	0.00	0.0557	0.0029	406.0	79.0	394.9	41.0	625.0	82.0	8.2
Temora_10	151	0.63	0.55	0.12	0.0655	0.0070	0.08	0.0604	0.0046	411.0	85.0	398.0	25.0	571.0	75.0	11.6
Temora_11	58	0.41	0.49	0.04	0.0656	0.0061	0.18	0.0544	0.0046	414.0	83.0	402.4	42.0	533.0	56.0	14.6
Temora_12	151	0.64	0.51	0.03	0.0655	0.0059	0.19	0.0572	0.0032	403.0	79.0	403.8	42.0	488.0	66.0	10.0
Temora_13	104	0.55	0.46	0.03	0.0654	0.0060	0.03	0.0512	0.0037	412.4	38.0	403.9	16.0	471.0	28.0	12.7
Temora_14	156	0.68	0.50	0.12	0.0656	0.0069	0.05	0.0550	0.0045	396.0	49.0	405.9	36.0	515.0	83.0	10.5
Temora_15	159	0.27	0.48	0.07	0.0659	0.0059	0.05	0.0527	0.0034	398.0	72.0	406.0	42.0	450.0	62.0	11.5
Temora_16	122	0.36	0.51	0.12	0.0660	0.0069	0.02	0.0568	0.0049	436.0	47.0	406.3	36.0	609.0	57.0	12.4
Temora_17	68	0.31	0.52	0.12	0.0659	0.0070	0.06	0.0556	0.0056	408.0	36.0	407.2	16.0	441.0	38.0	15.8
Temora_18	59	0.33	0.54	0.08	0.0661	0.0061	0.08	0.0583	0.0059	405.0	56.0	407.8	30.0	530.0	71.0	18.9
Temora_19	117	0.33	0.48	0.07	0.0660	0.0059	0.19	0.0536	0.0038	415.0	38.0	408.1	16.0	485.0	39.0	12.8
Temora_20	124	0.25	0.55	0.08	0.0661	0.0051	0.42	0.0591	0.0035	413.0	52.0	408.5	30.0	464.0	49.0	10.2
Temora_21	206	0.48	0.50	0.12	0.0662	0.0069	0.01	0.0545	0.0040	444.0	82.0	408.8	42.0	683.0	67.0	9.4
Temora_22	203	0.34	0.50	0.07	0.0662	0.0059	0.96	0.0556	0.0030	398.0	27.0	409.0	37.0	582.0	62.0	8.5
Temora_23	60	0.41	0.51	0.09	0.0662	0.0061	0.18	0.0577	0.0073	420.0	17.0	409.0	36.0	538.0	52.0	17.8
Temora_24	78	0.36	0.50	0.08	0.0663	0.0061	0.24	0.0556	0.0045	383.0	22.0	409.2	36.0	425.0	68.0	14.8
Temora_25	151	0.53	0.53	0.13	0.0663	0.0040	0.32	0.0565	0.0044	416.0	78.0	409.3	42.0	504.0	55.0	9.2
Temora_26	123	0.30	0.50	0.08	0.0663	0.0050	0.02	0.0534	0.0036	393.0	49.0	411.4	36.0	459.0	55.0	10.5
Temora_27	155	0.34	0.53	0.13	0.0664	0.0040	0.08	0.0571	0.0044	428.7	36.0	411.4	16.0	510.0	30.0	10.2
Temora_28	67	0.34	0.54	0.13	0.0665	0.0040	0.24	0.0589	0.0046	417.0	79.0	411.6	42.0	571.0	77.0	11.7
Temora_29	114	0.45	0.51	0.07	0.0665	0.0059	0.13	0.0561	0.0039	420.0	81.0	411.6	42.0	656.0	80.0	12.9
Temora_30	123	0.49	0.53	0.13	0.0665	0.0040	0.08	0.0575	0.0049	441.0	55.0	412.0	37.0	750.0	100.0	12.1
Temora_31	157	0.56	0.50	0.13	0.0665	0.0040	0.05	0.0565	0.0046	393.0	49.0	412.2	36.0	485.0	67.0	10.9
Temora_32	117	0.39	0.50	0.13	0.0665	0.0040	0.02	0.0543	0.0050	441.0	53.0	412.7	31.0	595.0	53.0	12.8
Temora_33	142	0.54	0.49	0.08	0.0666	0.0050	0.29	0.0543	0.0029	412.0	80.0	412.9	42.0	462.0	52.0	7.3
Temora_34	139	0.50	0.49	0.07	0.0666	0.0059	0.10	0.0527	0.0039	412.0	47.0	412.9	35.0	479.0	50.0	13.2
Temora_35	84	0.37	0.50	0.08	0.0666	0.0051	0.05	0.0547	0.0044	422.0	57.0	413.0	37.0	730.0	120.0	13.6
Temora_36	156	0.65	0.50	0.03	0.0666	0.0060	0.00	0.0551	0.0037	411.0	53.0	413.5	37.0	559.0	66.0	13.2
Temora_37	88	0.46	0.50	0.12	0.0667	0.0070	0.27	0.0554	0.0047	425.0	86.0	413.6	24.0	486.0	56.0	12.2
Temora_38	180	0.55	0.52	0.12	0.0666	0.0070	0.01	0.0577	0.0042	422.0	34.0	413.8	19.0	487.0	55.0	10.4
Temora_39	109	0.30	0.51	0.12	0.0668	0.0070	0.20	0.0549	0.0046	408.0	52.0	414.0	30.0	428.0	50.0	11.7
Temora_40	207	0.40	0.53	0.07	0.0669	0.0060	0.24	0.0574	0.0026	430.0	39.0	414.1	16.0	535.0	47.0	7.9
Temora_41	58	0.42	0.51	0.08	0.0668	0.0061	0.07	0.0568	0.0053	425.0	86.0	414.3	24.0	549.0	67.0	19.0
Temora_42	161	0.51	0.50	0.12	0.0671	0.0069	0.02	0.0542	0.0043	435.0	83.0	414.8	24.0	601.0	60.0	10.1
Temora_43	61	0.39	0.51	0.13	0.0672	0.0041	0.06	0.0555	0.0053	420.0	50.0	414.8	36.0	496.0	59.0	13.5
Temora_44	102	0.55	0.51	0.13	0.0672	0.0040	0.06	0.0551	0.0049	429.0	83.0	415.1	24.0	581.0	56.0	12.7
Temora_45	86	0.31	0.51	0.13	0.0674	0.0040	0.02	0.0557	0.0052	416.0	90.0	415.1	24.0	535.0	64.0	12.6
Temora_46	63	0.42	0.49	0.08	0.0676	0.0062	0.08	0.0529	0.0049	407.0	89.0	415.2	24.0	483.0	59.0	15.6
Temora_47	235	0.56	0.54	0.08	0.0676	0.0050	0.34	0.0569	0.0029	409.0	53.0	415.3	30.0	440.0	52.0	7.1
Temora_48	88	0.49	0.51	0.12	0.0677	0.0072	0.04	0.0541	0.0047	405.0	49.0	415.3	36.0	527.0	67.0	13.1
Temora_49	101	0.51	0.48	0.03	0.0677	0.0059	0.01	0.0521	0.0038	410.0	57.0	415.5	31.0	578.0	76.0	12.9
Temora_50	115	0.52	0.49	0.08	0.0678	0.0051	0.19	0.0527	0.0037	410.0	21.0	415.7	36.0	588.0	67.0	10.3
Temora_51	108	0.37	0.51	0.07	0.0676	0.0059	0.05	0.0544	0.0039	411.0	81.0	416.0	42.0	536.0	62.0	13.3
Temora_52	61	0.42	0.51	0.08	0.0678	0.0062	0.08	0.0564	0.0055	424.0	79.0	416.4	43.0	524.0	51.0	17.8
Temora_53	86	0.34	0.49	0.04	0.0679	0.0060	0.03	0.0535	0.0046	424.0	81.0	416.6	42.0	532.0	75.0	14.7
Temora_54	214	0.54	0.52	0.13	0.0680	0.0040	0.05	0.0554	0.0042	450.0	32.0	416.6	19.0	685.0	43.0	8.4
Temora_55	58	0.39	0.57	0.13	0.0681	0.0041	0.01	0.0602	0.0061	428.0	47.0	417.1	36.0	536.0	46.0	16.1
Temora_56	211	0.72	0.50	0.12	0.0681	0.0071	0.02	0.0537	0.0040	423.0	60.0	417.7	12.0	478.0	46.0	8.5
Temora_57	220	0.32	0.52	0.07	0.0682	0.0059	0.04	0.0547	0.0029	418.0	52.0	418.0	37.0	637.0	75.0	9.8
Temora_58	86	0.29	0.51	0.04	0.0682	0.0060	0.26	0.0540	0.0038	408.0	77.0	418.8	42.0	462.0	53.0	12.8
Temora_59	91	0.30	0.52	0.07	0.0682	0.0059	0.17	0.0555	0.0036	414.0	85.0	418.9	25.0	619.0	83.0	12.9
Temora_60	204	0.57	0.53	0.07	0.0683	0.0058	0.07	0.0567	0.0030	413.0	87.0	419.0	24.0	554.0	76.0	9.7
Temora_61	158	0.51	0.52	0.12	0.0684	0.0071	0.00	0.0556	0.0041	416.0	56.0	419.5	12.0	425.0	42.0	9.4

		Ratios								Age (Ma)						
Analysis	U ppm	Th/U	$^{207}Pb/^{235}U$	Err 2SE abs	$^{206}Pb/^{238}U$	Err 2SE abs	Rho	$^{207}Pb/^{206}Pb$	Err 2SE abs	$^{207}Pb/^{235}U$	Err 2SE abs	$^{206}Pb/^{238}U$	Err 2SE abs	$^{207}Pb/^{206}Pb$	Err 2SE abs	% Disc
Temora_62	105	0.31	0.51	0.13	0.0686	0.0040	0.02	0.0545	0.0046	419.0	86.0	420.1	24.0	584.0	80.0	11.2
Temora_63	58	0.29	0.50	0.12	0.0687	0.0072	0.18	0.0532	0.0052	410.0	52.0	421.0	37.0	614.0	87.0	15.2
Temora_64	679	0.51	0.54	0.12	0.0691	0.0069	0.12	0.0556	0.0034	435.0	51.0	421.6	30.0	545.0	51.0	5.5
Temora_65	113	0.36	0.50	0.09	0.0698	0.0071	0.26	0.0533	0.0062	419.0	84.0	422.0	44.0	571.0	65.0	12.7
Temora_66	117	0.32	0.57	0.09	0.0707	0.0052	0.24	0.0593	0.0047	395.0	22.0	422.2	36.0	490.0	77.0	14.4
Temora_67	1598	0.98	0.54	0.07	0.0713	0.0049	0.39	0.0549	0.0021	411.0	50.0	422.5	31.0	436.0	66.0	3.4
Temora_68	3050	1.32	0.52	0.07	0.0713	0.0059	0.85	0.0542	0.0012	454.6	53.0	422.6	12.0	601.0	34.0	2.4
Temora_69	157	0.58	0.62	0.13	0.0715	0.0040	0.21	0.0626	0.0045	410.0	49.0	422.8	35.0	535.0	78.0	9.8
Temora_70	136	0.56	0.56	0.08	0.0719	0.0052	0.22	0.0564	0.0036	407.0	57.0	423.0	38.0	718.0	87.0	11.1
Temora_71	160	0.62	0.49	0.06	0.0652	0.0026	0.18	0.0550	0.0029	410.0	26.0	423.2	36.0	492.0	69.0	4.2
Temora_72	113	0.50	0.51	0.06	0.0654	0.0027	0.07	0.0555	0.0032	424.0	86.0	424.2	24.0	470.0	51.0	5.5
Temora_73	390	0.53	0.53	0.06	0.0659	0.0026	0.18	0.0572	0.0027	462.0	82.0	424.5	25.0	718.0	82.0	3.5
Temora_74	105	0.56	0.53	0.06	0.0664	0.0027	0.11	0.0577	0.0036	414.0	78.0	424.8	43.0	391.0	53.0	6.8
Temora_75	460	0.52	0.50	0.06	0.0647	0.0026	0.12	0.0562	0.0028	424.0	47.0	425.2	36.0	504.0	61.0	3.7
Temora_76	456	0.51	0.52	0.09	0.0670	0.0021	0.05	0.0559	0.0043	413.0	24.0	425.5	36.0	507.0	57.0	5.2
Temora_77	827	0.84	0.53	0.09	0.0683	0.0019	0.01	0.0566	0.0042	422.0	50.0	425.5	36.0	562.0	70.0	4.5
Temora_78	655	0.97	0.51	0.09	0.0689	0.0020	0.10	0.0526	0.0045	432.0	46.0	425.6	35.0	518.0	57.0	6.7
Temora_79	1398	0.91	0.51	0.09	0.0672	0.0019	0.04	0.0551	0.0043	431.0	56.0	425.6	12.0	445.0	36.0	5.2
Temora_80	296	0.56	0.56	0.09	0.0678	0.0020	0.35	0.0595	0.0041	427.0	84.0	426.2	43.0	518.0	57.0	5.0
Temora_81	121	0.48	0.51	0.05	0.0663	0.0031	0.03	0.0562	0.0032	419.0	85.0	427.9	24.0	483.0	64.0	7.3
Temora_82	64	0.29	0.56	0.05	0.0668	0.0031	0.29	0.0625	0.0028	410.0	84.0	428.2	43.0	516.0	80.0	7.7
Temora_83	338	0.65	0.45	0.15	0.0582	0.0100	0.12	0.0563	0.0024	414.0	60.0	429.4	12.0	364.0	55.0	6.2
Temora_84	231	0.60	0.43	0.15	0.0593	0.0098	0.02	0.0522	0.0024	434.0	77.0	430.8	42.0	466.0	30.0	6.8
Temora_85	291	0.65	0.57	0.15	0.0604	0.0099	0.39	0.0684	0.0028	405.0	57.0	434.0	42.0	434.0	88.0	11.9
Temora_86	181	0.62	0.54	0.15	0.0602	0.0096	0.45	0.0615	0.0040	456.0	54.0	440.0	31.0	645.0	70.0	11.7
Temora_87	289	0.44	0.52	0.55	0.0604	0.0091	0.13	0.0664	0.0120	438.5	49.0	443.8	30.0	412.0	23.0	8.0
Temora_88	155	0.31	0.61	0.71	0.0629	0.0091	0.08	0.0547	0.0110	427.9	44.0	443.8	36.0	375.0	13.0	12.0
Temora_89	340	0.39	0.50	0.57	0.0583	0.0087	0.05	0.0584	0.0110	484.0	81.0	445.4	24.0	712.0	51.0	7.5
Temora_90	474	0.60	0.47	0.51	0.0588	0.0084	0.05	0.0568	0.0110	452.0	53.0	448.0	31.0	560.0	54.0	6.8
TSUPB007_1	6410	0.23	10.43	0.56	0.3810	0.0210	1.00	0.1979	0.0023	2426.0	26.0	2024.0	70.0	2804.8	7.8	27.0
TSUPB007_2	332	0.48	13.12	0.15	0.4786	0.0064	0.49	0.1976	0.0025	2687.4	11.0	2521.0	28.0	2814.5	7.9	9.3
TSUPB007_3	1000	0.56	8.87	0.64	0.3110	0.0210	0.99	0.2076	0.0040	2318.0	63.0	1733.0	100.0	2890.7	9.4	38.8
TSUPB007_4	533	0.62	9.37	0.19	0.3102	0.0072	0.90	0.2122	0.0024	2373.0	19.0	1741.0	35.0	2924.1	6.2	41.7
TSUPB007_5	930	0.47	13.19	0.52	0.4430	0.0170	0.99	0.2156	0.0037	2675.0	30.0	2337.0	60.0	2945.6	7.5	20.5
TSUPB007_6	786	0.63	16.84	0.35	0.5660	0.0110	0.91	0.2171	0.0025	2925.0	20.0	2888.0	47.0	2958.0	7.0	5.4
TSUPB007_7	1514	1.38	12.17	0.26	0.3920	0.0094	0.95	0.2184	0.0023	2614.0	21.0	2130.0	44.0	2964.9	5.3	29.9
TSUPB007_8	656	0.59	12.78	0.25	0.4274	0.0078	0.86	0.2169	0.0038	2662.0	18.0	2293.0	35.0	2965.8	8.1	21.8
TSUPB007_9	196	0.62	16.78	0.32	0.5620	0.0120	0.81	0.2178	0.0028	2920.0	18.0	2871.0	50.0	2967.6	8.5	6.3
TSUPB007_10	1601	0.40	13.99	0.26	0.4621	0.0085	0.95	0.2193	0.0023	2746.0	18.0	2447.0	38.0	2974.9	6.7	17.3
TSUPB007_11	2070	2.02	13.08	0.52	0.4330	0.0160	0.97	0.2190	0.0037	2674.0	36.0	2313.0	73.0	2976.0	7.0	21.6
TSUPB007_12	242	0.57	17.31	0.82	0.5740	0.0230	0.93	0.2194	0.0057	2947.0	44.0	2921.0	95.0	2978.0	25.0	6.1
TSUPB007_13	620	0.70	16.67	0.88	0.5490	0.0310	0.97	0.2209	0.0040	2916.0	55.0	2820.0	130.0	2980.9	7.7	14.0
TSUPB007_14	527	0.60	17.13	0.53	0.5670	0.0180	0.93	0.2195	0.0039	2936.0	30.0	2887.0	75.0	2982.4	8.6	8.9
TSUPB007_15	369	0.56	17.66	0.44	0.5840	0.0140	0.93	0.2197	0.0038	2976.0	25.0	2969.0	54.0	2983.6	6.4	5.7
TSUPB007_16	439	0.87	15.57	0.52	0.5080	0.0150	0.96	0.2206	0.0038	2842.0	33.0	2642.0	65.0	2987.1	7.5	11.7
TSUPB007_17	293	0.90	16.79	0.60	0.5490	0.0170	0.95	0.2207	0.0042	2925.0	34.0	2812.0	73.0	2987.5	9.0	6.8
TSUPB007_18	623	0.46	18.11	0.51	0.5880	0.0180	0.94	0.2212	0.0040	2991.0	27.0	2986.0	75.0	2987.7	8.2	7.4
TSUPB007_19	397	0.41	14.97	0.61	0.4910	0.0190	0.89	0.2222	0.0048	2807.0	40.0	2570.0	83.0	2988.0	16.0	13.2
TSUPB007_20	670	0.79	17.02	0.31	0.5615	0.0110	0.89	0.2212	0.0026	2938.0	17.0	2871.0	44.0	2988.1	7.7	6.2
TSUPB007_21	158	0.99	16.46	0.24	0.5361	0.0071	0.48	0.2212	0.0031	2903.0	14.0	2766.0	30.0	2990.0	11.0	7.5
TSUPB007_22	1272	0.71	16.25	0.41	0.5340	0.0130	0.96	0.2215	0.0036	2892.0	25.0	2755.0	57.0	2990.2	5.2	7.8
TSUPB007_23	236	0.58	17.63	0.23	0.5803	0.0073	0.49	0.2212	0.0042	2969.0	12.0	2949.0	30.0	2991.2	9.1	4.4

		Ratios								Age (Ma)						
Analysis	U ppm	Th/U	$^{207}Pb/^{235}U$	Err 2SE abs	$^{206}Pb/^{238}U$	Err 2SE abs	Rho	$^{207}Pb/^{206}Pb$	Err 2SE abs	$^{207}Pb/^{235}U$	Err 2SE abs	$^{206}Pb/^{238}U$	Err 2SE abs	$^{207}Pb/^{206}Pb$	Err 2SE abs	% Disc
TSUPB007_24	515	0.70	18.25	0.48	0.5990	0.0160	0.95	0.2215	0.0038	3000.0	25.0	3026.0	64.0	2991.4	5.8	7.1
TSUPB007_25	239	0.58	18.86	0.54	0.6160	0.0140	0.86	0.2210	0.0043	3033.0	28.0	3097.0	57.0	2994.0	12.0	4.9
TSUPB007_26	281	0.75	18.12	0.30	0.5937	0.0075	0.73	0.2213	0.0040	2994.0	16.0	3007.0	30.0	2997.0	7.3	3.6
TSUPB007_27	1431	0.11	16.73	0.92	0.5420	0.0270	0.98	0.2221	0.0024	2890.0	43.0	2780.0	100.0	2997.5	8.4	13.4
TSUPB007_28	272	0.54	16.17	0.55	0.5300	0.0190	0.97	0.2219	0.0052	2883.0	34.0	2737.0	80.0	2998.0	15.0	9.2
TSUPB007_29	795	0.65	17.84	0.23	0.5831	0.0076	0.82	0.2227	0.0037	2983.0	13.0	2963.0	32.0	3000.6	5.8	3.4
TSUPB007_30	316	0.56	17.14	0.26	0.5545	0.0082	0.83	0.2240	0.0038	2943.0	15.0	2842.0	34.0	3002.6	6.8	6.1
TSUPB007_31	485	1.13	16.06	0.98	0.5210	0.0300	0.99	0.2231	0.0038	2855.0	51.0	2700.0	120.0	3003.6	7.4	18.5
TSUPB007_32	617	0.41	15.39	0.82	0.4770	0.0240	0.99	0.2240	0.0038	2819.0	53.0	2490.0	110.0	3005.7	7.6	19.7
TSUPB007_33	300	0.62	17.70	0.33	0.5772	0.0089	0.77	0.2235	0.0043	2972.0	18.0	2941.0	37.0	3005.8	8.0	4.5
TSUPB007_34	454	1.19	17.34	0.33	0.5610	0.0097	0.87	0.2229	0.0039	2953.0	19.0	2869.0	40.0	3006.8	6.3	5.4
TSUPB007_35	39	0.08	14.95	0.34	0.4802	0.0089	0.23	0.2224	0.0053	2808.0	22.0	2527.0	39.0	3012.0	21.0	15.1
TSUPB007_36	313	0.65	17.85	0.30	0.5711	0.0110	0.87	0.2252	0.0040	2981.0	16.0	2911.0	44.0	3022.1	8.4	4.1
TSUPB007_37	56	0.04	15.73	0.33	0.4979	0.0084	0.63	0.2294	0.0048	2857.0	21.0	2607.0	37.0	3035.0	17.0	13.9
TSUPB007_38	32	0.05	15.63	0.41	0.4922	0.0096	0.48	0.2265	0.0052	2858.0	25.0	2578.0	42.0	3040.0	22.0	14.9
TSUPB007_39	2690	0.29	11.77	0.39	0.3710	0.0110	0.95	0.2298	0.0037	2578.0	30.0	2037.0	52.0	3046.9	5.4	34.6
TSUPB007_40	1500	0.44	14.68	0.35	0.4386	0.0097	0.94	0.2426	0.0037	2790.0	22.0	2347.0	44.0	3137.4	6.2	27.0
TSUPB007_41	326	0.23	21.35	0.37	0.6196	0.0079	0.80	0.2485	0.0045	3152.0	17.0	3107.0	31.0	3178.0	15.0	3.8
TSUPB007_42	1027	0.07	20.72	0.19	0.5968	0.0066	0.65	0.2521	0.0024	3125.8	8.6	3016.0	27.0	3196.5	5.1	6.0
TSUPB007_43	1792	0.57	20.22	0.23	0.5718	0.0083	0.91	0.2564	0.0022	3102.0	11.0	2914.0	34.0	3228.4	3.4	10.3
TSUPB007_44	568	0.58	22.63	0.49	0.6380	0.0140	0.93	0.2574	0.0026	3207.0	21.0	3179.0	54.0	3234.1	5.8	6.1
TSUPB008_1	2260	0.38	8.72	0.34	0.3117	0.0120	0.91	0.2023	0.0039	2299.0	36.0	1746.0	58.0	2836.0	20.0	37.1
TSUPB008_2	4780	1.01	9.77	0.83	0.3430	0.0260	0.99	0.2062	0.0038	2395.0	75.0	1880.0	120.0	2879.0	15.0	31.8
TSUPB008_3	1270	0.90	8.24	0.26	0.2724	0.0100	0.97	0.2152	0.0033	2257.0	29.0	1551.0	51.0	2946.0	6.5	49.2
TSUPB008_4	819	0.51	13.32	0.48	0.4440	0.0150	0.98	0.2168	0.0033	2691.0	34.0	2361.0	68.0	2960.9	6.4	19.0
TSUPB008_5	623	0.85	10.42	0.45	0.3390	0.0140	0.97	0.2173	0.0037	2467.0	40.0	1883.0	69.0	2962.0	10.0	38.5
TSUPB008_6	284	0.57	15.96	0.26	0.5309	0.0100	0.87	0.2192	0.0036	2874.0	16.0	2744.0	43.0	2977.7	7.6	7.9
TSUPB008_7	317	0.60	16.93	0.26	0.5610	0.0097	0.76	0.2202	0.0036	2931.0	15.0	2870.0	40.0	2979.3	8.3	4.9
TSUPB008_8	240	0.71	18.99	0.88	0.6180	0.0230	0.99	0.2216	0.0040	3019.0	34.0	3093.0	87.0	2983.0	11.0	7.3
TSUPB008_9	466	0.18	12.75	0.81	0.4110	0.0240	0.96	0.2213	0.0043	2613.0	67.0	2200.0	110.0	2983.0	19.0	26.6
TSUPB008_10	289	0.97	16.83	0.25	0.5556	0.0097	0.79	0.2217	0.0036	2925.0	14.0	2847.0	40.0	2990.0	7.6	5.0
TSUPB008_11	514	0.22	18.00	1.30	0.5840	0.0330	1.00	0.2220	0.0036	2952.0	22.0	2950.0	110.0	2992.2	7.9	5.0
TSUPB008_12	346	0.87	17.91	0.25	0.5894	0.0093	0.78	0.2227	0.0035	2985.0	14.0	2986.0	37.0	3002.6	8.4	3.6
TSUPB008_13	259	0.62	17.70	0.30	0.5763	0.0120	0.84	0.2235	0.0036	2975.0	16.0	2931.0	48.0	3008.3	8.0	5.2
TSUPB008_14	151	0.89	17.17	0.36	0.5564	0.0120	0.80	0.2241	0.0040	2946.0	21.0	2854.0	48.0	3010.0	11.0	6.0
TSUPB008_15	1170	0.33	8.31	0.19	0.2647	0.0079	0.91	0.2271	0.0035	2264.0	21.0	1513.0	40.0	3030.4	7.7	52.4
TSUPB008_16	832	0.58	14.42	0.34	0.4603	0.0110	0.93	0.2272	0.0035	2776.0	22.0	2438.0	50.0	3037.0	6.4	19.8
TSUPB008_17	635	0.48	13.71	0.56	0.4360	0.0170	0.98	0.2284	0.0038	2717.0	38.0	2327.0	74.0	3037.0	10.0	23.6
TSUPB008_18	1143	0.79	14.38	0.19	0.4568	0.0088	0.88	0.2284	0.0033	2774.0	13.0	2424.0	39.0	3041.6	4.8	20.3
TSUPB008_19	511	0.20	17.56	0.37	0.5490	0.0120	0.95	0.2321	0.0035	2963.0	20.0	2820.0	51.0	3064.7	5.8	8.7
TSUPB008_20	733	0.34	14.84	0.47	0.4610	0.0120	0.94	0.2347	0.0040	2800.0	29.0	2442.0	55.0	3084.0	16.0	21.0
TSUPB008_21	357	0.71	18.63	0.38	0.5762	0.0110	0.89	0.2348	0.0037	3020.0	19.0	2932.0	45.0	3087.5	7.3	6.0
TSUPB008_22	1494	0.83	10.74	0.20	0.3324	0.0082	0.89	0.2351	0.0034	2505.0	17.0	1849.0	40.0	3088.1	6.1	42.9
TSUPB008_23	4690	0.24	13.11	0.44	0.3880	0.0140	0.98	0.2459	0.0033	2687.0	32.0	2115.0	64.0	3159.7	6.9	36.4
TSUPB008_24	627	0.65	11.89	0.50	0.3500	0.0150	0.97	0.2472	0.0037	2581.0	40.0	1929.0	72.0	3164.6	7.3	42.8
TSUPB008_25	1368	0.75	12.69	0.69	0.3710	0.0180	0.99	0.2477	0.0037	2622.0	39.0	2008.0	77.0	3167.4	9.3	42.3
TSUPB008_26	454	0.50	19.30	0.40	0.5620	0.0120	0.95	0.2474	0.0035	3059.0	19.0	2874.0	51.0	3173.8	5.8	9.0
TSUPB008_27	235	1.29	13.51	0.60	0.3910	0.0160	0.97	0.2516	0.0041	2710.0	42.0	2121.0	77.0	3198.7	9.1	37.2
TSUPB008_28	688	0.64	17.10	1.20	0.4880	0.0320	0.99	0.2527	0.0036	2896.0	68.0	2530.0	140.0	3202.0	9.2	24.9
TSUPB008_29	239	0.70	23.25	0.60	0.6610	0.0170	0.96	0.2553	0.0037	3241.0	23.0	3265.0	64.0	3219.0	8.3	6.4
TSUPB008_30	245	0.85	20.73	0.35	0.5865	0.0120	0.91	0.2559	0.0037	3124.0	16.0	2973.0	46.0	3219.1	7.8	9.1
TSUPB008_31	920	0.71	16.00	1.10	0.4520	0.0300	1.00	0.2554	0.0037	2868.0	64.0	2400.0	130.0	3221.0	10.0	29.8

		Ratios								Age (Ma)						
Analysis	U ppm	Th/U	$^{207}Pb/^{235}U$	Err 2SE abs	$^{206}Pb/^{238}U$	Err 2SE abs	Rho	$^{207}Pb/^{206}Pb$	Err 2SE abs	$^{207}Pb/^{235}U$	Err 2SE abs	$^{206}Pb/^{238}U$	Err 2SE abs	$^{207}Pb/^{206}Pb$	Err 2SE abs	% Disc
TSUPB008_32	81	0.91	21.32	0.39	0.6027	0.0098	0.53	0.2577	0.0049	3153.0	17.0	3039.0	39.0	3238.0	15.0	7.5
TSUPB008_33	152	0.66	18.79	0.73	0.5240	0.0190	0.93	0.2605	0.0046	3018.0	40.0	2704.0	84.0	3247.0	12.0	18.1
TSUPB008_34	560	1.74	19.80	2.00	0.5430	0.0500	1.00	0.2616	0.0038	2995.0	60.0	2700.0	160.0	3253.8	9.2	25.9
TSUPB008_35	686	0.47	22.35	0.25	0.6179	0.0088	0.73	0.2632	0.0035	3198.2	11.0	3101.0	35.0	3267.0	6.4	4.9
TSUPB008_36	245	1.11	23.60	0.31	0.6477	0.0092	0.71	0.2647	0.0041	3251.0	13.0	3218.0	36.0	3277.3	9.6	4.5
TSUPB008_37	228	0.44	24.89	0.39	0.6790	0.0130	0.85	0.2661	0.0039	3304.0	15.0	3350.0	47.0	3287.7	9.5	5.6
TSUPB008_38	235	0.55	23.15	0.31	0.6323	0.0094	0.77	0.2667	0.0037	3237.0	13.0	3158.0	37.0	3288.0	7.4	4.6
TSUPB009_1	657	0.54	6.63	0.30	0.2440	0.0120	0.97	0.1974	0.0025	2057	41.0	1405.0	61.0	2808.0	12.0	46.9
TSUPB009_2	1120	1.05	10.05	0.78	0.3520	0.0260	0.99	0.2076	0.0019	2368	79.0	1920.0	120.0	2889.7	9.3	30.7
TSUPB009_3	223	0.85	17.62	0.34	0.5920	0.0120	0.81	0.2166	0.0027	2970	18.0	3001.0	48.0	2961.0	10.0	5.5
TSUPB009_4	555	0.84	19.20	1.50	0.6150	0.0400	1.00	0.2211	0.0019	3005	50.0	3060.0	140.0	2980.3	7.5	10.8
TSUPB009_5	453	1.16	18.35	0.75	0.5890	0.0260	0.97	0.2223	0.0023	3009	39.0	2970.0	110.0	3000.6	9.7	11.6
TSUPB009_6	1006	0.62	12.64	0.42	0.3700	0.0120	0.98	0.2466	0.0020	2653	30.0	2031.0	56.0	3161.9	6.0	39.7
TSUPB009_7	526	1.29	16.73	0.42	0.4760	0.0120	0.96	0.2553	0.0025	2923	24.0	2506.0	52.0	3215.4	8.0	24.1
TSUPB009_8	358	0.81	24.31	0.33	0.6649	0.0110	0.83	0.2633	0.0026	3281	13.0	3284.0	42.0	3271.0	7.0	5.0
TSUPB020_1	< 70	1.62	4.67	0.10	0.1787	0.0024	0.71	0.1894	0.0041	1761.5	18.0	1059.7	13.0	2735.4	6.8	54.2
TSUPB020_2	747	0.96	4.95	0.20	0.1878	0.0068	0.95	0.1909	0.0032	1823.0	34.0	1108.0	37.0	2749.0	15.0	53.3
TSUPB020_3	< 70	1.02	5.73	0.23	0.2151	0.0069	0.99	0.1930	0.0043	1928.0	35.0	1254.0	37.0	2768.0	13.0	49.7
TSUPB020_4	< 70	0.33	4.04	0.36	0.1440	0.0110	0.94	0.1981	0.0053	1607.0	68.0	862.0	61.0	2812.0	25.0	61.6
TSUPB020_5	736	0.67	6.72	0.18	0.2457	0.0060	0.97	0.1986	0.0029	2073.0	22.0	1416.0	31.0	2820.0	12.0	46.3
TSUPB020_6	17000	0.89	6.56	0.38	0.2260	0.0110	0.99	0.2101	0.0044	2035.0	51.0	1307.0	58.0	2906.0	13.0	54.0
TSUPB020_7	< 70	3.69	5.07	0.20	0.1755	0.0045	0.96	0.2095	0.0047	1830.0	33.0	1042.0	24.0	2908.0	16.0	61.7
TSUPB020_8	716	0.30	9.85	0.50	0.3410	0.0170	0.99	0.2101	0.0033	2415.0	47.0	1883.0	80.0	2915.0	13.0	34.3
TSUPB020_9	4870	1.73	9.48	0.44	0.3240	0.0130	0.75	0.2130	0.0046	2377.0	42.0	1806.0	64.0	2923.0	16.0	37.9
TSUPB020_10	< 70	2.41	11.69	0.28	0.3973	0.0092	0.97	0.2137	0.0041	2576.0	23.0	2155.0	42.0	2933.6	4.9	25.8
TSUPB020_11	< 70	3.14	16.85	0.20	0.5739	0.0051	0.59	0.2149	0.0045	2925.0	11.0	2923.0	21.0	2938.0	11.0	3.3
TSUPB020_12	434	0.93	12.48	0.49	0.4220	0.0160	0.95	0.2133	0.0031	2635.0	43.0	2260.0	75.0	2939.0	21.0	22.3
TSUPB020_13	< 70	1.72	10.74	0.34	0.3615	0.0120	0.93	0.2142	0.0046	2499.0	26.0	1989.0	39.0	2939.0	10.0	32.1
TSUPB020_14	74	1.06	17.14	0.21	0.5787	0.0055	0.47	0.2152	0.0034	2942.0	12.0	2943.0	23.0	2943.0	12.0	3.1
TSUPB020_15	127	1.39	17.29	0.14	0.5811	0.0059	0.43	0.2151	0.0031	2951.0	7.6	2953.0	24.0	2950.0	11.0	2.7
TSUPB020_16	< 70	1.30	13.25	0.23	0.4476	0.0071	0.80	0.2160	0.0040	2697.0	17.0	2385.0	32.0	2952.0	12.0	18.1
TSUPB020_17	< 70	1.35	16.31	0.41	0.5459	0.0051	0.50	0.2169	0.0046	2895.1	15.0	2808.0	21.0	2961.2	5.4	4.4
TSUPB020_18	< 70	1.80	14.68	0.15	0.4883	0.0042	0.63	0.2190	0.0042	2794.1	9.5	2563.0	18.0	2971.7	5.1	13.2
TSUPB020_19	< 70	1.75	7.75	0.16	0.2669	0.0045	0.91	0.2196	0.0042	2202.0	19.0	1525.0	23.0	2975.5	8.5	47.0
TSUPB020_20	< 70	1.69	16.22	0.22	0.5377	0.0060	0.50	0.2201	0.0042	2891.5	13.0	2774.0	26.0	2977.0	10.0	6.7
TSUPB020_21	< 70	1.66	13.83	0.18	0.4705	0.0053	0.72	0.2213	0.0044	2737.0	12.0	2488.0	23.0	2988.3	8.6	14.0
TSUPB020_22	< 70	2.27	10.26	0.23	0.3361	0.0074	0.92	0.2213	0.0043	2458.0	20.0	1866.0	36.0	2993.0	5.8	38.2
TSUPB020_23	1672	1.07	9.91	0.16	0.3212	0.0059	0.57	0.2214	0.0034	2426.0	15.0	1795.0	29.0	2994.6	9.6	40.7
TSUPB020_24	< 70	1.21	9.95	0.13	0.3249	0.0034	0.83	0.2227	0.0042	2429.7	13.0	1814.0	16.0	2997.6	5.0	40.5
TSUPB020_25	783	1.35	17.27	0.14	0.5639	0.0049	0.23	0.2227	0.0043	2950.5	7.5	2882.0	20.0	2999.3	7.2	4.2
TSUPB020_26	128	0.54	18.01	0.17	0.5895	0.0056	0.60	0.2230	0.0029	2991.0	8.9	2987.0	23.0	3001.4	9.2	2.2
TSUPB020_27	1240	1.34	17.37	0.26	0.5639	0.0094	0.61	0.2236	0.0042	2955.0	15.0	2882.0	40.0	3003.2	6.9	4.5
TSUPB020_28	< 70	0.05	17.33	0.27	0.5656	0.0080	0.51	0.2238	0.0042	2953.0	16.0	2890.0	34.0	3004.9	8.4	3.5
TSUPB020_29	< 70	0.83	13.34	0.31	0.4293	0.0080	0.93	0.2243	0.0043	2707.0	23.0	2308.0	37.0	3009.5	7.8	23.3
TSUPB020_30	< 70	2.13	9.83	0.33	0.3160	0.0053	0.98	0.2248	0.0049	2405.0	21.0	1769.0	26.0	3012.0	16.0	42.5
TSUPB020_31	< 70	2.49	15.95	0.23	0.5216	0.0070	0.11	0.2246	0.0043	2877.0	14.0	2706.0	30.0	3021.0	13.0	10.0
TSUPB020_32	< 70	0.94	10.58	0.50	0.3390	0.0140	0.98	0.2268	0.0049	2476.0	42.0	1879.0	64.0	3030.0	15.0	39.3
TSUPB020_33	< 70	1.58	14.07	0.40	0.4516	0.0120	0.81	0.2273	0.0042	2756.0	29.0	2402.0	55.0	3034.5	6.6	20.4
TSUPB020_34	557	0.60	10.05	0.45	0.3200	0.0110	0.98	0.2292	0.0045	2429.0	38.0	1786.0	56.0	3040.0	23.0	42.2
TSUPB020_35	3660	0.84	17.60	0.14	0.5627	0.0038	0.50	0.2277	0.0041	2969.1	7.8	2878.0	15.0	3042.2	5.6	5.1

		Ratios								Age (Ma)						
Analysis	U ppm	Th/U	$^{207}Pb/^{235}U$	Err 2SE abs	$^{206}Pb/^{238}U$	Err 2SE abs	Rho	$^{207}Pb/^{206}Pb$	Err 2SE abs	$^{207}Pb/^{235}U$	Err 2SE abs	$^{206}Pb/^{238}U$	Err 2SE abs	$^{207}Pb/^{206}Pb$	Err 2SE abs	% Disc
TSUPB020_36	168	0.45	18.19	0.19	0.5786	0.0060	0.56	0.2301	0.0031	3001.0	10.0	2943.0	24.0	3050.1	9.6	4.0
TSUPB020_37	< 70	2.20	19.12	0.21	0.6040	0.0048	0.73	0.2290	0.0043	3047.0	11.0	3045.0	19.0	3051.5	7.6	2.4
TSUPB020_38	129	0.80	20.54	0.42	0.6200	0.0130	0.86	0.2405	0.0030	3120.0	20.0	3115.0	51.0	3121.0	12.0	3.9
TSUPB020_39	799	0.18	9.91	0.43	0.2920	0.0110	0.89	0.2439	0.0036	2422.0	39.0	1651.0	54.0	3146.0	13.0	52.7
TSUPB020_40	< 70	0.94	18.99	0.50	0.5670	0.0050	0.86	0.2457		3041.0		2896.0		3164.0	9.1	8.3
TSUPB020_41	< 70	1.01	18.31	0.19	0.5384	0.0053	0.84	0.2480	0.0043	3005.6	9.9	2781.0	22.0	3167.7	9.4	12.5
TSUPB020_42	< 70	1.13	12.33	0.12	0.3578	0.0033	0.79	0.2507	0.0041	2629.7	9.0	1972.0	16.0	3186.9	4.1	42.8
TSUPB020_43	< 70	3.15	10.68	0.54	0.3060	0.0120	0.87	0.2510	0.0052	2504.0	52.0	1717.0	59.0	3191.0	17.0	52.0
TSUPB020_44	102	0.85	22.53	0.22	0.6352	0.0064	0.89	0.2567	0.0030	3206.0	9.7	3170.0	26.0	3223.0	14.0	3.0
TSUPB020_45	< 70	2.05	20.56	0.18	0.5813	0.0048	0.60	0.2577	0.0042	3118.8	8.5	2953.0	20.0	3230.0	5.5	9.0
TSUPB020_46	1022	1.22	16.98	0.23	0.4786	0.0072	0.90	0.2580	0.0042	2933.0	13.0	2520.0	31.0	3234.4	3.7	24.4
TSUPB020_47	165	0.76	22.44	0.23	0.6304	0.0081	0.29	0.2591	0.0040	3202.5	10.0	3150.0	32.0	3237.0	17.0	5.3
TSUPB020_48	128	1.43	23.20	0.27	0.6501	0.0068	0.49	0.2575	0.0047	3234.0	11.0	3228.0	27.0	3238.0	11.0	3.1
TSUPB020_49	742	0.58	19.12	0.32	0.5360	0.0079	0.91	0.2596	0.0042	3050.0	16.0	2765.0	34.0	3239.9	5.8	16.1
TSUPB020_50	< 70	0.77	18.34	0.19	0.5138	0.0053	0.78	0.2592	0.0042	3007.4	10.0	2672.0	23.0	3241.1	5.0	19.2
TSUPB020_51	< 70	0.61	23.08	0.20	0.6499	0.0063	0.79	0.2594	0.0043	3229.9	8.2	3227.0	25.0	3243.8	6.5	3.5
TSUPB020_52	< 70	0.94	23.59	0.17	0.6562	0.0048	0.40	0.2597	0.0043	3251.4	7.0	3252.0	18.0	3250.2	5.5	2.5
TSUPB020_53	< 70	1.24	24.05	0.25	0.6633	0.0053	0.48	0.2623	0.0044	3271.0	9.8	3280.0	21.0	3257.2	7.5	2.5
TSUPB020_54	2263	0.95	23.89	0.16	0.6598	0.0045	0.63	0.2614	0.0041	3263.6	6.6	3266.0	17.0	3258.9	5.1	2.0
TSUPB020_55	810	0.94	22.93	0.34	0.6378	0.0091	0.27	0.2628	0.0043	3224.0	15.0	3180.0	36.0	3260.0	14.0	3.7
TSUPB020_56	< 70	1.14	23.82	0.19	0.6587	0.0064	0.63	0.2630	0.0042	3260.5	8.0	3261.0	25.0	3264.2	5.7	3.3
TSUPB020_57	< 70	0.79	15.31	0.15	0.4200	0.0037	0.77	0.2630	0.0042	2834.3	9.6	2260.0	17.0	3266.7	5.8	35.3
TSUPB020_58	4550	1.64	23.92	0.19	0.6589	0.0044	0.69	0.2634	0.0041	3264.8	7.4	3263.0	17.0	3268.6	7.8	2.0
TSUPB020_59	< 70	3.05	19.69	0.15	0.5387	0.0039	0.49	0.2650	0.0043	3075.9	7.6	2778.0	16.0	3276.7	4.9	16.9
TSUPB020_60	836	1.31	23.67	0.26	0.6440	0.0065	0.56	0.2657	0.0043	3255.0	11.0	3209.0	26.0	3278.8	9.1	3.9
TSUPB020_61	< 70	2.33	23.08	0.17	0.6308	0.0043	0.55	0.2655	0.0041	3230.8	7.1	3152.0	17.0	3281.5	4.9	4.1
TSUPB020_62	< 70	2.02	24.35	0.19	0.6651	0.0046	0.41	0.2661	0.0043	3282.3	7.6	3287.0	18.0	3284.7	5.7	2.4
TSUPB020_63	< 70	2.00	24.37	0.21	0.6642	0.0051	0.84	0.2671	0.0042	3283.1	8.3	3283.0	20.0	3288.2	6.0	2.0
TSUPB020_64	< 70	1.33	21.26	0.32	0.5790	0.0066	0.84	0.2673	0.0044	3149.0	14.0	2943.0	27.0	3292.0	10.0	11.6
TSUPB020_65	1490	1.84	20.41	0.42	0.5483	0.0094	0.95	0.2703	0.0043	3113.0	21.0	2817.0	39.0	3309.4	7.7	16.1
TSUPB020_66	< 70	1.18	23.92	0.20	0.6400	0.0052	0.67	0.2707	0.0043	3266.2	8.4	3188.0	20.0	3311.3	6.5	4.1
TSUPB020_67	< 70	1.28	22.73	0.33	0.6137	0.0100	0.94	0.2708	0.0042	3215.0	15.0	3084.0	42.0	3312.0	9.7	7.0
TSUPB020_68	< 70	3.09	23.57	0.24	0.6235	0.0051	0.39	0.2732	0.0045	3250.0	9.8	3126.0	20.0	3327.3	8.3	6.4
TSUPB020_69	< 70	2.00	25.64	0.21	0.6702	0.0044	0.65	0.2786	0.0044	3332.7	8.1	3306.0	17.0	3355.3	8.1	2.2
TSUPB020_70	< 70	1.37	23.01	0.20	0.5928	0.0044	0.47	0.2835	0.0045	3228.1	8.6	3000.0	18.0	3379.9	8.8	12.9
TSUPB020CA_1	196	0.94	17.62	0.24	0.5814	0.0078	0.72	0.2166	0.0019	2969.0	13.0	2954.0	32.0	2955.0	14.0	0.3
TSUPB020CA_2	196	1.20	15.66	0.17	0.5277	0.0064	0.78	0.2187	0.0026	2856.0	11.0	2731.0	27.0	2975.0	18.0	8.7
TSUPB020CA_3	84	1.30	19.10	0.33	0.6050	0.0100	0.84	0.2207	0.0021	3046.0	17.0	3050.0	42.0	2985.0	15.0	-2.1
TSUPB020CA_4	192	0.74	18.28	0.19	0.5940	0.0048	0.84	0.2209	0.0014	3007.0	9.0	3005.0	20.0	2987.0	10.0	-0.5
TSUPB020CA_5	198	0.83	19.06	0.34	0.6040	0.0110	0.94	0.2216	0.0014	3043.0	17.0	3043.0	46.0	2992.0	10.0	-1.5
TSUPB020CA_6	191	0.88	17.73	0.20	0.5858	0.0077	0.77	0.2213	0.0016	2975.0	11.0	2979.0	33.0	2993.0	13.0	0.8
TSUPB020CA_7	156	0.93	19.07	0.34	0.6013	0.0079	1.00	0.2219	0.0020	3045.0	17.0	3035.0	32.0	2994.0	14.0	-1.2
TSUPB020CA_8	346	0.49	14.54	0.31	0.4751	0.0086	0.95	0.2229	0.0013	2786.0	21.0	2505.0	37.0	3001.1	9.2	16.3
TSUPB020CA_9	100	0.43	19.85	0.23	0.6119	0.0084	0.88	0.2268	0.0037	3084.0	11.0	3077.0	34.0	3029.0	26.0	-1.6
TSUPB020CA_10	187	0.70	19.01	0.19	0.6037	0.0061	0.93	0.2272	0.0022	3042.0	9.6	3044.0	25.0	3032.0	15.0	-0.5
TSUPB020CA_11	139	0.69	19.07	0.20	0.6048	0.0070	0.65	0.2290	0.0019	3045.0	10.0	3049.0	28.0	3044.0	13.0	-0.2
TSUPB020CA_12	182	0.67	19.84	0.28	0.6137	0.0061	0.35	0.2292	0.0035	3083.0	14.0	3085.0	24.0	3045.0	24.0	-1.5
TSUPB020CA_13	207	0.73	20.26	0.21	0.6186	0.0067	0.89	0.2290	0.0015	3103.5	9.8	3104.0	27.0	3045.0	10.0	-1.9
TSUPB020CA_14	205	1.03	19.08	0.18	0.6071	0.0055	0.54	0.2302	0.0022	3048.0	10.0	3058.0	22.0	3053.0	16.0	0.0
TSUPB020CA_15	157	0.58	20.32	0.38	0.6197	0.0092	0.70	0.2304	0.0018	3107.0	18.0	3108.0	37.0	3054.0	12.0	-1.8
TSUPB020CA_16	138	0.88	18.19	0.19	0.5703	0.0062	0.92	0.2325	0.0019	2999.0	10.0	2908.0	25.0	3069.0	13.0	5.2
TSUPB020CA_17	229	0.14	19.17	0.33	0.6075	0.0058	0.66	0.2327	0.0030	3050.0	17.0	3060.0	23.0	3070.0	21.0	0.2

		Ratios								Age (Ma)						
Analysis	U ppm	Th/U	$^{207}Pb/^{235}U$	Err 2SE abs	$^{206}Pb/^{238}U$	Err 2SE abs	Rho	$^{207}Pb/^{206}Pb$	Err 2SE abs	$^{207}Pb/^{235}U$	Err 2SE abs	$^{206}Pb/^{238}U$	Err 2SE abs	$^{207}Pb/^{206}Pb$	Err 2SE abs	% Disc
TSUPB020CA_18	92	0.57	21.58	0.34	0.6345	0.0060	0.32	0.2433	0.0038	3165.0	15.0	3167.0	24.0	3151.0	30.0	-0.8
TSUPB020CA_19	292	0.62	21.44	0.23	0.6313	0.0054	0.93	0.2474	0.0015	3158.0	10.0	3154.0	21.0	3167.8	9.8	0.4
TSUPB020CA_20	256	0.38	21.52	0.19	0.6340	0.0043	0.65	0.2481	0.0013	3162.1	8.5	3165.0	17.0	3172.1	8.4	0.3
TSUPB020CA_21	74	0.45	21.62	0.34	0.6350	0.0130	0.52	0.2489	0.0026	3166.0	15.0	3169.0	53.0	3177.0	17.0	-0.1
TSUPB020CA_22	50	0.34	22.47	0.26	0.6450	0.0160	0.75	0.2514	0.0042	3204.0	11.0	3205.0	64.0	3192.0	26.0	-0.5
TSUPB020CA_23	236	0.87	21.65	0.49	0.5930	0.0130	0.93	0.2560	0.0025	3172.0	21.0	2999.0	54.0	3222.0	16.0	6.9
TSUPB020CA_24	127	1.27	23.48	0.29	0.6576	0.0093	0.72	0.2585	0.0028	3246.0	12.0	3257.0	36.0	3237.0	17.0	-1.0
TSUPB020CA_25	159	0.35	24.69	0.35	0.6708	0.0092	0.88	0.2636	0.0017	3295.0	14.0	3308.0	35.0	3268.0	10.0	-1.2
TSUPB020CA_26	153	0.39	24.29	0.20	0.6634	0.0066	0.92	0.2640	0.0019	3279.9	8.0	3280.0	26.0	3270.0	11.0	-0.2
TSUPB020CA_27	129	0.72	23.30	0.25	0.6535	0.0070	0.42	0.2651	0.0025	3239.0	10.0	3241.0	28.0	3277.0	15.0	0.9
TSUPB020CA_28	73	0.82	25.58	0.50	0.6790	0.0130	0.76	0.2672	0.0040	3336.0	17.0	3341.0	49.0	3289.0	24.0	-1.5
TSUPB020CA_29	46	0.72	24.75	0.31	0.6732	0.0087	0.57	0.2676	0.0029	3297.0	12.0	3322.0	34.0	3291.0	17.0	-0.6
TSUPB020CA_30	102	1.23	24.49	0.54	0.6670	0.0110	0.27	0.2678	0.0038	3288.0	21.0	3296.0	43.0	3293.0	22.0	-0.4
TSUPB020CA_31	81	0.55	25.36	0.36	0.6762	0.0075	0.50	0.2706	0.0039	3322.0	14.0	3329.0	29.0	3308.0	23.0	-1.2
TSUPB020CA_32	176	0.71	25.40	0.26	0.6810	0.0100	0.61	0.2732	0.0032	3323.3	9.9	3350.0	38.0	3324.0	18.0	-0.5
TSUPB021_1	709	0.63	8.21	0.24	0.2937	0.0079	0.97	0.2026	0.0028	2250.0	26.0	1659.0	39.0	2846.7	8.1	39.3
TSUPB021_2	437	1.56	11.35	0.40	0.3990	0.0050	0.86	0.2065		2551.0		2164.0		2881.0	13.0	22.4
TSUPB021_3	618	1.25	10.10	0.21	0.3496	0.0066	0.94	0.2082	0.0029	2445.0	19.0	1937.0	31.0	2894.9	8.1	31.6
TSUPB021_4	307	0.68	15.29	0.38	0.5216	0.0130	0.94	0.2122	0.0028	2833.0	27.0	2706.0	56.0	2907.0	16.0	6.7
TSUPB021_5	331	1.11	13.43	0.20	0.4555	0.0064	0.50	0.2115	0.0028	2710.0	15.0	2420.0	29.0	2924.0	14.0	15.9
TSUPB021_6	618	0.62	9.28	0.37	0.3160	0.0130	0.81	0.2120	0.0029	2365.0	33.0	1770.0	61.0	2925.9	9.3	39.7
TSUPB021_7	820	0.91	13.880	0.230	0.4684	0.0075	0.93	0.2142	0.0026	2740.0	16.0	2476.0	33.0	2935.8	5.0	15.0
TSUPB021_8	754	0.52	9.600	0.650	0.3220	0.0170	0.89	0.2133	0.0033	2395.0	49.0	1800.0	79.0	2937.0	14.0	39.0
TSUPB021_9	411	0.58	17.030	0.300	0.5639	0.0096	0.72	0.2168	0.0027	2936.0	19.0	2883.0	40.0	2955.8	7.7	2.9
TSUPB021_10	152	0.69	17.550	0.170	0.5841	0.0069	0.48	0.2170	0.0029	2965.0	9.2	2965.0	28.0	2960.0	12.0	2.5
TSUPB021_11	258	0.87	17.440	0.130	0.5827	0.0053	0.53	0.2184	0.0029	2959.0	7.3	2959.0	22.0	2961.0	11.0	2.5
TSUPB021_12	240	0.60	17.750	0.420	0.5873	0.0140	0.82	0.2184	0.0027	2976.0	24.0	2978.0	56.0	2966.9	9.7	2.2
TSUPB021_13	7310	1.06	13.650	0.110	0.4463	0.0045	0.66	0.2188	0.0023	2725.4	7.7	2379.0	20.0	2968.7	6.8	20.2
TSUPB021_14	435	0.65	11.490	0.490	0.3810	0.0150	0.97	0.2184	0.0033	2553.0	40.0	2077.0	68.0	2969.0	15.0	30.2
TSUPB021_15	132	0.71	17.940	0.170	0.5904	0.0051	0.44	0.2194	0.0030	2986.0	9.3	2991.0	20.0	2972.0	12.0	2.4
TSUPB021_16	390	0.73	16.080	0.120	0.5309	0.0050	0.66	0.2189	0.0027	2882.3	7.4	2745.0	21.0	2972.6	7.3	7.6
TSUPB021_17	276	1.59	17.800	0.140	0.5878	0.0045	0.43	0.2196	0.0029	2978.9	7.4	2980.0	18.0	2974.3	7.5	1.6
TSUPB021_18	182	0.92	17.780	0.180	0.5863	0.0055	0.64	0.2205	0.0028	2978.0	9.7	2974.0	22.0	2983.0	11.0	2.4
TSUPB021_19	208	1.22	17.640	0.320	0.5692	0.0110	0.45	0.2214	0.0022	2970.0	19.0	2904.0	46.0	2994.0	19.0	3.5
TSUPB021_20	399	0.64	12.660	0.410	0.4110	0.0130	0.95	0.2228	0.0028	2653.0	33.0	2220.0	61.0	2996.8	9.1	25.5
TSUPB021_21	1241	1.70	17.800	0.220	0.5754	0.0053	0.68	0.2221	0.0023	2984.0	12.0	2930.0	22.0	2997.0	16.0	3.0
TSUPB021_22	1361	0.11	6.550	0.800	0.2210	0.0250	0.99	0.2213	0.0063	1995.0	89.0	1250.0	110.0	3000.0	39.0	59.1
TSUPB021_23	211	0.73	18.250	0.220	0.5926	0.0061	0.82	0.2239	0.0028	3002.0	11.0	2999.0	25.0	3012.4	6.4	2.4
TSUPB021_24	132	0.83	18.900	0.160	0.6015	0.0060	0.28	0.2251	0.0032	3037.0	8.4	3036.0	24.0	3019.0	10.0	2.3
TSUPB021_25	386	0.45	15.020	0.290	0.4847	0.0091	0.93	0.2253	0.0028	2817.0	18.0	2547.0	40.0	3022.2	6.5	15.4
TSUPB021_26	405	1.87	13.750	0.340	0.4340	0.0084	0.80	0.2282	0.0034	2731.0	25.0	2323.0	38.0	3033.0	50.0	24.4
TSUPB021_27	1002	0.98	18.560	0.140	0.5933	0.0050	0.56	0.2291	0.0022	3018.9	7.1	3002.0	20.0	3050.3	8.0	1.7
TSUPB021_28	426	0.11	16.150	0.510	0.5030	0.0170	0.95	0.2326	0.0029	2883.0	31.0	2624.0	71.0	3060.0	12.0	14.7
TSUPB021_29	340	0.14	15.760	0.440	0.4850	0.0130	0.93	0.2352	0.0033	2863.0	27.0	2548.0	56.0	3084.0	12.0	18.2
TSUPB021_30	261	0.06	20.680	0.140	0.6160	0.0044	0.29	0.2424	0.0029	3123.6	6.6	3094.0	18.0	3137.0	7.0	2.2
TSUPB021_31	629	0.69	11.780	0.250	0.3176	0.0058	0.94	0.2447	0.0028	2585.0	20.0	1777.0	29.0	3149.9	6.5	55.2
TSUPB021_32	393	0.43	17.980	0.810	0.5200	0.0240	1.00	0.2496	0.0029	2980.0	36.0	2692.0	94.0	3183.3	6.9	19.5
TSUPB021_33	75	0.26	19.680	0.310	0.5671	0.0087	0.49	0.2495	0.0032	3079.0	16.0	2895.0	36.0	3187.0	13.0	9.4
TSUPB021_34	75	0.41	22.710	0.210	0.6474	0.0058	0.31	0.2536	0.0034	3215.4	8.7	3218.0	23.0	3208.7	8.3	3.0
TSUPB021_35	661	1.01	10.580	0.230	0.2987	0.0049	0.91	0.2542	0.0032	2484.0	20.0	1685.0	24.0	3216.0	11.0	55.1
TSUPB021_36	481	1.02	15.630	0.450	0.4440	0.0120	0.99	0.2549	0.0029	2850.0	26.0	2368.0	53.0	3217.1	7.6	29.2
TSUPB021_37	32	0.41	23.030	0.390	0.6490	0.0100	0.47	0.2570	0.0041	3226.0	17.0	3225.0	41.0	3224.0	16.0	5.1

		Ratios								Age (Ma)						
Analysis	U ppm	Th/U	$^{207}Pb/^{235}U$	Err 2SE abs	$^{206}Pb/^{238}U$	Err 2SE abs	Rho	$^{207}Pb/^{206}Pb$	Err 2SE abs	$^{207}Pb/^{235}U$	Err 2SE abs	$^{206}Pb/^{238}U$	Err 2SE abs	$^{207}Pb/^{206}Pb$	Err 2SE abs	% Disc
TSUPB021_38	141	0.57	16.630	0.270	0.4720	0.0076	0.79	0.2579	0.0032	2915.0	16.0	2492.0	33.0	3227.8	9.3	24.7
TSUPB021_39	140	0.33	23.170	0.230	0.6523	0.0059	0.48	0.2576	0.0034	3233.8	9.4	3237.0	23.0	3228.3	9.2	2.9
TSUPB021_40	1269	1.23	16.200	0.320	0.4471	0.0083	0.89	0.2570	0.0021	2888.0	21.0	2382.0	38.0	3230.3	5.8	30.2
TSUPB021_41	39	0.72	23.010	0.380	0.6491	0.0085	0.73	0.2573	0.0040	3226.0	16.0	3224.0	33.0	3232.0	14.0	3.7
TSUPB021_42	534	0.64	12.520	0.410	0.3195	0.0092	0.96	0.2582	0.0034	2643.0	28.0	1787.0	44.0	3233.0	10.0	57.9
TSUPB021_43	199	0.21	23.520	0.190	0.6563	0.0051	0.54	0.2586	0.0030	3248.3	8.0	3253.0	20.0	3235.8	6.8	2.0
TSUPB021_44	356	0.48	20.880	0.160	0.5832	0.0053	0.53	0.2586	0.0030	3132.6	7.2	2964.0	22.0	3237.5	8.4	9.1
TSUPB021_45	339	0.55	19.170	0.180	0.5372	0.0057	0.79	0.2585	0.0028	3049.8	9.2	2771.0	24.0	3238.0	5.8	15.7
TSUPB021_46	538	0.55	14.410	0.880	0.4060	0.0220	0.97	0.2579	0.0095	2771.0	62.0	2191.0	90.0	3240.0	14.0	36.9
TSUPB021_47	232	1.48	21.180	0.180	0.5904	0.0050	0.49	0.2591	0.0031	3146.2	8.4	2991.0	20.0	3240.3	7.0	8.0
TSUPB021_48	310	0.98	23.370	0.150	0.6526	0.0049	0.37	0.2593	0.0028	3242.4	6.3	3238.0	20.0	3241.9	7.0	2.4
TSUPB021_49	307	0.79	20.920	0.220	0.5834	0.0078	0.70	0.2599	0.0030	3134.0	10.0	2962.0	31.0	3243.0	6.9	9.5
TSUPB021_50	238	0.40	23.700	0.160	0.6575	0.0048	0.56	0.2604	0.0029	3255.8	6.6	3257.0	19.0	3248.8	7.0	2.2
TSUPB021_51	156	0.60	23.790	0.180	0.6580	0.0061	0.52	0.2624	0.0030	3260.0	7.4	3259.0	24.0	3249.0	20.0	3.5
TSUPB021_52	175	0.73	23.710	0.160	0.6564	0.0056	0.63	0.2611	0.0029	3256.4	6.7	3253.0	22.0	3249.6	4.7	2.4
TSUPB021_53	391	0.43	23.520	0.130	0.6541	0.0053	0.84	0.2606	0.0028	3248.5	5.4	3244.0	21.0	3250.8	5.8	2.5
TSUPB021_54	220	0.78	23.560	0.180	0.6565	0.0057	0.63	0.2605	0.0030	3250.2	7.2	3253.0	22.0	3250.8	7.5	2.6
TSUPB021_55	337	0.76	23.330	0.160	0.6528	0.0051	0.60	0.2604	0.0029	3241.6	6.5	3239.0	20.0	3251.0	7.1	2.0
TSUPB021_56	170	0.66	23.570	0.170	0.6559	0.0050	0.52	0.2613	0.0031	3250.3	7.2	3251.0	20.0	3253.8	6.0	2.3
TSUPB021_57	2300	0.88	23.620	0.290	0.6530	0.0067	0.77	0.2610	0.0030	3251.0	13.0	3240.0	27.0	3254.0	16.0	3.0
TSUPB021_58	203	1.33	23.590	0.320	0.6544	0.0085	0.88	0.2624	0.0029	3253.0	13.0	3244.0	33.0	3258.8	7.9	3.2
TSUPB021_59	407	0.72	20.830	0.140	0.5795	0.0055	0.74	0.2618	0.0027	3130.2	6.5	2946.0	22.0	3260.1	5.1	10.3
TSUPB021_60	243	1.15	24.240	0.340	0.6554	0.0100	0.15	0.2621	0.0022	3278.2	15.0	3249.0	42.0	3261.0	11.0	1.8
TSUPB021_61	61	0.73	23.700	0.220	0.6562	0.0056	0.36	0.2624	0.0033	3257.1	9.3	3252.0	22.0	3261.2	8.2	2.3
TSUPB021_62	103	1.04	23.960	0.190	0.6601	0.0050	0.51	0.2629	0.0033	3267.0	7.7	3267.0	19.0	3264.0	13.0	2.2
TSUPB021_63	85	1.49	23.990	0.430	0.6567	0.0093	0.24	0.2625	0.0036	3268.0	18.0	3254.0	37.0	3264.0	14.0	2.9
TSUPB021_64	143	1.78	24.270	0.370	0.6565	0.0110	0.76	0.2626	0.0023	3279.0	16.0	3253.0	45.0	3267.8	7.5	2.4
TSUPB021_65	210	0.94	24.160	0.220	0.6611	0.0059	0.56	0.2641	0.0029	3274.0	9.0	3271.0	23.0	3269.0	10.0	2.7
TSUPB021_66	278	0.74	24.350	0.260	0.6639	0.0057	0.51	0.2630	0.0023	3282.4	11.0	3282.0	22.0	3270.6	5.7	2.2
TSUPB021_67	414	1.75	22.150	0.260	0.5990	0.0067	0.89	0.2641	0.0022	3189.0	11.0	3028.0	27.0	3271.8	4.2	8.8
TSUPB021_68	1655	1.61	24.400	0.280	0.6629	0.0066	0.84	0.2632	0.0023	3284.0	12.0	3278.0	26.0	3275.1	8.2	2.1
TSUPB021_69	4510	2.69	23.850	0.360	0.6499	0.0095	0.46	0.2642	0.0023	3265.0	16.0	3228.0	38.0	3276.2	9.3	2.6
TSUPB021_70	112	0.98	24.460	0.210	0.6662	0.0081	0.58	0.2649	0.0031	3286.8	8.5	3291.0	31.0	3276.2	8.3	2.9
TSUPB021_71	295	2.26	23.730	0.330	0.6367	0.0094	0.74	0.2644	0.0021	3257.0	14.0	3176.0	38.0	3281.0	7.3	3.8
TSUPB021_72	181	2.09	23.870	0.280	0.6466	0.0073	0.66	0.2660	0.0031	3265.0	12.0	3214.0	29.0	3283.0	12.0	4.3
TSUPB021_73	141	0.59	24.440	0.220	0.6649	0.0076	0.67	0.2672	0.0032	3286.0	9.3	3286.0	30.0	3285.7	9.0	2.7
TSUPB021_74	1242	1.68	23.330	0.380	0.6277	0.0092	0.60	0.2666	0.0022	3240.6	17.0	3140.0	37.0	3286.0	10.0	4.9
TSUPB021_75	146	0.59	23.070	0.210	0.6274	0.0066	0.81	0.2665	0.0028	3231.0	8.8	3139.0	27.0	3286.5	4.9	4.7
TSUPB021_76	262	2.57	23.620	0.360	0.6347	0.0100	0.32	0.2664	0.0024	3253.0	16.0	3168.0	42.0	3287.0	11.0	4.9
TSUPB021_77	524	0.62	23.760	0.380	0.6380	0.0110	0.87	0.2671	0.0023	3263.0	17.0	3181.0	44.0	3289.9	8.7	4.1
TSUPB021_78	128	1.10	22.380	0.400	0.5950	0.0050	0.86	0.2673		3200.0		3010.0		3297.3	7.1	10.3
TSUPB021_79	138	1.03	25.390	0.480	0.6721	0.0130	0.76	0.2699	0.0024	3323.0	20.0	3314.0	52.0	3305.4	7.3	2.4
TSUPB021_80	274	0.97	25.150	0.120	0.6731	0.0043	0.45	0.2707	0.0027	3313.9	4.8	3318.0	16.0	3310.1	5.8	1.6
TSUPB021_81	1013	2.78	16.640	0.380	0.4335	0.0076	0.90	0.2748	0.0032	2915.0	23.0	2320.0	34.0	3333.0	14.0	37.3
TSUPB021_82	546	1.70	21.400	0.310	0.5645	0.0056	0.71	0.2748	0.0028	3160.0	14.0	2885.0	23.0	3338.0	10.0	15.0
TSUPB021CA_1	182	0.62	17.210	0.170	0.5803	0.0050	0.71	0.2168	0.0014	2946.0	9.5	2950.0	20.0	2957.0	10.0	0.3
TSUPB021CA_2	323	1.01	17.230	0.180	0.5817	0.0051	0.54	0.2170	0.0017	2950.5	8.7	2955.0	21.0	2958.0	13.0	0.2
TSUPB021CA_3	226	0.66	17.740	0.380	0.5870	0.0150	0.89	0.2177	0.0025	2974.0	21.0	2977.0	60.0	2963.0	18.0	-0.4
TSUPB021CA_4	272	0.76	15.830	0.200	0.5233	0.0058	0.89	0.2183	0.0012	2866.0	12.0	2713.0	25.0	2968.2	8.6	8.5
TSUPB021CA_5	426	0.63	14.590	0.270	0.4815	0.0076	0.96	0.2190	0.0012	2787.0	17.0	2533.0	33.0	2972.8	9.1	14.8
TSUPB021CA_6	250	0.86	16.030	0.110	0.5471	0.0048	0.87	0.2193	0.0010	2878.5	6.6	2813.0	20.0	2975.2	7.4	5.6
TSUPB021CA_7	227	0.67	16.690	0.250	0.5585	0.0059	0.90	0.2195	0.0013	2919.0	14.0	2860.0	25.0	2976.3	9.6	3.9

		Ratios								Age (Ma)						
Analysis	U ppm	Th/U	$^{207}Pb/^{235}U$	Err 2SE abs	$^{206}Pb/^{238}U$	Err 2SE abs	Rho	$^{207}Pb/^{206}Pb$	Err 2SE abs	$^{207}Pb/^{235}U$	Err 2SE abs	$^{206}Pb/^{238}U$	Err 2SE abs	$^{207}Pb/^{206}Pb$	Err 2SE abs	% Disc
TSUPB021CA_8	173	1.08	16.980	0.140	0.5578	0.0038	0.48	0.2205	0.0015	2933.4	7.8	2857.0	16.0	2984.0	11.0	4.1
TSUPB021CA_9	260	0.68	17.910	0.140	0.5880	0.0049	0.68	0.2207	0.0014	2984.6	7.4	2981.0	20.0	2985.0	10.0	0.0
TSUPB021CA_10	289	0.62	17.790	0.170	0.5867	0.0053	0.52	0.2209	0.0018	2978.4	9.3	2976.0	21.0	2987.0	13.0	-0.1
TSUPB021CA_11	310	1.12	14.980	0.350	0.5030	0.0110	0.28	0.2209	0.0016	2811.0	23.0	2626.0	48.0	2987.0	12.0	12.5
TSUPB021CA_12	133	0.69	18.080	0.170	0.5907	0.0043	0.51	0.2211	0.0017	2995.0	8.6	2992.0	18.0	2988.0	12.0	-0.1
TSUPB021CA_13	148	0.87	17.950	0.170	0.5847	0.0044	0.90	0.2213	0.0012	2986.4	8.8	2967.0	18.0	2990.2	8.5	0.7
TSUPB021CA_14	213	0.67	17.720	0.140	0.5860	0.0056	0.65	0.2214	0.0017	2976.4	8.3	2973.0	23.0	2991.0	12.0	0.5
TSUPB021CA_15	263	0.63	18.030	0.150	0.5901	0.0042	0.70	0.2214	0.0011	2991.1	8.0	2992.0	16.0	2992.1	7.8	-0.1
TSUPB021CA_16	193	1.09	18.370	0.130	0.5966	0.0043	0.52	0.2217	0.0016	3009.2	7.0	3016.0	17.0	2993.0	12.0	-0.9
TSUPB021CA_17	196	0.99	16.680	0.210	0.5554	0.0085	0.89	0.2220	0.0012	2916.0	12.0	2847.0	35.0	2994.9	8.7	5.3
TSUPB021CA_18	253	0.87	17.990	0.190	0.5874	0.0054	0.52	0.2222	0.0020	2989.0	10.0	2979.0	22.0	2996.0	14.0	0.4
TSUPB021CA_19	230	0.86	17.880	0.140	0.5874	0.0055	0.60	0.2226	0.0016	2983.3	7.7	2979.0	22.0	2999.0	12.0	0.6
TSUPB021CA_20	311	0.98	17.770	0.110	0.5789	0.0044	0.67	0.2226	0.0011	2978.3	5.5	2947.0	19.0	2999.2	7.6	1.9
TSUPB021CA_21	260	0.58	17.720	0.160	0.5910	0.0110	0.45	0.2234	0.0033	2974.6	8.9	2995.0	43.0	3005.0	24.0	0.7
TSUPB021CA_22	232	0.22	19.320	0.160	0.6139	0.0051	0.92	0.2294	0.0012	3057.5	7.9	3085.0	20.0	3047.8	8.4	-1.0
TSUPB021CA_23	146	0.43	19.230	0.140	0.6059	0.0044	0.41	0.2300	0.0018	3054.1	7.1	3053.0	18.0	3053.0	13.0	-0.2
TSUPB021CA_24	203	0.69	19.110	0.130	0.6046	0.0039	0.28	0.2303	0.0017	3047.3	6.5	3048.0	16.0	3054.0	11.0	0.2
TSUPB021CA_25	271	0.46	19.430	0.220	0.6072	0.0061	0.86	0.2307	0.0014	3063.0	11.0	3058.0	25.0	3056.6	9.7	-0.2
TSUPB021CA_26	180	0.32	19.440	0.150	0.6062	0.0084	0.65	0.2312	0.0023	3063.5	7.7	3054.0	34.0	3060.0	16.0	0.1
TSUPB021CA_27	369	0.38	20.520	0.320	0.5836	0.0072	0.94	0.2532	0.0013	3115.0	15.0	2963.0	29.0	3204.5	7.9	7.5
TSUPB021CA_28	390	0.35	21.090	0.200	0.5992	0.0050	0.84	0.2541	0.0012	3143.9	9.1	3026.0	20.0	3210.1	7.7	5.9
TSUPB021CA_29	500	0.37	21.870	0.270	0.6350	0.0100	0.68	0.2550	0.0026	3178.0	12.0	3170.0	40.0	3216.0	16.0	1.7
TSUPB021CA_30	186	0.48	23.660	0.270	0.6579	0.0082	0.73	0.2573	0.0017	3254.0	11.0	3259.0	32.0	3230.0	10.0	-1.1
TSUPB021CA_31	307	0.50	22.600	0.350	0.6450	0.0120	0.90	0.2573	0.0018	3209.0	15.0	3209.0	48.0	3230.0	11.0	0.9
TSUPB021CA_32	148	0.78	21.420	0.190	0.6128	0.0072	0.69	0.2579	0.0021	3158.8	9.0	3080.0	29.0	3235.0	13.0	4.6
TSUPB021CA_33	192	0.81	23.190	0.170	0.6512	0.0049	0.99	0.2587	0.0014	3234.5	6.9	3233.0	19.0	3238.7	8.8	0.1
TSUPB021CA_34	193	0.31	23.000	0.230	0.6494	0.0070	0.80	0.2590	0.0016	3226.8	9.9	3226.0	27.0	3241.0	10.0	0.5
TSUPB021CA_35	140	0.44	23.680	0.240	0.6568	0.0062	0.54	0.2600	0.0022	3255.1	9.7	3254.0	24.0	3246.0	13.0	-0.3
TSUPB021CA_36	329	0.34	22.730	0.190	0.6349	0.0052	0.76	0.2600	0.0013	3215.1	8.1	3169.0	20.0	3246.7	7.9	2.4
TSUPB021CA_37	204	0.62	22.320	0.230	0.6431	0.0067	0.81	0.2603	0.0023	3197.5	9.8	3201.0	26.0	3248.0	14.0	1.8
TSUPB021CA_38	82	0.46	23.950	0.280	0.6608	0.0072	0.43	0.2599	0.0029	3266.0	11.0	3270.0	28.0	3249.0	16.0	-0.7
TSUPB021CA_39	359	1.13	23.350	0.320	0.6527	0.0056	0.87	0.2606	0.0014	3241.0	14.0	3238.0	22.0	3249.8	8.4	0.4
TSUPB021CA_40	109	0.59	23.480	0.250	0.6543	0.0068	0.61	0.2608	0.0020	3246.0	10.0	3245.0	26.0	3251.0	12.0	0.5
TSUPB021CA_41	100	0.67	23.180	0.240	0.6412	0.0062	0.44	0.2609	0.0023	3234.0	10.0	3193.0	24.0	3251.0	14.0	1.7
TSUPB021CA_42	177	0.65	23.350	0.230	0.6524	0.0057	0.65	0.2607	0.0021	3241.4	9.5	3237.0	22.0	3253.0	13.0	0.4
TSUPB021CA_43	139	1.04	23.080	0.730	0.6480	0.0230	0.99	0.2610	0.0024	3227.0	32.0	3218.0	92.0	3253.0	15.0	1.0
TSUPB021CA_44	347	0.64	22.620	0.150	0.6302	0.0044	0.63	0.2613	0.0012	3210.5	6.7	3150.0	18.0	3254.7	7.0	3.1
TSUPB021CA_45	113	0.47	23.270	0.170	0.6519	0.0045	0.48	0.2617	0.0016	3237.9	7.2	3235.0	18.0	3256.5	9.4	0.6
TSUPB021CA_46	361	0.23	21.390	0.140	0.5912	0.0049	0.74	0.2615	0.0013	3156.4	6.3	2994.0	20.0	3256.6	8.3	8.2
TSUPB021CA_47	160	0.81	23.900	0.210	0.6602	0.0069	0.66	0.2618	0.0021	3263.9	8.6	3267.0	27.0	3259.0	12.0	-0.3
TSUPB021CA_48	93	1.02	24.370	0.180	0.6650	0.0110	0.53	0.2627	0.0035	3283.3	7.4	3286.0	43.0	3263.0	21.0	-0.5
TSUPB021CA_49	264	0.62	24.400	0.150	0.6649	0.0042	0.74	0.2629	0.0015	3284.3	5.9	3286.0	16.0	3264.0	8.9	-0.5
TSUPB021CA_50	120	0.74	24.230	0.200	0.6646	0.0064	0.62	0.2640	0.0019	3277.4	8.1	3284.0	25.0	3270.0	11.0	-0.7
TSUPB021CA_51	277	0.78	23.840	0.150	0.6499	0.0039	0.37	0.2640	0.0018	3261.6	6.2	3227.0	15.0	3270.0	11.0	1.2
TSUPB021CA_52	98	0.81	24.400	0.290	0.6651	0.0071	0.57	0.2643	0.0023	3284.0	12.0	3286.0	27.0	3272.0	13.0	-0.5
TSUPB021CA_53	123	0.94	23.910	0.170	0.6528	0.0044	0.54	0.2643	0.0016	3264.3	7.0	3239.0	17.0	3272.1	9.5	0.9
TSUPB021CA_54	156	0.88	24.130	0.220	0.6640	0.0058	0.65	0.2644	0.0019	3273.4	9.0	3283.0	22.0	3273.0	12.0	-0.2
TSUPB021CA_55	106	0.99	24.350	0.210	0.6639	0.0077	0.40	0.2645	0.0027	3282.1	8.4	3282.0	30.0	3273.0	16.0	0.2
TSUPB021CA_56	160	0.65	24.250	0.240	0.6624	0.0063	0.85	0.2649	0.0017	3278.1	9.7	3282.0	27.0	3275.0	10.0	-0.1
TSUPB021CA_57	228	1.04	24.180	0.150	0.6602	0.0043	0.58	0.2655	0.0016	3275.7	6.0	3268.0	17.0	3279.2	9.6	0.4
TSUPB021CA_58	266	0.55	23.720	0.270	0.6571	0.0057	0.62	0.2656	0.0023	3257.0	11.0	3256.0	22.0	3280.0	14.0	0.6
TSUPB021CA_59	115	0.49	23.870	0.270	0.6600	0.0110	0.64	0.2662	0.0034	3263.0	11.0	3268.0	41.0	3283.0	20.0	0.4
TSUPB021CA_60	70	1.05	24.220	0.260	0.6631	0.0066	0.66	0.2670	0.0020	3278.8	9.9	3279.0	25.0	3290.0	12.0	0.6
TSUPB021CA_61	231	1.02	20.840	0.150	0.6253	0.0064	0.78	0.2706	0.0016	3133.4	7.1	3130.0	25.0	3309.1	9.3	5.3

		Ratios								Age (Ma)						
Analysis	U ppm	Th/U	$^{207}Pb/^{235}U$	Err 2SE abs	$^{206}Pb/^{238}U$	Err 2SE abs	Rho	$^{207}Pb/^{206}Pb$	Err 2SE abs	$^{207}Pb/^{235}U$	Err 2SE abs	$^{206}Pb/^{238}U$	Err 2SE abs	$^{207}Pb/^{206}Pb$	Err 2SE abs	% Disc
TSUPB021CA_62	218	0.84	21.960	0.270	0.6378	0.0080	0.31	0.2707	0.0014	3181.0	12.0	3180.0	31.0	3309.7	8.2	4.1
TSUPB021CA_63	193	0.95	25.470	0.310	0.6779	0.0065	0.63	0.2717	0.0024	3326.0	12.0	3336.0	25.0	3316.0	14.0	-0.3
TSUPB021CA_64	161	0.75	25.210	0.230	0.6733	0.0057	0.58	0.2721	0.0020	3315.9	9.0	3318.0	22.0	3318.0	12.0	-0.1
TSUPB001_1	115	0.49	12.820	0.310	0.4881	0.0110	0.75	0.1878	0.0042	2662.0	22.0	2565.0	48.0	2727.0	17.0	6.2
TSUPB001_2	922	0.79	14.230	0.360	0.5230	0.0130	0.95	0.1960	0.0033	2760.0	23.0	2707.0	53.0	2795.1	7.5	5.3
TSUPB001_3	477	1.03	13.600	0.210	0.4999	0.0088	0.73	0.1975	0.0034	2723.0	14.0	2613.0	38.0	2809.1	7.7	6.1
TSUPB001_4	87	0.67	14.630	0.260	0.5329	0.0095	0.57	0.1989	0.0042	2789.0	17.0	2757.0	41.0	2817.0	14.0	4.9
TSUPB001_5	115	0.64	15.240	0.260	0.5512	0.0096	0.60	0.1985	0.0039	2828.0	17.0	2829.0	40.0	2828.0	13.0	4.2
TSUPB001_6	73	0.59	14.870	0.410	0.5330	0.0130	0.64	0.2004	0.0049	2808.0	26.0	2751.0	53.0	2848.0	14.0	6.6
TSUPB001_7	117	0.67	15.760	0.280	0.5654	0.0100	0.70	0.2022	0.0041	2860.0	17.0	2888.0	42.0	2849.0	13.0	4.7
TSUPB001_8	86	0.71	14.380	0.250	0.5121	0.0083	0.11	0.2029	0.0047	2775.0	16.0	2665.0	36.0	2854.0	15.0	6.3
TSUPB001_9	168	0.93	23.770	0.760	0.6040	0.0170	0.91	0.2853	0.0046	3250.0	31.0	3038.0	70.0	3385.0	12.0	12.6
TSUPB001_10	213	0.45	30.090	0.760	0.6990	0.0170	0.96	0.3079	0.0047	3485.0	25.0	3411.0	66.0	3513.0	12.0	7.9
TSUPB003_1	508	0.11	11.480	0.930	0.3890	0.0290	0.99	0.2164	0.0038	2519.0	74.0	2090.0	130.0	2950.0	11.0	28.2
TSUPB003_2	111	0.27	16.780	0.360	0.5559	0.0099	0.60	0.2214	0.0048	2920.0	21.0	2849.0	41.0	2989.0	15.0	4.9
TSUPB003_3	89	0.58	17.750	0.250	0.5875	0.0110	0.37	0.2221	0.0043	2977.0	13.0	2978.0	43.0	2991.0	15.0	5.2
TSUPB003_4	221	0.11	16.770	0.240	0.5572	0.0085	0.45	0.2216	0.0040	2920.0	14.0	2854.0	35.0	2993.0	12.0	4.8
TSUPB003_5	114	0.53	16.260	0.280	0.5430	0.0096	0.70	0.2215	0.0041	2892.0	17.0	2795.0	40.0	2993.0	11.0	6.0
TSUPB003_6	84	0.28	16.640	0.490	0.5480	0.0160	0.86	0.2207	0.0042	2909.0	30.0	2833.0	66.0	2995.0	13.0	8.2
TSUPB003_7	156	0.08	17.750	0.290	0.5811	0.0093	0.57	0.2202	0.0041	2977.0	16.0	2952.0	38.0	2997.0	11.0	4.5
TSUPB003_8	273	0.10	18.000	0.330	0.5879	0.0100	0.81	0.2218	0.0037	2989.0	18.0	2984.0	43.0	2997.7	9.4	3.9
TSUPB003_9	181	0.34	16.730	0.470	0.5540	0.0160	0.91	0.2217	0.0038	2916.0	27.0	2835.0	68.0	2999.0	12.0	7.3
TSUPB003_10	177	0.32	15.750	0.310	0.5153	0.0120	0.85	0.2236	0.0037	2861.0	19.0	2682.0	50.0	3004.6	6.8	10.3
TSUPB003_11	289	0.28	16.850	0.280	0.5518	0.0097	0.73	0.2244	0.0038	2924.0	16.0	2832.0	40.0	3004.9	7.7	6.0
TSUPB003_12	298	0.47	16.910	0.400	0.5530	0.0130	0.97	0.2232	0.0036	2926.0	21.0	2833.0	53.0	3005.3	7.9	7.1
TSUPB003_13	356	0.54	17.270	0.270	0.5643	0.0100	0.83	0.2224	0.0034	2949.0	15.0	2883.0	41.0	3007.8	6.7	4.6
TSUPB003_14	105	0.98	16.660	0.300	0.5466	0.0096	0.51	0.2227	0.0046	2915.0	18.0	2820.0	40.0	3010.0	12.0	6.4
TSUPB003_15	206	0.30	17.240	0.340	0.5640	0.0120	0.73	0.2242	0.0042	2948.0	18.0	2881.0	51.0	3010.0	15.0	7.1
TSUPB003_16	128	0.41	17.770	0.270	0.5807	0.0090	0.59	0.2241	0.0040	2978.0	15.0	2951.0	37.0	3014.0	11.0	3.4
TSUPB003_17	183	0.27	15.020	0.280	0.4891	0.0100	0.76	0.2246	0.0040	2816.0	18.0	2565.0	44.0	3014.0	11.0	14.0
TSUPB003_18	218	0.34	15.680	0.200	0.5119	0.0077	0.32	0.2248	0.0038	2856.8	12.0	2665.0	33.0	3016.7	9.1	10.7
TSUPB003_19	217	0.48	17.410	0.280	0.5713	0.0097	0.66	0.2255	0.0039	2960.0	16.0	2912.0	40.0	3018.9	8.3	4.6
TSUPB003_20	40	0.10	18.220	0.380	0.5893	0.0110	0.47	0.2244	0.0056	3000.0	21.0	2985.0	45.0	3023.0	21.0	5.4
TSUPB003_21	331	0.44	17.210	0.340	0.5620	0.0120	0.86	0.2265	0.0036	2944.0	18.0	2873.0	48.0	3023.2	8.4	6.2
TSUPB003_22	578	0.57	10.640	0.370	0.3340	0.0130	0.96	0.2268	0.0035	2482.0	33.0	1853.0	65.0	3030.2	7.6	41.9
TSUPB003_23	181	0.20	16.340	0.360	0.5270	0.0130	0.87	0.2272	0.0039	2895.0	21.0	2727.0	57.0	3033.0	11.0	9.9
TSUPB003_24	345	0.41	16.150	0.260	0.5147	0.0091	0.69	0.2293	0.0037	2886.0	15.0	2676.0	39.0	3039.0	11.0	11.5
TSUPB003_25	491	0.14	12.980	0.270	0.4047	0.0098	0.84	0.2318	0.0037	2680.0	20.0	2189.0	45.0	3068.0	8.5	28.9
TSUPB005_1	1330	0.29	5.990	0.210	0.2234	0.0066	0.70	0.1983	0.0042	1975.0	30.0	1299.0	35.0	2813.0	17.0	49.8
TSUPB005_2	912	0.18	8.360	0.670	0.2880	0.0200	0.99	0.2057	0.0039	2238.0	69.0	1618.0	100.0	2868.0	11.0	41.9
TSUPB005_3	622	0.69	6.760	0.230	0.2401	0.0078	0.93	0.2051	0.0032	2084.0	29.0	1386.0	41.0	2872.0	13.0	49.5
TSUPB005_4	2037	0.20	7.188	0.100	0.2516	0.0054	0.82	0.2088	0.0023	2135.5	13.0	1446.0	28.0	2891.8	4.3	48.8
TSUPB005_5	870	0.64	7.780	0.470	0.2710	0.0160	0.99	0.2078	0.0028	2175.0	58.0	1535.0	82.0	2892.0	11.0	44.5
TSUPB005_6	899	0.20	7.394	0.120	0.2556	0.0059	0.91	0.2089	0.0025	2159.0	15.0	1467.0	31.0	2894.9	6.7	48.1
TSUPB005_7	728	0.21	7.950	0.450	0.2740	0.0130	0.96	0.2097	0.0047	2210.0	52.0	1558.0	67.0	2902.0	19.0	44.5
TSUPB005_8	1510	0.68	6.650	0.210	0.2214	0.0084	0.96	0.2107	0.0025	2062.0	29.0	1287.0	45.0	2910.0	7.9	56.4
TSUPB005_9	97	0.17	12.070	0.290	0.4113	0.0093	0.76	0.2098	0.0041	2609.0	22.0	2223.0	42.0	2914.0	15.0	21.7
TSUPB005_10	1094	0.48	9.430	0.240	0.3171	0.0070	0.95	0.2150	0.0037	2376.0	23.0	1775.0	34.0	2943.7	7.7	39.5

		Ratios								Age (Ma)						
Analysis	U ppm	Th/U	$^{207}Pb/^{235}U$	Err 2SE abs	$^{206}Pb/^{238}U$	Err 2SE abs	Rho	$^{207}Pb/^{206}Pb$	Err 2SE abs	$^{207}Pb/^{235}U$	Err 2SE abs	$^{206}Pb/^{238}U$	Err 2SE abs	$^{207}Pb/^{206}Pb$	Err 2SE abs	% Disc
TSUPB005_11	469	0.71	12.920	0.340	0.4310	0.0120	0.93	0.2168	0.0028	2669.0	25.0	2308.0	53.0	2954.5	6.6	20.6
TSUPB005_12	362	0.23	15.590	0.340	0.5180	0.0110	0.83	0.2180	0.0027	2850.0	21.0	2687.0	49.0	2961.5	7.4	9.0
TSUPB005_13	816	0.06	10.520	0.210	0.3505	0.0075	0.89	0.2177	0.0025	2479.0	18.0	1936.0	36.0	2964.5	6.4	34.5
TSUPB005_14	225	0.81	15.880	0.570	0.5320	0.0180	0.96	0.2184	0.0039	2866.0	36.0	2740.0	75.0	2966.4	9.4	8.4
TSUPB005_15	141	0.79	17.040	0.310	0.5623	0.0093	0.67	0.2183	0.0033	2936.0	17.0	2879.0	38.0	2970.0	11.0	4.8
TSUPB005_16	1150	0.22	11.500	0.620	0.3770	0.0180	0.98	0.2190	0.0039	2538.0	54.0	2049.0	88.0	2973.0	12.0	30.2
TSUPB005_17	736	0.56	11.150	0.400	0.3690	0.0130	0.95	0.2194	0.0029	2525.0	34.0	2022.0	60.0	2973.9	9.5	31.8
TSUPB005_18	153	0.71	17.330	0.310	0.5782	0.0083	0.69	0.2192	0.0031	2951.0	17.0	2944.0	35.0	2974.0	12.0	3.8
TSUPB005_19	325	1.25	14.290	0.270	0.4720	0.0086	0.77	0.2195	0.0030	2769.0	17.0	2491.0	37.0	2975.0	10.0	15.9
TSUPB005_20	180	0.95	17.450	0.440	0.5750	0.0140	0.89	0.2188	0.0030	2958.0	24.0	2933.0	56.0	2976.9	9.9	6.1
TSUPB005_21	264	0.62	16.490	0.310	0.5453	0.0087	0.79	0.2205	0.0042	2906.0	19.0	2804.0	36.0	2977.0	10.0	6.5
TSUPB005_22	325	0.52	15.630	0.310	0.5185	0.0086	0.78	0.2204	0.0042	2853.0	19.0	2692.0	37.0	2978.5	8.5	8.9
TSUPB005_23	283	0.78	16.150	0.290	0.5359	0.0089	0.84	0.2200	0.0028	2883.0	18.0	2765.0	37.0	2979.7	7.8	7.4
TSUPB005_24	97	0.92	17.980	0.390	0.5887	0.0100	0.70	0.2190	0.0039	2985.0	21.0	2982.0	42.0	2981.0	12.0	5.6
TSUPB005_25	284	0.83	15.550	0.550	0.5050	0.0160	0.97	0.2205	0.0038	2841.0	34.0	2636.0	71.0	2982.7	6.6	12.1
TSUPB005_26	329	0.95	17.940	0.220	0.5926	0.0063	0.80	0.2204	0.0036	2985.3	12.0	2999.0	25.0	2983.1	6.6	2.6
TSUPB005_27	308	0.48	16.980	0.350	0.5690	0.0110	0.79	0.2197	0.0045	2935.0	21.0	2900.0	45.0	2983.2	6.8	4.4
TSUPB005_28	146	0.89	17.500	0.430	0.5740	0.0110	0.82	0.2212	0.0045	2962.0	23.0	2921.0	47.0	2985.0	13.0	5.0
TSUPB005_29	303	1.11	17.930	0.430	0.5860	0.0110	0.64	0.2204	0.0055	2985.0	23.0	2974.0	43.0	2986.0	12.0	2.7
TSUPB005_30	327	1.23	17.550	0.350	0.5770	0.0110	0.96	0.2206	0.0037	2963.0	20.0	2934.0	46.0	2987.6	6.5	5.0
TSUPB005_31	313	1.05	14.760	0.400	0.4870	0.0130	0.88	0.2209	0.0033	2797.0	26.0	2561.0	56.0	2988.6	9.4	14.0
TSUPB005_32	340	0.85	18.000	0.320	0.5878	0.0082	0.77	0.2212	0.0039	2989.0	16.0	2983.0	34.0	2988.8	8.6	3.8
TSUPB005_33	242	1.08	17.840	0.270	0.5848	0.0081	0.73	0.2203	0.0041	2981.0	15.0	2971.0	32.0	2988.9	9.9	4.0
TSUPB005_34	280	0.40	17.860	0.350	0.5870	0.0120	0.85	0.2214	0.0029	2981.0	18.0	2973.0	48.0	2989.0	10.0	5.3
TSUPB005_35	152	0.69	17.880	0.340	0.5865	0.0098	0.68	0.2211	0.0033	2980.0	18.0	2973.0	40.0	2990.0	11.0	5.1
TSUPB005_36	328	0.41	15.040	0.450	0.4820	0.0140	0.94	0.2209	0.0030	2810.0	30.0	2532.0	64.0	2991.9	8.7	16.2
TSUPB005_37	391	1.42	13.660	0.200	0.4357	0.0074	0.80	0.2219	0.0030	2727.0	14.0	2330.0	33.0	2992.8	9.6	24.1
TSUPB005_38	181	0.28	16.110	0.220	0.5282	0.0073	0.64	0.2223	0.0030	2885.0	14.0	2733.0	31.0	2994.5	9.3	8.4
TSUPB005_39	368	0.39	15.830	0.490	0.5110	0.0140	0.89	0.2216	0.0044	2863.0	30.0	2660.0	61.0	2995.0	16.0	10.7
TSUPB005_40	525	1.03	11.680	0.240	0.3697	0.0086	0.90	0.2225	0.0028	2583.0	20.0	2026.0	40.0	2995.4	7.1	34.7
TSUPB005_41	286	1.20	17.860	0.300	0.5903	0.0086	0.71	0.2208	0.0041	2983.0	17.0	2990.0	35.0	2996.0	11.0	3.6
TSUPB005_42	151	0.98	17.730	0.300	0.5729	0.0082	0.59	0.2222	0.0034	2973.0	16.0	2919.0	34.0	2996.2	9.8	4.8
TSUPB005_43	207	0.88	17.370	0.270	0.5662	0.0094	0.68	0.2216	0.0030	2954.0	15.0	2891.0	39.0	2996.2	9.8	5.0
TSUPB005_44	103	0.32	18.130	0.330	0.5931	0.0082	0.32	0.2228	0.0036	2994.0	17.0	3001.0	33.0	2998.0	10.0	4.5
TSUPB005_45	719	0.46	12.930	0.480	0.4210	0.0140	0.97	0.2218	0.0038	2671.0	36.0	2264.0	66.0	2998.6	8.6	24.8
TSUPB005_46	221	0.35	17.440	0.260	0.5696	0.0082	0.76	0.2221	0.0042	2958.0	15.0	2906.0	34.0	2999.0	10.0	4.1
TSUPB005_47	779	0.52	12.950	0.400	0.4200	0.0120	0.98	0.2225	0.0038	2670.0	27.0	2257.0	52.0	3000.1	6.1	23.8
TSUPB005_48	258	1.11	17.130	0.400	0.5670	0.0120	0.85	0.2227	0.0040	2940.0	22.0	2895.0	51.0	3001.0	11.0	4.6
TSUPB005_49	167	1.19	17.670	0.200	0.5764	0.0068	0.40	0.2226	0.0029	2972.2	11.0	2934.0	28.0	3001.1	8.8	4.1
TSUPB005_50	195	1.00	18.460	0.230	0.5987	0.0069	0.52	0.2228	0.0041	3014.0	12.0	3024.0	28.0	3002.3	8.7	3.9
TSUPB005_51	469	0.50	12.890	0.410	0.4250	0.0120	0.76	0.2212	0.0054	2670.0	29.0	2284.0	52.0	3003.0	12.0	22.9
TSUPB005_52	207	1.13	17.810	0.350	0.5830	0.0110	0.65	0.2229	0.0046	2978.0	19.0	2961.0	44.0	3005.0	14.0	4.3
TSUPB005_53	151	0.55	18.060	0.380	0.5892	0.0099	0.69	0.2234	0.0040	2992.0	21.0	2984.0	40.0	3005.0	15.0	4.8
TSUPB005_54	433	0.39	12.290	0.500	0.4040	0.0140	0.94	0.2228	0.0043	2630.0	39.0	2193.0	64.0	3005.0	12.0	27.1
TSUPB005_55	177	0.96	17.680	0.280	0.5751	0.0078	0.46	0.2225	0.0034	2973.0	15.0	2928.0	32.0	3006.0	10.0	4.6
TSUPB005_56	71	0.71	17.910	0.380	0.5784	0.0110	0.51	0.2239	0.0045	2983.0	21.0	2940.0	44.0	3008.0	12.0	7.0
TSUPB005_57	389	0.37	15.280	0.350	0.4931	0.0100	0.89	0.2235	0.0039	2834.0	22.0	2581.0	44.0	3008.5	8.2	13.8
TSUPB005_58	849	0.19	9.860	0.360	0.3210	0.0130	0.97	0.2243	0.0027	2413.0	32.0	1789.0	62.0	3009.2	7.7	41.4
TSUPB005_59	303	0.78	18.510	0.390	0.6050	0.0110	0.90	0.2249	0.0039	3016.0	20.0	3048.0	46.0	3009.3	6.9	4.3
TSUPB005_60	348	0.51	15.970	0.350	0.5185	0.0100	0.58	0.2244	0.0058	2878.0	23.0	2692.0	43.0	3010.0	18.0	9.2
TSUPB005_61	156	0.43	18.710	0.270	0.6018	0.0070	0.57	0.2247	0.0041	3027.0	14.0	3036.0	28.0	3013.8	9.9	3.5
TSUPB005_62	273	0.29	16.760	0.570	0.5430	0.0170	0.95	0.2242	0.0042	2916.0	33.0	2794.0	72.0	3014.0	11.0	8.3
TSUPB005_63	126	0.59	17.770	0.290	0.5746	0.0100	0.38	0.2258	0.0052	2979.0	15.0	2926.0	41.0	3017.0	16.0	5.3
TSUPB005_64	103	0.74	18.220	0.380	0.5855	0.0098	0.66	0.2251	0.0039	2998.0	20.0	2974.0	39.0	3020.0	13.0	5.2

		Ratios								Age (Ma)						
Analysis	U ppm	Th/U	$^{207}Pb/^{235}U$	Err 2SE abs	$^{206}Pb/^{238}U$	Err 2SE abs	Rho	$^{207}Pb/^{206}Pb$	Err 2SE abs	$^{207}Pb/^{235}U$	Err 2SE abs	$^{206}Pb/^{238}U$	Err 2SE abs	$^{207}Pb/^{206}Pb$	Err 2SE abs	% Disc
TSUPB005_65	53	1.18	18.110	0.430	0.5849	0.0110	0.56	0.2247	0.0051	2998.0	23.0	2973.0	46.0	3022.0	17.0	7.3
TSUPB005_66	486	0.16	16.980	0.220	0.5451	0.0085	0.86	0.2260	0.0025	2934.0	12.0	2804.0	36.0	3022.6	7.3	7.1
TSUPB005_67	492	0.60	17.200	0.360	0.5510	0.0120	0.90	0.2261	0.0026	2942.0	20.0	2825.0	48.0	3022.9	5.8	7.2
TSUPB005_68	212	0.31	14.660	0.250	0.4526	0.0076	0.82	0.2253	0.0029	2791.0	16.0	2409.0	35.0	3025.5	9.7	22.1
TSUPB005_69	288	0.57	18.330	0.300	0.5885	0.0097	0.80	0.2265	0.0029	3007.0	16.0	2981.0	40.0	3027.4	6.7	4.8
TSUPB005_70	350	0.08	16.220	0.400	0.5220	0.0110	0.93	0.2261	0.0037	2886.0	24.0	2707.0	47.0	3027.4	7.5	9.9
TSUPB005_71	142	0.28	18.460	0.360	0.5918	0.0110	0.67	0.2264	0.0036	3011.0	19.0	2994.0	44.0	3030.0	11.0	5.5
TSUPB005_72	943	0.12	10.330	0.560	0.3310	0.0160	0.98	0.2271	0.0044	2459.0	51.0	1837.0	78.0	3031.0	14.0	40.9
TSUPB005_73	351	0.28	15.330	0.390	0.4883	0.0110	0.97	0.2277	0.0029	2831.0	23.0	2561.0	47.0	3032.6	8.3	15.0
TSUPB005_74	211	0.90	17.420	0.450	0.5556	0.0092	0.86	0.2275	0.0047	2953.0	24.0	2847.0	38.0	3033.0	18.0	5.8
TSUPB005_75	274	0.41	17.290	0.270	0.5469	0.0097	0.91	0.2286	0.0028	2949.0	16.0	2811.0	41.0	3037.7	7.2	7.9
TSUPB005_76	151	0.55	17.970	0.300	0.5704	0.0086	0.63	0.2286	0.0034	2986.0	16.0	2908.0	36.0	3042.0	11.0	5.3
TSUPB005_77	349	0.47	16.740	0.310	0.5237	0.0100	0.85	0.2311	0.0029	2921.0	17.0	2717.0	43.0	3051.0	7.8	11.0
TSUPB005_78	253	0.07	17.690	0.390	0.5560	0.0110	0.87	0.2310	0.0040	2977.0	21.0	2845.0	47.0	3055.8	9.6	7.2
TSUPB005_79	379	0.54	12.480	0.640	0.3720	0.0190	0.99	0.2290	0.0040	2625.0	53.0	2024.0	91.0	3056.5	9.5	38.9
TSUPB005_80	242	0.39	19.700	0.280	0.6109	0.0073	0.68	0.2329	0.0041	3077.0	14.0	3073.0	29.0	3070.7	8.6	3.4
TSUPB005_81	347	0.31	19.720	0.600	0.6110	0.0170	0.98	0.2332	0.0039	3070.0	31.0	3067.0	71.0	3076.3	8.1	6.9
TSUPB005_82	3000	0.06	10.710	0.410	0.3320	0.0110	0.96	0.2343	0.0039	2487.0	35.0	1845.0	54.0	3079.0	21.0	40.6
TSUPB005_83	530	0.19	15.610	0.410	0.4740	0.0140	0.93	0.2387	0.0028	2850.0	26.0	2495.0	59.0	3111.7	7.7	20.5
TSUPB005_84	169	0.59	22.010	0.300	0.6421	0.0081	0.72	0.2491	0.0030	3188.0	13.0	3196.0	32.0	3175.0	8.2	3.5
TSUPB030_1	8	0.36	17.500	0.650	0.5480	0.0270	0.72	0.2307	0.0094	2953.0	35.0	2820.0	110.0	3054.0	58.0	5.9
TSUPB030_2	27	0.22	18.500	0.570	0.5580	0.0200	0.66	0.2295	0.0056	3018.0	30.0	2872.0	85.0	3062.0	40.0	6.5
TSUPB006_1	3150	0.07	5.257	0.090	0.2179	0.0071	0.92	0.1751	0.0017	1860.0	15.0	1270.0	38.0	2606.3	8.3	42.6
TSUPB006_2	3330	0.03	11.720	0.430	0.4710	0.0210	0.98	0.1811	0.0018	2575.0	32.0	2478.0	90.0	2664.0	10.0	11.4
TSUPB006_3	6710	0.08	6.850	0.420	0.2710	0.0180	0.99	0.1831	0.0017	2069.0	50.0	1535.0	90.0	2679.3	8.9	39.1
TSUPB006_4	3930	0.05	5.810	0.150	0.2336	0.0084	1.00	0.1843	0.0015	1945.0	22.0	1351.0	44.0	2685.9	6.9	42.7
TSUPB006_5	7330	0.05	6.620	0.097	0.2604	0.0069	0.93	0.1854	0.0015	2062.0	13.0	1491.0	35.0	2697.3	4.8	39.1
TSUPB006_6	2610	0.05	12.860	0.710	0.4990	0.0310	0.98	0.1863	0.0031	2666.0	53.0	2590.0	130.0	2706.0	20.0	13.6
TSUPB006_7	3410	0.07	9.740	0.350	0.3820	0.0150	0.99	0.1860	0.0015	2400.0	33.0	2079.0	69.0	2707.4	4.9	20.4
TSUPB006_8	1200	0.02	9.190	0.680	0.3640	0.0290	0.96	0.1864	0.0044	2369.0	75.0	1990.0	140.0	2710.0	22.0	23.5
TSUPB006_9	1740	0.51	8.990	0.680	0.3490	0.0260	0.98	0.1873	0.0024	2315.0	66.0	1920.0	120.0	2716.0	12.0	26.0
TSUPB006_10	890	0.12	9.930	0.530	0.3910	0.0250	0.80	0.1884	0.0067	2436.0	54.0	2120.0	120.0	2717.0	35.0	21.9
TSUPB006_11	5390	0.05	6.940	0.130	0.2652	0.0074	0.97	0.1895	0.0013	2104.0	16.0	1515.0	38.0	2736.2	3.7	39.7
TSUPB006_12	5150	0.12	7.270	0.230	0.2793	0.0100	0.97	0.1891	0.0015	2138.0	28.0	1585.0	52.0	2737.2	6.6	37.7
TSUPB006_13	6400	0.40	3.740	0.620	0.1290	0.0190	0.98	0.1906	0.0020	1441.0	90.0	768.0	100.0	2739.0	10.0	60.7
TSUPB006_14	4240	0.16	5.750	0.320	0.2220	0.0140	0.99	0.1892	0.0016	1924.0	43.0	1285.0	74.0	2739.1	6.1	47.9
TSUPB006_15	3920	0.64	11.600	1.100	0.4360	0.0410	1.00	0.1900	0.0020	2517.0	76.0	2290.0	170.0	2739.3	9.7	23.4
TSUPB006_16	4530	0.08	11.470	0.770	0.4400	0.0330	0.99	0.1903	0.0022	2534.0	55.0	2300.0	130.0	2745.0	11.0	22.8
TSUPB006_17	3910	0.13	10.600	1.100	0.4070	0.0450	0.99	0.1908	0.0022	2420.0	85.0	2150.0	190.0	2747.0	12.0	30.5
TSUPB006_18	6800	0.06	5.310	0.680	0.2000	0.0270	1.00	0.1914	0.0021	1797.0	98.0	1150.0	140.0	2755.0	10.0	52.1
TSUPB006_19	2760	0.25	15.210	0.840	0.5670	0.0330	0.98	0.1924	0.0027	2816.0	50.0	2890.0	130.0	2760.0	16.0	11.9
TSUPB006_20	4170	0.08	9.610	0.470	0.3630	0.0200	0.99	0.1936	0.0016	2389.0	42.0	1988.0	89.0	2776.4	5.9	27.5
TSUPB006_21	6660	0.07	15.030	0.970	0.5680	0.0430	0.99	0.1943	0.0023	2791.0	61.0	2860.0	170.0	2777.0	16.0	21.8
TSUPB006_22	4120	0.08	10.260	0.590	0.3780	0.0240	0.99	0.1945	0.0028	2441.0	49.0	2050.0	110.0	2779.0	18.0	25.1
TSUPB006_23	524	0.23	8.020	0.390	0.2940	0.0130	0.97	0.1972	0.0028	2220.0	47.0	1658.0	66.0	2801.0	19.0	38.8
TSUPB006_24	5040	0.27	9.460	0.700	0.3460	0.0230	0.99	0.1967	0.0020	2356.0	62.0	1910.0	110.0	2802.0	11.0	28.1
TSUPB006_25	5330	0.07	8.470	0.220	0.3180	0.0120	0.97	0.1958	0.0016	2276.0	23.0	1774.0	58.0	2805.6	8.3	33.7
TSUPB006_26	11700	0.98	7.480	0.240	0.2710	0.0120	0.99	0.2011	0.0018	2164.0	27.0	1540.0	58.0	2832.9	9.2	43.3
TSUPB006_27	11400	0.12	9.820	0.420	0.3550	0.0180	0.98	0.2012	0.0025	2405.0	37.0	1947.0	85.0	2833.0	17.0	28.4
TSUPB006_28	10600	0.13	6.430	0.410	0.2350	0.0180	0.98	0.2015	0.0030	2023.0	59.0	1348.0	94.0	2835.0	20.0	48.9

		Ratios								Age (Ma)						
Analysis	U ppm	Th/U	$^{207}Pb/^{235}U$	Err 2SE abs	$^{206}Pb/^{238}U$	Err 2SE abs	Rho	$^{207}Pb/^{206}Pb$	Err 2SE abs	$^{207}Pb/^{235}U$	Err 2SE abs	$^{206}Pb/^{238}U$	Err 2SE abs	$^{207}Pb/^{206}Pb$	Err 2SE abs	% Disc
TSUPB006_29	6010	0.04	16.700	2.200	0.6050	0.0800	1.00	0.2013	0.0022	2910.0	120.0	2980.0	300.0	2838.0	16.0	28.3
TSUPB006_30	6560	0.12	10.900	1.100	0.3910	0.0430	1.00	0.2031	0.0026	2457.0	77.0	2050.0	170.0	2847.0	17.0	38.0
TSUPB006_31	8240	0.08	8.110	0.110	0.2867	0.0078	0.95	0.2040	0.0024	2242.0	12.0	1624.0	39.0	2860.0	14.0	41.6
TSUPB006_32	6210	0.29	8.740	0.300	0.3080	0.0120	0.92	0.2042	0.0026	2308.0	32.0	1725.0	58.0	2864.0	16.0	38.0
TSUPB006_33	5890	0.06	8.890	0.450	0.3130	0.0200	0.99	0.2072	0.0028	2310.0	41.0	1745.0	93.0	2883.0	17.0	40.1
TSUPB006_34	10880	0.33	7.226	0.095	0.2526	0.0073	0.86	0.2117	0.0018	2138.0	11.0	1451.0	37.0	2919.5	9.0	48.6
TSUPB011_1	9	0.00	10.260	0.620	0.4500	0.0160	0.13	0.1690	0.0110	2467.0	56.0	2387.0	73.0	2556.0	57.0	17.0
TSUPB011_2	19	0.00	10.530	0.440	0.4560	0.0130	0.34	0.1698	0.0074	2480.0	38.0	2416.0	59.0	2563.0	38.0	11.5
TSUPB011_3	12	0.00	11.660	0.670	0.4780	0.0170	0.50	0.1776	0.0090	2559.0	53.0	2511.0	73.0	2628.0	42.0	11.2
TSUPB011_4	18	0.00	11.530	0.460	0.4740	0.0140	0.52	0.1747	0.0058	2560.0	38.0	2498.0	62.0	2632.0	40.0	9.7
TSUPB011_5	26	0.00	11.310	0.430	0.4575	0.0100	0.29	0.1777	0.0068	2537.0	36.0	2426.0	46.0	2635.0	39.0	9.6
TSUPB011_6	19	0.00	11.460	0.730	0.4880	0.0150	0.12	0.1720	0.0120	2569.0	59.0	2558.0	65.0	2635.0	56.0	11.0
TSUPB011_7	10	0.00	12.150	0.690	0.4950	0.0160	0.27	0.1769	0.0095	2609.0	52.0	2596.0	69.0	2641.0	53.0	13.6
TSUPB011_8	18	0.00	11.240	0.460	0.4600	0.0140	0.47	0.1778	0.0068	2545.0	38.0	2436.0	63.0	2643.0	33.0	11.1
TSUPB011_9	14	0.00	12.400	0.610	0.5010	0.0170	0.48	0.1798	0.0082	2645.0	46.0	2612.0	71.0	2665.0	39.0	11.7
TSUPB011_10	16	0.00	12.360	0.540	0.4930	0.0150	0.46	0.1804	0.0071	2616.0	42.0	2591.0	63.0	2671.0	40.0	10.3
TSUPB011_11	13	0.00	13.610	0.630	0.5410	0.0160	0.41	0.1852	0.0072	2723.0	43.0	2790.0	67.0	2681.0	38.0	10.5
TSUPB011_12	17	0.00	13.270	0.540	0.5310	0.0140	0.42	0.1842	0.0070	2714.0	39.0	2741.0	60.0	2695.0	34.0	9.1
TSUPB011_13	45	0.01	14.110	0.630	0.5430	0.0170	0.74	0.1834	0.0055	2749.0	42.0	2800.0	68.0	2696.0	33.0	8.7
TSUPB011_14	29	0.00	13.330	0.430	0.5180	0.0130	0.46	0.1856	0.0060	2702.0	31.0	2687.0	57.0	2702.0	33.0	9.5
TSUPB011_15	10	0.00	11.950	0.780	0.4620	0.0190	0.35	0.1860	0.0110	2576.0	58.0	2466.0	78.0	2702.0	52.0	13.9
TSUPB011_16	38	0.00	12.420	0.390	0.4890	0.0140	0.38	0.1867	0.0060	2632.0	29.0	2562.0	59.0	2712.0	30.0	10.1
TSUPB011_17	26	0.03	12.560	0.500	0.5040	0.0140	0.41	0.1834	0.0072	2639.0	37.0	2627.0	61.0	2713.0	40.0	8.5
TSUPB011_18	36	0.00	13.790	0.550	0.5310	0.0150	0.67	0.1888	0.0055	2728.0	38.0	2742.0	61.0	2715.0	29.0	7.6
TSUPB011_19	34	0.00	14.730	0.580	0.5550	0.0140	0.78	0.1879	0.0049	2780.0	34.0	2843.0	57.0	2715.0	25.0	8.1
TSUPB011_20	13	0.00	12.940	0.660	0.5080	0.0180	0.39	0.1876	0.0075	2672.0	49.0	2639.0	76.0	2716.0	46.0	11.6
TSUPB011_21	27	0.00	13.880	0.400	0.5410	0.0140	0.36	0.1870	0.0050	2738.0	28.0	2782.0	57.0	2718.0	28.0	9.2
TSUPB011_22	44	0.03	13.460	0.400	0.5250	0.0170	0.47	0.1889	0.0051	2705.0	28.0	2715.0	72.0	2721.0	27.0	10.8
TSUPB011_23	24	0.00	13.260	0.490	0.5190	0.0130	0.24	0.1873	0.0075	2694.0	37.0	2701.0	52.0	2722.0	39.0	8.1
TSUPB011_24	26	0.00	11.760	0.380	0.4573	0.0110	0.41	0.1898	0.0059	2596.0	31.0	2430.0	51.0	2723.0	32.0	11.1
TSUPB011_25	44	0.00	13.250	0.340	0.5090	0.0130	0.53	0.1886	0.0041	2692.0	25.0	2648.0	53.0	2724.0	18.0	7.7
TSUPB011_26	35	0.00	13.180	0.400	0.5050	0.0120	0.56	0.1861	0.0051	2689.0	28.0	2644.0	50.0	2726.0	26.0	6.4
TSUPB011_27	19	0.00	13.460	0.570	0.5270	0.0160	0.32	0.1872	0.0080	2702.0	41.0	2732.0	70.0	2732.0	36.0	12.2
TSUPB011_28	26	0.00	13.420	0.470	0.5170	0.0160	0.51	0.1862	0.0065	2709.0	34.0	2691.0	71.0	2734.0	30.0	9.9
TSUPB011_29	25	0.00	13.680	0.530	0.5290	0.0150	0.58	0.1863	0.0061	2721.0	35.0	2731.0	65.0	2739.0	31.0	9.3
TSUPB011_30	47	0.00	12.540	0.340	0.4849	0.0110	0.38	0.1911	0.0049	2646.0	26.0	2546.0	49.0	2740.0	24.0	8.9
TSUPB011_31	11	0.00	12.720	0.740	0.4840	0.0170	0.30	0.1890	0.0110	2644.0	55.0	2539.0	74.0	2740.0	54.0	14.4
TSUPB011_32	40	0.00	13.900	0.410	0.5281	0.0110	0.42	0.1892	0.0054	2738.0	29.0	2731.0	47.0	2741.0	27.0	7.7
TSUPB011_33	33	0.00	13.460	0.510	0.5080	0.0130	0.41	0.1910	0.0076	2705.0	36.0	2646.0	55.0	2745.0	47.0	8.0
TSUPB011_34	17	0.00	13.390	0.540	0.5030	0.0150	0.44	0.1891	0.0072	2707.0	39.0	2621.0	65.0	2745.0	38.0	11.9
TSUPB011_35	42	0.00	13.030	0.370	0.5020	0.0120	0.45	0.1897	0.0045	2686.0	26.0	2620.0	50.0	2747.0	25.0	7.8
TSUPB011_36	22	0.00	14.480	0.550	0.5520	0.0170	0.39	0.1943	0.0066	2784.0	37.0	2827.0	68.0	2747.0	33.0	10.6
TSUPB011_37	40	0.06	12.500	0.460	0.4850	0.0160	0.68	0.1910	0.0052	2646.0	34.0	2549.0	71.0	2748.0	24.0	10.8
TSUPB011_38	36	0.00	13.180	0.330	0.5049	0.0110	0.38	0.1900	0.0050	2693.0	24.0	2632.0	48.0	2750.0	23.0	7.6
TSUPB011_39	44	0.00	13.230	0.410	0.5020	0.0130	0.59	0.1903	0.0047	2702.0	30.0	2621.0	55.0	2751.0	25.0	8.8
TSUPB011_40	22	0.02	14.140	0.430	0.5350	0.0150	0.37	0.1934	0.0065	2757.0	30.0	2758.0	64.0	2752.0	31.0	10.0
TSUPB011_41	44	0.00	13.510	0.390	0.5171	0.0110	0.49	0.1902	0.0051	2716.0	26.0	2684.0	48.0	2753.0	22.0	7.2
TSUPB011_42	46	0.02	14.290	0.360	0.5470	0.0130	0.62	0.1900	0.0043	2767.0	25.0	2810.0	55.0	2753.0	24.0	7.6
TSUPB011_43	29	0.23	13.840	0.650	0.5290	0.0210	0.64	0.1917	0.0068	2727.0	44.0	2741.0	85.0	2753.0	31.0	9.7
TSUPB011_44	34	0.00	13.640	0.410	0.5220	0.0130	0.47	0.1905	0.0055	2717.0	28.0	2702.0	57.0	2757.0	30.0	8.4
TSUPB011_45	46	0.00	12.580	0.340	0.4800	0.0140	0.55	0.1924	0.0049	2649.0	26.0	2524.0	63.0	2757.0	25.0	10.6
TSUPB011_46	41	0.00	13.750	0.410	0.5207	0.0110	0.40	0.1891	0.0053	2736.0	30.0	2700.0	48.0	2759.0	28.0	7.7

		Ratios								Age (Ma)						
Analysis	U ppm	Th/U	$^{207}Pb/^{235}U$	Err 2SE abs	$^{206}Pb/^{238}U$	Err 2SE abs	Rho	$^{207}Pb/^{206}Pb$	Err 2SE abs	$^{207}Pb/^{235}U$	Err 2SE abs	$^{206}Pb/^{238}U$	Err 2SE abs	$^{207}Pb/^{206}Pb$	Err 2SE abs	% Disc
TSUPB011_47	18	0.00	13.260	0.550	0.5120	0.0150	0.44	0.1931	0.0072	2700.0	39.0	2667.0	64.0	2759.0	36.0	10.1
TSUPB011_48	15	0.00	12.730	0.490	0.4940	0.0140	0.25	0.1872	0.0076	2668.0	36.0	2585.0	60.0	2762.0	45.0	12.2
TSUPB011_49	24	0.00	14.210	0.670	0.5470	0.0210	0.42	0.1914	0.0098	2771.0	41.0	2808.0	86.0	2765.0	54.0	10.8
TSUPB011_50	31	0.00	13.630	0.520	0.5180	0.0190	0.63	0.1924	0.0060	2718.0	36.0	2680.0	80.0	2767.0	25.0	11.1
TSUPB011_51	43	0.01	14.060	0.380	0.5415	0.0110	0.47	0.1905	0.0042	2755.0	25.0	2786.0	48.0	2769.0	23.0	7.4
TSUPB011_52	25	0.00	13.560	0.440	0.5140	0.0140	0.33	0.1958	0.0063	2711.0	30.0	2671.0	59.0	2769.0	33.0	9.1
TSUPB011_53	28	0.01	12.940	0.480	0.5010	0.0140	0.52	0.1926	0.0065	2683.0	39.0	2615.0	60.0	2772.0	30.0	9.1
TSUPB011_54	43	0.00	14.870	0.400	0.5537	0.0110	0.51	0.1951	0.0050	2800.0	26.0	2838.0	48.0	2774.0	22.0	7.0
TSUPB011_55	38	0.00	14.160	0.390	0.5310	0.0130	0.32	0.1958	0.0052	2756.0	26.0	2742.0	55.0	2775.0	29.0	7.2
TSUPB011_56	40	0.00	13.910	0.340	0.5247	0.0110	0.35	0.1939	0.0048	2754.0	25.0	2716.0	48.0	2783.0	20.0	7.3
TSUPB011_57	33	0.00	13.300	0.430	0.5033	0.0110	0.46	0.1934	0.0057	2702.0	30.0	2632.0	47.0	2784.0	30.0	7.6
TSUPB011_58	39	0.00	14.620	0.390	0.5340	0.0130	0.44	0.1959	0.0052	2785.0	25.0	2755.0	55.0	2784.0	24.0	7.7
TSUPB011_59	43	0.00	12.690	0.300	0.4776	0.0100	0.48	0.1959	0.0045	2655.0	23.0	2515.0	45.0	2786.0	20.0	9.4
TSUPB011_60	30	0.00	13.370	0.420	0.5020	0.0130	0.58	0.1939	0.0052	2706.0	30.0	2627.0	56.0	2787.0	24.0	8.7
TSUPB011_61	44	0.00	14.490	0.430	0.5390	0.0120	0.62	0.1941	0.0049	2779.0	28.0	2776.0	51.0	2788.0	23.0	8.0
TSUPB011_62	45	0.00	14.380	0.410	0.5380	0.0130	0.72	0.1960	0.0037	2774.0	26.0	2769.0	55.0	2789.0	18.0	8.0
TSUPB011_63	91	-0.01	11.840	0.450	0.4440	0.0140	0.87	0.1967	0.0045	2579.0	41.0	2365.0	67.0	2790.0	23.0	12.7
TSUPB011_64	36	0.00	14.140	0.440	0.5300	0.0130	0.56	0.1939	0.0053	2754.0	29.0	2736.0	54.0	2791.0	26.0	7.6
TSUPB011_65	22	0.00	14.590	0.510	0.5390	0.0150	0.14	0.1964	0.0061	2783.0	32.0	2774.0	62.0	2791.0	30.0	8.9
TSUPB011_66	17	0.00	13.870	0.590	0.5260	0.0160	0.47	0.1937	0.0071	2736.0	39.0	2719.0	66.0	2791.0	42.0	11.5
TSUPB011_67	32	0.00	13.080	0.360	0.4928	0.0110	0.37	0.1942	0.0059	2683.0	25.0	2580.0	49.0	2793.0	22.0	10.1
TSUPB011_68	41	0.00	14.150	0.390	0.5315	0.0110	0.42	0.1975	0.0051	2753.0	27.0	2746.0	47.0	2795.0	27.0	7.5
TSUPB011_69	16	0.00	12.880	0.420	0.4820	0.0140	0.22	0.1953	0.0070	2667.0	31.0	2535.0	60.0	2796.0	30.0	13.1
TSUPB011_70	24	0.02	13.480	0.610	0.4940	0.0130	0.60	0.1947	0.0070	2702.0	42.0	2592.0	60.0	2799.0	30.0	10.9
TSUPB011_71	45	0.00	14.450	0.400	0.5450	0.0130	0.62	0.1952	0.0047	2781.0	26.0	2807.0	52.0	2800.0	18.0	7.5
TSUPB011_72	24	0.01	13.650	0.720	0.5070	0.0210	0.34	0.1982	0.0100	2729.0	47.0	2674.0	98.0	2800.0	45.0	10.5
TSUPB011_73	23	0.02	13.920	0.490	0.5270	0.0150	0.43	0.1907	0.0064	2742.0	34.0	2725.0	63.0	2803.0	36.0	9.6
TSUPB011_74	32	0.00	14.130	0.460	0.5220	0.0140	0.32	0.2002	0.0061	2758.0	31.0	2704.0	58.0	2804.0	30.0	9.0
TSUPB011_75	41	0.00	15.000	0.430	0.5490	0.0140	0.56	0.1986	0.0049	2819.0	26.0	2818.0	56.0	2806.0	22.0	8.4
TSUPB011_76	35	0.00	14.620	0.440	0.5470	0.0130	0.53	0.1954	0.0050	2794.0	29.0	2808.0	53.0	2808.0	26.0	7.3
TSUPB011_77	27	0.01	14.820	0.460	0.5390	0.0140	0.51	0.1968	0.0056	2803.0	30.0	2777.0	59.0	2819.0	24.0	7.3
TSUPB011_78	47	0.20	12.880	0.450	0.4688	0.0100	0.65	0.2018	0.0069	2661.0	32.0	2482.0	44.0	2823.0	44.0	12.4
TSUPB011_79	31	0.00	14.020	0.680	0.5180	0.0180	0.34	0.1973	0.0095	2753.0	44.0	2687.0	76.0	2825.0	49.0	7.9
TSUPB011_80	32	0.00	14.920	0.640	0.5500	0.0150	0.47	0.1994	0.0079	2810.0	39.0	2825.0	60.0	2834.0	34.0	7.1
TSUPB011_81	14	0.00	13.390	0.540	0.4880	0.0150	0.38	0.2001	0.0077	2714.0	38.0	2561.0	63.0	2837.0	35.0	12.5
TSUPB011_82	27	0.00	15.070	0.480	0.5350	0.0120	0.27	0.2048	0.0064	2819.0	29.0	2765.0	50.0	2879.0	28.0	8.5
TSUPB011_83	14	0.00	13.700	1.100	0.4960	0.0240	0.12	0.2060	0.0150	2752.0	71.0	2590.0	100.0	2882.0	85.0	14.4
TSUPB011_84	23	0.43	15.760	0.610	0.5420	0.0190	0.71	0.2136	0.0065	2854.0	37.0	2784.0	80.0	2935.0	29.0	12.0
TSUPB011_85	300	0.41	16.520	0.340	0.5604	0.0100	0.90	0.2150	0.0022	2910.0	19.0	2867.0	42.0	2946.8	9.5	4.1
TSUPB004_1	3720	1.32	4.401	0.140	0.1663	0.0048	0.97	0.1935	0.0035	1711.0	26.0	991.0	26.0	2772.7	5.5	57.6
TSUPB004_2	1020	0.18	5.660	0.610	0.2070	0.0200	0.99	0.1962	0.0042	1892.0	91.0	1200.0	110.0	2801.0	18.0	52.7
TSUPB004_3	608	0.17	6.770	0.330	0.2422	0.0110	0.99	0.2011	0.0027	2076.0	42.0	1394.0	56.0	2835.0	12.0	48.5
TSUPB004_4	1125	0.26	6.157	0.140	0.2204	0.0045	0.73	0.2026	0.0037	1999.0	21.0	1284.0	24.0	2846.7	6.8	51.9
TSUPB004_5	1044	0.16	7.410	0.230	0.2650	0.0075	0.97	0.2043	0.0037	2157.0	27.0	1514.0	38.0	2857.0	8.7	44.9
TSUPB004_6	646	0.19	7.001	0.110	0.2491	0.0055	0.79	0.2043	0.0024	2110.6	14.0	1434.0	28.0	2863.2	9.0	48.0
TSUPB004_7	1187	0.23	6.637	0.150	0.2335	0.0044	0.75	0.2050	0.0036	2063.0	20.0	1352.0	23.0	2863.6	6.1	50.9
TSUPB004_8	709	0.17	8.340	0.420	0.2970	0.0140	0.98	0.2048	0.0027	2266.0	45.0	1683.0	70.0	2865.0	11.0	40.3
TSUPB004_9	1108	0.17	7.750	0.200	0.2737	0.0064	0.93	0.2062	0.0036	2200.0	23.0	1562.0	32.0	2873.8	7.6	44.2
TSUPB004_10	1840	0.19	8.290	0.440	0.2940	0.0140	0.99	0.2063	0.0035	2259.0	46.0	1664.0	72.0	2875.6	5.9	40.1
TSUPB004_11	867	0.16	8.030	0.240	0.2823	0.0072	0.95	0.2062	0.0037	2232.0	26.0	1602.0	36.0	2879.4	8.4	42.1
TSUPB004_12	1623	0.25	7.357	0.140	0.2581	0.0044	0.80	0.2068	0.0036	2155.0	17.0	1480.0	23.0	2880.7	4.5	47.2
TSUPB004_13	718	0.20	8.880	0.270	0.3106	0.0100	0.95	0.2068	0.0025	2325.0	28.0	1741.0	50.0	2888.5	6.5	38.5

		Ratios								Age (Ma)						
Analysis	U ppm	Th/U	$^{207}Pb/^{235}U$	Err 2SE abs	$^{206}Pb/^{238}U$	Err 2SE abs	Rho	$^{207}Pb/^{206}Pb$	Err 2SE abs	$^{207}Pb/^{235}U$	Err 2SE abs	$^{206}Pb/^{238}U$	Err 2SE abs	$^{207}Pb/^{206}Pb$	Err 2SE abs	% Disc
TSUPB004_14	925	0.21	11.400	1.200	0.3910	0.0390	1.00	0.2084	0.0029	2472.0	79.0	2050.0	150.0	2890.0	14.0	32.9
TSUPB004_15	821	0.16	8.980	0.320	0.3148	0.0100	0.98	0.2091	0.0037	2335.0	33.0	1761.0	50.0	2896.4	6.8	37.5
TSUPB004_16	1048	0.14	8.910	0.160	0.3083	0.0047	0.83	0.2091	0.0036	2327.0	17.0	1732.0	23.0	2897.0	6.5	39.2
TSUPB004_17	921	0.14	7.557	0.150	0.2636	0.0045	0.80	0.2088	0.0035	2178.9	17.0	1508.0	23.0	2898.1	5.1	47.0
TSUPB004_18	856	0.22	8.290	0.190	0.2876	0.0060	0.91	0.2093	0.0037	2261.0	21.0	1629.0	30.0	2898.6	6.7	42.5
TSUPB004_19	1096	0.18	8.493	0.150	0.2959	0.0045	0.83	0.2087	0.0035	2284.4	16.0	1671.0	22.0	2901.7	4.8	41.0
TSUPB004_20	650	0.15	11.420	0.510	0.3930	0.0170	0.99	0.2088	0.0029	2540.0	49.0	2131.0	80.0	2905.6	9.8	26.7
TSUPB004_21	837	0.14	9.760	0.330	0.3362	0.0110	0.97	0.2100	0.0033	2404.0	31.0	1865.0	54.0	2906.0	13.0	33.6
TSUPB004_22	653	0.15	11.870	0.760	0.4060	0.0250	0.98	0.2097	0.0027	2564.0	62.0	2180.0	110.0	2909.0	10.0	24.6
TSUPB004_23	449	0.14	10.750	0.220	0.3697	0.0080	0.95	0.2105	0.0026	2499.0	19.0	2027.0	38.0	2909.2	7.6	28.8
TSUPB004_24	545	0.24	9.580	0.130	0.3281	0.0062	0.77	0.2105	0.0026	2395.0	12.0	1829.0	30.0	2910.9	8.5	36.1
TSUPB004_25	1119	0.15	10.220	0.250	0.3532	0.0092	0.93	0.2108	0.0024	2456.0	24.0	1948.0	44.0	2911.8	8.4	32.5
TSUPB004_26	1158	0.20	10.760	0.450	0.3700	0.0150	0.98	0.2108	0.0025	2489.0	37.0	2021.0	69.0	2914.2	9.3	30.4
TSUPB004_27	849	0.30	8.150	0.200	0.2804	0.0064	0.92	0.2113	0.0037	2244.0	23.0	1592.0	32.0	2916.0	7.6	44.3
TSUPB004_28	871	0.17	9.150	0.170	0.3151	0.0051	0.87	0.2116	0.0036	2352.0	17.0	1765.0	25.0	2916.9	4.6	38.5
TSUPB004_29	817	0.19	8.730	0.170	0.2997	0.0050	0.89	0.2117	0.0036	2309.0	18.0	1689.0	25.0	2918.8	5.5	41.4
TSUPB004_30	718	0.17	9.120	0.220	0.3100	0.0084	0.96	0.2123	0.0022	2347.0	22.0	1739.0	41.0	2921.6	5.1	40.0
TSUPB004_31	1000	0.17	9.400	0.350	0.3214	0.0110	0.98	0.2118	0.0036	2379.0	34.0	1798.0	51.0	2924.4	7.9	37.4
TSUPB004_32	340	0.13	14.700	0.510	0.4990	0.0170	0.97	0.2126	0.0025	2786.0	34.0	2601.0	72.0	2931.6	7.0	11.7
TSUPB004_33	735	0.16	11.100	0.700	0.3820	0.0230	0.99	0.2132	0.0036	2514.0	58.0	2070.0	110.0	2931.7	7.7	27.8
TSUPB004_34	633	0.17	10.550	0.430	0.3600	0.0130	0.98	0.2135	0.0036	2476.0	38.0	1976.0	63.0	2932.7	6.5	31.9
TSUPB004_35	1110	0.18	10.570	0.280	0.3597	0.0090	0.97	0.2146	0.0036	2485.0	25.0	1991.0	45.0	2935.6	4.7	31.4
TSUPB004_36	1098	0.23	7.720	0.180	0.2626	0.0058	0.90	0.2147	0.0036	2199.0	21.0	1503.0	29.0	2946.2	7.2	49.1
TSUPB004_37	837	0.13	15.500	0.380	0.5250	0.0110	0.93	0.2161	0.0026	2844.0	24.0	2717.0	49.0	2954.7	6.2	8.5
TSUPB004_38	417	0.14	15.620	0.230	0.5184	0.0090	0.91	0.2163	0.0023	2852.0	14.0	2691.0	38.0	2954.7	6.3	8.8
TSUPB004_39	725	0.12	15.820	0.240	0.5286	0.0082	0.88	0.2166	0.0024	2864.0	14.0	2734.0	35.0	2955.4	6.1	7.2
TSUPB004_40	372	0.12	15.230	0.340	0.5120	0.0120	0.93	0.2167	0.0025	2828.0	22.0	2661.0	50.0	2956.4	8.3	9.3
TSUPB004_41	761	0.12	16.090	0.290	0.5325	0.0100	0.85	0.2174	0.0027	2883.0	17.0	2750.0	43.0	2963.6	6.8	7.1
TSUPB004_42	1536	0.34	6.630	0.210	0.2194	0.0066	0.95	0.2193	0.0036	2058.0	28.0	1277.0	35.0	2976.2	5.6	58.1
TSUPB004_43	669	0.13	11.540	0.220	0.3842	0.0070	0.92	0.2192	0.0036	2569.0	19.0	2095.0	33.0	2978.5	5.9	29.5
TSUPB004_44	714	0.13	10.730	0.190	0.3557	0.0061	0.88	0.2196	0.0036	2498.0	17.0	1964.0	30.0	2979.5	4.4	34.1
TSUPB004_45	489	0.15	11.370	0.380	0.3760	0.0140	0.97	0.2207	0.0026	2545.0	32.0	2054.0	65.0	2981.0	11.0	32.1
TSUPB004_46	1122	0.17	7.400	0.230	0.2434	0.0073	0.97	0.2211	0.0036	2164.0	28.0	1407.0	38.0	2987.4	6.2	54.3
TSUPB004_47	642	0.20	12.190	0.340	0.3990	0.0120	0.98	0.2222	0.0035	2615.0	27.0	2158.0	55.0	3000.3	4.8	28.2
TSUPB004_48	1070	0.16	9.250	0.540	0.3030	0.0170	0.99	0.2232	0.0036	2351.0	52.0	1707.0	85.0	3004.7	6.1	44.2
TSUPB004_49	875	0.10	8.278	0.120	0.2677	0.0062	0.76	0.2231	0.0027	2264.0	13.0	1529.0	31.0	3006.0	10.0	50.9
TSUPB004_50	822	0.19	10.780	0.170	0.3487	0.0052	0.84	0.2258	0.0036	2505.0	15.0	1930.0	25.0	3017.0	5.9	37.0
TSUPB004_51	1240	0.17	6.570	0.250	0.2114	0.0082	0.98	0.2253	0.0038	2048.0	32.0	1234.0	43.0	3018.8	9.2	61.2
TSUPB012_1	923	0.50	5.790	0.350	0.2170	0.0120	0.99	0.1907	0.0037	1929.0	53.0	1261.0	66.0	2749.0	14.0	48.9
TSUPB012_2	230	0.24	5.080	0.480	0.1840	0.0240	0.98	0.1930	0.0110	1828.0	81.0	1090.0	130.0	2773.0	61.0	54.6
TSUPB012_3	769	0.39	6.340	0.290	0.2380	0.0110	0.96	0.1950	0.0039	2029.0	40.0	1373.0	56.0	2786.0	15.0	46.4
TSUPB012_4	671	0.59	6.220	0.280	0.2260	0.0100	0.98	0.1977	0.0037	1996.0	39.0	1318.0	55.0	2803.0	12.0	48.8
TSUPB012_5	936	0.94	5.930	0.340	0.2160	0.0120	0.98	0.1976	0.0036	1946.0	48.0	1255.0	63.0	2807.0	13.0	52.2
TSUPB012_6	868	0.45	7.630	0.160	0.2735	0.0076	0.90	0.2016	0.0033	2188.0	19.0	1558.0	38.0	2836.9	5.7	42.9
TSUPB012_7	1200	0.30	7.320	0.290	0.2526	0.0100	0.96	0.2036	0.0038	2149.0	34.0	1450.0	52.0	2854.0	12.0	49.7
TSUPB012_8	602	0.45	8.920	0.210	0.3150	0.0086	0.89	0.2060	0.0035	2329.0	21.0	1764.0	42.0	2874.9	7.9	37.2
TSUPB012_9	1311	0.93	9.410	0.270	0.3300	0.0110	0.96	0.2063	0.0034	2373.0	28.0	1836.0	54.0	2877.8	6.2	35.0
TSUPB012_10	1860	0.33	8.770	0.350	0.3060	0.0130	0.98	0.2077	0.0033	2308.0	36.0	1715.0	62.0	2884.4	6.4	38.9
TSUPB012_11	1032	0.24	5.510	0.180	0.1865	0.0084	0.95	0.2074	0.0034	1909.0	29.0	1105.0	45.0	2887.5	7.9	62.1
TSUPB012_12	766	0.33	9.220	0.490	0.3220	0.0170	0.99	0.2075	0.0035	2337.0	49.0	1791.0	82.0	2888.0	8.9	36.1
TSUPB012_13	696	0.26	9.790	0.210	0.3422	0.0086	0.92	0.2080	0.0034	2414.0	20.0	1896.0	41.0	2893.4	7.9	33.2
TSUPB012_14	1269	0.29	9.480	0.290	0.3256	0.0100	0.96	0.2093	0.0034	2379.0	28.0	1819.0	51.0	2896.9	6.6	36.6

		Ratios								Age (Ma)						
Analysis	U ppm	Th/U	$^{207}Pb/^{235}U$	Err 2SE abs	$^{206}Pb/^{238}U$	Err 2SE abs	Rho	$^{207}Pb/^{206}Pb$	Err 2SE abs	$^{207}Pb/^{235}U$	Err 2SE abs	$^{206}Pb/^{238}U$	Err 2SE abs	$^{207}Pb/^{206}Pb$	Err 2SE abs	% Disc
TSUPB012_15	242	0.58	10.710	0.350	0.3709	0.0110	0.88	0.2094	0.0045	2493.0	29.0	2032.0	54.0	2905.0	17.0	28.1
TSUPB012_16	630	0.95	9.510	0.180	0.3281	0.0081	0.84	0.2101	0.0035	2387.0	17.0	1829.0	39.0	2907.8	8.8	36.8
TSUPB012_17	466	0.36	9.540	0.190	0.3301	0.0078	0.87	0.2101	0.0036	2391.0	18.0	1838.0	38.0	2909.0	10.0	35.5
TSUPB012_18	443	0.51	12.800	1.000	0.4310	0.0320	0.99	0.2121	0.0037	2634.0	78.0	2280.0	150.0	2918.0	11.0	21.7
TSUPB012_19	468	0.85	9.800	1.100	0.3340	0.0370	0.99	0.2126	0.0043	2330.0	120.0	1820.0	180.0	2920.0	15.0	36.1
TSUPB012_20	399	0.99	12.210	0.490	0.4200	0.0170	0.96	0.2118	0.0037	2612.0	38.0	2251.0	78.0	2922.7	8.2	21.8
TSUPB012_21	797	0.44	10.070	0.310	0.3333	0.0120	0.97	0.2125	0.0033	2441.0	29.0	1851.0	56.0	2924.4	5.6	38.8
TSUPB012_22	281	0.34	13.160	0.420	0.4480	0.0140	0.93	0.2126	0.0038	2683.0	29.0	2383.0	63.0	2928.1	7.7	17.1
TSUPB012_23	399	0.51	13.060	0.250	0.4406	0.0090	0.92	0.2138	0.0036	2684.0	17.0	2352.0	40.0	2929.9	7.6	18.4
TSUPB012_24	482	0.52	10.680	0.230	0.3655	0.0096	0.85	0.2127	0.0036	2496.0	20.0	2007.0	45.0	2933.0	8.7	30.5
TSUPB012_25	374	0.31	14.490	0.200	0.4930	0.0085	0.71	0.2139	0.0037	2781.0	13.0	2583.0	37.0	2934.1	8.8	11.3
TSUPB012_26	282	0.37	14.900	0.530	0.5040	0.0190	0.97	0.2139	0.0036	2803.0	36.0	2620.0	83.0	2935.7	8.0	10.2
TSUPB012_27	424	0.58	12.540	0.420	0.4260	0.0140	0.95	0.2138	0.0037	2650.0	32.0	2283.0	62.0	2936.0	10.0	21.3
TSUPB012_28	456	0.85	10.400	0.460	0.3420	0.0150	0.97	0.2132	0.0036	2460.0	42.0	1889.0	71.0	2936.0	10.0	37.2
TSUPB012_29	975	0.42	12.760	0.210	0.4360	0.0082	0.86	0.2142	0.0033	2662.0	15.0	2332.0	37.0	2939.9	6.2	19.7
TSUPB012_30	372	0.36	13.450	0.380	0.4550	0.0130	0.93	0.2154	0.0036	2709.0	27.0	2427.0	57.0	2946.3	9.3	17.0
TSUPB012_31	336	0.40	13.940	0.570	0.4740	0.0190	0.96	0.2151	0.0037	2744.0	40.0	2492.0	85.0	2949.4	6.5	14.4
TSUPB012_32	340	0.36	13.990	0.400	0.4670	0.0150	0.95	0.2159	0.0036	2743.0	29.0	2474.0	65.0	2951.9	8.6	16.5
TSUPB012_33	240	0.39	16.060	0.200	0.5369	0.0084	0.62	0.2160	0.0038	2879.8	12.0	2770.0	35.0	2952.3	9.2	6.2
TSUPB012_34	546	0.43	16.240	0.250	0.5429	0.0098	0.87	0.2173	0.0033	2891.0	15.0	2798.0	41.0	2959.3	6.1	5.5
TSUPB012_35	286	0.44	17.140	0.290	0.5687	0.0110	0.80	0.2177	0.0037	2940.0	16.0	2901.0	44.0	2961.3	8.2	4.4
TSUPB012_36	551	0.53	17.580	0.230	0.5803	0.0087	0.82	0.2192	0.0035	2966.0	12.0	2949.0	35.0	2974.6	5.8	2.8
TSUPB012_37	175	0.35	17.880	0.300	0.5917	0.0094	0.81	0.2186	0.0038	2981.0	16.0	2995.0	38.0	2974.8	9.7	3.9
TSUPB012_38	410	0.45	17.190	0.270	0.5683	0.0100	0.87	0.2187	0.0037	2944.0	15.0	2905.0	45.0	2975.5	7.7	4.9
TSUPB012_39	560	0.49	17.450	0.220	0.5770	0.0080	0.82	0.2193	0.0033	2960.0	12.0	2936.0	33.0	2976.3	5.7	2.3
TSUPB028_1	2230	0.46	4.864	0.170	0.1787	0.0100	0.92	0.2006	0.0012	1795.0	29.0	1060.0	54.0	2830.4	6.5	56.8
TSUPB028_2	643	0.74	13.890	0.310	0.4620	0.0140	0.90	0.2119	0.0014	2740.0	23.0	2449.0	61.0	2908.0	12.0	17.4
TSUPB028_3	790	1.13	13.760	0.340	0.4310	0.0140	0.92	0.2126	0.0017	2734.0	24.0	2308.0	64.0	2924.8	8.0	25.9
TSUPB028_4	321	0.22	14.180	0.220	0.4765	0.0110	0.77	0.2129	0.0019	2761.0	15.0	2512.0	47.0	2925.1	8.1	14.5
TSUPB028_5	393	0.48	12.310	0.210	0.4135	0.0120	0.75	0.2129	0.0017	2627.0	16.0	2230.0	52.0	2931.8	8.1	23.2
TSUPB028_6	515	0.87	16.240	0.310	0.5652	0.0150	0.84	0.2144	0.0016	2890.0	19.0	2888.0	61.0	2937.9	8.8	2.5
TSUPB028_7	387	1.04	16.320	0.430	0.5670	0.0180	0.93	0.2154	0.0017	2894.0	27.0	2894.0	78.0	2942.6	7.7	4.6
TSUPB028_8	484	0.81	15.410	0.400	0.5282	0.0170	0.59	0.2164	0.0016	2841.0	28.0	2734.0	74.0	2945.0	21.0	6.0
TSUPB028_9	514	1.04	14.750	0.430	0.4930	0.0180	0.93	0.2144	0.0016	2798.0	35.0	2584.0	84.0	2945.0	10.0	12.7
TSUPB028_10	403	0.47	15.440	0.950	0.5130	0.0330	0.54	0.2158	0.0019	2846.0	79.0	2669.0	150.0	2956.0	16.0	9.1
TSUPB029_1	1490	0.56	2.005	0.560	0.0813	0.0095	0.95	0.1667	0.0110	1113.0	190.0	503.0	24.0	2525.0	22.0	62.9
TSUPB029_2	3180	1.11	4.650	0.550	0.1839	0.0120	0.99	0.1792	0.0110	1750.0	92.0	1086.0	46.0	2640.0	11.0	50.8
TSUPB029_3	2166	0.90	4.090	0.530	0.1574	0.0110	0.98	0.1794	0.0100	1645.0	110.0	941.0	37.0	2644.9	6.4	57.6
TSUPB029_4	508	0.54	4.950	0.890	0.1295	0.0094	0.80	0.1817	0.0110	1808.0	150.0	785.0	16.0	2667.6	8.3	90.4
TSUPB029_5	1016	0.03	2.536	0.170	0.0985	0.0099	0.88	0.1839	0.0026	1279.0	46.0	606.0	11.0	2690.0	21.0	64.4
TSUPB029_6	2570	0.50	4.680	0.560	0.1748	0.0130	0.99	0.1843	0.0110	1751.0	100.0	1036.0	51.0	2694.0	11.0	56.8
TSUPB029_7	3760	0.71	5.460	0.570	0.2023	0.0120	0.99	0.1918	0.0110	1887.0	90.0	1185.0	45.0	2758.0	10.0	53.0
TSUPB029_8	2990	0.72	6.190	0.560	0.2245	0.0110	0.99	0.1944	0.0110	1999.0	81.0	1311.0	40.0	2778.6	6.5	50.5
TSUPB029_9	1426	0.17	6.210	0.180	0.2400	0.0110	0.82	0.1945	0.0015	2005.0	25.0	1386.0	14.0	2783.6	9.2	43.6
TSUPB029_10	1797	0.34	5.924	0.170	0.2204	0.0100	0.88	0.1947	0.0012	1964.0	25.0	1284.0	17.0	2786.4	7.4	49.9
TSUPB029_11	4060	0.14	3.150	0.540	0.1360	0.0140	0.98	0.1963	0.0110	1445.0	130.0	816.0	63.0	2800.0	26.0	56.2
TSUPB029_12	2262	0.95	6.378	0.160	0.2490	0.0100	0.51	0.1973	0.0012	2028.8	22.0	1433.4	7.5	2802.2	6.3	41.8
TSUPB029_13	1490	0.67	6.450	0.510	0.2490	0.0210	1.00	0.1975	0.0018	2020.0	70.0	1423.0	91.0	2807.0	14.0	42.0
TSUPB029_14	1813	0.94	5.780	0.600	0.2040	0.0130	0.99	0.1984	0.0110	1943.0	92.0	1196.0	54.0	2810.0	18.0	55.0
TSUPB029_15	1096	0.80	16.730	1.000	0.5720	0.0380	0.90	0.1980	0.0110	2919.0	49.0	2917.0	70.0	2811.0	13.0	3.8

		Ratios								Age (Ma)						
Analysis	U ppm	Th/U	$^{207}Pb/^{235}U$	Err 2SE abs	$^{206}Pb/^{238}U$	Err 2SE abs	Rho	$^{207}Pb/^{206}Pb$	Err 2SE abs	$^{207}Pb/^{235}U$	Err 2SE abs	$^{206}Pb/^{238}U$	Err 2SE abs	$^{207}Pb/^{206}Pb$	Err 2SE abs	% Disc
TSUPB029_16	1801	0.45	4.960	0.530	0.1730	0.0090	0.92	0.1976	0.0110	1813.0	87.0	1028.0	19.0	2811.0	16.0	62.1
TSUPB029_17	2090	0.46	2.830	0.630	0.0937	0.0110	0.98	0.1982	0.0110	1335.0	180.0	575.0	41.0	2812.0	23.0	74.6
TSUPB029_18	1138	0.88	8.830	0.940	0.3150	0.0300	1.00	0.1994	0.0110	2288.0	97.0	1750.0	140.0	2817.0	11.0	37.7
TSUPB029_19	892	0.49	13.730	0.580	0.4930	0.0150	0.82	0.1996	0.0110	2731.0	42.0	2583.0	41.0	2823.3	9.8	8.6
TSUPB029_20	1379	0.50	8.310	0.840	0.2780	0.0220	0.99	0.1998	0.0110	2240.0	100.0	1570.0	97.0	2825.0	11.0	47.2
TSUPB029_21	850	0.54	7.119	0.170	0.2550	0.0100	0.73	0.2013	0.0016	2125.9	22.0	1464.0	13.0	2833.9	9.6	46.1
TSUPB029_22	1765	0.59	13.100	0.540	0.4544	0.0110	0.91	0.2012	0.0100	2690.0	39.0	2414.0	34.0	2837.2	5.4	15.7
TSUPB029_23	509	0.39	12.370	0.680	0.4430	0.0190	0.15	0.2018	0.0110	2632.0	58.0	2364.0	25.0	2839.0	30.0	15.4
TSUPB029_24	1736	0.83	8.990	0.620	0.2978	0.0096	0.85	0.2021	0.0110	2334.0	63.0	1680.0	20.0	2841.8	8.7	43.8
TSUPB029_25	1530	0.41	11.400	0.830	0.3950	0.0260	0.96	0.2021	0.0110	2550.0	68.0	2150.0	110.0	2843.0	12.0	25.1
TSUPB029_26	647	0.52	14.520	0.640	0.5182	0.0190	0.62	0.2048	0.0110	2784.0	44.0	2691.0	18.0	2858.0	14.0	5.2
TSUPB029_27	1182	0.55	8.020	0.390	0.3020	0.0150	0.99	0.2039	0.0015	2223.0	44.0	1697.0	57.0	2861.4	8.4	34.7
TSUPB029_28	1799	0.53	5.260	0.340	0.1970	0.0150	1.00	0.2042	0.0019	1846.0	56.0	1154.0	62.0	2869.0	13.0	54.1
TSUPB029_29	825	0.64	13.610	0.550	0.4685	0.0120	0.72	0.2053	0.0100	2723.0	39.0	2477.0	25.0	2870.0	11.0	13.7
TSUPB029_30	943	0.27	10.390	0.550	0.3494	0.0110	0.81	0.2059	0.0110	2471.0	49.0	1931.0	31.0	2881.0	6.7	34.1
TSUPB029_31	983	0.65	9.160	0.640	0.2940	0.0120	0.96	0.2072	0.0110	2355.0	64.0	1660.0	40.0	2883.7	6.9	48.0
TSUPB029_32	492	0.65	15.700	0.200	0.5448	0.0110	0.76	0.2072	0.0013	2858.0	13.0	2803.0	31.0	2886.7	5.9	3.0
TSUPB029_33	1600	0.59	9.172	0.510	0.3161	0.0096	0.70	0.2081	0.0110	2355.1	51.0	1770.0	21.0	2889.6	5.9	38.3
TSUPB029_34	484	0.73	12.830	1.400	0.2886	0.0250	0.95	0.2086	0.0130	2676.0	180.0	1634.0	40.0	2894.0	17.0	76.5
TSUPB029_35	606	0.07	14.970	0.640	0.5470	0.0250	0.97	0.2087	0.0015	2810.0	57.0	2810.0	100.0	2895.0	15.0	3.8
TSUPB029_36	1667	0.44	9.830	0.380	0.3539	0.0160	0.98	0.2092	0.0012	2416.0	34.0	1952.0	46.0	2898.4	4.4	29.2
TSUPB029_37	385	0.59	15.590	0.220	0.5391	0.0120	0.73	0.2094	0.0015	2851.0	14.0	2779.0	20.0	2900.0	10.0	3.8
TSUPB029_38	521	0.43	8.950	0.720	0.2366	0.0130	0.97	0.2090	0.0110	2328.0	73.0	1367.0	47.0	2900.0	7.7	73.3
TSUPB029_39	854	0.15	10.250	0.220	0.3760	0.0110	0.88	0.2097	0.0016	2456.0	20.0	2057.0	22.0	2906.6	8.1	24.1
TSUPB029_40	1345	0.96	11.540	0.950	0.3840	0.0160	1.00	0.2116	0.0110	2535.0	50.0	2093.0	61.0	2907.0	18.0	28.7
TSUPB029_41	149	0.42	8.670	0.650	0.2860	0.0150	0.96	0.2101	0.0110	2297.0	70.0	1616.0	61.0	2908.0	9.0	46.2
TSUPB029_42	1717	0.60	6.110	0.610	0.2150	0.0130	0.99	0.2101	0.0110	1980.0	86.0	1253.0	53.0	2908.0	20.0	54.4
TSUPB029_43	869	0.66	17.470	0.610	0.5820	0.0150	0.79	0.2104	0.0110	2961.0	35.0	2956.0	40.0	2908.9	8.5	2.9
TSUPB029_44	334	0.69	13.610	0.560	0.4524	0.0110	0.62	0.2107	0.0110	2722.0	39.0	2405.0	25.0	2911.6	8.1	18.3
TSUPB029_45	777	0.52	14.800	0.290	0.5430	0.0150	0.31	0.2107	0.0012	2802.0	20.0	2796.0	18.0	2913.5	8.8	1.7
TSUPB029_46	923	0.81	14.710	0.350	0.5332	0.0170	0.80	0.2124	0.0013	2796.0	25.0	2754.0	41.0	2918.0	11.0	2.5
TSUPB029_47	369	0.75	15.120	0.370	0.5490	0.0170	0.86	0.2115	0.0019	2821.0	23.0	2822.0	42.0	2919.0	11.0	3.3
TSUPB029_48	349	0.48	11.770	1.100	0.2900	0.0200	0.99	0.2119	0.0110	2574.0	83.0	1634.0	89.0	2922.6	7.3	67.7
TSUPB029_49	617	0.58	15.680	0.260	0.5411	0.0130	0.84	0.2129	0.0014	2857.0	16.0	2788.0	35.0	2922.9	9.4	4.5
TSUPB029_50	558	0.69	5.647	0.590	0.1863	0.0094	0.70	0.2126	0.0120	1922.9	91.0	1101.0	17.0	2925.4	9.7	64.2
TSUPB029_51	1099	0.48	14.390	0.670	0.4450	0.0150	0.96	0.2127	0.0110	2780.0	45.0	2370.0	50.0	2927.1	5.7	24.1
TSUPB029_52	618	0.49	16.410	0.560	0.5668	0.0150	0.96	0.2132	0.0110	2900.0	34.0	2894.0	41.0	2927.9	7.6	3.6
TSUPB029_53	495	0.59	15.410	0.330	0.5540	0.0150	0.89	0.2137	0.0015	2839.0	21.0	2843.0	42.0	2931.7	7.9	3.4
TSUPB029_54	690	0.66	15.340	0.600	0.4952	0.0110	0.73	0.2132	0.0110	2843.0	37.0	2593.0	40.0	2932.0	15.0	13.7
TSUPB029_55	997	0.42	11.290	0.630	0.3554	0.0120	0.94	0.2138	0.0110	2544.0	53.0	1959.0	35.0	2933.0	5.2	38.2
TSUPB029_56	518	0.86	9.260	1.100	0.2500	0.0240	1.00	0.2144	0.0120	2338.0	110.0	1440.0	120.0	2933.0	23.0	66.8
TSUPB029_57	451	0.64	16.060	1.200	0.3454	0.0180	0.88	0.2139	0.0110	2879.0	97.0	1912.0	39.0	2933.0	15.0	68.4
TSUPB029_58	605	0.67	15.460	0.290	0.5524	0.0140	0.84	0.2131	0.0013	2847.0	19.0	2835.0	38.0	2934.3	8.9	2.4
TSUPB029_59	390	0.62	15.570	0.230	0.5305	0.0120	0.46	0.2131	0.0017	2850.8	14.0	2743.0	23.0	2934.7	9.7	5.8
TSUPB029_60	456	0.66	14.530	0.600	0.4511	0.0097	0.52	0.2141	0.0110	2787.0	39.0	2400.0	22.0	2935.0	12.0	22.4
TSUPB029_61	802	0.24	12.680	0.200	0.4301	0.0110	0.74	0.2144	0.0013	2656.0	15.0	2309.0	22.0	2936.8	6.2	20.4
TSUPB029_62	308	0.50	16.550	0.670	0.5014	0.0130	0.78	0.2146	0.0110	2908.0	38.0	2618.0	41.0	2936.9	9.6	15.0
TSUPB029_63	414	0.66	19.020	0.690	0.6040	0.0170	0.78	0.2140	0.0110	3042.0	38.0	3046.0	42.0	2938.0	12.0	2.0
TSUPB029_64	474	0.58	14.190	0.500	0.4644	0.0100	0.67	0.2143		2762.0		2459.0	32.0	2941.0	13.0	17.5
TSUPB029_65	200	0.45	19.400	1.400	0.4450	0.0270	0.99	0.2156	0.0110	3043.0	69.0	2360.0	110.0	2950.7	8.1	44.5
TSUPB029_66	122	0.01	15.360	0.240	0.5524	0.0140	0.49	0.2179	0.0025	2837.0	16.0	2834.0	37.0	2954.0	15.0	4.1
TSUPB029_67	574	0.72	15.140	0.520	0.5193	0.0110	0.73	0.2159	0.0110	2826.1	35.0	2696.0	27.0	2954.0	10.0	6.8
TSUPB029_68	1122	0.50	10.640	0.520	0.3495	0.0095	0.55	0.2158	0.0110	2493.3	46.0	1932.0	21.0	2955.2	6.8	35.4
TSUPB029_69	2930	0.13	10.800	1.300	0.3060	0.0340	1.00	0.2170	0.0110	2460.0	93.0	1690.0	160.0	2958.7	7.7	53.4

		Ratios								Age (Ma)						
Analysis	U ppm	Th/U	$^{207}Pb/^{235}U$	Err 2SE abs	$^{206}Pb/^{238}U$	Err 2SE abs	Rho	$^{207}Pb/^{206}Pb$	Err 2SE abs	$^{207}Pb/^{235}U$	Err 2SE abs	$^{206}Pb/^{238}U$	Err 2SE abs	$^{207}Pb/^{206}Pb$	Err 2SE abs	% Disc
TSUPB029_70	568	0.51	18.080	0.660	0.5690	0.0140	0.68	0.2170	0.0110	2994.0	38.0	2905.0	74.0	2960.0	24.0	5.8
TSUPB029_71	426	0.30	11.360	0.750	0.3670	0.0190	0.98	0.2178	0.0110	2547.0	65.0	2006.0	91.0	2964.4	6.7	34.4
TSUPB029_72	292	0.64	20.670	0.840	0.4960	0.0180	0.96	0.2200	0.0110	3120.0	40.0	2591.0	65.0	2983.8	6.3	31.7
TSUPB029_73	204	0.53	18.080	0.620	0.5840	0.0140	0.44	0.2212	0.0120	2994.0	36.0	2967.0	45.0	2984.0	12.0	2.6
TSUPB029_74	597	0.44	14.910	0.280	0.4838	0.0130	0.84	0.2212	0.0021	2808.0	18.0	2543.0	36.0	2990.3	8.4	14.8
TSUPB029_75	634	0.36	8.000	0.970	0.1760	0.0160	0.99	0.2243	0.0110	2216.0	110.0	1037.0	76.0	3010.4	9.7	98.8
TSUPB029_76	310	0.57	17.980	0.650	0.5800	0.0140	0.78	0.2295	0.0120	2989.0	37.0	2947.0	54.0	3046.0	13.0	3.5
TSUPB029_77	771	0.48	8.840	0.640	0.3012	0.0140	0.97	0.2293	0.0120	2325.0	68.0	1702.0	47.0	3050.9	8.2	41.8
TSUPB029_78	733	0.73	12.080	0.590	0.4036	0.0110	0.85	0.2319	0.0120	2610.0	45.0	2185.0	25.0	3063.0	5.4	25.4
TSUPB029_79	1774	0.11	13.700	0.280	0.4244	0.0110	0.86	0.2327	0.0016	2727.0	19.0	2280.0	28.0	3072.0	10.0	26.9
TSUPB029_80	1458	0.34	8.200	0.900	0.1747	0.0120	0.94	0.2359	0.0120	2237.0	100.0	1036.0	45.0	3083.0	29.0	100.9
TSUPB029_81	6830	0.16	3.830	0.630	0.1022	0.0100	0.99	0.2393	0.0110	1600.0	140.0	626.0	33.0	3117.0	11.0	91.1
TSUPB029_82	2270	0.39	2.230	0.600	0.0695	0.0092	0.90	0.2505	0.0130	1193.0	200.0	433.0	13.0	3192.0	35.0	78.8
TSUPB029_83	859	0.33	3.853	0.570	0.1176	0.0091	0.40	0.2520	0.0120	1603.3	120.0	716.4	7.9	3200.0	11.0	80.1
TSUPB029_84	3900	0.09	1.800	0.620	0.0517	0.0120	0.97	0.2579	0.0130	1001.0	200.0	322.0	52.0	3244.0	34.0	87.2
TSUPB029CA_1	490	1.13	9.830	0.170	0.3488	0.0067	0.94	0.2042	0.0011	2417.0	15.0	1928.0	32.0	2859.9	8.9	32.6
TSUPB029CA_2	600	0.61	13.700	0.310	0.4759	0.0087	0.93	0.2079	0.0010	2727.0	21.0	2508.0	38.0	2890.5	8.5	13.2
TSUPB029CA_3	387	0.49	12.970	0.370	0.4530	0.0120	0.96	0.2082	0.0014	2681.0	26.0	2412.0	52.0	2893.0	11.0	16.5
TSUPB029CA_4	253	1.02	16.380	0.360	0.5685	0.0093	0.76	0.2095	0.0024	2898.0	21.0	2901.0	38.0	2901.0	18.0	0.0
TSUPB029CA_5	182	0.53	17.730	0.170	0.5856	0.0082	0.82	0.2099	0.0019	2974.7	9.5	2971.0	33.0	2906.0	15.0	-1.9
TSUPB029CA_6	307	0.48	16.890	0.210	0.5741	0.0074	0.75	0.2102	0.0021	2928.0	12.0	2924.0	30.0	2906.0	16.0	-0.1
TSUPB029CA_7	291	0.76	14.410	0.220	0.4974	0.0064	0.76	0.2101	0.0018	2776.0	15.0	2602.0	28.0	2906.0	14.0	10.4
TSUPB029CA_8	180	1.43	17.740	0.300	0.5869	0.0093	0.86	0.2105	0.0021	2974.0	16.0	2976.0	38.0	2908.0	16.0	-2.4
TSUPB029CA_9	259	0.85	16.420	0.160	0.5440	0.0056	0.84	0.2106	0.0012	2902.9	9.2	2800.0	24.0	2910.1	9.2	3.6
TSUPB029CA_10	305	0.64	16.710	0.300	0.5739	0.0090	0.85	0.2108	0.0013	2920.0	17.0	2923.0	37.0	2911.0	10.0	-0.4
TSUPB029CA_11	458	0.69	16.340	0.190	0.5671	0.0075	0.72	0.2112	0.0019	2896.0	11.0	2895.0	31.0	2914.0	14.0	0.6
TSUPB029CA_12	222	0.65	16.780	0.130	0.5739	0.0042	0.91	0.2113	0.0011	2922.0	7.3	2924.0	17.0	2915.6	8.3	-0.3
TSUPB029CA_13	381	0.93	16.770	0.230	0.5745	0.0097	0.92	0.2112	0.0013	2921.0	13.0	2925.0	39.0	2916.0	10.0	-0.3
TSUPB029CA_14	198	0.83	17.610	0.290	0.5819	0.0086	0.76	0.2121	0.0023	2968.0	16.0	2956.0	35.0	2922.0	18.0	-2.1
TSUPB029CA_15	131	0.52	17.640	0.220	0.5824	0.0093	0.71	0.2129	0.0023	2970.0	12.0	2957.0	38.0	2927.0	18.0	-1.3
TSUPB029CA_16	142	0.52	16.990	0.180	0.5773	0.0058	0.68	0.2130	0.0019	2935.7	9.9	2941.0	23.0	2927.0	14.0	-0.4
TSUPB029CA_17	177	0.62	17.040	0.140	0.5772	0.0043	0.34	0.2132	0.0018	2936.8	8.1	2937.0	18.0	2929.0	14.0	-0.3
TSUPB029CA_18	183	0.56	17.610	0.290	0.5864	0.0097	0.62	0.2135	0.0027	2968.0	16.0	2974.0	39.0	2936.0	22.0	-1.3
TSUPB029CA_19	454	0.49	16.280	0.200	0.5488	0.0056	0.83	0.2145	0.0015	2892.0	12.0	2820.0	24.0	2941.0	11.0	4.4
TSUPB015_1	634	0.97	9.100	0.320	0.3699	0.0110	0.92	0.1710	0.0100	2346.0	33.0	2028.0	53.0	2568.0	10.0	18.1
TSUPB015_2	191	0.73	13.240	0.320	0.5203	0.0120	0.86	0.1747	0.0100	2696.0	23.0	2699.0	50.0	2600.1	9.1	3.3
TSUPB015_3	357	0.89	9.080	0.290	0.3514	0.0096	0.88	0.1759	0.0100	2345.0	29.0	1941.0	46.0	2621.0	8.0	24.7
TSUPB015_4	444	0.68	14.050	0.360	0.5224	0.0099	0.84	0.1876	0.0110	2753.0	25.0	2709.0	42.0	2720.8	9.9	2.6
TSUPB015_5	369	0.49	13.080	0.380	0.4964	0.0120	0.85	0.1887	0.0110	2684.0	28.0	2597.0	52.0	2729.0	10.0	4.9
TSUPB015_6	354	1.09	15.090	0.350	0.5498	0.0110	0.85	0.1895	0.0100	2821.0	22.0	2824.0	46.0	2743.2	6.2	1.4
TSUPB015_7	679	0.49	12.180	0.330	0.4449	0.0110	0.87	0.1910	0.0100	2620.0	24.0	2372.0	48.0	2753.3	8.4	13.8
TSUPB015_8	585	0.65	13.590	0.350	0.4862	0.0098	0.68	0.1940	0.0110	2721.0	24.0	2554.0	42.0	2791.9	8.8	9.1
TSUPB015_9	162	2.67	3.255	0.360	0.1189	0.0095	0.62	0.2013	0.0140	1469.0	84.0	724.0	54.0	2825.0	23.0	66.9
TSUPB015_10	531	1.01	11.010	0.320	0.3940	0.0089	0.59	0.2012	0.0100	2524.0	27.0	2141.0	41.0	2837.2	6.0	23.0
TSUPB015_11	281	0.72	14.830	0.380	0.5188	0.0092	0.54	0.2066	0.0120	2804.0	24.0	2694.0	39.0	2869.0	19.0	6.3
TSUPB015_12	547	0.87	13.600	0.400	0.4724	0.0110	0.94	0.2060	0.0130	2720.0	28.0	2493.0	50.0	2878.0	12.0	12.8
TSUPB015_13	220	0.66	12.640	0.350	0.4424	0.0099	0.73	0.2074	0.0120	2652.0	26.0	2361.0	44.0	2885.0	11.0	16.5
TSUPB015_14	182	0.48	12.680	0.540	0.4330	0.0140	0.87	0.2066	0.0120	2652.0	39.0	2317.0	65.0	2889.0	30.0	20.3
TSUPB015_15	384	0.99	17.150	0.330	0.5755	0.0100	0.76	0.2105	0.0130	2943.1	18.0	2930.0	43.0	2908.2	9.2	2.1
TSUPB015_16	661	0.80	12.920	0.510	0.4310	0.0140	0.95	0.2116	0.0110	2675.0	35.0	2308.0	62.0	2916.0	18.0	21.3

		Ratios								Age (Ma)						
Analysis	U ppm	Th/U	$^{207}Pb/^{235}U$	Err 2SE abs	$^{206}Pb/^{238}U$	Err 2SE abs	Rho	$^{207}Pb/^{206}Pb$	Err 2SE abs	$^{207}Pb/^{235}U$	Err 2SE abs	$^{206}Pb/^{238}U$	Err 2SE abs	$^{207}Pb/^{206}Pb$	Err 2SE abs	% Disc
TSUPB015_17	417	0.55	16.730	0.370	0.5737	0.0120	0.62	0.2118	0.0130	2920.0	22.0	2923.0	48.0	2920.0	17.0	2.3
TSUPB015_18	736	0.90	13.830	0.350	0.4739	0.0110	0.87	0.2121	0.0110	2737.0	25.0	2500.0	49.0	2920.0	12.0	13.5
TSUPB015_19	659	1.04	12.220	0.420	0.4230	0.0140	0.95	0.2118	0.0120	2618.0	33.0	2272.0	64.0	2923.9	7.0	20.4
TSUPB015_20	484	1.10	11.470	0.340	0.3663	0.0120	0.74	0.2148	0.0110	2561.0	28.0	2011.0	56.0	2938.0	23.0	34.2
TSUPB015_21	301	0.57	17.640	0.350	0.5884	0.0100	0.44	0.2150	0.0130	2970.2	19.0	2983.0	41.0	2941.0	11.0	1.9
TSUPB015_22	662	0.99	15.850	0.410	0.5271	0.0120	0.90	0.2160	0.0130	2867.0	25.0	2729.0	50.0	2947.4	7.9	7.5
TSUPB015_23	492	0.99	11.670	0.300	0.3881	0.0110	0.68	0.2159	0.0110	2578.5	24.0	2113.0	50.0	2948.3	9.4	28.5
TSUPB015_24	815	1.06	10.990	0.720	0.3590	0.0150	0.94	0.2194	0.0130	2525.0	61.0	1977.0	71.0	2968.0	31.0	35.2
TSUPB015_25	546	0.39	15.920	0.390	0.5216	0.0120	0.88	0.2206	0.0120	2872.0	24.0	2706.0	51.0	2980.9	8.1	9.6
TSUPB015_26	822	0.53	13.050	0.550	0.4400	0.0200	0.97	0.2207	0.0120	2681.0	40.0	2349.0	88.0	2992.0	18.0	19.6
TSUPB015_27	497	0.81	15.960	0.450	0.5279	0.0110	0.81	0.2217	0.0130	2873.0	26.0	2732.0	47.0	2994.0	16.0	8.4
TSUPB015_28	326	0.62	18.710	0.460	0.5983	0.0130	0.88	0.2289	0.0140	3026.0	24.0	3022.0	51.0	3047.4	8.5	3.7
TSUPB015_29	405	0.56	18.570	0.390	0.5852	0.0097	0.80	0.2310	0.0130	3019.5	20.0	2970.0	39.0	3059.1	8.3	2.9
TSUPB015_30	357	0.58	19.280	0.410	0.6065	0.0099	0.51	0.2311	0.0140	3057.3	20.0	3056.0	40.0	3060.2	5.3	1.6
TSUPB015_31	358	0.53	14.250	0.410	0.4458	0.0098	0.59	0.2310	0.0140	2767.0	27.0	2376.0	44.0	3061.0	12.0	22.9
TSUPB015_32	776	1.32	11.400	0.500	0.3591	0.0120	0.92	0.2321	0.0120	2551.0	39.0	1977.0	56.0	3066.0	16.0	36.0
TSUPB015_33	360	1.17	17.340	0.410	0.5365	0.0098	0.64	0.2331	0.0140	2953.5	23.0	2768.0	41.0	3072.2	6.8	10.3
TSUPB015_34	533	0.46	16.640	0.580	0.5110	0.0140	0.93	0.2354	0.0140	2913.0	33.0	2661.0	62.0	3090.0	39.0	13.8
TSUPB015_35	577	0.78	17.400	0.430	0.5377	0.0110	0.73	0.2374	0.0140	2956.0	24.0	2774.0	48.0	3101.0	15.0	10.1
TSUPB015_36	294	0.96	16.160	0.470	0.4954	0.0110	0.92	0.2395	0.0140	2885.0	28.0	2594.0	46.0	3114.0	15.0	16.7
TSUPB015_37	1890	0.85	6.380	0.420	0.1926	0.0110	0.87	0.2416	0.0140	2024.0	56.0	1135.0	57.0	3136.0	27.0	69.9
TSUPB015_38	729	0.39	14.590	0.450	0.4354	0.0110	0.80	0.2475	0.0140	2788.0	29.0	2330.0	51.0	3164.0	13.0	28.1
TSUPB015_39	817	0.44	13.470	0.560	0.3890	0.0140	0.90	0.2555	0.0140	2710.0	39.0	2125.0	61.0	3222.0	17.0	37.7
TSUPB015_40	2374	1.61	12.240	0.580	0.3530	0.0140	0.99	0.2571	0.0120	2622.0	44.0	1948.0	69.0	3227.0	46.0	42.3
TSUPB015_41	1378	1.02	10.910	0.390	0.3164	0.0120	0.87	0.2585	0.0120	2514.0	34.0	1771.0	59.0	3238.0	15.0	50.2
TSUPB015_42	313	0.91	11.420	0.480	0.3188	0.0110	0.94	0.2595	0.0130	2562.0	40.0	1788.0	53.0	3247.0	10.0	52.8
TSUPB015_43	910	1.12	13.000	0.510	0.3498	0.0120	0.97	0.2663	0.0140	2678.0	38.0	1933.0	59.0	3279.0	17.0	49.3
TSUPB026_1	2950	1.17	0.720	0.091	0.0355	0.0041	0.95	0.1461	0.0025	548.0	55.0	225.0	26.0	2301.0	29.0	90.3
TSUPB026_2	4000	0.50	0.608	0.076	0.0260	0.0029	0.93	0.1702	0.0055	478.0	48.0	165.0	18.0	2556.0	55.0	93.6
TSUPB026_3	1400	1.50	1.200	0.056	0.0491	0.0031	0.92	0.1724	0.0041	799.0	25.0	309.0	19.0	2578.0	39.0	88.1
TSUPB026_4	1100	0.12	2.790	0.120	0.1163	0.0066	0.94	0.1720	0.0037	1360.0	36.0	709.0	38.0	2582.0	34.0	72.1
TSUPB026_5	5200	0.62	0.580	0.100	0.0229	0.0034	0.99	0.1735	0.0041	453.0	67.0	146.0	21.0	2590.0	39.0	94.4
TSUPB026_6	1120	0.28	2.020	0.140	0.0817	0.0065	0.94	0.1771	0.0035	1116.0	48.0	506.0	39.0	2625.0	33.0	81.2
TSUPB026_7	1020	0.21	1.720	0.240	0.0712	0.0093	0.97	0.1773	0.0050	999.0	94.0	442.0	56.0	2625.0	48.0	83.2
TSUPB026_8	1020	0.23	1.134	0.045	0.0464	0.0020	0.83	0.1773	0.0036	769.0	21.0	292.0	12.0	2626.0	33.0	88.8
TSUPB026_9	1110	0.14	0.962	0.028	0.0389	0.0010	0.50	0.1790	0.0045	684.0	15.0	246.2	5.9	2642.0	42.0	90.7
TSUPB026_10	420	0.22	1.530	0.130	0.0615	0.0055	0.89	0.1823	0.0070	935.0	52.0	384.0	33.0	2668.0	64.0	85.5
TSUPB026_11	1180	0.41	1.757	0.056	0.0699	0.0017	0.89	0.1829	0.0033	1029.0	20.0	436.0	10.0	2679.0	30.0	83.6
TSUPB026_12	3480	0.47	0.211	0.028	0.0083	0.0011	0.97	0.1836	0.0065	194.0	23.0	53.3	7.2	2682.0	57.0	98.0
TSUPB026_13	2120	0.47	3.040	0.310	0.1200	0.0110	0.98	0.1836	0.0034	1402.0	91.0	731.0	64.0	2685.0	30.0	73.0
TSUPB026_14	3280	0.41	0.607	0.036	0.0245	0.0014	0.97	0.1847	0.0036	481.0	23.0	155.8	8.6	2695.0	33.0	94.2
TSUPB026_15	1230	0.30	2.450	0.200	0.0946	0.0066	0.98	0.1850	0.0033	1251.0	60.0	582.0	39.0	2697.0	29.0	78.5
TSUPB026_16	668	0.33	3.150	0.160	0.1221	0.0062	0.85	0.1853	0.0035	1452.0	36.0	742.0	36.0	2700.0	32.0	72.6
TSUPB026_17	2700	0.69	0.322	0.017	0.0126	0.0006	0.95	0.1873	0.0044	283.0	13.0	80.5	3.8	2717.0	39.0	97.0
TSUPB026_18	1098	0.13	2.954	0.098	0.1145	0.0031	0.94	0.1871	0.0018	1393.0	25.0	699.0	18.0	2719.0	16.0	74.3
TSUPB026_19	2040	0.55	0.311	0.023	0.0123	0.0007	0.78	0.1883	0.0049	274.0	18.0	78.7	4.3	2721.0	43.0	97.2
TSUPB026_20	1220	0.34	2.170	0.084	0.0838	0.0039	0.90	0.1885	0.0030	1171.0	26.0	519.0	23.0	2729.0	27.0	81.0
TSUPB026_21	1440	0.49	2.010	0.140	0.0780	0.0050	0.95	0.1899	0.0047	1114.0	51.0	484.0	30.0	2739.0	41.0	82.2
TSUPB026_22	810	0.28	2.580	0.170	0.0965	0.0079	0.85	0.1876	0.0063	1289.0	50.0	593.0	46.0	2750.0	58.0	78.3
TSUPB026_23	1520	0.38	1.120	0.230	0.0408	0.0078	0.99	0.1954	0.0045	730.0	120.0	257.0	49.0	2786.0	38.0	90.9
TSUPB026_24	760	0.29	3.080	0.610	0.1070	0.0190	0.99	0.1956	0.0050	1400.0	140.0	690.0	130.0	2788.0	41.0	76.6
TSUPB026_25	1340	0.62	0.563	0.053	0.0206	0.0019	0.95	0.1978	0.0082	451.0	35.0	131.0	12.0	2801.0	68.0	95.3

		Ratios								Age (Ma)						
Analysis	U ppm	Th/U	$^{207}Pb/^{235}U$	Err 2SE abs	$^{206}Pb/^{238}U$	Err 2SE abs	Rho	$^{207}Pb/^{206}Pb$	Err 2SE abs	$^{207}Pb/^{235}U$	Err 2SE abs	$^{206}Pb/^{238}U$	Err 2SE abs	$^{207}Pb/^{206}Pb$	Err 2SE abs	% Disc
TSUPB026_26	790	0.47	2.870	0.290	0.1060	0.0100	0.99	0.1972	0.0034	1380.0	87.0	648.0	61.0	2802.0	28.0	77.0
TSUPB026_27	402	0.47	6.730	0.320	0.2430	0.0140	0.93	0.1982	0.0032	2075.0	43.0	1403.0	72.0	2811.0	26.0	49.2
TSUPB026_28	627	0.39	3.780	0.340	0.1380	0.0130	0.95	0.1986	0.0047	1582.0	70.0	833.0	75.0	2813.0	39.0	71.3
TSUPB026_29	606	0.29	5.300	0.330	0.1950	0.0110	0.75	0.1986	0.0031	1863.0	56.0	1145.0	61.0	2814.0	25.0	59.5
TSUPB026_30	2110	0.26	1.670	0.160	0.0632	0.0059	0.97	0.1981	0.0050	1012.0	55.0	395.0	36.0	2818.0	36.0	85.9
TSUPB026_31	510	0.32	1.800	0.230	0.0659	0.0071	0.97	0.1988	0.0078	1045.0	75.0	411.0	43.0	2822.0	60.0	85.8
TSUPB026_32	510	0.37	2.890	0.200	0.1059	0.0068	0.94	0.1993	0.0057	1374.0	52.0	648.0	39.0	2827.0	49.0	77.6
TSUPB026_33	260	0.41	5.340	0.450	0.1940	0.0160	0.98	0.2009	0.0028	1844.0	76.0	1136.0	85.0	2831.0	23.0	60.0
TSUPB026_34	620	0.34	5.270	0.800	0.1890	0.0280	1.00	0.2008	0.0028	1830.0	140.0	1110.0	150.0	2832.0	23.0	60.9
TSUPB026_35	910	0.33	2.840	0.140	0.1023	0.0056	0.92	0.2010	0.0044	1363.0	39.0	628.0	33.0	2833.0	36.0	77.8
TSUPB026_36	570	0.15	5.900	0.260	0.2121	0.0091	0.81	0.2018	0.0031	1958.0	39.0	1239.0	48.0	2840.0	25.0	56.3
TSUPB026_37	1060	0.36	1.360	0.110	0.0481	0.0044	0.93	0.2016	0.0065	866.0	48.0	303.0	27.0	2848.0	56.0	89.3
TSUPB026_38	562	0.84	2.720	0.200	0.0981	0.0078	0.83	0.2037	0.0077	1340.0	59.0	603.0	46.0	2850.0	59.0	78.7
TSUPB026_39	580	1.02	4.250	0.330	0.1500	0.0094	0.96	0.2031	0.0031	1694.0	71.0	900.0	53.0	2851.0	25.0	68.7
TSUPB026_40	350	0.36	8.700	1.100	0.3130	0.0370	1.00	0.2032	0.0017	2290.0	120.0	1780.0	170.0	2852.0	14.0	37.8
TSUPB026_41	217	0.30	7.360	0.720	0.2600	0.0250	0.98	0.2023	0.0034	2158.0	89.0	1480.0	130.0	2852.0	31.0	48.1
TSUPB026_42	550	0.22	4.780	0.730	0.1720	0.0260	0.99	0.2038	0.0044	1750.0	150.0	1010.0	150.0	2862.0	33.0	64.4
TSUPB026_43	650	0.22	3.330	0.240	0.1162	0.0074	0.89	0.2052	0.0067	1481.0	55.0	708.0	43.0	2864.0	53.0	75.3
TSUPB026_44	4600	0.74	0.670	0.160	0.0239	0.0055	1.00	0.2050	0.0030	507.0	98.0	152.0	35.0	2866.0	24.0	94.7
TSUPB026_45	670	0.31	7.530	0.690	0.2690	0.0240	1.00	0.2057	0.0015	2166.0	90.0	1530.0	120.0	2872.0	12.0	46.6
TSUPB026_46	431	0.24	6.260	0.380	0.2220	0.0160	0.97	0.2060	0.0039	2007.0	55.0	1292.0	83.0	2873.0	32.0	55.6
TSUPB026_47	690	0.53	3.020	0.230	0.1073	0.0075	0.95	0.2048	0.0057	1404.0	64.0	656.0	44.0	2873.0	49.0	77.6
TSUPB026_48	500	0.45	7.250	0.580	0.2540	0.0200	0.99	0.2064	0.0033	2127.0	79.0	1450.0	110.0	2876.0	26.0	49.4
TSUPB026_49	440	0.29	7.100	1.300	0.2440	0.0370	0.98	0.2066	0.0047	2090.0	160.0	1400.0	190.0	2878.0	37.0	51.9
TSUPB026_50	570	0.33	6.600	1.200	0.2320	0.0390	1.00	0.2079	0.0024	2050.0	160.0	1330.0	210.0	2889.0	19.0	54.1
TSUPB026_51	690	0.29	4.260	0.270	0.1468	0.0091	0.97	0.2082	0.0044	1679.0	56.0	882.0	51.0	2889.0	34.0	69.6
TSUPB026_52	309	0.22	7.480	0.740	0.2580	0.0280	0.99	0.2074	0.0032	2148.0	96.0	1470.0	150.0	2890.0	26.0	49.0
TSUPB026_53	860	0.30	5.200	0.680	0.1820	0.0230	0.99	0.2084	0.0040	1800.0	150.0	1070.0	130.0	2891.0	31.0	62.9
TSUPB026_54	420	0.54	9.160	0.790	0.3200	0.0280	0.98	0.2087	0.0047	2344.0	84.0	1790.0	140.0	2894.0	37.0	39.8
TSUPB026_55	263	0.64	8.610	0.370	0.2990	0.0100	0.94	0.2089	0.0034	2294.0	40.0	1688.0	50.0	2896.0	26.0	41.8
TSUPB026_56	401	0.45	7.430	0.910	0.2560	0.0320	0.99	0.2091	0.0031	2150.0	120.0	1460.0	160.0	2898.0	24.0	49.4
TSUPB026_57	410	0.60	6.500	1.500	0.2310	0.0500	1.00	0.2093	0.0057	2010.0	210.0	1330.0	260.0	2899.0	45.0	54.1
TSUPB026_58	413	0.36	10.560	0.260	0.3695	0.0089	0.96	0.2097	0.0028	2492.0	28.0	2041.0	50.0	2902.0	22.0	29.5
TSUPB026_59	989	0.42	2.485	0.082	0.0850	0.0032	0.57	0.2098	0.0049	1267.0	24.0	526.0	19.0	2902.0	37.0	81.9
TSUPB026_60	533	0.16	9.340	0.310	0.3250	0.0120	0.96	0.2098	0.0017	2371.0	31.0	1813.0	58.0	2904.0	13.0	38.1
TSUPB026_61	290	0.42	9.000	0.530	0.3110	0.0170	0.97	0.2103	0.0037	2330.0	59.0	1741.0	84.0	2906.0	29.0	40.2
TSUPB026_62	220	0.41	4.560	0.390	0.1590	0.0140	0.95	0.2103	0.0043	1730.0	73.0	951.0	77.0	2906.0	33.0	67.7
TSUPB026_63	261	0.31	13.040	0.840	0.4460	0.0300	0.98	0.2104	0.0040	2672.0	67.0	2370.0	140.0	2907.0	31.0	18.5
TSUPB026_64	419	0.25	6.570	0.440	0.2290	0.0150	0.98	0.2103	0.0036	2048.0	60.0	1329.0	81.0	2907.0	28.0	55.1
TSUPB026_65	380	0.44	6.000	0.760	0.2080	0.0240	0.99	0.2108	0.0049	1970.0	120.0	1210.0	130.0	2909.0	37.0	58.5
TSUPB026_66	325	0.42	8.500	1.800	0.2980	0.0560	1.00	0.2107	0.0062	2260.0	200.0	1670.0	280.0	2910.0	47.0	42.7
TSUPB026_67	112	0.51	9.170	0.280	0.3049	0.0078	0.74	0.2110	0.0038	2354.0	28.0	1715.0	39.0	2913.0	29.0	41.4
TSUPB026_68	700	0.37	2.340	0.160	0.0802	0.0044	0.94	0.2108	0.0040	1232.0	50.0	497.0	26.0	2918.0	27.0	83.0
TSUPB026_69	301	0.31	8.510	0.420	0.2950	0.0120	0.87	0.2120	0.0048	2282.0	46.0	1666.0	58.0	2919.0	37.0	42.6
TSUPB026_70	389	0.32	9.820	0.470	0.3420	0.0130	0.98	0.2121	0.0028	2414.0	46.0	1897.0	65.0	2921.0	21.0	34.6
TSUPB026_71	458	0.64	6.670	0.570	0.2210	0.0220	0.97	0.2125	0.0064	2055.0	79.0	1310.0	110.0	2921.0	49.0	58.2
TSUPB026_72	362	1.08	4.560	0.470	0.1580	0.0150	0.99	0.2125	0.0029	1713.0	87.0	938.0	84.0	2923.0	22.0	68.0
TSUPB026_73	204	0.44	15.100	1.100	0.5110	0.0390	0.90	0.2135	0.0080	2808.0	73.0	2650.0	170.0	2925.0	63.0	9.3
TSUPB026_74	537	0.40	5.800	0.250	0.1980	0.0085	0.94	0.2130	0.0035	1944.0	37.0	1164.0	46.0	2927.0	26.0	60.4
TSUPB026_75	509	0.50	4.820	0.170	0.1641	0.0066	0.88	0.2130	0.0045	1787.0	31.0	979.0	37.0	2927.0	34.0	66.6
TSUPB026_76	299	0.33	12.820	0.410	0.4310	0.0140	0.92	0.2133	0.0037	2665.0	31.0	2311.0	66.0	2930.0	28.0	22.0
TSUPB026_77	480	0.51	9.700	1.600	0.3390	0.0540	1.00	0.2138	0.0025	2420.0	150.0	1860.0	270.0	2934.0	19.0	36.3
TSUPB026_78	319	0.37	8.720	0.890	0.3060	0.0320	0.96	0.2140	0.0046	2360.0	68.0	1710.0	160.0	2934.0	34.0	41.1
TSUPB026_79	70	0.47	14.560	0.620	0.5060	0.0190	0.88	0.2140	0.0039	2785.0	40.0	2640.0	82.0	2935.0	30.0	8.5

		Ratios								Age (Ma)						
Analysis	U ppm	Th/U	$^{207}Pb/^{235}U$	Err 2SE abs	$^{206}Pb/^{238}U$	Err 2SE abs	Rho	$^{207}Pb/^{206}Pb$	Err 2SE abs	$^{207}Pb/^{235}U$	Err 2SE abs	$^{206}Pb/^{238}U$	Err 2SE abs	$^{207}Pb/^{206}Pb$	Err 2SE abs	% Disc
TSUPB026_80	338	0.44	8.900	0.980	0.3080	0.0350	0.97	0.2144	0.0064	2300.0	120.0	1720.0	180.0	2935.0	48.0	40.8
TSUPB026_81	420	0.50	9.010	0.510	0.3030	0.0150	0.98	0.2144	0.0036	2332.0	56.0	1703.0	77.0	2937.0	27.0	43.2
TSUPB026_82	266	0.70	14.250	0.800	0.4840	0.0240	0.99	0.2144	0.0026	2758.0	57.0	2540.0	110.0	2938.0	20.0	13.7
TSUPB026_83	248	0.25	8.520	0.720	0.2920	0.0230	0.97	0.2144	0.0043	2275.0	82.0	1640.0	120.0	2938.0	33.0	43.8
TSUPB026_84	172	0.32	13.620	0.670	0.4680	0.0200	0.96	0.2145	0.0022	2720.0	47.0	2471.0	86.0	2939.0	17.0	15.7
TSUPB026_85	175	0.43	11.630	0.530	0.3950	0.0170	0.96	0.2146	0.0033	2571.0	44.0	2142.0	78.0	2940.0	25.0	27.2
TSUPB026_86	189	0.87	7.720	0.270	0.2605	0.0099	0.97	0.2146	0.0022	2194.0	33.0	1490.0	51.0	2946.0	15.0	49.2
TSUPB026_87	463	0.45	9.500	1.300	0.3100	0.0340	0.98	0.2159	0.0018	2370.0	120.0	1830.0	240.0	2950.0	13.0	41.1
TSUPB026_88	500	0.31	9.500	2.100	0.3350	0.0780	1.00	0.2160	0.0064	2370.0	210.0	1850.0	380.0	2951.0	47.0	37.0
TSUPB026_89	183	0.35	17.060	0.690	0.5770	0.0200	0.95	0.2169	0.0036	2935.0	40.0	2932.0	84.0	2956.0	27.0	1.0
TSUPB026_90	500	0.29	6.450	0.440	0.2180	0.0140	0.96	0.2170	0.0051	2032.0	62.0	1271.0	75.0	2956.0	37.0	57.0
TSUPB026_91	354	0.18	11.290	0.900	0.3820	0.0320	0.98	0.2170	0.0035	2535.0	78.0	2080.0	150.0	2957.0	26.0	29.4
TSUPB026_92	189	0.40	13.400	1.100	0.4540	0.0250	0.97	0.2174	0.0045	2691.0	81.0	2410.0	110.0	2960.0	33.0	19.1
TSUPB026_93	352	0.34	12.420	0.430	0.4160	0.0170	0.95	0.2174	0.0028	2634.0	33.0	2240.0	79.0	2961.0	21.0	24.5
TSUPB026_94	576	0.44	4.370	0.310	0.1490	0.0130	0.95	0.2180	0.0092	1702.0	56.0	892.0	75.0	2961.0	67.0	69.7
TSUPB026_95	156	0.25	17.530	0.930	0.5850	0.0260	0.97	0.2179	0.0042	2958.0	54.0	2970.0	110.0	2964.0	31.0	-0.3
TSUPB026_96	168	0.25	16.400	1.000	0.5540	0.0260	0.98	0.2180	0.0029	2890.0	66.0	2840.0	110.0	2965.0	21.0	4.6
TSUPB026_97	583	0.30	4.420	0.180	0.1457	0.0058	0.80	0.2196	0.0063	1714.0	35.0	876.0	32.0	2976.0	46.0	70.1
TSUPB026_98	248	0.51	13.430	0.550	0.4330	0.0210	0.98	0.2205	0.0036	2707.0	40.0	2316.0	94.0	2983.0	26.0	22.8
TSUPB026_99	167	0.35	17.620	0.380	0.5850	0.0160	0.94	0.2211	0.0027	2969.0	21.0	2970.0	64.0	2988.0	20.0	0.1
TSUPB026_100	249	0.50	14.370	0.440	0.4640	0.0120	0.68	0.2229	0.0056	2773.0	29.0	2456.0	55.0	3012.0	36.0	18.4
TSUPB026_101	524	0.17	3.550	0.260	0.1133	0.0090	0.94	0.2248	0.0056	1534.0	58.0	692.0	52.0	3014.0	40.0	77.0
TSUPB026_102	840	0.59	9.100	1.200	0.2940	0.0390	0.98	0.2250	0.0044	2370.0	130.0	1640.0	200.0	3015.0	31.0	45.7
TSUPB026_103	221	0.41	13.990	0.470	0.4580	0.0150	0.92	0.2254	0.0034	2747.0	32.0	2430.0	68.0	3019.0	24.0	19.9
TSUPB026_104	287	0.51	15.820	0.610	0.4970	0.0230	0.89	0.2280	0.0051	2864.0	38.0	2622.0	91.0	3036.0	36.0	14.6
TSUPB026_Rim2_1	22900	0.51	0.045	0.006	0.0024	0.0004	0.97	0.1434	0.0069	44.7	6.0	15.6	2.8	2268.0	83.0	99.3
TSUPB026_Rim2_2	29000	0.46	0.033	0.006	0.0018	0.0005	0.90	0.1440	0.0150	33.1	5.4	11.5	3.0	2280.0	180.0	99.5
TSUPB026_Rim2_3	16900	0.47	0.072	0.019	0.0036	0.0010	0.99	0.1541	0.0062	71.0	18.0	22.9	6.3	2392.0	68.0	99.0
TSUPB026_Rim2_4	9600	0.46	0.124	0.022	0.0055	0.0007	1.00	0.1701	0.0069	119.0	20.0	35.3	4.7	2557.0	68.0	98.6
TSUPB026_Rim2_5	6900	0.45	0.161	0.018	0.0070	0.0010	0.83	0.1720	0.0200	151.0	15.0	45.1	6.4	2570.0	200.0	98.2
TSUPB026_Rim2_6	4060	0.47	0.255	0.045	0.0103	0.0020	0.99	0.1847	0.0088	230.0	37.0	66.0	12.0	2694.0	79.0	97.6
TSUPB026_Rim2_7	1970	0.51	0.307	0.010	0.0120	0.0004	0.74	0.1870	0.0130	272.1	7.5	77.0	2.8	2710.0	110.0	97.2
TSUPB026_Rim2_8	1850	0.52	0.356	0.047	0.0137	0.0020	0.91	0.1905	0.0076	309.0	35.0	88.0	13.0	2746.0	65.0	96.8
TSUPB026_Rim2_9	2273	0.56	0.375	0.034	0.0144	0.0018	0.18	0.1950	0.0360	323.0	25.0	92.0	12.0	2760.0	320.0	96.6
TSUPB026_Rim2_10	2970	0.52	0.317	0.008	0.0122	0.0001	1.00	0.1924	0.0033	279.3	6.2	78.1	0.5	2762.0	28.0	97.2
TSUPB026_Rim2_11	2170	0.50	0.380	0.049	0.0143	0.0014	0.78	0.1952	0.0057	327.0	36.0	91.5	9.0	2786.0	48.0	96.7
TSUPB026_Rim2_12	1750	0.61	0.426	0.042	0.0160	0.0030	1.00	0.1960	0.0170	360.0	30.0	102.0	19.0	2790.0	140.0	96.3
TSUPB016_1	801	0.29	5.110	0.590	0.1680	0.0150	1.00	0.2097	0.0130	1833.0	96.0	997.0	83.0	2904.0	30.0	65.7
TSUPB016_2	3800	0.09	1.720	0.360	0.0557	0.0089	0.93	0.2140	0.0150	1006.0	140.0	349.0	54.0	2925.0	50.0	77.3
TSUPB016_3	366	0.27	15.240	0.410	0.4993	0.0110	0.86	0.2122	0.0130	2830.0	25.0	2611.0	48.0	2928.0	10.0	11.9
TSUPB016_4	1443	0.15	9.120	0.430	0.3054	0.0130	0.98	0.2138	0.0130	2346.0	43.0	1716.0	64.0	2934.0	6.1	42.2
TSUPB016_5	207	0.47	17.370	0.400	0.5806	0.0110	0.65	0.2160	0.0130	2955.0	22.0	2951.0	46.0	2942.5	6.1	2.0
TSUPB016_6	325	0.32	15.240	0.420	0.4999	0.0130	0.73	0.2163	0.0140	2830.0	26.0	2613.0	55.0	2949.0	6.0	12.8
TSUPB016_7	375	0.34	15.730	0.510	0.5150	0.0170	0.96	0.2167	0.0130	2859.0	31.0	2676.0	72.0	2955.2	4.4	9.6
TSUPB016_8	272	0.46	17.360	0.380	0.5684	0.0095	0.82	0.2166	0.0130	2954.6	21.0	2901.0	39.0	2958.8	6.7	2.8
TSUPB016_9	458	0.29	17.350	0.670	0.5790	0.0270	0.96	0.2191	0.0130	2952.0	38.0	2940.0	110.0	2973.0	10.0	6.5
TSUPB016_10	168	0.45	17.390	0.440	0.5807	0.0130	0.43	0.2193	0.0130	2956.0	24.0	2951.0	53.0	2977.0	17.0	3.2
TSUPB016_11	208	0.19	12.680	0.380	0.4168	0.0097	0.70	0.2191	0.0140	2656.0	28.0	2246.0	44.0	2980.0	13.0	24.6
TSUPB016_12	295	0.36	10.380	0.540	0.3320	0.0140	0.86	0.2211	0.0130	2462.0	48.0	1847.0	66.0	2981.0	14.0	38.3
TSUPB016_13	384	0.46	13.700	0.410	0.4616	0.0100	0.69	0.2194	0.0130	2729.0	28.0	2446.0	45.0	2982.0	12.0	15.8

		Ratios								Age (Ma)						
Analysis	U ppm	Th/U	$^{207}Pb/^{235}U$	Err 2SE abs	$^{206}Pb/^{238}U$	Err 2SE abs	Rho	$^{207}Pb/^{206}Pb$	Err 2SE abs	$^{207}Pb/^{235}U$	Err 2SE abs	$^{206}Pb/^{238}U$	Err 2SE abs	$^{207}Pb/^{206}Pb$	Err 2SE abs	% Disc
TSUPB016_14	521	0.50	11.020	0.470	0.3584	0.0120	0.91	0.2203	0.0130	2529.0	41.0	1973.0	58.0	2982.0	20.0	35.2
TSUPB016_15	359	0.33	17.070	0.360	0.5781	0.0120	0.37	0.2228	0.0130	2938.8	20.0	2941.0	47.0	2999.0	9.5	1.8
TSUPB016_16	178	0.28	18.580	0.390	0.5850	0.0110	0.76	0.2224	0.0130	3020.0	20.0	2969.0	44.0	3001.6	8.6	2.5
TSUPB016_17	218	0.30	18.520	0.410	0.5862	0.0130	0.77	0.2230	0.0140	3019.0	21.0	2973.0	53.0	3005.0	14.0	4.0
TSUPB016_18	277	0.34	18.140	0.430	0.5920	0.0140	0.71	0.2247	0.0140	2997.0	23.0	2996.0	59.0	3020.0	14.0	3.2
TSUPB016_19	161	0.25	18.070	0.370	0.5649	0.0100	0.78	0.2268	0.0140	2993.0	20.0	2886.0	42.0	3024.6	6.9	6.1
TSUPB016_20	404	0.33	16.220	0.380	0.5353	0.0100	0.44	0.2266	0.0130	2892.0	25.0	2764.0	42.0	3030.5	9.4	7.0
TSUPB016_21	457	0.35	14.770	0.520	0.4740	0.0150	0.91	0.2294	0.0130	2804.0	32.0	2498.0	66.0	3045.6	7.3	17.3
TSUPB016_22	320	0.49	16.210	0.400	0.4943	0.0110	0.70	0.2295	0.0130	2889.0	24.0	2589.0	46.0	3050.2	7.8	17.0
TSUPB016_23	432	0.25	16.020	0.390	0.5183	0.0130	0.88	0.2297	0.0130	2878.0	23.0	2691.0	54.0	3055.0	15.0	10.9
TSUPB016_24	512	0.43	12.160	0.400	0.3823	0.0100	0.93	0.2311	0.0140	2615.0	31.0	2087.0	47.0	3055.0	17.0	33.2
TSUPB016_25	136	0.17	17.360	0.460	0.5403	0.0120	0.88	0.2301	0.0140	2954.0	25.0	2784.0	48.0	3057.5	6.8	9.3
TSUPB016_26	1370	0.34	4.698	0.350	0.1447	0.0096	0.80	0.2314	0.0140	1766.0	61.0	871.0	54.0	3059.0	28.0	74.4
TSUPB016_27	533	0.68	17.530	0.420	0.5433	0.0100	0.93	0.2317	0.0130	2963.0	23.0	2797.0	42.0	3061.6	5.9	9.3
TSUPB016_28	89	0.21	14.840	0.380	0.4792	0.0097	0.27	0.2317	0.0140	2805.0	24.0	2524.0	42.0	3065.0	13.0	16.1
TSUPB016_29	1307	0.09	5.280	0.640	0.1500	0.0140	0.85	0.2340	0.0160	1835.0	110.0	899.0	78.0	3067.0	65.0	77.0
TSUPB016_30	366	0.31	16.970	0.510	0.5430	0.0160	0.88	0.2355	0.0140	2932.0	29.0	2797.0	67.0	3083.0	20.0	8.0
TSUPB016_31	951	0.25	4.433	0.340	0.1358	0.0088	0.37	0.2341	0.0140	1718.4	63.0	821.0	50.0	3083.0	21.0	77.8
TSUPB016_32	474	0.11	3.960	0.350	0.1205	0.0091	0.97	0.2337	0.0140	1623.0	72.0	733.0	52.0	3083.0	13.0	79.8
TSUPB016_33	166	0.13	15.950	0.380	0.5017	0.0096	0.60	0.2361	0.0140	2873.0	23.0	2621.0	41.0	3092.7	8.6	14.1
TSUPB016_34	385	0.49	15.010	0.370	0.4450	0.0096	0.69	0.2359	0.0130	2816.0	24.0	2373.0	43.0	3093.0	12.0	26.8
TSUPB016_35	952	0.31	8.840	0.390	0.2673	0.0110	0.95	0.2386	0.0140	2319.0	41.0	1526.0	58.0	3094.0	24.0	56.9
TSUPB016_36	234	0.20	14.960	0.410	0.4707	0.0110	0.88	0.2394	0.0140	2813.0	26.0	2487.0	50.0	3115.0	11.0	18.8
TSUPB016_37	243	0.24	12.510	0.390	0.3761	0.0110	0.90	0.2424	0.0140	2647.0	32.0	2057.0	50.0	3136.0	11.0	37.6
TSUPB016_38	311	0.33	19.480	0.440	0.5651	0.0110	0.65	0.2439	0.0130	3065.0	22.0	2887.0	45.0	3146.0	16.0	10.9
TSUPB016_39	952	0.36	6.498	0.340	0.1896	0.0089	0.87	0.2450	0.0130	2045.0	47.0	1119.0	48.0	3151.7	6.8	73.0
TSUPB016_40	791	0.40	13.520	0.440	0.4070	0.0160	0.97	0.2451	0.0130	2716.0	31.0	2200.0	74.0	3156.0	12.0	31.9
TSUPB016_41	618	0.44	11.070	0.390	0.3208	0.0089	0.63	0.2459	0.0140	2529.0	33.0	1794.0	44.0	3158.0	15.0	50.0
TSUPB016_42	636	0.34	13.330	0.490	0.4080	0.0140	0.72	0.2462	0.0150	2703.0	35.0	2204.0	66.0	3162.0	36.0	29.7
TSUPB016_43	538	0.20	8.650	0.550	0.2407	0.0093	0.57	0.2530	0.0170	2296.0	58.0	1390.0	48.0	3194.0	64.0	67.4
TSUPB016_44	220	0.12	14.100	0.440	0.3930	0.0150	0.89	0.2563	0.0140	2756.0	30.0	2138.0	70.0	3218.0	25.0	40.2
TSUPB016_45	619	0.72	13.770	0.520	0.3699	0.0110	0.70	0.2611	0.0140	2733.0	35.0	2029.0	53.0	3264.0	22.0	45.8
TSUPB016_46	282	0.18	19.360	0.420	0.5340	0.0150	0.29	0.2668	0.0150	3060.0	21.0	2755.0	65.0	3287.0	38.0	15.7
TSUPB016_47	1137	0.58	8.340	0.370	0.2249	0.0090	0.85	0.2706	0.0130	2267.0	40.0	1310.0	50.0	3307.0	16.0	73.6
TSUPB016_48	813	0.26	12.230	0.460	0.3123	0.0120	0.97	0.2842	0.0140	2619.0	37.0	1751.0	60.0	3380.0	15.0	61.1

Appendix 6: U-Pb apatite data table.

	Ratios										Age (Ma)							
Analysis	$^{207}Pb/^{235}U$	Err 2SE abs	$^{206}Pb/^{238}U$	Err 2SE abs	Rho	$^{238}U/^{206}Pb$	Err 2SE abs	$^{207}Pb/^{206}Pb$	Err 2SE abs	Rho	$^{206}Pb/^{238}U$ Age	Err 2SE abs	$^{207}Pb/^{235}U$ Age	Err 2SE abs	$^{207}Pb/^{206}Pb$ Age	Err 2SE abs	^{207}Pb Corrected Age	Err 2SE abs
McClure_1	4.04	0.13	0.1136	0.0025	0.028134	8.802816901	0.193724	0.2622	0.0098	0.67696	693.6	15.3	1642.3	52.8	3260.0	121.8	528.5	14.0
McClure_2	4.79	0.16	0.1204	0.0023	0.22756	8.305647841	0.1586627	0.293	0.01	0.37223	732.9	14.0	1783.1	59.6	3433.6	117.2	532.2	13.3
McClure_3	2.427	0.095	0.0994	0.0019	-0.001911	10.06036217	0.1923007	0.1806	0.0079	0.061395	610.9	11.7	1250.6	49.0	2658.4	116.3	523.5	11.3
McClure_4	2.46	0.1	0.1004	0.0018	-0.0046717	9.960159363	0.1785686	0.1787	0.0079	0.42859	616.8	11.1	1260.4	51.2	2640.8	116.7	530.0	10.9
McClure_5	1.882	0.069	0.0951	0.0014	0.037485	10.51524711	0.1547986	0.1405	0.0056	0.023111	585.6	8.6	1074.8	39.4	2233.4	89.0	529.3	8.5
McClure_6	1.637	0.064	0.0934	0.0015	-0.037664	10.70663812	0.1719481	0.1265	0.0053	0.3407	575.6	9.2	984.6	38.5	2049.9	85.9	529.7	9.1
McClure_7	4.51	0.23	0.1162	0.0026	-0.048734	8.605851979	0.1925578	0.279	0.015	0.074034	708.7	15.9	1732.8	88.4	3357.3	180.5	526.0	17.2
McClure_8	4.9	0.23	0.1188	0.0029	0.25536	8.417508418	0.2054779	0.29	0.014	0.046306	723.7	17.7	1802.3	84.6	3417.6	165.0	528.0	17.5
McClure_9	5.41	0.37	0.1226	0.0042	0.21341	8.156606852	0.279427	0.315	0.023	0.40733	745.5	25.5	1886.4	129.0	3545.6	258.9	522.0	27.1
McClure_10	2.455	0.085	0.1015	0.0017	0.15709	9.852216749	0.1650125	0.176	0.0062	0.27989	623.2	10.4	1258.9	43.6	2615.5	92.1	537.7	9.9
McClure_11	2.58	0.1	0.1009	0.0018	-0.024941	9.910802775	0.1768032	0.1952	0.0085	0.041296	619.7	11.1	1295.0	50.2	2786.5	121.3	520.4	11.0
McClure_12	2.595	0.093	0.1024	0.0018	0.24207	9.765625	0.1716614	0.1912	0.0069	0.32277	628.5	11.0	1299.2	46.6	2752.5	99.3	530.9	10.5
McClure_13	2.266	0.076	0.0999	0.0018	0.079102	10.01001001	0.1803605	0.1704	0.0056	0.41262	613.8	11.1	1201.8	40.3	2561.6	84.2	533.5	10.2
McClure_14	2.086	0.072	0.0978	0.0015	-0.073161	10.22494888	0.1568244	0.1536	0.0054	0.37192	601.5	9.2	1144.2	39.5	2386.4	83.9	534.6	8.9
McClure_15	4.26	0.12	0.1144	0.0016	0.21431	8.741258741	0.1222554	0.2671	0.0079	0.33336	698.3	9.8	1685.7	47.5	3289.1	97.3	528.1	9.8
McClure_16	2.62	0.11	0.101	0.002	-0.018616	9.900990099	0.1960592	0.1883	0.0077	0.39938	620.3	12.3	1306.3	54.8	2727.4	111.5	526.0	11.7
McClure_17	2.041	0.079	0.0958	0.0017	0.089479	10.43841336	0.1852328	0.1525	0.0061	0.26674	589.7	10.5	1129.3	43.7	2374.1	95.0	524.7	10.0
McClure_18	2.057	0.081	0.0977	0.0015	-0.0084793	10.23541453	0.1571456	0.1502	0.0064	0.41584	600.9	9.2	1134.6	44.7	2348.2	100.1	536.5	9.2
McClure_19	3.51	0.12	0.1074	0.002	0.17319	9.310986965	0.173389	0.2324	0.0081	0.37949	657.6	12.2	1529.5	52.3	3068.6	107.0	523.8	11.5
McClure_20	1.722	0.064	0.0942	0.0014	0.15034	10.61571125	0.1577707	0.1307	0.0052	0.16729	580.3	8.6	1016.8	37.8	2107.4	83.8	530.6	8.5
McClure_21	2.848	0.065	0.1071	0.0032	0.11115	9.337068161	0.2789787	0.1944	0.0061	0.26644	655.9	19.6	1368.3	31.2	2779.7	87.2	551.1	16.8
McClure_22	4.49	0.7	0.1147	0.003	0.16358	8.718395815	0.2280313	0.265	0.018	-0.074406	700.0	18.3	1729.1	269.6	3276.7	222.6	529.0	20.5
McClure_23	3.43	0.55	0.1024	0.0018	-0.076894	9.765625	0.1716614	0.245	0.046	0.080925	628.5	11.0	1511.3	242.3	3152.7	591.9	488.2	36.2
McClure_24	3.63	0.1	0.1111	0.0021	0.98046	9.00090009	0.170134	0.2384	0.0072	-0.010898	679.1	12.8	1556.1	42.9	3109.3	93.9	534.8	11.6
McClure_25	1.912	0.049	0.0972	0.0014	0.0074806	10.28806584	0.148182	0.1435	0.0037	0.51915	598.0	8.6	1085.3	27.8	2269.9	58.5	537.9	8.0
McClure_26	2.368	0.056	0.0971	0.0016	0.032641	10.29866117	0.1696999	0.1784	0.0049	0.49632	597.4	9.8	1233.0	29.2	2638.1	72.5	512.0	9.0
McClure_27	2.83	0.082	0.0995	0.0016	-0.04796	10.05025126	0.1616121	0.2059	0.0066	0.21801	611.5	9.8	1363.5	39.5	2873.5	92.1	503.9	9.4
McClure_28	2.066	0.045	0.0931	0.0014	0.02921	10.74113856	0.1615209	0.1586	0.0041	0.57021	573.8	8.6	1137.6	24.8	2440.8	63.1	505.1	8.0
McClure_29	4.14	0.15	0.1122	0.0042	0.57909	8.912655971	0.3336288	0.263	0.011	0.40343	685.5	25.7	1662.2	60.2	3264.8	136.5	519.3	21.2
McClure_30	3.01	0.11	0.1007	0.0023	-0.080292	9.930486594	0.2268135	0.2109	0.0088	0.59317	618.5	14.1	1410.2	51.5	2912.5	121.5	506.1	13.1
McClure_31	2.91	0.13	0.102	0.0021	0.16544	9.803921569	0.2018454	0.211	0.016	-0.076294	626.1	12.9	1384.5	61.9	2913.2	220.9	512.5	16.0
TSUPB015_1	-57000	29000	-410	210	0.96548	-0.002439024	0.001249256	1.081	0.051	0.0039947	-	-	-	-	5346.6	252.2	0.0	454890.4
TSUPB015_2	1820	530	10.3	1.2	0.99666	0.097087379	0.01131115	1.061	0.052	-0.011848	15631.3	1821.1	7622.6	2219.8	5320.4	260.8	0.0	4948.9
TSUPB015_3	898	47	6.63	0.35	0.8599	0.150829563	0.007962345	0.95	0.025	0.27811	13099.7	691.5	6905.9	361.4	5165.2	135.9	-15982.7	16736.5
TSUPB015_4	1024	61	7.72	0.59	0.20451	0.129533679	0.009899595	1.024	0.031	-0.063833	13960.5	1066.9	7039.1	419.3	5270.7	159.6	0.0	2217.8
TSUPB015_5	1690	130	11.31	0.81	0.59621	0.08841733	0.006332276	1.034	0.032	-0.05529	16183.2	1159.0	7547.4	580.6	5284.3	163.5	0.0	3323.8
TSUPB015_6	1540	100	10.79	0.66	0.77241	0.092678406	0.005668929	1.01	0.033	-0.020542	15904.9	972.9	7453.1	484.0	5251.4	171.6	0.0	3142.6
TSUPB015_7	1095	62	7.84	0.46	0.84348	0.12755102	0.007483861	1.014	0.031	0.25683	14048.6	824.3	7107.1	402.4	5256.9	160.7	0.0	2161.5
TSUPB015_8	1267	81	8.94	0.54	0.75125	0.111856823	0.006756452	1.005	0.032	-0.030894	14804.6	894.2	7255.1	463.8	5244.4	167.0	0.0	2526.9
TSUPB015_9	1097	57	8.5	0.55	0.19065	0.117647059	0.007612457	1.001	0.03	0.38933	14512.8	939.1	7108.9	369.4	5238.8	157.0	0.0	2285.2
TSUPB015_10	1007	69	7.38	0.56	0.85274	0.135501355	0.01028195	0.998	0.028	0.064888	13704.1	1039.9	7022.1	481.2	5234.6	146.9	0.0	1910.8
TSUPB015_11	1354	81	9.96	0.6	0.92347	0.100401606	0.00604829	0.97	0.025	0.22857	15434.3	929.8	7322.5	438.1	5194.5	133.9	0.0	2242.3
TSUPB015_12	-189000	82000	-780	450	0.97935	-0.001282051	0.000739645	1.073	0.029	-0.067094	-	-	-	-	5336.2	144.2	0.0	893058.8
TSUPB015_13	894	42	6.46	0.31	0.7384	0.154798762	0.007428424	1.016	0.032	0.32346	12954.4	621.7	6901.4	324.2	5259.7	165.7	0.0	1803.1
TSUPB015_14	819	56	5.65	0.27	0.2229	0.17699115	0.008457984	0.998	0.037	-0.014372	12213.5	583.7	6812.5	465.8	5234.6	194.1	0.0	1786.0
TSUPB015_15	745	37	5.61	0.31	0.59213	0.178253119	0.009849994	0.977	0.032	0.31116	12174.6	672.7	6716.5	333.6	5204.7	170.5	-20412.4	35280.4
TSUPB015_16	1115	68	7.94	0.48	0.51728	0.125944584	0.007613778	1.01	0.028	0.044054	14121.1	853.7	7125.5	434.6	5251.4	145.6	0.0	2013.7
TSUPB015_17	3740	420	25.9	3.2	0.95893	0.038610039	0.004770352	1.058	0.028	-0.0074929	21222.4	2622.1	8353.7	938.1	5316.5	140.7	0.0	8481.4
TSUPB015_18	-350000	100000	-2560	710	0.97993	-0.000390625	0.000108337	1.09	0.031	-0.086575	-	-	-	-	5358.2	152.4	0.0	1620089.6
TSUPB015_19	126.1	3.5	1.303	0.038	-0.024866	0.767459708	0.02238179	0.692	0.025	0.21931	5377.7	156.8	4919.5	136.5	4714.2	170.3	3154.2	304.2
TSUPB015_20	2160	250	14.9	1.8	0.99994	0.067114094	0.008107743	1.051	0.03	-0.028153	17832.8	2154.3	7796.4	902.4	5307.2	151.5	0.0	4936.7
TSUPB015_21	1770	160	11.82	0.98	0.96809	0.084602369	0.00701441	1.034	0.023	-0.028809	16444.8	1363.4	7594.4	686.5	5284.3	117.5	0.0	2845.4
TSUPB015_22	1780	210	13	2.4	0.99985	0.076923077	0.01420118	1.042	0.037	0.19244	17012.5	3140.8	7600.1	896.6	5295.1	188.0	0.0	5706.3
TSUPB015_23	194.4	6	1.735	0.052	-0.00058646	0.576368876	0.01727446	0.821	0.042	0.11491	6485.9	194.4	5356.2	165.3	4958.6	253.7	1127.9	505.8
TSUPB015_24	3260	920	24.3	5.4	0.97069	0.041152263	0.009144947	1.011	0.042	0.01599	20827.1	4628.2	8214.2	2318.1	5252.7	218.2	0.0	11487.7
TSUPB015_25	2800	280	19.4	2	0.96873	0.051546392	0.005314061	1.067	0.038	-0.05511	19439.4	2004.1	8059.8	806.0	5328.3	189.8	0.0	7228.6

	Ratios										Age (Ma)							
Analysis	$^{207}Pb/^{235}U$	Err 2SE abs	$^{206}Pb/^{238}U$	Err 2SE abs	Rho	$^{238}U/^{206}Pb$	Err 2SE abs	$^{207}Pb/^{206}Pb$	Err 2SE abs	Rho	$^{206}Pb/^{238}U$ Age	Err 2SE abs	$^{207}Pb/^{235}U$ Age	Err 2SE abs	$^{207}Pb/^{206}Pb$ Age	Err 2SE abs	^{207}Pb Corrected Age	Err 2SE abs
TSUPB015_26	1800	130	12.28	0.86	0.94479	0.081433225	0.005702978	1.023	0.03	0.017727	16672.1	1167.6	7611.4	549.7	5269.3	154.5	0.0	3388.2
TSUPB015_27	1044	58	7.57	0.43	0.63583	0.132100396	0.007503721	0.997	0.028	0.018715	13848.6	786.6	7058.7	392.2	5233.2	147.0	0.0	1892.7
TSUPB015_28	1206	66	8.35	0.41	0.90775	0.119760479	0.005880455	1.029	0.026	0.18617	14410.2	707.6	7205.0	394.3	5277.5	133.3	0.0	1971.1
TSUPB015_29	1420	130	9.96	0.93	0.87593	0.100401606	0.009374849	1.012	0.033	0.089486	15434.3	1441.2	7370.8	674.8	5254.1	171.3	0.0	3075.1
TSUPB015_30	95.9	2.4	1.088	0.026	0.58256	0.919117647	0.02196421	0.628	0.014	0.48268	4745.9	113.4	4644.0	116.2	4574.2	102.0	2954.6	146.5
TSUPB015_31	1192	67	8.62	0.51	0.89063	0.116009281	0.006863658	0.993	0.026	0.29609	14593.7	863.4	7193.2	404.3	5227.5	136.9	0.0	2030.6
TSUPB015_32	1680	130	13.3	1.4	0.34332	0.07518797	0.007914523	0.98	0.038	0.0061527	17149.1	1805.2	7541.4	583.6	5209.0	202.0	0.0	4535.8
TSUPB015_33	842	54	6	0.39	0.5128	0.166666667	0.01083333	1.001	0.036	-0.022687	12544.1	815.4	6840.6	438.7	5238.8	188.4	0.0	1885.4
TSUPB015_34	978	65	6.83	0.41	0.60285	0.146412884	0.00878906	1.008	0.037	0.056581	13266.5	796.4	6992.5	464.7	5248.6	192.7	0.0	2192.5
TSUPB015_35	1079	73	8.23	0.73	0.32696	0.121506683	0.01077763	1.011	0.038	0.037018	14326.9	1270.8	7092.2	479.8	5252.7	197.4	0.0	2815.6
TSUPB015_36	910	47	6.72	0.35	0.58763	0.148809524	0.007750496	0.982	0.025	0.085985	13175.3	686.2	6919.4	357.4	5211.8	132.7	0.0	1505.5
TSUPB015_37	4470	740	29.3	4.4	0.99885	0.034129693	0.005125278	1.055	0.035	-0.011275	21989.7	3302.2	8534.7	1412.9	5312.5	176.2	0.0	11670.7
TSUPB015_38	-77000	32000	-600	280	0.60937	-0.001666667	0.000777778	1.027	0.056	0.0038511	-	-	-	-	5274.8	287.6	0.0	518013.7
TSUPB016_1	30.9	0.77	0.6	0.012	0.41048	1.666666667	0.03333333	0.3716	0.0089	0.36006	3029.8	60.6	3515.9	87.6	3798.0	91.0	2417.2	61.8
TSUPB016_2	24.97	0.58	0.5894	0.0094	0.22288	1.696640652	0.02705874	0.3076	0.0071	0.041909	2987.0	47.6	3307.0	76.8	3508.9	81.0	2628.1	54.1
TSUPB016_3	39.3	0.98	0.672	0.016	0.39903	1.488095238	0.03543084	0.428	0.012	0.2204	3313.6	78.9	3753.2	93.6	4010.5	112.4	2495.9	82.8
TSUPB016_4	21.21	0.65	0.5442	0.0097	0.11703	1.837559721	0.03275327	0.2845	0.0084	0.10455	2801.0	49.9	3148.2	96.5	3387.8	100.0	2482.3	55.6
TSUPB016_5	18.64	0.59	0.518	0.01	0.13114	1.930501931	0.03726838	0.2621	0.0086	0.28373	2690.7	51.9	3023.4	95.7	3259.4	106.9	2426.2	57.0
TSUPB016_6	20.07	0.51	0.5345	0.0087	0.031621	1.87090739	0.03045256	0.2712	0.0066	0.18378	2760.4	44.9	3094.7	78.6	3313.0	80.6	2480.0	48.7
TSUPB016_7	34.11	0.87	0.651	0.013	0.32252	1.53609831	0.03067477	0.3796	0.0094	0.4714	3232.1	64.5	3613.2	92.2	3830.2	94.8	2628.5	71.1
TSUPB016_8	15.86	0.33	0.491	0.014	0.20401	2.036659878	0.05807177	0.2344	0.0049	0.2942	2575.0	73.4	2868.4	59.7	3082.3	64.4	2377.2	72.5
TSUPB016_9	29.89	0.98	0.613	0.013	0.11386	1.63132137	0.03459572	0.352	0.011	-0.020278	3082.0	65.4	3483.2	114.2	3715.7	116.1	2563.3	73.7
TSUPB016_10	34.39	0.88	0.641	0.012	0.43259	1.560062402	0.02920554	0.3885	0.0098	0.078463	3192.9	59.8	3621.3	92.7	3865.2	97.5	2538.1	66.1
TSUPB016_11	27.82	0.78	0.595	0.011	0.36654	1.680672269	0.03107125	0.3421	0.009	0.27018	3009.7	55.6	3412.8	95.7	3672.2	96.6	2515.5	61.0
TSUPB016_12	28.86	0.78	0.586	0.011	0.48716	1.706484642	0.03203299	0.3512	0.0083	0.08564	2973.2	55.8	3448.8	93.2	3712.2	87.7	2434.5	57.8
TSUPB016_13	53.2	1.1	0.764	0.016	0.39182	1.308900524	0.02741153	0.502	0.012	0.48723	3658.9	76.6	4054.1	83.8	4247.1	101.5	2504.5	83.3
TSUPB016_14	26.78	0.75	0.56	0.012	0.18618	1.785714286	0.03826531	0.343	0.011	0.44809	2866.6	61.4	3375.5	94.5	3676.2	117.9	2342.6	65.3
TSUPB016_15	24.18	0.6	0.5606	0.0091	0.13368	1.783803068	0.02895578	0.3103	0.0077	0.034121	2869.1	46.6	3275.7	81.3	3522.4	87.4	2469.8	51.1
TSUPB016_16	33.9	1	0.622	0.012	0.2388	1.607717042	0.03101705	0.393	0.011	0.022286	3117.9	60.2	3607.1	106.4	3882.5	108.7	2428.1	66.5
TSUPB016_17	47.9	1.4	0.726	0.013	0.36176	1.377410468	0.02466437	0.476	0.013	0.29878	3518.5	63.0	3949.6	115.4	4168.6	113.8	2488.0	78.4
TSUPB016_18	27.88	0.66	0.607	0.011	0.60773	1.647446458	0.02985488	0.3289	0.007	0.030386	3058.0	55.4	3414.9	80.8	3612.0	76.9	2631.5	60.0
TSUPB016_19	37.7	1.2	0.643	0.015	0.13128	1.555209953	0.03628017	0.423	0.013	-0.037657	3200.8	74.7	3712.1	118.2	3992.9	122.7	2388.0	79.5
TSUPB016_20	43.7	2	0.705	0.024	0.059486	1.418439716	0.04828731	0.451	0.02	0.03929	3439.6	117.1	3858.4	176.6	4088.5	181.3	2529.6	130.2
TSUPB016_21	61.9	1.9	0.826	0.022	0.27471	1.210653753	0.03224502	0.535	0.018	-0.016248	3881.6	103.4	4205.3	129.1	4340.7	146.0	2563.0	123.0
TSUPB016_22	18.13	0.46	0.538	0.01	0.19194	1.858736059	0.034549	0.2426	0.0072	0.45284	2775.1	51.6	2996.7	76.0	3137.1	93.1	2600.3	58.7
TSUPB016_23	23.1	1.4	0.576	0.02	-0.0044422	1.736111111	0.06028164	0.292	0.017	0.11005	2932.4	101.8	3231.2	195.8	3428.3	199.6	2619.8	118.9
TSUPB016_24	36.62	0.97	0.683	0.015	0.5404	1.464128843	0.0321551	0.386	0.01	0.012751	3355.9	73.7	3683.3	97.6	3855.4	99.9	2760.3	84.2
TSUPB016_25	46.1	1.3	0.707	0.016	0.19835	1.414427157	0.03200967	0.47	0.014	0.4097	3447.1	78.0	3911.5	110.3	4149.8	123.6	2437.0	87.0
TSUPB016_26	59.5	2.4	0.82	0.027	0.043025	1.219512195	0.04015467	0.525	0.02	0.058712	3860.3	127.1	4165.8	168.0	4313.0	164.3	2605.2	143.6
TSUPB016_27	40.7	2.1	0.703	0.018	0.427	1.422475107	0.03642184	0.41	0.018	-0.088789	3432.0	87.9	3787.9	195.4	3946.2	173.2	2738.1	116.9
TSUPB016_28	42.2	2.9	0.727	0.03	0.18152	1.375515818	0.05676131	0.404	0.018	-0.24648	3522.2	145.3	3823.8	262.8	3924.0	174.8	2898.2	172.3
TSUPB016_29	22.85	0.66	0.549	0.01	0.28661	1.821493625	0.03317839	0.2946	0.0082	0.39846	2821.0	51.4	3220.6	93.0	3442.1	95.8	2469.9	56.0
TSUPB016_30	28.28	0.81	0.59	0.012	0.43111	1.694915254	0.03447285	0.344	0.009	0.099275	2989.4	60.8	3428.9	98.2	3680.6	96.3	2483.1	64.1
TSUPB016_31	22.71	0.63	0.5529	0.0099	0.45057	1.808645325	0.03238486	0.2928	0.0077	0.0094794	2837.2	50.8	3214.6	89.2	3432.5	90.3	2496.4	55.2
TSUPB016_32	23.37	0.67	0.5596	0.0097	0.10362	1.786990708	0.03097536	0.3021	0.0087	0.026012	2865.0	49.7	3242.5	93.0	3481.0	100.2	2495.8	56.0
TSUPB016_33	24.79	0.71	0.568	0.012	0.02443	1.76056338	0.037195	0.3112	0.0087	0.0054346	2899.6	61.3	3300.0	94.5	3526.9	98.6	2503.6	65.2
TSUPB016_34	20.8	0.44	0.5506	0.0085	0.24502	1.816200509	0.02803797	0.27	0.0057	0.047556	2827.7	43.7	3129.3	66.2	3306.0	69.8	2568.8	47.9
TSUPB016_35	38.2	1.1	0.666	0.025	0.35308	1.501501502	0.05636267	0.414	0.011	0.61957	3290.4	123.5	3725.1	107.3	3960.7	105.2	2536.6	113.8
TSUPB016_36	33.51	0.71	0.659	0.012	0.36453	1.517450683	0.02763188	0.365	0.0081	0.45302	3263.3	59.4	3595.7	76.2	3770.8	83.7	2739.0	67.9
TSUPB031_1	103.1	5.4	1.286	0.078	0.66212	0.777604977	0.04716422	0.642	0.024	0.057896	5329.9	323.3	4716.8	247.0	4606.1	172.2	-	-
TSUPB031_2	107.3	5.4	1.24	0.058	0.94941	0.806451613	0.03772112	0.66	0.022	0.24245	5198.9	243.2	4757.0	239.4	4646.0	154.9	3416.5	421.9
TSUPB031_3	352	45	3.47	0.49	0.4811	0.288184438	0.04069463	0.839	0.041	-0.00032848	9652.8	1363.1	5956.7	761.5	4989.4	243.8	-96.3	1198.2
TSUPB031_4	30.1	2.1	0.665	0.016	0.15841	1.503759398	0.03618068	0.337	0.012	-0.0045751	3286.5	79.1	3490.1	243.5	3649.2	129.9	2909.5	102.6
TSUPB031_5	109.1	9.6	1.3	0.11	0.15433	0.769230769	0.06508876	0.643	0.028	0.076056	5369.3	454.3	4773.7	420.1	4608.3	200.7	2999.0	492.6
TSUPB031_6	120.7	7.3	1.343	0.085	0.89168	0.744601638	0.04712669	0.709	0.025	0.19904	5488.7	347.4	4875.4	294.9	4749.1	167.5	3019.4	361.7
TSUPB031_7	198	13	1.95	0.13	0.9114	0.512820513	0.03418803	0.776	0.027	0.13579	6973.8	464.9	5374.7	352.9	4878.3	169.7	910.7	419.6
TSUPB031_8	145.3	8.6	1.73	0.18	0.47859	0.578034682	0.06014234	0.728	0.028	0.39403	6474.1	673.6	5062.4	299.6	4787.0	184.1	2562.1	490.6
TSUPB031_9	187	16	1.8	0.13	0.91971	0.555555556	0.04012346	0.791	0.031	0.084713	6637.4	479.4	5317.0	454.9	4905.6	192.3	2806.0	480.5

	Ratios										Age (Ma)							
Analysis	$^{207}Pb/^{235}U$	Err 2SE abs	$^{206}Pb/^{238}U$	Err 2SE abs	Rho	$^{238}U/^{206}Pb$	Err 2SE abs	$^{207}Pb/^{206}Pb$	Err 2SE abs	Rho	$^{206}Pb/^{238}U$ Age	Err 2SE abs	$^{207}Pb/^{235}U$ Age	Err 2SE abs	$^{207}Pb/^{206}Pb$ Age	Err 2SE abs	^{207}Pb Corrected Age	Err 2SE abs
TSUPB031_10	450	42	3.69	0.36	0.96481	0.27100271	0.02643929	0.936	0.045	0.49324	9962.5	972.0	6205.5	579.2	5144.3	247.3	0.0	1950.5
TSUPB031_11	650	140	5.2	1.1	0.99968	0.192307692	0.04068047	0.929	0.049	-0.0095286	11761.8	2488.1	6578.2	1416.8	5133.7	270.8	-5743.7	5248.0
TSUPB031_12	68.9	3.8	0.953	0.046	0.93519	1.049317943	0.05064913	0.577	0.021	-0.081189	4315.0	208.3	4312.4	237.8	4451.1	162.0	2815.5	212.3
TSUPB031_13	157.8	8.7	1.56	0.086	0.95522	0.641025641	0.03533859	0.784	0.034	0.47488	6059.7	334.1	5145.6	283.7	4892.9	212.2	2056.0	362.8
TSUPB031_14	167.7	9.3	1.71	0.1	0.97459	0.584795322	0.03419856	0.766	0.027	0.41838	6426.7	375.8	5207.0	288.8	4859.8	171.3	0.0	367.7
TSUPB031_15	137	9.1	1.473	0.085	0.65152	0.678886626	0.0391754	0.71	0.029	0.232	5836.8	336.8	5003.0	332.3	4751.1	194.1	1429.3	340.9
TSUPB031_16	25.9	1	0.627	0.016	0.8303	1.594896332	0.04069911	0.3082	0.0088	-0.20032	3137.7	80.1	3342.8	129.1	3511.9	100.3	2830.1	93.5
TSUPB031_17	89.6	6.6	1.097	0.06	0.98491	0.911577028	0.04985836	0.602	0.019	-0.064347	4773.6	261.1	4575.8	337.1	4512.8	142.4	3380.2	388.7
TSUPB031_18	391	27	3.27	0.22	0.95457	0.305810398	0.0205744	0.903	0.035	0.32101	9357.7	629.6	6063.1	418.7	5093.6	197.4	-9116.3	4467.6
TSUPB031_19	71.1	3.3	0.959	0.042	0.81832	1.042752868	0.04566801	0.568	0.019	0.1664	4334.8	189.8	4343.9	201.6	4428.2	148.1	2930.6	206.9
TSUPB031_20	592	95	5.14	0.8	0.91107	0.194552529	0.03028055	0.914	0.054	0.01211	11699.1	1820.9	6483.4	1040.4	5110.7	301.9	-4349.4	4375.2
TSUPB031_21	146	14	1.49	0.1	0.9848	0.67114094	0.04504302	0.701	0.023	0.17474	5881.0	394.7	5067.2	485.9	4732.8	155.3	-	-
TSUPB031_22	67.2	5.7	0.891	0.045	0.54135	1.122334456	0.05668356	0.535	0.023	0.0047369	4107.0	207.4	4287.4	363.7	4340.7	186.6	2870.1	226.2
TSUPB031_23	303	31	2.65	0.27	0.91919	0.377358491	0.03844785	0.883	0.045	0.20517	8346.3	850.4	5805.0	593.9	5061.9	258.0	0.0	1615.9
TSUPB031_24	290	22	2.67	0.32	0.37945	0.374531835	0.04488771	0.886	0.036	0.4925	8381.6	1004.5	5760.6	437.0	5066.7	205.9	0.0	1613.0
TSUPB031_25	153.4	7.9	1.504	0.067	0.79063	0.664893617	0.0296196	0.743	0.025	0.3163	5917.1	263.6	5117.1	263.5	4816.2	162.1	3073.9	361.5
TSUPB031_26	37.6	2.5	0.714	0.025	0.92742	1.400560224	0.04903922	0.391	0.017	-0.025842	3473.5	121.6	3709.5	246.6	3874.8	168.5	2900.2	150.4
TSUPB031_27	150.2	9	1.513	0.086	0.66838	0.660938533	0.03756822	0.734	0.027	0.37066	5940.2	337.6	5095.8	305.3	4798.8	176.5	3514.5	729.7
TSUPB031_28	135	11	1.312	0.052	0.27694	0.762195122	0.03020895	0.707	0.024	-0.0037663	5402.8	214.1	4988.2	406.4	4745.0	161.1	2888.9	270.2
TSUPB031_29	45.7	2.7	0.737	0.017	0.15268	1.356852103	0.03129781	0.436	0.012	0.092832	3559.4	82.1	3902.9	230.6	4038.1	111.1	2766.7	95.7
TSUPB031_30	105.8	4.5	1.188	0.044	0.908	0.841750842	0.03117596	0.645	0.022	-0.03831	5047.5	186.9	4742.8	201.7	4612.8	157.3	3317.3	322.1
TSUPB031_31	35.8	1.6	0.698	0.021	0.93759	1.432664756	0.04310309	0.372	0.013	-0.064207	3413.1	102.7	3661.0	163.6	3799.6	132.8	2915.2	125.5
TSUPB032_1	224	17	1.93	0.12	0.77627	0.518134715	0.03221563	0.827	0.018	-0.077908	6929.9	430.9	5499.4	417.4	4969.0	108.2	1240.7	267.4
TSUPB032_2	39.43	0.7	0.722	0.011	0.57243	1.385041551	0.02110174	0.3998	0.0055	0.4652	3503.5	53.4	3756.5	66.7	3908.3	53.8	2894.7	61.5
TSUPB032_3	161.7	4.9	1.56	0.055	0.10055	0.641025641	0.02260026	0.764	0.018	0.38752	6059.7	213.6	5170.2	156.7	4856.1	114.4	2695.7	232.5
TSUPB032_4	385	18	3.127	0.078	0.22303	0.319795331	0.007976986	0.939	0.017	-0.010127	9138.1	227.9	6047.5	282.7	5148.8	93.2	0.0	599.9
TSUPB032_5	60.9	1.4	0.859	0.052	0.28504	1.164144354	0.07047207	0.5239	0.0089	0.35281	3997.0	242.0	4189.0	96.3	4309.9	73.2	2796.7	205.8
TSUPB032_6	44.16	0.82	0.754	0.014	0.12014	1.326259947	0.02462552	0.4299	0.007	0.34209	3622.2	67.3	3868.8	71.8	4017.1	65.4	2891.8	76.2
TSUPB032_7	589	42	4.37	0.32	0.36544	0.228832952	0.01675665	0.964	0.02	-0.031217	10835.3	793.4	6478.3	461.9	5185.8	107.6	-7346.4	2541.5
TSUPB032_8	1050	62	7.48	0.43	0.16852	0.13368984	0.007685378	1.033	0.028	-0.01447	13780.6	792.2	7064.5	417.1	5283.0	143.2	0.0	1914.3
TSUPB032_9	63.5	2.1	0.875	0.023	0.13819	1.142857143	0.03004082	0.518	0.017	0.29505	4052.3	106.5	4230.8	139.9	4293.3	140.9	2924.2	143.4
TSUPB032_10	187	17	1.79	0.15	0.77382	0.558659218	0.04681502	0.779	0.022	-0.24798	6614.3	554.3	5317.0	483.4	4883.8	137.9	3575.1	1129.3
TSUPB032_11	116.1	3.2	1.211	0.047	0.11696	0.825763832	0.03204864	0.699	0.021	-0.15948	5114.9	198.5	4836.3	133.3	4728.7	142.1	2551.4	202.7
TSUPB032_12	179.4	8.4	1.689	0.095	0.26902	0.592066311	0.03330154	0.781	0.019	0.56483	6376.6	358.7	5275.1	247.0	4887.5	118.9	2702.5	294.6
TSUPB032_13	49.19	0.9	0.765	0.013	0.35874	1.307189542	0.02221368	0.4661	0.0093	-0.005483	3662.5	62.2	3976.1	72.7	4137.4	82.6	2727.5	72.8
TSUPB032_14	77.9	1.9	0.999	0.026	0.095441	1.001001001	0.02605208	0.573	0.011	0.26851	4465.1	116.2	4435.4	108.2	4441.0	85.3	3102.3	142.9
TSUPB032_15	143.6	3.3	1.432	0.063	0.24826	0.698324022	0.03072236	0.745	0.015	0.66583	5729.0	252.0	5050.5	116.1	4820.1	97.0	2629.4	203.1
TSUPB032_16	112.7	3.5	1.184	0.052	0.15619	0.844594595	0.03709368	0.672	0.016	-0.043249	5035.7	221.2	4806.4	149.3	4672.0	111.2	2842.1	204.1
TSUPB032_17	99.6	2.7	1.111	0.028	0.47868	0.900090009	0.02268454	0.655	0.016	-0.047202	4816.5	121.4	4682.1	126.9	4635.0	113.2	2725.7	148.2
TSUPB032_18	235.9	7.2	2.067	0.056	0.61269	0.483792937	0.01310711	0.831	0.015	0.34156	7224.5	195.7	5551.7	169.4	4975.8	89.8	1297.5	239.5
TSUPB032_19	54.5	3.2	0.824	0.027	0.80662	1.213592233	0.03976576	0.472	0.016	-0.39825	3874.5	127.0	4078.2	239.5	4156.1	140.9	2996.6	159.1
TSUPB032_20	167	16	1.61	0.12	0.60364	0.621118012	0.04629451	0.745	0.026	-0.090926	6184.4	460.9	5202.8	498.5	4820.1	168.2	0.0	389.5
TSUPB032_21	466	17	3.58	0.15	0.62108	0.279329609	0.01170375	0.959	0.017	-0.072655	9809.5	411.0	6240.9	227.7	5178.5	91.8	-4966.8	1206.6
TSUPB032_22	35.09	0.95	0.685	0.014	0.75989	1.459854015	0.02983643	0.3668	0.0061	0.21297	3363.5	68.7	3641.2	98.6	3778.3	62.8	2870.1	76.8
TSUPB032_23	65.5	2.6	0.879	0.022	0.33296	1.137656428	0.02847377	0.531	0.017	-0.012507	4066.0	101.8	4261.8	169.2	4329.7	138.6	2841.4	135.0
TSUPB032_24	456	17	3.51	0.15	0.5418	0.284900285	0.01217523	0.95	0.019	0.26351	9710.2	415.0	6218.9	231.8	5165.2	103.3	-4328.1	1157.3
TSUPB032_25	74.8	2	0.942	0.025	0.63649	1.061571125	0.02817333	0.576	0.011	0.25409	4278.6	113.6	4394.7	117.5	4448.6	85.0	2771.3	113.9
TSUPB032_26	76.2	2.9	0.952	0.024	0.45805	1.050420168	0.02648118	0.569	0.011	-0.03496	4311.7	108.7	4413.3	168.0	4430.8	85.7	2884.8	118.2
TSUPB032_27	782	39	5.56	0.23	0.39145	0.179856115	0.007440091	1.008	0.023	0.1704	12125.6	501.6	6765.6	337.4	5248.6	119.8	0.0	1157.0
TSUPB032_28	45	1.8	0.759	0.017	0.018627	1.317523057	0.02950974	0.429	0.018	0.04928	3640.6	81.5	3887.5	155.5	4014.0	168.4	2924.7	126.6
TSUPB032_29	171.6	5.5	1.56	0.046	0.26036	0.641025641	0.01890204	0.805	0.032	0.009902	6059.7	178.7	5230.2	167.6	4930.6	196.0	1370.4	341.5
TSUPB032_30	109.1	4.5	1.176	0.038	0.8585	0.850340136	0.02747698	0.671	0.015	-0.23173	5012.0	162.0	4773.7	196.9	4669.8	104.4	2817.1	168.6
TSUPB032_31	60.4	1.4	0.852	0.019	0.13159	1.17370892	0.02617426	0.513	0.011	0.095616	3972.7	88.6	4180.7	96.9	4279.0	91.8	2843.7	101.6
TSUPB032_32	203	13	1.88	0.17	0.19291	0.531914894	0.04809869	0.793	0.026	0.086782	6819.0	616.6	5399.9	345.8	4909.2	161.0	3199.2	651.7
TSUPB032_33	55	1.4	0.822	0.019	0.10688	1.216545012	0.02811965	0.481	0.016	0.63604	3867.4	89.4	4087.3	104.0	4184.0	139.2	2920.8	126.0
TSUPB032_34	1091	40	7.85	0.29	0.67793	0.127388535	0.004706073	1.009	0.018	-0.065542	14055.9	519.3	7103.4	260.4	5250.0	93.7	0.0	1336.5
TSUPB032_35	482	90	3.66	0.76	0.99996	0.273224044	0.05673505	0.959	0.04	-0.01625	9921.1	2060.1	6275.1	1171.7	5178.5	216.0	-5133.6	3036.7
TSUPB032_36	201.2	8.3	1.847	0.076	0.38335	0.541418517	0.02227818	0.81	0.016	0.48599	6744.7	277.5	5390.9	222.4	4939.4	97.6	1997.7	226.7
TSUPB032_37	265	12	2.191	0.078	0.56343	0.456412597	0.01624837	0.858	0.019	-0.023418	7480.0	266.3	5669.4	256.7	5021.2	111.2	-1487.7	483.5
TSUPB032_38	769	29	5.49	0.21	0.14592	0.182149362	0.006967462	0.995	0.016	-0.023886	12056.5	461.2	6748.6	254.5	5230.3	84.1	0.0	854.0

Appendix 7: Major element, trace element and Sm-Nd isotope data table.

	3GaTTG	TSUPB023	TSUPB024	TSUPB033	TSUPB034	TSUPB036	TSUPB039	TSUPB040
	*	C6.2	C6.2	C6.12	C6.12	C6.12	N2E	N2E
SiO2	*	47.33	44.48	51.24	44.77	46.53	48.75	47.73
TiO2	*	0.27	0.81	0.57	0.33	0.47	0.65	1.33
Al2O3	*	6.23	15.02	13.97	9.23	11.53	14.14	13.75
Fe2O3	*	12.02	13.42	11.61	11.92	12.22	12.28	20.21
FeO	*	10.81	12.08	10.44	10.73	11.00	11.05	18.18
MnO	*	0.16	0.19	0.15	0.16	0.21	0.17	0.21
MgO	*	21.00	9.38	8.43	18.87	12.38	5.77	5.62
CaO	*	8.64	13.76	9.65	7.93	12.38	14.17	5.72
Na2O	*	0.08	1.99	2.84	0.23	0.94	1.76	4.86
K2O	*	bdl	bdl	0.25	0.06	0.47	bdl	0.00
P2O5	*	0.02	0.04	0.06	0.03	0.04	0.05	0.10
LOI	*	4.30	0.91	1.22	6.46	2.85	2.28	0.47
CIA	*	28.30	34.75	38.45	38.42	32.04	33.11	43.06
Mg#	*	80.3	61.9	62.9	78.7	70.2	52.3	39.3
Li	*	11140	14360	22040	9344	34020	12640	17780
Be	*	95.51	171	189.5	108.2	167.8	164.1	261.4
Sc	*	24550	46710	42980	28830	37230	45120	43170
Ti	*	*	*	3730000	1841000	3049000	3958000	7486000
V	52000	*	*	258300	155200	222700	272400	395200
Cr	50000	3475000	247200	482100	2524000	1431000	285300	2747
Co	*	*	*	52400	88730	69650	52060	75880
Ni	21000	1410000	135000	103100	759400	397800	147300	38310
Cu	*	44990	108900	5023	40250	41730	110800	295300
Zn	*	73860	94430	85640	80170	84430	76450	137400
Ga	*	7700	13830	13600	8616	11530	13900	16290
As	*	246.2	75.34	130.4	94.21	178.1	380.1	3835
Rb	67000	701.4	768.7	1003	477.8	20500	691.1	272.1
Sr	541000	40380	102400	125700	13740	137000	140200	173800
Y	11000	7213	16190	14150	8402	11930	15420	26540
Zr	154000	10320	21430	23360	10110	24220	7363	69740
Nb	7000	861.3	1530	1292	686.3	1160	1429	3038
Mo	*	130.9	202.9	297.1	87.05	65.79	90.53	240.3
Ag	*	33.47	49.62	*	*	*	*	*
Cd	*	57.62	76.97	57.55	53	61.14	57.03	87.01
In	*	29.8	59.2	47.27	32.79	42.63	52.65	80.69
Sn	*	239.6	434.1	329.4	250.8	283.5	377	398.2
Sb	*	35.5	28.15	98.81	56.33	107	120.2	381.8
Cs	*	1154	127.1	127.2	467.1	1352	24.47	92.02
Ba	847000	1093	15130	52140	1008	531400	15380	8782
La	30800	784.2	1734	1655	891.5	1358	1709	4190
Ce	58500	2160	4901	4600	2553	3758	4742	10960
Pr	*	351.6	817.2	743.6	415.3	610	781.6	1677
Nd	23200	1864	4293	3859	2172	3224	4169	8380
Sm	3500	672.9	1527	1367	779.3	1145	1495	2790
Eu	900	282.6	593	501.6	294.5	425.7	583.4	967.4
Gd	2300	1026	2259	2004	1165	1678	2159	3911
Tb	*	190.4	417.1	375.7	220.2	313.7	406.2	718
Dy	1600	1273	2814	2515	1471	2089	2713	4700
Ho	*	285.9	638	566	331.8	470.1	610.6	1045
Er	750	817	1863	1618	968.1	1356	1755	2966
Tm	*	122.4	283	247.1	146.3	204.9	266.5	446.2
Yb	630	784.2	1815	1597	962.7	1339	1729	2874
Lu	120	115.7	268.3	232.7	142	199.4	253.7	424.8
Hf	*	326.9	680.2	707.7	321.9	717.9	348.9	1949
Ta	*	46.38	96.97	86.14	43.6	71.2	91.26	190.7
W	*	*	*	13500	3705	5571	7390	9409
Tl	*	10.11	6.494	10.94	6.218	128.4	6.739	2.193
Pb	*	194.2	1118	2397	282.4	1488	362.5	338
Th	*	72.64	151.5	168.5	83.07	132.1	130.7	535.2
U	*	23.56	34.89	39.88	21.94	36.17	38.27	138.7
$^{143}Nd/^{144}Nd$	*	0.5132	0.5131	*	*	*	*	*
Initial $^{143}Nd/^{144}Nd$	*	0.5089	0.5089	*	*	*	*	*
εNd (3.0 Ga)	*	3.5737	2.7443	*	*	*	*	*
$T_{DM(3000)}$	*	2950	3009	*	*	*	*	*

	TSUPB041	TSUPB042	TSUPB002	TSUPB009	TSUPB013	TSUPB014	TSUPB018	TSUPB019
	N2E	N2E	C67	WB	C67	C67	C67	C67
SiO2	44.68	43.04	60.15	58.69	65.66	53.23	57.19	62.86
TiO2	0.32	0.55	2.09	1.90	1.84	1.27	2.00	1.88
Al2O3	8.88	9.85	15.80	12.54	14.56	14.52	15.60	15.74
Fe2O3	12.64	14.35	8.21	14.65	9.15	14.79	11.41	5.81
FeO	11.37	12.91	7.38	13.18	8.24	13.30	10.27	5.23
MnO	0.17	0.16	0.10	0.23	0.06	0.15	0.14	0.07
MgO	18.00	18.72	2.72	1.77	1.73	5.24	2.51	1.46
CaO	9.22	8.49	5.10	5.01	2.05	6.13	6.89	5.56
Na2O	0.85	0.67	0.89	1.60	1.18	3.43	1.64	0.96
K2O	0.16	bdl	1.85	2.31	1.08	0.08	0.66	2.70
P2O5	0.02	bdl	0.40	0.42	0.38	0.26	0.39	0.42
LOI	5.07	4.23	2.69	0.89	2.30	0.90	1.56	2.55
CIA	32.71	37.31	57.30	48.68	71.04	47.19	50.99	53.61
Mg#	76.8	75.2	43.6	22.0	30.6	45.2	33.9	36.9
Li	11380	9283	28760	13120	15260	13250	25940	14420
Be	116.6	155	881.7	1182	677.9	590.7	873.1	865.3
Sc	24590	34340	41520	40730	34040	33230	37310	37560
Ti	1918000	3192000	11390000	10520000	9450000	7348000	11030000	10330000
V	152300	269300	185300	127700	148700	136600	176300	183700
Cr	2453000	3077000	13050	5881	18670	63710	19670	23360
Co	83170	118600	*	*	*	*	*	*
Ni	798500	1028000	14400	8043	15640	27150	13190	14110
Cu	155000	450400	18740	3397	20380	25300	33900	21530
Zn	77250	68530	202800	118000	78810	123900	251700	214500
Ga	9601	11130	23060	21280	21430	19730	23250	23010
As	950.7	711	625.9	*	1107	425.5	911.3	2721
Rb	317.2	262.1	55860	63730	31200	2652	22490	72210
Sr	56550	63900	105000	88960	108700	167000	232400	180500
Y	9855	10620	32890	36510	31850	23930	31490	32840
Zr	15560	27040	151600	189700	149300	96160	145600	153800
Nb	776.2	1103	7423	7924	6968	4882	7261	7390
Mo	143.8	190.2	602	1254	884.7	482.7	881	969.8
Ag	*	*	114.8	217.7	82.63	58.99	101.6	112.1
Cd	50.04	60.84	122.8	98.13	65.21	114.3	79.61	65.38
In	32.15	39.2	101.9	85.44	96.52	67.77	98.63	104.4
Sn	248.1	374.3	1273	1225	1353	827.1	1029	1650
Sb	279.5	118.4	953.9	99.37	881.3	725.2	1192	768.6
Cs	292.7	81.12	1795	1303	1093	243.4	2039	2264
Ba	6442	8459	618000	521100	440200	75770	613400	802800
La	1247	590.3	24100	26310	24430	16160	26150	26570
Ce	3393	2028	49850	53420	49110	32700	53830	55620
Pr	572.8	393	5829	6510	5825	3957	6265	6439
Nd	3063	2254	22860	26140	22940	15980	24980	25640
Sm	1095	856.6	5244	6162	5126	3678	5586	5748
Eu	344.2	404.4	1596	1908	1603	1283	1726	1739
Gd	1512	1399	5879	6891	5767	4196	6098	6335
Tb	271.1	275.1	982.1	1180	959.2	695.7	982.6	1025
Dy	1748	1866	6142	7317	6013	4335	6056	6350
Ho	382.2	425.5	1328	1558	1296	943.9	1289	1352
Er	1081	1236	3794	4397	3642	2650	3618	3757
Tm	161.3	184.8	566.2	662.3	545.2	395.6	541.3	562.2
Yb	1036	1191	3659	4337	3499	2532	3453	3552
Lu	152	179.3	541.5	657.9	520.5	378.2	516.7	522.4
Hf	454.3	785.7	4045	4519	3967	2524	3861	4030
Ta	46.99	73.18	573.4	615.3	548.3	372.7	546.8	562.4
W	2501	3205	*	*	*	*	*	*
Tl	3.945	3.087	404	420.5	148.5	18.46	158.2	450.7
Pb	390.9	624.2	6882	7153	5137	5355	10480	6374
Th	97.54	173.2	8535	8717	8171	5600	9852	9061
U	28.79	41.1	2310	2697	2141	1564	1920	2205
$^{143}Nd/^{144}Nd$	*	*	*	*	*	0.5115	0.5114	0.5114
Initial $^{143}Nd/^{144}Nd$	*	*	*	*	*	0.5087	0.5087	0.5088
εNd (3.0 Ga)	*	*	*	*	*	0.0152	0.1023	0.4129
$T_{DM(3000)}$	*	*	*	*	*	3196	3190	3169

	TSUPB022	TSUPB044	TSUPB045	TSUPB047	TSUPB007	TSUPB004	TSUPB008	TSUPB012
	WB	TAMAYA	TAMAYA	TAMAYA	WB	C6.12	WB	*
SiO2	50.19	53.45	52.67	64.82	71.00	70.66	71.85	71.70
TiO2	0.49	1.92	1.88	1.51	0.32	0.25	0.37	0.24
Al2O3	16.51	13.49	13.02	9.52	14.38	15.42	16.26	16.81
Fe2O3	9.92	16.97	17.74	13.56	0.73	1.94	1.80	0.69
FeO	8.93	15.27	15.97	12.20	0.66	1.74	1.62	0.62
MnO	0.10	0.17	0.17	0.15	0.04	0.02	0.03	bdl
MgO	8.44	3.91	4.14	1.84	1.54	0.64	0.33	0.32
CaO	8.31	4.52	4.34	5.89	4.88	3.06	1.97	2.93
Na2O	2.81	3.81	3.29	1.96	2.13	4.88	4.15	5.59
K2O	0.07	0.95	1.97	0.10	2.06	1.96	1.87	0.93
P2O5	0.04	0.42	0.33	0.33	0.10	0.12	0.08	0.11
LOI	3.12	0.39	0.46	0.31	2.81	1.05	1.30	0.69
CIA	45.58	48.15	47.03	41.83	50.02	50.01	57.04	52.39
Mg#	66.5	34.9	35.2	24.1	83.1	43.6	29.8	51.7
Li	13430	18180	35380	6767	22460	9863	11830	14380
Be	501.4	814.6	866.8	816.1	967.4	1065	1098	662.3
Sc	43840	37900	36280	29370	6248	3625	6086	2428
Ti	3279000	11030000	10800000	8482000	2138000	1729000	2365000	1904000
V	229600	137200	206900	78740	43650	35770	44140	27260
Cr	196200	4504	471.9	790.6	37100	11480	76310	6377
Co	*	35440	45350	24900	*	*	*	*
Ni	72640	6137	10560	1277	25860	10700	30510	4758
Cu	59470	5149	13270	*	20740	1022	26120	11800
Zn	91400	122300	120300	60630	55770	23520	43030	43600
Ga	13600	23340	21060	17790	17460	19280	18760	18290
As	56.62	1171	785.9	994.6	*	*	*	*
Rb	5585	23520	77300	1264	78760	26580	56630	33230
Sr	130100	148200	201300	158200	225200	1009000	263600	447400
Y	12230	38700	29490	29080	8677	6275	9365	3858
Zr	51300	159600	123000	117400	144900	109600	200700	135200
Nb	2346	7765	6278	6458	5297	3460	7270	3106
Mo	200.3	624.8	2475	530.8	2099	299.5	1614	479.6
Ag	48.37	*	*	*	117.8	51.33	169	100.9
Cd	72.91	106.5	58.75	65.28	89.79	45.07	91.98	45.09
In	48.01	88.06	80.28	89.61	27.06	14.95	29.2	16.46
Sn	700.7	646	1143	1137	1032	555.1	1205	514.2
Sb	59.38	221.9	276.5	262.5	85.36	116.3	65.16	15.54
Cs	250	482.9	7081	42.27	2450	735.1	1450	679.1
Ba	86710	456000	857900	126800	485600	1517000	785400	371800
La	7139	27600	25270	27620	27110	32940	30340	24510
Ce	13890	55590	47470	50270	51390	68180	56860	43390
Pr	1650	6675	5496	5752	5643	7972	6013	4813
Nd	6519	26560	21500	22130	19390	28160	20170	16280
Sm	1603	6091	4797	4912	3216	4040	3258	2317
Eu	526.1	1817	1498	1703	606.7	846.5	716.9	600.8
Gd	1890	6838	5276	5416	2292	2378	2395	1480
Tb	335.8	1134	868.5	876.6	297.6	250	322.2	166.1
Dy	2234	7062	5430	5425	1660	1229	1790	829.8
Ho	505.7	1525	1165	1153	322.3	223.8	349.3	144.8
Er	1490	4269	3268	3209	857.6	561.1	954.9	374.1
Tm	235.1	631.1	488.9	477.6	131.4	82.57	148.7	53.65
Yb	1554	4076	3125	3097	835.3	542.1	992.1	325.8
Lu	235.6	603.2	463	454.9	128.4	80.92	152.2	49.01
Hf	1375	4315	3321	3220	3739	2901	4869	3249
Ta	185.8	619.3	486.3	489.4	440.3	210.1	692.6	266.2
W	*	13660	11660	17570	*	*	*	*
Tl	32.25	101.6	476.6	7.301	337	136.3	301.4	168.3
Pb	4074	4896	3255	2911	11570	8573	13090	5213
Th	2663	8745	6810	6644	8925	7565	11750	5183
U	727.3	2694	2017	1882	2626	3027	3228	749.2
$^{143}Nd/^{144}Nd$	0.5116	*	*	*	*	*	*	*
Initial $^{143}Nd/^{144}Nd$	0.5087	*	*	*	*	*	*	*
εNd (3.0 Ga)	-1.0876	*	*	*	*	*	*	*
$T_{DM(3000)}$	3268	*	*	*	*	*	*	*

	TSUPB028	TSUPB029	TSUPB030	TSUPB001	TSUPB003	TSUPB005	TSUPB010	TSUPB011
	OGN	OGN	C67	C67	C67	TFW	WB FW	WB HW
SiO2	65.93	73.17	75.50	66.10	64.66	69.43	50.84	76.09
TiO2	0.37	0.20	0.13	2.02	0.43	0.47	1.65	0.22
Al2O3	16.68	16.05	14.34	16.38	17.03	16.37	18.53	14.13
Fe2O3	2.52	1.15	0.23	5.24	2.50	2.69	9.47	bdl
FeO	2.27	1.04	0.21	4.71	2.25	2.42	8.53	bdl
MnO	0.03	0.02	0.01	0.07	0.01	0.04	0.15	bdl
MgO	2.10	0.16	0.50	1.38	2.45	1.04	1.13	bdl
CaO	4.46	1.56	2.66	3.36	4.44	2.76	7.80	2.27
Na2O	5.77	4.73	3.99	1.74	3.28	4.20	4.01	4.16
K2O	1.26	2.42	1.03	1.60	2.92	1.72	3.02	1.65
P2O5	0.23	0.07	0.06	0.45	0.14	0.10	0.33	0.08
LOI	0.65	0.46	1.56	1.67	2.13	1.19	3.08	1.89
CIA	47.51	55.10	53.73	63.03	51.12	54.74	44.35	52.92
Mg#	66.0	24.7	83.3	38.0	69.5	47.3	21.7	*
Li	50300	42160	10440	17350	15900	30640	9313	5866
Be	1096	979.8	633.7	938.1	777.3	872.1	1214	795
Sc	8002	1944	4656	33170	10710	7394	36310	3460
Ti	2687000	1552000	1335000	11520000	2789000	2311000	8816000	1571000
V	74250	11220	37490	175200	80090	55720	150400	29300
Cr	47960	5504	8167	18510	69420	60400	97100	26490
Co	*	7594	1867	*	*	*	*	*
Ni	34670	3080	4913	10820	31130	32160	18640	22490
Cu	20510	1154	8900	15690	27720	25280	25400	11010
Zn	63560	56830	40490	326900	51570	49080	37110	22990
Ga	21310	18890	13850	25610	22390	18540	23840	17040
As	*	*	*	*	*	*	1066	*
Rb	23960	71220	15750	41920	92270	40740	68570	49320
Sr	535600	251800	155500	260900	294400	571000	154300	390200
Y	7225	3752	5648	28500	5689	7159	25660	2869
Zr	111800	163700	78260	165600	103800	118100	124000	119100
Nb	3161	4968	1410	8311	1950	3825	6046	3343
Mo	569.9	306.5	227.6	1122	1244	1243	575.8	420.5
Ag	130.3	106.9	29.5	76.05	85.78	133.7	209.7	96.98
Cd	72.08	58.44	50.87	49.32	58.54	63.89	56.07	44.68
In	31.05	28.54	22.17	97.42	36.01	26.22	86.27	15.31
Sn	903.3	2094	596.2	1685	730.2	651.3	1186	520.1
Sb	13.31	12.75	291.8	1504	211.9	94.31	109.7	365.3
Cs	1937	2081	380	1606	1013	1393	878.9	794.6
Ba	480700	759300	157600	695100	615200	610100	429100	561500
La	36900	31200	12010	26590	13380	22030	21610	13730
Ce	54870	43160	20520	53510	28320	43360	42290	27210
Pr	9567	5144	2990	6472	3611	4902	5055	2707
Nd	36520	15920	10830	25430	14400	17530	19980	9121
Sm	5849	2213	1890	5782	2661	2859	4492	1438
Eu	1326	334.6	464.2	1747	701.9	721.7	1502	367.9
Gd	3511	1332	1463	6013	2002	2070	4962	988.4
Tb	351	151.4	192.5	926.3	238.2	262	806.1	122.6
Dy	1616	768.6	1103	5625	1272	1421	4903	593.2
Ho	274.1	131.3	208.1	1189	233.1	277	1039	107.9
Er	660.3	319.5	541.6	3242	588	720.7	2884	276.1
Tm	92.28	43.32	71.83	468.7	85.77	106	424.1	38.63
Yb	516.3	262.7	439.9	2964	526.4	644.4	2673	254.8
Lu	77.17	37.8	64.42	426.8	79.61	98.99	398.6	36.79
Hf	2799	4131	2115	4454	2797	2924	3210	2865
Ta	166	187.2	80.53	631.7	113.9	239.4	457.2	266.3
W	*	*	1001	*	*	*	*	*
Tl	232.3	544.9	134.4	159.6	295.4	246.1	323.7	301.7
Pb	8127	16600	9976	8481	6786	9949	6152	7084
Th	8143	17880	1409	8861	2064	4931	6453	3478
U	11020	1557	339.9	1973	684.3	1432	1635	1183
$^{143}Nd/^{144}Nd$	*	*	*	*	*	*	*	*
Initial $^{143}Nd/^{144}Nd$	*	*	*	*	*	*	*	*
εNd (3.0 Ga)	*	*	*	*	*	*	*	*
$T_{DM(3000)}$	*	*	*	*	*	*	*	*

	TSUPB020	TSUPB021	TSUPB006	FZ-12-02
	WB HW	WB FW	TFW	Piment
SiO2	80.04	78.81	74.35	35.59
TiO2	0.21	0.21	bdl	0.03
Al2O3	11.85	12.13	15.65	1.54
Fe2O3	0.15	0.63	bdl	59.52
FeO	0.14	0.56	bdl	53.56
MnO	bdl	0.01	0.23	0.29
MgO	0.37	0.36	bdl	1.77
CaO	1.13	1.72	0.32	1.19
Na2O	3.69	3.05	5.03	bdl
K2O	1.78	1.89	3.54	0.45
P2O5	0.04	0.04	0.04	0.03
LOI	0.74	1.15	0.84	-0.30
CIA	54.32	54.60	55.40	37.47
Mg#	84.9	57.1	*	6.5
Li	25060	11560	34000	8787
Be	710	827.6	1726	740.2
Sc	4151	3852	1108	1562
Ti	1779000	1658000	106000	328900
V	31170	29410	1300	11080
Cr	76560	57420	1122	16790
Co	*	*	*	*
Ni	25570	23750	760.6	14080
Cu	31460	21890	1012	7471
Zn	51190	32460	6200	24490
Ga	14180	13710	24430	2759
As	*	*	*	4289
Rb	42470	57710	269500	42540
Sr	222700	175300	12970	36570
Y	7652	8192	18290	4589
Zr	135100	161300	37750	13760
Nb	4718	5499	20360	906
Mo	1145	1388	422.2	494.1
Ag	166.2	123.3	66.1	17.78
Cd	81.73	69.28	80.05	30.22
In	19.35	17.41	37.7	3.498
Sn	850.4	928.8	4100	176.9
Sb	9.266	86.6	9.947	8437
Cs	1713	1937	6964	2312
Ba	841700	662700	13460	118200
La	45160	31400	2876	4602
Ce	82040	56580	6161	8760
Pr	8419	5908	798.1	995.8
Nd	27190	19260	2878	3688
Sm	3817	2869	1210	673.1
Eu	719.3	568.4	19.92	293.1
Gd	2467	2089	1708	663.5
Tb	301.1	268.7	448	97.81
Dy	1611	1562	3018	591.8
Ho	305	310.7	575.1	135.6
Er	801.3	865.4	1725	398
Tm	119.6	132.5	335	59.65
Yb	746.8	895.6	2647	376.3
Lu	112.4	134.7	365.5	58.48
Hf	3364	4012	2343	370.8
Ta	442	617.5	1599	74.84
W	*	*	*	*
Tl	230.8	299.9	1295	68.59
Pb	12880	12180	16990	1543
Th	14950	12840	3943	1171
U	3705	3192	3982	154
$^{143}Nd/^{144}Nd$	*	*	*	*
Initial $^{143}Nd/^{144}Nd$	*	*	*	*
εNd (3.0 Ga)	*	*	*	*
$T_{DM(3000)}$	*	*	*	*

Appendix 8: Pb-Pb data table.

Analysis	$^{206}Pb/^{204}Pb$	Err 2SE abs	$^{207}Pb/^{204}Pb$	Err 2SE abs	$^{208}Pb/^{204}Pb$	Err 2SE abs
TSUPB004_1	15.74	0.48	14.91	0.31	34.92	0.93
TSUPB004_2	16.15	0.39	15.38	0.34	35.61	0.70
TSUPB004_3	15.71	0.42	14.72	0.30	35.40	1.00
TSUPB004_4	16.51	0.53	15.37	0.32	36.30	0.88
TSUPB004_5	15.41	0.38	15.08	0.38	34.13	0.76
TSUPB004_6	16.16	0.60	15.10	0.53	35.54	0.98
TSUPB004_7	16.12	0.61	14.91	0.43	35.70	1.10
TSUPB004_8	14.49	0.37	14.89	0.37	33.30	0.98
TSUPB012_1	16.23	0.56	15.26	0.44	36.08	0.98
TSUPB012_2	15.88	0.75	14.89	0.40	36.40	1.30
TSUPB012_3	16.64	0.54	15.09	0.41	36.26	0.87
TSUPB012_4	16.67	0.57	15.17	0.34	36.74	0.83
TSUPB012_5	16.73	0.63	15.01	0.38	36.16	0.97
TSUPB012_6	16.12	0.52	15.08	0.33	35.79	0.83
TSUPB012_7	16.62	0.62	14.93	0.31	36.10	1.10
TSUPB012_8	16.80	0.59	15.50	0.38	37.29	0.89
TSUPB012_9	15.50	0.47	14.66	0.33	35.27	0.83
TSUPB012_10	16.40	0.51	15.52	0.39	37.40	1.00
TSUPB028_1	13.34	0.49	14.28	0.40	32.89	0.93
TSUPB028_2	13.35	0.42	14.44	0.47	33.40	1.20
TSUPB028_3	13.59	0.36	14.46	0.35	33.93	0.94
TSUPB028_4	13.81	0.50	14.51	0.53	33.80	1.20
TSUPB028_5	13.04	0.49	14.29	0.57	32.80	1.20
TSUPB028_6	13.48	0.51	14.48	0.53	32.90	1.10
TSUPB028_7	13.17	0.61	14.45	0.59	33.10	1.40
TSUPB028_8	13.21	0.51	14.46	0.54	33.00	1.20
TSUPB028_9	13.30	0.42	14.55	0.45	33.50	1.00
TSUPB029_1	13.67	0.31	14.64	0.33	33.10	0.69
TSUPB029_2	13.98	0.33	14.93	0.38	34.08	0.79
TSUPB029_3	14.08	0.36	14.65	0.37	33.61	0.86
TSUPB029_4	13.98	0.41	14.55	0.39	33.75	0.84
TSUPB029_5	13.83	0.37	14.98	0.39	33.46	0.73
TSUPB029_6	13.96	0.38	15.06	0.40	34.16	0.95
TSUPB029_7	13.93	0.33	15.01	0.39	34.11	0.82
TSUPB030a_1	14.63	0.21	15.01	0.19	34.27	0.48
TSUPB030a_2	14.55	0.37	14.77	0.40	33.98	0.94
TSUPB030a_3	14.08	0.16	14.75	0.17	33.47	0.39
TSUPB030a_4	14.43	0.29	15.01	0.20	34.12	0.49
TSUPB030a_5	14.64	0.16	14.78	0.18	34.08	0.39
TSUPB030a_6	13.88	0.21	14.56	0.20	33.21	0.45
TSUPB030a_7	13.98	0.21	14.54	0.20	32.97	0.45
TSUPB030a_8	14.07	0.15	14.69	0.16	33.37	0.37
TSUPB030f_1	14.06	0.20	14.68	0.20	33.43	0.42
TSUPB030f_2	14.11	0.16	14.76	0.15	33.62	0.46
TSUPB030f_3	14.88	0.30	15.42	0.31	35.22	0.76
TSUPB030f_4	13.84	0.15	14.77	0.17	33.19	0.34
TSUPB030f_5	14.02	0.14	14.98	0.15	33.75	0.34
TSUPB015_1	14.50	1.50	15.40	1.50	33.60	3.20
TSUPB015_2	15.71	0.92	15.52	0.99	34.20	2.10
TSUPB015_3	15.02	0.80	15.85	0.90	30.00	11.00
TSUPB016_1	13.07	0.17	14.29	0.23	32.91	0.67
TSUPB016_2	12.86	0.36	14.20	0.43	32.30	1.20
TSUPB016_3	12.94	0.21	14.07	0.28	31.82	0.79
TSUPB016_4	12.85	0.28	13.92	0.36	31.70	1.30
TSUPB016_5	12.77	0.18	13.76	0.27	30.67	0.74
TSUPB031_1	13.82	0.41	14.47	0.46	32.20	1.30
TSUPB032_1	13.89	0.24	14.85	0.32	33.44	0.86
TSUPB032_2	14.13	0.85	14.77	0.99	34.10	2.20
TSUPB032_3	14.00	0.40	14.97	0.46	33.60	1.10
NIST612_1	17.09	0.14	15.52	0.10	37.02	0.30
NIST612_2	17.09	0.10	15.42	0.12	36.80	0.26
NIST612_3	17.19	0.13	15.65	0.11	36.93	0.27
NIST612_4	17.15	0.14	15.55	0.12	37.10	0.33
NIST612_5	17.05	0.16	15.50	0.14	37.04	0.29
NIST612_6	17.10	0.14	15.53	0.11	37.04	0.30
NIST612_7	16.95	0.15	15.32	0.15	36.75	0.36
NIST612_8	17.10	0.13	15.55	0.13	36.98	0.28
NIST612_9	17.05	0.11	15.38	0.12	37.00	0.27
NIST612_10	16.91	0.23	15.38	0.22	36.86	0.49
NIST612_11	17.21	0.25	15.69	0.22	37.16	0.54
NIST612_12	17.33	0.26	15.66	0.24	37.48	0.54
NIST612_13	17.05	0.27	15.65	0.27	36.97	0.59
NIST612_14	17.01	0.25	15.56	0.21	36.98	0.49
NIST612_15	16.94	0.11	15.33	0.10	37.06	0.29
NIST612_16	17.13	0.12	15.39	0.09	37.00	0.22
NIST612_17	17.29	0.15	15.63	0.14	37.05	0.36
NIST612_18	17.22	0.15	15.62	0.10	37.15	0.25
NIST612_19	17.00	0.16	15.47	0.13	36.69	0.27
NIST612_20	16.95	0.12	15.31	0.14	36.85	0.31
NIST612_21	17.02	0.14	15.42	0.15	36.97	0.29
NIST612_22	17.06	0.17	15.61	0.10	37.07	0.29
NIST612_23	17.01	0.21	15.44	0.16	36.63	0.39
NIST612_24	17.09	0.19	15.43	0.18	36.91	0.38
NIST612_25	17.07	0.15	15.51	0.16	37.21	0.34
NIST612_26	16.95	0.16	15.53	0.13	36.66	0.30
NIST612_27	17.23	0.17	15.50	0.14	37.36	0.32
NIST612_28	17.12	0.15	15.56	0.13	36.97	0.31
NIST612_29	17.16	0.17	15.55	0.17	37.13	0.42
NIST612_30	17.30	0.19	15.66	0.15	37.29	0.39
NIST612_31	16.90	0.16	15.36	0.13	36.64	0.33

Ore Geology Reviews xxx (2015) xxx–xxx

Contents lists available at ScienceDirect

Ore Geology Reviews

journal homepage: www.elsevier.com/locate/oregeorev

The Tasiast deposit, Mauritania

Kyle Heron [a], Mark Jessell [b,c,*], Keith Benn [d], Esther Harris [e], Quentin G. Crowley [f]

[a] Department of Geology, School of Natural Sciences, Trinity College, Dublin 2, Ireland
[b] Laboratoire GET, Université Toulouse 3 Paul Sabatier, IRD, CNRS UMR 5563, Observatoire Midi-Pyrénées, 31400 Toulouse, France
[c] Centre for Exploration Targeting, The University of Western Australia, 35 Stirling Highway, Crawley, WA 6009, Australia
[d] Terracognita Geological Consulting Inc., P.O. Box 100, 4874 St. Clair Parkway, Port Lambton, ON N0P 2B0, Canada
[e] Mineral Exploration Consultant, 96 Marlow St, Wembley, WA 6014, Australia
[f] Department of Geology, School of Natural Sciences, Trinity College Dublin 2, Ireland

ARTICLE INFO

Article history:
Received 18 June 2015
Received in revised form 18 August 2015
Accepted 21 August 2015
Available online xxxx

Keywords:
Tasiast
Gold
Mauritania
BIF
Zircon geochronology

ABSTRACT

The Tasiast gold deposits are hosted within Mesoarchean rocks of the Aouéouat greenstone belt, Mauritania. The Tasiast Mine consists of two deposits hosted within distinctly different rock types, both situated within the hanging wall of the west-vergent Tasiast thrust. The Piment deposits are hosted within metasedimentary rocks including metaturbidites and banded iron formation where the main mineral association consists of magnetite-quartz-pyrrhotite ± actinolite ± garnet ± biotite. Gold is associated with silica flooding and sulphide replacement of magnetite in the turbidites and in the banded iron formation units. The West Branch deposit is hosted within meta-igneous rocks, mainly diorites and quartz diorites that lie stratigraphically below host rocks of the Piment deposits. Most of the gold mineralisation at West Branch is hosted by quartz–carbonate veins within the sheared and hydrothermally altered meta-diorites that constitute the Greenschist Zone. At Tasiast, gold mineralisation has been defined over a strike length > 10 km and to vertical depths of 740 m. All of the significant mineralised bodies defined to date dip moderately to steeply (45° to 70°) to the east and have a south–southeasterly plunge. Gold deposits on the Tasiast trend are associated with second order shear zones that are splays cutting the hanging wall block of the Tasiast thrust. An age of 2839 ± 36 Ma obtained from the hydrothermal overgrowth on zircons from a quartz vein is interpreted to represent the age of mineralisation.

© 2015 Elsevier B.V. All rights reserved.

1. Introduction

There are five principal geological domains within the borders of Mauritania (Fig. 1a). The Reguibat Shield to the north of the country, hosts Archean and Palaeoproterozoic metamorphic sequences and granites that form the northwestern limit of the West African Craton (Ennih and Liegeois, 2008; Key et al., 2008). Further south the craton margin coincides with the Mauritanides, a Hercynian tectonic belt that consists of Neoproterozoic and Palaeozoic metamorphosed sediments and volcanoclastic formations and that also includes parts of the basement (Villeneuve, 2008). To the east of the Mauritanide belt lies the vast Mesoproterozoic (Teal and Kah, 2005; Rooney et al., 2010) to Palaeozoic Taoudeni basin. Finally to the West of the Mauritanides lies the northern limit of the Mauritania–Senegal–Gambia–Bissau–Conarky Basin, which is a Mesozoic–Cenozoic continental margin basin overlying a Palaeozoic (and probably Archean) basement.

Mauritania is a significant source of copper, gold, and iron ore and was the second ranked exporter and producer of iron ore in Africa, after South Africa, in 2012. In addition to iron ore, Mauritania produces cement, copper, crude oil, gold, gypsum, quartz, salt, and steel (Taib, 2012). The Tasiast gold deposit (location coordinates: 15.5124° W, 20.5786° N) is a >10 million ounce deposit located within the south-western part of the Reguibat Shield, in the administrative region (Wilaya) of Inchiri, 250 km northeast of the capital Nouakchott.

Before discovery of the Tasiast deposit, the area had been subject to three regional exploration programmes during the 1960s and 1970s with various non-gold targets as summarized in Table 1 (Stuart, 2010). The area was identified as being anomalous in gold during the first regional-scale geological mapping and geochemical sampling programme of the European Development Fund project undertaken between 1993 and 1996 by the Bureau de Recherches Géologiques et Minières (BRGM) and the Office Mauritanien de Recherche Géologique (OMRG). The primary mission of the project was to locate new mineral indices of potential economic importance in the Tasiast area. More detailed soil sampling followed, resulting in the identification of a series of geochemical anomalies which were later tested by manual trenching. One of the soil geochemical anomalies, then called the C6–9 anomaly, eventually became the main Tasiast prospect (Stuart, 2010).

Exploration programmes were conducted by a series of companies, beginning with Normandy La Source Development in 1996 who defined two principal areas of gold mineralisation within the Tasiast prospect (Mining Journal, 2006). Commercial production began in January 2008

* Corresponding author at: Centre for Exploration Targeting, The University of Western Australia, 35 Stirling Highway, Crawley, WA, 6009, Australia.
E-mail address: mark.jessell@uwa.edu.au (M. Jessell).

http://dx.doi.org/10.1016/j.oregeorev.2015.08.020
0169-1368/© 2015 Elsevier B.V. All rights reserved.

Please cite this article as: Heron, K., et al., The Tasiast deposit, Mauritania, Ore Geol. Rev. (2015), http://dx.doi.org/10.1016/j.oregeorev.2015.08.020

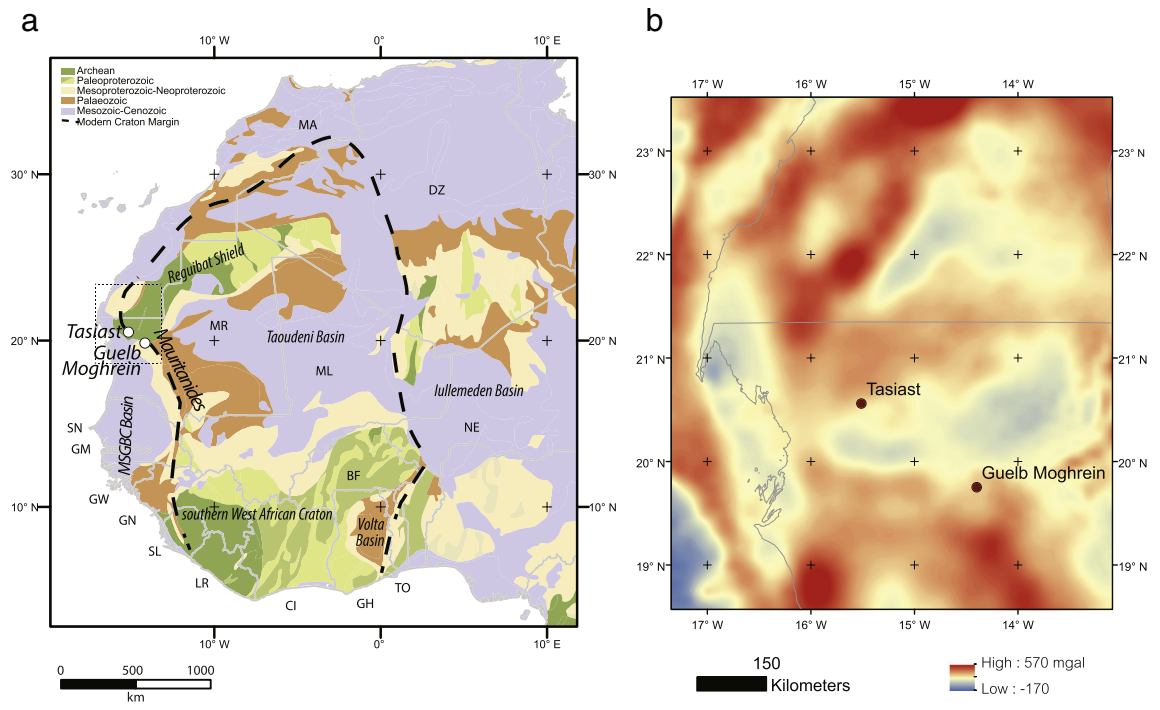


Fig. 1. a) Geological Framework of the West African Craton, showing the location of the Tasiast deposit (gold) in Mauritania, together with the ages of the major terranes, modified from the Geological Survey of Canada 1:35 M map of the world (Chorlton, 2007). The approximate limit of the present day WAC is shown as a heavy dashed line (after Ennih and Liegeois, 2008), and the limit of the gravity data shown in Fig. 1b is shown as a dotted rectangle. Two-letter country codes: BF: Burkina Faso; CI: Côte d'Ivoire; DZ: Algeria; GH: Ghana; GM: The Gambia; GN: Guinea; GW: Guinea Bissau; LR: Liberia; MA: Morocco; ML: Mali; MR: Mauritania; NE: Niger; SL: Sierra Leone; SN: Senegal; and TO: Togo. b) Free Air gravity image of Northern Mauritania showing location of principal deposits.

when the mine was owned and operated by Red Back Mining B.V. (Stuart, 2010). The Tasiast mine is currently 100% owned and operated by the Kinross Gold Corporation. Kinross currently estimates the gold resource to be 12.8 million ounces at an average grade of 1.5 g/t (Table 2). In 2013, 2.5 Mt. ore yielding 144,000 oz. Au at a grade of 1.96 g/t in addition to 104,000 oz. of dump leach gold for a total of 248,000 oz. Au were produced (Table 3) (Sims, 2014).

2. Geological overview

The Tasiast gold deposit is located within one of three principal Precambrian greenstone belts that form part of the Tasiast–Tijirit Terrane located in the western part of the Reguibat Shield (Fig. 1a). The Reguibat Shield consists of a series of west to east accreted, north–south trending Archean and Paleoproterozoic metavolcano-sedimentary belts and domal basement gneiss complexes. The majority of rocks that have been dated in the Tasiast–Tijirit Terrane have been gneiss, TTG and granite samples, and are all between 2.97 Ga and 2.91 Ga in age (Chardon, 1997, Key et al., 2008; Schofield et al., 2012; Gärtner et al., 2013; Montero et al., 2014). There have been two older TTG samples dated in the north of the region between 3.03 Ga and 3.01 Ga (Gärtner et al., 2013; Montero et al., 2014). The single other lithology to be dated in the region is a felsic volcanic obtained from drill core at the Tasiast deposit, which yielded an age of 2.97 Ga (Key et al., 2008), which is currently the best constraint for the age of the host rocks at Tasiast. Although no crystallization events older than 3.03 Ga are preserved in the Tasiast–Tijirit Terrane, whole rock Nd T_{DM} ages ranging from 3.60 Ga–2.95 Ga (Chardon, 1997, Key et al., 2008; Montero et al., 2014) suggest a contribution of older crustal material was involved in its creation.

The Aouéouat greenstone belt lies on the edge of one of a series of ENE oriented long-wavelength gravity and magnetic anomalies (Fig. 1b; Jessell et al., 2015). The Tasiast deposit is hosted within the north–south trending Aouéouat greenstone belt that is continuous for about 75 km strike length and shows as a series of high magnitude parallel anomalies in airborne magnetic data (Fig. 2b). The mine geology is characterized by a mafic to felsic meta-igneous succession, overlain by the remains of a sedimentary basin (Fig. 2a) that formed during rifting in a sinistral transtensional tectonic regime (Kruse, 2013). The preserved sedimentary stratigraphy includes abundant greywackes, siltstones, turbidite sequences and minor amounts of silica facies and

Table 1
Early exploration history of the Tasiast region (after Stuart, 2010).

Period	Operator	Activity	Exploration Scale
1962–1963	BRGM	The pegmatite Mission (for Be and Li)	Regional
1972	BRGM	Nickel Sulphide Mission	Regional
1973–1975	SNIM	Iron Ore Mission	Regional
1993–1996	BRGM + OMRG	European Development Fund project	Regional and infill

BRGM — Bureau de Recherches Géologique et Minières (French Geological Survey).
SNIM — Société Nationale Industrielle et Minière (Majority Mauritanian State-owned mining company).
OMRG — Office Mauritanien de Recherches Géologiques (Mauritanian Geological Survey).

Table 2
Mineral reserve and resource summary as of December 31, 2014.

Gold	Tonnes (×1000)	Grade (g/t)	Ounces (×1000)
Proven and probable reserves	161,822	1.77	9196
Measured and indicated resources[a]	85,573	1.14	3148
Inferred resources	8915	1.71	492
Total[b]	256,310	1.56	12,836

After www.kinross.com/operations/operation-tasiast-mauritania.aspx.
[a] Measured and Indicated Resources exclude Proven and Probable Reserves.
[b] 'Total' Grade is the weighted average of the three cited grades according to tonnes.

Please cite this article as: Heron, K., et al., The Tasiast deposit, Mauritania, Ore Geol. Rev. (2015), http://dx.doi.org/10.1016/j.oregeorev.2015.08.020

Table 3
Production summary.
Table 3 from Sims (2014).

Year	Tonnes milled (Mt)	Grade (g/t)	Gold produced ('000 oz.)	Dump leach gold produced ('000 oz.)	Total gold produced ('000 oz.)
2013	2.50	1.96	144	104	248
2012	2.55	1.54	114	71	185
2011	2.61	2.53	153	48	201
2010	2.14	2.46	151	36	187
2009	1.69	2.87	143	16	159
2008	1.49	3.10	140	0	140
2007	0.22	4.77	21	0	21

possibly some oxide facies banded iron formations (BIF). The siliciclastic sedimentary rocks contain detritus derived from gneissic basement rocks as well as from younger volcanic and intrusive rocks that formed prior to the rifting event.

Gold mineralisation formed during the approximately E–W bulk shortening event that accompanied inversion of the Tasiast sedimentary basin (Fig. 3). That deformation resulted in tight to isoclinal, upright to overturned folds, thrusting and transcurrent shearing throughout the Aouéouat belt (Fig. 4a). According to the present understanding the Tasiast deposits were formed during that single, possibly transpressive tectonic event. In all the Piment deposits, gold is associated with silica flooding and sulfidation of magnetite. At West Branch, the gold is hosted by quartz–carbonate veins that are folded and locally transposed parallel to the principal foliation that is axial planar to the folds. Several families of northeast and northwest striking brittle faults crosscut the folds and locally offset geological units.

The rocks of the Aouéouat belt, including the host rocks of the Piment and West Branch deposits, preserve upper greenschist to lower amphibolite peak metamorphic mineral assemblages, and a younger supergene alteration history. Mineral parageneses including cordierite and andalusite indicative of HT-LP peak metamorphism have been locally identified within metasedimentary units and may be associated with the emplacement of intrusive bodies of diorite and granodiorite compositions. Gold deposition occurred under middle greenschist post-peak metamorphic conditions as indicated by the presence of retrograde mineral assemblages including chlorite that are associated with mineralised veins and shear zones.

3. Gold mineralisation

The Tasiast Mine consists of two deposits hosted within distinctly different rock types. Both deposits are situated within the hanging wall block of the west vergent Tasiast thrust.

The Piment deposits are currently exploited as three main pits (North, Central and South) (Fig. 3) and are all hosted within metasedimentary rocks including metaturbidites and minor banded iron formation. Gold is associated with silicification and sulphide replacement of magnetite as observed within the turbidites and the banded iron formation units. In the Piment deposits the iron rich rocks represented a chemically reactive host for gold mineralization. The alteration mineral assemblage is principally associated with brittle–ductile splay thrusts that branch off the Tasiast thrust.

i. The West Branch deposit hosts the bulk of the gold at Tasiast. It is hosted within meta-igneous rocks, predominantly diorites and quartz diorites that lie stratigraphically below the host rocks of the Piment deposits. The dioritic host rocks are situated within the core of an overturned antiformal fold and are bounded above and below by felsic metavolcanic rocks. The diorites are thought to have been the preferred host for gold because they represented a

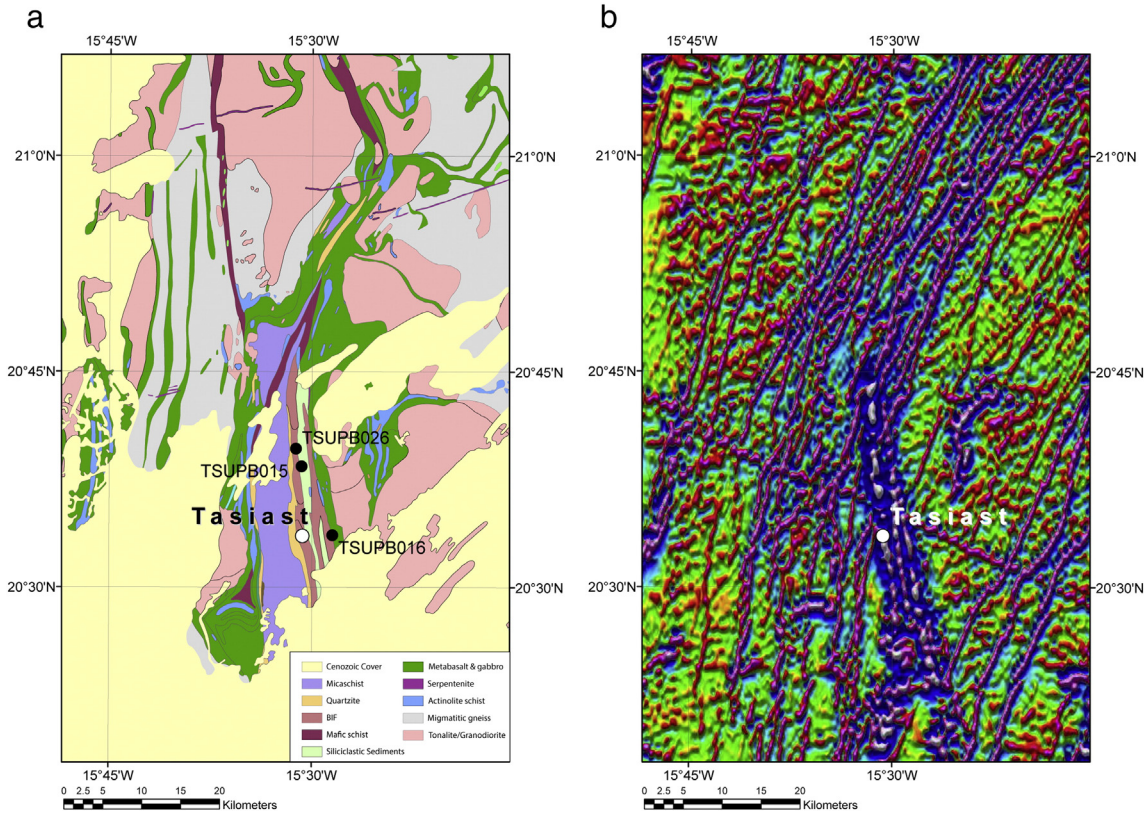


Fig. 2. a) Geological setting of the Tasiast deposit, (After PRISM 1:500 k geological map). b) First Vertical Derivative of the Reduced to the Pole airborne magnetic data. The principal anomalies seen are the NNW traces of the BIFs, together with two sets of dykes, one solitary dyke trending NW just north of the Tasiast deposit, and a dense swarm of dykes trending N to NE that obscure much of the geological signal.

Please cite this article as: Heron, K., et al., The Tasiast deposit, Mauritania, Ore Geol. Rev. (2015), http://dx.doi.org/10.1016/j.oregeorev.2015.08.020

ARTICLE IN PRESS

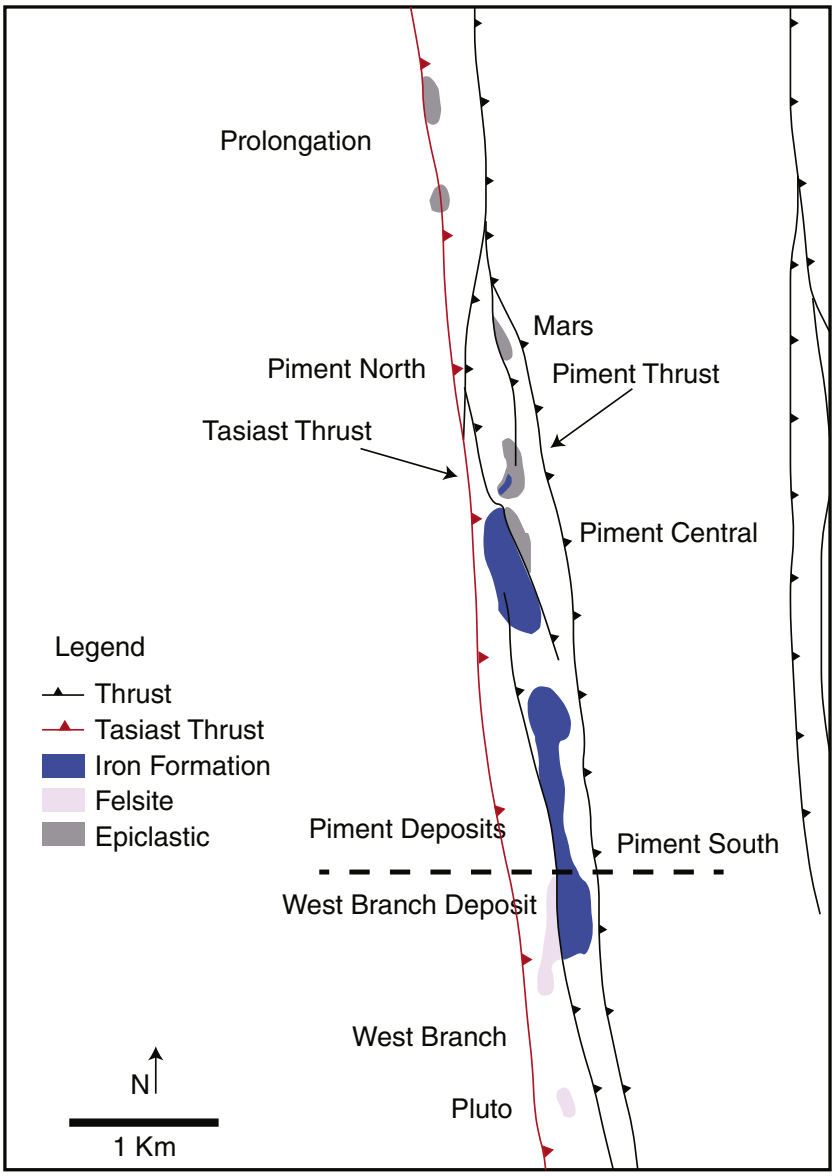


Fig. 3. Location of principal deposits and their host rocks, as well as the main structural features. After Stuart (2010).

less ductile lithology that the enveloping felsic rocks, such that they efficiently localized high strains within shear zones that channelled fluids and that acted as structural traps. At West Branch several facies of veins are recognized within the so-called Greenschist Zone and include the following (in order of paragenesis):Early milky white quartz veins that are commonly tightly to isoclinally folded, and boudinaged at a low angle to the foliation.

ii. Quartz–albite–tourmaline veins that are also boudinaged at low angles to foliation.
iii. Greenish grey to translucent quartz ± native gold veins with a silica selvedge at low angles to foliation.
iv. Quartz–amphibole–biotite–carbonate–pyrite ± garnet veins at low angles to the foliation.
v. Quartz–carbonate–biotite ± actinolite ± pyrite ± pyrrhotite ± tourmaline ± magnetite ± garnet veins that crosscut foliation at a high-angle.

The first four vein facies listed above are clearly syn-orogenic, probably having formed in extensional or shear fractures and were subsequently folded, boudinaged and locally transposed into the folation plane, or nearly so, during progressive deformation. Facies (i), (ii) and (iii) are observed to be cross-cut by veinlets of facies (iv) and visible gold is commonly associated with the carbonate-pyrite ± biotite rich veinlets. Facies (v) may be late orogenic, as those veins tend to be planar and undeformed to weakly deformed. The same facies of veins have been documented at satellite exploration targets along the Tasiast trend.

Metallic mineralogy within the Greenschist Zone is dominated by pyrrhotite, pyrite and native gold that occur as vein infill and alteration spots along the foliation, mainly in proximity to the veins. Pyrrhotite and pyrite occur together in many places but in variable ratios, with pyrrhotite being the predominant sulphide. Zones of pyrite-only and pyrrhotite-only mineralisation are rare. Blake (2011a,b in Sims, 2014) studied the nature, grain size and mode of occurrence of native gold grains in seven composites from two drill holes that intersected Greenschist Zone-style mineralisation. Results from the study concluded that the volume of coarse (>100 μm) Au grains account for the majority of contained Au and greater than 60% of grains occur in the liberated form and a lesser portion associated with gangue minerals and micrometre grains detected in slimes. At Piment the minerals of interest include native gold, pyrrhotite and pyrite.

Please cite this article as: Heron, K., et al., The Tasiast deposit, Mauritania, Ore Geol. Rev. (2015), http://dx.doi.org/10.1016/j.oregeorev.2015.08.020

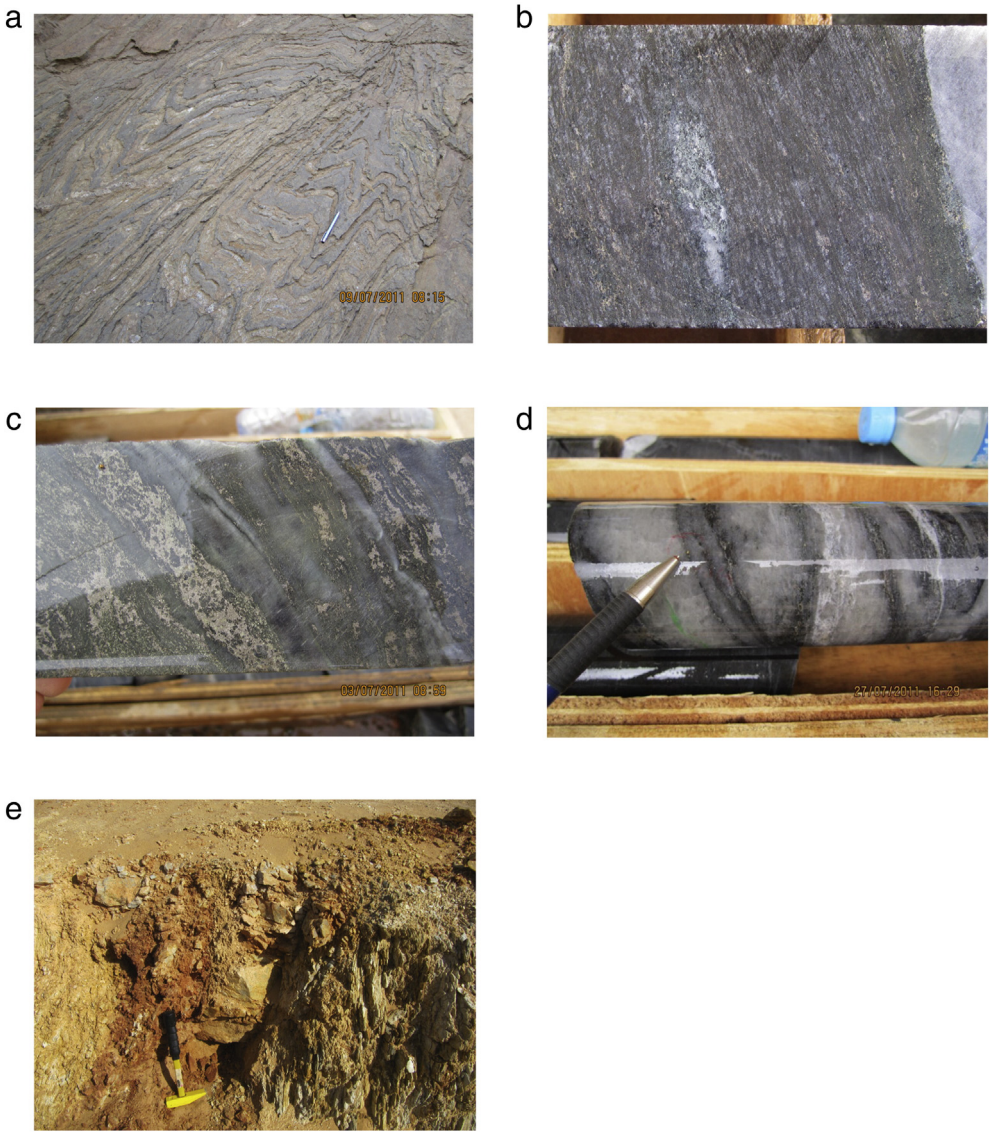


Fig. 4. a) Isoclinally folded sediments that are representative of the host rocks for all the Piment deposits, Tasiast Mine, pen for scale. b) Strongly foliated meta-diorite from West Branch typical of the Greenschist Zone. c) Silica flooding and extensive sulphide mineralisation, mainly pyrrhotite, parallel to bedding in the metaturbidites at Piment. d) Visible gold hosted in a quartz–carbonate vein, in drill core taken from the West Branch deposit. e) Field location of quartz–carbonate vein TSUPB026. All cores are 63.5 mm in diameter.

Other sulphide minerals are recognized at both deposits in minor to trace abundances. These include electrum, chalcopyrite, arsenopyrite, sphalerite, galena, covellite, pentlandite and petzite.

4. Ore body characteristics

Gold mineralisation at the West Branch and Piment deposits has been defined over a strike length of about 10 km and to vertical depths of 740 m. Other mineralised exploration targets extend the strike length of the Tasiast camp several kilometres to the north and south. The deposits defined to date dip moderately to steeply (45° to 70°) to the east and have a south–southeasterly plunge; at some satellite exploration targets the mineralisation dips steeply to the west.

Piment mineralisation is largely hosted along splay faults and within the adjacent altered and veined iron formation and turbiditic units. Individual mineralised shoots are continuous over 300 m and to vertical depths of at least 260 m.

Most of the gold mineralisation at West Branch is hosted by quartz–carbonate veins in hydrothermally altered meta-diorites (Greenschist Zone, Fig. 4b). The meta-diorites are enveloped by a felsite unit that occurs on the footwall and hanging wall sides of the Greenschist zone, defining an overturned antiformal fold in the hanging wall of the Tasiast thrust. The Greenschist Zone is characterized by intervals of mineralisation averaging 40 m to 100 m in thickness. Individual shoots are continuous over a strike length of at least 1000 m.

5. Geometric and kinematic controls

Gold mineralisation is associated with shear zones, quartz-veining (mainly at West Branch) and silica-flooding and sulphidation of magnetite (mainly at Piment, Fig. 4c). Gold deposits on the Tasiast trend are spatially associated with second order shear zones that are splay thrusts cutting the hanging wall block of the Tasiast thrust. Coarse visible gold is common within the quartz–carbonate veins (Fig. 4d).

Thrusting and tight to isoclinal folding has resulted in thickening of the stratigraphic package at Tasiast. The dominant foliation in the mine sequence is moderately to steeply east-dipping (45°–70°). Individual shear zones are typically 0.5 m to 10 m thick and are characterized by planar-laminated foliation with mylonitic textures locally observed. The shearing is commonly localized at contacts of lithologic

Please cite this article as: Heron, K., et al., The Tasiast deposit, Mauritania, Ore Geol. Rev. (2015), http://dx.doi.org/10.1016/j.oregeorev.2015.08.020

units. The current structural interpretation of the mine area suggests that mineralisation is associated with second order shear zones that formed in the tightly to isoclinally folded rocks within the hanging wall of the west-vergent Tasiast thrust. The shear zones developed preferentially along the limbs of, and within the cores of very tight to isoclinal folds. Vein sets occur subparallel and oblique to foliation in styles that include boudinaged, buckled and planar.

6. Alteration

The following hydrothermal alteration and mineralisation history (Japan International Cooperation Agency (JICA)/OMRG, 2005) is thought to be a down-temperature time sequence, based on mineralogy and fluid inclusion analysis:

i. Tungsten mineralisation suggests a temperature maximum of about 280 °C. The salinity of the ore-forming fluid is assumed to have been about 37 wt.% NaCl eq. and is thought to have been oxidizing, based on chromium dissolution recognized in the tungsten mineralised region.
ii. White mica alteration occurred at a temperature of about 200 °C. Based on the clay mineralogy, the ore-forming fluid is assumed to have been neutral to weakly acidic, while intensive dissolution of iron from BIFs suggests it also acted as the reducing agent.
iii. Gold was produced at a temperature of about 150 °C. The salinity of the ore-forming fluid is assumed to have been about 26 wt.% NaCl eq.

Supergene alteration has resulted in an oxide zone characterized by leaching of quartz–carbonate veins and sulphides, and precipitation of calcrete and iron hydroxides in voids and fractures. No well-defined transition zone was identified as the strongly weathered upper portion of the deposits grades into fresh rock at depth. The depth of oxidation is in the order of 30 m to 60 m, at an average of 40 m. No supergene enrichment of gold is apparent in the upper profile.

7. Age of mineralisation

Previous studies attempting to date the age of Tasiast mineralisation have relied on K–Ar dating of low potassium sericite, which gave an age of 1.9 Ga from a white argillized zone at the surface (Marutani et al., 2005). Dating of two distinct morphological types of hydrothermal monazite and xenotime from the Guelb Moghrein copper deposit yielded in situ U–Pb ages of 2492 ± 9 and 1742 ± 12 Ma respectively (Meyer et al., 2006) so a Meso-Proterozoic remobilisation remains a possibility in this part of the Reguibat Shield.

Apart from the results above, which do not seem to correlate with significant tectonic or magmatic activity in this region, there have been no previous attempts to directly date mineralisation at the Tasiast deposit. In order to address this we collected four samples of mineralised quartz veins from the Tasiast Mine and from several nearby exploration targets within the Aouéouat belt; three samples from drill core and one from an exploration trench. Three of these samples represent exploration target rocks, with the fourth being from the operational West Branch deposit. The primary purpose was to extract any minerals that could be used to date the formation of the quartz veins with a focus on hydrothermal zircon, monazite or xenotime. Zircon was separated from three of the four quartz veins, with the West Branch vein the only sample returning no zircons. Neither monazite nor xenotime were recovered from any of the samples.

Samples were crushed and zircons separated using standard techniques (Gemini water table, Frantz magnetic separation, and MI heavy-liquid separation), mounted in 1 in. diameter epoxy resin mounts, and polished to expose a near-equatorial section through the crystals. Analysis was carried out at the Geology Department, Trinity College Dublin, using Q-LA-ICP-MS (Thermo Scientific iCAP Qs, Photon Machines 193 nm ArF Excimer laser; see Crowley et al. (2014) for operating conditions). Zircon 91,500 (Wiedenbeck et al., 1995) was used as the primary standard, with Plešovice (Sláma et al., 2008) and Temora (Black et al., 2003) as secondary standards. The VizualAge data reduction scheme (Petrus and Kamber, 2012) within Iolite (Paton et al., 2011) was used to process data and Isoplot 4.15 (Ludwig, 2003) was used for data plotting. It is worth noting a large proportion of zircons analysed are discordant in nature, exhibiting varying degrees of Pb-loss. This is not unusual in Archean and Proterozoic terranes, and has been apparent in previous studies on the Tasiast–Tijirit Terrane (e.g. Key et al., 2008; Gärtner et al., 2013). The results of U–Pb dating from the three quartz veins containing zircon are presented below, and in Supplementary Material Table 1.

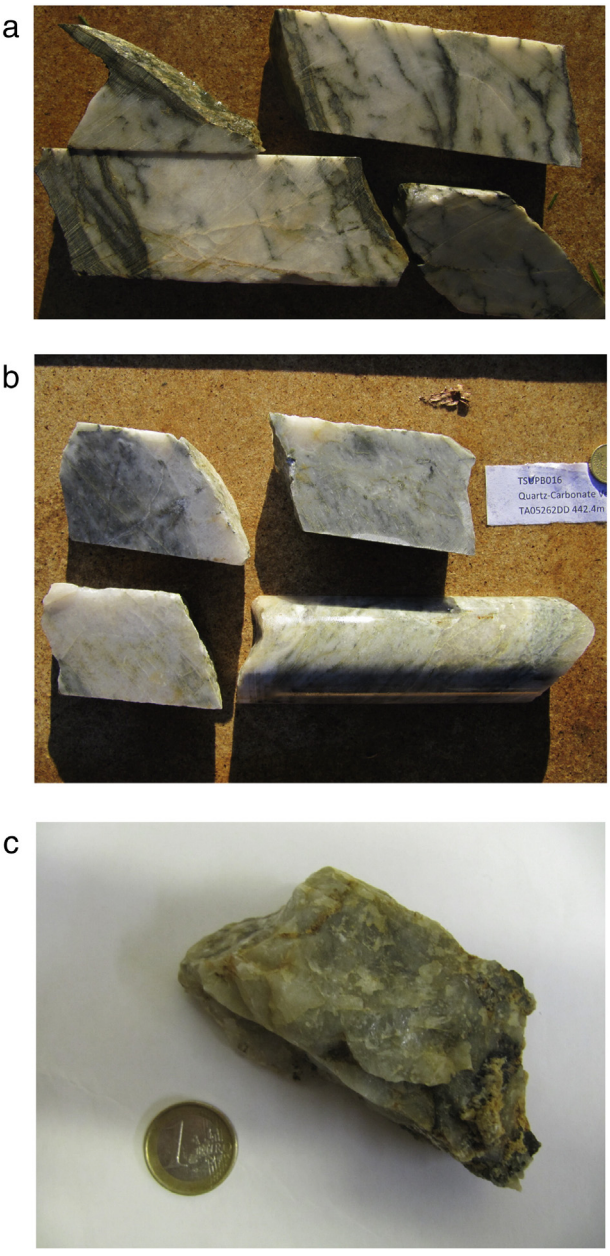


Fig. 5. Samples used for zircon analysis. a) TSUPB015 is a sample of drill core from a hole located 7 km north of the Piment Central deposit in target C6.7 showing pervasive quartz–carbonate veining. b) TSUPB016 is a sample of drill core from a hole located 4 km east of the Piment deposits in target C6.12, showing pervasive quartz–carbonate veining. c) TSUPB026 was collected as a field sample of a quartz–carbonate vein from an exploration trench in the Fennec target, 10 km north of the Piment deposits. All core are 63.5 mm in diameter.

Please cite this article as: Heron, K., et al., The Tasiast deposit, Mauritania, Ore Geol. Rev. (2015), http://dx.doi.org/10.1016/j.oregeorev.2015.08.020

TSUPB015, Quartz–Carbonate Vein (Drill Collar Location 446,500, 2,282,415 UTM WGS84 Zone 28Q).

TSUPB015 is a sample of drill core from a hole located 5 km north of the Piment deposits in target C6.7 and it yielded 43 zircons (Fig. 5a). The vein includes facies (iii) cross-cut by facies (iv). CL-images of the zircons show oscillatory zoning in most indicating they are igneous in nature, with metamict cores present in some (Fig. 6a). The zircons are therefore almost certainly xenocrystic. A number of zircons possess an extremely thin (<10 μm) overgrowth seen by the dark CL rim surrounding the zircon on all sides (Fig. 6a), interpreted as hydrothermal in origin. Of the 43 zircon analyses, 15 were <10% discordant, with Concordia ages of 3037 ± 29 Ma and 2946 ± 26 Ma obtained from time-resolved components of these least discordant analyses. A further two analyses overlapping with Concordia were obtained from this sample, with Concordia ages of 2819 ± 19 and 2695 ± 18 Ma, the latter of which is attributed to Pb-loss (Fig. 7a).

TSUPB016, Quartz–Carbonate Vein (Drill Collar Location 450250 2273595 UTM WGS84 Zone 28Q).

TSUPB016 is a sample of drill core from a hole located 5 km east of the Piment deposits in target C6.12 and yielded 48 zircons (Fig. 5b). The vein is of the tourmaline bearing facies (ii). CL-images show oscillatory zoning again with some metamict cores indicating these too are xenocrystic, however none show evidence of hydrothermal overgrowths (Fig. 6b). This is confirmed by the U–Pb data, with the 14 analyses <10% discordant containing one concordant population at 2953 ± 11 Ma (Fig. 7b), and a total range of $^{207}Pb/^{206}Pb$ ages of c. 3080–2945 Ma (Fig. 7c).

TSUPB026, Quartz–Carbonate Vein (Outcrop Location 445849 2284695 UTM WGS84 Zone 28Q).

TSUPB026 was collected as a field sample of a quartz vein from an exploration trench in the Fennec target, 10 km north of the Piment deposits (Fig. 4e, 5c). The sample exhibited strong signs of weathering, breaking apart where transected by thin carbonate veinlets. The quartz itself however remained intact. The vein includes facies (iii) cross-cut by facies (iv). This sample, partially due to the ability to obtain a larger volume of rock than from drill core, yielded ample zircon, and so an initial set of 104 grains were analysed. CL-images show igneous zircon with oscillatory zoning, some with more complex zoning, and a number possessing cores (Fig. 6c). All zircons from this sample had an obvious, generally <10 μ thick, overgrowth which again has been interpreted as hydrothermal in origin. The entire population gave an upper-intercept age of 2950 ± 11 Ma, with six zircons <10% discordant giving an upper intercept age of 2958 Ma ± 14 Ma (MSWD = 0.92) which is the preferred age for this sample (Fig. 7d & e).

Due to the ubiquitous presence of hydrothermal overgrowths on the zircons extracted from this sample, a second set of ten zircons were hand-picked, pre-treated in dilute HNO_3, and mounted on double-sided sticky tape without polishing. The exterior crystal faces were then ablated in two-second increments in an attempt to sample only the hydrothermal overgrowths. Five of the ten analyses exhibited extreme Pb-loss resulting in errors >140 Ma, which was not unexpected, since the rim of a zircon is the most likely part of a crystal to be affected by Pb-loss (Krogh, 1982). Three analyses did not produce any meaningful data and one sample gave a similar age to those obtained above, highlighting the lack of an overgrowth. This left one analysis providing usable data. An upper-intercept age of the two-second increments gave an age of 2839 ± 36 Ma (Fig. 7f).

The ages between c. 3060 and 2945 Ma obtained from all three quartz veins are interpreted as xenocrystic inherited zircons from neighbouring country rocks, or from deeper unexposed rock, and so provide a window on the ages of rocks present in the Aouéouat stratigraphy. Most of these ages overlap within error of previous ages obtained from the Tasiast–Tijirit Terrane gneiss and TTG rocks (Chardon, 1997, Key et al., 2008; Gärtner et al., 2013; Montero et al., 2014) which confirms this interpretation. The minor older component, up to 3080 Ma is within error of zircon T_{DM} Hf model ages (c. 3080 to 3030 Ma) calculated from c. 2950 to 2910 Ma granitic and TTG intrusions in the Tasiast–Tijirit Terrane (Key et al., 2008). The 2839 ± 36 Ma age obtained from the hydrothermal overgrowth from the Fennec sample is within error of a concordant age obtained from C6.7 (2819 ± 19 Ma). The dated

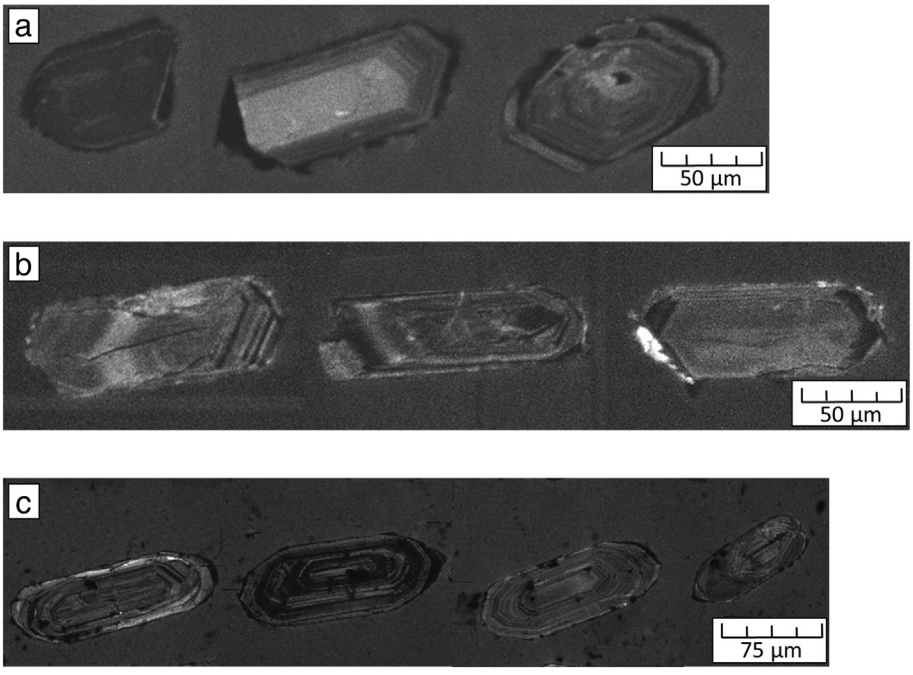


Fig. 6. Representative CL-images of zircons used for U–Pb dating. a) TSUPB015 CL-images show oscillatory zoning in most grains indicating they are igneous in nature, with some showing metamict cores. Some of these xenocrystic zircons show a thin (<10 μm) overgrowth seen by the dark CL rim surrounding the zircon on all sides, interpreted as hydrothermal in origin. b) TSUPB016 CL-images show oscillatory zoning with some metamict cores indicating they are xenocrystic, however none show evidence of hydrothermal overgrowths. c) TSUPB026 sample CL-images show igneous zircon with oscillatory zoning, some with more complex zoning, and a number possessing cores. All zircons from this sample had an obvious, generally <10 μ thick, overgrowth which is interpreted as hydrothermal in origin.

Please cite this article as: Heron, K., et al., The Tasiast deposit, Mauritania, Ore Geol. Rev. (2015), http://dx.doi.org/10.1016/j.oregeorev.2015.08.020

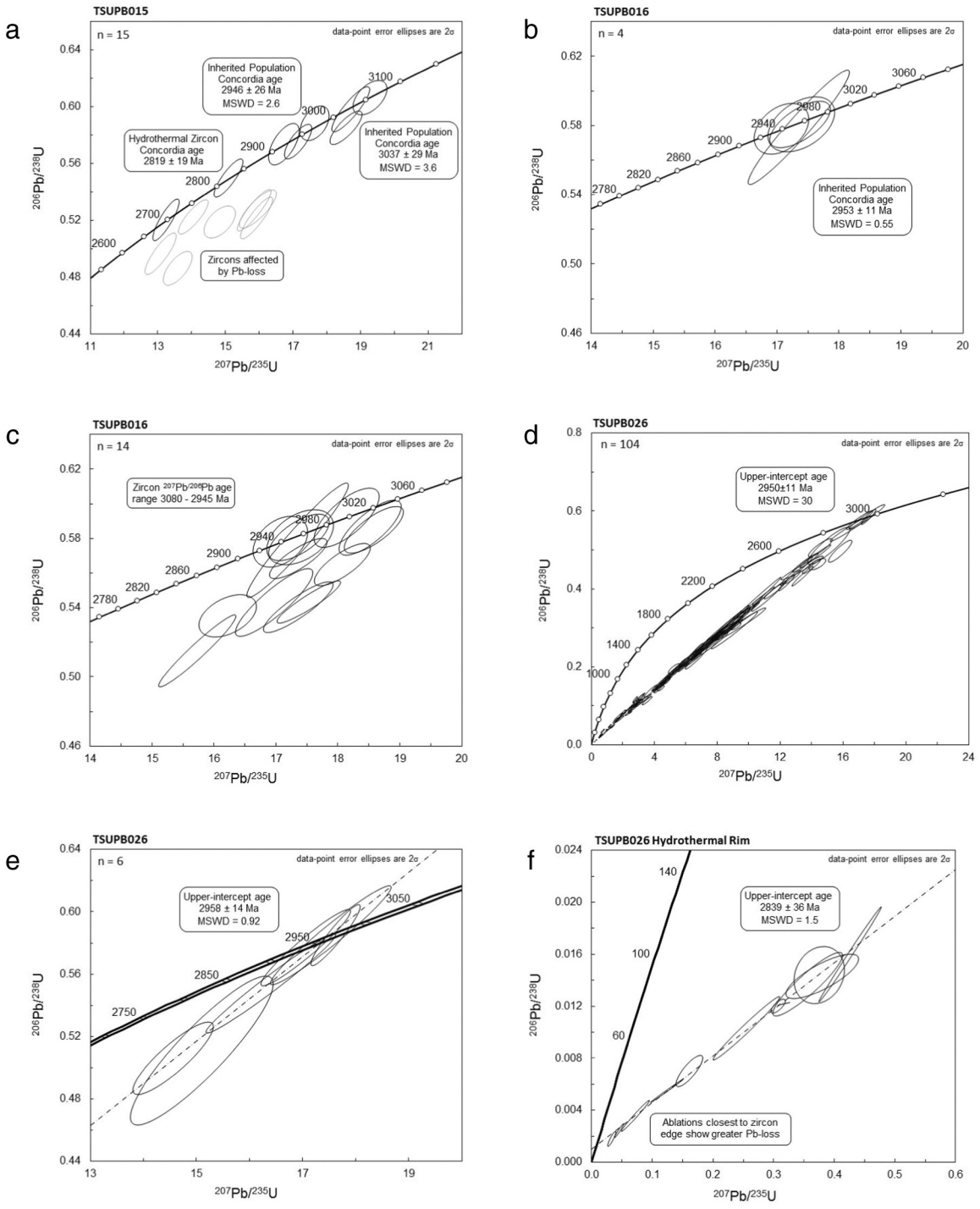


Fig. 7. U–Pb Concordia plots a) TSUPB015 analyses <10% discordant. b) TSUPB016 upper-intercept plot of concordant population. c) TSUPB016 analyses <10% discordant. d) TSUPB026. e) TSUPB026 upper intercept plot of analyses <10% discordant. f) TSUPB026 upper-intercept plot of hydrothermal overgrowth.

vein is of a known visible gold bearing generation. This age is interpreted as the crystallization age of the hydrothermal quartz veins, and therefore the mineralisation age of the Tasiast deposit.

8. Summary

The Tasiast gold deposit is situated on the flank of a long-wavelength gravity ENE oriented gravity high and a north–south oriented BIF which appears clearly in regional aeromagnetic data. The deposit mineralisation is focused in splay shears off the west-vergent Tasiast thrust and is associated with an alteration sequence interpreted to show a down-temperature evolution with time. Mineralization is controlled by both chemical traps (especially at the Piment deposits) and structural traps (shear zones), epigenetic in style and was coincident with early stages of post-peak metamorphic retrograde greenschist P–T conditions. An age of 2839 ± 36 Ma obtained from the hydrothermal overgrowth on zircons from a quartz vein is interpreted to represent the age of mineralisation.

Supplementary data to this article can be found online at http://dx.doi.org/10.1016/j.oregeorev.2015.08.020.

Please cite this article as: Heron, K., et al., The Tasiast deposit, Mauritania, Ore Geol. Rev. (2015), http://dx.doi.org/10.1016/j.oregeorev.2015.08.020

ARTICLE IN PRESS

Acknowledgements

Our thanks go to Kim Hein for improvements to the manuscript. We wish to gratefully acknowledge AMIRA International and the industry sponsors, as well as AusAID and the ARC Linkage Project LP110100667, for their support of the WAXI project (P934A). We are also appreciative of the contribution of the various Geological Surveys/Department of Mines in West Africa as sponsors in kind of WAXI. We wish to recognize our WAXI research colleagues from the various Institutions from around the world. We would like to thank SIGM for their permission to republish PRISM geological maps and magnetic data. We acknowledge the use of gravity data supplied by the BGI. Finally our thanks go to Kinross Gold Corporation for their permission to publish this paper.

References

Black, L.P., Kamo, S.L., Allen, C.M., Aleinikoff, J.N., Davis, D.W., Korsch, R.J., Foudoulis, C., 2003. TEMORA 1: a new zircon standard for Phanerozoic U–Pb geochronology. Chem. Geol. 200, 155–170.

Blake, C. 2011a. Mineralogical characterisation of five gold-bearing samples from the Tasiast mine, Mauritania for Kinross Gold Corporation. Internal unpublished report (February, 2011).

Blake, C. 2011b. Mineralogical characterisation of seven gold-bearing composite samples from the Tasiast Mine, Mauritania for Kinross Gold Corporation. Internal unpublished report (September, 2011).

Chardon, D. 1997. Les deformations continentals Archéennes. Examples naturels et modèlisation thermomécanique. Mémoires de Géosciences, Rennes, 76.

Chorlton, L.B. 2007. Generalized geology of the world: bedrock domains and major faults in GIS 416 format: a small-scale world geology map with an extended geological attribute database. 417 Geological Survey of Canada, Open File 5529, 2007; 48 pages; 1 CD-ROM, 418 http://dx.doi.org/10.4095/223767.

Crowley, Q.G., Heron, K., Riggs, N., Kamber, B., Chew, D., McConnell, B., Benn, K., 2014. Chemical abrasion applied to LA-ICP-MS U–Pb zircon geochronology. Minerals 4, 503–518.

Ennih, N., Liegeois, J.-P. (Eds.), 2008. The Boundaries of the West African CratonLondon, Special Publications 297. Geological Society.

Gärtner, A., Villeneuve, M., Linnemann, U., Archi, A.E., Hervé, B., 2013. An exotic terrane of Laurussian affinity in the Mauritanides and Souttoufides (Moroccan Sahara). Gondwana Res. 24, 687–699.

Jessell, M.W., Begg, G.C., Miller, M.S., 2015. The Geophysical Signatures of the West African Craton. Precambrian Research http://dx.doi.org/10.1016/j.precamres.2015.08.010 (in press).

JICA/OMRG Report on the Tasiast Gold Deposit. http://www.omrg.mr/spip.php?article88.

Key, R.M., Loughlin, S.C., Horstwood, M.S.A., Gillespie, M., Pitfield, P.E.J., Henney, P.J., Crowley, Q.G., Del Rio, M., 2008. Two Mesoarchaean Terranes in the Reguibat Shield of NW Mauritania. In: Ennih, N., Liégeois, J.-P. (Eds.), Boundaries of the West African Craton vol. 297. Special Publication of the Geological Society, London, pp. 33–52.

Krogh, T.E., 1982. Improved accuracy of U–Pb zircon ages by the creation of more concordant systems using an air abrasion technique. Geochimica et Cosmochimica Acta Vol. 46, 637–649.

Kruse, S., 2013. Regional geometry and tectonic evolution of the Aouéouat greenstone belt and Tasiast metallogenic district. Unpublished Internal Report for Kinross Tasiast, Terrane Geoscience Inc.

Ludwig, K.R., 2003. Isoplot 3.00: a geochronological toolkit for Microsoft Excel. Berkeley. Geochronol. Cent. Spec. Publ. 4, 0–71.

Marutani, M., Higashihara, M., Watanabe, Y., Murakami, H., Kojima, G., Dioumassi, B., 2005. Metallic ore deposits in the Islamic Republic of Mauritania. Resour. Geol. 55, 59–70.

Meyer, F.M., Kolb, J., Sakellaris, G.A., Gerdes, A., 2006. New ages from the Mauritanides Belt: recognition of Archean IOCG mineralization at Guelb Moghrein. Terra Nova 18, 345–352.

Mining Journal, 2006. Mauritania: London, Mining Journal Special Publication, February 2006 12 pp.

Montero, P., Haissen, F., Archi, A.E., Rjimati, E., Bea, F., 2014. Timing of Archean crust formation and cratonisation in the Awsard–Tichla zone of the NW Reguibat Rise, West African Craton. A SHRIMP, Nd–Sr isotopes, and geochemical reconnaissance study. Precambrian Research 242, 112–137.

Paton, C., Hellstrom, J., Paul, B., Woodhead, J., Hergt, J., 2011. Iolite: freeware for the visualisation and processing of mass spectrometric data. J. Anal. At. Spectrom. 26, 2508–2518.

Petrus, J.A., Kamber, B.S., 2012. Vizualage: a novel approach to laser ablation ICP-MS U–Pb geochronology data reduction. Geostand. Geoanalytical Res. 36, 247–270.

Rooney, A.D., Selby, D., Houzay, J.-P., Renne, P.R., 2010. Re–Os geochronology of a Mesoproterozoic sedimentary succession, Taoudeni basin, Mauritania: implications for basin wide correlations and Re–Os organic-rich sediments systematic. Earth Planet. Sci. Lett. v. 289 (3–4), 486–496.

Schofield, D.I., Horstwood, M.S.A., Pitfield, P.E.J., Gillespie, M., Darbyshire, F., O'Connor, E.A., Abdouloye, T.B., 2012. U–Pb dating and Sm–Nd isotopic analysis of granitic rocks from the Tiris Complex: new constraints on key events in the evolution of the Reguibat Shield, Mauritania. Precambrian Res. 204-205, 1–11. http://dx.doi.org/10.1016/j.precamres.2011.12.008.

Sims, J., 2014. Tasiast Project Mauritania National Instrument 43-101 Technical Report, Prepared for Kinross Gold Corporation 253 pp.

Sláma, J., Košler, J., Condon, D.J., Crowley, J.L., Gerdes, A., Hanchar, J.M., Horstwood, M.S., Morris, G.A., Nasdala, L., Norberg, N., 2008. Plešovice zircon — a new natural reference material for U–Pb and Hf isotopic microanalysis. Chem. Geol. 249, 1–35.

Stuart, H. 2010. Technical Report on the Tasiast Gold Mine Islamic Republic of Mauritania for Red Back Mining Inc.: unpublished technical report prepared for Red Back Mining Inc., effective date 6 September 2010. 104 pp.

Taib, M., 2012. The Mineral Industry of Mauritania, USGS Minerals Yearbook 2012 (Advance Release) 6 pp.

Teal, D.J., Kah, L.C., 2005. Using C-isotopes to constrain interbasinal stratigraphic correlations, Mesoproterozoic Atar Group, Mauritania. Geol. Soc. Am. 37, 45 Abstracts with Programs.

Villeneuve, M., 2008. Review of the orogenic belts on the western side of the West African craton: the Bassarides, Rokelides and Mauritanides. In: Ennih, N., Liégeois, J.-P. (Eds.), Boundaries of the West African Craton. Special Publication of the Geological Society vol. 297, pp. 169–201 London.

Wiedenbeck, M., Alle, P., Corfu, F., Griffin, W., Meier, M., Oberli, F., Quadt, A.v., Roddick, J., Spiegel, W., 1995. Three natural zircon standards for U–Th–Pb, Lu–Hf, trace element and REE analyses. Geostand. Newslett. 19, 1–23.

Please cite this article as: Heron, K., et al., The Tasiast deposit, Mauritania, Ore Geol. Rev. (2015), http://dx.doi.org/10.1016/j.oregeorev.2015.08.020

Minerals **2014**, *4*, 1-x manuscripts; doi:10.3390/min40x000x

OPEN ACCESS

minerals

ISSN 2075-163X

Article

Chemical Abrasion Applied to LA-ICP-MS U-Pb Zircon Geochronology

Quentin G. Crowley [1,*], Kyle Heron [1], Nancy Riggs [2], Balz Kamber [1], David Chew [1], Brian McConnell [3], Keith Benn [4]

[1] Department of Geology, School of Natural Sciences, Trinity College, Dublin 2, Ireland; E-Mails: heronky@tcd.ie (K.H.); kamberbs@tcd.ie (B.K.); chewd@tcd.ie (D.C.)

[2] School of Earth Sciences and Environmental Sustainability, Northern Arizona University, Flagstaff, Arizona 86011, USA; E-Mail: nancy.riggs@nau.edu

[3] Geological Survey of Ireland, Beggars Bush, Dublin 4, Ireland; E-Mail: brian.mcconnell@gsi.ie

[4] Tasiast Mauritanie Limited SA, ZRA 741, BP 5051, Nouakchott, Mauritania, West Africa; E-Mail: keith.benn@kinross.com

***** Author to whom correspondence should be addressed; E-Mail: crowleyq@tcd.ie; Tel.: +353-1-8962403; Fax: +353-1-6711199.

Received: / Accepted: / Published:

Abstract: Zircon ($ZrSiO_4$) is the most commonly used mineral in U-Pb geochronology. Although it has proven to be a robust chronometer, it can suffer from Pb-loss or elevated common Pb, both of which impede precision and accuracy of age determinations. Chemical abrasion of zircon involves thermal annealing followed by relatively low temperature partial dissolution in HF acid. It was specifically developed to minimize or eliminate the effects of Pb-loss prior to analysis using Thermal Ionization Mass Spectrometry (TIMS). Here we test the application of chemical abrasion to Laser Ablation Inductively Coupled Plasma Mass Spectrometry (LA-ICP-MS) by analyzing zircons from both untreated and chemically abraded samples. Rates of ablation for non-treated zircons are up to 25% faster than chemically abraded equivalents. Ablation of 91500 zircon reference material demonstrates a c. 3% greater down-hole fractionation of $^{206}Pb/^{238}U$ for non-treated zircons. These disparities necessitate using chemical abrasion for both primary reference material and unknowns to avoid applying an incorrect laser induced fractionation correction. All treated samples display a marked increase in the degree of concordance and / or lowering of common Pb, thereby illustrating the effectiveness of chemical abrasion to LA-ICP-MS U-Pb zircon geochronology.

Keywords: U-Pb geochronology; zircon; chemical abrasion; LA-ICP-MS; Pb-loss

1. Introduction

U-Pb geochronology is a widely used radiometric dating tool applied to geological time-scales from 800 thousand years to >4 billion years. This is made possible due to dual uranium parent isotopes of ^{235}U and ^{238}U decaying to ^{207}Pb and ^{206}Pb with half-lives of c. 704 million years and c. 4.468 billion years respectively. U–Pb geochronology was initially developed in the mid-1950s [1-3] and only made possible by earlier advances in mass spectrometry [4]. Thermal Ionization Mass Spectrometry (TIMS) is the method of choice for studies requiring the highest precision U-Pb data. Micro-beam techniques such as Secondary Ionization Mass Spectrometry (SIMS) and Laser Ablation Inductively Coupled Plasma Ionization Mass Spectrometry (LA-ICP-MS) are generally used when there is a requirement for a greater number of analyses at a lower analytical precision, or where a spatial resolved analysis is beneficial. Zircon ($ZrSiO_4$) is the most commonly used mineral in U–Pb geochronology and is found in a wide compositional range of igneous, metamorphic and sedimentary rocks. In terms of crystal structure and composition, zircon has a tetrahedral Si site and a distorted octahedral Zr site [5]. Hf, U, Th, Ti, rare earth elements, Y and Sc may enter the Zr site, but only relatively small amounts of Pb are accepted. As a result of this, U is compatible but Pb is incompatible in the zircon crystal structure, so that common (or initial) Pb is preferentially excluded at the time of zircon formation, whereas ^{206}Pb and ^{207}Pb can reside within zircon following *in-situ* radioactive decay from the parent U isotopes. The exact mode of incorporation and place of residence of radiogenic Pb in the zircon crystal structure is thought to be strongly dependent on composition, such as the presence or absence of phosphate or hydrous phases [6].

Zircon commonly occurs as an accessory phase following high-grade metamorphism and partial melting and demonstrates a high closure temperature for Pb (> 900°C [7,8]), yet paradoxically the U–Pb isotope system may be disturbed at low temperatures resulting in Pb-loss. Conditions resulting in zircon being susceptible to Pb-loss may arise from the crystal lattice being damaged by the emission of alpha particles and alpha recoil processes [9]. In this manner, high-U zircons or high-U domains within zircons may accumulate radiation damage and be susceptible to Pb-loss. This effect is particularly pronounced at low temperatures where there is insufficient thermal energy to repair (anneal) radiation damage to the crystal lattice. The seemingly contradictory behavior of Pb in zircon may be explained by a difference in valence states for ^{204}Pb, compared to ^{206}Pb and ^{207}Pb. Although uncertainty exists, it is possible that ^{204}Pb is divalent, in contrast to ^{206}Pb and ^{207}Pb which may exist in tetravalent states [10,11]. Prevalence of tetravalent Pb in zircon may be enhanced by a strong oxidizing environment at α-recoil sites and maintained by the continuous loss of β-particles [12]. Considering that divalent Pb is incompatible in zircon, any fluid-induced reduction of Pb^{4+} to Pb^{2+} may result in loss of Pb. Aside from Pb-loss being related to radiation damage, it can also arise following physical distortion of the crystal lattice structure during rock deformation processes (e.g. shearing). This phenomenon results in mobilization of Pb from distorted zircons and can occur at lower metamorphic grade than in undistorted counterparts [13]. The U–Pb isotope system in zircon may therefore be disturbed by a process of Pb-loss causing erroneous younger apparent ages.

Although it is possible to obtain meaningful radiometric ages from zircons that have suffered Pb-loss, a greater number of analyses are usually required to construct a statistically valid discordia array and intercept ages. Additionally, these intercept ages are generally less precise than ages (e.g. a concordia age or weighted mean $^{206}Pb/^{238}U$ age) calculated from a uniform population of zircons with no Pb-loss. In order to reduce uncertainties due to Pb-loss a method of "air-abrasion" was developed to physically abrade the exterior portions of zircons [14]. This results in less discordant or concordant zircon analyses when compared with non-abraded samples and was widely adopted for over two decades as a zircon pretreatment for TIMS analysis. More recently a method termed "chemical abrasion" was perfected by Mattinson [15] following a series of similar but less successful attempts [16-20] to chemically pre-treat zircons and lessen or remove the effects of Pb-loss. Chemical abrasion of zircon involves two steps; (1) thermally annealing grains between 850 and 1000^{o}C for 48 hrs and (2) subjecting annealed grains to HF acid attack for 12 hrs at temperatures below which full dissolution normally takes place. This two-step process whereby alpha track damage is thermally annealed and higher-U domains are preferentially dissolved from the entire grain also has the effect of removing more soluble forms of Pb.

Chemical abrasion was specifically developed as a pre-treatment to eliminate or minimize Pb-loss in zircons prior to TIMS analysis. This method has been adapted for incrementally dissolving complex single grains to produce high-precision TIMS ages not discernible using micro-beam techniques [21]. Chemical abrasion has also been demonstrated to be effective for SIMS U-Pb zircon geochronology [22]. This study aims to investigate if chemical abrasion can be applied to LA-ICP-MS U-Pb zircon geochronology to reduce discordance. Although the technique has previously been applied to a small number of LA-ICP-MS U-Pb zircon studies [23-25], it has not been rigorously assessed. We test a modified chemical abrasion technique by applying an annealing-leaching treatment to zircon reference materials and a range of zircons of unknown age. Comparisons of data are made between treated and un-treated zircons to assess physical and chemical effects and evaluate the method as a pretreatment utility prior to LA-ICP-MS analysis.

2. Experimental Section

2.1. Sample Preparation

Samples were crushed and zircons separated by standard techniques (Rogers water table, Frantz magnetic separation, and heavy-liquid separation). Representative zircons were hand-picked under a binocular microscope; some of these were then thermally annealed at 850^{o}C in quartz glass beakers for 60 hours. The annealed crystals were then ultrasonically washed in 4N HNO_3, rinsed in ultra-pure water, then further washed in warm 4N HNO_3 prior to rinsing with ultra-pure water to remove surface contamination. The annealed and cleaned zircon fractions were then chemically abraded in 200µl 29N HF and 20µl 8N HNO_3 at 180^{o}C in modified 1.5ml Teflon micro-centrifuge tubes in a Parr bomb for 12 hours. Following several cleaning steps in 3N HCl and ultra-pure water, treated and untreated zircons were mounted in separate epoxy plugs, ground down to expose grain interiors and polished with 6µm and 1µm diamond paste. All sample preparation was undertaken at the Department of Geology, Trinity College Dublin (TCD).

2.2. Instrumentation

Samples were analysed either at the Department of Earth Science, University of California Santa Barbara (UCSB) by Multi-Collector (MC) LA-ICP-MS (Nu Plasma) [26] or by Quadrupole (Q-) LA-ICP-MS (Thermo Scientific iCAP Qs) at the Department of Geology, TCD. Both laboratories utilized a Photon Machines 193 nm ArF Excimer laser equipped with a HeLex ablation cell, 91500 zircon [27] as a primary reference material and Plešovice [28] as a secondary reference material. For analyses conducted at TCD the LA-ICP-MS system was tuned while ablating a line raster on NIST SRM 612 synthetic glass in order to obtain optimal sensitivity for Pb, Th and U, while keeping ThO+ ⁄ Th low and Th ⁄U close to 1. ThO+ ⁄ Th and Th ⁄U were typically < 0.002 and > 0.9, respectively. Full instrument set-up conditions are given in Table 1.

Table 1. Running conditions for ICP-MS and laser ablation at University of California Santa Barbara and Trinity College Dublin.

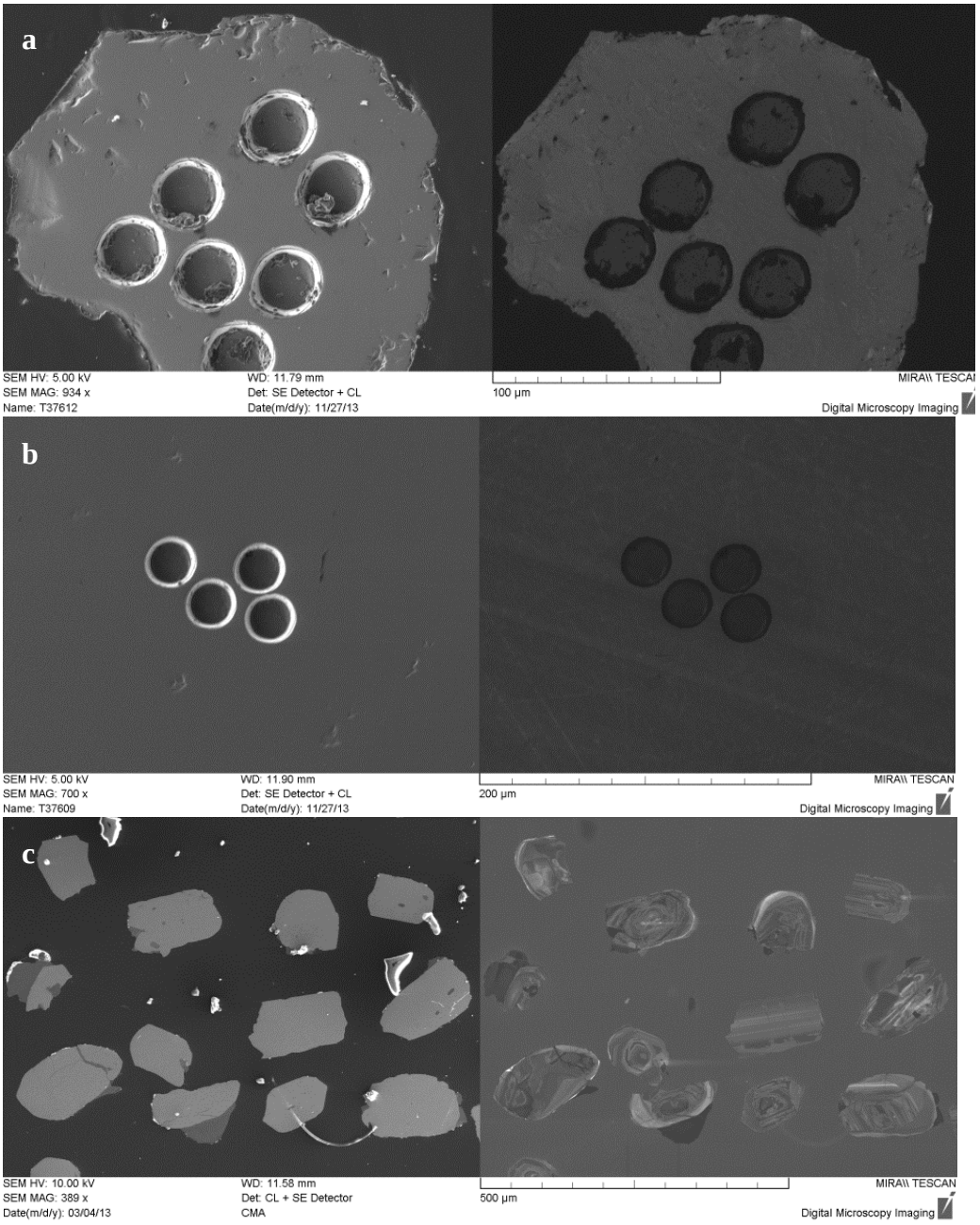
	UCSB	**TCD**
ICP Instrument model	Nu Plasma HR MC-ICP-MS	Thermo-Scientific iCAP-Qs (quadrupole)
Plasma RF power (W)	1300	1450
Plasma gas flow (lit/m)	0.8	0.7
Monitored masses	^{238}U, ^{232}Th, ^{208}Pb, ^{207}Pb, ^{206}Pb, ^{204}Pb/^{204}Hg	^{238}U, ^{232}Th, ^{208}Pb, ^{207}Pb, ^{206}Pb, ^{204}Pb/^{204}Hg, ^{200}Hg, ^{91}Zr, ^{88}Sr
LA Instrument Model	Photon Machines Analyte 193	Photon Machines Analyte 193
Laser	ATLEX-SI 193 nm ArF excimer	ATLEX-SI 193 nm ArF excimer
Fluence (J/cm^2)	6	7
Repetition Rate (Hz)	4	5
Delay between analyses (s)	20	15
Ablation duration (s)	30	30
Carrier gas flow (lit/m)	0.25 (He)	0.70 (He), 0.006 (N_2)
Spot diameter (µm)	30	30

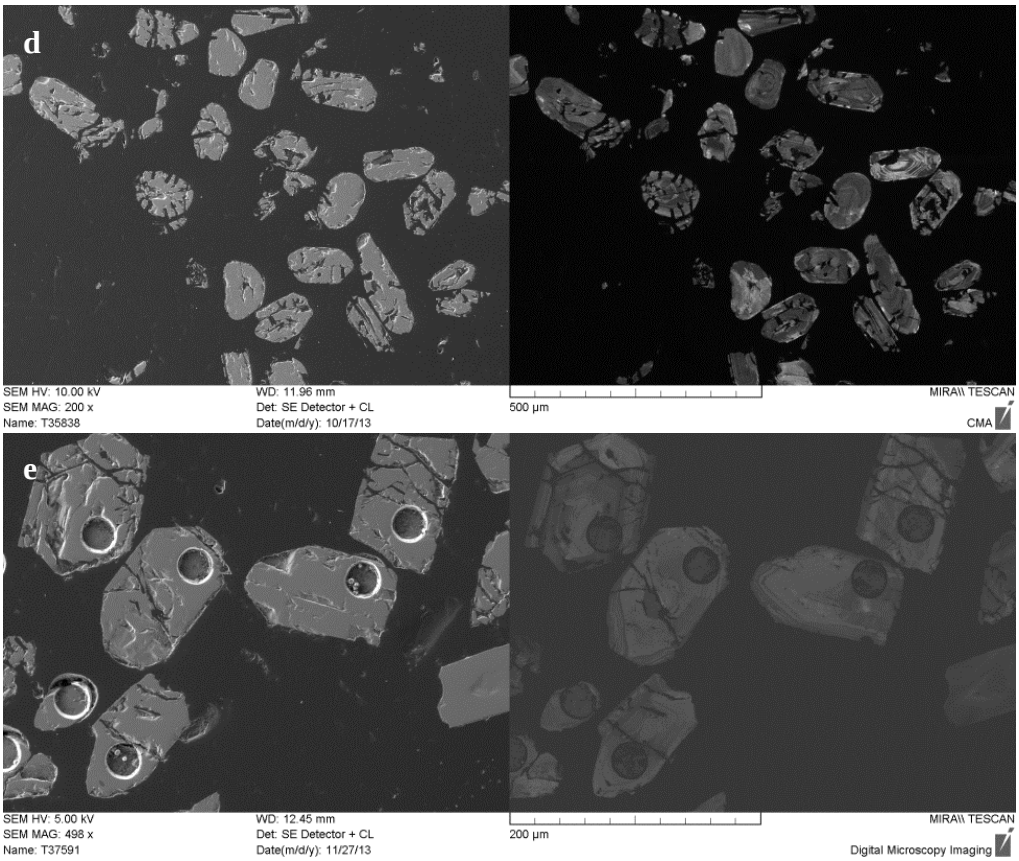
2.3. Sample Description

Untreated and chemically abraded zircons were analyzed from four samples, comprising two natural reference materials 91500 [27] and Penglai [29] and two unknowns TSUPB021 and 10/225.

The 91500 zircon reference material is thought to have come from a syenite pegmatite near Kuehl Lake in Ontario, Canada. The original sample consisted of a single 238g crystal, part of which was split into a large number of 200µm to 2mm fragments and made available to geochronology laboratories worldwide. 91500 zircon has an accepted U-Pb age of c. 1065 million years (Ma) [27]. Back-scattered secondary electron (BSEM) and cathodoluminesence (CL) images of a chemically abraded 91500 zircon fragment (Fig. 1a) show slight pitting in the grain interior, resulting from etching by HF acid. Note that all zircons were polished down to reveal grain interiors after chemical abrasion; this signifies that HF acid vapour penetrated into central portions of even large (c. 150 µm diameter)

Figure 1. Back-scattered secondary electron (left) and cathodoluminesence (right) images of representative zircons from (**a**) 91500-CA; (**b**) Penglai-CA; (**c**) TSUPB021; (**d**) TSUPB021-CA; (**e**) 10/225-CA. Note that "-CA" indicates zircons have been subjected to chemical abrasion.





grains. Faint oscillatory zoning of the 91500 fragment evident in CL is consistent with the igneous origin of this zircon.

Penglai zircons [29] are sourced from early Pliocene alkaline basalts from the northern Hainan Island of South China. Due to their abundance and large size, they were originally suggested as reference material for micro-beam analysis of Hf-O isotopes and for U-Pb geochronology. Penglai zircons however, define a linear discordant array on a Tera-Wasserburg diagram with a "preferred" $^{206}Pb/^{238}U$ age of 4.4 ±0.1 Ma [29]. This discordance makes Penglai unsuitable for use as a primary reference material for U-Pb geochronology, unless a common Pb correction is undertaken [30]. As with 91500, slight pitting due to chemical abrasion is evident in the BSEM image and oscillatory zoning is obvious in CL (Fig. 1b), the latter being consistent with an igneous origin.

TSUPB021 is an Archean greywacke from the Tasiast terrane of Mauritania, West Africa. Zircons are sub-angular to rounded, 150-100 x 100-80 x 80-60 µm and typically display oscillatory zoning in CL images (Fig. 1c) indicating an igneous provenance. Metamict zircons are also evident from CL images indicating that substantial radiation damage has occurred. TSUPB021 zircons subjected to chemical abrasion have been visibly and severely affected, with widespread partial dissolution along micro-cracks, radiating fractures and dark CL (high U) domains throughout the grains (Fig. 1d).

Sample 10/225 is a granite cobble from an Ordovician sedimentary sequence in South Mayo, west of Ireland. Zircons are euhedral to subhedral, 100-50 x 80-60 x 60-40 µm and display oscillatory zoning and metamict domains in CL. Chemically abraded zircons from this sample display widespread severe pitting and dissolution zones along fractures through entire grains (Fig. 1e).

2.4. Data processing

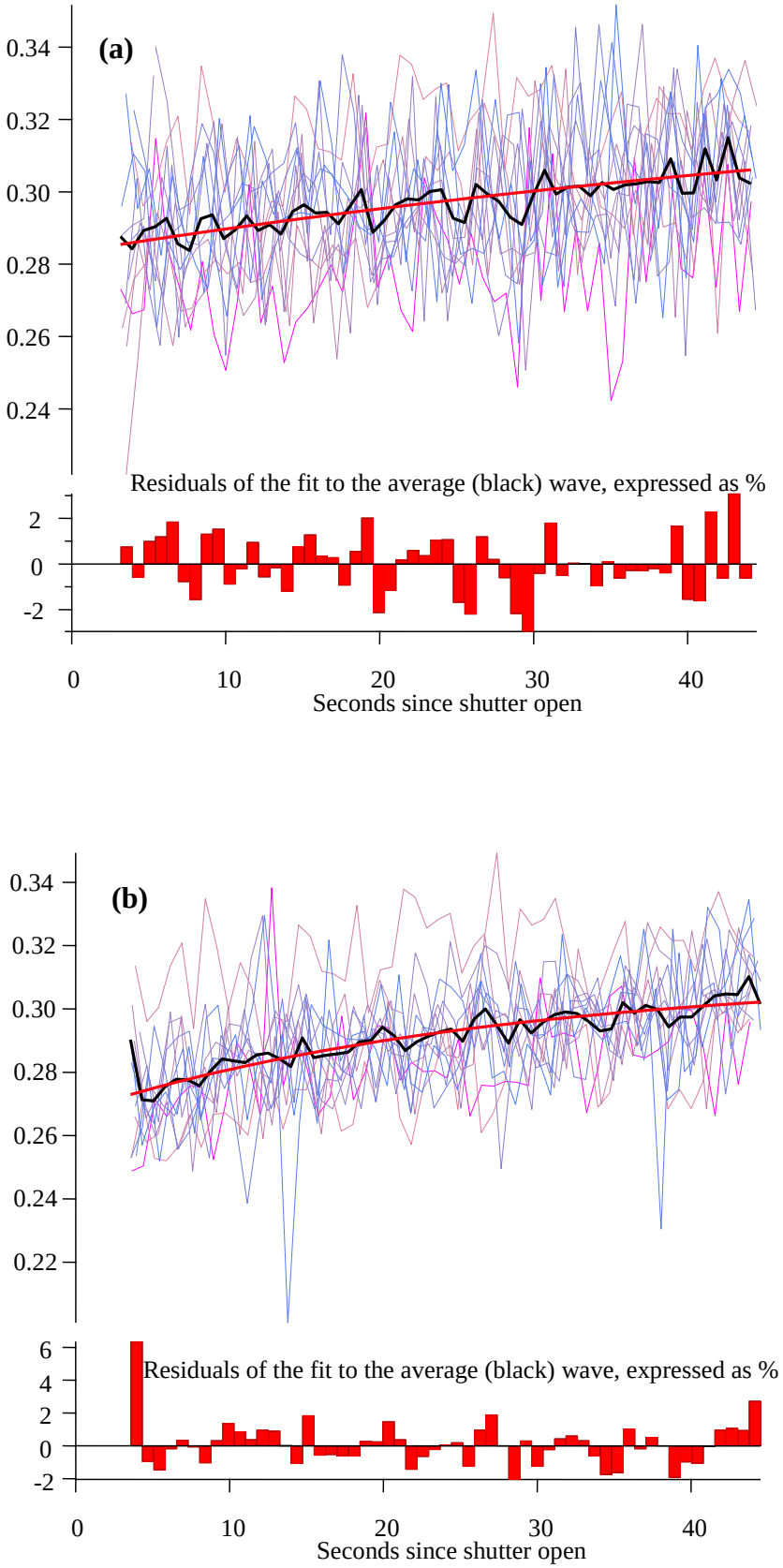
All data reduction was performed using the Iolite software package (http://www.iolite.org.au) [31-33] which operates within Igor Pro (http://www.wavemetrics.com). Although Iolite has been available for only a few years, it has become widely adopted for its visual and interactive approach to processing very large time-integrated datasets. Once raw data have been imported from the mass spectrometer software, Iolite uses several steps to process the data. These include (1) baseline corrections, (2) defining integrations for U–Pb primary reference materials, (3) calculating a down-hole U-Th-Pb fractionation correction, (4) defining integrations for secondary reference materials and unknowns and (5) applying a session-wide fractionation and instrumental drift corrections. The VizualAge data reduction scheme [34] within Iolite was used to process data presented here. It has the capability of producing "live concordia" diagrams for visualising data while selecting integration intervals during data processing.

3. Results and Discussion

3.1. Characterizing Ablation Profiles and Down-Hole Fractionation

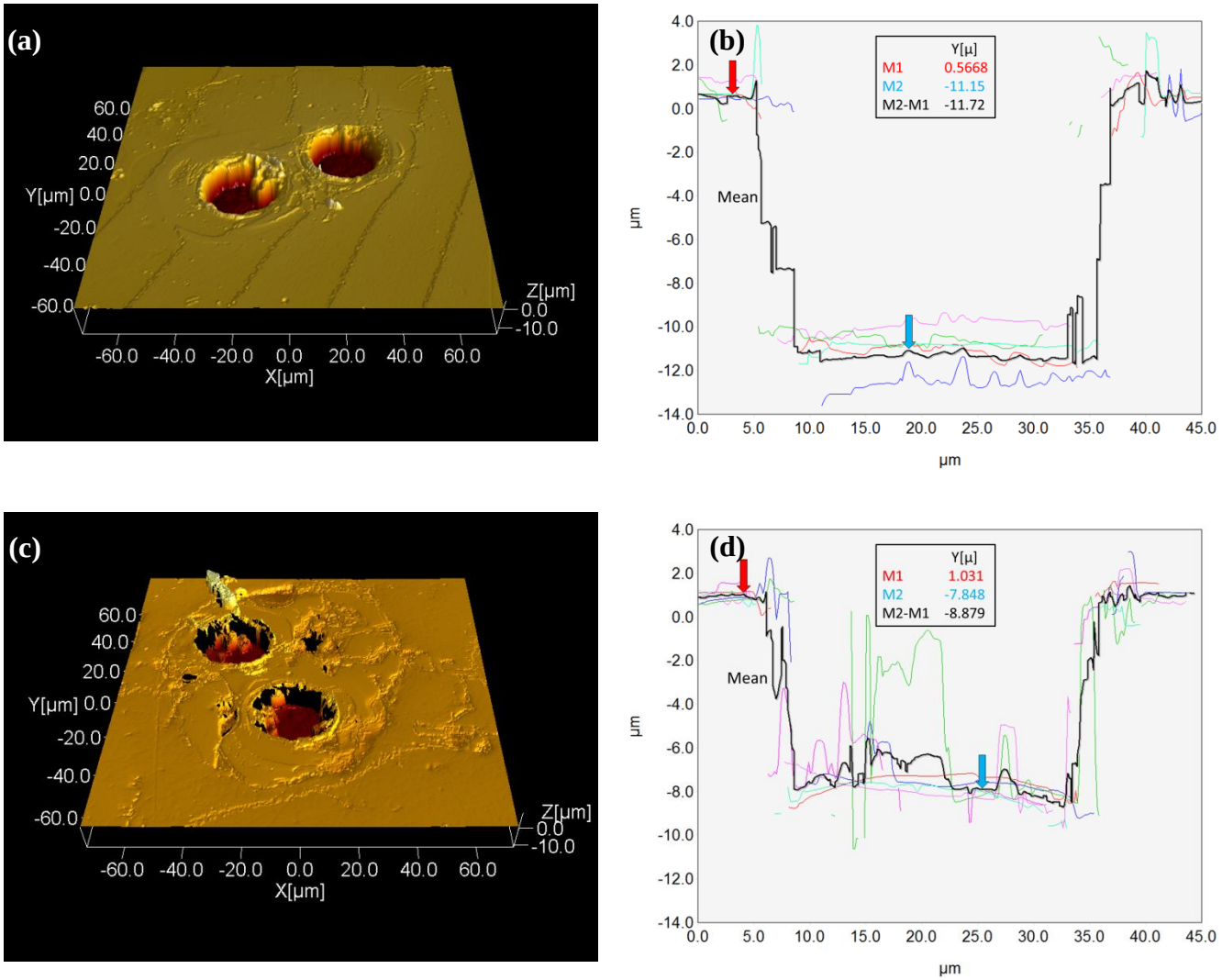
Natural variation in the U concentration of zircon, and hence the amount of accumulated radiation damage, has a direct influence on zircon ablation rates [35,36]. Generally, high U zircons (e.g. 3000 ppm U; Plešovice zircon reference material [28]) are expected to ablate at higher rates than those with lower U concentrations. Since down-hole fractionation in LA-ICP-MS increases with an increase in ablation pit depth, it is important to use a primary reference material that approximates the U concentration of unknowns. For the analyses conducted at TCD, both untreated and chemically abraded 91500 zircon reference material was used as a primary standard to correct for down-hole fractionation and instrument drift. Assessment of down-hole fractionation of $^{206}Pb/^{238}U$ for untreated and chemically abraded 91500 zircons reveals a distinct difference (Fig. 2), with a c. 3% higher fractionation factor calculated for untreated analyses. This demonstrates chemical abrasion of these zircons has affected their physical response to laser ablation. Visualization and measurement of pit depths on several zircons from sample TSUPB021 using optical interferometry reveals a difference in ablation profiles, despite identical ablation parameters being used for both sets of analyses (Fig. 3). In general, untreated zircons ablated in a more uniform manner (Fig. 3a and c). In terms of ablation depths, untreated zircons typically yielded c. 11 to 12 μm (n=5) pits, whereas chemically abraded zircons consistently yielded shallower pits of c. 8 to 9 μm (n=6). This equates to c. 70 nm and c. 50 nm ablation depths per laser shot for untreated and chemically abraded zircons respectively. The reasons for this disparity are unclear but may be due to elimination of the alpha-dose-induced crystal lattice damage in the annealed zircons, a factor which is considered to contribute to a so-called "matrix effect" in LA-ICP-MS analyses [35]. A smaller difference in the ablation rate of untreated and annealed zircon reference materials has previously been noted [36], but this may have become more extreme with the addition of a subsequent HF acid treatment step. At least some of this observed difference in ablation rates may result from less effective coupling of the excimer laser in the chemically abraded zircons due to small-scale etching and the creation of a 3-dimensional porous texture.

Figure 2. Comparison of down-hole fractions of the $^{206}Pb/^{238}U$ ratio in (**a**) untreated 91500 zircon and; (**b**) chemically abraded 91500 zircon reference materials.



This observation has important implications for the use of chemical abrasion in LA-ICP-MS analyses of zircon. A c. 25% discrepancy in ablation depths for identical analytical protocols is the likely primary cause of a c. 3% difference in down-hole $^{206}Pb/^{238}U$ fractionation between untreated and chemically abraded zircon, as calculated from analyses of the 91500 zircon reference material.

Figure 3. Ablation pit profiles from sample TSUPB021; (**a**) 3D view of untreated zircons; (**b**) cross-sectional view of untreated zircons; (**c**) 3D view of chemically abraded zircons; (**d**) cross-sectional view of chemically abraded zircons.



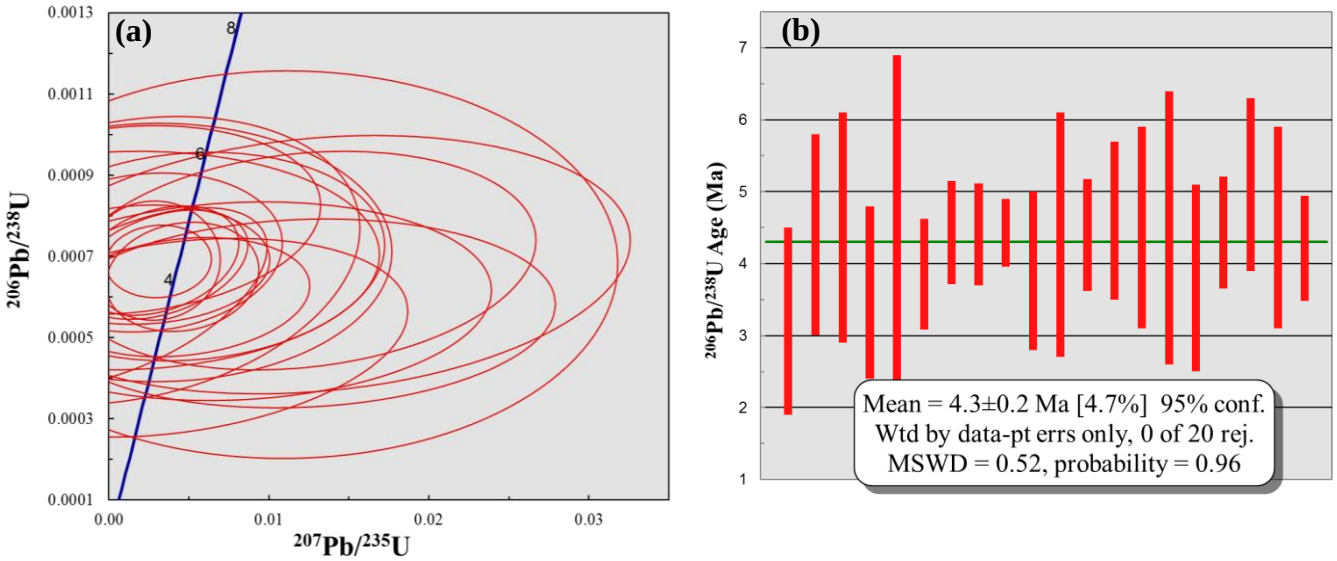
3.2. U-Th-Pb data

U-Th-Pb data for all samples are provided in the in the supplementary material. Errors and uncertainties are presented at a 2σ confidence level. Chemically abraded 91500 zircon was used as a primary reference material for chemically abraded secondary reference material and chemically abraded unknowns. All reported data are non-common Pb corrected.

3.2.1. Penglai Zircon Reference Material

Representative sub-samples of several large mm-size zircon fragments were chemically abraded and analysed by Q-ICP-MS at TCD. All analyses are concordant and define a mean $^{206}Pb/^{238}U$ age of 4.3 ± 0.2 Ma (Fig. 4), within error of the "preferred age" of 4.4 ± 0.1 Ma [29]. In order to be consistent with ablation protocols, a 30 µm spot diameter was used for all analyses in this study. The resultant error of our calculated mean $^{206}Pb/^{238}U$ age for Penglai zircons (4.7% 2σ, including decay constant uncertainties) could likely be reduced with a larger spot size. The concordant nature of our data is in contrast to all published U-Pb data for this reference material [29,30,34]. This serves to demonstrate that chemical abrasion has preferentially and effectively removed common Pb from these zircons and opens the possibility of using Penglai as a primary reference material for micro-beam U-Pb zircon geochronology, especially when analysing young (<10 Ma) material.

Figure 4. U-Pb data for chemically abraded Penglai zircon reference material (a) Concordia plot; (b) weighted mean $^{206}Pb/^{238}U$ age. Error ellipses and box heights are 2σ.



3.2.2. Sample TSUPB021

Both untreated (n=77) and chemically abraded (n=60) zircons from this sample were analysed by Q-ICP-MS at TCD. A significant proportion of untreated zircons (c. 30%) are discordant due to severe Pb-loss (Fig. 5a), which is quite typical of zircons from Archean rocks. This contrasts dramatically with chemically abraded zircons where only 3% of analyses are discordant and the remaining analyses plot close to the concordia curve (Fig. 5b). Although untreated zircons from this sample display a greater range of U concentration (c. 30 to 7300 ppm, but mostly within c. 30 to 1000 ppm) compared to those which were chemically abraded (c. 70 to 500 ppm) (Fig. 6a), importantly all age spectra present in the untreated sample are evident in the chemically abraded counterpart (Fig. 6b).

Figure 5. U-Pb concordia diagrams for sample TSUPB021; **(a)** non-treated zircons; **(b)** chemically abraded zircons. Data-point error ellipses are 2σ. Red ellipses signify analyses >10% discordant.

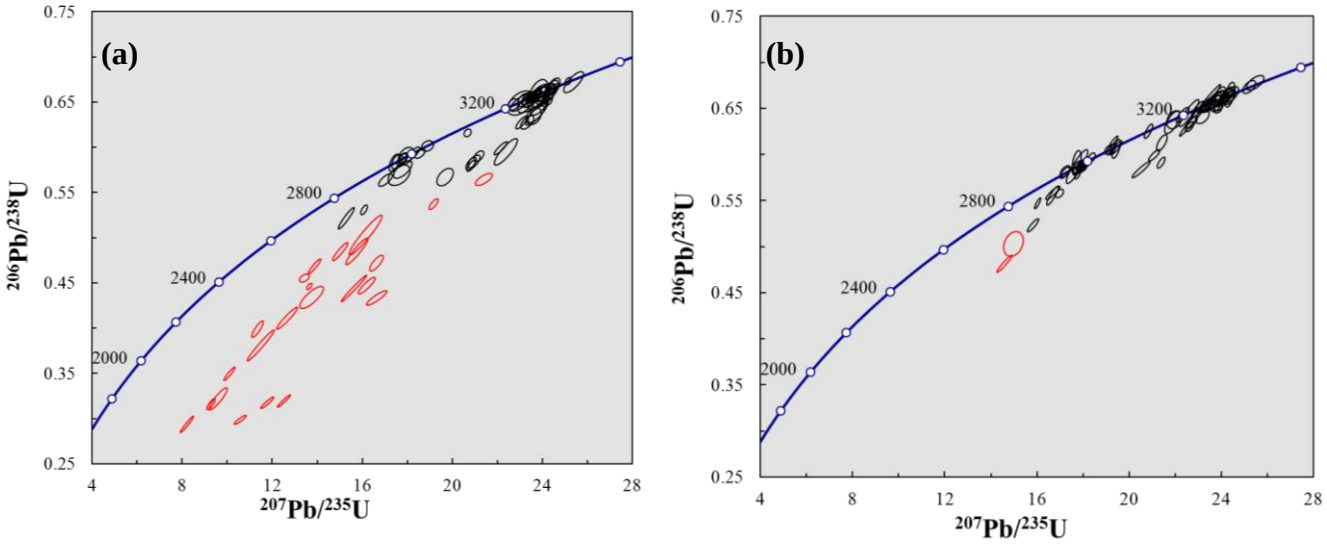
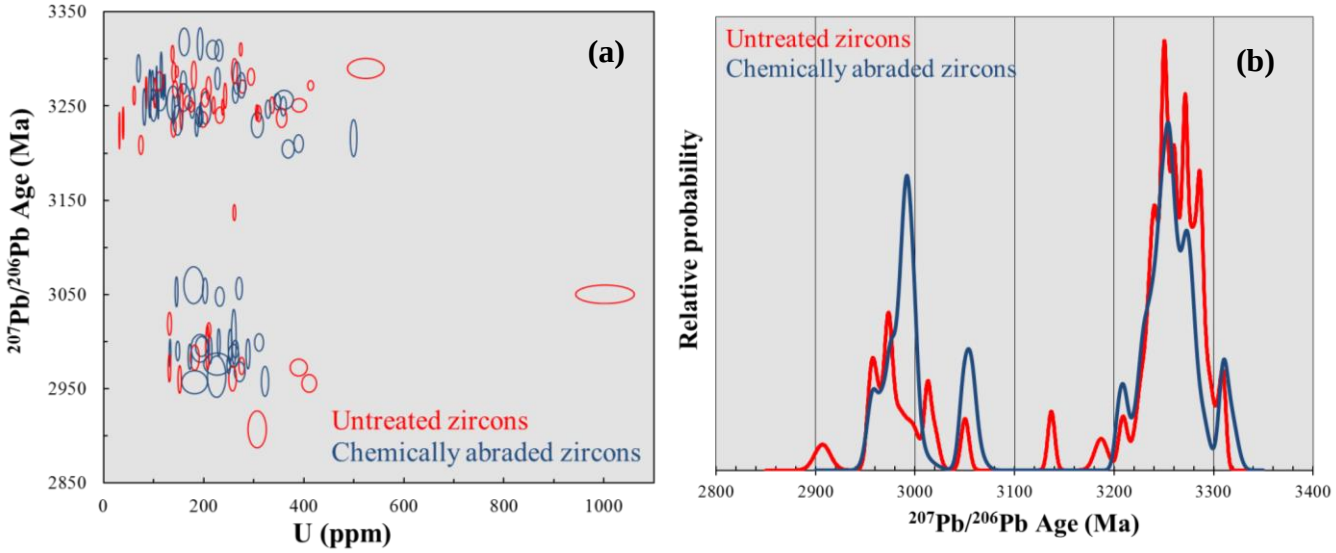


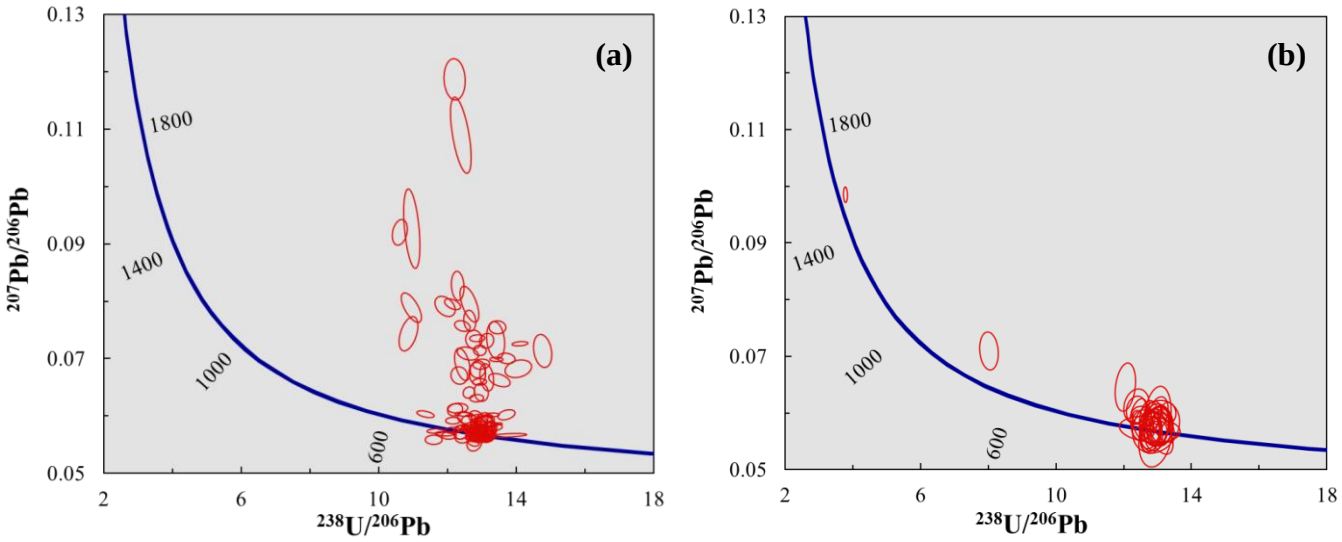
Figure 6. Chemical and age data for sample TSUPB021; **(a)** U ppm vs. $^{207}Pb/^{206}Pb$ age (Ma), note that analyses > c. 1100 ppm U have not been plotted but do not define any ages not already represented in the diagram, error ellipses are 2σ; **(b)** probability-age plot for both untreated and chemically abraded zircons for analyses <10% discordant.



3.2.3. Sample 10/225

Untreated zircons from sample 10/225 were analysed at the UCSB facility. U-Pb data show a concordant cluster at c. 480 Ma and a large number of discordant analyses with a high degree of scatter (Fig. 7a). This scatter and discordance most likely result from a combination of elevated common Pb, Pb-loss and possibly some degree of inheritance. Despite the large number of analyses (n=109) and the relatively high-precision nature of the U-Pb data, this scatter impedes a robust weighted mean age calculation. Analysis of chemically abraded zircons from the same sample (n=33) demonstrates a tight cluster of data overlapping with the concordia curve and four discordant analyses (Fig. 7b), with the latter likely reflecting a "mixed age" due to sampling of an inherited component and magmatic overgrowth. The "TuffZirc" algorithm [37] returns an age of 479.90 ± 1.2 Ma for the non-treated (n=46/109) and 479.65 + 5.25 / - 2.15 Ma for the chemically abraded (n=24/33) zircon populations respectively.

Figure 7. Tera-Wasserburg plots for sample 10/225, error ellipses are 2σ; **(a)** untreated zircons analysed at UCSB by LA-MC-ICP-MS; **(b)** chemically abraded zircons analysed by LA-Q-ICP-MS at TCD.



4. Conclusions

Chemical abrasion of zircon is an effective pre-treatment to minimize Pb-loss and elevated common Pb in zircon prior to LA-ICP-MS U-Pb analysis. All our chemically abraded U-Pb zircon data demonstrate a substantial improvement in concordance when compared with un-treated zircon analyses from the same samples. Reduced radiogenic Pb (^{206}Pb and ^{207}Pb) has a tendency to occupy sites affected by accumulated radiation damage and alteration, whereas common Pb may be incorporated into the zircon crystal lattice in small amounts, or present in micro-inclusions. Both reduced radiogenic Pb and common Pb are considered to exist in divalent form. Discordance is eliminated or minimized by removal of divalent Pb during exposure to HF acid at moderate temperatures (180^{o}C), while leaving the remainder of the zircon crystal lattice relatively unaffected. The extent to which zircon is visibly

affected by chemical abrasion, however seems to primarily depend on U concentration and the presence of physical defects such as fractures. Zircons that display some or all of these attributes are inherently more likely to have suffered Pb-loss, so there is an apparent correlation between the extent of Pb-loss and the physical effects of chemical abrasion. Although this physical effect on concordant zircons appears minimal, comparison of down-hole fractionation of $^{206}Pb/^{238}U$ in untreated and chemically abraded 91500 reference material reveals a c. 3% difference, with the untreated zircons displaying a greater degree of laser-induced fractionation effects. This disparity is likely depth dependant, as ablated pits in chemically abraded zircons known to have suffered Pb-loss are up to 25% shallower than ablation pits in untreated zircons from the same sample. Although this may be an extreme example, it does serves to illustrate that primary reference materials should be chemically abraded when analysing chemically abraded unknowns. It does not, however, eliminate the possibility that reference materials and unknowns will respond differently to the treatment, thereby resulting in differing down-hole fractionation of U-Pb and Th-Pb isotopes. Accurate measurement and comparison of ablation depths may help to minimize a mis-match between reference materials and sample down-hole fractionation corrections.

Analysis of zircons from an Archean sample (TSUPB021) demonstrates preferential dissolution of zircon at U concentrations greater than c. 1100 ppm, the majority of which are severely discordant as measured in untreated counterparts. In this particular case age spectra between untreated and chemically abraded zircons are identical, although it would in theory be possible to bias a sample by preferential dissolution of high-U zircons with a distinct age signature. Although higher U zircons (up to 1400 ppm) have been reported to have survived intact following chemical abrasion [22], these instances have been from considerably younger zircons. The chemical abrasion technique should therefore be used with caution when dealing with Archean zircons with elevated U concentrations.

In summary, although initially developed for TIMS U-Pb geochronology, chemical abrasion can easily and routinely be applied as a "pre-treatment" protocol to improve concordance for the majority of samples for LA-ICP-MS U-Pb geochronology.

Acknowledgments

Thanks to Tony Simonetti for his suggestion to write this research paper, to Andrew Kylander-Clark at UCSB for his help with analyses, to Cora McKenna for assistance with mass spectrometry at TCD and to reviewers xxx and yyy.

Author Contributions

QGC developed the experiment design, carried out the majority of sample analyses and drafted the paper. All co-authors contributed to the writing of this paper. KH collected sample TSUPB021, carried out rock crushing and mineral separation of samples TSUPB021 and 10/225, analysed sample TSUPB021, performed CL imaging and measurement of pit depth profiles. NR carried out analysis of the non-treated sample 10/225 at UCSB. BK supplied Penglai zircon reference material. DC supplied 91500 zircon reference material. BMcC assisted with collection of sample 10/225. KB assisted with collection of sample TSUPB021.

Conflicts of Interest

The authors declare no conflict of interest.

References and Notes

1. Kulp, J.L.; Bate, G.L.; Broecker, W.S. Present status of the lead method of age determination. *Am. J. Sci.* **1954**, *252*, 345-365.
2. Tilton, G.R.; Patterson, C.; Brown, H.; Inghram, M.; Hayden, R.; Hess, D.; Larsen, E. Isotopic composition and distribution of lead, uranium, and thorium in a Precambrian granite. *Geol. Soc. Am. Bull.* **1955**, *66*, 1131-1148.
3. Wetherill, G.W. Discordant uranium-lead ages: 2. Disordant ages resulting from diffusion of lead and uranium. *Journal of Geophysical Research* **1963**, *68*, 2957-2965.
4. Nier, A.O. Variations in the relative abundances of the isotopes of common lead from various sources. *Journal of the American Chemical Society* **1938**, *60*, 1571-1576.
5. Finch, R.J.; Hanchar, J.M. Structure and chemistry of zircon and zircon-group minerals. *Reviews in mineralogy and geochemistry* **2003**, *53*, 1-25.
6. Kogawa, M.; Watson, E.B.; Ewing, R.C.; Utsunomiya, S. Lead in zircon at the atomic scale. *American Mineralogist* **2012**, *97*, 1094-1102.
7. Cherniak, D.; Watson, E. Pb diffusion in zircon. *Chemical Geology* **2001**, *172*, 5-24.
8. Lee, J.K.; Williams, I.S.; Ellis, D.J. Pb, U and Th diffusion in natural zircon. *Nature* **1997**, *390*, 159-162.
9. Nasdala, L.; Hanchar, J.M.; Kronz, A.; Whitehouse, M.J. Long-term stability of alpha particle damage in natural zircon. *Chemical Geology* **2005**, *220*, 83-103.
10. Tanaka, K.; Takahashi, Y.; Horie, K.; Shimizu, H.; Murakami, T. Determination of the oxidation state of radiogenic Pb in natural zircon using x-ray absorption near-edge structure. *Physics and Chemistry of Minerals* **2010**, *37*, 249-254.
11. Xu, X.-S.; Zhang, M.; Zhu, K.-Y.; Chen, X.-M.; He, Z.-Y. Reverse age zonation of zircon formed by metamictisation and hydrothermal fluid leaching. *Lithos* **2012**, *150*, 256-267.
12. Kramers, J.; Frei, R.; Newville, M.; Kober, B.; Villa, I. On the valency state of radiogenic lead in zircon and its consequences. *Chemical Geology* **2009**, *261*, 4-11.
13. MacDonald, J.M.; Wheeler, J.; Harley, S.L.; Mariani, E.; Goodenough, K.M.; Crowley, Q.; Tatham, D. Lattice distortion in a zircon population and its effects on trace element mobility and U-Th-Pb isotope systematics: Examples from the Lewisian Gneiss Complex, northwest Scotland. *Contributions to Mineralogy and Petrology* **2013**, *166*, 21-41.
14. Krogh, T. Improved accuracy of U-Pb zircon ages by the creation of more concordant systems using an air abrasion technique. *Geochimica et Cosmochimica Acta* **1982**, *46*, 637-649.
15. Mattinson, J.M. Zircon U–Pb chemical abrasion ("CA-TIMS") method: Combined annealing and multi-step partial dissolution analysis for improved precision and accuracy of zircon ages. *Chemical Geology* **2005**, *220*, 47-66.
16. Krogh, T.; Davis, G. Alteration in zircons with discordant U-Pb ages. *Carnegie Inst. Washington Yearb* **1974**, *73*, 560-567.
17. Krogh, T.; Davis, G. Alteration in zircons and differential dissolution of altered and metamict zircon. *Carnegie Inst Washington Yearb* **1975**, *74*, 619-623.
18. Mattinson, J.M. A study of complex discordance in zircons using step-wise dissolution techniques. *Contributions to Mineralogy and Petrology* **1994**, *116*, 117-129.
19. McClelland, W.C.; Mattinson, J.M. Resolving high precision U-Pb ages from tertiary plutons with complex zircon systematics. *Geochimica et Cosmochimica Acta* **1996**, *60*, 3955-3965.
20. Todt, W.A.; Büsch, W. U-Pb investigations on zircons from pre-variscan gneisses—i. A study from the schwarzwald, west germany. *Geochimica et Cosmochimica acta* **1981**, *45*, 1789-1801.

21. Crowley, Q.; Key, R.; Noble, S. High-precision U–Pb dating of complex zircon from the lewisian gneiss complex of scotland using an incremental ca-id-tims approach. *Gondwana Research* **2014**.
22. Kryza, R.; Crowley, Q.G.; Larionov, A.; Pin, C.; Oberc-Dziedzic, T.; Mochnacka, K. Chemical abrasion applied to SHRIMP zircon geochronology: An example from the Variscan Karkonosze Granite (Sudetes, SW Poland). *Gondwana Research* **2012**, *21*, 757-767.
23. McConnell, B.; Riggs, N.; Crowley, Q.G. Detrital zircon provenance and Ordovician terrane amalgamation, western Ireland. *Journal of the Geological Society* **2009**, *166*, 473-484.
24. Riggs, N.R.; Barth, A.P.; González-León, C.M.; Jacobson, C.E.; Wooden, J.L.; Howell, E.R.; Walker, J.D. Provenance of upper Triassic strata in southwestern North America as suggested by isotopic analysis and chemistry of zircon crystals. *Mineralogical and Geochemical Approaches to Provenance: Geological Society of America Special Paper 487* **2012**, 13-36.
25. Riggs, N.; Reynolds, S.; Lindner, P.; Howell, E.; Barth, A.; Parker, W.; Walker, J. The early Mesozoic cordilleran arc and late Triassic paleotopography: The detrital record in upper Triassic sedimentary successions on and off the Colorado Plateau. *Geosphere* **2013**, *9*, 602-613.
26. Kylander-Clark, A.R.; Hacker, B.R.; Cottle, J.M. Laser-ablation split-stream ICP petrochronology. *Chemical Geology* **2013**, *345*, 99-112.
27. Wiedenbeck, M.; Alle, P.; Corfu, F.; Griffin, W.; Meier, M.; Oberli, F.; Quadt, A.v.; Roddick, J.; Spiegel, W. Three natural zircon standards for U-Th-Pb, Lu-Hf, trace element and REE analyses. *Geostandards newsletter* **1995**, *19*, 1-23.
28. Sláma, J.; Košler, J.; Condon, D.J.; Crowley, J.L.; Gerdes, A.; Hanchar, J.M.; Horstwood, M.S.; Morris, G.A.; Nasdala, L.; Norberg, N. Plešovice zircon—a new natural reference material for U–Pb and Hf isotopic microanalysis. *Chemical Geology* **2008**, *249*, 1-35.
29. Li, X.H.; Long, W.G.; Li, Q.L.; Liu, Y.; Zheng, Y.F.; Yang, Y.H.; Chamberlain, K.R.; Wan, D.F.; Guo, C.H.; Wang, X.C. Penglai zircon megacrysts: A potential new working reference material for microbeam determination of Hf–O isotopes and U–Pb age. *Geostandards and Geoanalytical Research* **2010**, *34*, 117-134.
30. Chew, D.; Petrus, J.; Kamber, B. U–Pb LA–ICPMS dating using accessory mineral standards with variable common Pb. *Chemical Geology* **2014**, *363*, 185-199.
31. Hellstrom, J.; Paton, C.; Woodhead, J.; Hergt, J. Iolite: Software for spatially resolved LA-(QUAD and MC) ICPMS analysis. *Mineralogical Association of Canada short course series* **2008**, *40*, 343-348.
32. Woodhead, J.; Hellstrom, J.; Paton, C.; Hergt, J.; Greig, A.; Maas, R. A guide to depth profiling and imaging applications of LA–ICP–MS. *Laser ablation ICP–MS in the Earth sciences: Current practices and outstanding issues. Mineralogical Association of Canada, Short Course Series* **2008**, 135-145.
33. Paton, C.; Hellstrom, J.; Paul, B.; Woodhead, J.; Hergt, J. Iolite: Freeware for the visualisation and processing of mass spectrometric data. *Journal of Analytical Atomic Spectrometry* **2011**, *26*, 2508-2518.
34. Petrus, J.A.; Kamber, B.S. Vizualage: A novel approach to laser ablation icp-ms u-pb geochronology data reduction. *Geostandards and Geoanalytical Research* **2012**, *36*, 247-270.
35. Allen, C.M.; Campbell, I.H. Identification and elimination of a matrix-induced systematic error in LA–ICP–MS $^{206}Pb/^{238}U$ dating of zircon. *Chemical Geology* **2012**, *332*, 157-165.
36. Marillo-Sialer, E.; Woodhead, J.; Hergt, J.; Greig, A.; Guillong, M.; Gleadow, A.; Evans, N.; Paton, C. The zircon 'matrix effect': Evidence for an ablation rate control on the accuracy of U–Pb age determinations by LA-ICP-MS. *Journal of Analytical Atomic Spectrometry* **2014**.
37. Ludwig, K.; Mundil, R. Extracting reliable U-Pb ages and errors from complex populations of zircons from phanerozoic tuffs. *Geochimica et Cosmochimica Acta* **2002**, A463-A463.

© 2014 by the authors; licensee MDPI, Basel, Switzerland. This article is an open access article distributed under the terms and conditions of the Creative Commons Attribution license (http://creativecommons.org/licenses/by/3.0/).